PB81-204364

THE SIMULATION OF EARTHQUAKE-LIKE GROUND MOTIONS WITH HIGH EXPLOSIVES

by

Cornelius J. Higgins
Roy L. Johnson
and
George E. Triandafilidis

REPORT DOCUMENTATION PAGE	NSF/RA-780752	PB81 204364

4. Title and Subtitle
Simulation of Earthquake-Like Ground Motions with High Explosives, Final Report

5. Report Date
July 1978

6.

7. Author(s)
C. J. Higgins, R. L. Johnson, G. E. Triandafilidis

8. Performing Organization Rept. No.
CE-45(78)NSF-507-1

9. Performing Organization Name and Address
University of New Mexico
Department of Civil Engineering
Albuquerque, NM 87131

10. Project/Task/Work Unit No.

11. Contract(C) or Grant(G) No.
(C)
(G) ENG7521580

12. Sponsoring Organization Name and Address
Office of Planning and Resources Management (OPRM)
National Science Foundation
1800 G Street, N.W.
Washington, D.C. 20550

13. Type of Report & Period Covered
Final

14.

15. Supplementary Notes

16. Abstract (Limit: 200 words)

Assessment of the technical and economic feasibility of using high explosive detonations to simulate the effects of earthquakes on engineering structures is reported. The investigation comprised eight tasks: (1) identification of potential simulation methods; (2) development of simulation criteria; (3) analysis of existing ground motion; (4) development of a numerical calculation approach involving over 30 one- and two-dimensional calculations to expand the data base by providing insight into explosive ground motion phenomena and revealing relationships between governing parameters; (5) numerical calculations to enhance ground motions from explosive sources; (6) synthesis of data and calculation results into predictive relations; (7) application of explosives to simulate an earthquake-like environment to a specific structure; and (8) presentation of the economic feasibility of using explosives to simulate earthquake-like systems. Results indicate that explosive simulation of earthquake-like ground motions on engineering systems is technically feasible.

17. Document Analysis a. Descriptors

Earthquakes
Explosive charges
Detonators
Buildings
Simulation
Earth movements
Structures
Dynamic structural analysis

b. Identifiers/Open-Ended Terms

c. COSATI Field/Group

18. Availability Statement	19. Security Class (This Report)	21. No. of Pages
NTIS	20. Security Class (This Page)	22. Price

THE SIMULATION OF EARTHQUAKE-LIKE GROUND MOTIONS WITH HIGH EXPLOSIVES

by

Cornelius J. Higgins
Roy L. Johnson
and
George E. Triandafilidis

Final Report No. CE-45(78)NSF-507-1

The University of New Mexico
Department of Civil Engineering
and
Bureau of Engineering Research
Albuquerque, New Mexico 87131

Work Performed under
Contract No. NSF ENG 75-21580

July 1978

ACKNOWLEDGEMENTS

The authors wish to acknowledge Mr. David K. Rudeen, who performed all of the two-dimensional calculations and analyzed the two-dimensional experiment results. Mr. Frank B. Guros performed the calculations concerned with material property scaling in elastic materials and analyzed the results. He and Mr. Duane Labreche aided in reducing the calculational data.

This work was supported by National Science Foundation Grant ENV75-21580.

ABSTRACT

Experimental data are needed to verify or improve earthquake-resistant design techniques. Such data must come from actual or simulated earthquakes. Simulations are needed because data from actual earthquakes are limited and will continue to be limited because of uncertainties with regard to time and place of occurrence.

An investigation was made of the technical and econimic feasibility of simulating earthquake-like ground motions with high explosives. This form of simulation appears most applicable to evaluations of soil-structure interaction where structure response is coupled with the response of the medium through which the ground motion waves propagate.

Eight tasks were undertaken in the investigation. The first task identified potential simulation methods. Second, an approach was developed for simulation criteria. Existing ground motion data were analyzed as a third task. Because the data base was not sufficient for a high confidence assessment of feasibility, a numerical calculation approach was developed to expand the data base in the fourth task. Over 30, one-dimensional and two-dimensional calculations were performed to provide insigut into explosive ground motion phenomena and to reveal relationships between the governing parameters. As a fifth task, numerical calculations aimed at enhancing ground motions from explosive sources were performed. The data and calculation results were synthesized into prediction relations in the sixth task. The application of explosive to simulate on earquake-like environment to a specific structure was studied in the seventh task. Finally, the economic feasibility using explosive to simulate earthquake-like systems was presented in task eight.

The investigation concludes that explosive simulation of earthquake-like ground motions on engineering systems is technically feasible. Explosives in various arrays can produce motion amplitudes and frequency content which are in the range of those expected in large earthquakes. Further, the wave structure from planar explosive arrays contains significant shear wave contributions to the horizontal motion. This is similar to what is thought to occur in actual earthquakes. Multiple cycles of motion and long time durations can be obtained from multiple, sequenced explosions. Explosive ground motions in dry alluvial materials can be predicted with reasonable confidence using methods developed in the investigation.

TABLE OF CONTENTS

TABLE OF CONTENTS (Continued)

TABLE OF CONTENTS (Continued)

TABLE OF CONTENTS (Continued)

LIST OF FIGURES

LIST OF FIGURES (Continued)

LIST OF FIGURES (Continued)

LIST OF FIGURES (Continued)

LIST OF FIGURES (Continued)

LIST OF FIGURES (Continued)

LIST OF FIGURES (Continued)

LIST OF FIGURES (Continued)

LIST OF FIGURES (Continued)

LIST OF FIGURES (Continued)

LIST OF FIGURES (Continued)

LIST OF TABLES

LIST OF TABLES (Continued)

LIST OF TABLES (Continued)

SECTION I
INTRODUCTION

1. BACKGROUND

The design of engineering structures to resist the effects of earthquakes is one of the most significant problems facing the United States and world technical communities. The potential loss of property and life in the United States from large size earthquakes is astounding. The moderate San Fernando Earthquake of 1971 resulted in 64 deaths and monetary losses approaching a billion dollars (ref. I-1). Had the earthquake occurred nearer to a more densely populated area or been of larger size, the resulting loss would have been unestimable.

Analytical methods are now and must remain the prime basis for the design of engineering structures subjected to the effects of earthquakes. It is practically and economically impossible to test every structure under every potentially damaging environment. However, experimental data are needed to verify current design techniques and/or to provide the basis for new or improved techniques, fully analytical or semi-empirical. Such data must come from actual or simulated earthquakes.

Response measurements and post-event observations of actual earthquakes are a significant source of data on the behavior of prototype structures and such data have demonstrated serious deficiencies in our understanding of phenomena and associated design procedures (refs. I-2

and I-3). However, the available data from actual earthquakes are severely limited and will continue to be limited by uncertainties with regard to time and place of earthquake occurrence and by the limited amount of in-place instrumentation to record response. A more complete and adequate data base must, therefore, come from simulations.

Simulation sources include field shaking machines, shake tables and explosions, either nuclear or high explosive. Field shaking machines are limited by low levels of input energy and, as a result, low vibration levels are induced within limited regions. Shake tables are very useful because they are able to reproduce ground shaking from past or projected earthquakes with a high degree of precision. The largest shake table in the United States, located at the Richmond Field Station of the University of California, is 20 feet by 20 feet (ref. I-4). A shake table of 100 feet by 100 feet has been proposed (ref. I-5) but is of extremely high cost. The major limitations of shake tables are size (similitude is required to extrapolate the prototype size structures), some limitation on maximum displacement, and almost a complete inability to simulate effects on soil and soil-structure systems. This last limitation is very serious. Being composed of or surrounded to a large extent by the medium through which the earthquake waves propagate, the response of such systems cannot be adequately evaluated independently of the medium. Actually, the use of a shake table for any system is somewhat in error because it enforces a condition of minimum interaction between the model and the source of shaking. The behavior of underground conduits, subways, mines, earthdams, retaining structures and nuclear power structures are only a few of the numerous important problems which are not

satisfactorily resolved by current understanding and testing techniques and which cannot be evaluated with shake tables.

For soil and soil-structure systems, potential earthquake simulation sources which have not seen any significant use are explosions, both nuclear and high explosive. Although high energy explosions cannot reproduce all of the motion characteristics of strong earthquakes, knowledge of explosion-phenomena has reached a level where, with additional research, explosions may be used in combination with enhancement techniques to simulate motions closely resembling earthquakes. The evaluation and development of explosive sources for planned scientific simulation experiments is the only viable alternative to waiting for major earthquakes to identify deficiencies in current understanding and design procedures. It is not clear that the latter alternative is either economically or morally justified.

The Russians have been considering earthquake simulation with explosions for some time (ref. I-6) and the need in the United States is strongly emphasized by the conclusions of a recent National Academy of Engineering Workshop on the Simulation of Earthquake Effects on Structures (ref. I-7). The Panels on Building Structures and Special Structures recommended study and development of explosive methods and the Panel on Soils, Rocks and Foundations, in particular, recommended the establishment of a national test site where ground shaking is created by explosives. The steering committee of the workshop concluded that "a much more detailed study of its (explosive simulation) technical and economic feasibility is required."

Although nuclear explosions provide a significant potential simula-

tion source, high explosives are preferable because they offer less environmental hazards, more safety, smaller cost, and greater flexibility in charge size and configuration. In addition, high explosive events can be fielded in a wide range of geologies while nuclear events in the continental United States are restricted to the Nevada test site. Accordingly, this report addresses the topic of high explosive simulation techniques.

2. RESEARCH OBJECTIVES AND METHODOLOGY

The major objective of this research was the assessment of the technical feasibility of using high explosive detonations to simulate the effects of earthquakes on engineering structures. Achievement of the objective required the accomplishment of seven major tasks:

a. Development of an approach for the establishment of simulation criteria.

b. Identification of potential simulation methods in relation to existing applicable ground motion data.

c. Analysis of existing data and identification of data base deficiencies.

d. Development and application of a numerical calculation approach to expand the experimental data base.

e. Synthesis of experimental data and calculation results into general relations for analyzing, scaling and predicting ground motions from various explosive simulation arrays.

f. Illustration of the application of the prediction relations in combination with simulation criteria for the design of a simulation experiment.

g. Cost feasibility of using high explosives to simulate an earthquake environment.

The first task was considered a very important one because no technique, explosive or otherwise, is capable of simulating every aspect of an earthquake. Accordingly, it is necessary to establish some basis for determining those characteristics of an earthquake which must be simulated for a credible test on a particular structure. Since specific criteria for simulation will vary from structure to structure, the development of an approach for the establishment of criteria was emphasized in this research.

The second and third tasks deal with the existing high explosive experimental data base. Although the objectives of the experiments which led to the data differed from those of interest in this research, there exists sufficient data for identification of potential simulation methods and a partial assessment of the technical feasibility of simulation with high explosives.

A high confidence assessment requires that detailed insight be obtained into data trends and that the data be extrapolated to motion regimes and time durations for which data does not exist. The fourth task was designed to provide the basis for this extrapolation. A numerical calculation procedure, using finite continuum mechanics codes, was developed and applied. The calculations, viewed as numerical experiments, can provide insight into important explosive ground motion phenomena and quantitative relationships between governing parameters which were not immediately evident by the experimental data alone.

The synthesis of the data and calculation results was accomplished in the fifth task. The synthesis led to general relations which can be used for the design of simulation experiments. Application of these re-

lationships, in combination with simulation criteria for an example structure, to demonstrate the technical feasibility for one class of structures performed as the sixth major task.

Finally a cost feasibility study was conducted to illustrate the economic feasibility of utilizing high explosive techniques to simulate earthquake-like ground motions.

3. APPROACH

The report is divided into sections basically following the tasks mentioned above. Section II summarizes previous work applicable to explosive simulation including the ground motions resulting from high explosives and the use of high explosives as a ground motion source for evaluating general structural response. Section III describes the importance of simulation criteria and provides an approach to criteria development. Prototype earthquake ground motion characteristics are summarized and methods for evaluating those aspects of a prototype earthquake which are important for a particular engineering system are presented.

Section IV describes high explosive configurations and enhancements with potential for simulating earthquake effects. Existing data from spherical, cylindrical and planar charges, and the effect of various enhancement techniques are presented and analyzed. Data deficiencies are identified. Section V describes for single shots the numerical calculation approach for expanding the experimental data base. Calculation results are presented and analyzed. Section VI deals with numerical calculations pertaining to ground motion enhancement techniques. The calculation results and experimental data including enhancement techniques are synthesized in Section VII. Empirical and semi-empirical

relationships are developed which relate configuration, charge size, array dimensions, range and other important parameters to ground motion amplitude and duration characteristics.

The ground motion prediction relations are discussed in relation to a potential application for a structural problem in Section VIII. Simulation criteria for the structure are developed and the design of a suitable simulation experiment is presented. This application demonstrates the technical feasibility of high explosive simulation of earthquake ground motion effects for at least the structure described therein. Section IX presents a cost feasibility study in using high explosives to simulate earthquake-like ground motions, and finally Section X summarizes the conclusions of the research, lists remaining uncertainties and presents recommendations for future research.

Supporting information is provided in Appendices. Explosive equivalency information, which was evaluated to enable reduction of ground motion data from different types of explosives to a common base, is presented in Appendix A. Appendices B and C contain methods for predicting and minimizing the extranneous explosive environments (in the sense that they do not occur in earthquakes) of cratering and debris, and airblast, respectively. Detailed output from typical calculations is presented in Appendix D.

4. REFERENCES

I-1 The San Fernando Earthquake of February 9, 1971, National Academy of Sciences, National Academy of Engineering, Washington, D.C., 1971.

I-2 Housner, G.W., "Earthquake Environment Simulation: An Overview," Earthquake Environment Simulation, Final Report and Proceedings of a Workshop on Simulation of Earthquake Effects on Structures, National Academy of Engineering, Washington, D.C., 1974.

I-3 Ambraseys, N.N., "Dynamics and Response of Foundation Materials in Epicentral Regions of Strong Earthquakes," Proc. 5th World Conference on Earthquake Engineering, Rome, 1973.

I-4 Rea, D. and Penzien, J., "Dynamic Response of a 20 ft. x 20 ft. Shaking Table," Proc. 5th World Conference on Earthquake Engineering, Rome, 1973.

I-5 Penzien, J., Bouwkamp, J.G., Clough, R.W. and Rea, D., Feasibility Study, Large-Scale Earthquake Simulator Facility, EERC-67-1, Earthquake Engineering Research Center, University of California, Berkeley, California, September 1967.

I-6 Zarubin, U., Institute of Mechanics and Seismic Stability, Sotsialistecheskaya, Industriyz, No. 90, p. 4, April 16, 1972, (Foriegn Technology Division, Air Force Systems Command, Wright-Patterson AFB, Ohio,Translation).

I-7 Earthquake Environment Simulation, Final Report and Proceedings, Workshop on Simulation of Earthquake Effects on Structures, National Academy of Engineering, Washington, D.C., 1974.

SECTION II

PREVIOUS WORK ON HIGH EXPLOSIVES AND THEIR USE IN SIMULATING EARTHQUAKE-LIKE GROUND MOTIONS

1. INTRODUCTION

No previous studies of the direct application of high explosives for simulating specific earthquake effects on engineering structures are known to exist. However, data and information which provide a partial basis for evaluating the technical feasibility of simulating earthquake ground motion effects exist in two areas:

- Ground Motion Effects from High Explosives
- High Explosives Used as Vibration Sources

Significant work in these areas is summarized in the following.

2. GROUND MOTION EFFECTS FROM HIGH EXPLOSIVES

Single or multiple explosive charges detonated in various arrays and firing sequences and in combination with various enhancement techniques will be used in the simulation approach. Large amounts of data on single point charges and lesser amounts on cylindrical, arrayed, and enhanced charges are available in the literature. The major sources of data and conclusions with regard to effects are summarized in the following paragraphs. Major emphasis is placed on deeply buried charges, since earthquake simulation applications will require maximum coupling and minimization of energy converted into airblast. Specific applicable data are presented and analyzed in detail in Section IV.

a. National Defense Research Committee Tests

The earliest systematic evaluation in the United States of the ground motions created by high explosive detonations was performed in the period 1941 through 1945. The results of the evaluations are summarized by Lampson (ref. II-1), including empirical and semi-empirical relations between ground shock parameters and charge size, explosive type, range, material properties, and depth of burst.

The relation for soil pressure is

$$P = FEk\,(R/W^{\frac{1}{3}})^{-n} \qquad \text{(II-1)}$$

where

P = peak pressure in lb/in^2

R = distance in feet

W = weight of explosive in pounds

k = a soil characteristic in lb/in^2

F = a coupling coefficient determined by depth of burial

E = an energy factor determined by type of explosive

n = an exponent whose value is determined by the depth of burial or the depth of the measurement gage.

The exponent n was found to be 3 for depths of burial deeper than $3/2W^{\frac{1}{3}}$ feet, and 4 for shallower depths. Explosive factors (E) are given in table II-1, and the energy coupling factor (F) as a function of depth of burst is given in figure II-1. It can be seen in figure II-1 that maximum coupling is achieved at a depth of burst of about $2.1W^{\frac{1}{3}}$ feet. The soil characteristics (k) for various sites are given in table II-2. A correlation between k and soil density and seismic velocity, accurate to

Table II-1

Explosive Factors for Pressure (ref. II-1)

Explosive	Explosive factor E
TNT	1.00
Amatol	1.04
Comp. B	1.04
Tritonal	1.17
Minol 2	1.34
HBX 2	1.39

Table II-2

Soil Constants for Pressure as Function of Soil Type and Location (ref. II-1)

Soil type	Location	k(min)	k(max)	k(avg)
Loess	Natchez, Miss	400	1,700	800
Clay silt (loam)	Princeton, N.J.	1,300	2,500	2,000
Silty clay	Camp Gruber, Okla.	1,300	9,000	5,100
Clay, unsaturated	Houston, Tex.	10,000	20,000	15,000
Clay, saturated	Houston, Tex.	50,000	150,000	100,000

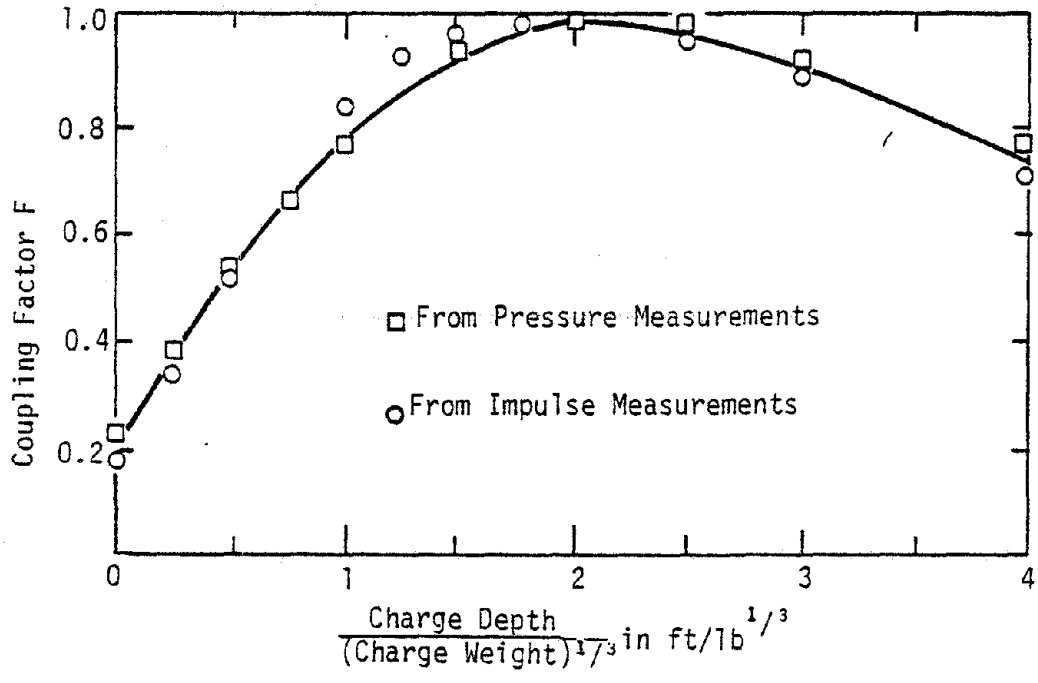

Figure II-1. Explosive Coupling Factor as Function of Charge Depth in Clay Silt (ref. II-1)

within ± 25 percent, was found to be

$$k = 1/25\ \rho c^2 \qquad \text{(II-2)}$$

where

ρ = soil mass density

c = seismic velocity

The impulse due to the compressive phase of the pressure pulse was found (ref. II-1) to be

$$I = E'Fk'W^{\frac{1}{3}}(R/W^{\frac{1}{3}})^{-\frac{5}{2}} \qquad \text{(II-3)}$$

where

I = impulse per unit area in lb-sec/in^2

E' = an explosive factor for impulse

k' = a impulse soil constant in lb-sec/in^3

and the other parameters are as defined previously. The explosive factor (E') and soil constant (k') differ from those for pressure and are given in tables II-3 and II-4, respectively. The soil constant is related to the mass density and seismic velocity by

$$k' = 1.15\rho c = 5.5\rho^{\frac{1}{2}}k^{\frac{1}{2}} \qquad \text{(II-4)}$$

although the correlation is not as good as for k.

The correlation for acceleration due to TNT at the depth of maximum coupling ($2.1W^{\frac{1}{3}}$ feet) is

$$a = \frac{k}{\rho W^{\frac{1}{3}}}\left(120(R/W^{\frac{1}{3}})^{-4} + 0.3(R/W^{\frac{1}{3}})^{-2} + 0.04(R/W^{\frac{1}{3}})^{-1}\right) \times 10^{-5} \qquad \text{(II-5)}$$

Table II-3

Explosive Factors For Impulse (ref. II-1)

Explosive	Explosive factor E'
TNT	1.00
Amatol	1.04
Comp. B	0.97
Tritonal	1.27
Minol 2	1.38
HBX 2	1.50

Table II-4

Soil Constants For Impulse For Various Soils (ref. II-1)

Soil	Location	k' (avg)
Loess	Natchez, Miss.	1.60
Clay silt (loam)	Princeton, N.J.	4.77
Silty clay	Camp Gruber, Okla.	5.44
Clay	Houston, Tex.	6.64

where a = horizontal or vertical acceleration in g's (i.e. relative to the acceleration due to gravity).

Relations of less confidence are given for particle velocity and dislacement from TNT at the depth of maximum coupling ($2.1W^{\frac{1}{3}}$ feet). The relation for velocity is

$$v = \frac{Bk^{\frac{1}{2}}}{\rho^{\frac{1}{2}}} (R/W^{\frac{1}{3}})^{-3.5} \qquad \text{(II-6)}$$

where

v = particle velocity in in/sec

B = a numerical constant which depends on the stress strain curve (0.7 for a silty clay described in reference II-1)

The relation for displacement is

$$d = \frac{1}{8} W^{\frac{1}{3}} k^{\frac{1}{3}} (R/W^{\frac{1}{3}})^{-3} \qquad \text{(II-7)}$$

where d = displacement in inches

Reference II-1 notes that, in the absence of other data, the relations for acceleration and velocity can be applied to other explosive types and depths of burst using the factors E and F for pressure. No recommendation is made for displacement.

Reference II-1 presents a few examples of the data from which the relations II-1 through II-7 were derived, but the amount of data and information about the specific experiments from which the data were obtained are not sufficient to allow detailed analysis in this program. However, the relations are compared with other more recent data in Section IV.

b. Underground Explosion Test Program (UET)

The Underground Explosion Test Program was undertaken in 1951 to study the generation and propagation of explosive produced waves from underground detonations, and their effects on structures. Tests were conducted in three soils and three rocks, and involved charges ranging from 8 lbs to 320,000 lbs of TNT. The soil results (ref. II-2) are of most interest to earthquake simulation and are discussed herein.

The three soils involved were roughly categorized as dry clay, dry sand, and wet clay, although the sites were relatively nonuniform in nature. The dry clay site consisted of a deep bed of lake sediments containing thin sand lenses and, below 20 ft, sand beds 1 to 10 ft thick. A white marl layer of varying thickness was also present. Significant nonuniformity was introduced by two major joint sets, one north-south and one east-west, with joints as wide as 2 inches filled with loose clay. Reference II-2 states that these joints had a significant effect on results. Seismic surveys at the site indicated seismic velocities of 1000 ft/sec at 3.7 ft, 6150 ft/sec at 93 ft, and 5400 ft/sec at 138 ft. The water table was below 138 ft, but capillary saturation extended in two drill holes to 136 feet.

The dry sand site was in a dune area having very irregular topography (20 ft from troughs to ridges common over short distances). The depth of sand was greater than 100 ft, but there were lenses of clay and thin beds of white marl near the surface. Some gravel and gravel lenses were present in the lower sand. The water table was below 170 ft, but the material was damp a few inches below the surface. Seismic velocities

were 800 to 1000 ft/sec in the dune sands, 1500 to 2000 ft/sec in the moist sands (the bulk of the sand layer), and 8000 to 9000 ft/sec at 100 ft. Because of the topographic irregularity, the shot sites were leveled and in some cases filled. Also, most areas had been backfilled previously in 1948. Reference II-2 notes that variations in density and moisture content occurred and the site properties were significantly altered by excavation and backfilling.

The wet clay site was flat and consisted of wet clay to 62 feet, below which interbedded clays and sands were present. The clay exhibited thin layering in color, but was physically homogeneous. There were some joints, mostly in the north-south direction, but they were not as wide as at the dry site. Seismic velocities were measured as 2800 ft/sec to 3.5 ft (thought to be the water table depth) and 5600 ft/sec below.

The characteristics of the test detonations are summarized in table II-5. Measurements consisted of pressure, horizontal accelerations, some vertical accelerations and permanent surface displacements. The bulk of the data and discussions of reference II-2 deals with accelerations, and derived particle velocities. No pressure data are presented.

Accelerations were measured at various ranges and depths with respect to the detonations and reference II-2 presents least square power fits to the horizontal peak accelerations for each round. Correlations amongst the various rounds, however, are relatively poor. For example, figure II-2 shows scaled peak horizontal accelerations for various charge sizes at a common scaled depth of burst. Reference II-2 attributes the

Table II-5

Summary of Underground Explosion Test Detonations (ref. II-2)

Site	Charge Wt (lb)	Charge Scale *	No. of Charges	Site Location
Dry Clay	8	0.029	2	Dugway Proving Ground, Utah
	110	0.07	1	
	320	0.1	9	
	2,560	0.2	5	
	40,000	0.5	1	
	320,000	1.0	1	
Dry Sand	8	0.029	2	Dugway Proving Ground, Utah
	320	0.1	10	
	2,560	0.2	3	
	40,000	0.5	1	
Wet Clay	8	0.029	2	Dugway Proving Ground, Utah
	320	0.1	2	
	2,560	0.2	1	
Limestone	320	0.1	2	Dugway Proving Ground, Utah
Granite	320	0.1	10	Unaweep Canyon, near Grand Junction, Colorado
	2,560	0.2	2	
Sandstone	320	0.1	8	Buckhorn, Wash, near Castle Dale, Utah
	1,080	0.15	1	
	2,560	0.02	3	
	10,000	0.315	1	
	40,000	0.5	3	
	320,000	1.0	1	

* The 320,000 pound charge was arbitrarily assigned a scale of 1.0; the charge scale is proportional to the cube root of the charge weight.

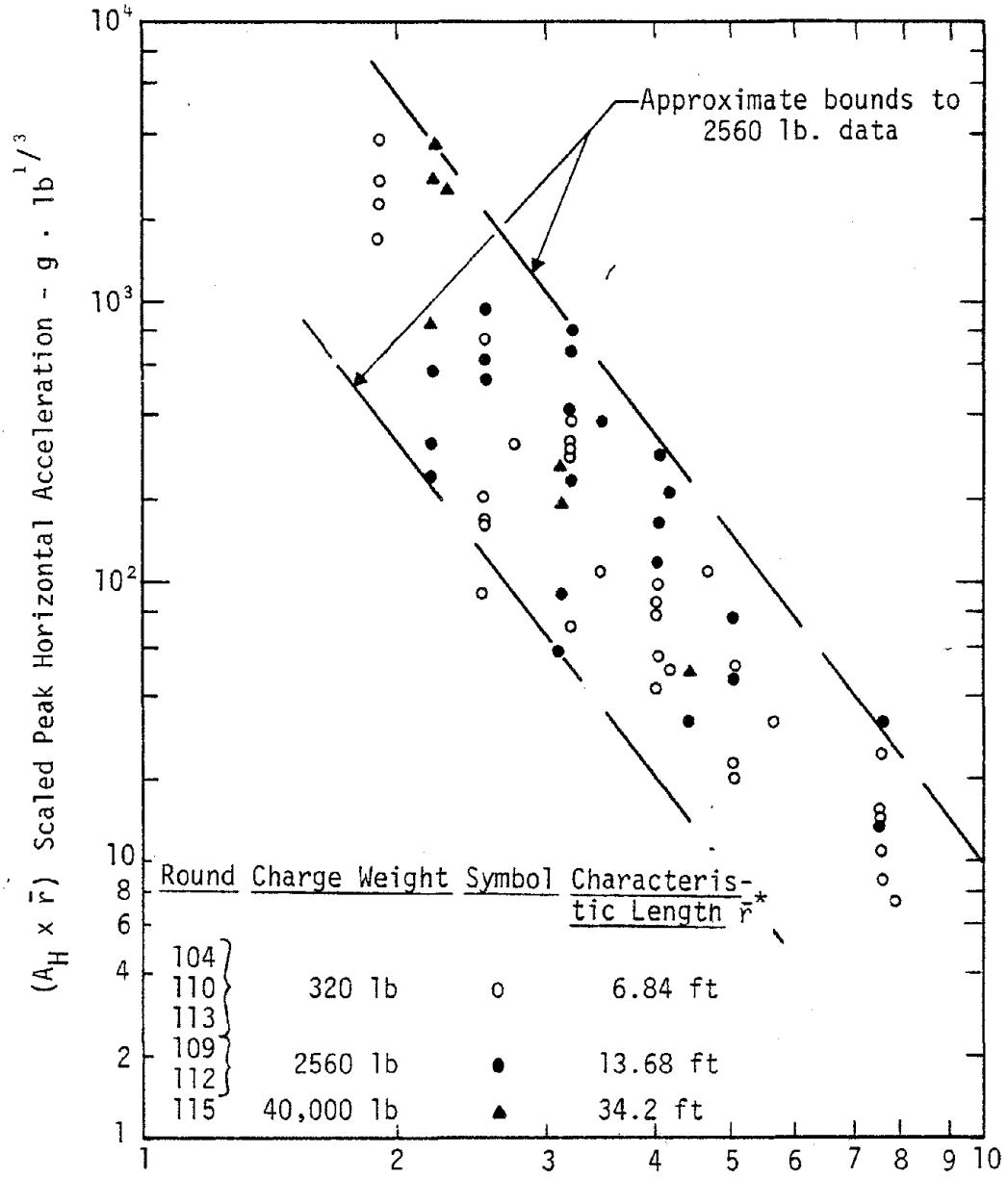

Figure II-2. Peak Horizontal Acceleration Scaled to Charge Size for Rounds with Scaled Charge Depth of 0.51-Dry Sand (ref. II-2)

large scatter to variation and lack of understanding of soil properties, although it appears that the inclusion of all data regardless of depth, and the fact that the peak acceleration was not or could not be resolved into the radial direction also contributes to the scatter. It is also possible that instrumentation placement, in the early stages of development at the time of the UET experiments, may have contributed to the data scatter. It is interesting that the bounds to the 2650 lb charge data encompass most of the data from smaller and larger charges. Unfortunately, reference II-2 does not provide sufficient definition of the specific data so that the data could be reevaluated according to depth. In spite of some shortcomings with respect to using the motion data of reference II-2 for new analysis, reference II-2 draws several conclusions which are of significant interest.

Symmetry evaluations indicated definite asymmetries which were relatively random in nature. Measurements of acceleration at the same range but different azimuths indicated variations of a factor of 2 to 3 occurred and these could not be correlated with any systematic cause. This nonuniformity and random scatter, as will be noted in later discussions, has been observed in every well instrumented experiment, regardless of the apparent uniformity of the site.

Reference II-2 identified four types of waveforms in the acceleration data which were described as follows:

Type 1 - a direct compressional waveform having a simple pulse form of high amplitude.

Type 2 - a waveform, thought to be a transverse wave, which prop-

agates at a lower wave speed and has higher frequency content than the direct compression waveform.

Type 3 - a waveform having multiple peaks and large negative peaks which tended to occur in lieu of the direct compression wave.

Type 4 - a waveform which occurred at larger ranges, especially at shallow depths, and appeared to be the break up of the simple compression waveform into a more complicated wave train.

Figure II-3 shows the records from round 109 in dry sand. The type 1 and type 2 waveforms are evident in the data.

On the basis of waveform types, reference II-2 classified detonations according to scaled depth of burst. Deep bursts, with scaled depths of burst below 0.5, contained primarily type 1 waveforms, while those for shallow bursts above a scaled depth of 0.5 were type 3. This differentiation is also evident in the amplitude and decay rate data as a function of depth of burst. Figure II-4 shows least square fits to dry clay data at various depths of burst. The decay rate increases rapidly with increasing depth of burst from -1.5 at the shallowest burst depth to -3.5 at a scaled burst depth of 0.51 after which it increases only slightly. On the basis of amplitude, maximum initial amplitude (i.e., coupling) for acceleration is achieved at a scaled burst depth of about 2.0. Particle velocity amplitude (fig. II-5) also seems to achieve a maximum at a scaled depth of burst of about 2. These results are in agreement with the conclusions of Lampson (ref. II-1) for maximum coupling for pressure and impulse which were presented earlier.

Information on attenuation rates for acceleration and particle velocity are also available from reference II-2. Table II-6 presents data

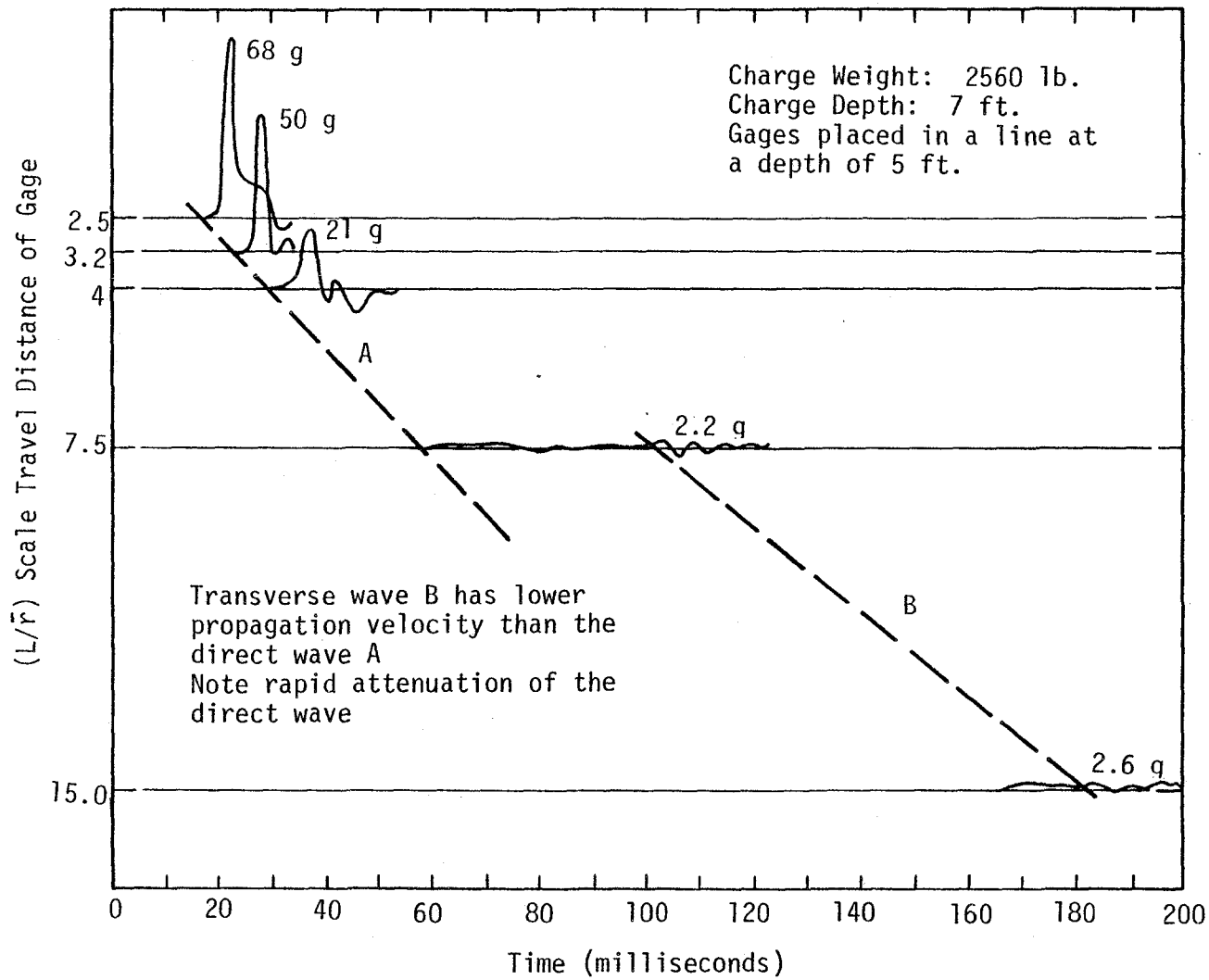

Figure II-3. Horizontal Acceleration, Round 109-Dry Sand (ref. II-2)

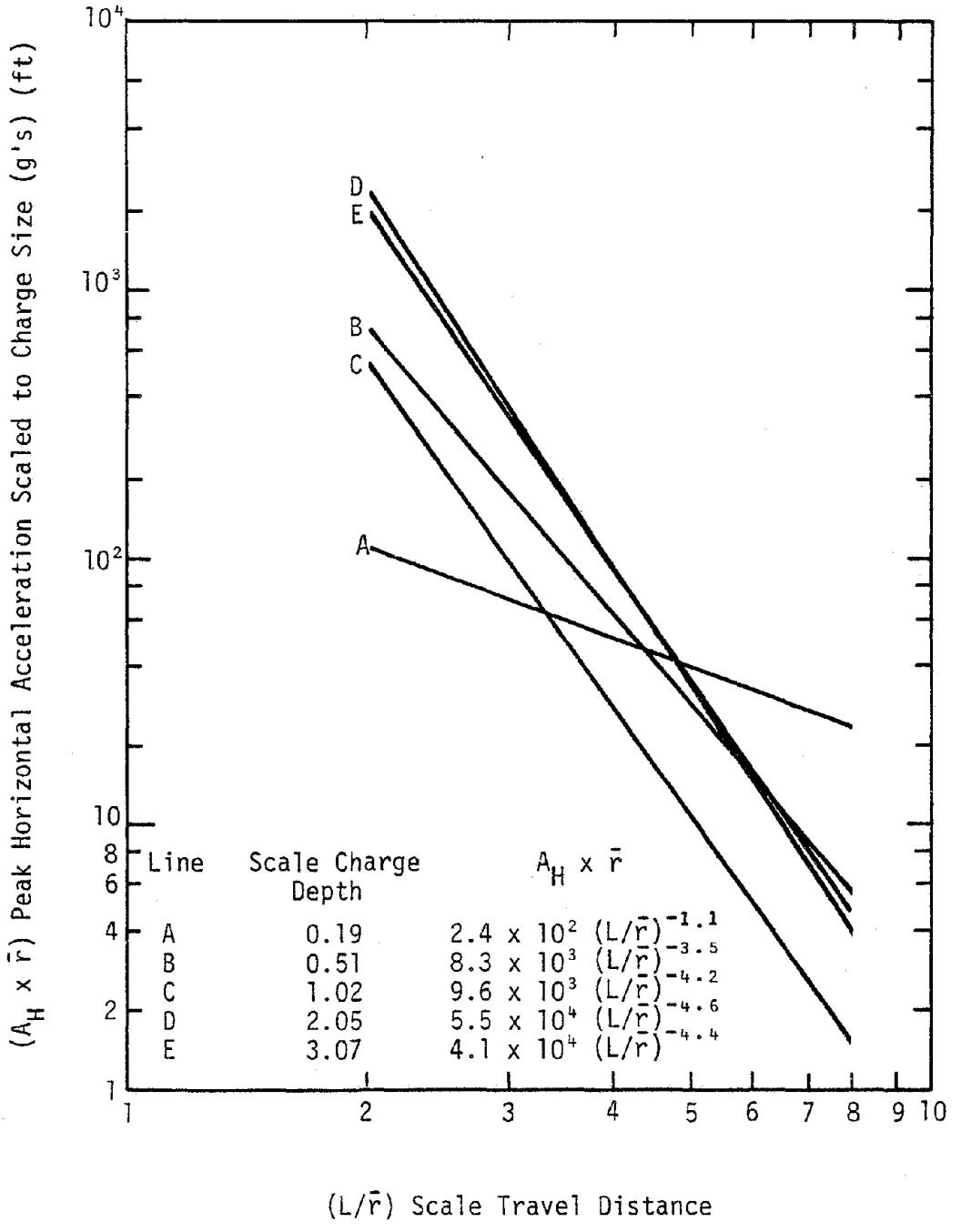

Figure II-4. Effect of Charge Depth on Peak Horizontal Acceleration-Dry Clay (ref. II-2)

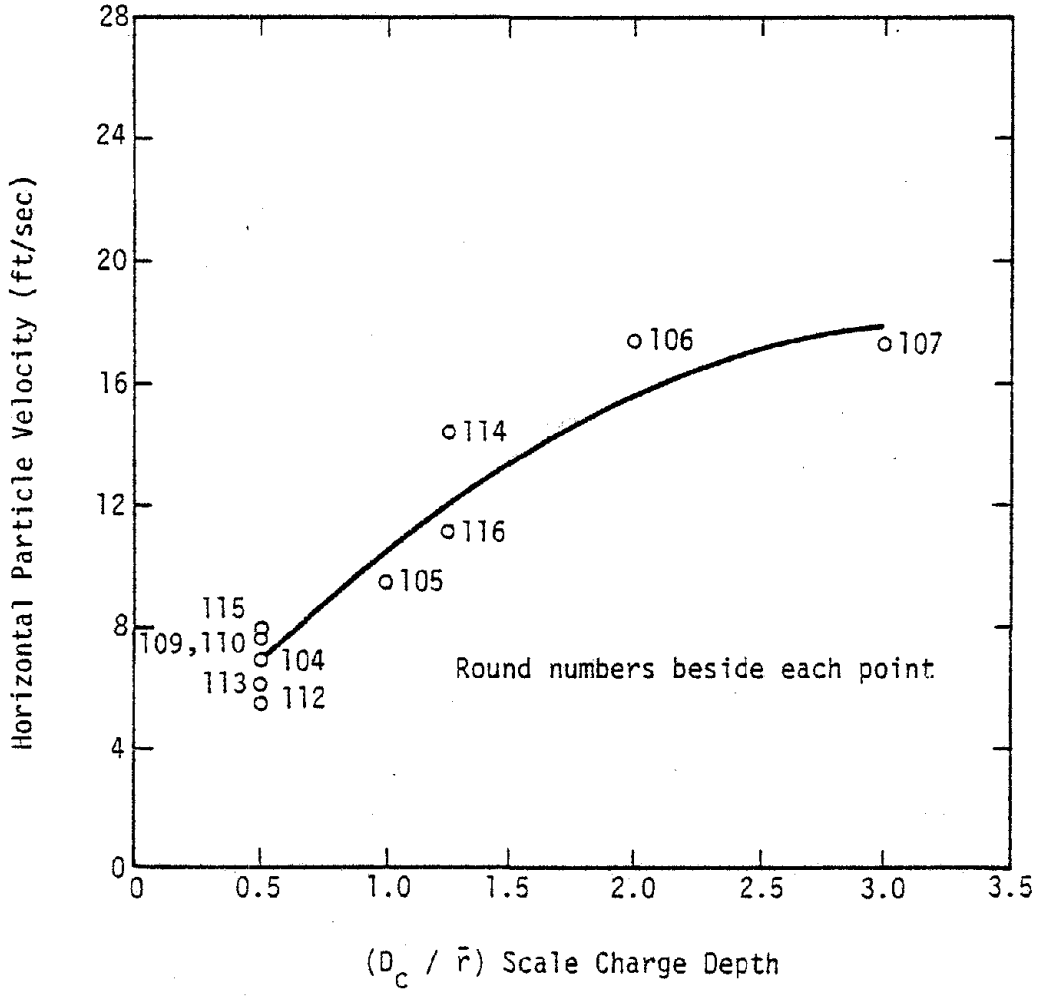

Figure II-5. Variation of Initial Values of Horizontal Particle Velocity with Scale Charge Depth (Scale Travel Distance $L/\bar{r} = 2$) (ref. II-2)

Table II-6

Attenuation of Peak Horizontal Acceleration Scaled to Charge Size, $A_H \times \bar{r}$, for Charges with Scaled Depth of 0.51 (ref. II-2)

Dry Sand			Dry Clay		
Round No.	Charge Weight (pounds)	$A_H \times \bar{r}$	Round No.	Charge Weight (pounds)	$A_H \times \bar{r}$
104	320	$1.4 \times 10^4 (L/\bar{r})^{-3.6}$	304	320	$4.7 \times 10^2 (L/\bar{r})^{-1.9}$
110	320	$3.2 \times 10^4 (L/\bar{r})^{-4.1}$	310	320	$1.6 \times 10^3 (L/\bar{r})^{-2.8}$
113	320	$1.9 \times 10^3 (L/\bar{r})^{-2.7}$	313	320	$1.1 \times 10^3 (L/\bar{r})^{-2.4}$
109	2560	$3.5 \times 10^4 (L/\bar{r})^{-3.9}$	317	2560	$2.2 \times 10^4 (L/\bar{r})^{-4.6}$
112	2560	$6.2 \times 10^3 (L/\bar{r})^{-3.7}$	319	2560	$3.6 \times 10^4 (L/\bar{r})^{-4.7}$
115	40,000	$2.1 \times 10^5 (L/\bar{r})^{-5.8}$	315	40,000	$2.5 \times 10^4 (L/\bar{r})^{-3.2}$
			318	320,000	$1.3 \times 10^5 (L/\bar{r})^{-4.3}$

fitting from reference II-2 to the dry clay and dry sand data at a scaled charge depth of 0.51. The average attenuation rate in dry sand is -4 while that in dry clay is -3.4. In spite of the lack of correlation from test to test, the attenuation rates on the average are consistent and credible. Available least square fits for horizontal particle velocity are given in table II-7. The average attenuation rate in dry sand is -2.6 while that in dry clay is -2.9. Within the data scatter, the attenuation rates in dry sand and dry clay appear about the same.

Very few vertical accelerations were measured in the UET series but the few data available from near surface measurement indicate that the vertical accelerations are on the same order as the horizontal.

c. Project Mole

Project Mole (ref. II-3) was conducted in the period June 1952 through October 1954, and produced one of the largest banks of data on small spherical TNT explosions in existence. The project was conducted by Stanford Research Institute for the U.S. Army Corps of Engineers. It had as its objective the investigation of height and depth of burst effects on the ground shock and airblast produced by explosives of a single size in various soils. The program involved 45 rounds of spherically shaped, 256 pound charges of TNT detonated in four different soil types.

Volume I of reference II-3 presents basic information on the test series, plots of various peak parameters versus range, comparisons with data from other sources, and a thorough discussion of instrumentation and the qualitative differences between the results of the different shots.

Table II-7

Least Square Equations For Horizontal Particle Velocity (ref. II-2)

Dry Sand							
Round No.	Horizontal Velocity U_H (feet per second)	Charge Weight (pounds)	Scaled Depth of Burst	Round No.	Charge Weight (pounds)	Scaled Depth of Burst	Horizontal Velocity U_H (feet per second)
104	$42(L/\bar{r})^{-2.6}$	320	0.51	110	320	0.51	$74(L/\bar{r})^{-3.3}$
105	$40(L/\bar{r})^{-2.1}$	320	1.02	112	2560	0.51	$17(L/\bar{r})^{-2.2}$
106 shallow	$42(L/\bar{r})^{-2.3}$	320	2.04	113	320	0.51	$46(L/\bar{r})^{-2.6}$
deep	$98(L/\bar{r})^{-2.5}$	320	2.04	114	8	1.0	$100(L/\bar{r})^{-2.8}$
107	$98(L/\bar{r})^{-2.5}$	320	4.08	115	40,000.	0.51	$69(L/\bar{r})^{-3.2}$
109	$37(L/\bar{r})^{-2.3}$	2560	0.51	116	320	1.28	$89(L/\bar{r})^{-3.0}$
Dry Clay							
Round No.	Horizontal Velocity U_H (feet per second)	Charge Weight (pounds)	Scaled Depth of Burst	Round No.	Charge Weight (pounds)	Scaled Depth of Burst	Horizontal Velocity U_H (feet per second)
306	$170(L/\bar{r})^{-2.6}$	320	2.04	310	320	0.51	$100(L/\bar{r})^{-3.4}$
307	$110(L/\bar{r})^{-2.4}$	320	4.08	319	2560	0.51	$260(L/\bar{r})^{-3.9}$

Volume II presents the detailed data including the directly measured time histories, tables of peak amplitude and characteristic time parameters for each gage, and time of arrival curves for each round. Also included in reference II-3 are results from some UET rounds in dry clay which are not provided in reference II-2, as well as data in an unclassified form from the JANGLE HE test series, the JANGLE nuclear test series and the TEAPOT ESS (shot 7) nuclear event.

The soil types in Project Mole were dry clay (DC), dry sand-gravel mix (S-G), wet sand (WS) and moist clay (MC), where the initials in parentheses are the abbreviations for the soil types used in reference II-3. A summary of the Mole rounds is given in table II-8. The mole rounds are identified by a 3 digit number, the first digit of which designates the series number which is associated with the test location. The last two digits are simply sequential designations of the individual tests in the series.

The 100 series, consisting of 12 shots, was conducted at Dugway Proving Ground, Utah in the same dry clay used in the UET program. The properties of the site determined in the UET program and described previously are applicable for the Mole dry clay tests. First arrival wave speeds in the Mole experiments averaged 1540 ft/sec and the in-situ density was about 99 lbs/ft^3. The 200 series, with 13 shots, was conducted in the Yucca Flat area of Nevada Test Site, near the JANGLE HE site. The soil in this area consists of alluvial fill in a basin-range valley. The constituents consist largely of sands, gravels and silts, hence, the designation sand-gravel mix. The site is very dry with only a trace of moisture detected in one drill hole at a depth of 1500

Table II-8

Summary of Mole Rounds
(ref. II-3)

Scaled Charge Depth (λ_c)*	Round No.	Date	Actual Charge Depth (ft)	Remarks
Utah Dry Clay				
1.00	101	6/28/52	6.35	First attempt at firing failed
1.00	105	7/17/52	6.35	
0.50	102	7/3/52	3.18	All records lost due to relay failure
0.50	102A	7/6/52	3.18	
0.26	106	7/19/52	1.65	
0.13	103	7/10/52	0.83	Partial detonation, data not reported
0.00	107	8/20/52	0.0	
-0.13	104	7/13/52	-0.83	
-0.26	111	8/26/52	-1.65	
-0.50	109	8/24/52	-3.18	
-0.50	110	8/26/52	-3.18	
-1.00	108	8/24/52	-6.35	
Nevada Sand-Gravel Mix				
1.00	201	9/11/52	6.35	Partial detonation, data not reported
1.00	202	9/14/52	6.35	Records from one camera lost
1.00	212	10/24/52	6.35	
0.50	203	9/19/52	3.18	
0.26	204	10/4/52	1.65	
0.13	205	10/8/52	0.83	
0.00	206	10/11/52	0.0	
-0.13	207	10/15/52	-0.83	
-0.26	211	10/21/52	-1.65	Records from one camera very faint
-0.26	211A	10/22/52	-1.65	
-0.50	209	10/19/52	-3.18	
-0.50	210	10/19/52	-3.18	Records from one camera lost
-1.00	208	10/16/52	-6.35	Twelve records lost due to oscillator imbalance
1.00	404	10/30/54	6.35	
0.75	402	10/26/54	4.77	
0.50	401	10/23/54	3.18	
0.50	406	10/4/54	3.18	
0.26	405	11/2/54	1.65	
0.13	403	10/28/54	0.83	
California Wet Sand				
0.75	304	9/23/53	4.77	Shot in 303 crater
0.50	302	9/18/53	3.17	
0.50	301	9/15/53	3.17	Most records off-scale
0.50	309	10/16/53	3.17	
0.50	310	10/17/53	3.17	
0.50	305A	10/5/53	3.17	Dynamite, data not reported
0.25	303	9/22/53	1.6	Partial detonation, data not reported
0.25	305	9/26/53	1.6	
0.13	306	10/8/53	0.83	
0.00	307	10/10/53	0.0	
-0.13	308	10/13/53	-0.83	
California Moist Clay				
0.5	311	10/20/53	3.18	
0.5	312	10/22/53	3.18	
-0.13	313	10/24/53	-0.83	

* $\lambda_c = \frac{\text{Depth of Burst}}{(\text{charge weight})^{\frac{1}{3}}}$

feet. The vertical seismic profile of the site indicates 3000 ft/sec velocity from the surface to 100 ft, 4000 to 4500 ft/sec from 100 to 350 feet and 5000 to 5500 ft/sec below 350 feet. First arrival wave speeds in the experiments averaged 3600 ft/sec. The in-situ density averaged 99 lbs/ft^3.

The 300 series was conducted at Camp Cooke, California. Eleven tests in wet sand were conducted on the banks of a lagoon formed by the mouth of the Santa Ynez River. The top 2 feet consisted of silty sand mixed with organic material. This material was underlain by saturated sand to a depth of 20 feet where Monterey shale was encountered. Three tests were conducted in a moist clay at a nearby site where the ground surface was about 5 feet above the water table. The upper 5 feet consisted of hard clay-silt which was underlain by moist sandy clay to a depth of 22 feet. Seismic data for these sites are not given in reference II-3, but reference II-3 gives measured wave speeds in the explosive experiments of about 5000 ft/sec in the wet sand and 4020 to 7550 ft/sec in the moist clay. In-situ densities were 114 and 124 lbs/ft^3 in the wet sand and moist clay, respectively.

The 400 series, consisting of 6 shots, was conducted at the Nevada Test Site about 7000 feet from the site of the 200 series tests. The purpose was to obtain data near the site of the TEAPOT ESS nuclear event. The soils of the site were assumed in reference II-3 to be similar to those at the 200 series site. Measured first arrivals in the experiments indicated a wave speed of 2900 ft/sec suggesting some differences in the properties from a seismic viewpoint.

Measurements in Project Mole included soil pressure, soil stress, soil strain, particle acceleration, airblast overpressure, residual earth displacement and crater profiles. The instruments were placed at depths of 1, 2.5, and 5 feet with most of the instruments at 2.5 and 5 feet. Since the depths of burst of the buried charges ranged from 0.83 to 6.35 feet, not appreciably different from the gage depths, the horizontal measurements can probably be assumed as representative of the radial behavior without introducing as much suspected scatter as occurred in the UET results by this assumption. Accelerations were integrated to obtain particle velocities and doubly integrated to obtain displacements.

Reference II-3 discusses qualitative differences amongst the data quite thoroughly. In addition, the data is scaled for comparison with large scale high explosive data or nuclear data where available. Typical waveforms derived for various parameters are shown in figures II-6, II-7, and II-8. The peak parameters and characteristic times shown in the figures are tabulated in Volume II of reference II-3. A typical travel time plot, useful in discriminating direct induced effects from airblast induced effects, and in evaluating the wavespeeds in the experiment against measured seismic wavespeeds, is given in figure II-9. Examples of peak motion parameter data in dry clay are shown in figures II-10, II-11, and II-12. The data show a tendency toward increasing amplitude with increasing depth of burst. Comparisons of scaled data from series 400 with TEAPOT ESS are given in figure II-13. The $W^{\frac{1}{3}}$ scaling used in reference II-3 did not bring these events into close agreement.

Very little quantitative analysis of the results of the tests is

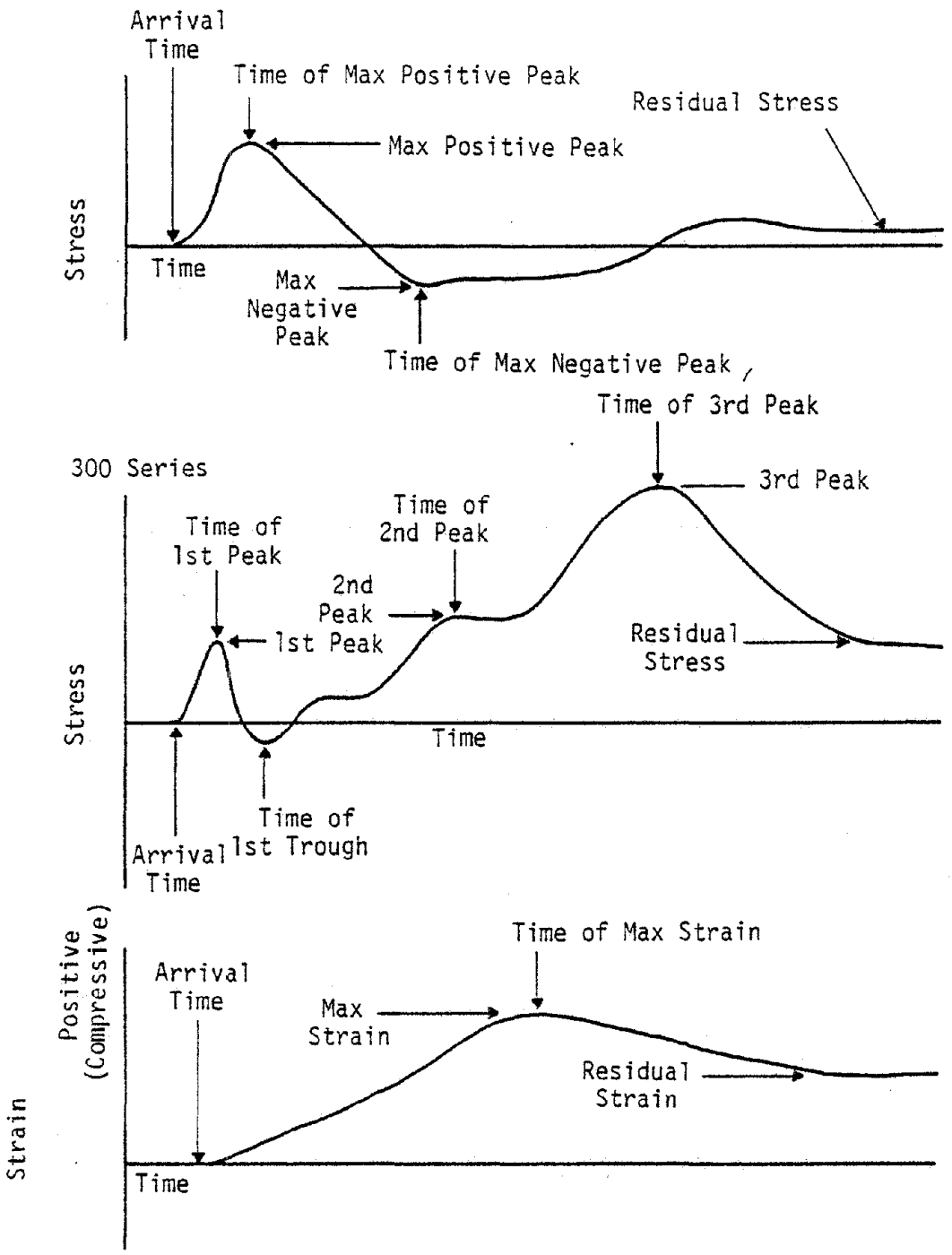

Figure II-6. Typical Soil Stress and Strain Waveforms (ref. II-3)

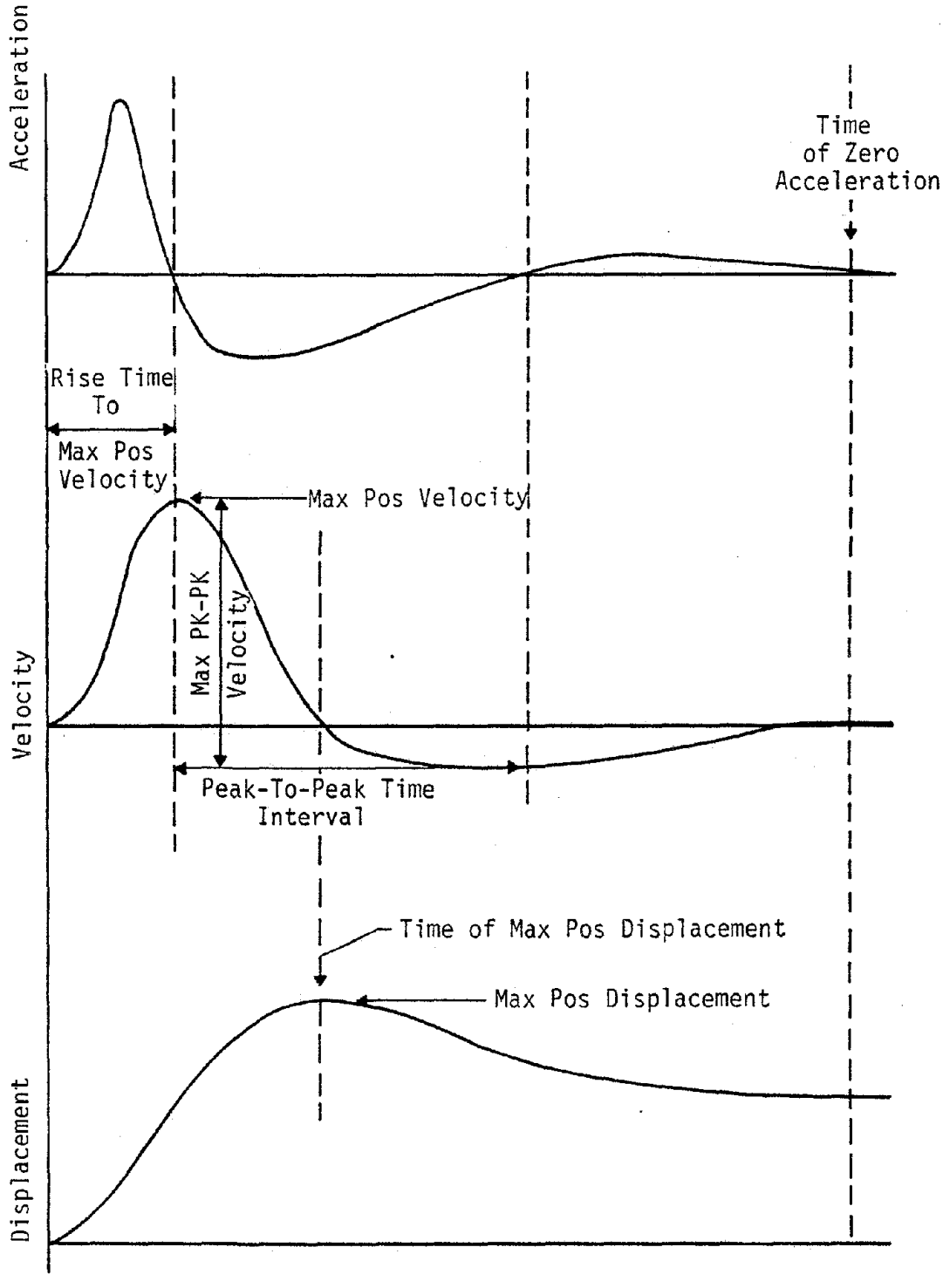

Figure II-7. Typical Particle Velocity and Displacement Waveforms (ref. II-3)

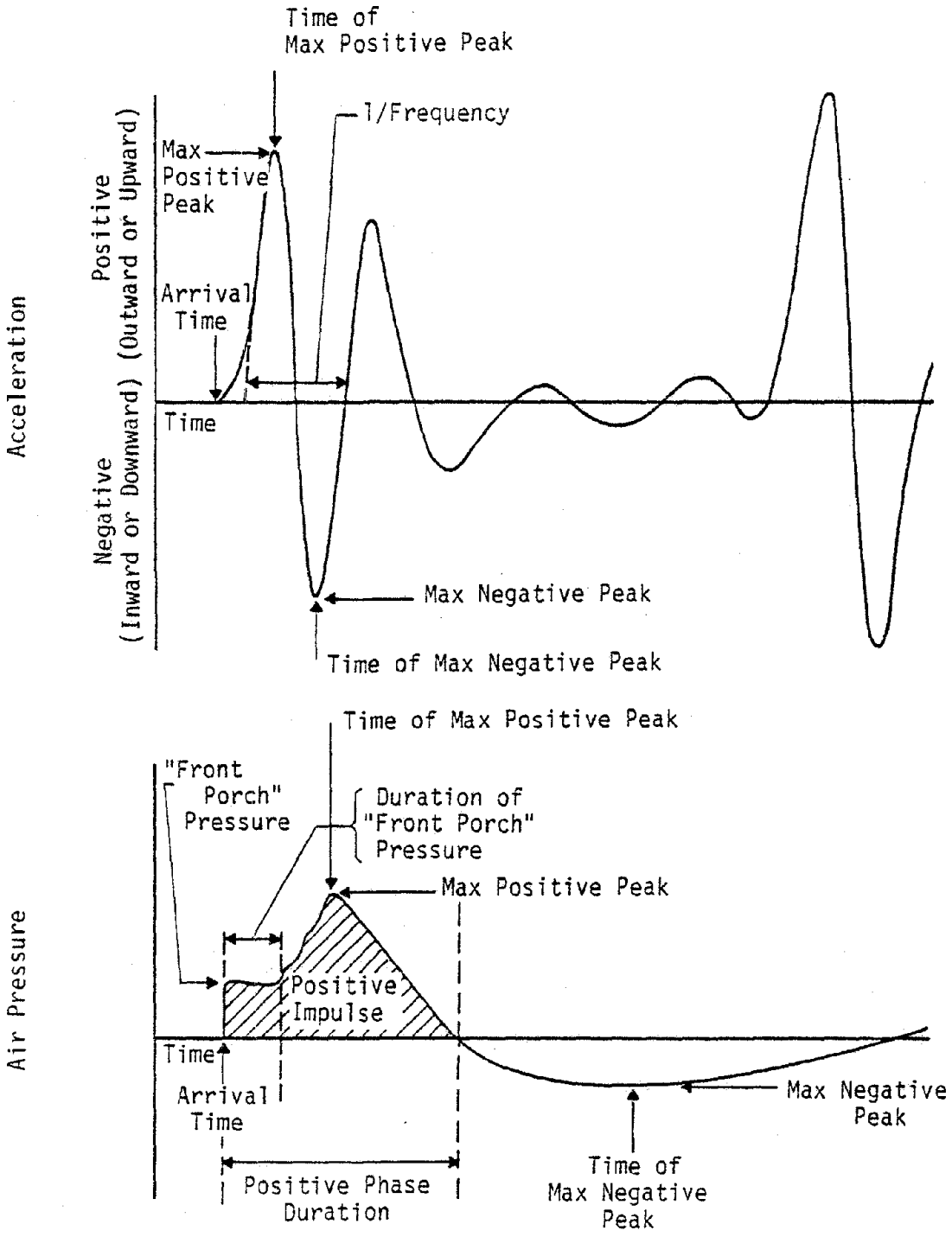

Figure II-8. Typical Soil Acceleration and Airblast Pressure Waveforms (ref. II-3)

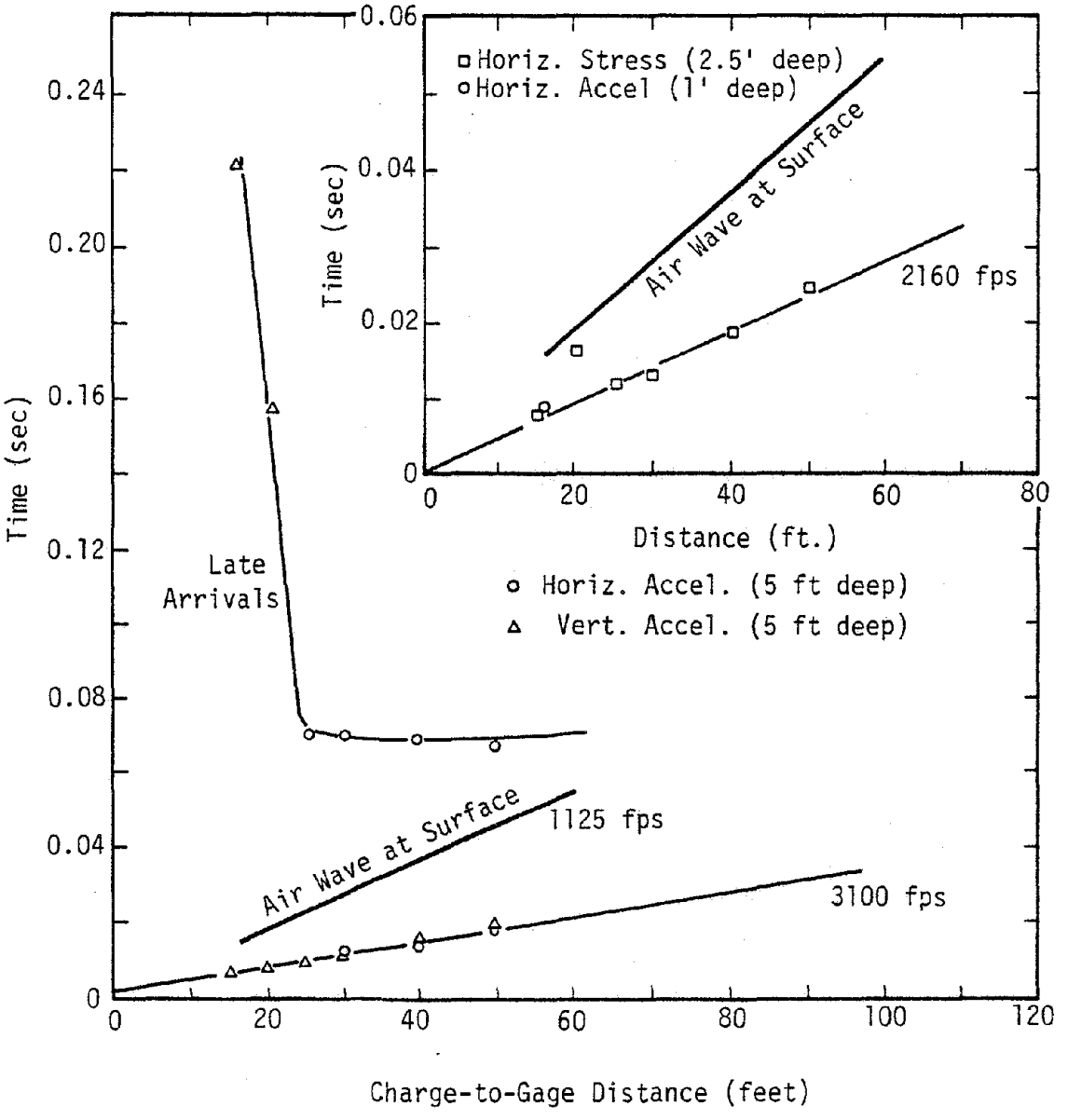

Figure II-9. Travel-Time Plot, Nevada Sand-Gravel Mix, Round 404 (Scaled Charge Depth = 1.0) (ref. II-3)

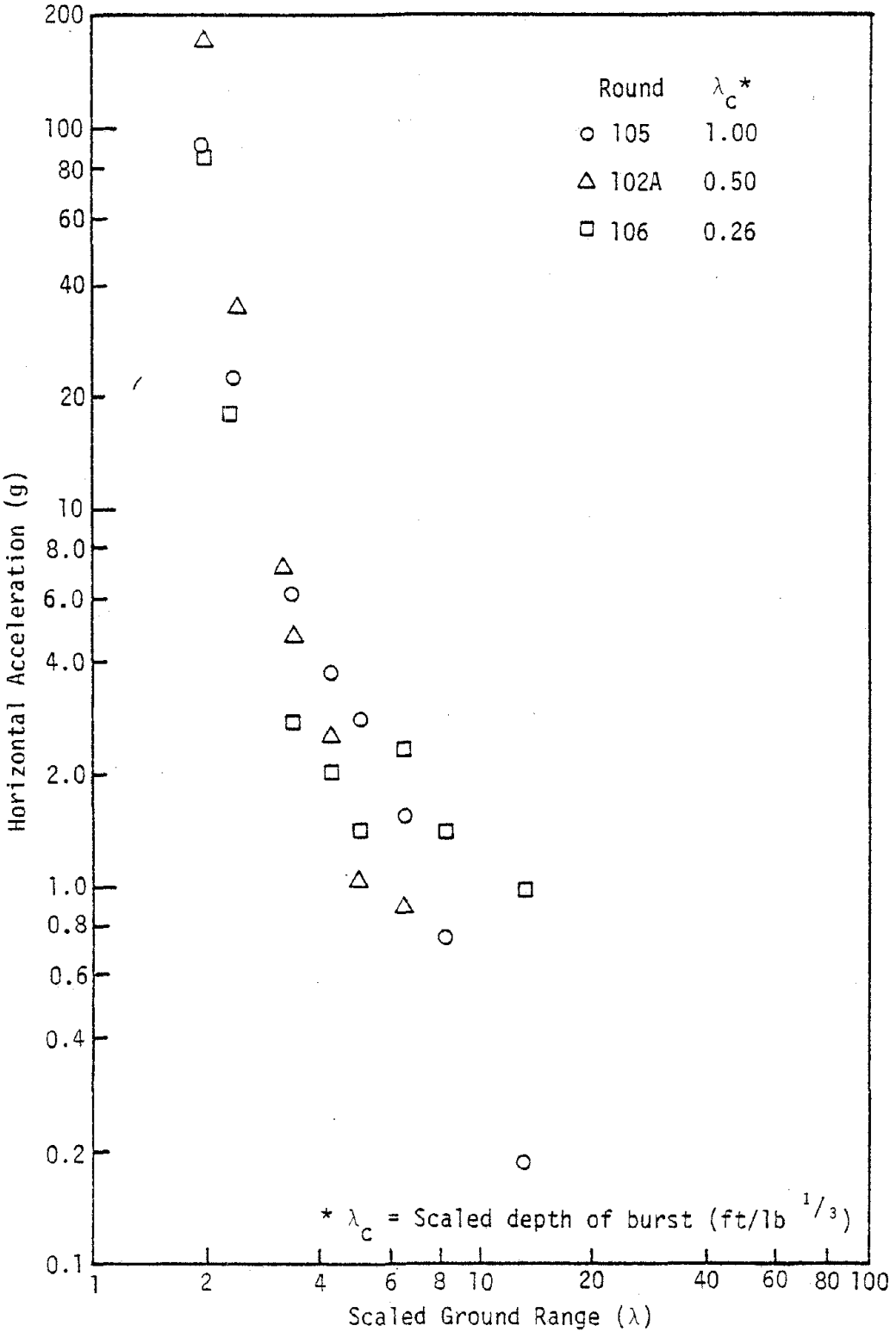

Figure II-10. Charge Depth Effect, Maximum Horizontal Earth Acceleration, Utah Dry Clay, Underground Shots (ref. II-3)

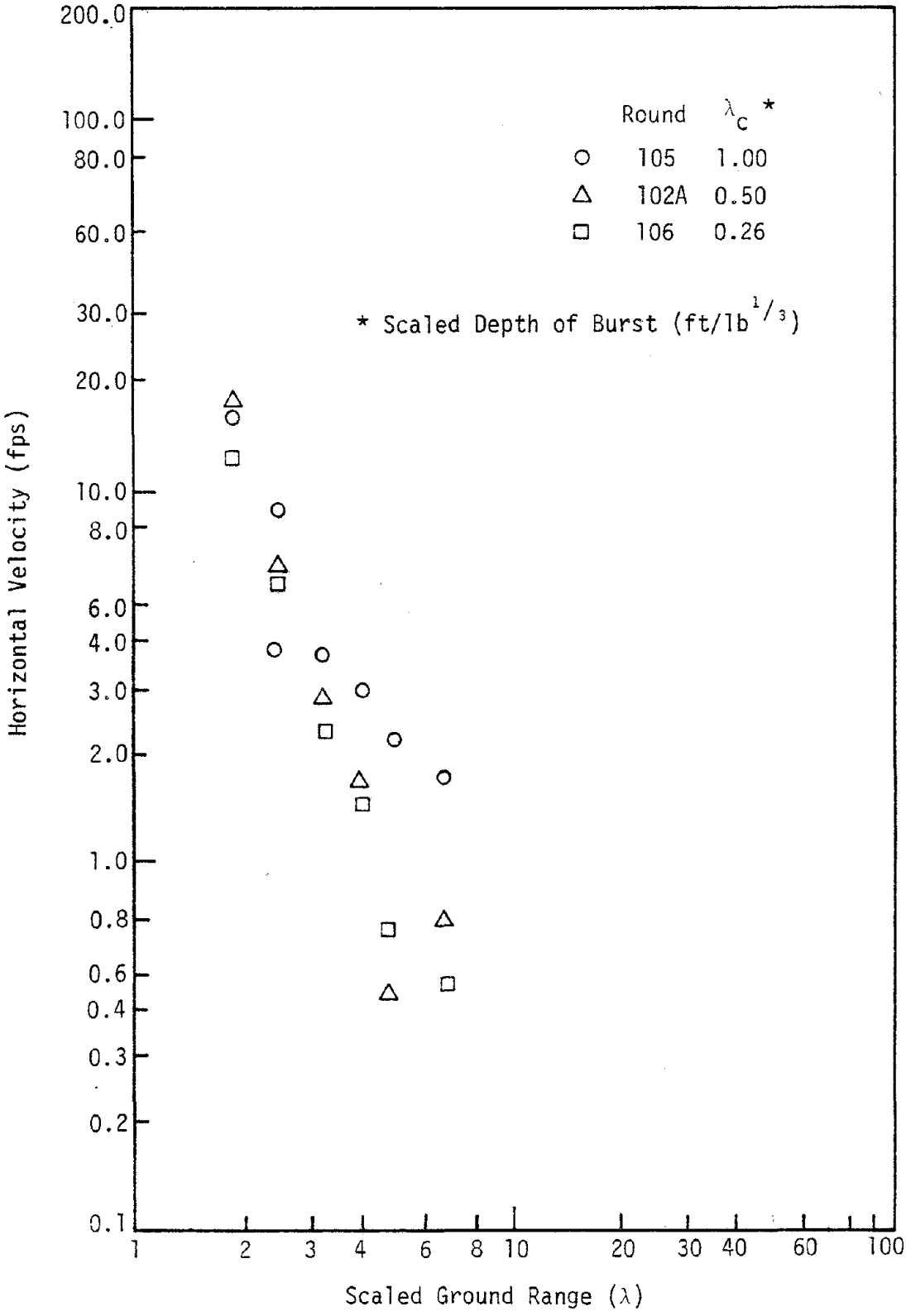

Figure II-11. Charge Depth Effect, Maximum Horizontal Velocity, Utah Dry Clay (ref. II-3)

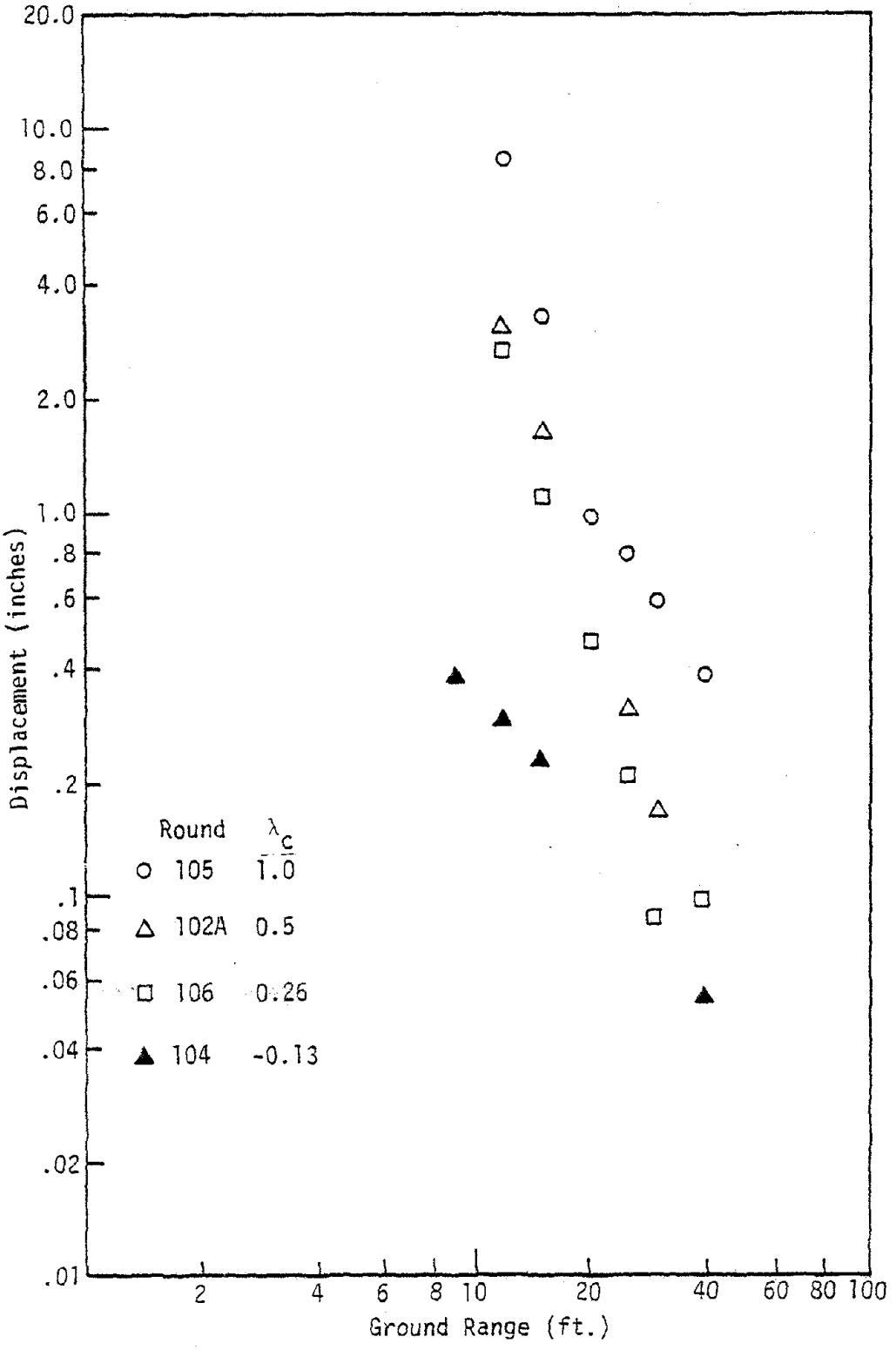

Figure II-12. Charge Depth Effect, Maximum Horizontal Displacement, Utah Dry Clay (ref. II-3)

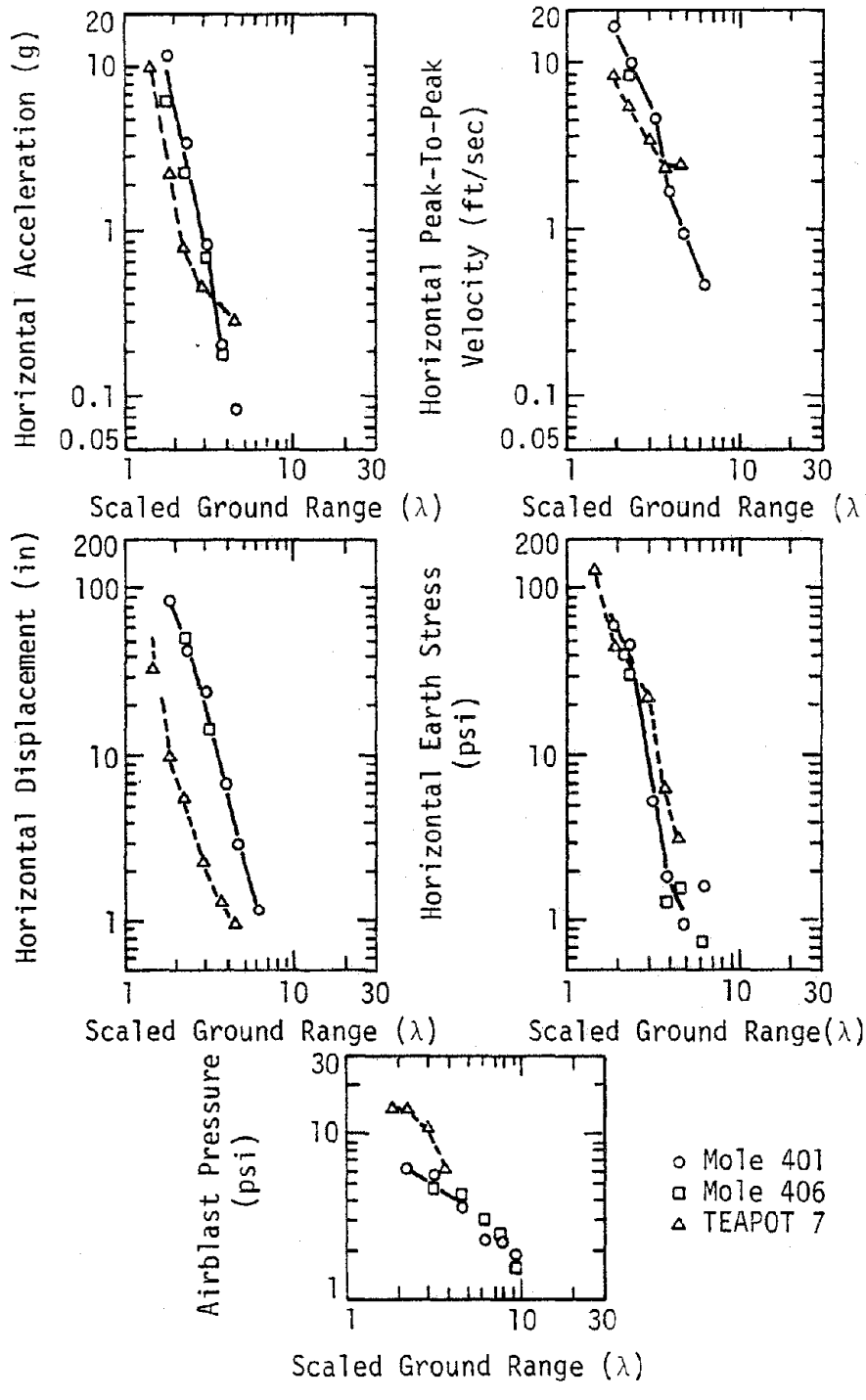

Figure II-13. Maximum Values of Earth Response and Airblast Pressure, Scaled to TEAPOT Shot 7, Nevada Sand-Gravel Mix, $\lambda_c = 0.5$ (ref. II-3)

presented in reference II-3 and, hence, the major benefit of the project is the availability of the data for further analysis. Ground motion data applicable to the simulation objective of this research effort is analyzed quantitatively in Section IV.

Some of the major general conclusions of reference II-3 are as follows:

(1) Ground shock response from underground explosions is highly dependent upon medium characteristics.

(2) The response is much larger in wet and damp soils than in dry soils.

(3) Response to small explosions can be quite sensitive to localized inhomogeneities.

(4) Ground response increases with increasing depth of burst while airblast effects decrease.

(5) Comparisons with higher yield explosions indicate that $W^{\frac{1}{3}}$ scaling may not work. Also, nuclear radiochemical equivalent yield may not be the appropriate yield for comparison with conventional high explosives.

(6) Crater radius may be a more appropriate scaling parameter than $W^{\frac{1}{3}}$ for near-surface explosions which cause craters.

Reference II-3 attributes the difficulty in scaling small and large charges at the same scaled depth of burst to the inelasticity of the soils. In general, properties vary with depth, even within a material which appears uniform. The variation is related to changes in moisture

content and increasing overburden stress with depth, as well as the existence of distinct material interfaces. These changes are usually manifested in an increasing seismic velocity with depth. The varying properties will have little effect upon small charges, but the ground response to larger charges will be influenced by a considerable variation in properties even from continuously varying seismic velocity. The property changes will be particularly important where faults, water tables, and rock interfaces are encountered. Reference II-3 also notes that differences between the hydrodynamic and thermodynamic behavior of high explosives and nuclear explosives complicate the determination of appropriate scaled yields for nuclear explosions.

d. Some Russian Work

Reference II-4 describes a relatively large experimental study of the ground motions caused by charges of various sizes in a geology consisting of loess loam* overlying clay. The experiments were performed in the fall of 1957 at a site in southern Kazakhstan. Charges ranged from 10kg (22.05 lbs) to 1000 metric tons (1100 tons) of Ammonite 6 explosive and were placed at scaled depths of burst of 0.4 to 0.7 $m/kg^{\frac{1}{3}}$ (1.01 to 1.76 $ft/lb^{\frac{1}{3}}$) with the exception of two 1000 kg explosions which were detonated at a scaled depth of burst of 1.5 $m/kg^{\frac{1}{3}}$ (3.78 $ft/lb^{\frac{1}{3}}$).

The test sites consisted of loess loam which varied in thickness from 1 to 25 m overlying clays. Area 1, having flat relief and involving 13 explosions having sizes of 10, 80, and 1000 kg, had a surface

*The definition of loam varies from place to place. In general, it refers to texture and denotes a mixture of particles of sand, silt and clay sizes without precise specification of relative amounts. Clayey loam usually means a sufficient amount of clay so that the texture is fine and the material is plastic when moist.

layer of loam of 1 to 2 m thick with seismic velocity of 240 to 280 m/sec (800 to 900 ft/sec), underlain by a main loess layer 15 to 20 m thick having a seismic velocity of 400 to 500 m/sec (1300 to 1600 ft/sec). Area 2 had significantly more relief, and the recording stations were on the slope of a hill having a 2 degree slope. Five explosions of 1000 kg each were detonated at varying depths of burst in area 2. The site of the explosions had about 1 m of loess-like loam with a density of 1.6 g/cm^3 (100 lbs/ft^3) underlain by a 0.5 m layer of sand. A layer of chestnut green clay with a density of 1.9 g/cm^3 (120 lb/ft^3) was present to a depth of 5 m, below which existed blue clay with a density of 2 gm/cm^3 (125 lb/ft^3). Seismic velocities are not reported, and the authors note that the stratum were not uniform over the field of observation, but the degree of nonuniformity is not known.

Charges of 90, 105, 120, 1000 and 10,000 kg were detonated in area 3 which had a geology similar to that of area 2, but with a flatter topography. The upper layer was fissured loess-like loam for 1 m, underlain by a layer of chestnut green clay to a depth of 7 m with a seismic velocity of 1750 m/sec (5750 ft/sec). Below 7 m was a layer of blue clay with a density of 2g/cm^3 (125 lb/ft^3) and a seismic velocity of 1800 m/sec (5900 ft/sec). The single 1000 metric ton charge was detonated in area 4, which consisted of 6 to 12 m of loess-like loam overlying clays. Seismic surveys indicated the loam had a seismic velocity of 430 to 500 m/sec (1400 to 1650 ft/sec). A chestnut green clay, with a seismic velocity of 1750 m/sec (5700 ft/sec), and a thickness of 2.5 to 3 m was beneath the loam. Blue clays, with a seismic velocity of 1900 m/sec (6200 ft/sec), extended to an undetermined depth.

Measurements on all explosions consisted of direct measurements of particle velocity and displacement at various ranges using seismometers. The majority of the measurements were made at the surface. Reference II-4 analyzed the results of the experiments in great detail. Peak amplitude parameters, characteristic times, waveforms, and particle trajectories were evaluated and interpreted with regard to their variation with range and the underlying phenomena which controlled the parameters. Figure II-14 shows typical measured particle velocities and figure II-15 shows typical displacement waveforms, measured in area 1. Individual wave components on the displacement waveforms are identified by capital letters R_1, N_0, etc. It is important to note that the peak amplitude occurs at the first motion cycle at near ranges, but in later cycles at more distant ranges, the waveforms becoming increasingly complicated with increasing range. At close distances, reference II-4 interprets the first main forward and upward motion (R_1^X, R_1) to be associated with the initial compression wave from the explosion. At greater distance the waveforms become more complex and their nature is not as evident. The R motion at far distances has an ellipsoidal counter-clockwise trajectory and has a propagation velocity of 210 to 250 m/sec (700 to 820 ft/sec). Thus, reference II-4 identifies the motion as a Rayleigh type surface wave in the loam layer. The transition area is vague. The N motion phase has been tentatively hypothesized by reference II-4 to be due to headwaves in the surface layer which were formed by a transverse wave refracted into the underlying clays, although reference II-4 notes that this hypothesis lacks a clear physical concept and is not consistent with all data.

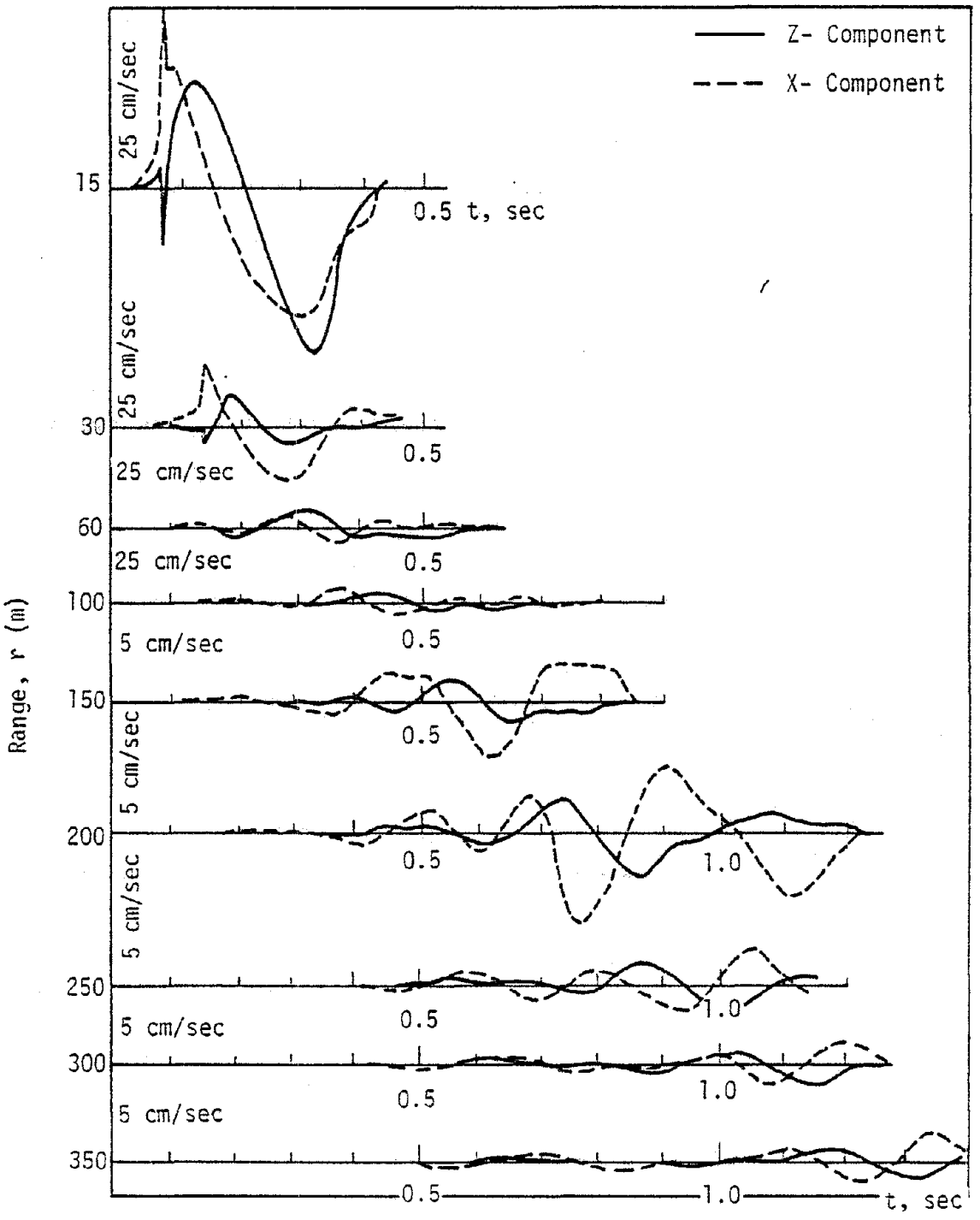

Figure II-14. Ground Particle Velocity at Various Epicentral Distances Explosion No. 4 (C=1000 kg; h=7 m) in Area 1 (ref. II-4)

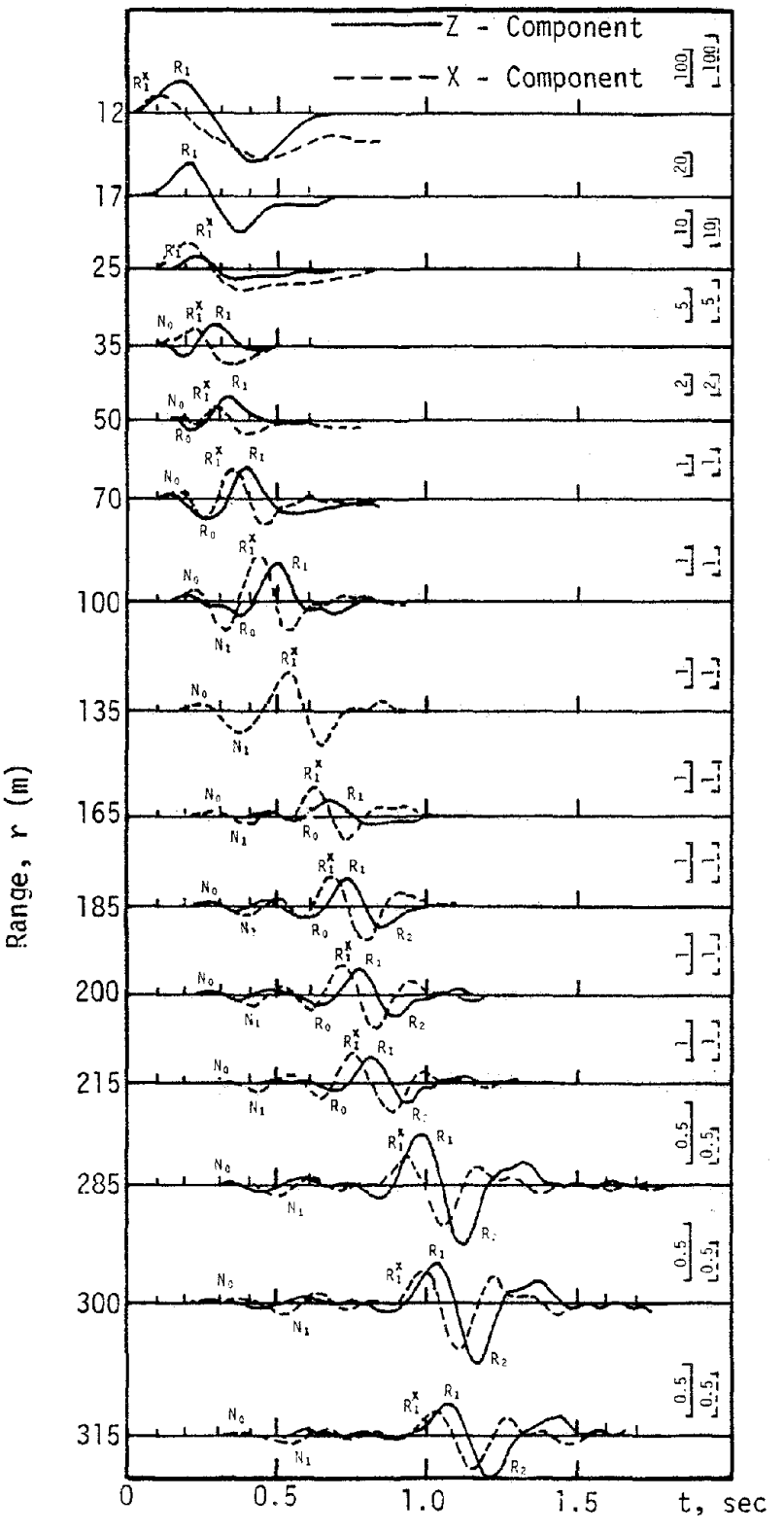

Figure II-15. Ground Motion at Various Epicentral Distances. Explosion No. 2 (C=1000 kg; h=5 m) in Area 1 Amplitude Scales in Millimeters (ref. II-4)

Reference II-4 provides an interesting evaluation of scaling laws using the results from areas 2 and 3, whicn were geologically similar. Explosive weights were 100, 1000, and 10,000 kg. Two scaling approaches are considered, designated in reference II-4 as Cauchy and Froude scaling. Cauchy scaling applies to systems where elastic forces predominate in controlling phenomena and is what is commonly called Lampson scaling or $W^{\frac{1}{3}}$ scaling in the United States. Froude scaling applies to systems where gravity exerts major control on phenomena and is commonly called gravity scaling in the United States. The scale factors for the physical quantities of interest for the two types of scaling are given in table II-9. The scale factors for 3 quantities can be taken arbritrarily and they were selected by reference II-3 as 1 for density (i.e. same material density in model and prototype), α for length (i.e. model lengths are $1/\alpha$ those of the prototype) and 1 for modulus of elasticity for Cauchy scaling or for the acceleration due to gravity for Froude scaling.

Selecting the amount of explosive C* as a convenient scale magnitude, using 1 kg as a standard, and taking the charge energy as proportional to the charge size for the same explosive, the scale for length is:

$$\text{Cauchy Scaling} = 1/C^{\frac{1}{3}} \qquad \text{(II-8)}$$

$$\text{Froude Scaling} = 1/C^{\frac{1}{4}} \qquad \text{(II-9)}$$

where C = charge weight in kg

Table II-9 can then be easily converted to table II-10 which presents the scale factors in terms of the charge weight C. Reference II-4 tested

*C is used in the Russian work; W is the common symbol in U.S. literature

Table II-9

Scaling Factors in Different Modeling (ref. II-4)

Quantity	Modeling after Cauchy	Modeling after Froude	Quantity	Modeling after Cauchy	Modeling after Froude
Length r	α	α	Velocity u	1	$\alpha^{1/2}$
Density γ	1	1	Acceleration w	α^{-1}	1
Modulus of elasticity E	1	-	Mass m	α^3	α^3
Acceleration of gravity g	-	1	Force K	α^2	α^3
Time t	α	$\alpha^{1/2}$	Stress σ	1	α
			Energy Q	α^3	α^4

Table II-10

Scale Factors Relative to Charge Weight in Different Modeling (ref. II-4)

Quantity	Modeling after Cauchy	Modeling after Froude	Quantity	Modeling after Cauchy	Modeling after Froude
Length r	$\frac{1}{C^{\frac{1}{3}}}$	$\frac{1}{C^{\frac{1}{4}}}$	Mass m	$\frac{1}{C}$	$\frac{1}{C^{\frac{3}{4}}}$
Density	1	1			
Modulus of elasticity E	1	-	Force K	$\frac{1}{C^{\frac{2}{3}}}$	$\frac{1}{C^{\frac{3}{4}}}$
Acceleration of gravity g	1	1	Stress σ	1	$\frac{1}{C^{\frac{3}{4}}}$
Time t	$\frac{1}{C^{\frac{1}{3}}}$	$\frac{1}{C^{\frac{1}{8}}}$			
Velocity u	1	$\frac{1}{C^{\frac{1}{8}}}$	Energy Q	$\frac{1}{C}$	$\frac{1}{C}$
Acceleration	$C^{\frac{1}{3}}$	1			

the validity of each type of scaling for the parameters of the initial phase of motion (the compression phase) from different charge sizes in areas No. 2 and 3. The first phase on the vertical (Z) component is designated P and on the horizontal (X) component as N_o. Figure II-16 shows the results of $C^{\frac{1}{3}}$ scaling for the vertical component of velocity, while figure II-17 shows the results for the horizontal component. Vertical velocity can be expressed as

$$U_p^Z = 600\left(\frac{r}{C^{\frac{1}{3}}}\right)^{-2} \qquad \text{(II-10)}$$

where

U_p^Z = peak vertical velocity in initial compression phase in cm/sec

r = range in meters

C = charge weight in kg

The corresponding expression for horizontal velocity is

$$U_{N_o}^X = 900\left(\frac{r}{C^{\frac{1}{3}}}\right)^{-2.3} \qquad \text{(II-11)}$$

where $U_{N_o}^X$ = peak horizontal velocity in initial compression phase in cm/sec

It should be noted that these relations do not correlate the absolute peak velocity since the absolute peak occurs in later phases of the waveforms for scaled ranges greater than about 7 $m/kg^{\frac{1}{3}}$ (17.6 $ft/lb^{\frac{1}{3}}$).

Scaled data for maximum vertical displacement (A_p^Z) and the rise time to maximum displacement (τ_2) are shown in figure II-18. Similar data for horizontal displacement are shown in figure II-19. It can be seen that $C^{\frac{1}{4}}$ (Froude) scaling seems to provide a better reduction of

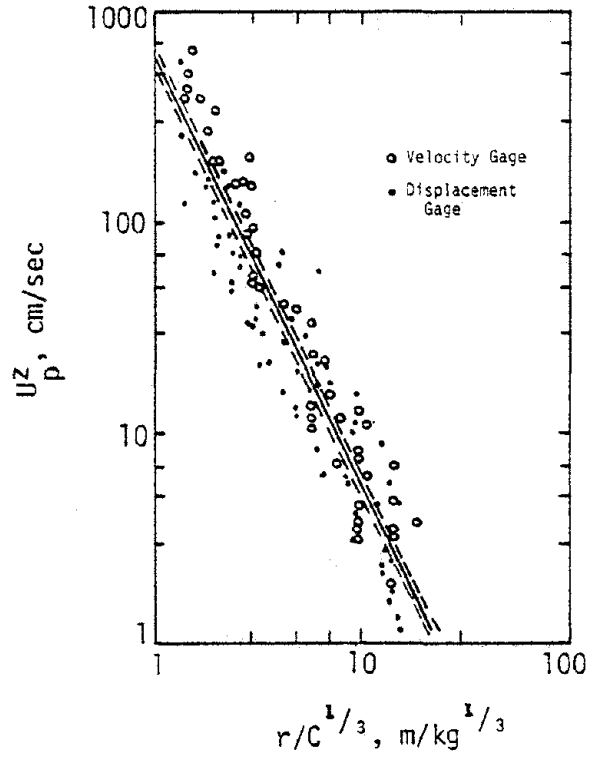

Figure II-16. Maximum Vertical Soil Particle Velocity in the Compression Wave Versus Scaled Distance in Areas No. 2 and 3 (ref. II-4)

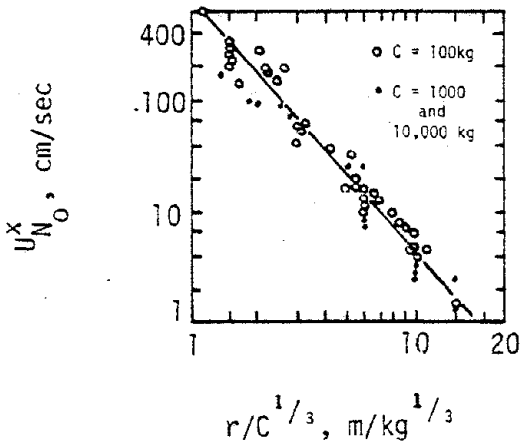

Figure II-17. Maximum Horizontal Particle Velocity in the N_o Phase Versus Scaled Distance in Areas No. 2 and 3 (ref. II-4)

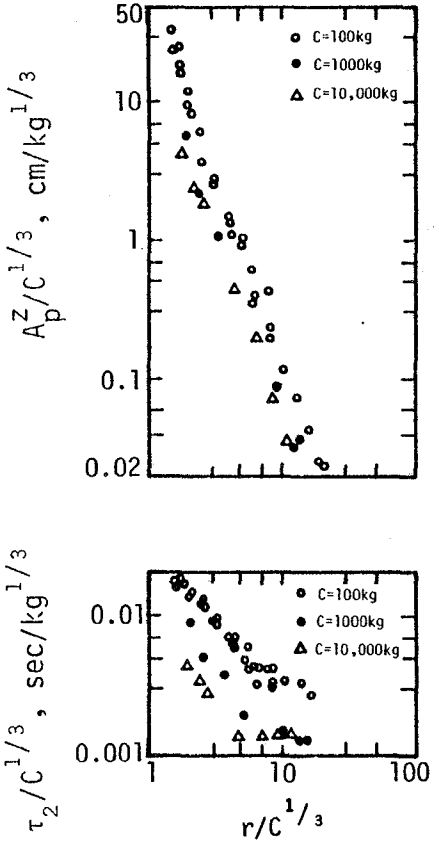

(a) Cauchy Scaling

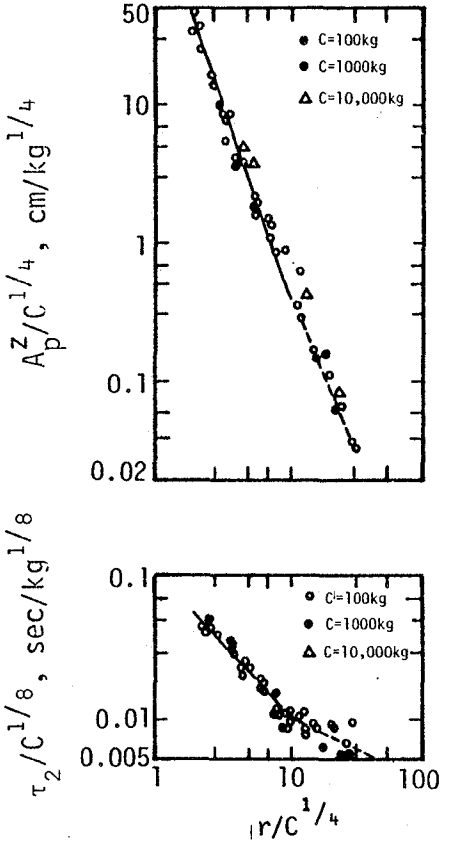

(b) Froude Scaling

Figure II-18. Maximum Vertical Displacement In The Compression Wave (A_p^z) and Its Time of Occurrence (τ_2) Scaled After Cauchy and Froude (ref. II-4)

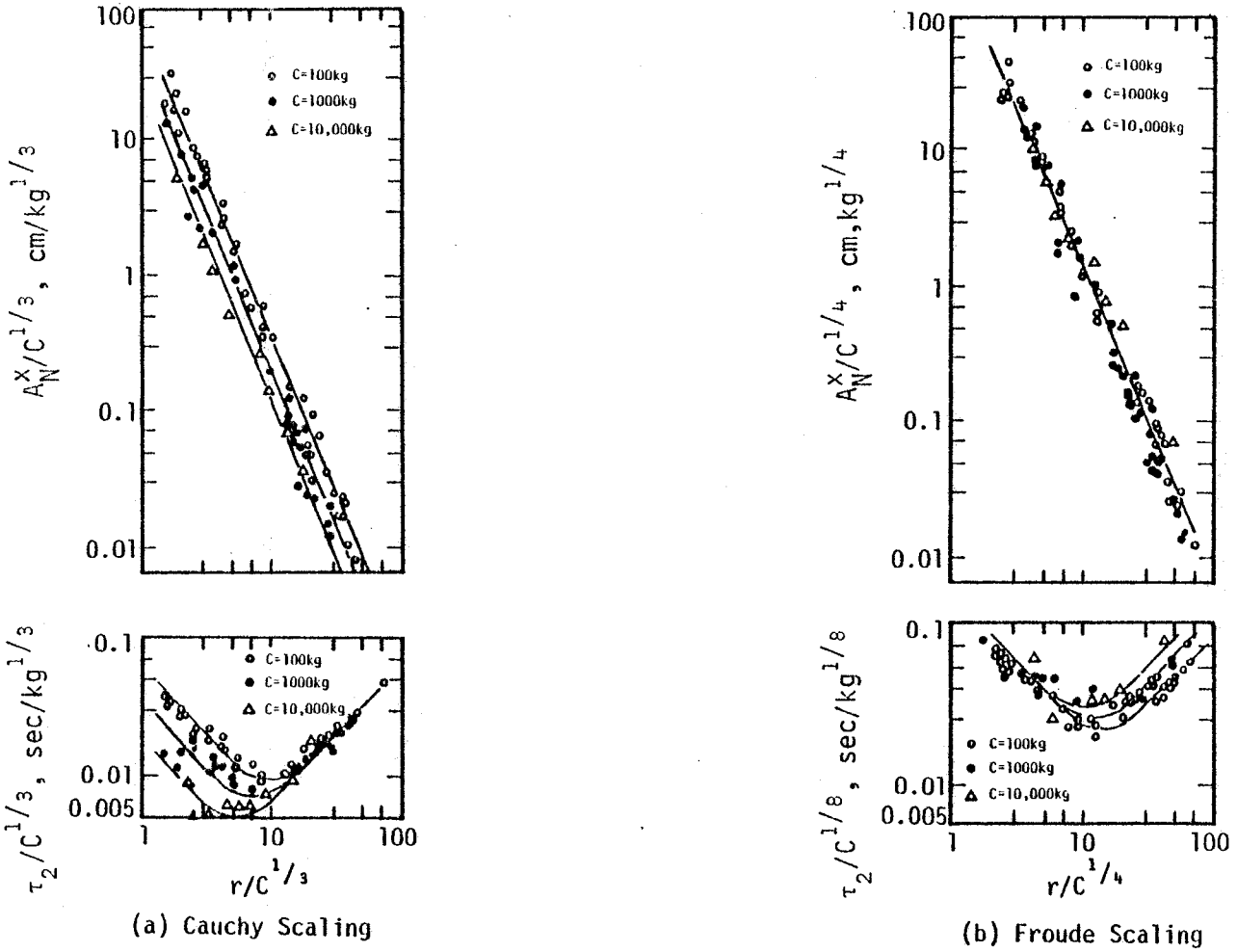

(a) Cauchy Scaling

(b) Froude Scaling

Figure II-19. Maximum Horizontal Displacement (A_N^X) and Its Time of Occurence (τ_2) Scaled After Cauchy and Froude (ref. II-4)

the peak displacements to a common fit and reference II-4 arrives at the conclusions that in the immediate vicinity of explosions in soil, gravity creates the greatest effect on the formulation of seismic waves.

The expressions for displacement are:

vertical component

$$A_p^z = 500 \frac{C}{r^3} \qquad \text{(II-12)}$$

where A_p^z = vertical displacement in cm

horizontal component

$$A_{N_o}^x = 300 \frac{C^{0.825}}{r^{2.3}} \qquad \text{(II-13)}$$

where $A_{N_o}^x$ = horizontal displacement in cm.

The characteristic time, τ_2, indicates that the transition from gravity influence to elastic force influence (i.e. $C^{\frac{1}{4}}$ scaling to $C^{\frac{1}{3}}$ scaling) occurs at a scaled range of about 10 m/kg$^{\frac{1}{3}}$. The characteristic time seems to decrease to this scaled range and increase thereafter. In addition, it is apparent that the times are grouped better by $W^{\frac{1}{4}}$ scaling up to this range and by $W^{\frac{1}{3}}$ scaling thereafter.

Reference II-4 notes several points which limit the conclusions of their results including the facts that the geologic layers were not modeled and the composition of the sites varied somewhat from explosion to explosion, and between areas 2 and 3. The smaller shots were conducted in loams and fissured clays while the 10,000 kg shot was in the deeper clay. Also, the natural attenuation rate of the parameter influ-

ences the degree to which scaling can be evaluated. Reference II-4 notes that if the velocity attenuates as $r^{-1.5}$ then $C^{\frac{1}{3}}$ and $C^{\frac{1}{4}}$ scaling give the same result, i.e.

$$u = A \frac{C^{0.5}}{r^{1.5}} \qquad \text{(II-14)}$$

where

u = velocity

A = a constant

Since reference II-4 finds the velocity attenuation rate to be between $r^{-1.6}$ and r^{-2}, the good agreement for $C^{\frac{1}{3}}$ scaling shown in figure II-16 does not completely verify the scaling. Because all measurements were made at the surface, it is possible that gravity (i.e. cratering) might be exerting a stronger influence on response than at greater depths.

Reference II-4 does not perform a similar modeling comparison for the surface wave (R) components of the motion because of the lack of layer depth modeling which strongly influences surface wave development and dispersion.

A short discussion of the meaning of $C^{\frac{1}{4}}$ or Froude scaling is appropriate here. Gravity scaling can be physically interpreted as meaning that the effect of material properties is small. Indeed, near the explosion, the shear strength of most soils is so small that all soils can be considered equally strong. It has been observed in numerous cratering experiments (e.g. ref. II-5) that the peak displacement is strongly dependent on the positive phase of the upward and outward velo-

city. The displacement results from severe shear failure and flow of the material. Initially the duration is long but it diminishes with range as the stresses drop and shear strength becomes important. In the range where shear strength is essentially zero, it is reasonable to expect that duration might be controlled by gravity. Peak velocity, however, is controlled by bulk or stiffness properties of the medium which are significant even at near ranges. Hence, $C^{\frac{1}{3}}$ scaling for velocity would be indicated. However, since duration strongly controls displacement, it is possible that $C^{\frac{1}{4}}$ scaling might be a better way to scale close-in displacements.

e. Defense Nuclear Agency (DNA) High Explosive Events

The Defense Nuclear Agency (formerly Defense Atomic Support Agency) has sponsored a large number of near-surface high explosive events from 1966 through the present. Table II-11 lists some of the important high explosive ground motion experiments. Reference II-6 summarizes major characteristics of many of the test events, and lists references for sources of the basic data and analyses. A large amount of the data has been accumulated in a computer accessible master file (ref. II-7) and is available for future analysis by interested technical personnel.

With the exception of MINERAL LODE, all the DNA sponsored events were conducted at or above the ground surface. As a result, airblast effects are major and, therefore, most of the basic data and analyses are not directly applicable to the earthquake simulation problem. MINERAL LODE was deeply buried in rock. Although at some future time rock may be of interest, this research is primarily concerned with soil response.

Table II-11

Some DNA Sponsored High Explosive Ground Motion Experiments

EVENT	YIELD	EXPLOSIVE	CONFIGURATION	HEIGHT OF BURST (ft)	SCALED HEIGHT OF BURST ($ft/ton^{\frac{1}{3}}$)	GEOLOGY
Distant Plain VI	100 Tons	TNT	Surface Tangent Sphere	8	1.72	Silty Clay Alluvium (Glacial)
Prairie Flat	500 Tons	TNT	Surface Tangent Sphere	13.5	1.70	Silty Clay Alluvium (Glacial)
Mine Under	100 Tons	TNT	Sphere- above 2 Charge Radii above	14.2	3.06	Quartz Diorite
Mine Ore	100 Tons	TNT	Sphere-base buried 0.1 Charge Radii	7.2	1.55	Quartz Diorite
Mineral Lode	15.8 Tons	Ammonium Nitrate Slurry	Buried Sphere	-100	-40	Quartz Diorite
Mineral Rock	100 Tons	TNT	Sphere-Base Buried 0.1 Charge Radii	7.2	1.55	Quartz Diorite
Dial Pack	500 Tons	TNT	Surface Tangent Sphere	13.5	1.70	Silty Clay Alluvium (Glacial)
Snowball	500 Tons	TNT	Hemisphere on Surface	6.4	0.81	Silty Clay Alluvium (Glacial)
Mixed II	20 Tons	TNT	Surface Tangent Sphere	4.6	1.70	Sand/Sandstone
Company III	500 Tons	TNT	Surface Tangent Sphere	13.5	1.70	Sand/Sandstone
Middle Gust I	20 Tons	TNT	Sphere-Half Buried	0	0	"Wet" Clay/Shale
II	100 Tons	TNT	Sphere-2 Charge Radii above	16.0	3.45	"Wet" Clay/Shale
III	100 Tons	TNT	Surface Tangent Sphere	8.0	1.72	"Wet" Clay/Shale
IV	100 Tons	TNT	Surface Tangent Sphere	8.0	1.72	"Dry" Clay/Shale
V	20 Tons	TNT	Sphere-Half Buried	0	0	"Dry" Clay/Shale

f. Underground Nuclear Explosions

Several underground nuclear tests events have been conducted by the United States, and their results are summarized in reference II-8. Table II-12 lists some of the important events and their characteristics. Although coupling effects between conventional high explosives and nuclear explosives differ, information on attenuation rates and geologic dependencies are available from nuclear data. Reference II-8 divides the available data into separate categories for hard rock, soft rock, and dry soil. Those categories were established by generalizing the observation that data from various types of hard rock were encompassed by the data bounds for granite. The bounds on the particle motions for the three categories are shown in figures II-20, II-21, and II-22, where the bounds have been established from measured data.

The peak ground motions at intermediate ranges due to contained bursts in hard rock may be estimated by the following relations which define the average and approximate bounds of granite data.

$$v = 200 \text{ ft/sec} \left(\frac{W}{1MT}\right)^{\frac{2}{3}} \left(\frac{R}{1kft}\right)^{-2} \quad \pm \text{ a factor of } 2.5 \qquad \text{(II-15)}$$

$$d = 200 \text{ in} \left(\frac{W}{1MT}\right)^{\frac{5}{6}} \left(\frac{R}{1kft}\right)^{-\frac{3}{2}} \quad \pm \text{ a factor of } 2 \qquad \text{(II-16)}$$

$$a = 3500 \text{ g} \left(\frac{W}{1MT}\right) \left(\frac{R}{1kft}\right)^{-4} \quad \pm \text{ a factor of } 2.5 \qquad \text{(II-17)}$$

where

d = peak displacement

v = peak particle velocity

a = peak acceleration

W = yield

R = range

Table II-12

Some Contained Nuclear Tests Providing Direct-Induced Ground Shock Data (ref. II-8)

Medium	Shot Name	Yield
Alluvium*	FISHER	13.3kT
	HAYMAKER	48kT
	HOGNOSE	**
	RINGTAIL	4.9kT
Tuff (Seismic Velocity - 7000 fps)	RAINIER	1.7kT
	EVANS	55 tons
	TAMALPAIS	72kT
	MADISON	**
Granite (Seismic Velocity - 18000 to 19000 fps)	HARDHAT	5.9kT
	SHOAL	12kT
	PILEDRIVER	61kT
Dolomite (Seismic Velocity - 14,100 fps)	HANDCAR	10kT
Andesite (Seismic Velocity - 14,100 fps)	LONGSHOT	81kT
	MILROW	1MT
	CANNIKIN	5MT
Salt (Seismic Velocity - 13,400 fps)	GNOME	3kT

* Seismic velocity varies with depth ranging from 3000 fps (914 m/sec) from 175 feet (53 m) to 650 feet (198 m) to 10,000 fps (3050 m/sec) below 650 feet (198 m).

** Classified Field

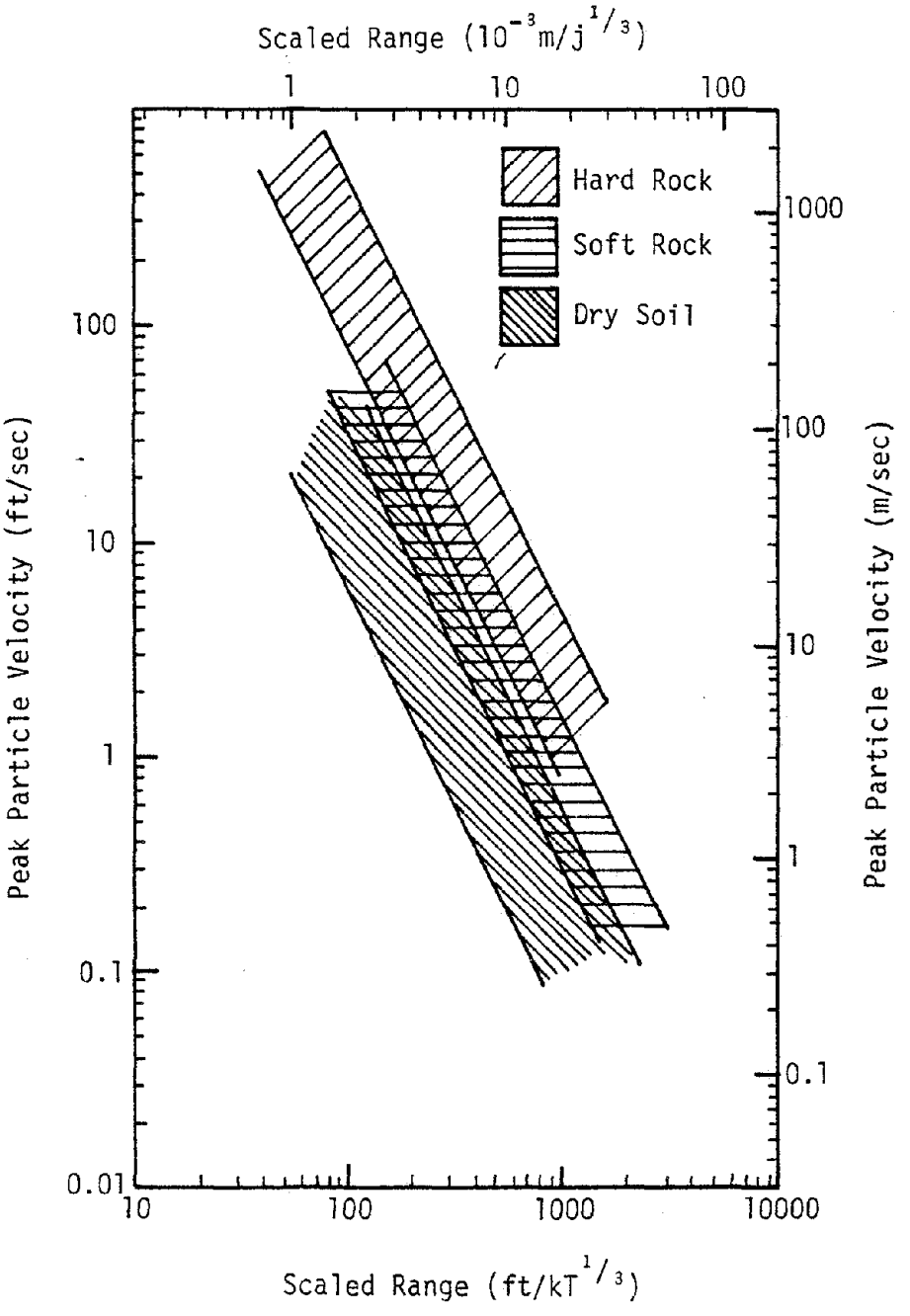

Figure II-20. Peak Particle Velocity Bounds for Hard Rock, Soft Rock, and Dry Soil (Ref. II-8)

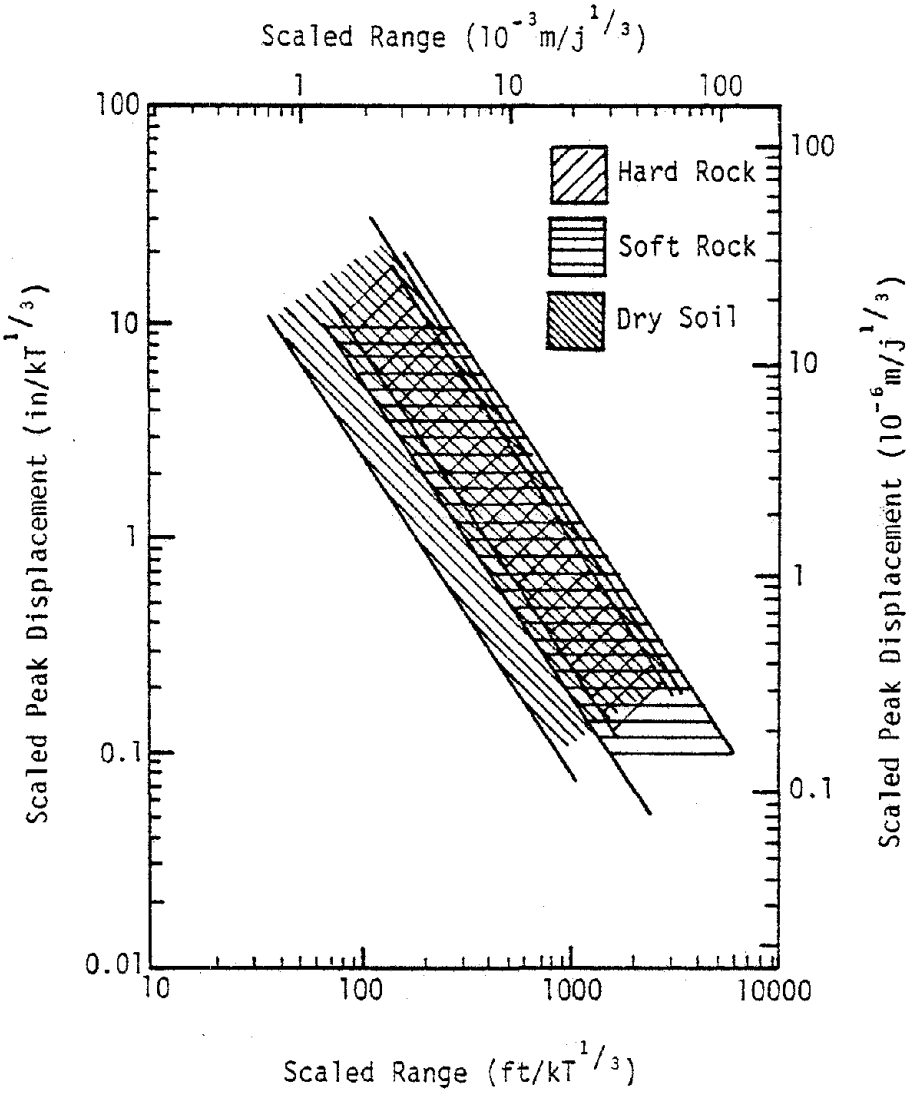

Figure II-2T. Scaled Peak Displacement Bounds for Hard Rock, Soft Rock, and Dry Soil (ref. II-8)

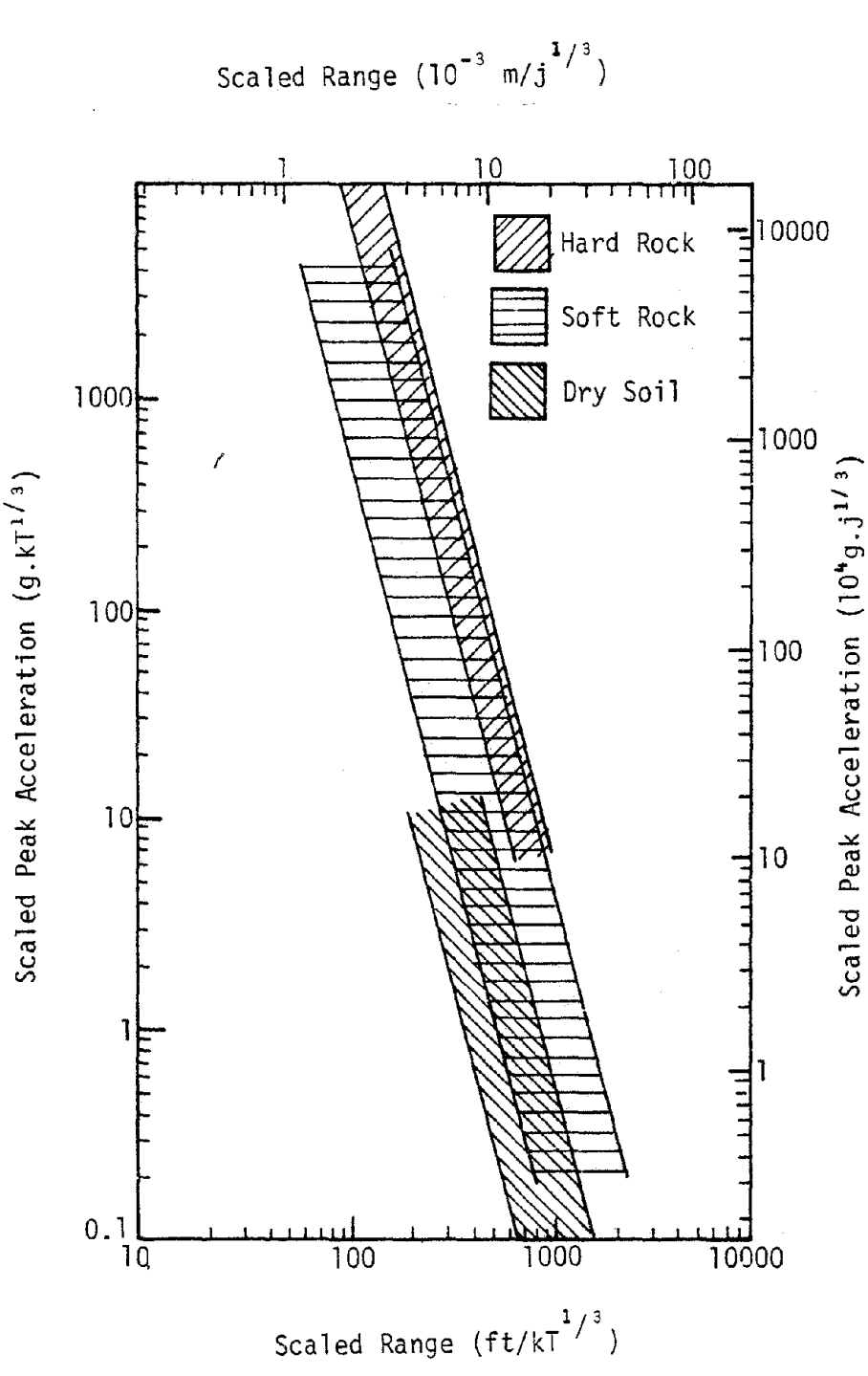

Figure II-22. Scaled Peak Acceleration Bounds for Hard Rock, Soft Rock, and Dry Soil (Ref. II-8)

The corresponding relations for soft rock, defined by the approximate bounds for tuff, are the following

$$v = 80 \text{ ft/sec} \left(\frac{W}{1MT}\right)^{\frac{2}{3}} \left(\frac{R}{1kft}\right)^{-2} \quad \pm \text{ a factor of 2} \qquad \text{(II-18)}$$

$$d = 160 \text{ in} \left(\frac{W}{1MT}\right)^{\frac{5}{6}} \left(\frac{R}{1kft}\right)^{-\frac{3}{2}} \quad \pm \text{ a factor of 3} \qquad \text{(II-19)}$$

$$a = 600 \text{ g} \left(\frac{W}{1MT}\right) \left(\frac{R}{1kft}\right)^{-4} \quad \pm \text{ a factor of 5} \qquad \text{(II-20)}$$

The bounds of the alluvium data, given below, are recommended for estimates of peak motion quantities at intermediate ranges due to contained burst in dry soils.

$$v = 20 \text{ ft/sec} \left(\frac{W}{1MT}\right)^{\frac{3}{2}} \left(\frac{R}{1kft}\right)^{-2} \quad \pm \text{ a factor of 3} \qquad \text{(II-21)}$$

$$d = 100 \text{ in} \left(\frac{W}{1MT}\right)^{\frac{5}{6}} \left(\frac{R}{1kft}\right)^{-\frac{3}{2}} \quad \pm \text{ a factor of 4} \qquad \text{(II-22)}$$

$$a = 120 \text{ g} \left(\frac{W}{MT}\right) \left(\frac{R}{kft}\right)^{-4} \quad \pm \text{ a factor of 5} \qquad \text{(II-23)}$$

Reference II-8 notes that particle velocities (fig. II-20) at a given range are, on the average, highest for hard rock, intermediate for soft rock and lowest for dry soil. The particle velocity trend is in agreement with the concept that the more hysteretic a material the greater the close-in peak stress and velocity attenuation. A similar trend exists in the acceleration data (fig. II-22) and is also in agreement with existing knowledge of material behavior. Increases in rise time and attenuations of peak particle velocity and, therefore, attenuation of acceleration are directly related to material nonlinearity and hysteresis.

Peak displacements (fig. II-21) are not as readily interpretable.

Peak displacements in tuff are, on the average, higher than in hard rock while displacements in dry soil are less than in hard rock. In a homogeneous elastic medium, peak displacement is directly proportional to impulse and inversely proportional to characteristic impedance (density X wave velocity). Assuming the impulse delivered at a given range is the same in both hard rock and soft rock, displacement will be greater in soft rock because soft rock has a lower characteristic impedance, in agreeement with hard rock and tuff data. The impulse argument does not explain the alluvium data, however. Since peak displacement is a late time phenomena, displacement is easily affected by free surface effects (which ultimately occur in all contained events) and reflections. Free surface and/or reflection effects may be playing a stronger role in alluvium events than in events in rock. In any case, reference II-8 states that the observed displacement differences between the materials are believed real and should be expected in future events in similar geologies.

g. DIHEST Improvement Program (DIP)

In the late 1960's the Air Force developed a method for simulating the direct induced ground shock effects from a weapon burst. The method, called the DIHEST technique (Direct Induced High Explosive Simulation Technique), involved the use of high explosives in various arrays in which the array size, shape, and explosive loading density were varied to obtain the desired ground motion effects. Early large scale applications were in rock. However, in the early 1970's the University of New Mexico, as contractor to the Air Force Weapons Laboratory, under-

took a program to apply the DIHEST technique in soils. The results of the work are reported in references II-9 through II-13.

Reference II-9 reports the results of 13 developmental tests performed in a silty sand at the McCormick Ranch Test site south of Albuquerque. The experiments were designed to investigate enhancement techniques with potential for lengthening motion duration and sustaining large displacements, while maintaining relatively low levels of velocity, acceleration, and stress. Although the motion levels of interest were higher than those of interest in earthquakes, the objectives are directly applicable to earthquake simulation. Techniques tested were focusing, decoupling, and boundary relief.

The focusing concept employs a geometric arrangement of explosives to concentrate energy from a large array into a small region to increase durations and displacements in the region. Decoupling is the detonation of charges in closed air cavities in the soil to reduce the input pressure to the soil and extend the duration of the driving function. Boundary relief consists of providing a reflective boundary in the test medium (usually by trenching) to obtain reflections which maintain displacement and velocity intensities over longer periods of time.

Table II-13 summarizes the characteristics of the experiments and their ofjectives. Figures II-23 and II-24 show the layout and some results for the decoupled (Shots 6 and 7) and coupled (Shot 8) cylindrical experiments. Within the scatter of the data there does not appear to be a significant difference in the peak velocity amplitudes between decoupled and coupled charges. Frequency content, however, does appear

Table II-13

DIHEST Enhancement Program
Explosive Placement, Geometry and Array Parameters (Information from ref. II-9)

Shot #	Explosive Array	ARRAY GEOMETRY					EXPLOSIVES					OBJECTIVES
					Array Details				Placement	Density		
		L ft.	H ft.	S ft.	Arc Angle degrees	R ft.	Type	W lbs	N Holes	α lbs/ft^2	γ lbs/ft	
1	Planar	12	4	4	-	-	PETN	48	C	1	*	Focusing (1 vs 2)
2	V-Shape	12	4	4	60	-	PETN	48	C	1	-	Focusing (1 vs 2)
3	Planar	20	6.7	6	-	-	PETN	133	16	1	(1.24)	Focusing (3 vs 4,5)
4	Curved	20	6.7	6	120	9.5	PETN	133	16	1	(1.24)	Focusing (3 vs 4)
5	Curved	20	6.7	6	120	9.5	PETN	133	16	1	(1.24)	Repeat of 4
6	Cylindrical	-	12.	6	-	-	PETN	60	1	-	5	Decoupling (6,7 and 8)
7	Cylindrical	-	12.	6	-	-	PETN	60	1	-	5	Decoupling (6,7 and 8)
8	Cylindrical	-	12.	6	-	-	PETN	60	1	-	5	Coupling (6,7 and 8)
9	Planar	40	13.3	8	-	-	PETN	2133	11	4	(14.5)	Relief (9A vs 9B)
10	Curved	40	13.3	8	120	19	PETN	2133	11	4	(14.5)	Focusing (9A vs 10)
11	Curved	40	13.3	8	120	19	PETN	2133	7	4	(22.9)	Decoupl.in Arr.(10 vs 11)
12	Cylindrical	-	13.3	8	-	-	PETN	305	1	-	22.9	Yield Variation(12 vs 6,7)
13	Planar	40	13.3	8	-	-	PETN	533	11	1	(3.6)	Relief Variation(9 vs 13)

NOTES: 1. Figures in ( ), indicate equivalent line (cylindrical) charge per drill-hole

2. C indicates continuous charge density in a trench configuration.

3. Symbols: L = array length, H = array height, S = height of surcharge above explosive, W = explosive weight, α = areal charge density in two dimensional array, γ = line charge density in cylindrical charge, R = radius of curved array

* Absence of a value for γ indicates explosive was distributed uniformly in a trench.

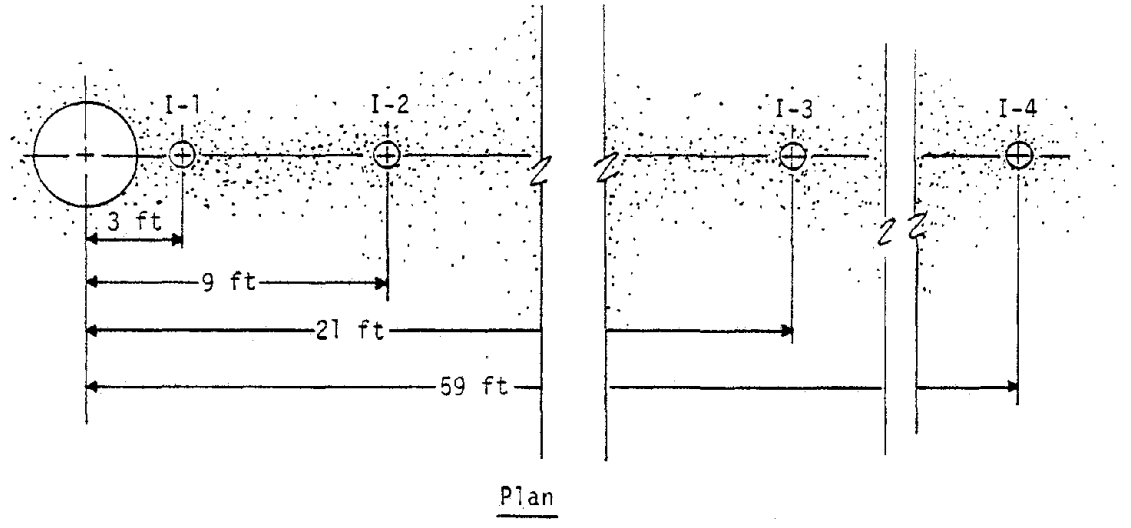

Note: Shot 6, D = 3 ft, Decoupled, Distributed Charge
Shot 7, D = 3 ft, Decoupled, Charge concentrated on centerline
Shot 8, D = 9 in, Grouted, Charge concentrated on centerline

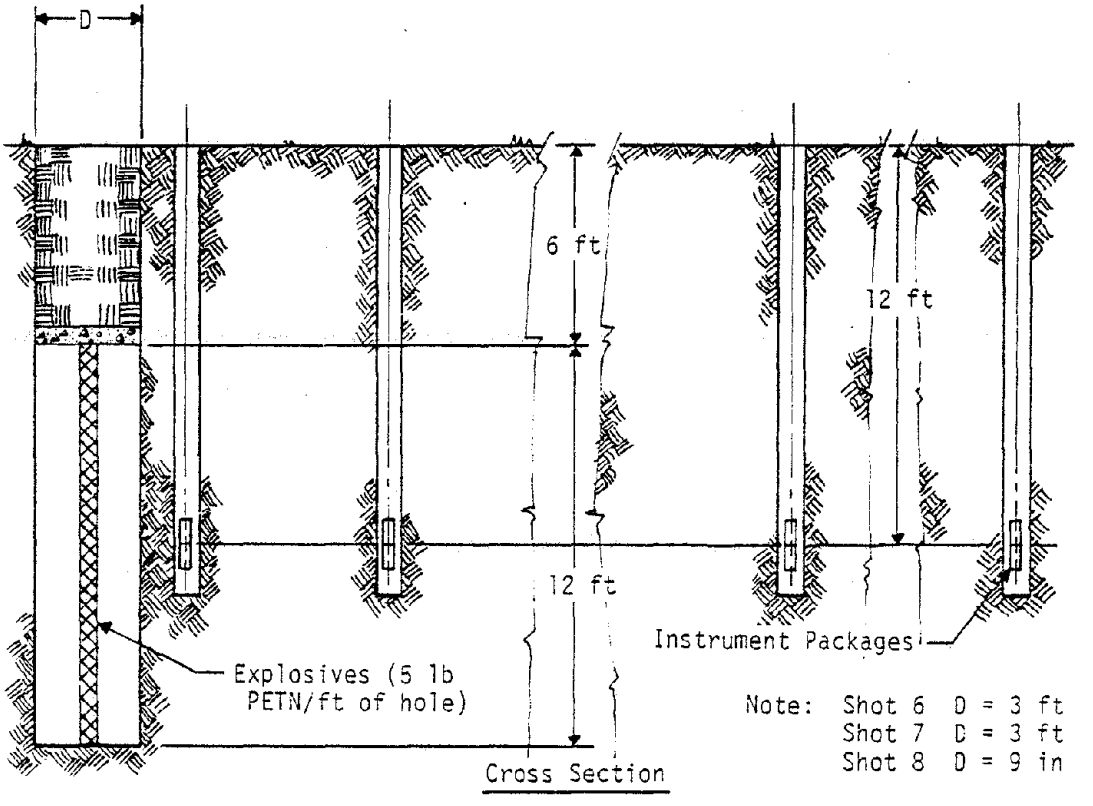

Figure II-23. Shots 6, 7, and 8 Testbed Layout (ref. II-9)

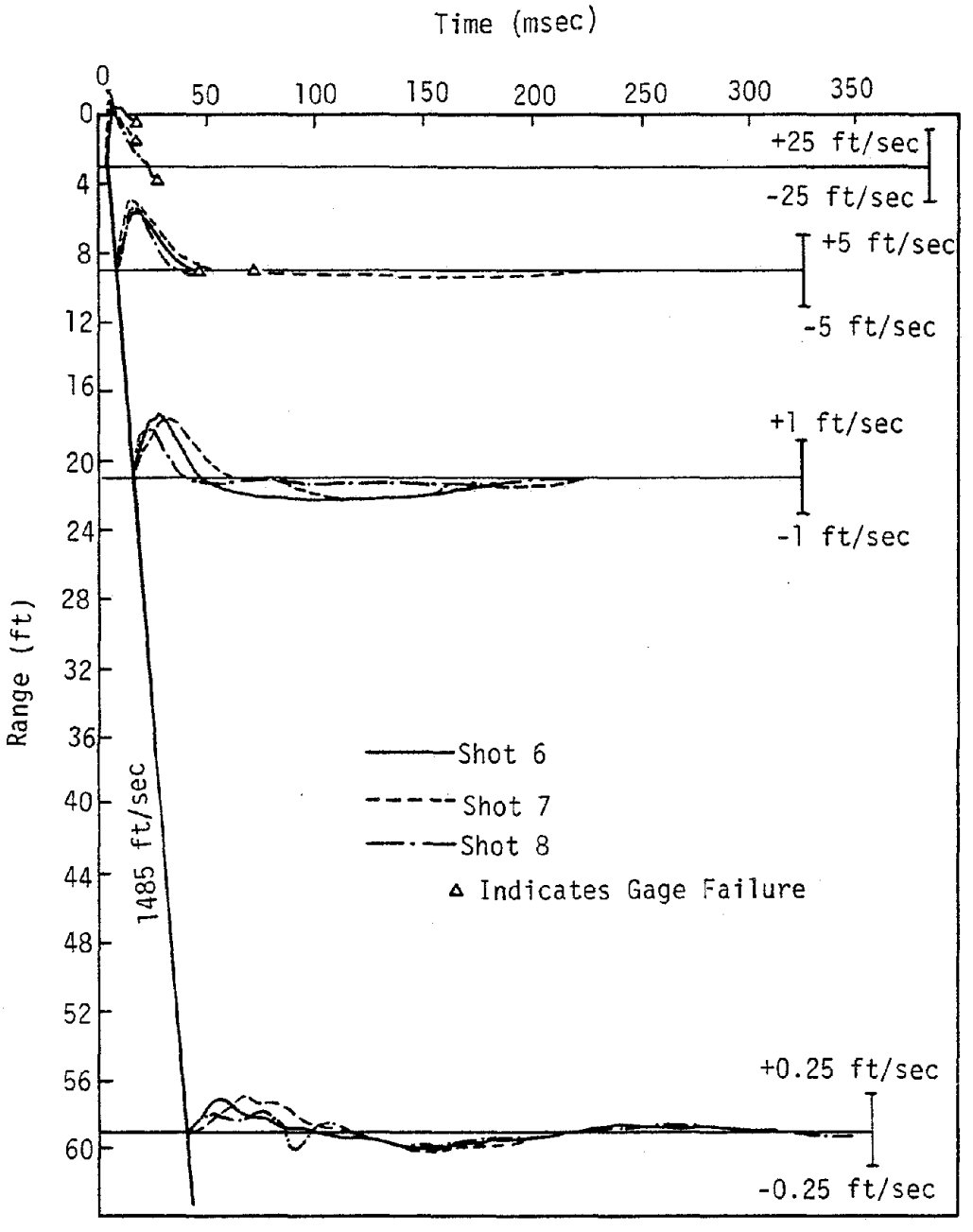

Figure II-24. Integrated Accelerations (Velocity Time Histories) from Cylindrical Shots of DIHEST Enhancement Study (Data from ref. II-9)

to be affected. Figure II-25 shows the layout for Shots 3 and 4 which were intended to evaluate the effect of focusing from arrays. It was hoped that the same instrumentation could be used for both shots. Shot 3 was fired first and destroyed instrument holes I-1 and I-2. In addition, reference II-9 suspected that the medium properties were significantly altered by Shot 3 and, as a result, questioned the validity of Shot 4. Shot 5 was performed as a repeat of Shot 4. The results of Shots 3 and 5 are compared in table II-14 where the ratios between ground shock parameters measured in Shot 5 and those measured in Shot 3 are tabulated at each range. It can be seen that focusing significantly increases the ground shock amplitude.

The configurations and results for two boundary relief experiments (ref. II-9) are shown in figures II-26 and II-27, respectively. Test 9 consisted of a 40-ft by 13-1/3-ft rectangular array of PETN explosive buried 8-ft with a charge density of 4 lb/ft^2. A free boundary was created by an 80-ft by 3-1/2-ft deep trench located 40-ft from the explosive array. Instrumentation was located on both sides of the array allowing comparison of the effect of relief and no relief. It can be seen in figure II-27 that the boundary has no effect upon peak acceleration. However, attenuation of velocity decreases at a distance about halfway to the relief trench and displacements are enhanced throughout the instrumented region.

Test 13 was similar to Test 9 except that the charge density was reduced to 1 lb/ft^2 and partial relief was provided on one side of the explosive array with a rectangular pattern of 3-ft diameter, 25-ft deep drill holes over an area 100-ft by 12-ft, and 1-ft diameter relief holes

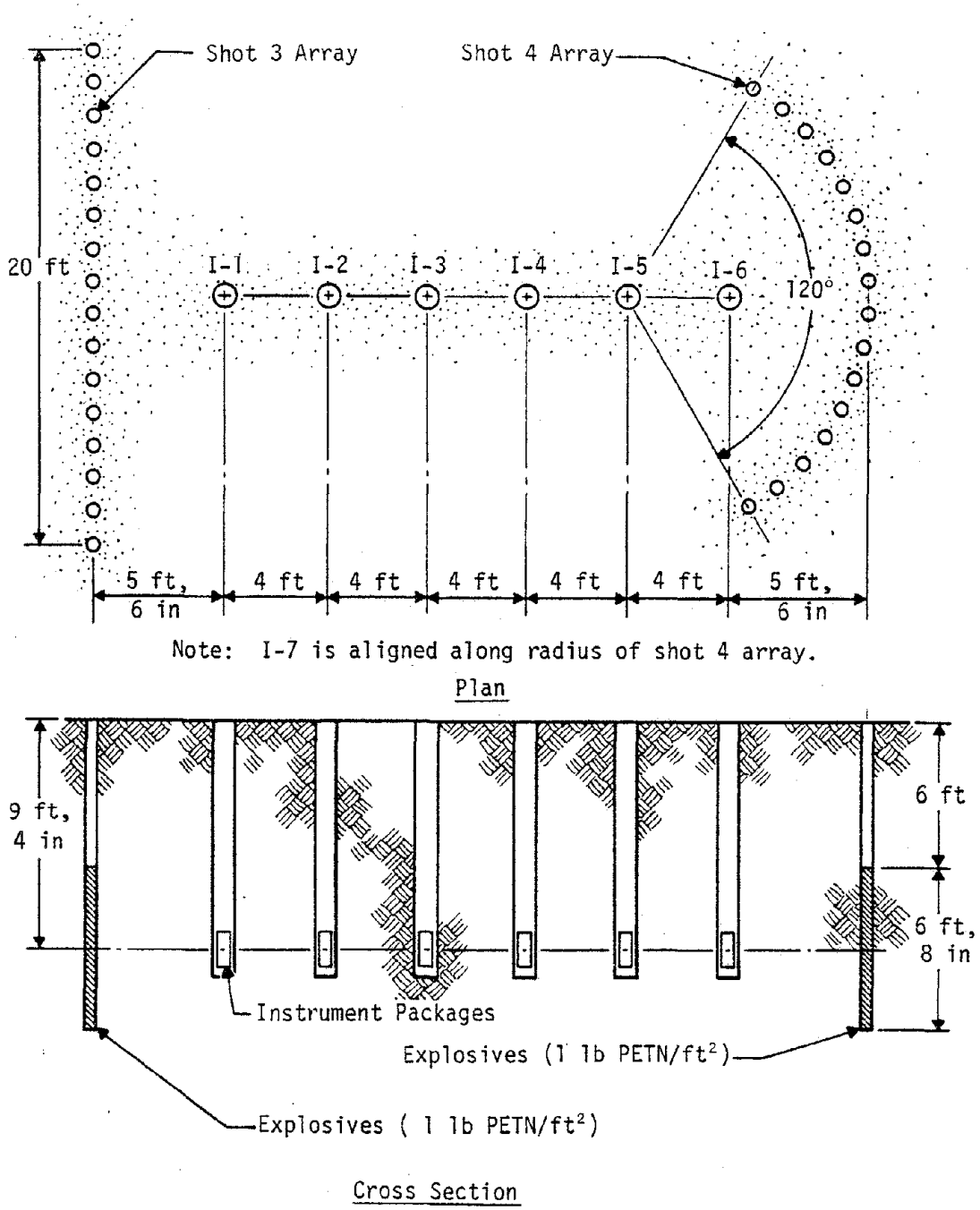

Figure II-25. Test 3 and Test 4 Layout (ref. II-9)

Table II-14

Comparison of Shots 3 and 5 Peak Values*
(Focusing Comparison(ref. II-9)

PARAMETER	RANGE, FT.					AVERAGE INCREASE %
	9-1/2**	13-1/2	17-1/2	21-1/2	25-1/2	
VELOCITY	1.28	2.19	1.17	0.55	2.00	44
DISPLACEMENT	1.04	1.78	1.06	0.55	2.25	34
ACCELERATION	1.28	3.56	2.76	1.39	2.11	122
STRESS	1.89	1.43	0.95	4.80	2.00	121

* Shot 5 Peak Values Divided by Shot 3 Peak Values.

** Focal Point on Shot 5.

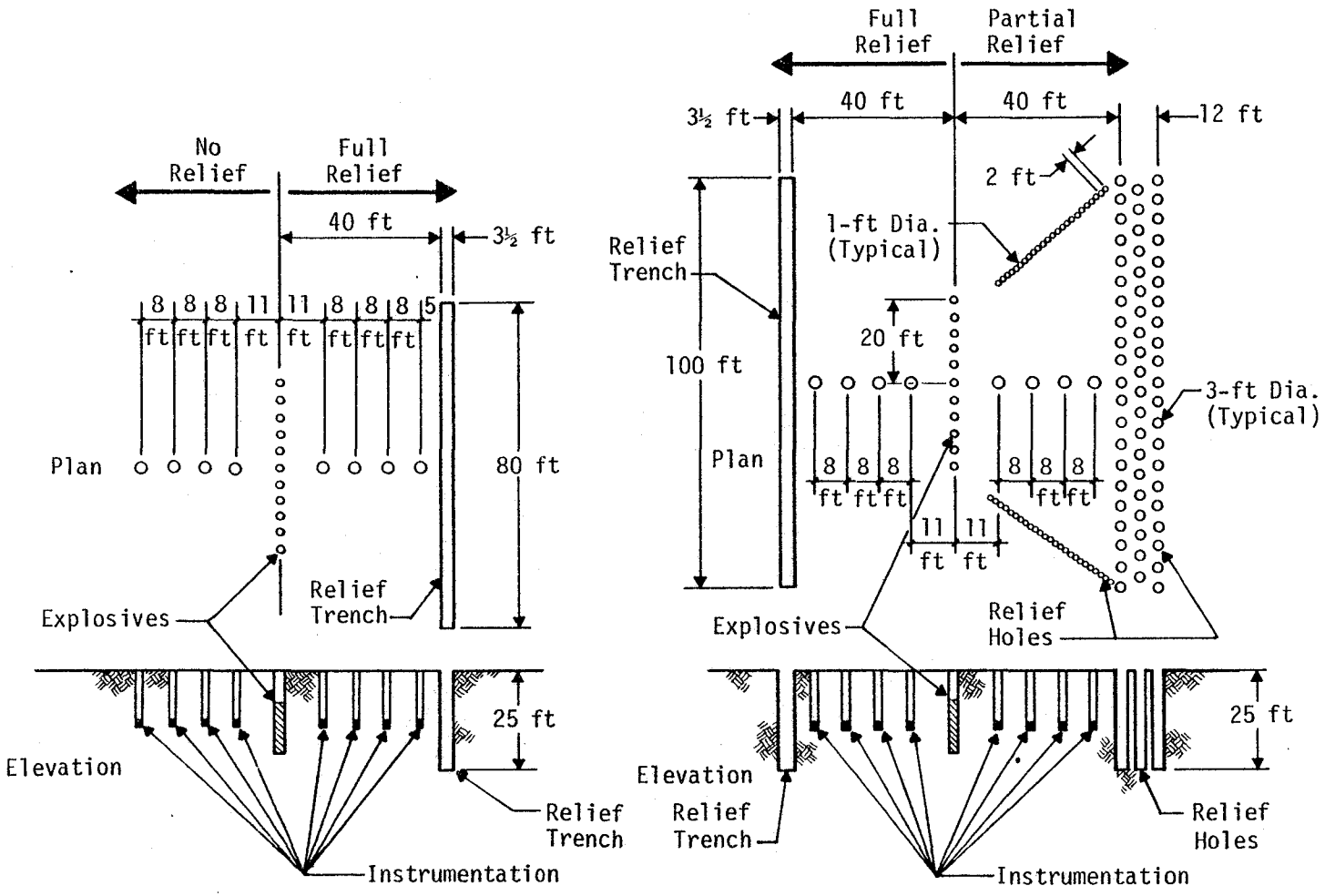

(a) Shot No. 9 Test Layout

(b) Shot No. 13 Test Layout

Figure II-26. Configurations of the Boundary Relief Experiments (ref. II-9)

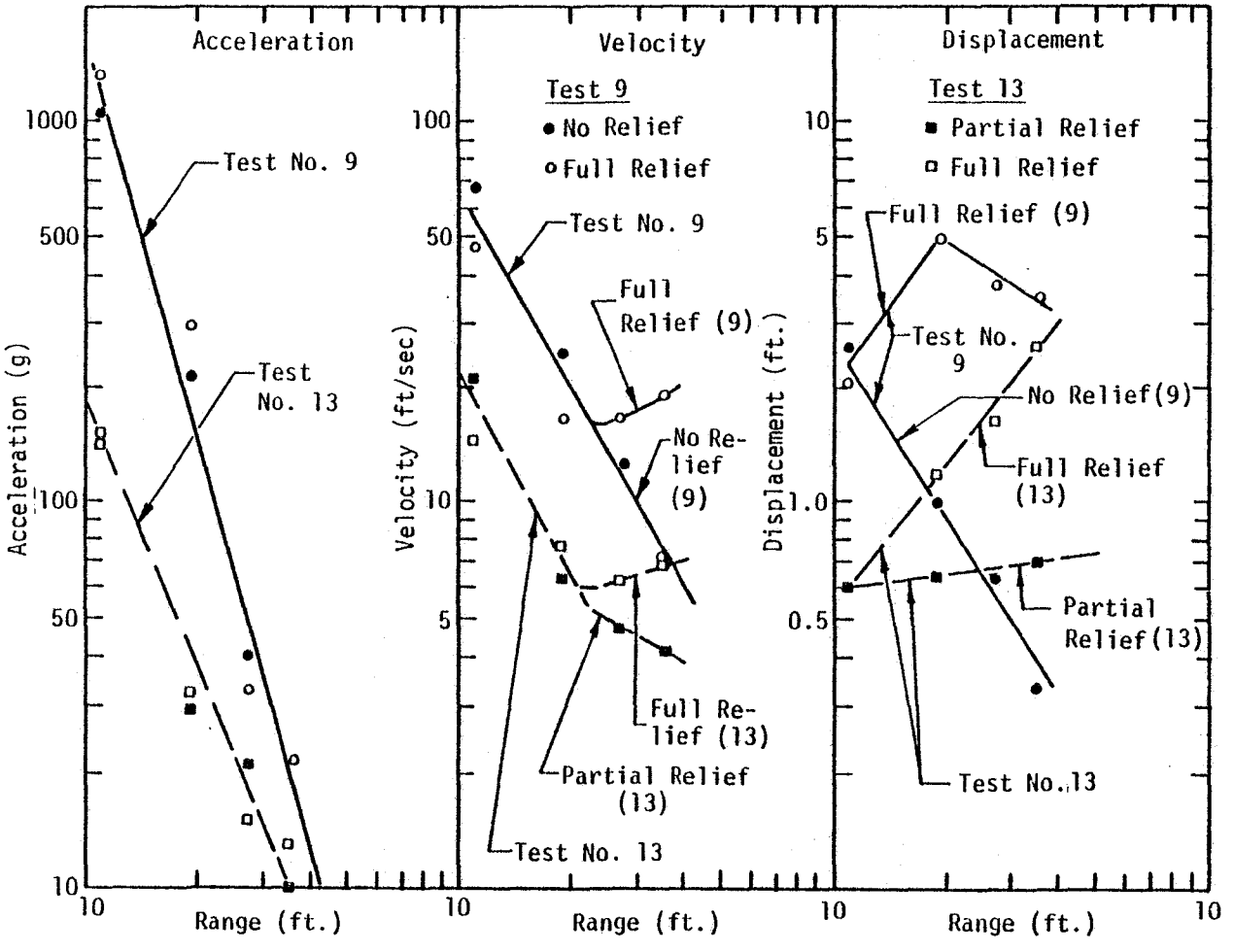

Figure II-27. Effect of Boundary Relief on Ground Motion Parameters (ref. II-9)

along the side boundaries of the test area. As in Test 9, a relief trench was provided on the opposite side of the explosive array. The reduced charge density results in overall reduced motions as can be seen in figure II-27. As in Test 9, the relief condition does not affect accelerations. Partial relief provides effects on velocities and displacements which are intermediate between the complete relief and no relief conditions. Reference II-9 concluded that boundary relief produces the greatest increase of displacements and duration, followed by decoupling and then focusing. In addition, boundary relief reduces the attenuation of particle velocity with range.

In addition to the enhancement study, five relatively large events (DIP IA through VA) were conducted to evaluate the effects of DIHEST in soil on a large scale. The important characteristic of the tests are given in table II-15.

DIP IA (ref. II-10), conducted in March 1971, was a large fully contained single concentrated charge which was intended to provide a basis for comparing array response with single charge response. The charge consisted of 40-tons of IRECO DBA-22M slurry in a cylindrical shape 10-ft in diameter and 10-ft, 4-in high. The charge was buried 40 feet to its center. Reference II-10 considered the 40 tons of slurry approximately equivalent to 50 tons of TNT.

The test was conducted at the McCormick Ranch Test Site. Reference II-10 provides a simplified soil profile and the results of triaxial tests from samples at the site. This soil data are considered in combination with other available data in more detail in a later section.

Table II-15

Parameters for Large Soil DIHEST Events

Event	Array Type	ARRAY GEOMETRY L ft	H ft	S ft	EXPLOSIVES Type	W Tons	No. of Holes	Density α lbs/ft^2	Density γ lbs/ft	Remarks	Reference
DIP IA	Concentrated Charge	-	-	40*	DBA-22M Slurry	40	-	-	-	Large concentrated charge	II-10
DIP IIA	Planar Array	208	35	30	DBA-22M Slurry	40	29	11.4	(78.8)	Largest charge density array	II-11
DIP IIIA	Planar Array	107.5	33	20	DBA-22M Slurry	3.3	15	1.86	(13.33)	Boundary relief Experiment	II-12
DIP IVA	Concentrated Charge	-	-	10.75*	DBA-22M Slurry	0.5	-	-	-	Small concentrated charge	II-13
DIP VA	Planar Array	1134	204	30	65T2 Slurry	40	16	0.35	(24.5)	Largest size array smallest charge density	II-13

* Depth to center of concentrated charge

Notes and nomenclature are the same as for table 13.

Measurements in the test event consisted of particle velocity, acceleration and soil stress in three orthogonal directions at 53 locations. Velocity was the primary measurement. The quality of the measured data, however, was poor. Reference II-10 states that the pre-test predictions were low. As a result, most of the gages either failed or band-edged. The close-in data in reference II-10, therefore, has little direct use. Far-field measurements, however, were reliable and they are given in figure II-28). Seusy (ref. II-14) has made an unpublished interpretation of some of the radial failed and band-edged gages and the results are given in table II-16.

DIP IIA (ref. II-11), conducted at McCormick Ranch in June 1971, was a large planar array test involving 40 tons of IRECO DBA-22M slurry placed in 29 drill holes which were 7-ft 2-in on center. Important test parameters are given in table II-15. The configuration approximated a planar array 208-ft long by 35-ft deep loaded with 11.4 lbs/ft^2 of slurry explosive. The test contained the largest areal charge density of any soil DIHEST conducted.

The test layout, including instrumentation holes, is shown in figure II-29. Instrumentation recovery was quite good. Peak horizontal velocities and displacements from reference II-11 are shown in figures II-30 and II-31. The large scatter is due to the fact that all data, without regard to depth, are plotted together. Radial seismic motions are shown in figure II-32. A typical horizontal velocity measured in DIP IIA is shown in figure II-33. It is believed that the characteristics of the motion are of the type of interest in earthquake simulation.

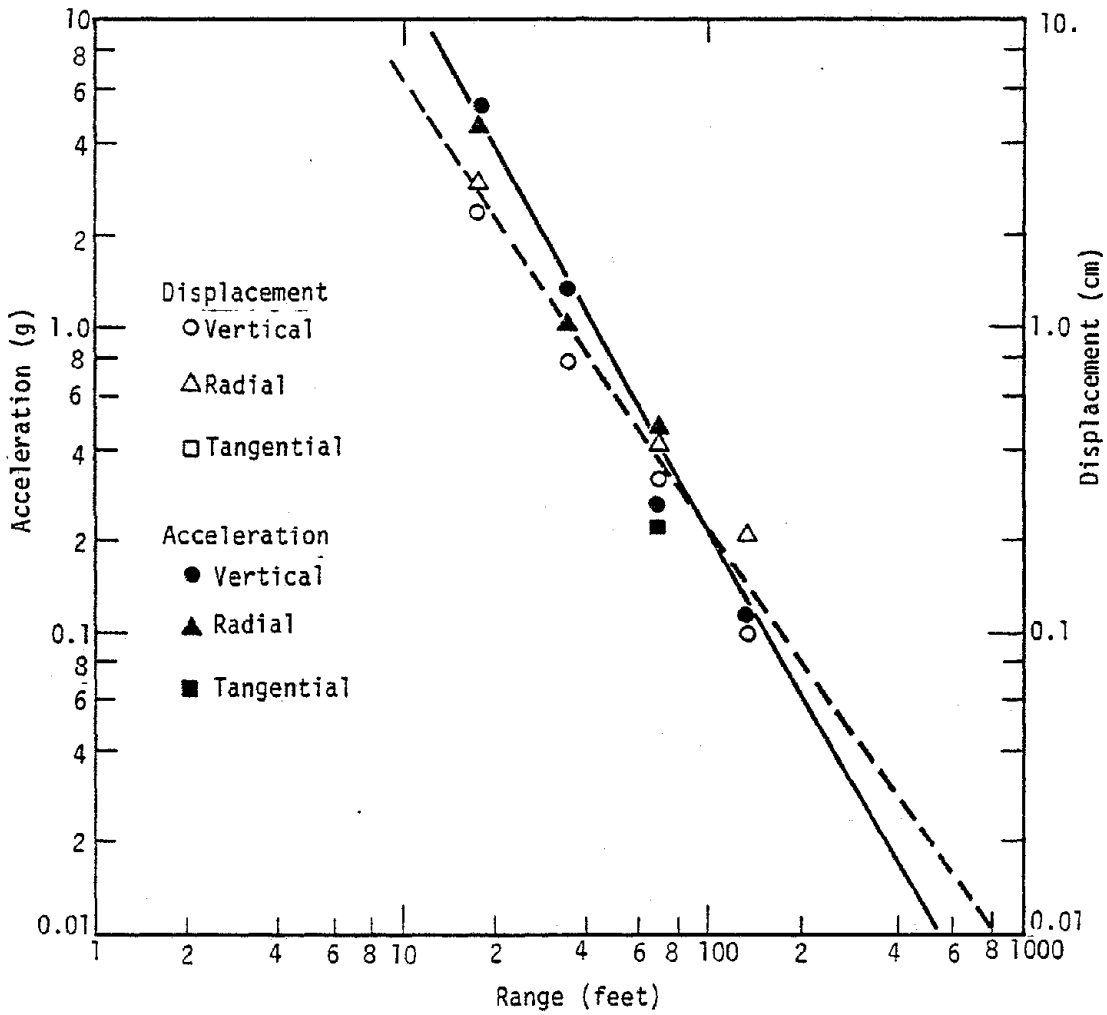

Figure II-28. DIP IA Strong Motion Surface Accelerations and Displacements (ref. II-10)

Table II-16

Approximate Radial Motion From DIP IA (ref. II-14)

Range (ft)	Acceleration (g)	Velocity (ft/sec)	Displacement (in)
40	-	-	-
60	219	37.5	-
90	11.3	14.6	26.8
135	1.2	3.2	6.2
200	0.69	1.5	2.6

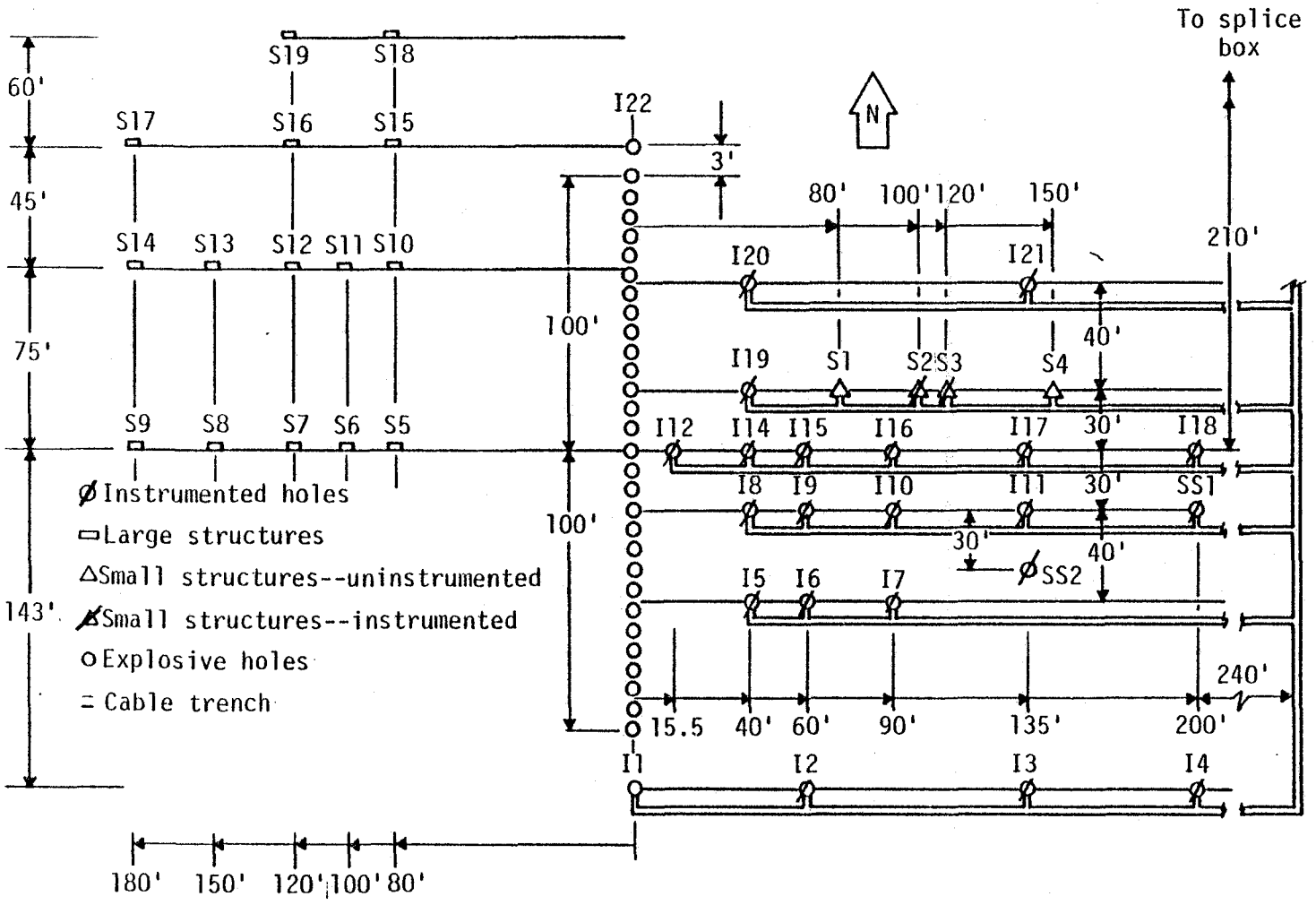

Figure 29. DIP IIA Testbed Layout (ref. II-11)

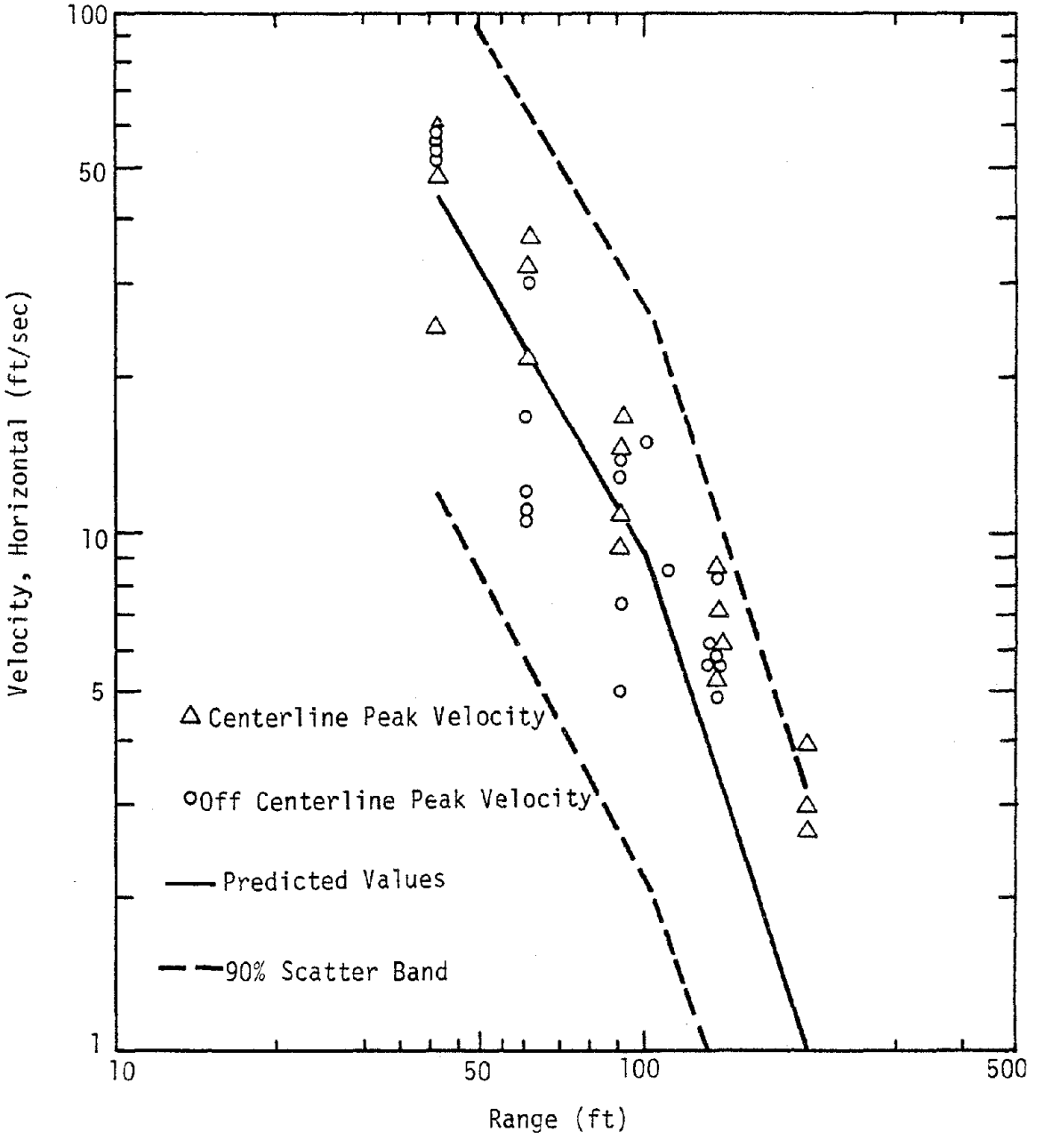

Figure II-30. Comparison of Predicted and Measured Velocities on DIP IIA (ref. II-11)

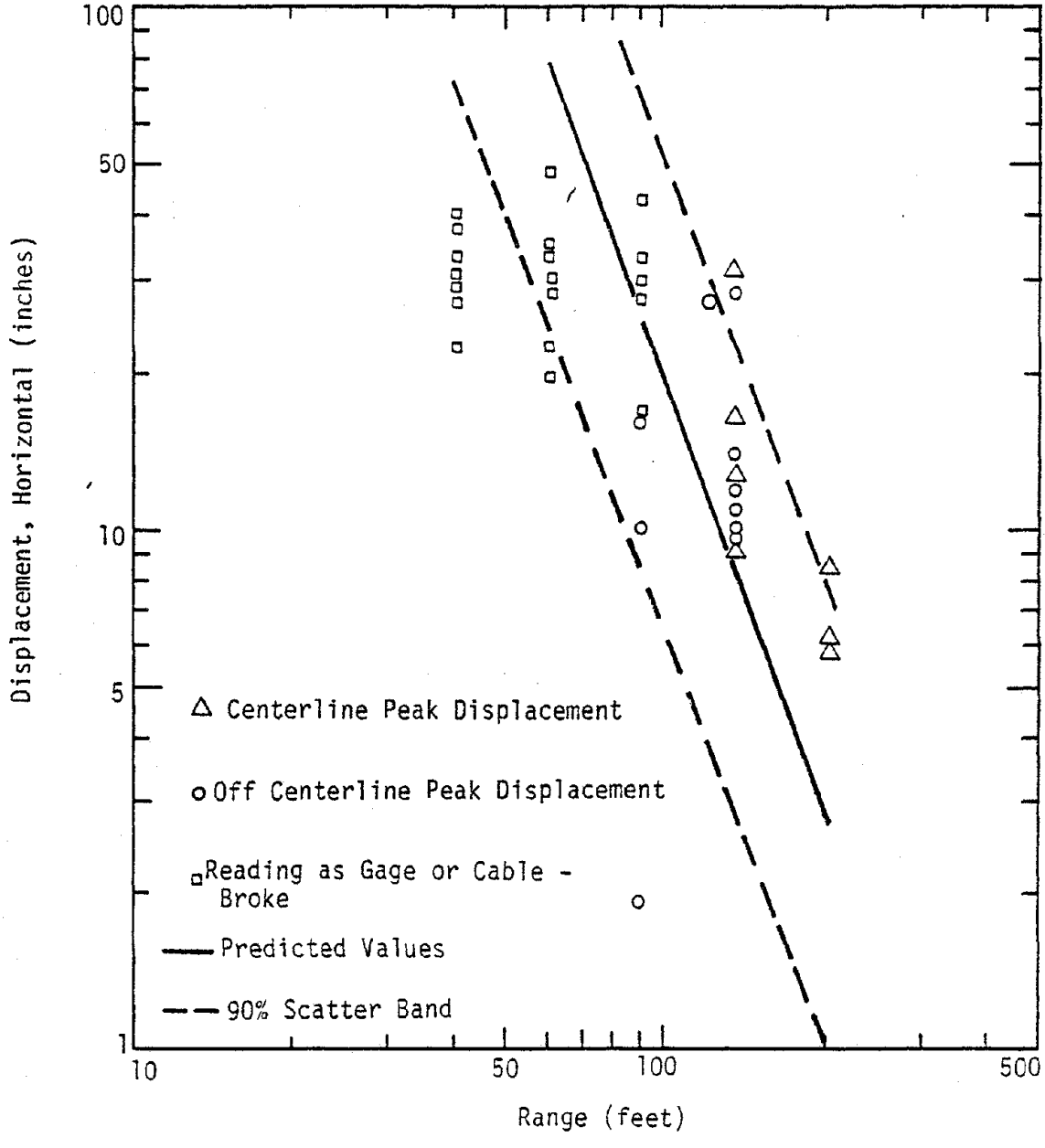

Figure II-31. Comparison of Predicted and Measured Displacements on DIP IIA (ref. II-11)

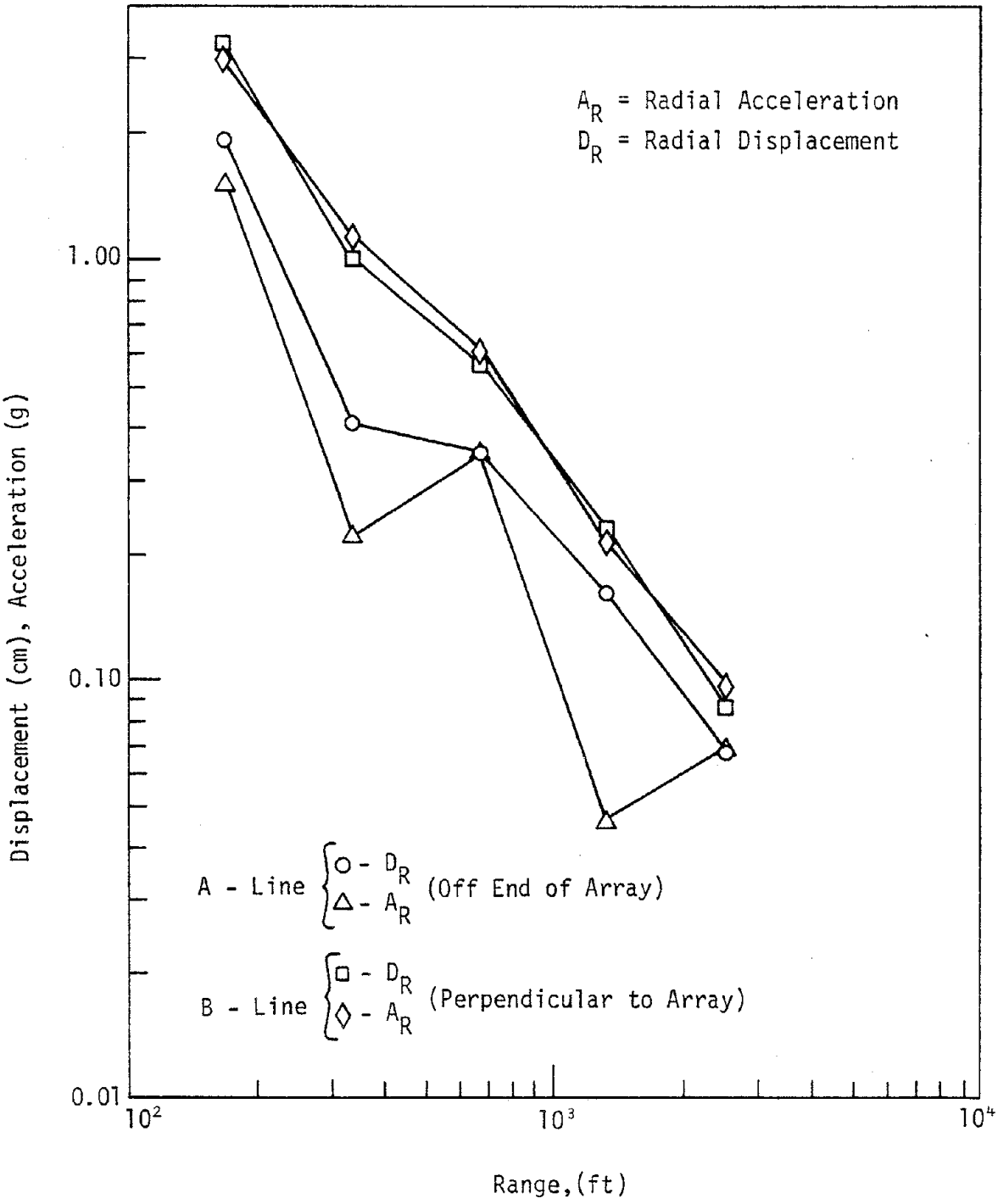

Figure II-32. Radial Seismic Motions of DIP IIA (ref. II-11)

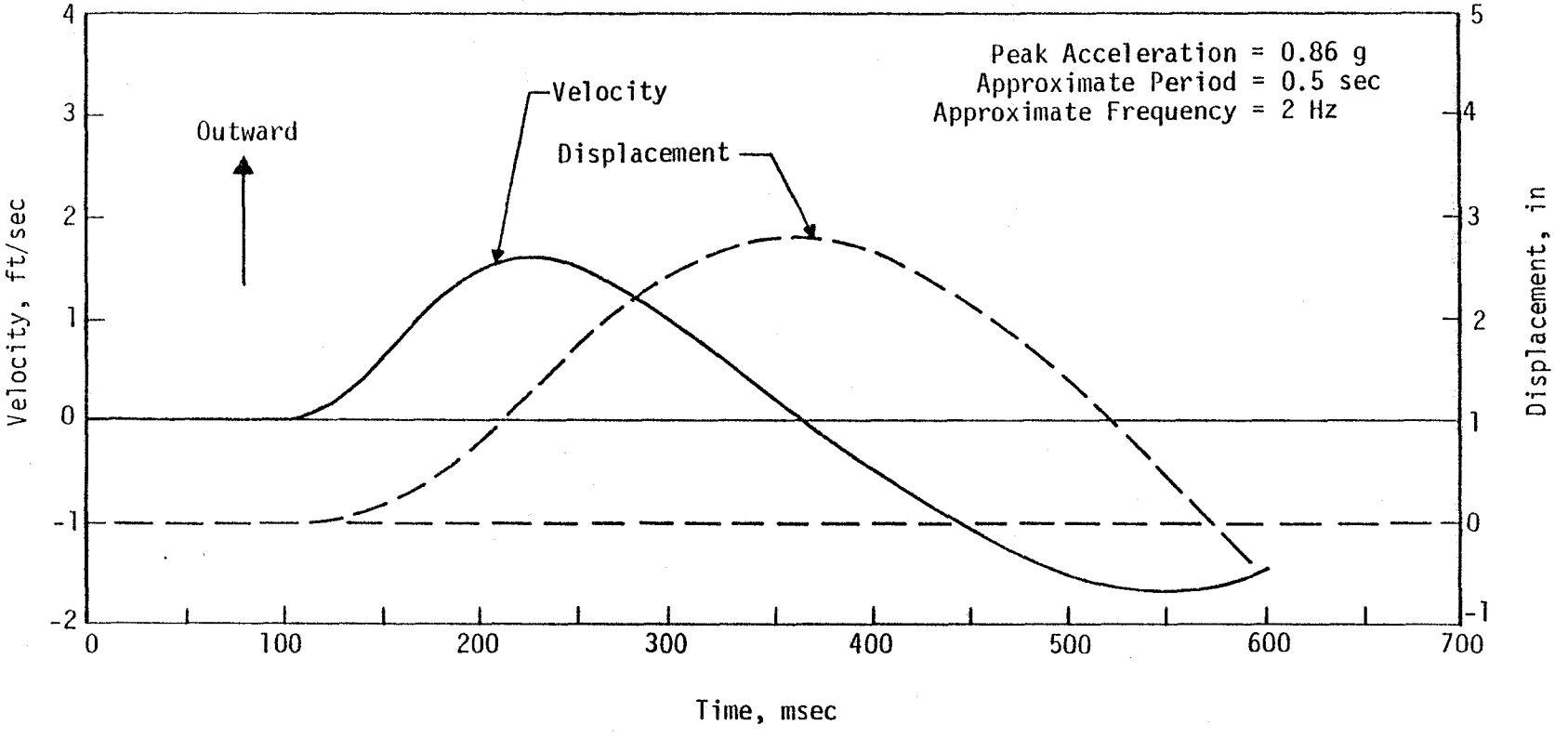

Figure II-33. Horizontal Longitudinal Velocity Integration at 200-Foot Range and 20-Foot Depth on DIP IIA (ref. II-11)

DIP IIIA (ref. II-12), conducted at McCormick Ranch in May 1972, was a planar array test designed to further evaluate boundary relief. The array was loaded with 6600 lbs of DBA-22M slurry in 15 holes 7-ft 2-in on center. The configuration approximated a 107.5-ft long by 33-ft deep planar array loaded with 1.86 lb/ft^2 of slurry. The incident ground shock was assumed symmetric about the array and, therefore, measurements were made on both sides. The test layout is shown in figure II-34. A 62-ft deep trench, 5-ft wide was placed on one side of the array while a series of 62-ft deep relief holes was placed on the opposite side. Figures II-35 and II-36 present the peak horizontal velocities and displacements measured on the centerline on the trenched side of the array while figures II-37 and II-38 present similar data on the relief hole side. Reference II-12 makes no detailed interpretation of the results nor does it compare the results with those of reference II-9. The results will be discussed in Section IV, which deals with data analysis.

DIP IVA (ref. II-13) was conducted at McCormick Ranch in August 1973. The event was a single concentrated charge of 1000 lbs of DBA-22M slurry detonated at a depth of 10-ft 9-in, considered by reference II-13 to be the approximate optimum depth of burst. The objective, as with DIP IA, was to obtain baseline concentrated charge data for comparison with the planar arrays. Unfortunately, as with DIP IA, data recovery was poor. Reference II-13 attributes the poor instrumentation performance to moisture penetration into the gage canisters. The few peak velocity data available are shown in figure II-39.

DIP VA (ref. II-13) was also conducted at McCormick Ranch in August

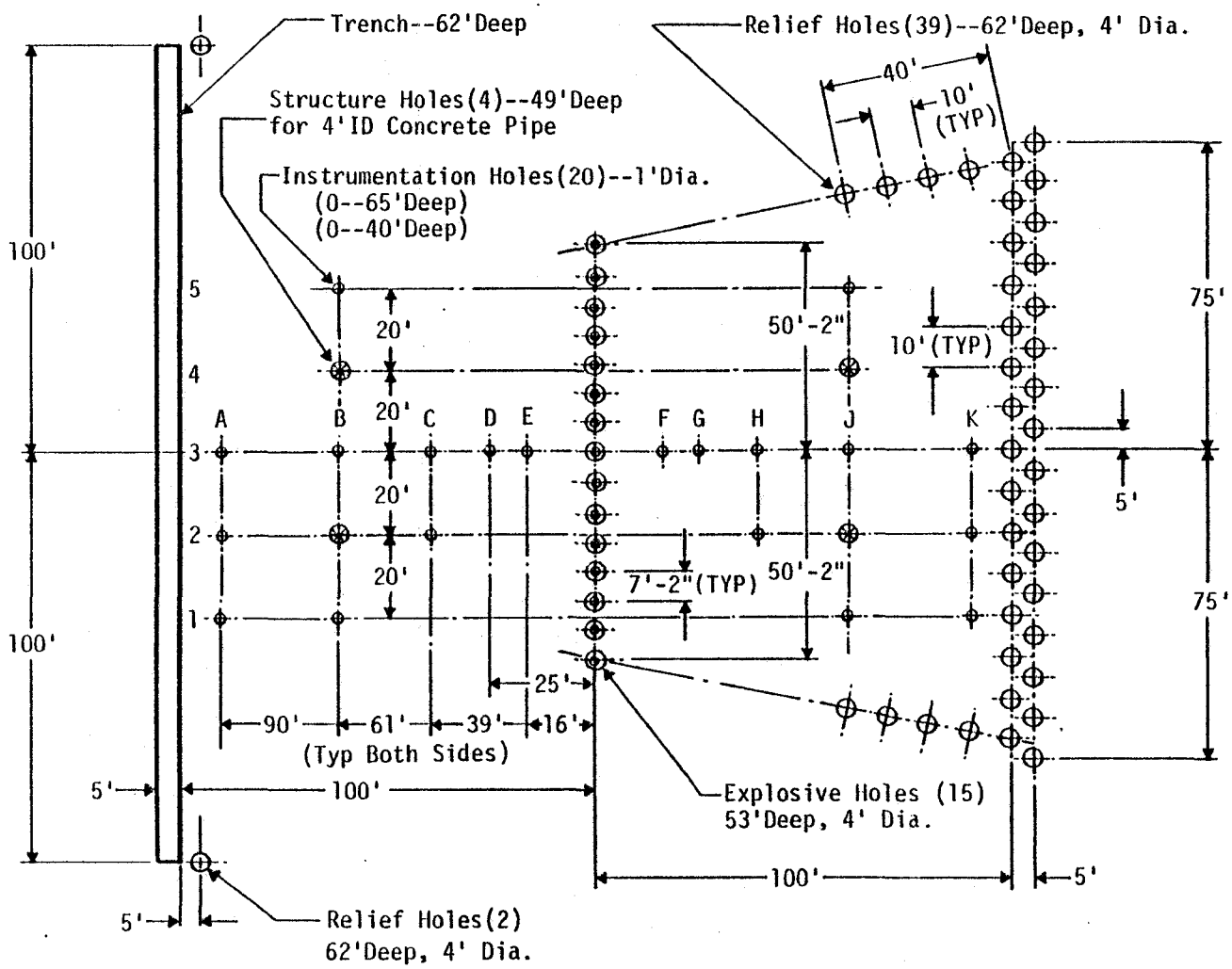

Figure II-34. DIP IIIA Layout (ref. II-12)

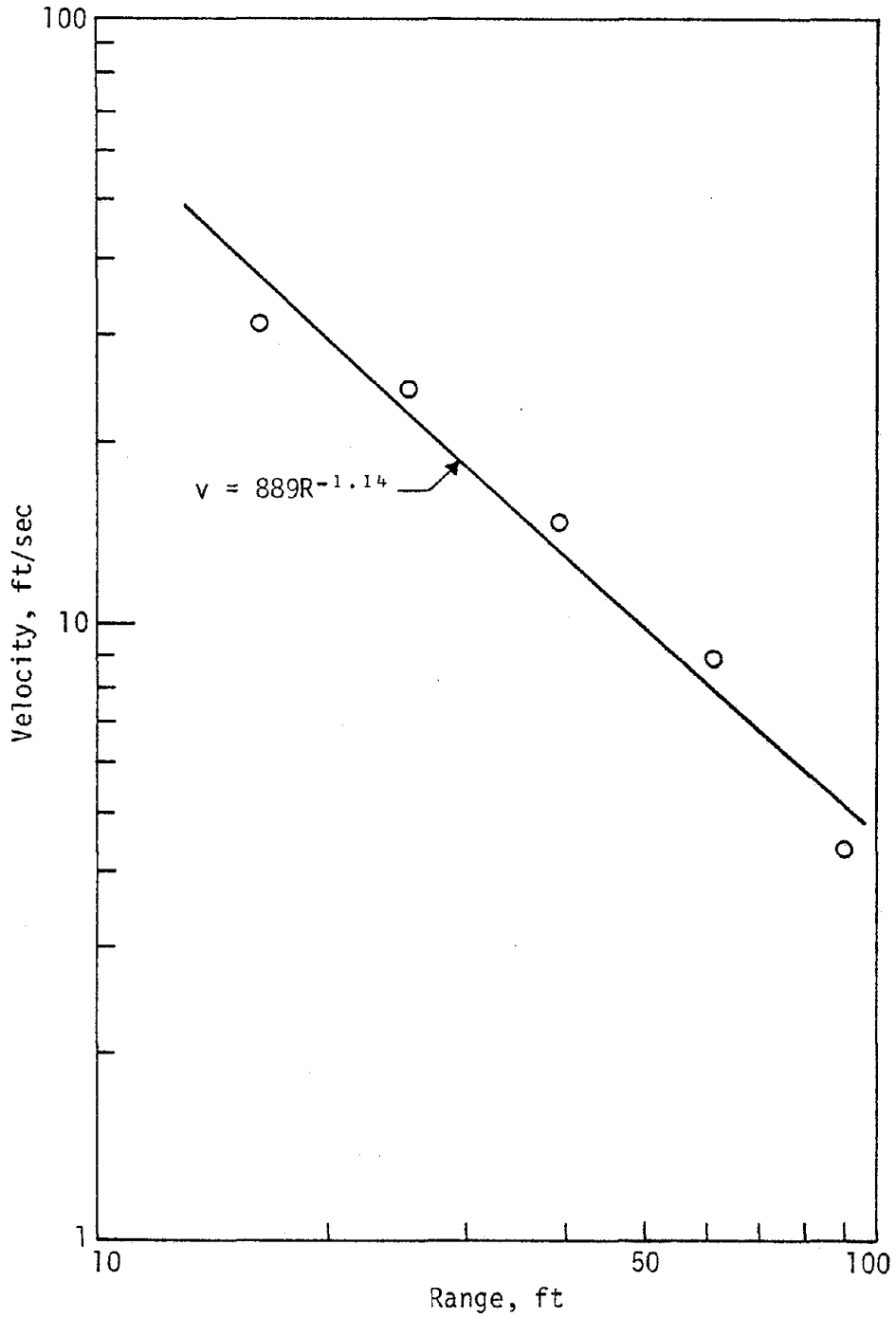

Figure II-35. Centerline Horizontal Velocity on Trench Side of Array (ref. II-12)

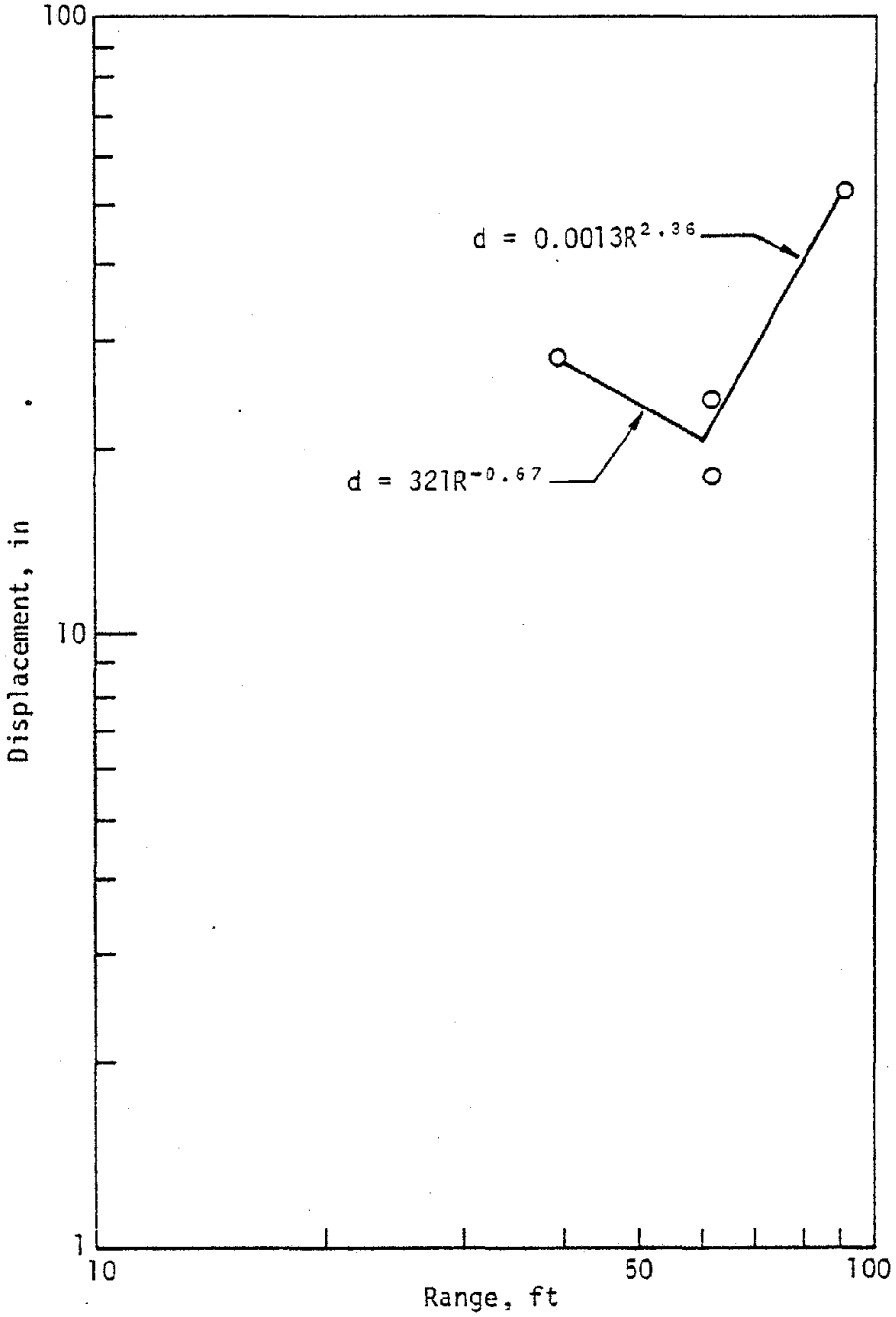

Figure II-36. Centerline Horizontal Displacement on Trench Side of Array (ref. II-12)

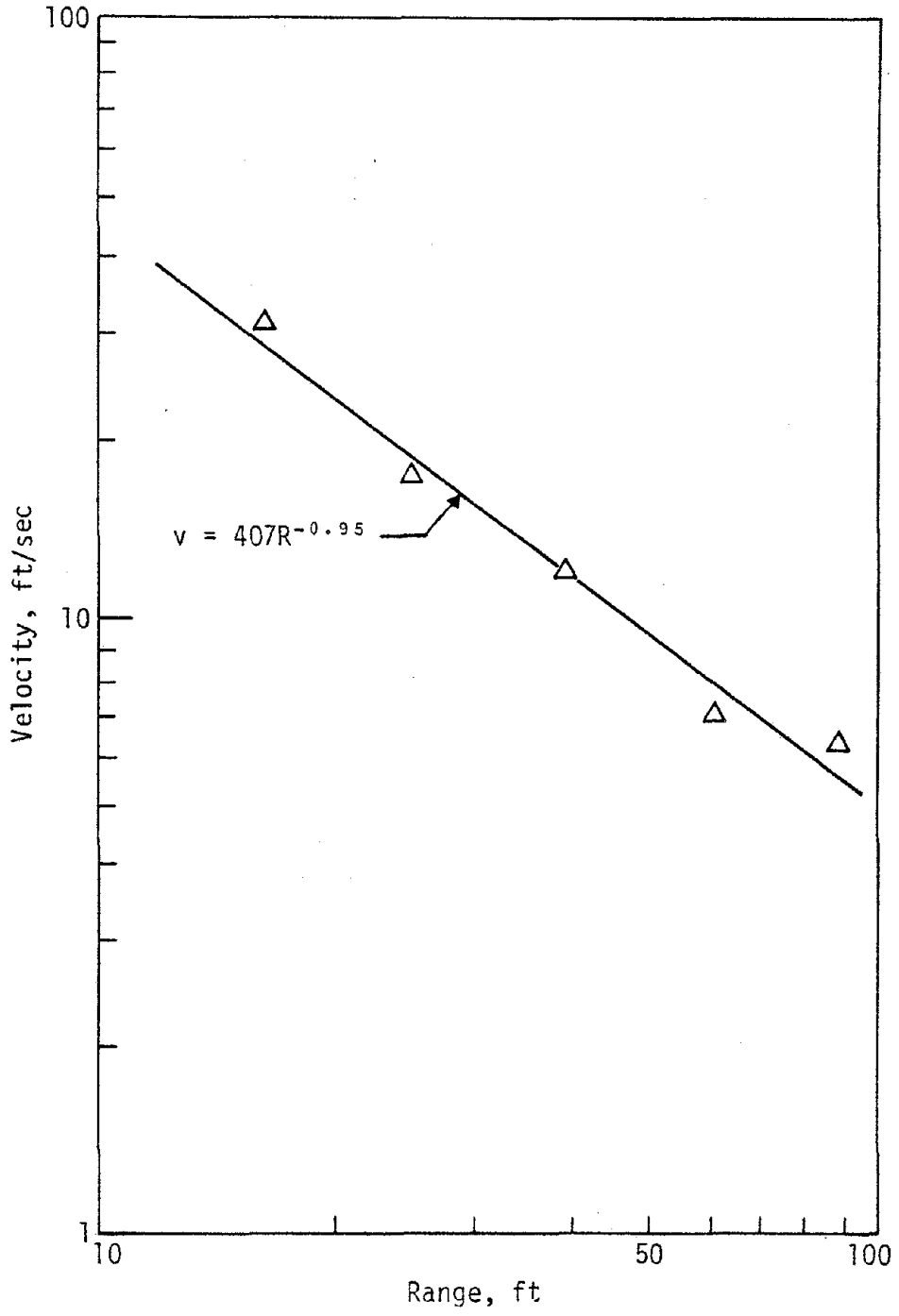

Figure II-37. Centerline Horizontal Velocity on Hole Side of Array (ref. II-12)

Figure II-37. Centerline Horizontal Velocity on Hole Side of Array (ref. II-12)

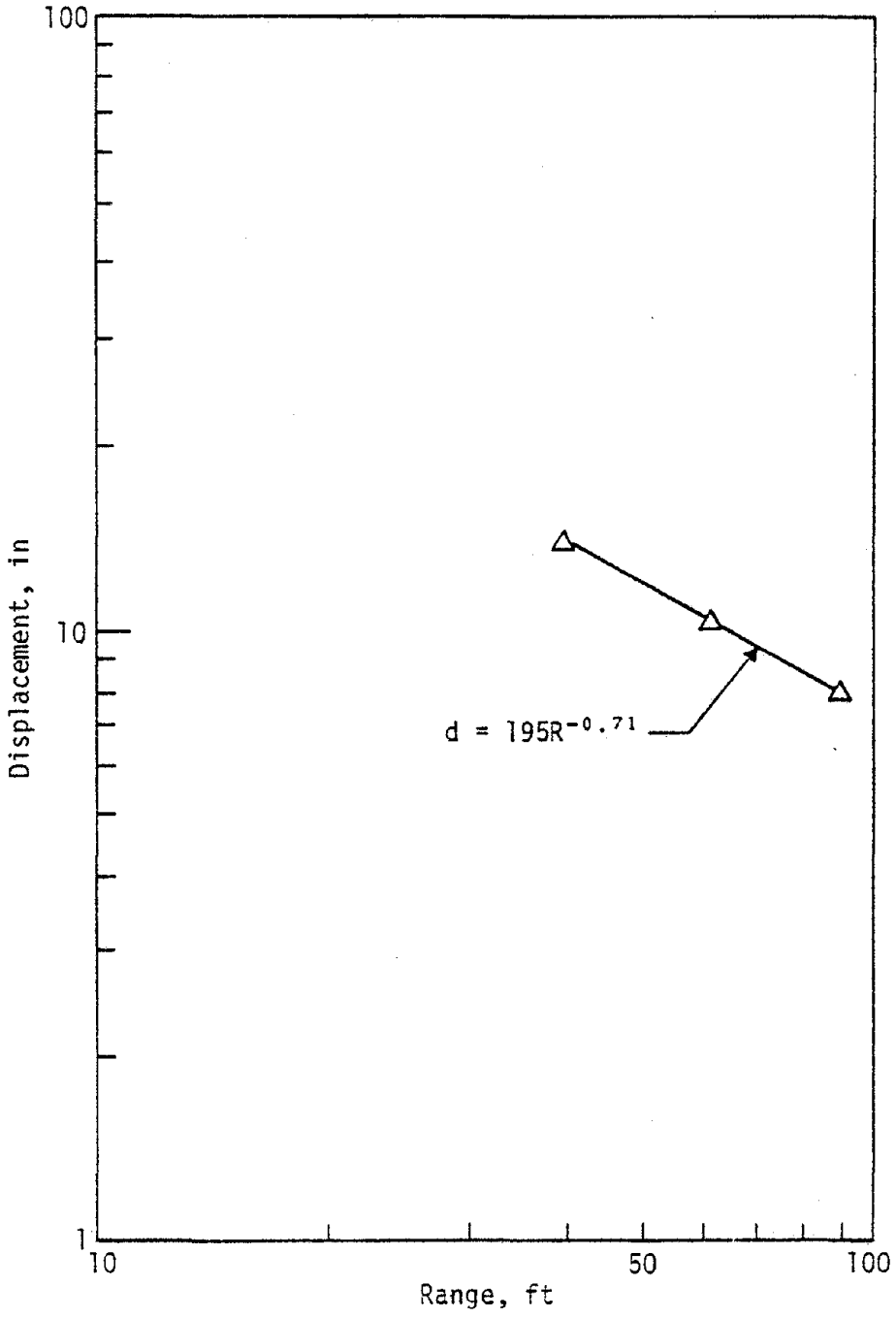

Figure II-38. Centerline Horizontal Displacement on Hole Side of Array (ref. II-12)

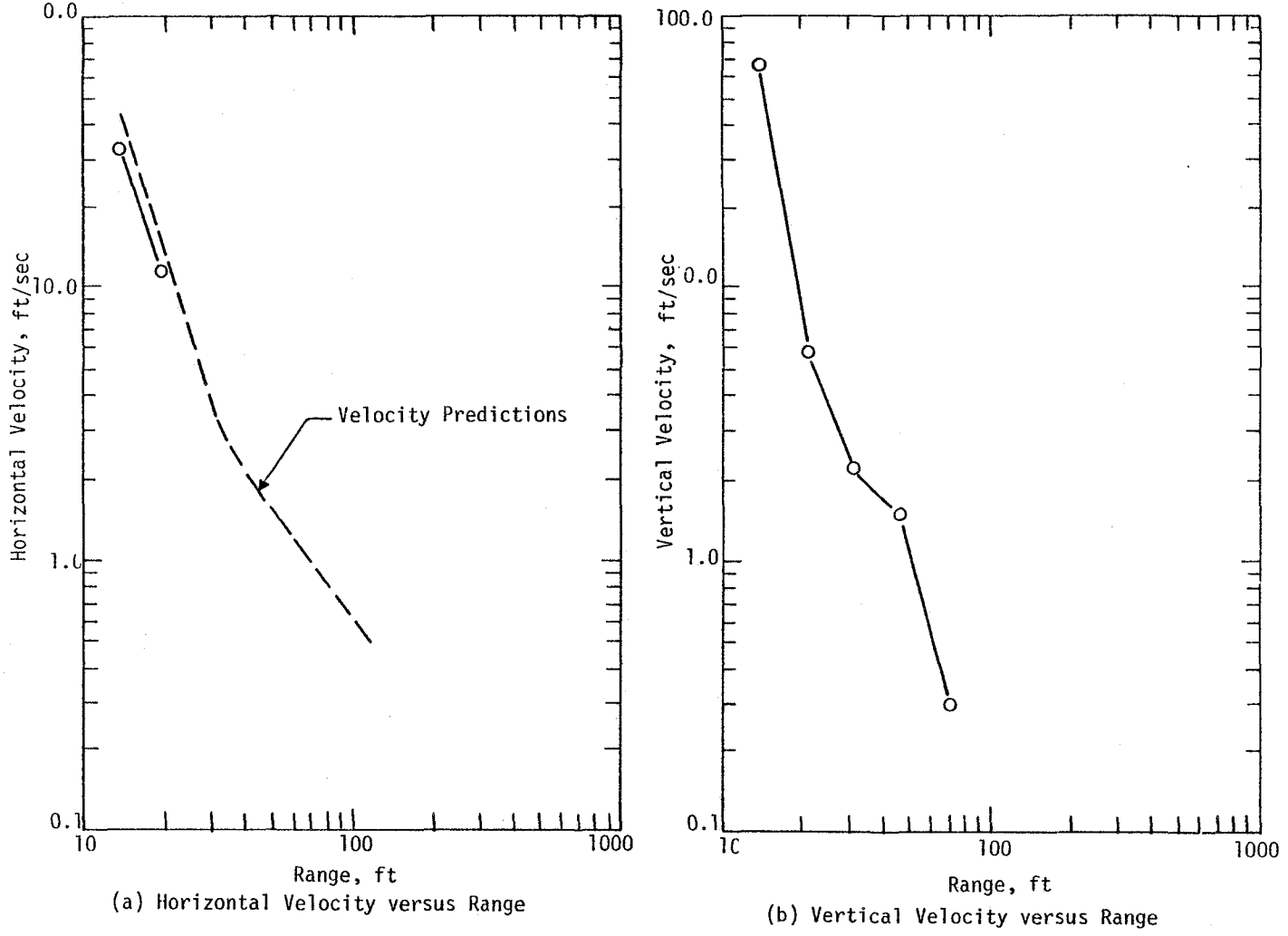

Figure II-39. DIP IVA Peak Velocity Plots (ref. II-13)

1973. Its objective was to provide data which could be used to evaluate the effects of a very large planar array and a very low areal charge density. The event contained 40 tons of IRECO 65T2 slurry in 16 holes which were 71 feet on center. The explosive loading approximated a planar array 1134 feet long by 204 feet deep loaded at an areal density of 0.35 lbs/ft^2 of slurry. The 65T2 slurry is similar to the DBA-22M used in prior events except 20 percent of the ammonium nitrate is replaced with TNT pellets. The TNT allows the slurry to be detonated in deep holes where the hydrostatic pressure is high. Data from IRECO, the firm which manufactured both slurries, presented in reference II-13, indicates the explosive energy of the two slurries is about the same. Only velocity measurements were made on DIP VA. Figure II-40 shows the layout of DIP VA and figures II-41, II-42, and II-43 present measured peak horizontal velocities as a function of range, depth and distance from the experiment centerline.

3. USE OF HIGH EXPLOSIVES AS VIBRATION SOURCES

Applications of high explosives for the specific simulation of definite characteristics of an earthquake have not been found in the literature. However, there have been studies where high explosives were used to provide a ground motion excitation for prototype structures. These applications demonstrate several advantages of ground motion excitation over forced vibration methods and are briefly discussed below.

a. UCLA Studies

Reference II-15 summarizes the results of three test programs in which high explosive charges were used to induce ground motion effects

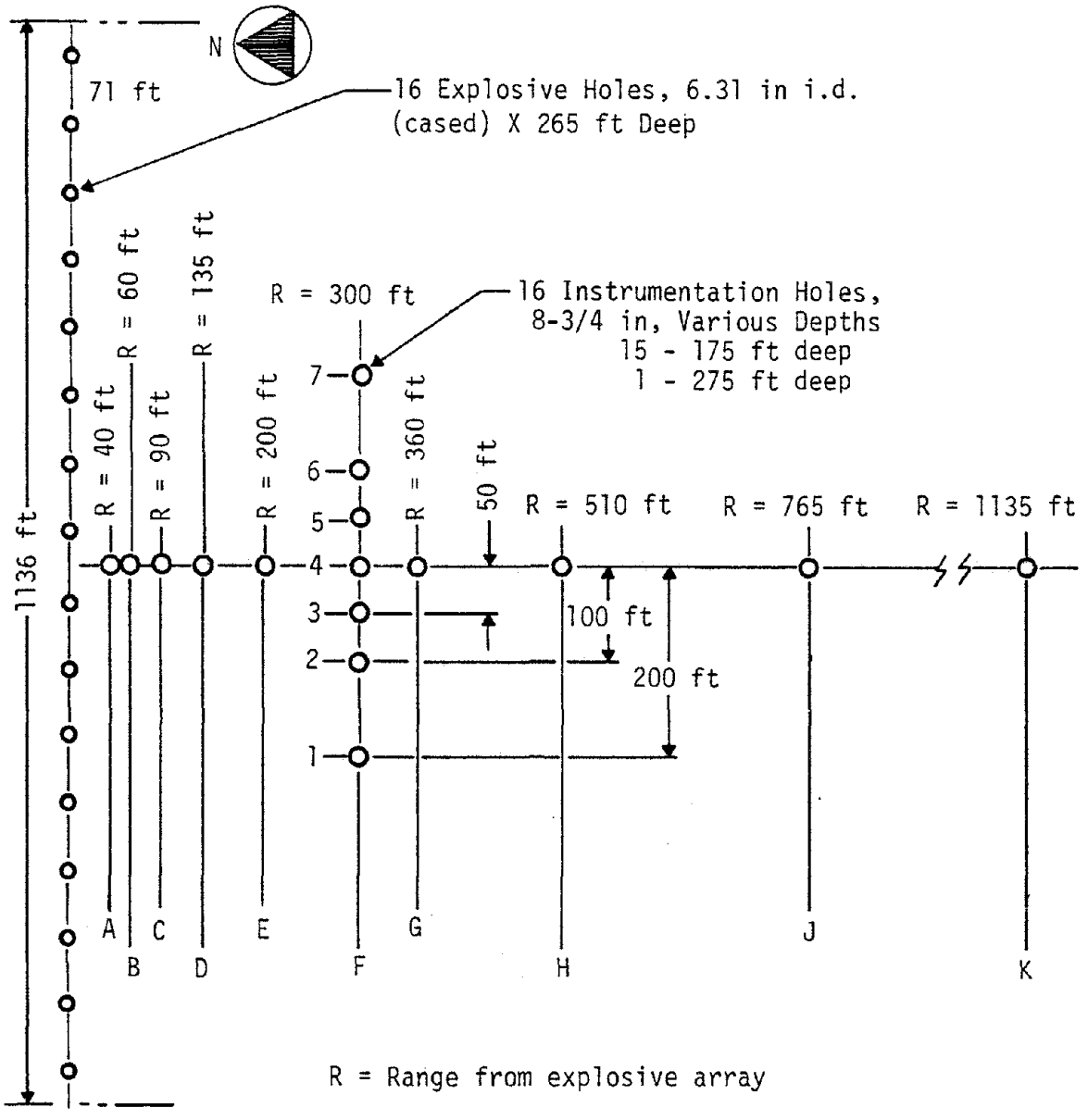

Figure II-40. DIP VA Testbed Layout (ref. II-13)

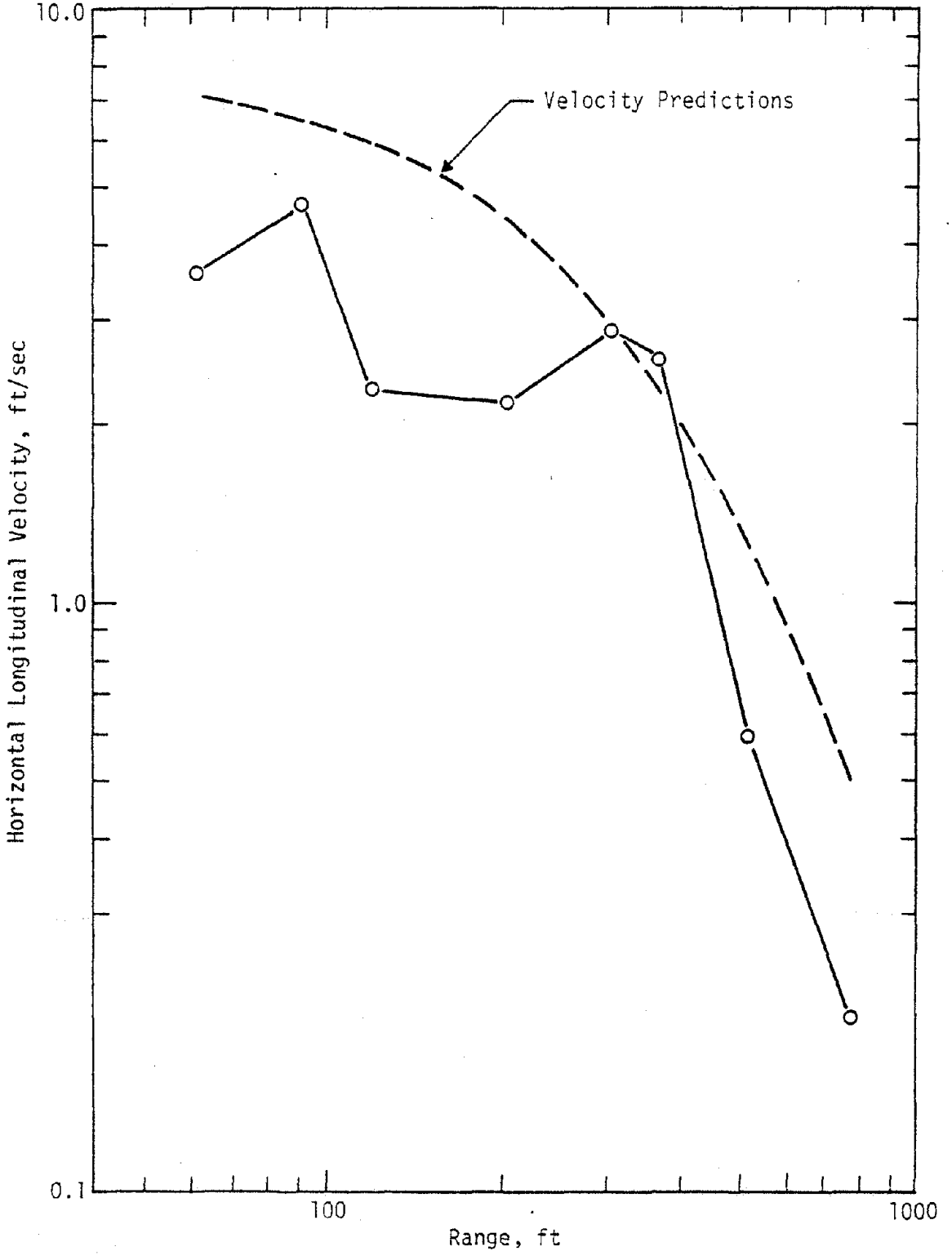

Figure II-41. Longitudinal Centerline Peak Velocities from DIP VA (ref. II-13)

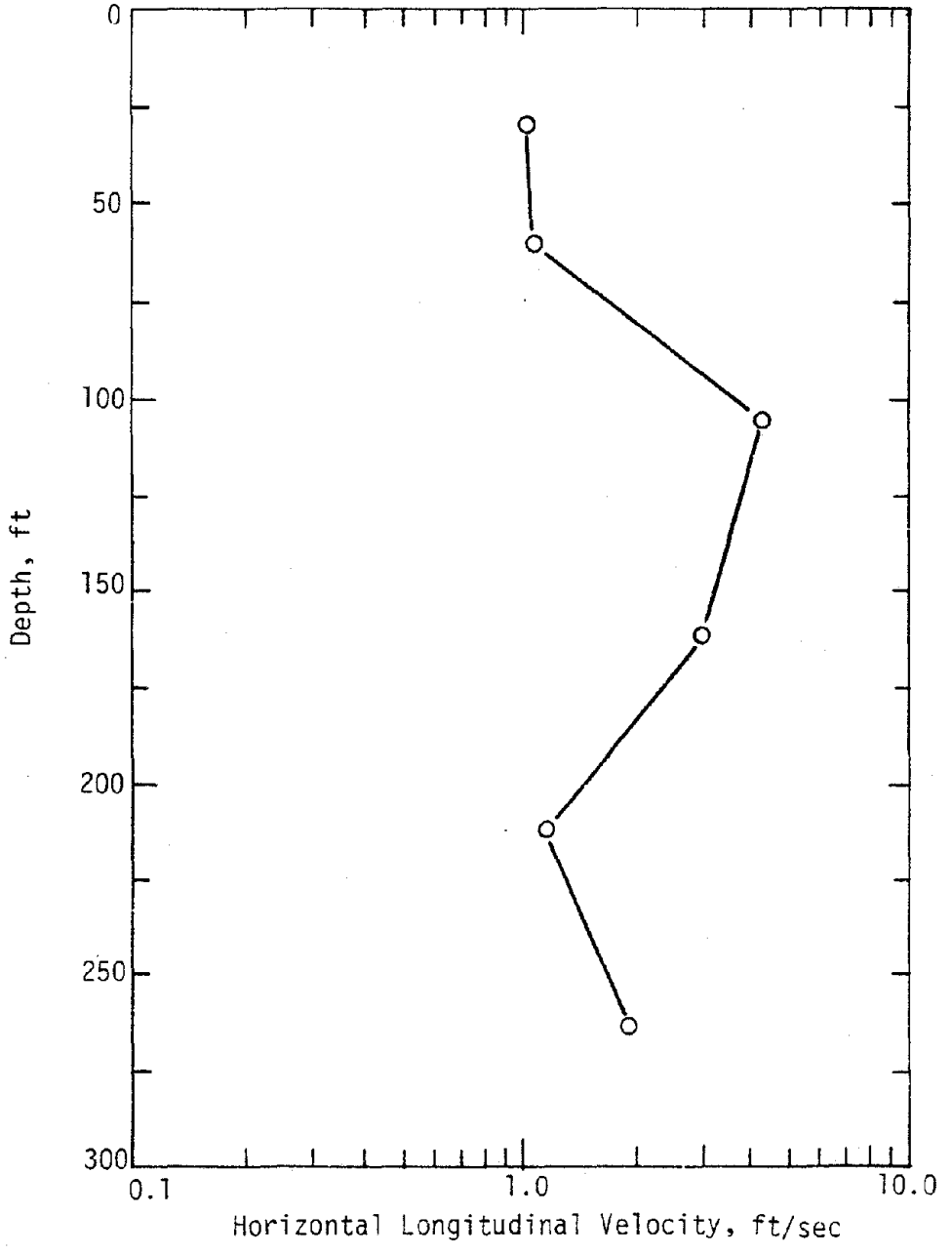

Figure II-42. Peak Velocity versus Depth at 300-Foot Range from DIP VA (ref. II-13)

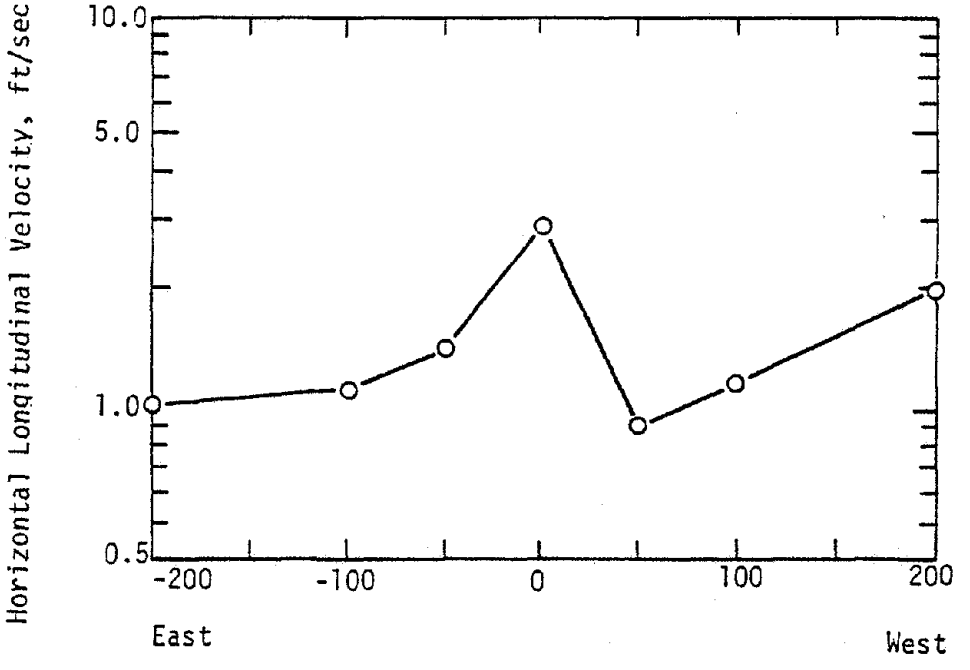

Figure II-43. Peak Velocity versus Distance from Centerline at 300-Foot Range from DIP VA (ref. II-13)

on large structures. As stated by the authors, the objective of the tests was "to determine the feasibility of simulating strong ground motion earthquake effects using dynamite blasts." Blast induced structural response was measured in tests at:

(1) Enrico Fermi Nuclear Power Plant, Monroe, Michigan

(2) Experimental Gas - Cooled Reactor Facility (EGCR), at Oak Ridge National Laboratory, Tennessee

(3) UCLA Field Station

Reference II-16 provides additional detail on the EGCR and UCLA Field Station Tests.

The measurements at the Enrico Fermi plant were made in December 1969, as an adjunct to a study by Dames and Moore. Dames and Moore were attempting to obtain soils data for use in planning future excavations and construction at the site. The ground motion measurements are not reported. UCLA's concern was with the response of the structures.

Seven tests involving single charges weighing 25-lbs were detonated at distances from 875 to 1000 ft from the reactor core. The small charge size and large distances involved caused excitations at the structure which were small and could only be detected by instruments. Instrumentation consisted of accelerometers placed on the reactor and other important facility components. Data were analyzed by fast Fourier transform (FFT) techniques to identify system natural frequencies. It was found that the frequencies observed in the spectra for the blast were in excellent agreement with frequencies interpreted from ambient vibrations, in spite of the fact that ambient vibration amplitudes were an order of magnitude less than those induced by the blast. In addition,

it was observed that the blasts excited coupled response between the various components of the facility, and permitted insight into the coupling. This coupling was not excited by ambient vibrations.

The EGCR tests were conducted in July and August 1970 and had as their objectives the evaluation of soil-structure interaction effects, containment building response, and equipment response. The charge size and distance parameters for the tests are summarized in table II-17. The tests were designed primarily to study structural response, and references II-15 and II-16 do not present the measured soil response data. Some frequency domain analyses are provided in reference II-16, However, the results are subject to some uncertainty (ref. II-16), and cannot be used directly in this report.

FFT techniques were used to interpret the structural response. Real and imaginary parts of the spectrum, power spectral density, and cross power spectra were generated. Both Fourier modulus and phase were used in evaluating soil-structure interaction. The modulus indicated the dominant motion frequencies at various structure locations. In-phase response at various positions in the basement indicated vertical response of the entire basement as a body, while out of phase response indicated structural rocking and, therefore, the presence of soil-structure interaction and the dominant frequencies of the motion. The measured data indicated the presence of coupled rocking-translation in two modes. With regard to structure and equipment response, it was found that the blasts could be used to excite and identify the system modes, even when closely coupled.

Table II-17

Tests Conducted at EGCR
6-7 July 1970 (ref. II-15)

Test #	Run #	Excitation	Charge Weight, W (lbs)	Depth, d (ft)	Distance, r (ft)	Scale factor, $S=W^{\frac{1}{3}}$	Depth Factor, h $ft/lb^{\frac{1}{3}}$	Distance Factor $ft/lb^{\frac{1}{3}}$	Comments
1	1	Blast	55	50[a]	500	3.8	13.1[a]	131	See Note a.
1	2	Blast	25	25	500	2.92	8.5	171	
1	3	Blast	25	16	500	2.92	5.5	171	
1	4	Blast	60	40	300	3.9	10.2	77	
2	1	Blast	10	7	500	2.15	3.3	232	Shallow blast, crater
2	2	Blast	50	10	650	3.7	2.7	176	Shallow blast, crater
2	3	Blast	10	7	500	2.15	3.3	232	Shallow blast, crater
2	4	Displacement of steam generator----------							
2	5	Displacement of steam generator----------							
2	6	Blast	80	60	290	4.3	14	68	
2	7	Blast	160	60	290	5.4	11.2	54	Multiple blast; 2-80# charges in holes 20' apart fired simultaneously.
2	8	Blast	160	55	290	5.4	10.2	54	Delayed blast; 2-80# charges in holes 20' apart fired with a 50 millisec delay

Note: a) 30 lbs at a depth of 50', 25 lbs at a depth of 30'. Values obtained by averaging.

Table II-17 (continued)

Tests Conducted at CGCR
19-24 August 1970 (ref. II-15)

Test #	Run	Excitation	Charge Weight, W (lbs)	Depth, d (ft)	Distance, r (ft)	Scale Factor, $S=W^{\frac{1}{3}}$	Depth Factor, h $ft/lb^{\frac{1}{3}}$	Distance Factor $ft/lb^{\frac{1}{3}}$	Comments
1	1	Blast	1	60	289	1.00	60.0	289	
1	2	Blast	10	57	289	2.15	26.5	134	
2	1	Blast	10	8	281	2.15	3.72	130	Shallow surface blast.
2	2	Blast	100	52	289	4.64	11.2	62.2	
2	3	Blast	600	44	285	8.42	7.5(b)	38.8	200# in each of 3 bore holes detonated simultaneously
2	4	Blast	2000	41	283	12.6	3.5(b)	22.5	1600# in one hole; 400# in second hole detonated simultaneously
3	1	Blast	10	57	251	2.15	26.5	117	
3	2	Blast	100	51	262	4.64	11.0	56.2	
3	3	Blast	600	45	262	8.42	7.70(b)	31.0	200# in each of 3 bore holes; 200# detonated instantaneously, 200# 135 msec later, 200# 320 msec later.
3	4	Blast	2000	54	272	12.6	5.2(b)	21.5	This shot consisted of 1100# in one hole, 675# in second hole, 225# in third hole fired simultaneously

Note: (b) for one hole. If size of charge per hole varied, the largest was used.

The major conclusions of the EGCR tests were that excellent agreement existed between frequencies determined from the blast tests and those determined earlier by shaker tests. In addition, the blast tests provided deeper insight into nonlinear behavior, soil-structure interaction and coupled response.

The UCLA field station tests were conducted in March 1971 to evaluate methods for controlling the excitation created by explosive blasts. Specifically, the objectives of the tests were to investigate

(1) the effect of detonation rate and explosive bulk strength on the frequency of the ground motion

(2) amplitude and frequency sensitivity to distance

(3) the feasibility of producing arbitrary blast durations using time delayed explosions.

In addition, the blasts were used to excite a three story test structure. The test characteristics are shown in table II-18 and the test layout in figure II-44.

Figure II-45 shows the measured radial accelerations at the structure base from three tests involving 3-lb charges of dynamite having three different detonation rates. There is no significant difference in the peak amplitudes or the time histories. Thus, reference II-15 concluded that detonation rate does not significantly affect the form of the acceleration time history. Figure II-46 compares the radial base accelerations from two tests in which the total weight of Hercomite 7X-A was varied (3-lbs in Test 2, 10.71 lbs in Test 9). The effect upon the acceleration time history is insignificant. Test 9 had the same bulk

Table II-18

Blast Test Program (ref. II-16)

Date: Wednesday, March 24, 1971; UCLA Field Station

Three-degree-of-freedom structure
9 accelerometers

Test No.	DYNAMITE	CHARGE SIZE	DISTANCE	DELAYS
1.	Hercomite • 7X-A	3.06 lbs.	100 ft. transverse	———
2.	Hercomite 7X-A	3.06 lbs.	100 ft.	———
3.	Hercol 2	2.92 lbs.	100 ft.	———
4.	Gelaprime-F	3.00 lbs.	100 ft.	———
5.	Hercomite 7X-A	3-3-3-3 lbs.	110 ft.	0,#4,#7,#10
6.	Hercomite 7X-A	3-3-3-3 lbs.	105 ft.	0,#4,#7,#10
7.	Hercol 2	3-3-3-3 lbs.	95 ft.	0,#4,#7,#10
8.	Gelaprime-F	3-3-3-3 lbs.	100 ft.	0.#4,#7,#10
9.	Hercomite 7X-A	10.71 lbs.	95 ft.	.50/14 x 3#
10.	Hercomite 7X-A	7.7 lbs.	25 ft.	———
11.	Hercol 2	10 lbs.	36 ft.	———
12.	Hercol 2	5-5-5-5-5 lbs.	50 ft. quart circle	———
13.	Gelaprime-F	7-7-7-7-7 lbs.	75 ft. quart. circle	———

	Bulk Strength	Detonation Rate
Hercomite 7X-A	14%	6,400 ft/sec
Hercol 2	50%	10,500 ft/sec
Gelaprime-F	54%	20,800 ft/sec

Delays

0 .012 sec.
#4 .100 sec.
#7 .205 sec.
#10 .320 sec.

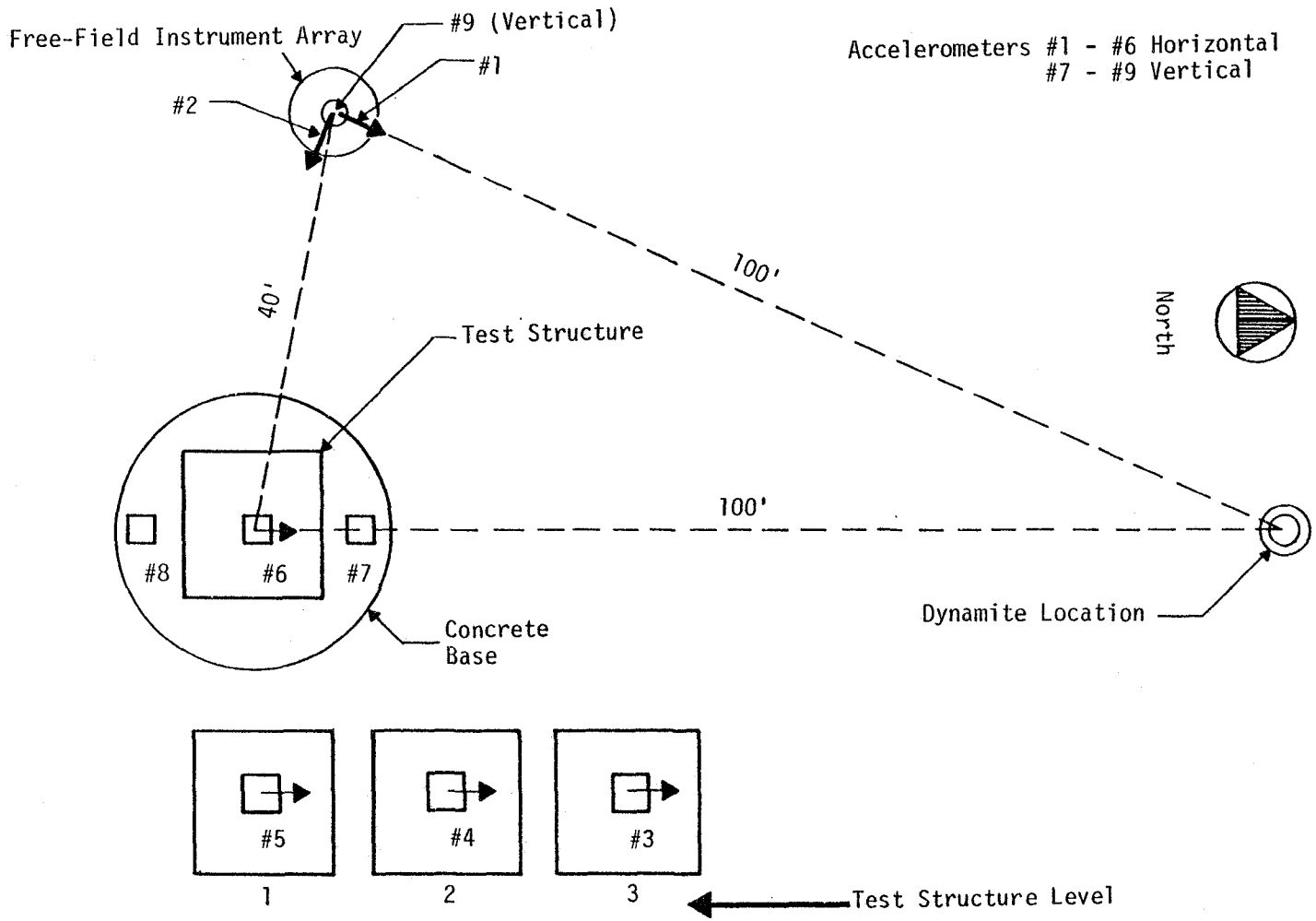

Figure II-44. Accelerometer Locations During Tests 2 - 4 (ref. II-16)

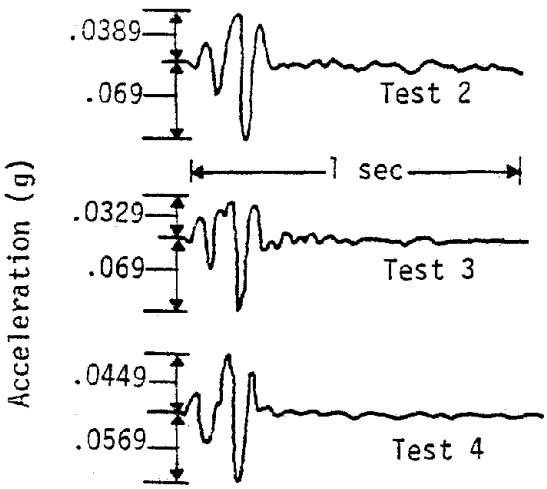

Figure II-45. Radial Acceleration at Base of Test Structure (Tests 2-4) (ref. II-15)

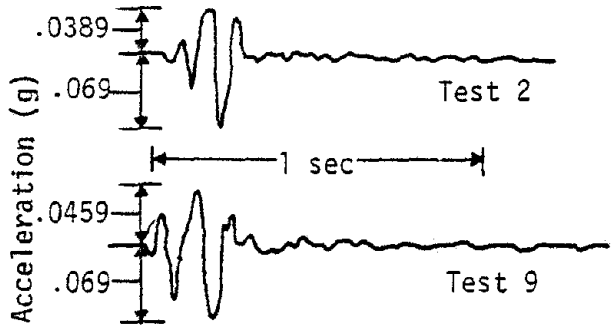

Figure II-46. Radial Acceleration at Base of Test Structure (Tests 2 and 9) (ref. II-15)

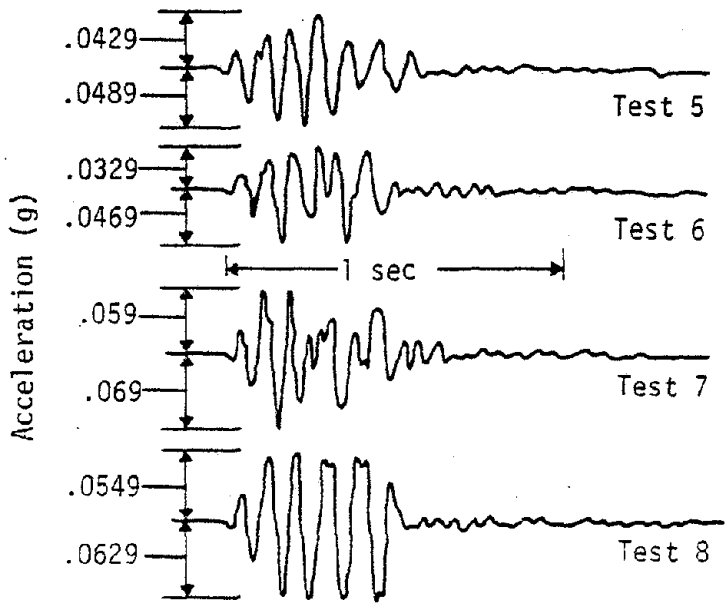

Figure II-47. Radial Acceleration at Base (time delayed blasts) (ref. II-15)

dynamite (10.71-lbs, 14 percent bulk strength*) as Tests 3 and 4 (3-lbs, 50 percent bulk strength). Since the results of Test 9 coincide closely with the results of Tests 3 and 4, references II-15 and II-16 concluded that matching total bulk dynamite on the basis of bulk strength was a valid method for obtaining equivalent responses from different dynamites at the same range.

Figure II-47 presents measured base radial accelerations for tests involving time delayed charges. The results indicate that the use of time delays is a viable method for introducing multiple cycles of motion and extending the time duration of the ground motion excitation.

With regard to structure response, reference II-16 notes that, where allowances were made for nonlinear effects, blast results yielded model frequencies that were in good agreement with the results for forced vibration tests. The mode shapes and damping values did not compare as well. Reference II-16 attributes the differences to the fact that the levels of response in the forced vibration tests were higher than in the blast tests, leading to higher damping values in the forced vibration tests.

An important conclusion stated in reference II-16 is that criticisms of blast testing based upon the high frequency content of the input and the lack of a precise simulation of an earthquake-like motion are not completely relevant. Reference II-6 noted that although early structural response contained a substantial high frequency content, this response quickly diminished and transitioned to a free vibration response at the

*Bulk Strength is the strength of the dynamite relative to the strength of pure nitorglycerin.

natural frequencies of the systems. This response lasted for 20-seconds or more in many cases, and was the prime basis for the UCLA analyses. Reference II-16 states that this response is a significant response in that it reflects the structure providing the driving force for the internal equipment.

The UCLA results are important in that they demonstrate the usefulness of a ground excitation created by explosives in gaining understanding of structural response. In addition, the results indicate the feasibility of using time delays for varying the frequency and duration of the input excitation.

b. Explosive Excited Forced Vibration Tests in the Soviet Union

Reference II-17 reports the results of two tests on a three story test structure in which high explosives were used to generate ground motion excitation of the structure. The tests were conducted at a test site near Laur, Tadzhik, S.S.R. The first test involved the detonation of a 2 metric ton concentrated charge at a range of about 175 m (576 ft) from the structure. The second test, which was designed to generate longer duration shaking, involved six 2-metric ton explosions detonated at 0.5 second intervals. The layouts for both tests are shown in figure II-48. The explosive used was black powder in bags (ref. II-18).

The test site consisted of what is described by the Russian engineers as dry homogeneous loess-like clayey loam with some sand and plastic

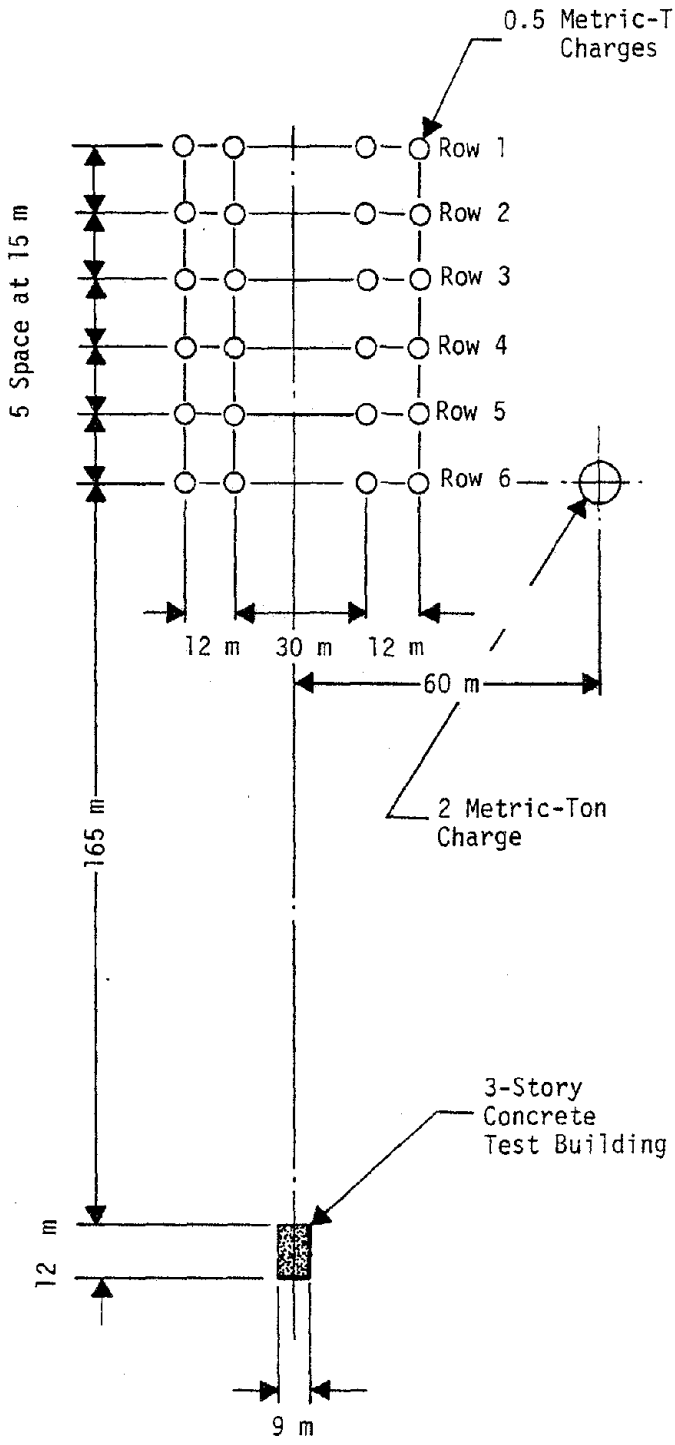

Figure II-48. Layout for Soviet Tests of a 3-Story Concrete Test Building (ref. II-18)

material* extending to a depth of 60 m (200-ft) (ref. II-18). The wet density of the soil was 1.4-1.5 gm/cc (87-94 lb/ft^3) and the moisture content ranged from 6 to 17 percent. The porosity averaged 50 percent and the specific gravity of the solids was 2.68. Seismic velocities at the site were 390 to 420 m/sec (1300-1400 ft/sec) to a depth of 60 m (200 ft), 800 m/sec (2600 ft/sec) from 60 to 95 m (200 to 310 ft), and 1400 m/sec (4600 ft/sec) at greater depth.

Measurements consisted of horizontal and vertical accelerometers placed on the structure: one horizontal and one vertical on the roof, one horizontal on each of the second and third floors, and a triaxial package on the foundation. No measurements were taken on or in the soil. Acceleration measurements, and their integrations, taken on the foundation during the single charge test are shown in figures II-49, II-50, and II-51. Similar data for the sequenced event are shown in figures II-52, II-53, and II-54. These records were obtained from Rojahn (ref. II-18), and he notes that they are preliminary and have not been evaluated in detail with regard to variations in accelerometer sensitivity, filtering, and baseline corrections.

Table II-19 summarizes peak kinematic parameters and some frequency and duration characteristics which have been crudely extracted visually from the plotted time histories. In general, the amplitudes of the motions are significant, but well below the amplitudes which would be expected in the near-field of a strong earthquake. The small amplitudes

*The definition of loam varies from place to place. In general, it refers to texture and denotes a mixture of particles of sand, silt and clay sizes without precise specification of relative amounts. Clayey loam usually means a sufficient amount of clay so that the texture is fine and the material is plastic when moist.

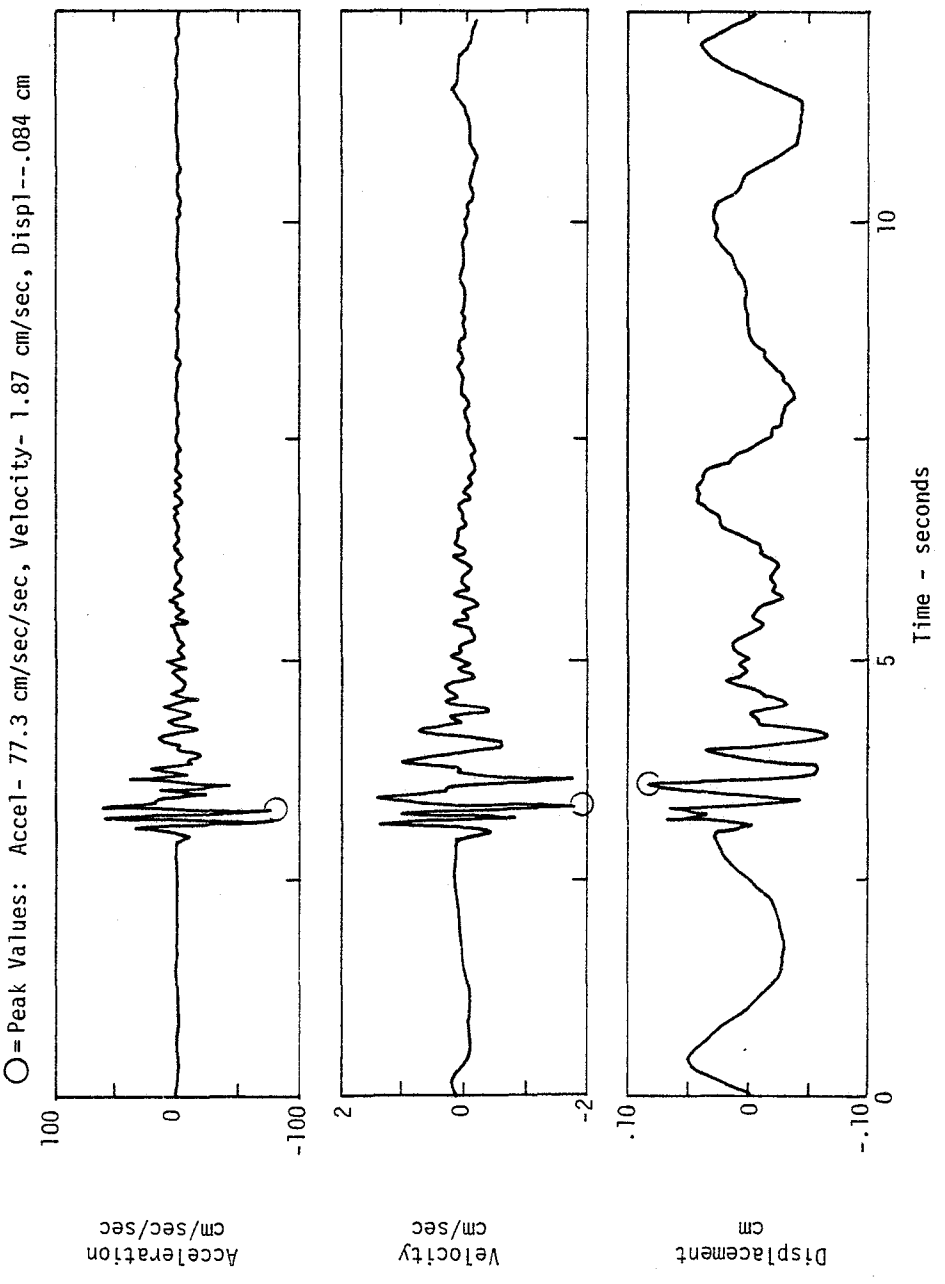

Figure II-49. N-S (Longitudinal) Motion at Ground Level, Single Charge Test (ref. II-18)

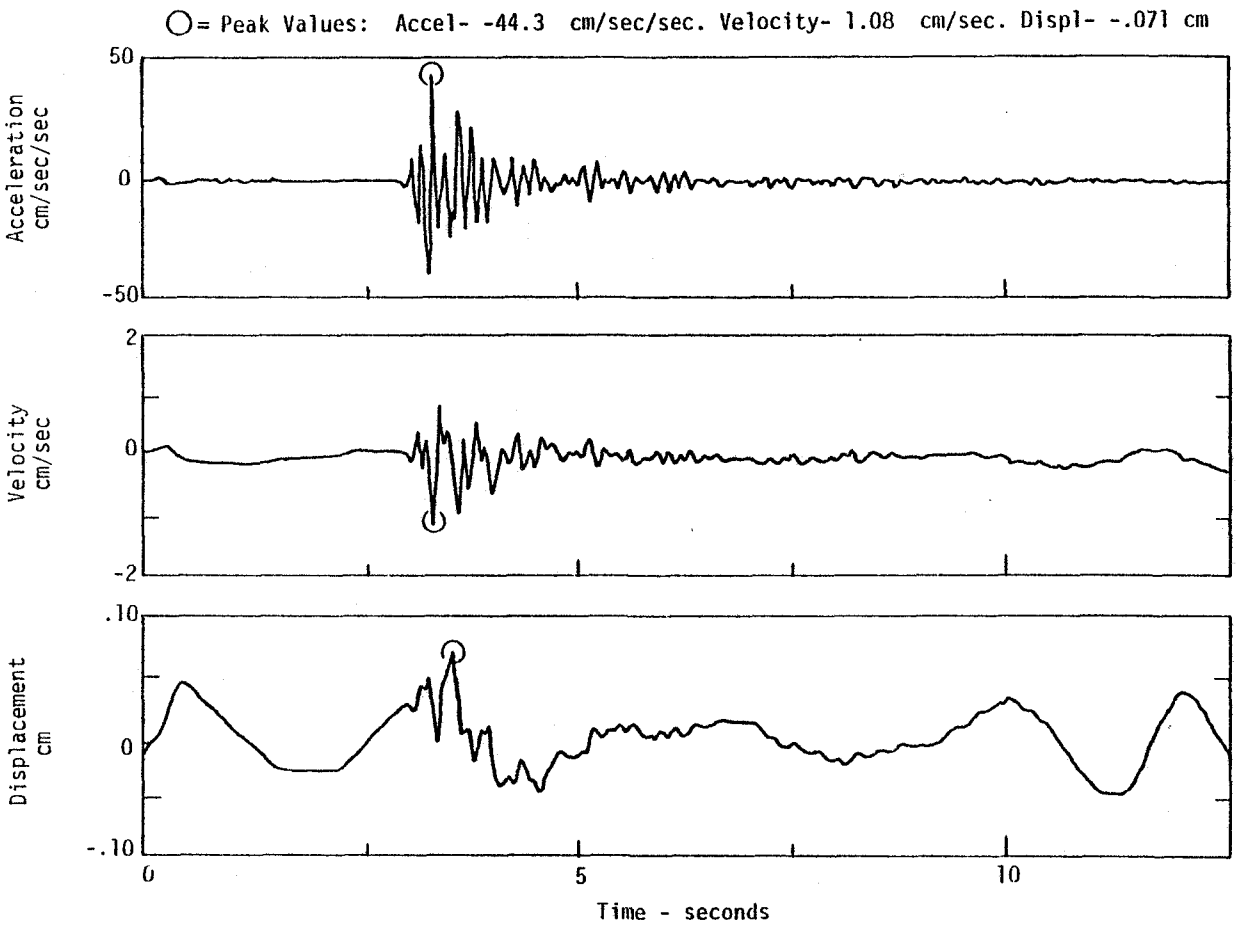

Figure II-50. E-W (Transverse) Motion at Ground Level, Single Charge Test (ref. II-18)

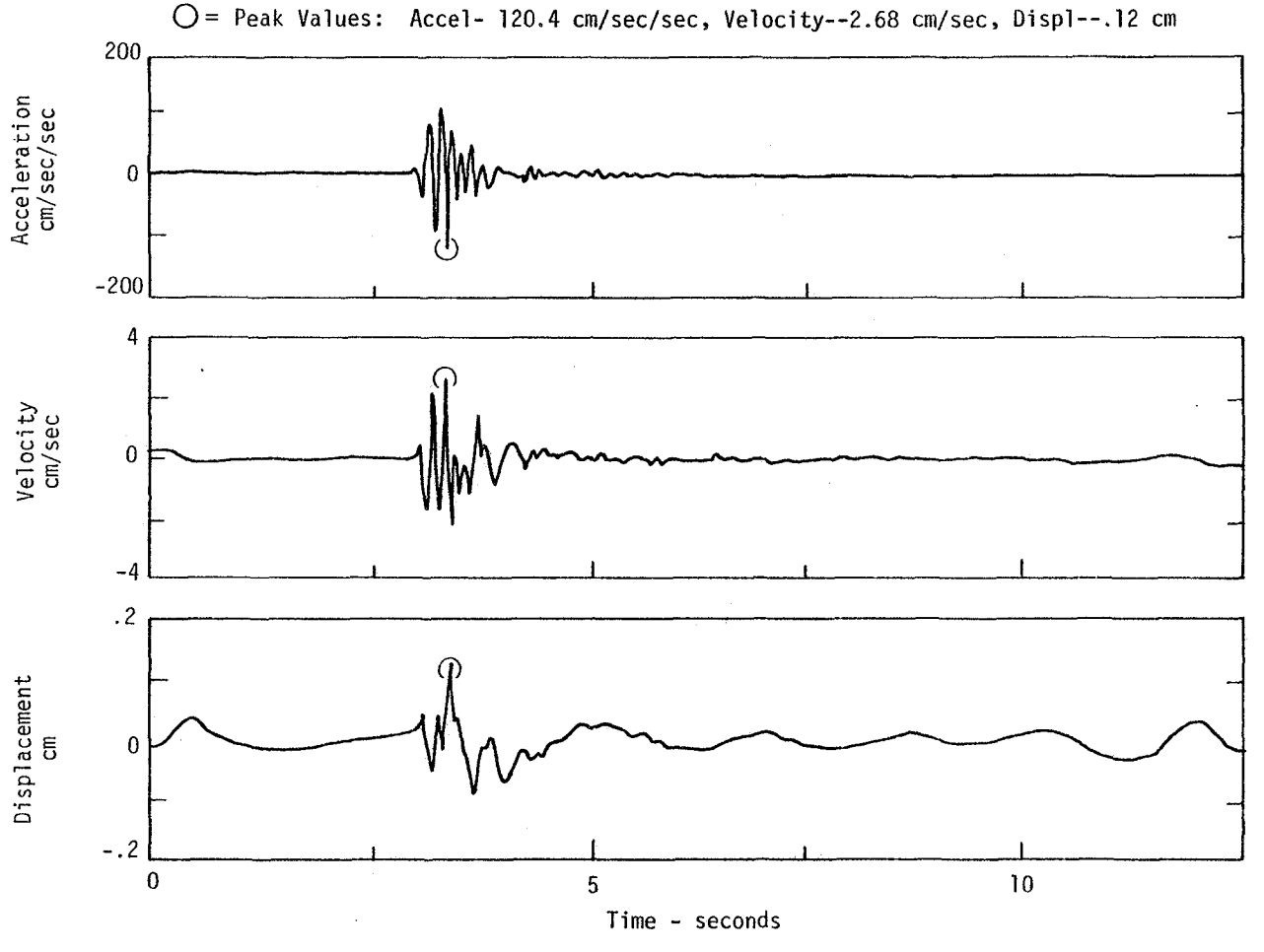

Figure II-51. Vertical Motion at Ground Level, Single Charge Test (ref. II-18)

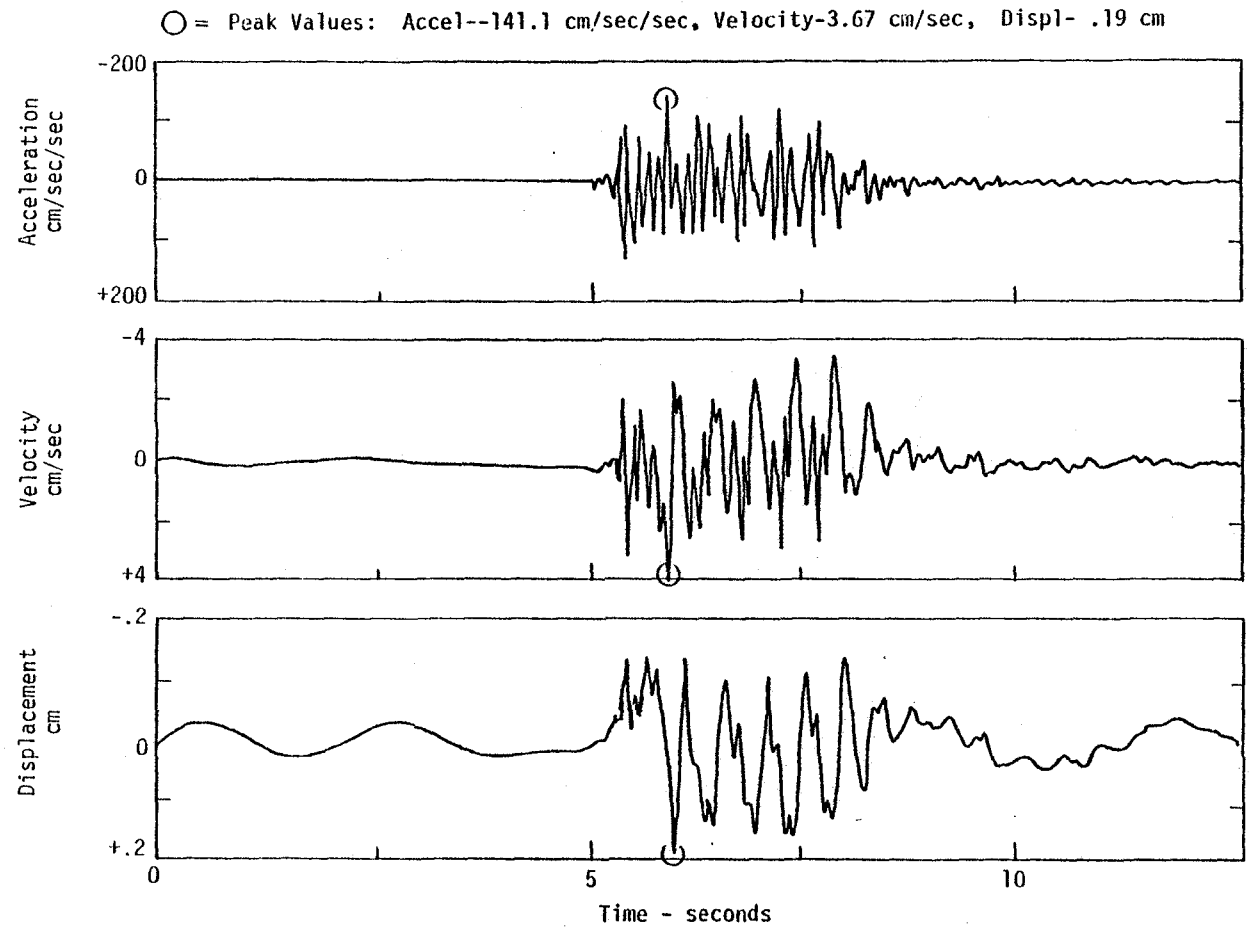

Figure II-52. N-S (Longitudinal) Motion at Ground Level, Multiple Charge Test (ref. II-18)

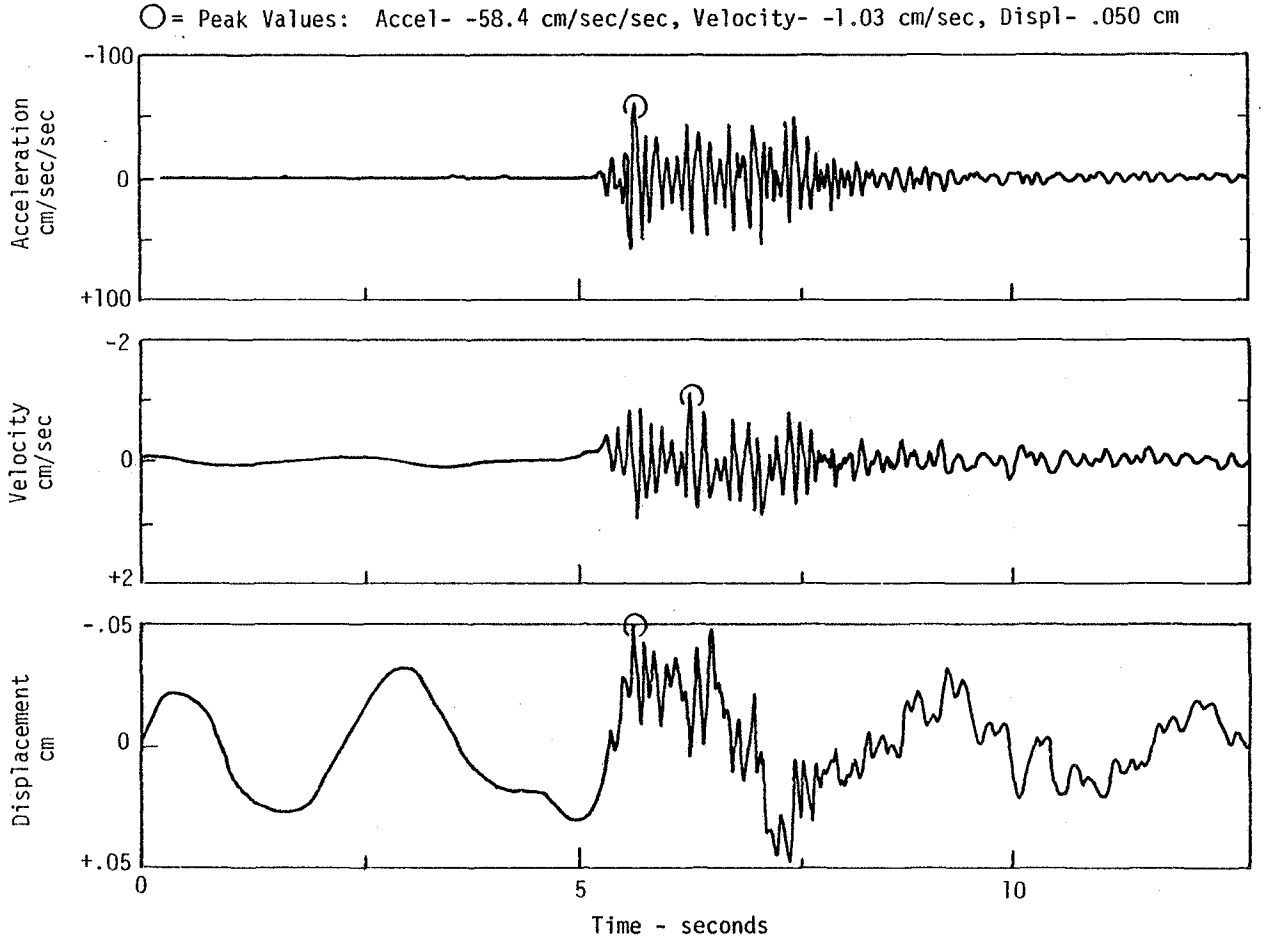

Figure II-53. E-W (Transverse) Motion at Ground Level, Multiple Charge Test (ref. II-18)

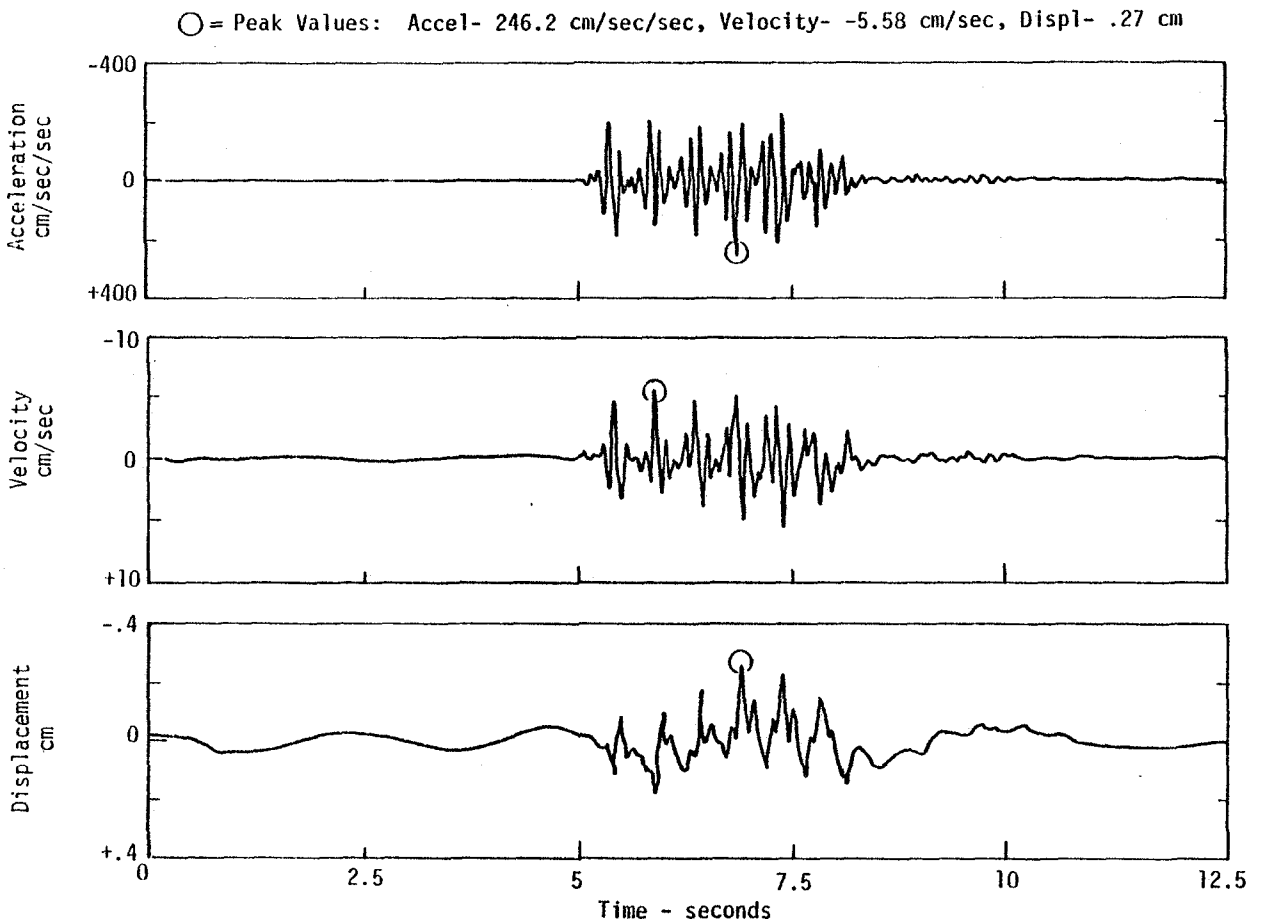

Figure II-54. Vertical Motion at Ground Level, Multiple Charge Test (ref. II-18)

Table II-19

Peak Motions and Time Characteristics at Structure Foundation in Soviet Tests (Extracted from data of reference II-18)

(a) Test 1 - 2 Metric Ton Charge Structure Range: 175m (580 feet)						
Parameter	N-S*	E-W	Vertical	Major Frequencies, H_z	Duration Above 10% Peak, Sec	Duration Above 20% Peak, sec
Acceleration, cm/sec^2(g) Velocity, cm/sec(ft/sec) Displacement, cm(in)	77.3(0.079) 1.87(0.061) 0.084(0.033)	44.3(0.045) 1.08(0.035) 0.071(0.028)	120.4(0.123) 2.63(0.088) 0.12(0.047)	2.8,7 2.8,7 2.8,7	1.7 1.7 1.7	0.9 0.9 0.9
(b) Test 2 - Six 0.5 Metric Ton Sequenced Charges (0.5 sec delay) Structure Range: 165m (540 feet)						
Parameter	N-S	E-W	Vertical	Major Frequencies, H_z	Duration Above 10% Peak, sec	Duration Above 20% Peak, sec
Acceleration, cm/sec^2(g) Velocity, cm/sec(ft/sec) Displacement, cm(in)	141.(0.144) 3.67(0.12) 0.19(0.075)	58.4(0.06) 1.63(0.053) 0.05(0.02)	246.2(0.25) 5.58(0.18) 0.27(0.11)	7 2.2,2.8,7 2.2,2.8,7	3.8 3.8 3.8	3.45 3.45 3.45

*N-S is longitudinal; E-W is transverse.

are due to the large distance from the explosives to the structure in each test (a scaled range of $R/W^{\frac{1}{3}}$ = 45 ft/lb$(TNT)^{\frac{1}{3}}$ for the single charge test where black powder has been taken about one-half as effective as TNT*). The single charge event seems to contain significant motion contributions at 2.8 and 7 Hz. The sequenced event also contains these frequencies but, in addition, there is a 2.2 Hz component evident in the velocity and displacement. This frequency seems to correspond to the firing time delay of 0.5 seconds (2.0 Hz). Only the 7 Hz component could be visually ascertained from the acceleration record of the sequenced event due to the overlap caused by the multiple firings. The 10 percent and 20 percent durations (amplitudes equal to or greater than 10 or 20 percent of the peak) of the sequenced event correspond well with six times the time delay (6 x 0.5 sec = 3.0 sec) plus the appropriate 10 percent or 20 percent duration of the single charge event.

The vertical motion components in both events are 40 to 80 percent (50 percent average) higher than the corresponding N-S (longitudinal) component. The E-W (transverse) components averaged about 67 percent of the N-W components on the single charge event and about 40 percent of the N-W components on the multiple charge event.

The peak amplitudes in the sequenced event are 30 to 125 percent (85 percent average) higher than in the single charge event. This effect may be due partially to the fact that the structure was nearer the explosive in the sequenced event than in the single charge event (165 m vs 175 m) and partially due to the effect of the superposition of the

*See appendix A

second sequenced explosion on the first (the peaks occur during the time period of the second explosion). Analysis beyond these observations is not possible due to the few available data.

c. Explosive Vibration Test of a Reinforced Earth Wall

Reference II-19 describes a study in which dynamite blasts were used to excite a reinforced earth wall at the UCLA Engineering Field Station in Sangus, California. The overall study was designed to check a seismic design procedure on a full-scale test wall and supplement data from laboratory model tests. Dynamite blasts were included in the program because forced vibration tests provided only low levels of dynamic excitation (shear strains less than 0.001 percent) while the authors believed higher levels were necessary to evaluate nonlinear soil response. In addition, it was desired to obtain data from random type dynamic loadings.

A total of 20 explosive tests were conducted employing a wide variety of explosive types, detonation rates, locations, and depths of burial. Evaluations of initial small (0.3 to 2.7 lbs) tests by the authors indicated that a slow detonating explosive produced a greater wall response than the same amount of fast detonating explosive. As a result, the stronger tests utilized a slow detonating explosive. The large tests involved 5 to 20 lb charges of HP-90A dynamite and caused peak wall accelerations of up to 1.46 g horizontally and 1.25 g vertically. These accelerations were associated with small vibration periods, usually less than 0.1 sec.

Four of the larger tests involved multiple delayed explosions, but the delay caps available to the investigators were not adequate for properly phasing the explosions into a continuous wave train. Reference II-19 suggests that larger amounts of explosives at greater distances and the use of many multiple delay charges may be necessary to simulate realistic strong earthquake motions.

Reference II-19 analyzed the forced vibration and blast response of the wall to estimate values of the wall's first vibration mode frequency, the damping, and the maximum peak to peak soil shear strain adjacent to the wall. The results are shown in figure II-55. The frequency was obtained by performing a fast Fourier transform (FFT) of the acceleration at the top of the wall, while the strain was calculated as a ratio of the peak dynamic wall displacement divided by the wall height. The damping ratio was estimated using the log decrement method during the ring down phase of the wall vibration. Reference II-19 compared the results with estimates based on work by Seed and Idriss (ref. II-20) and found good agreement even to strains as high as near 1 percent. The disagreement of the damping ratios for the forced vibration tests (much higher than indicated by the blast results) were attributed in reference II-19 to geometric damping caused by the small size of the vibrator.

d. Structure Response to Quarry Blasts

Building and ground responses have been measured in the vicinity of several large quarry blasts. Reference II-21 describes the measurements made in a steel frame mill building located about 1000 ft

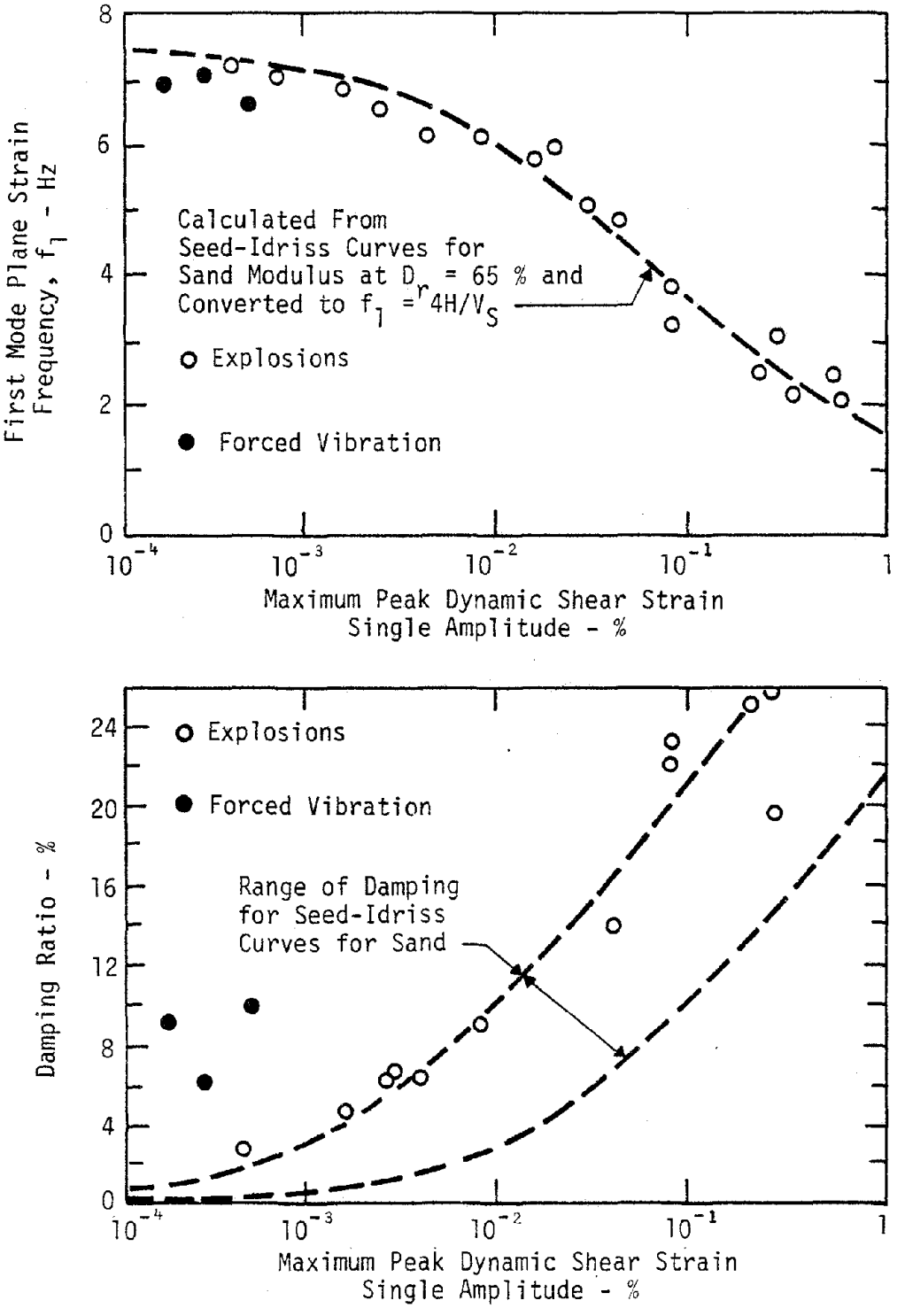

Figure II-55. Field Measured Dynamic Properties of Backfill Soil at UCLA Test Wall Compared with Published Data (ref. II-19)

from a 185 ton explosive charge. The peak ground acceleration near the structure was 0.12 g and reference II-21 notes that the acceleration time history shape was similar to that of the initial portion of a strong earthquake. Reference II-22 also observes that large quarry blasts generate ground accelerations in their vicinity which are comparable in amplitude and other characteristics to strong earthquakes.

4. CONCLUSIONS

The previous paragraphs have outlined some of the significant existing work which deals with explosive ground motions per se or with the use of explosively generated ground motions to excite structures. The major conclusions which can be drawn from this previous work are the following.

a. There is a very large existing base of data on the ground motions which result from single point sources. These data encompass varying depths of burst and material types. Significant, but lesser, amounts of data exist on cylindrical charges and planar charges. Data to define the effects of charge dimensions and various material types are lacking for these types of charges.

b. In spite of the large amounts of ground motion data available, there does not exist a common unified explanation of the data nor a general theory or scaling method for relating the complete data base. Data analyses consist in large part of a qualitative description of the results and the effects of different parameters in specific test series. An important conclusion from all of the data is that the results from a single well instrumented experiment or from identical experiments scatter over a relatively large range.

c. High explosives have been used to generate ground motion excitation of large structures. The results have indicated significant usefulness of such tests including the determination of as-built structure dynamic properties and the obtaining of insight into some nonlinear effects. However, the vibration levels in the experiments were relatively small. Specially designed experiments to simulate specific aspects of a strong earthquake ground motion environment have not been conducted. In addition, there has been no analysis of the criteria necessary to define simulation requirements.

d. Specific data from several ground motion experiments suggest some potential methods for designing an explosive experiment to simulate ground motions which approach earthquake levels, durations, and frequency content. The UCLA tests (refs. II-16 and II-19) indicate a strong potential use for delayed explosions in lengthening durations. The University of New Mexico DIHEST enhancement experiments (ref. II-9) suggest several potential methods for varying ground motion attenuation rates and tailoring ground motion amplitudes.

5. REFERENCES

II-1 Lampson, C.W., "Explosions in Earth," in Effects of Impact and Explosion, Summary Technical Report of Division 2, National Defense Research Committee, Vol. 1, Washington, D.C., 1946.

II-2 Underground Explosion Test Program, Final Report, Vol. I - Soil, Engineering Research Associates, Armour Research Foundation, Rensselaer Polytechnic Institute, 30 August 1952.

II-3 Sachs, D.C. and Swift, L.M., Small Explosion Tests, Project Mole, Vols. I and II, Final Report AFSWP-291, Stanford Research Institute, Menlo Park, California, December 1955.

II-4 Kuzmina, N.V. et al, "Seismic Effect of Eruptive Explosions in Nonrock Coherent Ground," Problems of Engineering Seismology, Edited by S.V. Medvedev (Translation from Russian), Consultants Bureau, New York, 1966.

II-5 Higgins, C.J. and Schreyer, H.L., An Analysis of Outrunning Ground Motions, AFWL-TR-74-220, Air Force Weapons Laboratory, Kirtland AFB, New Mexico, May 1975.

II-6 Harner, E.L et al, A Compilation of Test Information From a Series of DNA Sponsored Non-Nuclear Explosive Experiments, DASIAC SR-161, DASIAC, General Electric Company - Tempo, Santa Barbara, California, 15 November 1976.

II-7 Malthan, J.A., DNA Master File of Ground Shock, Airblast and Structure Response Data, DNA 3741F, prepared by Agbabian and Associates for Defense Nuclear Agency, Washington, D.C. 20305, 1 November 1975.

II-8 Crawford, R.E., Higgins, C.J., and Bultmann, E.H., The Air Force Manual for Design and Analysis of Hardened Structures, AFWL-TR-74-102, Air Force Weapons Laboratory, Kirtland AFB, New Mexico, October 1974.

II-9 Simmons, K.B., Soil DIHEST Motion Enhancement Techniques, AFWL-TR-72-233, Air Force Weapons Laboratory, Kirtland AFB, New Mexico, September 1973.

II-10 Schlater, D.R., DIHEST Improvement Program Test DIP IA, Data Report, AFWL-TR-71-120, Air Force Weapons Laboratory, Kirtland AFB, New Mexico, January 1972.

II-11 Schlater, D.R., DIHEST Improvement Program Test DIP IIA, Data Report, AFWL-TR-72-35, Air Force Weapons Laboratory, Kirtland AFB, New Mexico, April 1972.

II-12 Schlater, D.R., DIHEST Improvement Program Test DIP IIIA, Data Report, AFWL-TR-74-16, Air Force Weapons Laboratory, Kirtland AFB, New Mexico, April 1974.

II-13 Simmons, K.B., DIHEST Improvement Program Tests DIP IVA and DIP VA, AFWL-TR-74-238, Air Force Weapons Laboratory, Kirtland AFB, New Mexico, April 1975.

II-14 Seusy, E., Private Communication, Air Force Weapons Laboratory, Kirtland AFB, New Mexico, January 1977.

II-15 Bleiweis, P.B. et al, "Simulation of Strong Motion Earthquake Effects on Structures Using Explosive Blasts," Nuclear Engineering and Design, Vol. 25, pp 126-149, 1973.

II-16 Chrostowski, J., et al, Simulating Strong Motion Earthquake Effects on Nuclear Power Plants Using Explosive Blasts, UCLA-34P193-10, UCLA-ENG-7119, Nuclear Energy Laboratory and Earthquake Engineering and Structures Laboratory, School of Engineering and Applied Science, University of California at Los Angeles, February 1972.

II-17 Rojahn, C. and Negmatullaev, S.H., "Forced-Vibration Tests of a Three-Story Reinforced Concrete Frame and Shear-Wall Building in Tadzhik, S.S.R.," Proceedings, ASCE, Conference on Dynamic Response of Structures: Instrumentation, Testing Methods, and System Identification, University of California at Los Angeles, March 1976.

II-18 Rojahn, C., Personal Communications, Menlo Park, California, August and October 1976.

II-19 Richardson, G.N., et al, "Seismic Testing of Reinforced Earth Walls," Journal of the Geotechnical Engineering Division, ASCE, Vol. 103, No. GT1, January 1977.

II-20 Seed, H.B. and Idriss, I.M., Soil Moduli and Damping Factors for Dynamic Response Analyses, Report No. EERC 70-10, University of California, Berkeley, California, December 1970.

II-21 Hudson, D.E., Alford, J.L., and Housner, G.W., "Measured Response of a Structure to an Explosive-Generated Ground Shock," Bull. Seism. Soc. Am., 44(3), July 1954.

II-22 Hudson, D.E., Alford, J.L. and Iwang, W.D., "Ground Accelerations Caused by Large Quarry Blasts," Bull. Seism. Soc. Am., 51(2), April 1961.

SECTION III
SIMULATION CRITERIA

1. THE SIMULATION CONCEPT

The word simulation generally implies that the prototype environment cannot be generated at will and that some features or characteristics of the prototype environment will not be reproduced exactly in a simulation. In developing or designing a simulation technique, it is necessary to determine those characteristics of the full-scale environment which are essential to adequately evaluate the system of interest. Note that the system of interest is a major consideration. Certain features of earthquakes may be important for one structure but not for another. For example, aboveground structures founded on soil may be adequately tested by simulating certain kinematic features of earth motion (acceleration, frequency content, duration) while belowground structures may require both a kinematic and dynamic simulation (i.e. both motions and stresses).

The dynamic response characteristics of a structure are of major importance in designing a simulation experiment. For example, if an earthquake of interest has a given acceleration, frequency content and duration, the important features which must be simulated for a particular structure are directly related to the response characteristics of the structure itself. If the characteristics are such that maximum response will be achieved at, say, one-fourth the duration of the earth-

quake, then it may not be necessary to simulate the complete duration. If the structure is not acceleration sensitive but velocity or displacement sensitive, then certain acceleration amplitude features of the prototype earthquake may be compromised while still achieving an adequate simulation. The major point to be made here is that the adequacy of a simulation cannot simply be judged by the degree with which it matches the prototype environment, but must be judged by the degree to which the response of the system of interest matches or yields insight into prototype response. Obviously, it will not be possible to define prototype response in every detail so that precise simulation requirements can be defined. However, it is believed that analytical studies and engineering judgement can be applied to establish reasonable simulation needs.

An important point to be recognized is that no simulation, shake table, explosive or otherwise, will fully reproduce every feature of an earthquake and its interaction with an engineering system. However, explosive simulation can produce environments equally as complex as earthquake environments and excite structures of prototype size. It is believed that the most important value of such simulation is that both the excitation and the response can be used to judge the ability of current analytical techniques to predict response. Also, the experimental results provide a data base for developing new or improved techniques. If analytical techniques provide satisfactory prediction and/or understanding of a complex simulated dynamic environment and response, then the technical community will gain improved confidence that the same techniques can be adequately applied to prototype earthquake environments.

In developing simulation criteria for a particular engineering system, it will be necessary to consider the two primary aspects of the prototype problem:

a. The characteristics of the prototype earthquake environment.

b. The dynamic characteristics of the engineering system.

The remainder of this section discusses these problems in general terms. Detailed criteria cannot be given because the criteria will vary with the earthquake threat in a particular region and the specific system of interest. However, the approach given in the following should provide a guide to criteria development. An example for a specific problem is given in Section VIII.

2. EARTHQUAKE CHARACTERISTICS

a. Introduction

The characteristics of an earthquake environment which are of interest include motion amplitude, time history and/or frequency content, duration and as much detail as possible on individual wave components and associated stresses. These characteristics will be dependent upon the earthquake source mechanism, the source size, the geology, and properties of the geologic materials between the source and the structure location. Ideally, it would be desirable to combine these factors into a consistent physical theory so that effects could be predicted under any combination of conditions. Unfortunately, the state of understanding of earthquakes has not advanced to that stage. Current understanding is based upon empirical measurements and observations combined with elementary theories.

b. Earthquake Mechanisms

Major earthquakes are caused by tectonic processes i.e., processes that cause deformation of the earth's crust. Specific mechanisms however, are subject to some controversy. The most widely accepted theory, at least for the shallow focus (less than 60 km) earthquakes of the Western United States, is that they result from the sudden release of strain energy by rupture of a fault (refs. III-1, III-2, and III-3). This theory, known as the elastic rebound theory, is due originally to H.F. Reid who developed it after study of the San Francisco earthquake of 1908. The theory holds that tectonic forces in various parts of the earth are causing strains in the crustal rocks. When these strains exceed the strength of the rock, a rupture takes place and the strained rock rebounds under its elastic stresses until the strain is relieved. The release of strain energy which occurs as the rock rebounds gives rise to the strong earthquake waves which propagate away from the fault.

The original elastic rebound theory has subsequently been modified to account for aftershocks by hypothesizing that after rebound there is a readjustment and repartitioning of the remaining strain in the region (ref. III-1). The stress may grow on a section of the fault, which may have been weakened by the main fracture, until local slip occurs again. This readjustment can continue to occur until everywhere the strains are below those necessary for rupture. The modified elastic rebound theory is consistent with aftershocks and with the observation that surface deformation in the form of fault rupture, surface uplift, or subsidence often accompanies shallow focus earthquakes of moderate to large energy

release. Reference III-1 also notes that analyses of P-wave first motions in a large number of cases suggest a line source which lies within a few degrees of a major fault in the vicinity. Exceptions, where observable faulting is not evident in major earthquakes, include the Charleston earthquake of 1886, the New Madrid, Mo. earthquake of 1811 and shallow focus earthquakes in Japan and Europe (ref. III-1). However, the elastic rebound theory is consistent with most available evidence in the Western United States.

The tectonic model which leads to the crustal strains is described in reference III-2 as based upon magnetic variations which show that the sea floors have spread outward from the mid-oceanic ridges to plunge finally beneath the ocean trenches. The model proposes that the earth's surface is divided into a small number of geological plates. These plates move outward from the mid-oceanic ridges causing plate motion over the entire earth. Earthquakes occur mainly along the mid-oceanic ridges and the edges of the plates. The San Andreas fault appears to form the western boundary of the North American plate which extends to the Mid-Atlantic ridge. Along the San Andreas, the North American plate is moving west while the Pacific plate is moving northwest; both at different velocities.

If the discussion is restricted to earthquakes which are generated by fault slip, then it can be seen that the source of the earthquake is extended in space. The term focus or hypocenter is used to designate the point at which rupture starts (i.e., the source of the first waves to arrive at a point). Epicenter refers to the point on the ground surface immediately above the source of energy release. The focus, however,

may not be the center of energy release if faulting occurs over a large region since the focus, or point of initiation, may lie anywhere on the fault.

The energy released in an earthquake can be quantified in a relative way by the Richter magnitude of the earthquake. The magnitude is defined (ref. III-3) as:

$$M = \log_{10} \frac{A}{A_o} \qquad \text{(III-1)}$$

where

M = magnitude

A = maximum amplitude in thousandths of a millimeter recorded by Wood-Anderson seismograph at a distance of 100 km from the epicenter

A_o = an amplitude of one-thousandth of a millimeter

In practice, measurements are made at various distances and must be extrapolated to 100 km. Reference III-1 provides the following empirical relation between magnitude and energy:

$$\text{Log } E - \text{Log } E_o = aM \qquad \text{(III-2)}$$

where

E = energy in ergs

$E_o = 2.5 \times 10^{11}$ ergs

a = 1.5

The relation indicates that for a 1 unit increase in magnitude there is a 32 fold increase in energy.

The energy released by an earthquake is directly related to the

faulting characteristics. Reference III-2 states that the energy is proportional to the length of faulting and the square of the fault slip. This assumes (ref. III-4) that the shear stress drop on the fault is approximately the same for small earthquakes as for large earthquakes. A large earthquake is associated with a failure over a large region leading to a large release of strain energy. The size of the earthquake or slipped area is manifested in the frequency content, duration, and lowered geometric attenuation of the seismic waves with distance. The amplitude of the ground motion at the source seems more related to the stress drop and local geologic conditions (ref. III-2).

Earthquakes of magnitude 5.0 and greater generate ground motions sufficiently severe to be potentially damaging to engineering systems (ref. III-4). The vertical and horizontal dimensions of the slipped region are about the same for earthquake magnitudes less than about 6.0. Larger earthquakes may involve slipped regions extending for tens to hundreds of miles. This relation between magnitude and slipped length gives added engineering importance to magnitude in that it indicates the approximate size of the source and, therefore, the approximate area affected by ground shaking.

c. Seismic Waves Generated by Earthquakes

Elastic wave propagation theory predicts that dilatational (P), shear (S), and Rayleigh waves (R) will result from any disturbance in a medium which contains a free surface. Even a pure dilatational source will generate shear waves and Rayleigh waves upon reflection from the free surface. Layered media introduce P and S waves from wave inter-

actions at layer interfaces and, in addition, surface waves with strong horizontal surface motion transverse to the direction of propagation, known as Love waves. The theoretical wave velocities of P, S, and surface waves indicate that P-waves travel the fastest, S-waves next and lastly surface waves. The S-wave velocity is related to the P-wave velocity by the following relation

$$C_S = \sqrt{\frac{(1 - 2\nu)}{2(1 - \nu)}}\, C_p \qquad \text{(III-3)}$$

where

C_S = shear wave velocity

ν = Poisson's ratio

C_p = dilatational wave velocity

In an elastic half-space, the Rayleigh wave speed can be computed as the real root of

$$4 \left(1 - \frac{C_R^2}{C_p^2}\right)^{\frac{1}{2}} \left(1 - \frac{C_R^2}{C_S^2}\right)^{\frac{1}{2}} = \left(2 - \frac{C_R^2}{C_S^2}\right)^2 \qquad \text{(III-4)}$$

where C_R = Rayleigh wave velocity.

For a Poisson's ratio of 0.25, a representative value for many rocks,

$$C_R = 0.92C_S = 0.53C_p \qquad \text{(III-5)}$$

In layered geologies, the velocities of surface waves, Rayleigh or Love, are more complicated because the waves are dispersive in nature, i.e., the phase velocity of a particular frequency component is a function of the frequency which, in turn, is related to the layer depths and the source characteristics (ref. III-5). This dispersive

nature will cause a transient pulse at the source to spread into a wave train as it propagates outward.

With regard to geometric attenuation, P and S waves attenuate spherically in amplitude at large distances from the source, in proportion to the range, R, while surface waves (which are confined to the near-surface region) attenuate cylindrically in proportion to $\sqrt{R}$ (ref. III-6). As a result, surface waves predominate at the more distant ranges.

Although elastic wave theory accounts for many of the observed wave phenomena in earthquakes, the detailed motions, including amplitude, frequency content and individual wave components, are dominated by source characteristics, material inelasticity, viscosity, anisotropy and non-homogeneity. Lack of understanding and major uncertainties in all of these parameters make theoretical predictions of seismic waves emanating from a fault break beyond the state-of-the-art at this time.

However, it is possible to make qualitative assessments of expected motions from general knowledge of the effects of the various parameters and from available recorded motions. Prime interest is the focal region, where P, S, and surface wave effects are intermixed, because that is the region where potential damage to engineering structures is most severe. Reference III-1 notes that ground shaking produced by progressive rupture on a fault will be different than if it were produced, for example, by an explosion. Since the fault slip is essentially a shearing mechanism, it would be expected that a primary effect in the near region

perpendicular to the fault would be due to shear waves while off the ends of the fault dilatational and compressional waves might be relatively important. The actual character of the waves would be sensitive to the type of faulting (e.g., strike-slip, dip-slip or some combination).

Focal depth is an important earthquake parameter in that shallow focus (less than 60 km) earthquakes cause the greatest damage (ref. III-1). In addition, focal depth seems to affect the relative importance of the wave components in the near field. Reference III-1 notes that deep foci do not excite strong surface wave motions. In addition, theoretical work (ref. III-7) on underground disturbances indicates that the amplitude of Rayleigh waves is insignificant compared to P and S waves out to distances as much as 5 times the focal depth. Reference III-2 notes that S-waves provide the greatest transverse ground shaking within a few tens of kilometers from the fault. They generally move upward from the fault at depth.

Reference III-8 follows this same reasoning and notes that, due to the decreasing wave speed with increasing height above the fault, the waves are refracted into nearly vertical ray paths. As a result, surface response can be computed from basement rock motion with a one-dimensional model. Reference III-9 and III-10 describe one-dimensional models for shear wave propagation. Given the rock motion, the response of the surface of an arbitrary site can be computed or, alternatively, the rock motion can be estimated from measured surface motions at a site. The major difficulty with verifying this approach, as well as other pos-

tulations of motion in the source region, is the absence of a significant amount of data in the focal region of major earthquakes, especially on rock or at depth.

d. Earthquake Ground Motion Amplitudes

As is evident from the preceding discussions of earthquake mechanisms and resulting waves, the state-of-the-art in fundamental earthquake understanding is not sufficient for the quantitative prediction of ground motion amplitudes and time histories. The current information on ground motion amplitudes is based upon recorded accelerations, most of which were taken on alluvium. It appears from the literature that there is no generally accepted synthesis of the available data into a consistent empirical prediction method which can relate ground motions to factors such as magnitude, distance from the causative fault and geologic parameters. However, several investigators have presented prediction relations and a few of the results are reviewed in the following.

Reference III-11 proposes an upper limit of 0.5 g for the maximum acceleration possible in the vicinity of a major earthquake based upon an extrapolation of data available at that time (1965), suggesting that the maximum acceleration should be related to stress drop on the fault which is upper bounded by the failure strength of rock. Extending the argument, estimating the stress drop to be about 500 to 1000 psi based upon surface strain measurements from large earthquakes, and assuming reasonable rock properties, reference III-11 proposes an upper bound for the area (approximately the peak velocity) of an acceleration pulse

of 0.5 g to be about 2.0-ft/sec. This velocity implies a square acceleration pulse with a time width of 0.25 sec.

Other investigators and more recent data suggest that the proposed upper bound of reference III-11 is too low. The maximum recorded acceleration at Poicoma Dam (ref. III-12) was 1.25 g and reference III-6 indicates that the maximum acceleration in the 1897 Assam earthquake was at least 1.0 g and perhaps 1.5 g. Reference III-13 suggests that at the source very high accelerations are possible, perhaps as high as 2.0 g or greater. Whether this acceleration reaches the surface is dependent upon the local geology. Reference III-13 also suggests an upper bound of 1.5 m/sec (5 ft/sec) for the maximum rock velocity near the fault break which, as with peak acceleration, may or may not reach the surface depending on geology.

Correlations between magnitude, distance, and ground motions in the near-field are subject to significant uncertainty. However, some correlations have been proposed as the basis for the development of design criteria. Reference III-14 presents the curves of displacement, velocity, and acceleration versus distance and magnitude which are shown in figure III-1. The development of the curves is not discussed although the authors state that they are based upon sparse data and are conservative.

Reference III-15 presents the following equations for relating acceleration, velocity, and displacement to magnitude and distance:

$$a = 1230e^{0.8}\ (R + 25)^{-2} \qquad \text{(III-6)}$$

$$v = 15e^{M}\ (R + 0.17e^{0.59M})^{-1.7} \qquad \text{(III-7)}$$

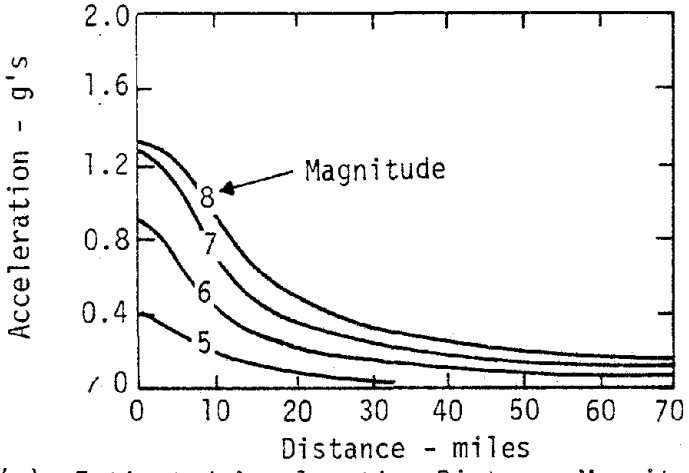

(a) Estimated Acceleration-Distance-Magnitude Relationships

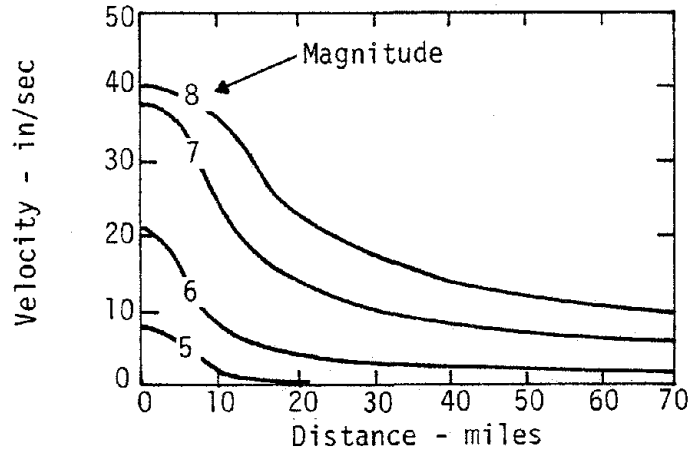

(b) Estimated Velocity-Distance-Magnitude Relationships

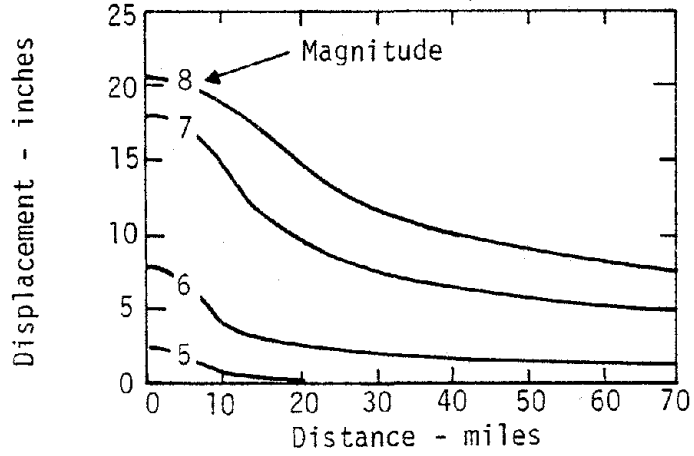

(c) Estimated Displacement-Distance-Magnitude Relationships

Figure III-1. Estimated Motion-Distance-Magnitude Relationships (ref. III-14)

$$d = \frac{v^2}{a}\left(1 + \frac{400}{R^{0.6}}\right) \qquad \text{(III-8)}$$

where

a = acceleration in cm/sec^2

v = particle velocity in cm/sec

d = displacement in cm

R = range in km

M = Richter Magnitude

e = base of the natural logarithm

The accelerations and velocities predicted by equations III-6 and III-7 are compared with the recommendations of reference III-14 in figures III-2 and III-3, respectively. The near-field peak acceleration recommendations of reference III-4 are also included in figure III-2. The correlations from the three sources differ so markedly that it is difficult to even describe the differences qualitatively. Comparisons of displacements are not presented because equation III-8 leads to displacements which are so large that they appear to be unreasonable compared to available data and other correlations.

Reference III-8 proposes the basis for a somewhat different approach to the prediction of ground motion. The authors estimate bedrock horizontal peak accelerations by combining the measured rock motions from the San Fernando earthquake of 1971 (the largest number of rock motion records available), rock motions which were estimated from measurements on soil by using soil property estimates and a one-dimensional shear wave model, and attenuation assumptions to obtain a correlation between peak rock acceleration, earthquake magnitude and dis-

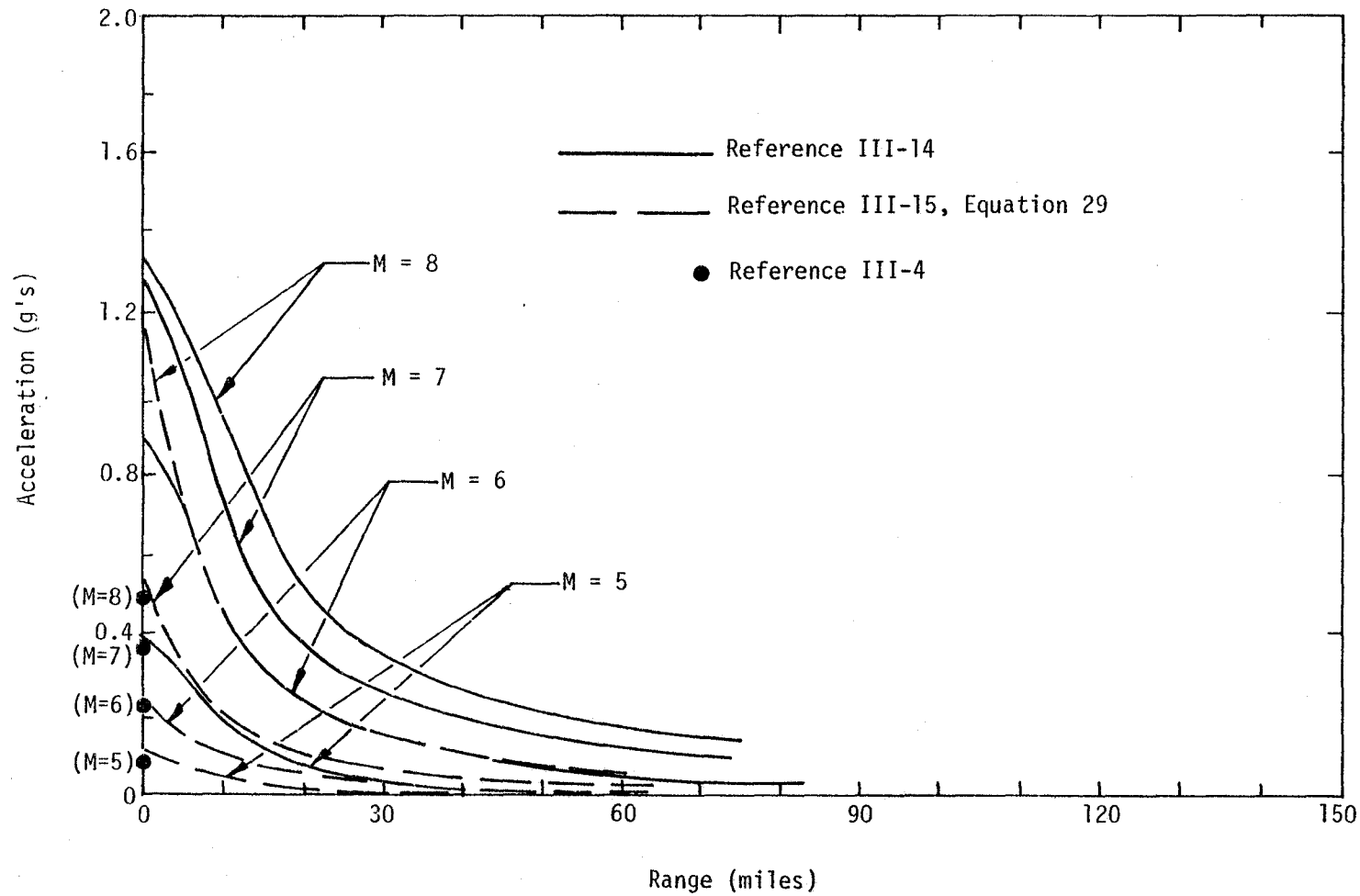

Figure III-2. Some Correlations Between Peak Acceleration, Range, and Earthquake Magnitude

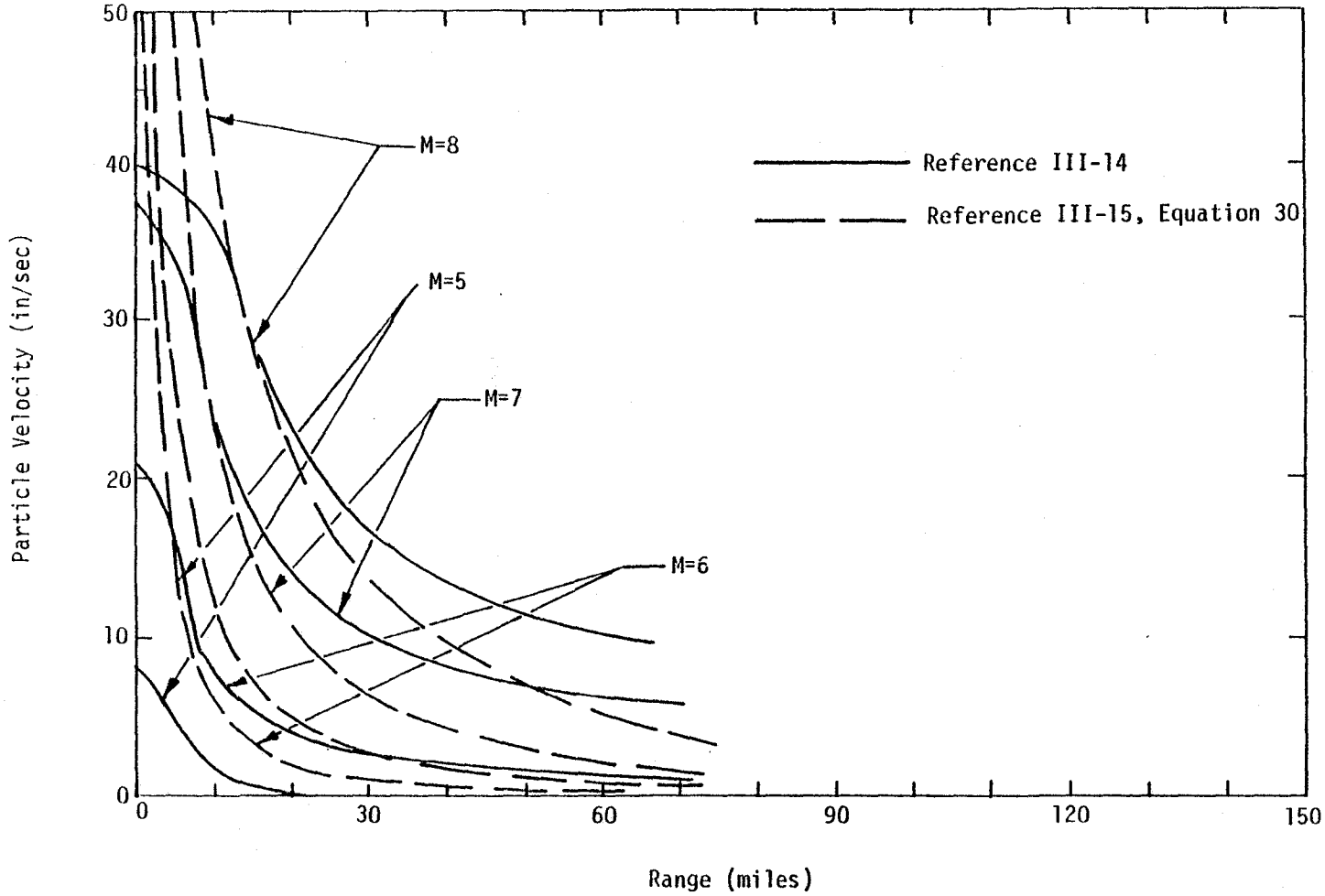

Figure III-3. Some Correlations Between Peak Particle Velocity, Range, and Earthquake Magnitude

tance. The correlation for average maximum accelerations is shown in figure III-4. Uncertainty ranges are shown in figure III-5. The use of the rock acceleration correlations requires a knowledge of the detailed soil properties at the site, an assumed normalized acceleration time history and the calculation of the motion transmission to the surface with a wave propagation code.

In addition to empirical methods which attempt to correlate motions as a function of range and magnitude, information is available in the literature on base ground motions used for design of various systems. For example, reference III-16 outlines the design earthquake ground motions used for the Trans-Alaska pipeline. The ground motions for the "contingency plan" earthquake (i.e., system designed to survive contingency earthquake but not necessarily continue operation) are given in table III-1. Various magnitude earthquakes are given because the design earthquake varies along the pipeline. The authors state that the values given are "effective" values of such motions and are not the maximum spikes or possible maximum instrumentation readings that might be recorded. They do not define the meaning of "effective" or how the "effective" peaks are determined. The values of table III-1 can be compared with the proposed correlations of reference III-14 (fig. III-1) at a range which yields the same velocity. For the magnitude 8 earthquake, reference III-14 predicts a 29 in/sec velocity at a range of 15 miles. The corresponding acceleration and displacement are 0.7 g and 17 in, respectively, about 15 percent higher on acceleration and 15 percent lower on displacement. For the magnitude 7 event, the corresponding range for a 14 in/sec velocity is 20 miles, which yields an acceleration of 0.38 g

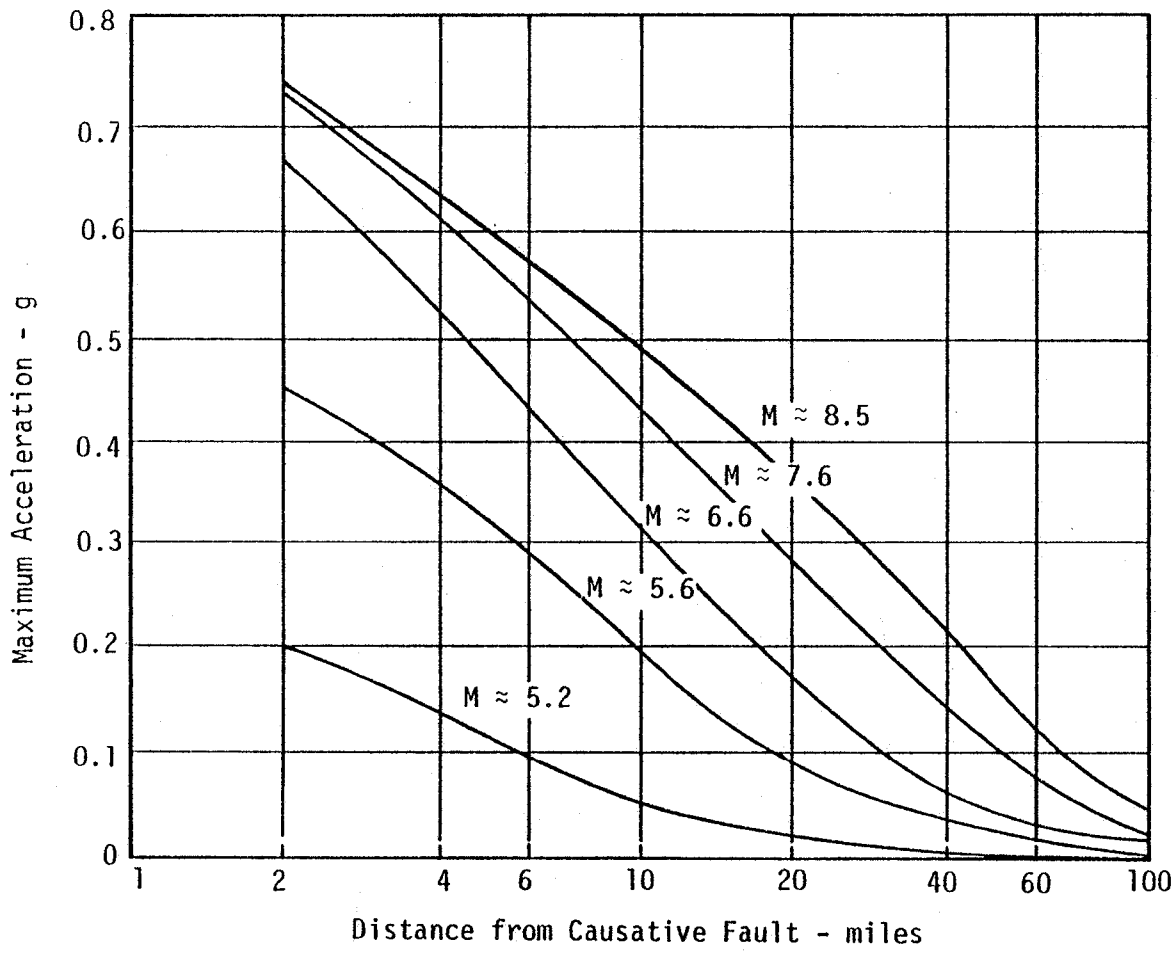

Figure III-4. Average Values of Maximum Accelerations in Rock (ref. III-8)

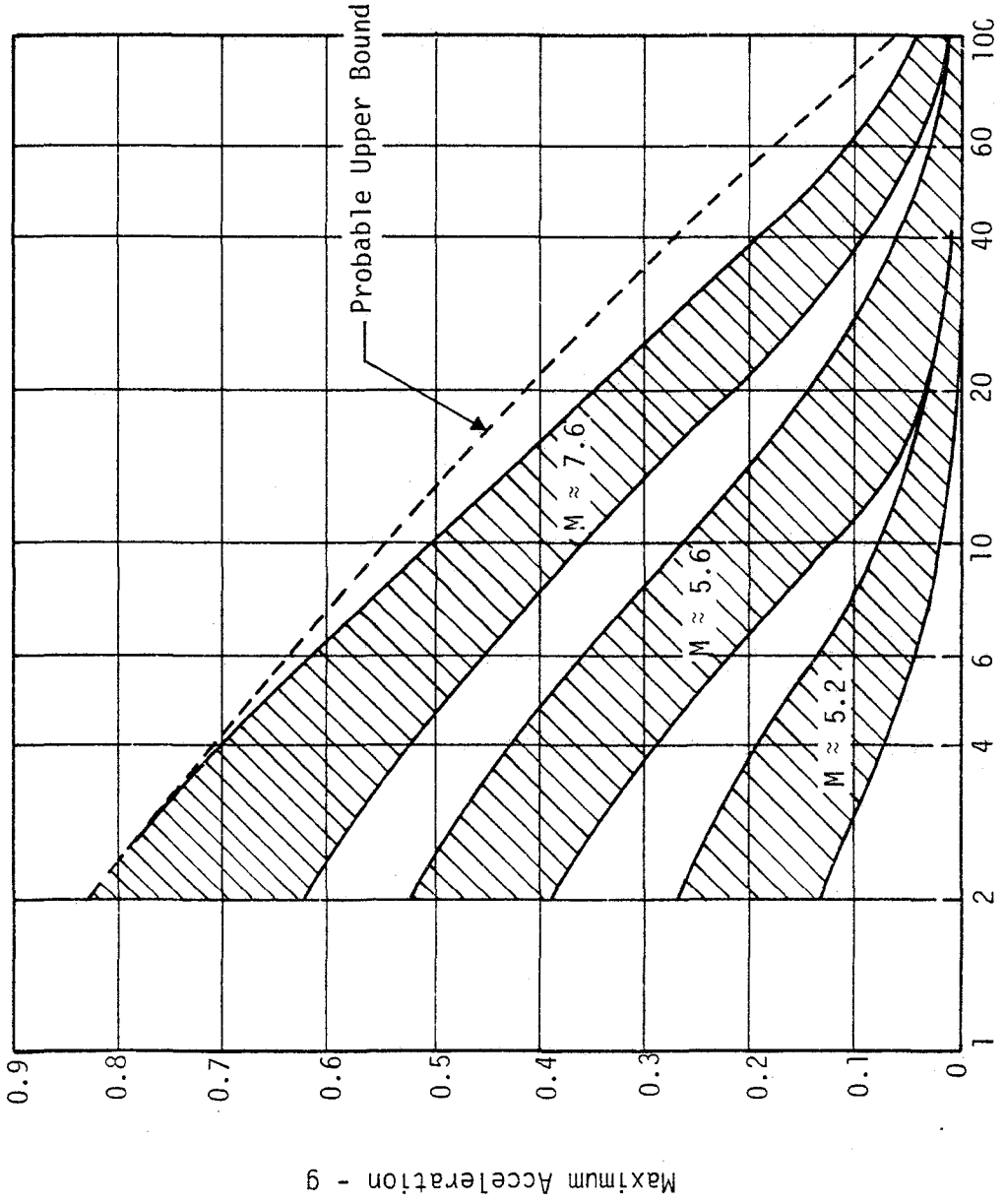

Figure III-5. Ranges of Maximum Accelerations in Rock (ref. III-8)

Table III-1
Contingency Plan Ground Motions for Trans-Alaska Pipeline (ref. III-16)

Magnitude	Acceleration (g)	Velocity (in/sec)	Displacement (in)
8.0	0.60	29	22
7.5	0.45	22	17
7.0	0.30	14	10
5.5	0.12	6	5

and a displacement of 9.5 in. The acceleration is about 27 percent higher and the displacement about 5 percent lower. The agreement for the 5.5 magnitude earthquake is not as good. Although the proposals of reference III-14 are not in precise agreement with the design criteria of reference III-16, the agreement is far better than with reference III-15.

Seismic design spectra for nuclear power plants are discussed in reference III-17. Spectra will be discussed in some detail in a later paragraph, but of interest here are proposed maximum ground motions. Without citing a specific earthquake magnitude, reference III-17 notes that for a 1 g ground acceleration in alluvium, the corresponding maximum ground velocity is 48 in/sec and maximum displacement is 36 in. On hard rock, the values are 28 in/sec and 12 in. Again comparing with reference III-14, and selecting a magnitude 8 earthquake, it is found that 1 g corresponds to a range of 8 miles. The velocity and displacement at this range are 37 in/sec and 18 in, about 25 percent and 50 percent less than the alluvium proposals of reference III-17.

Although the literature does not yield motion amplitude correlations universally agreed upon, the recently proposed correlation of reference III-14 and the proposed motion amplitudes of reference III-16 and III-17 are not grossly in disagreement. The results of these separate investigators provide at least a trend toward the bounds on strong motions which can be expected. The results of reference III-15 predate these other three, are in significant disagreement with them, and will not be considered further herein.

Very little direct attention is given to vertical ground motions in the existing literature. Usually vertical ground motion amplitudes are related in magnitude to the horizontal component. Reference III-4 notes that the vertical peak acceleration is 1/3 to 2/3 the horizontal and usually has higher frequency components. With regard to response spectra, reference III-4 states that the vertical spectra values are usually given as 1/2 and 2/3 the horizontal. Reference III-17 gives maximum vertical motion amplitudes of 2/3 g, 29 in/sec and 33 in for alluvium and 2/3 g, 17 in/sec and 11 in for rock. These values are 66.6 percent (2/3), 60 percent and 29 percent the maximum horizontal amplitudes.

e. Earthquake Ground Motion Durations

Reference III-11 presents a correlation of ground motion duration with earthquake magnitude for magnitudes greater than 5 which can be written as

$$T = 11.2M-53 \qquad \text{(III-9)}$$

where

T = duration of strong ground shaking in seconds.

M = Richter magnitude

Equation III-9 is restricted to regions very near the source and estimates the duration of the strong shaking phase. Shaking of lesser intensity will occur for a relatively long period of time.

Reference III-18 provides an estimate of ground motion duration given by

$$T = 0.02e^{0.47M} + 0.3R \qquad \text{(III-10)}$$

where R = range in kilometers

A recent statistical study of ground motion duration based upon 188 acceleration records is given in reference III-19. The authors note that a major difficulty in studying duration is determining a suitable definition of duration. Reference III-19 selects a definition based on the mean-square integral of the motion (acceleration, velocity or displacement) which is closely related to that part of the strong motion which makes a significant contribution to the seismic energy arriving at a point. The recommended correlation is

$$T = aS + bM + c\Delta \pm \sigma \qquad \text{(III-11)}$$

where

T = duration in seconds

S = a site dependent constant

M = magnitude

Δ = range in kilometers

σ = one standard deviation

a,b,c = constants

The site constant S is 0, 1 or 2 depending upon whether the site is soft (alluvium), intermediate or hard (crystalline rock), respectively. The constants a, b and c and the standard deviation given in table III-2, depend upon whether the acceleration, velocity, or displacement is being considered. The correlations of reference III-11, III-18, and III-19 are compared for acceleration in figure III-6. Comparisons with reference

Table III-2

Coefficients for Estimates of Earthquake Ground Motion Duration (ref. III-19)

Duration $\left\{\begin{matrix}\text{acceleration}\\ \text{velocity}\\ \text{displacement}\end{matrix}\right\} = as + bM + c\Delta \pm \sigma;$

Component	a	b	c	σ
		Acceleration		
Vertical	-6.29	2.90	0.172	10.89
Horizontal	-4.88	2.33	0.149	10.67
		Velocity		
Vertical	-6.51	4.50	0.100	12.13
Horizontal	-5.60	3.55	0.141	12.16
		Displacement		
Vertical	-5.82	5.32	0.0307	13.61
Horizontal	-4.08	4.07	0.107	13.72

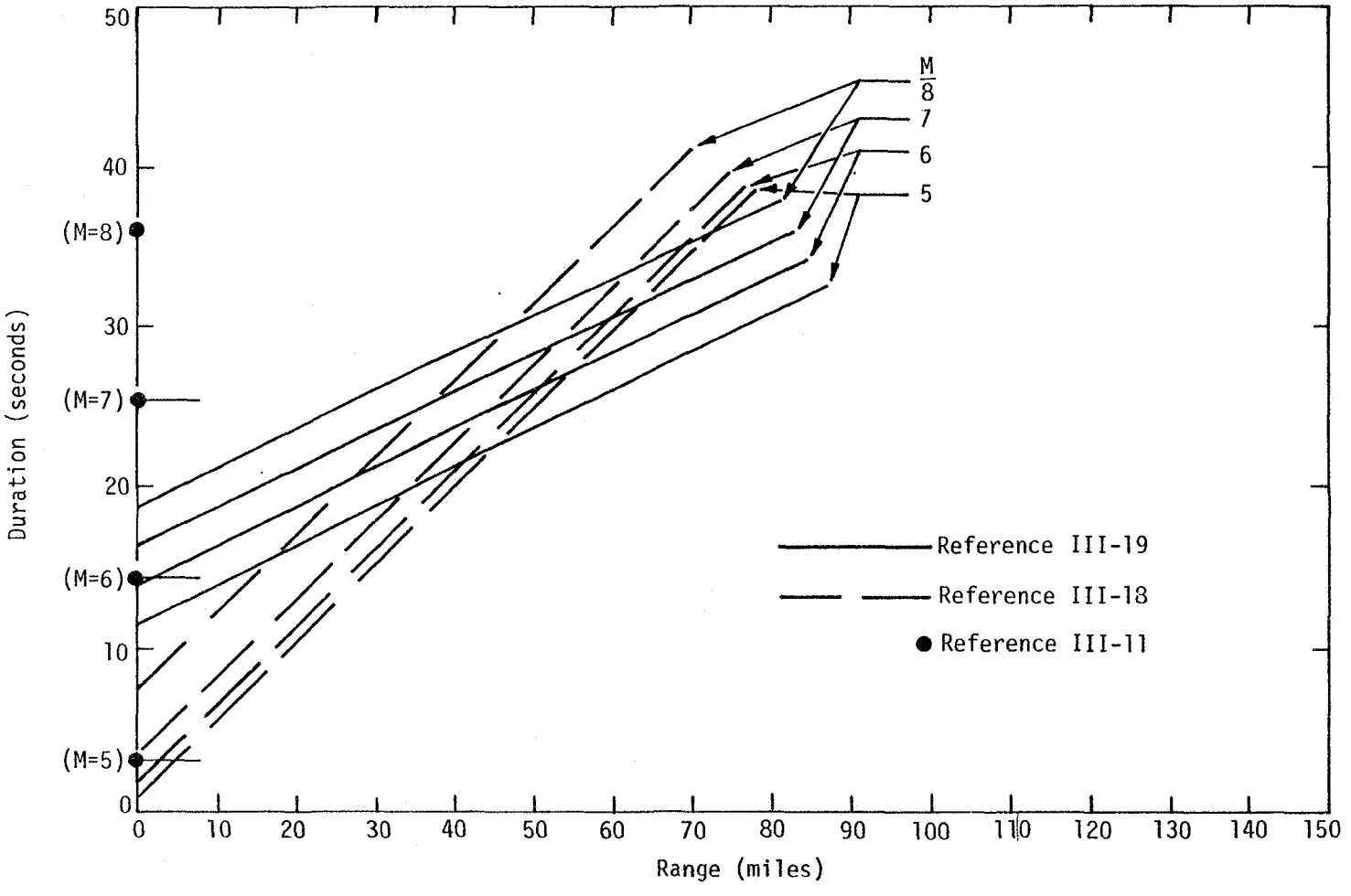

Figure III-6. Some Correlations Between Strong Motion Duration, Range and Earthquake Magnitude

III-19 results for velocity and displacement are similar. There does not appear to be a consistent relation between the three sources at all. It may be due to the lack of a consistent definition of duration among the three sources. The results of reference III-19 are the most recent and are based on the analysis of a large amount of data; therefore, rather arbitrarily, duration estimates, where required herein, will be based on reference III-19 results.

f. Ground Motion Time Histories

There is no available method, empirical or otherwise, which allows the prediction of an earthquake ground motion. However, a large number of the strong motion accelerograms recorded in the United States have been digitized, corrected and integrated. These records and their integrations are given in plotted and print-out form in reference III-20, and are available on punched cards or magnetic tape from the Earthquake Engineering Research Laboratory at the California Institute of Technology. An example of the available plotted ground motion data is given in figure III-7.

g. Response Spectra

The frequency content of earthquake ground motions is usually analyzed and interpreted through the use of response spectra or Fourier spectra. Response spectra are discussed here. Fourier spectra are discussed in a later paragraph. A useful way of expressing the effect of a ground motion on an engineering system, including the effects of both amplitude and frequency content is through the use of a response

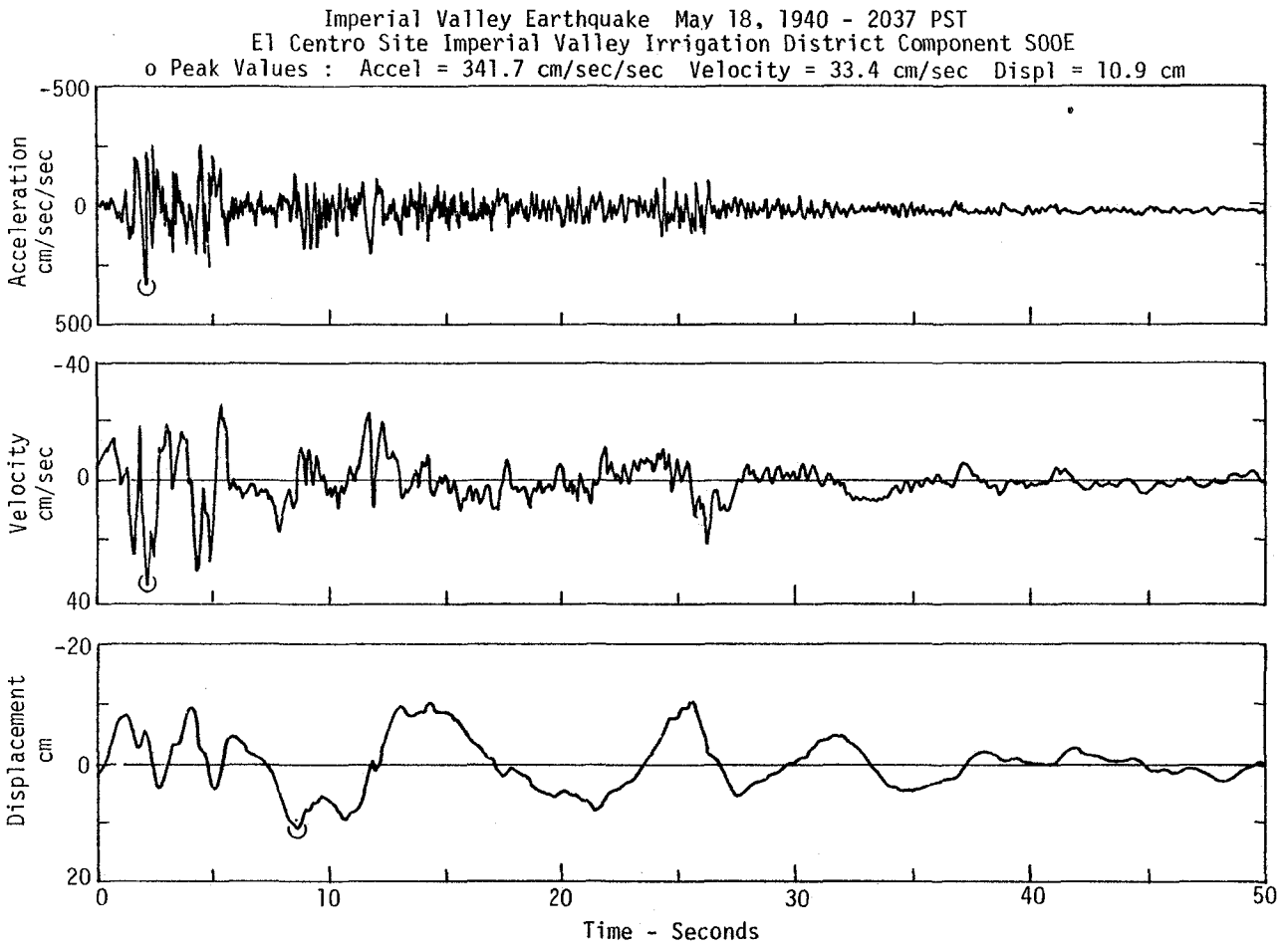

Figure III-7. Typical Earthquake Ground Motion Time History (ref. III-20)

spectrum. The response spectrum concept is reviewed in detail below because of its potential use in developing simulation criteria.

Response spectra give the maximum response of a single degree of freedom system as a function of the frequency or period of the system. Consider the single degree of freedom system shown in figure III-8 having mass m, a linear spring of stiffness k, viscous damping c, and subjected to a base motion. The equation of motion of the mass is

$$m\ddot{u}(t) + c\dot{u}(t) + ku(t) = -m\ddot{y}(t) \qquad \text{(III-12)}$$

or

$$\ddot{u}(t) + 2\beta\omega_n\dot{u}(t) + \omega_n^2 u(t) = -\ddot{y}(t) \qquad \text{(III-13)}$$

where

$y(t)$ = base displacement as a function of time

$x(t)$ = absolute displacement of the mass

$u(t)$ = relative displacement between the mass and the base = $x(t) - y(t)$.

$\beta = \frac{c}{2\sqrt{km}}$ = damping ratio or fraction of critical damping

$\omega_n = \sqrt{k/m}$ = undamped natural frequency

and a dot ($\cdot$) above a variable indicates the usual differentiation with respect to time.

For zero initial conditions equation III-12 has the solution (e.g. ref. III-21)

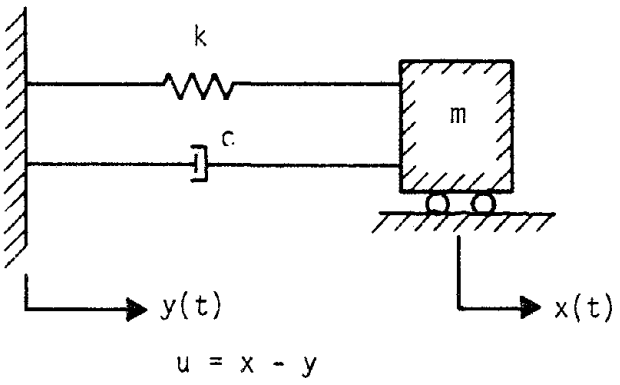

Figure III-8. Single Degree of Freedom System Subjected to Base Motion

$$u = (x - y) = \frac{-1}{\omega_n\sqrt{1-\beta^2}} \int_o^t \ddot{y}(\tau) e^{-\beta\omega_n(t-\tau)} \sin\omega_n\sqrt{1-\beta^2}\,(t-\tau)d\tau \qquad \text{(III-14)}$$

Successive differentiation of equation III-14 with respect to time and the use of the relation between absolute and relative acceleration lead to the following expressions for relative velocity and absolute acceleration

$$\dot{u} = (\dot{x} - \dot{y}) = -\int_o^t \ddot{y}(\tau) e^{-\beta\omega_n(t-\tau)} \cos\omega_n\sqrt{1-\beta^2}\,(t- \quad d\tau \qquad \text{(III-15)}$$

$$+ \frac{\beta}{\sqrt{1-\beta^2}} \int_o^t \ddot{y}(\tau) e^{-\beta\omega_n(t-\tau)} \sin\omega_n\sqrt{1-\beta^2}\,(t-\tau)d\tau$$

$$\ddot{x} = \omega_n \frac{(1-2\beta^2)}{\sqrt{1-\beta^2}} \int_o^t \ddot{y}(\tau) e^{-\beta\omega_n(t-\tau)} \sin^{\omega}{}_n\sqrt{1-\beta^2}\,(t-\tau)d\tau \qquad \text{(III-16)}$$

$$+ 2\omega_n\beta \int_o^t \ddot{y}(\tau) e^{-\beta\omega_n(t-\tau)} \cos\omega_n\sqrt{1-\beta^2}\,(t-\tau)d\tau$$

The maximum values of $u(t)$, $\dot{u}(t)$ and $\ddot{x}(t)$ have important engineering significance and their values may be written as

$$\begin{aligned} S_d &= |u(t)|_{max} \\ S_v &= |\dot{u}(t)|_{max} \\ S_a &= |\ddot{x}(t)|_{max} \end{aligned} \qquad \text{(III-17)}$$

Any one of the quantities S_a, S_v, or S_d can be computed as a function of the natural frequency or period and damping of the system for any given base motion and plotted as a function of frequency or period. The resulting curves are known as the maximum relative displacement

spectrum, relative velocity spectrum or absolute acceleration spectrum, depending upon the quantity plotted. Any one of the individual spectra is commonly called a response spectrum. An example relative velocity spectrum (ref. III-22) is shown in figure III-9. Also shown in figure III-9 is the Fourier amplitude spectrum whose relation to the relative velocity spectrum is discussed later. In the blast response community, the response spectrum is often called a shock spectrum and often the terms response spectra or shock spectra are used to refer to all or any of the individual spectra.

All three spectra have uses. The relative velocity spectrum has good definition at both high and low values of frequency while the relative displacement and acceleration spectra become obscured due to the frequency or period multipliers in equations III-14 and III-16. The maximum relative velocity gives a direct measure of the maximum energy per unit mass in the system. The relative displacement spectrum is important because it is directly related to system strain. The absolute acceleration spectrum is important because it is directly proportional to the seismic coefficient or lateral force coefficient commonly used in building codes, i.e., if

$$F_{max} = CW \tag{III-18}$$

where

F_{max} = the maximum force on the mass

W = weight of the mass

C = seismic coefficient

then

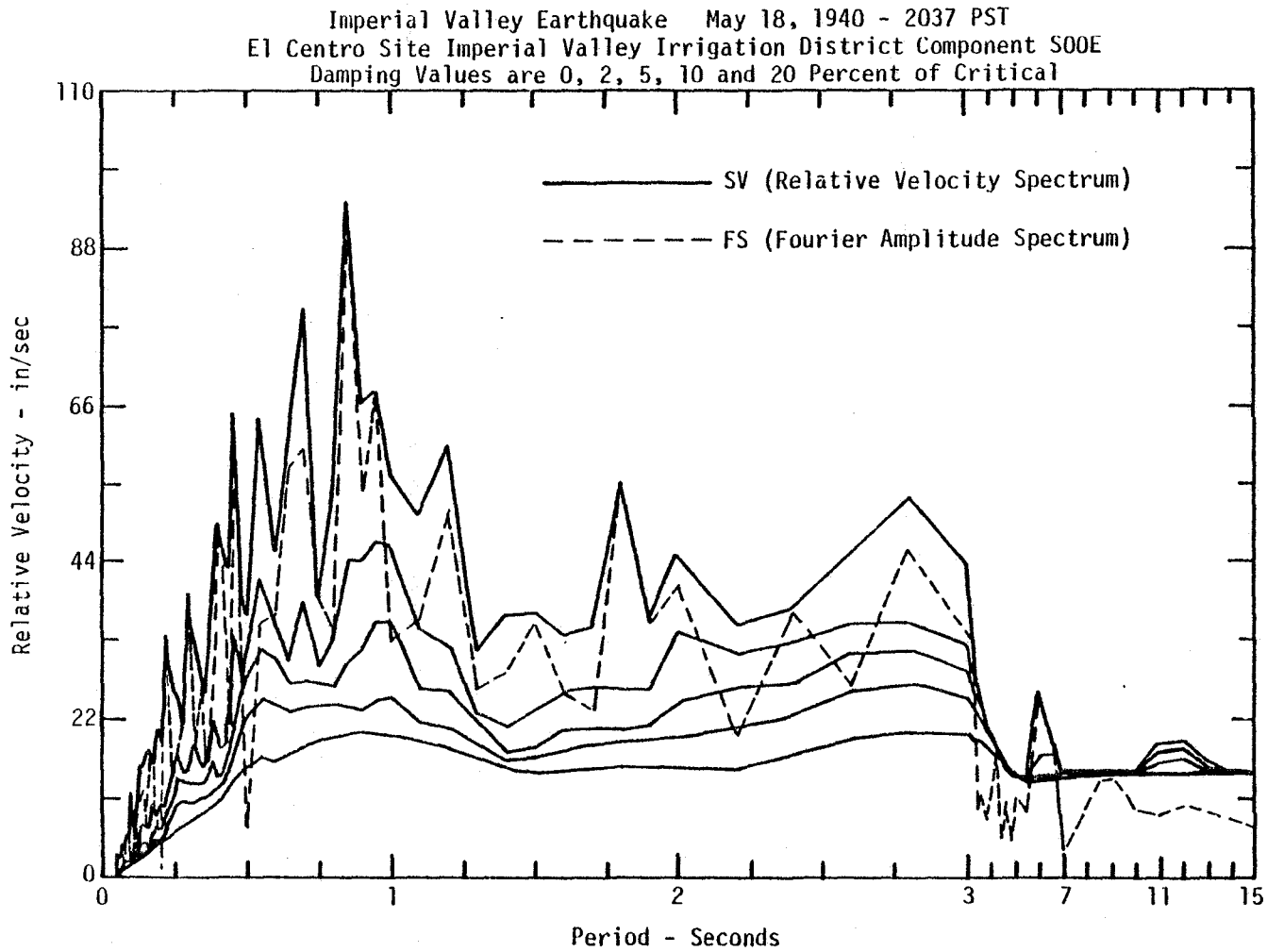

Figure III-9. Example Relative Velocity Response Spectrum (ref. III-22)

$$C = \frac{1}{g}(\omega_n S_v) = \frac{1}{g}\left(\frac{2\pi}{T} S_v\right) \qquad \text{(III-19)}$$

where g = acceleration due to gravity

and the term in parenthesis is the maximum absolute acceleration of the system.

For small damping (β less than about 0.2), $\sqrt{1-\beta^2} \approx 1$ and equation III-14 can be simplified to

$$u = (y - x) = \frac{-1}{\omega_n}\int_0^t \ddot{y}(\tau)e^{-\beta\omega_n(t-\tau)}\sin\omega_n(t-\tau)d\tau \qquad \text{(III-20)}$$

and ignoring terms in β and β^2, equations III-15 and III-16 can be simplified to

$$\dot{u} = (\dot{x} - \dot{y}) = -\int_0^t \ddot{y}(\tau)e^{-\beta\omega_n(t-\tau)}\cos\omega_n\sqrt{1-\beta^2}\,(t-\tau)d\tau \qquad \text{(III-21)}$$

$$\ddot{x} = \omega_n\int_0^t \ddot{y}(\tau)e^{-\beta\omega_n(t-\tau)}\sin\omega_n\sqrt{1-\beta^2}\,(t-\tau)d\tau \qquad \text{(III-22)}$$

A comparison of equations III-20 and III-22 indicates that the same integral appears in both expressions and, therefore, there is a unique relationship between the relative displacement and absolute acceleration spectra for small damping, namely

$$S_{pa} = \omega_n^2 S_d \qquad \text{(III-23)}$$

where S_{pa} = pseudo-acceleration which is usually very close to the absolute acceleration (ref. III-6).

It would be convenient to have a unique relation joining the three parameters S_a, S_v, and S_d under small damping conditions. If the cosine function under the integral in equation III-21 is replaced with the sine function then the maximum value of equation III-21 is called the pseudo-velocity, S_{pv}, and is related to S_{pa} and S_d by

$$\frac{1}{\omega_n} S_{pa} = S_{pv} = \omega_n S_d \qquad \text{(III-24)}$$

The parameters S_{pa}, S_{pv}, and S_d are sometimes expressed as A, V, and D. Reference III-4 notes that S_{pv} and S_v do not differ much for most earthquakes, although they can be significantly different when the system period is much longer than the duration of the earthquake.

Because of the convenient relation between the spectra expressed by equation III-24, S_{pa}, S_{pv}, and S_d can be displayed together on a tripartite logarithmic plot as, for example, is shown in figure III-10. So long as one is careful in interpreting the pseudo-velocity, i.e., it is applied under conditions where $S_v \approx S_{pv}$, the tripartite plot provides the pertinent peak parameters of maximum relative displacement, relative velocity and absolute acceleration on a single plot.

Reference III-23 lists several useful features of the response spectra, in spite of its definition in terms of a single degree of freedom system, including:

(1) The effect of system damping in limiting the dynamic stresses in a system is often apparent from the response spectrum. Undamped spectra for earthquakes often show irregular peaks suggesting dominant periods in the input and large responses for certain system periods. However, small amounts of damping, as illustrated in figures III-9 and III-10,

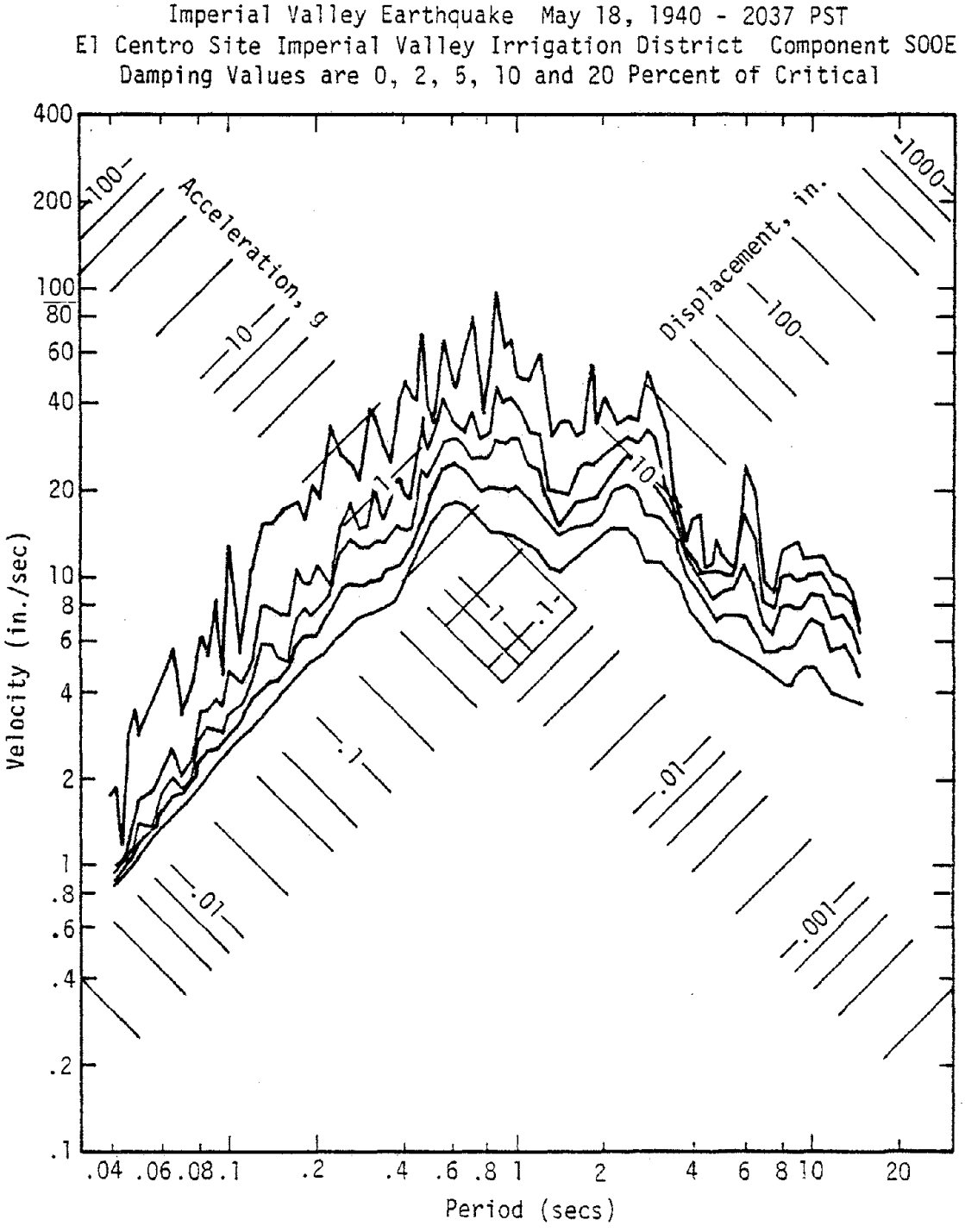

Figure III-10. Example Tripartite Logarithmic Response Spectra Plot (ref. III-22)

removes most of the peaks. Reference III-23 notes that damped response spectra for a number of earthquakes indicate that there are no dominant periods as far as most structures with some damping are concerned.

(2) Response spectra can provide an upper bound to response for multi-degree of freedom systems which can be decoupled into a series of single degree of freedom systems. The method is described in several available references, reference III-24 for example.

(3) Many complex structures behave as single degree of freedom systems under some circumstances, and the response spectra can be applied directly.

(4) The response spectra gives the energy input into the system directly.

Response spectra for a large number of recorded earthquake ground motions are available in reference III-22. Many of these spectra have been analyzed statistically and the results are summarized in reference III-17. The authors considered various partitions of the available data in terms of geologic conditions, motion intensity and other variables, but could not draw statistically significant inferences. They recommend horizontal spectra on alluvium type soil based upon computed mean spectra plus one standard deviation, which corresponds to a probability of 84.1 percent that the spectra will not be exceeded. The recommended amplification factors are given in table III-3 for specified design spectrum frequency control points. The amplication factors are applied to a ground motion peak displacement of 36 in and a peak acceleration of 1 g. The corresponding peak ground velocity is 48 in/sec. The design spectra obtained from the recommendations are shown in figure III-11.

Table III-3

Recommended Amplification Factors for
Design Spectrum Control Points (Ref. III-17)

Damping, percentage critical (1)	AMPLIFICATION FACTORS FOR CONTROL POINTS			
	Acceleration*			Displacement*
	A (33 Hz) (2)	B (9 Hz) (3)	C (2.5 Hz) (4)	D (0.25 Hz) (5)
0.5	1.0	4.96	5.95	3.20
2.0	1.0	3.54	4.25	2.50
5.0	1.0	2.61	3.13	2.05
7.0	1.0	2.27	2.72	1.88
10.0	1.0	1.90	2.28	1.70

* Maximum ground displacement is taken proportional to maximum ground acceleration and is 36 in. (910 mm) for ground acceleration of 1.0 g.

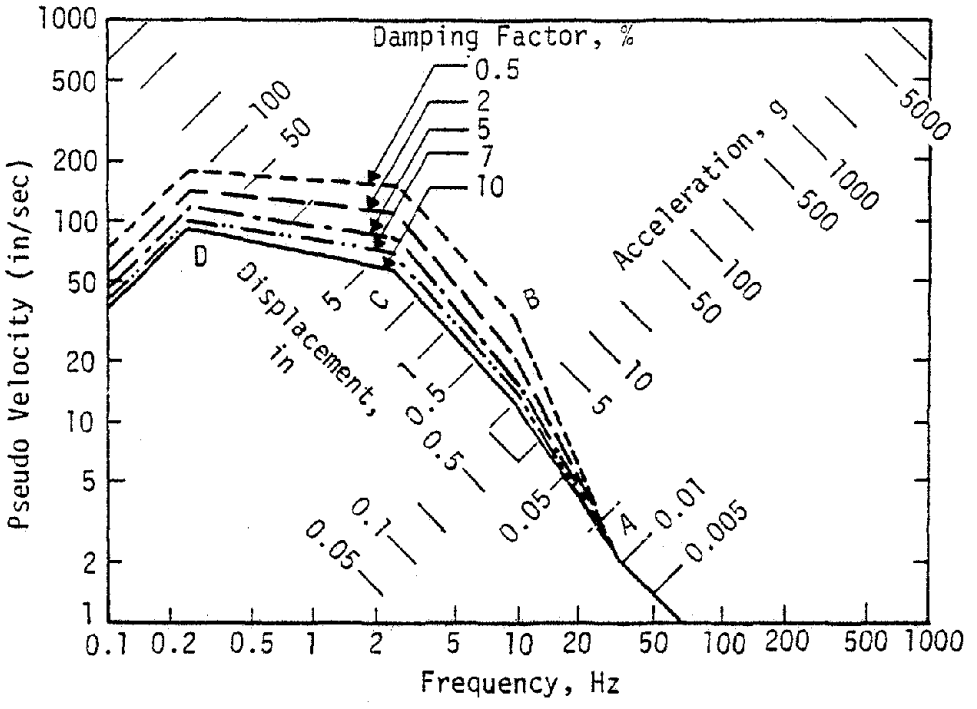

Figure III-11. Design Spectra for Various Damping Factors (ref. III-17)

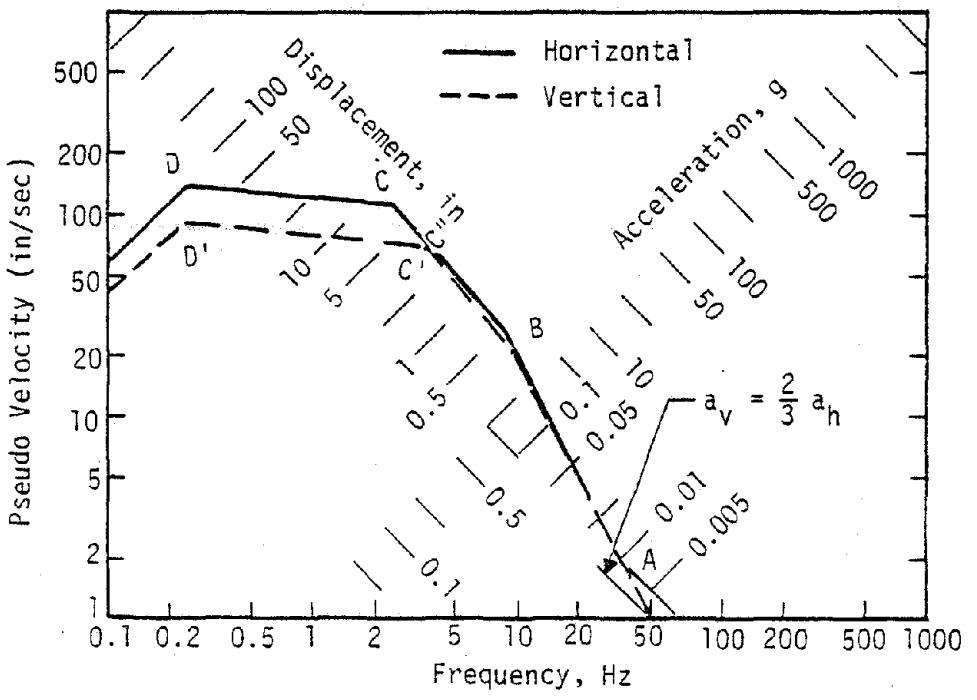

Figure III-12. Relation Between Vertical and Horizontal Design Spectra (ref. III-17)

The recommended vertical response spectrum is obtained by taking two-thirds of the horizontal design spectrum from very low frequencies through points D (0.25 Hz) and C (2.5 Hz) as illustrated for 2 percent damping in figure III-12. The corresponding control points on the vertical spectrum are D' and C'. The line D'-C' is extended to point C, where the vertical design spectrum becomes equal to the horizontal spectrum. At point A the vertical spectrum deviates again and merges into the estimated peak vertical ground acceleration at about 50 Hz.

h. Fourier Spectra

The Fourier amplitude spectrum is a convenient way of exhibiting the frequency content of any function of time such as a measured ground motion. In addition, the complete Fourier spectrum (both amplitude and phase) can be used in relating input excitation to system response for linear systems.

The Fourier transform of an acceleration time history with a duration T is defined by

$$F(\omega) = \int_0^T \ddot{y}(t) e^{-\omega t} dt \qquad \text{(III-25)}$$

The Fourier amplitude spectrum is given by the square-root of the sum of the squares of the real and imaginary parts of $F(\omega)$, i.e.

$$|F(\omega)| = \left\{ \left(\int_0^T \ddot{y}(t) \cos\omega t \, dt \right)^2 + \left(\int_0^T \ddot{y}(t) \sin\omega t dt \right)^2 \right\}^{\frac{1}{2}} \qquad \text{(III-26)}$$

The peaks in the Fourier amplitude spectrum represent periods or frequencies at which relatively large amounts of energy are contained

in the ground motion. Reference III-25 presents Fourier amplitude spectra for a large number of recorded ground motions, as well as recorded motions at other positions within structures. These latter spectra are included because the basement spectra and the spectra from other locations in the structure can be used to obtain information on the transfer functions in the structure. Figure III-13 provides an example Fourier amplitude spectrum determined for one of the horizontal acceleration components measured at El Centro during the Imperial Valley earthquake of May 18, 1940.

There is a relation between the Fourier amplitude spectra and the exact relative velocity response spectra for an undamped (β=0) single degree of freedom system. The exact relative velocity with β=0 follows from equation III-17 as

$$\dot{u}(t) = (\dot{x} - \dot{y}) = -\int_0^t \ddot{y}(\tau)\cos\omega_n(t-\tau)d\tau \qquad \text{(III-27)}$$

Equation III-27 can be expanded to

$$\dot{u}(t) = -\cos\omega_n t\int_0^t y(\tau)\cos\omega_n\tau d\tau - \sin\omega_n t\int_0^t y(\tau)\sin\omega_n\tau d\tau \qquad \text{(III-28)}$$

which from the definition of S_v is

$$S_v = \left|\dot{u}(t)\right|_{max} = \left\{\left(\int_0^{t_{max}} y(\tau)\cos\omega_n\tau d\tau\right)^2 + \left(\int_0^{t_{max}} \ddot{y}(\tau)\sin\omega_n\tau d\tau\right)^2\right\}^{\frac{1}{2}} \qquad \text{(III-29)}$$

where t_{max} = the time at which maximum response occurs. A comparison of equations III-26 and III-29 indicates that they are the same except that the Fourier amplitude spectrum results from the integration over the entire duration of the motion while the relative velocity response spectrum for β=0 results from the integration up to time of maximum response.

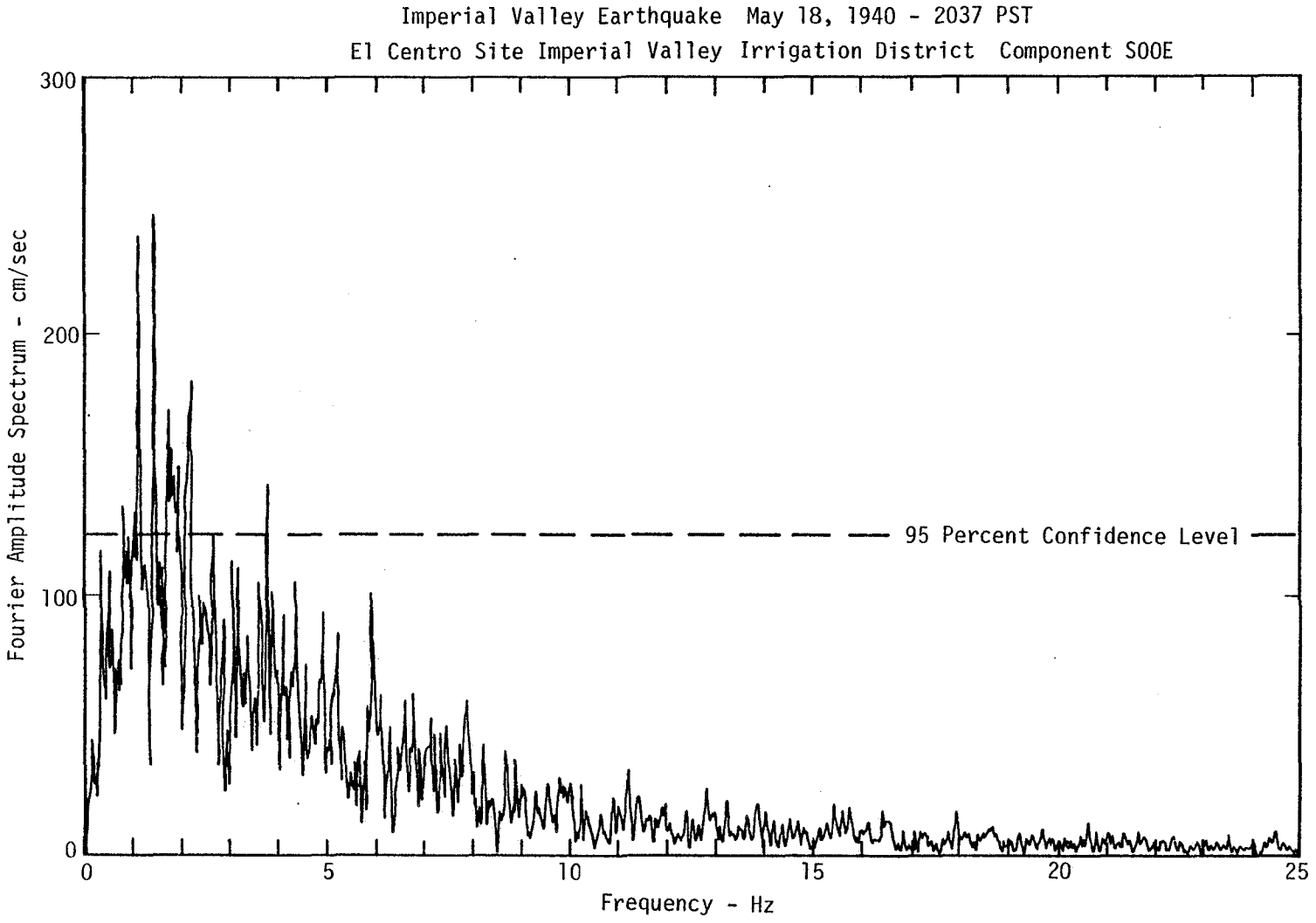

Figure III-13. Example Fourier Amplitude Spectra (ref. III-24)

As a result, the shape of the two spectra are similar (fig. III-9). If t_{max} coincides with T the two spectra are identical. In general, however, t_{max} is less than T and the undamped relative velocity response spectrum is always greater than the Fourier amplitude spectrum (ref. III-25).

3. DEVELOPMENT OF SIMULATION CRITERIA

The previous paragraphs provide a description of the state of knowledge of characteristics of prototype earthquake environments. The characteristics and their amplitude bounds provide a partial basis against which high explosive test methods can be compared to partially evaluate their suitability as a simulation method. It remains, however, to evaluate the response characteristics of engineering systems and their effect on simulation requirements.

The important characteristics of earthquakes in terms of structural response and criteria for a good simulation are not clearly stated nor universally agreed upon in the existing literature. Many American engineers and most U.S. design codes focus on peak acceleration as a baseline parameter. Housner (ref. III-26) suggests that the greatest area of acceleration pulse (a velocity measure) is a more significant parameter than peak acceleration by itself. Cloud and Perez (ref. III-27) consider the time duration above some acceleration level a more important duration criterion for response than simply total duration. Russian structural design criteria (ref. III-28) are based upon peak particle velocity, in agreement with Housner, but the effect of duration and number of cycles of motion are also considered important (ref. III-29).

Watabe (ref. III-30) suggests that the motions given in table III-4 are credible earthquake motion bounds but that shake table simulators must be capable of producing somewhat different motions because of similitude requirements, the need to determine structural dynamic characteristics, and physical limits on displacements which can be achieved.

Sozen (ref. III-31) suggests that in simulation it is not necessary to reproduce a precise acceleration time history, but demonstration that model response is similar to prototype response is the most important factor. He also considers response spectra, but notes that response spectra are rather insensitive to many time history details. It is believed that Sozen's approach is a reasonable one. It is proposed, therefore, that simulation criteria be developed around the system response concept.

In the prototype situation, the ground shock environment created at a point in the ground will be determined by the incoming wave or waves, the stresses associated with these waves, and the motions which are generated by the waves through the inelastic interactions between the stresses and the media material properties. The response of a structure to this environment will be governed by the structure characteristics (mass, mass moment of inertia, size and shape, stiffnesses, interface conditions, etc.), and the inelastic interaction between the structure and the surrounding media. At one extreme, simulation criteria could require that the simulated environment contain a precise duplication of the prototype waves, and their stress and motion time histories. This would insure precise duplication of structure response for a full size prototype structure.

Table III-4

Suggested Bounds for Earthquake Motions (ref. III-30)

Acceleration (g's)	Velocity (ft/sec)	Displacement* (inches)	Frequency (Hz)
0.1 to 1.5	0.2 to 4	0.01 to 200	0.1 to 20

* Displacements approaching the upper limit of Watabe's bounds are possible in the immediate vicinity of surface faulting. The simulation of such faulting, however, would require special treatment not intended to be addressed in this program.

Such a severe criteria specification would be economically impractical and technically difficult to achieve. Indeed, it is inconsistent with the state-of-knowledge of the prototype environment and understanding of the inelastic interactions which occur. A more realistic approach is to consider the type of structure, its dynamic characteristics, anticipated response in the prototype environment and the major uncertainities in the anticipated response. Simulation criteria should then be specified to insure similar response in the simulation, especially exercise of the structure in such a way that the major uncertainties can be evaulated.

The criteria will probably vary from structure to structure and may include any or all of the following:

a. Wave Types (P, SV, SH or R)

b. Stress-time history associated with the waves

c. Motion-time history at a point or points

d. Some level and type of response in the structure.

The wave types and associated stresses might be important for underground or partially buried structures which are loaded directly by the waves. The stress fields associated with various wave types differ and the stress fields may be important for evaluation of the structural integrity of systems loaded by the stresses. Another aspect of wave type relates to the propagation velocity of the different waves. Some aspects of the response of systems which are long (i.e., bridges, tunnels, dams) may be affected by the transit time of the wave across the structure and phase differences in the ground motion along the structure length.

For structures in which the stress system is not of major importance, i.e., where the structural strength is sufficient to withstand the incident stresses regardless of their distribution and type, then the specification of a motion time history at a point in the ground may be a sufficient criteria for simulation. This would normally be the case where the ground motion excites structure base motion which in turn excites motion and stresses in other parts of the structure not directly loaded by the incident waves (internal or above-ground components). This is a common problem in seismic design and is the one which most design codes treat for above-ground structures. Figure III-14 illustrates the idealized generation of the same horizontal motion time history at the ground surface from two different wave types. The P-wave illustrated travels horizontally and contains a high horizontal stress component while the S-wave travels vertically and contains no horizontal or vertical stress component. For properly selected P and S wave stress amplitudes, the two waves can produce exactly the same horizontal motion time history. The illustration shows that if only motion time history at a point is of interest there is a wide range of wave types or combinations which can be used to produce it. It is interesting to note that the use of shake tables is implicitly founded on this principle in that the motion of the table is created by mechanisms which do not contain the wave characteristics which are present in earthquakes. Shake tables also contain a more severe restriction compared to the use of some other kind of wave excitation because they effectively eliminate interaction between the structure and the shaking source.

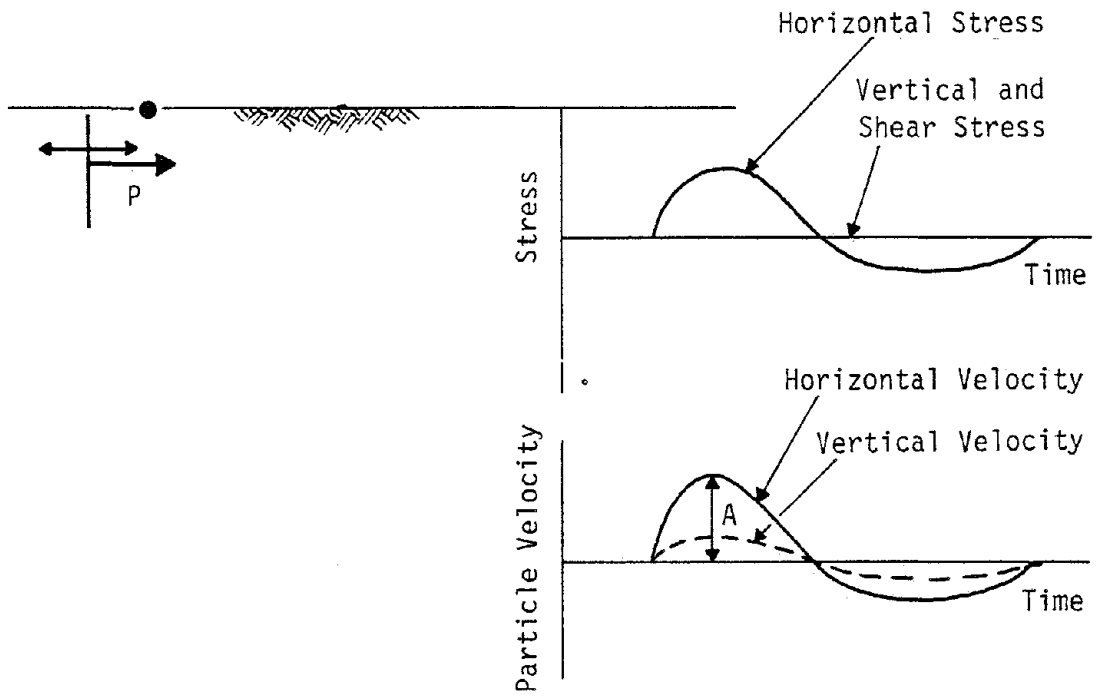

a) Horizontally Traveling P-Wave

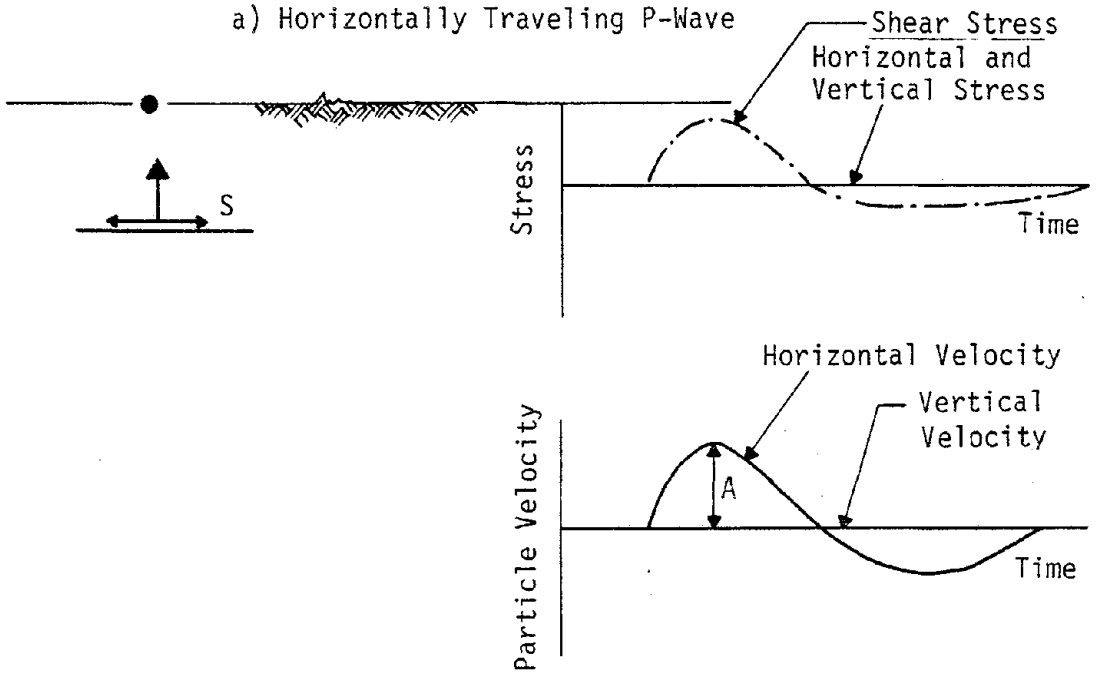

b) Vertically Traveling S-Wave

Figure III-14. Idealized Velocity and Stress Time Histories at a Point at the Ground Surface in an Elastic Medium Due to Different Wave Types

The least restrictive simulation criteria in terms of defining the waves, stresses, or ground motions is the use of some structural response parameter or parameters as a measure of simulation. Normally, a designer or analyst is interested in the behavior of various critical members or locations in a structure. The behavior of interest, which determines whether the structure or some internal component is safe, may be defined by some level of stress, strain, displacement, velocity or acceleration at the location of interest. Strain, for example, may be of interest in a problem of structural integrity or if one is interested in the inelastic interaction between the foundation soil and the structure. Relative displacement between an internal component and its attachment points may be of interest in a shock isolation problem. Acceleration may be a major concern in evaluating the behavior of electrical or electronic components, such as relays and servo-control systems. Whatever the parameter of interest, it is the level and type of response which is important rather than the specific details of the excitation causing the response. The response spectrum discussed in detail previously is a convenient tool for relating the characteristics of an input excitation to the response of a system. Although it is defined in terms of a single degree of freedom system, it can be used to estimate response of multi-degree of freedom systems under some circumstances and, in addition, many systems can be approximated as single degree of freedom systems. It is believed that the use of a response spectrum is a reasonable and practical approach to defining simulation criteria for a large number of earthquake problems.

Consider the idealized response spectra shown in figure III-15. The

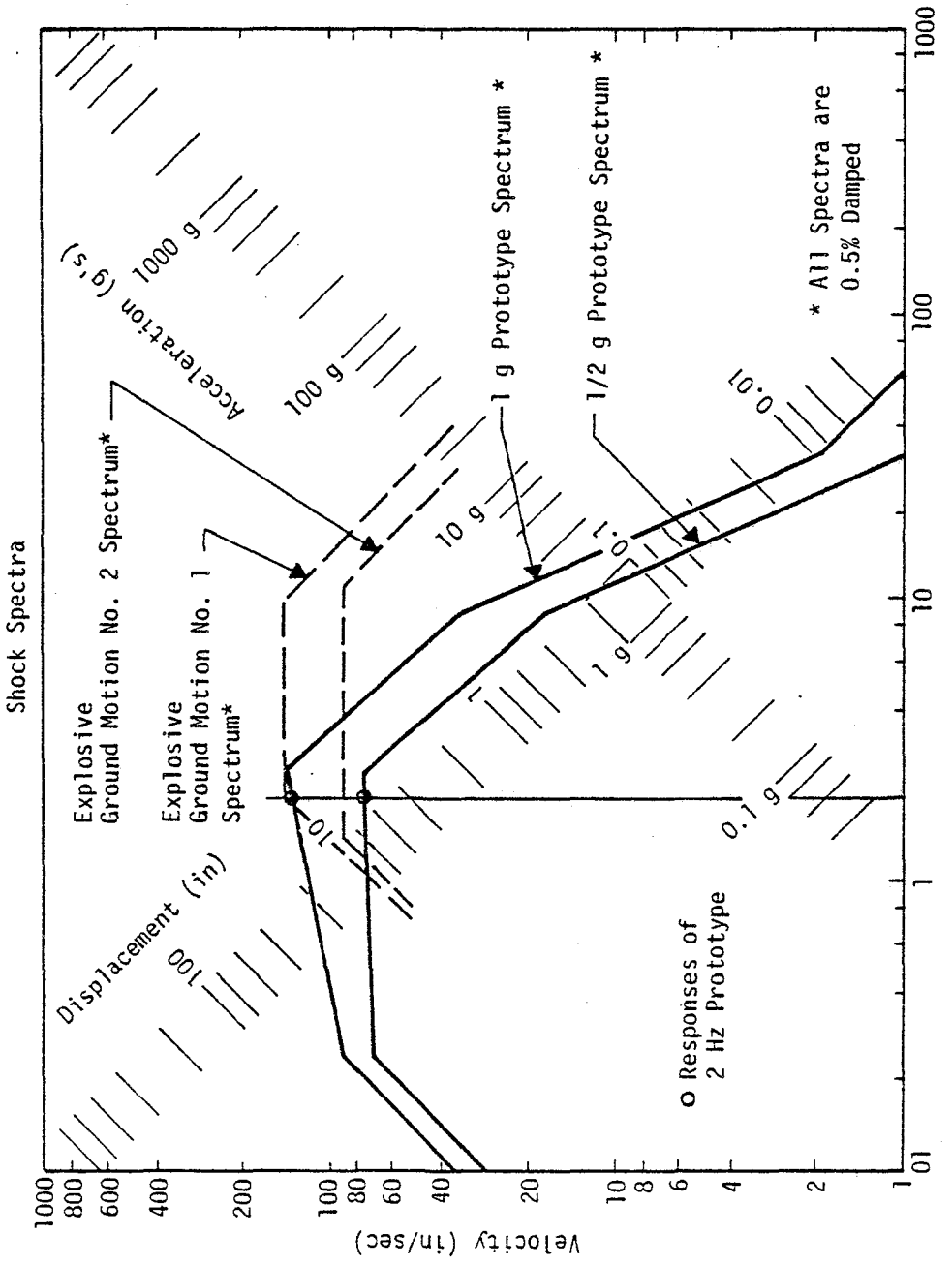

Figure III-15. Illustration of the Use of Response Spectra for Evaluating System Response

spectra designated "prototype" are estimated spectra for 1 g and 1/2 g magnitude 8 earthquakes using the base ground motions of reference III-14 (fig. III-1) and the spectral amplification factors for 0.5 percent damping of reference III-17 (table III-3). The spectra designated "explosive ground motion" are credible spectra from hypothetical (but unspecified) ground motion experiments. The fact that the "explosive" spectra are shifted to the right relative to the earthquake spectra is a manifestation of the higher frequency content and higher accelerations of the explosive ground motion. The estimation of spectra from actual explosive ground motions is addressed in a later section.

Suppose that a 2.0 Hz lightly damped system were of interest. Its peak responses to the 1 g and 1/2 g earthquakes are represented by the circled points on the "prototype" spectra. The spectrum for "explosive ground motion No. 1" passes nearly through the same point and, therefore, the peak response of the system would be about the same as in the 1 g earthquake in spite of the higher frequency content and higher acceleration of the high explosive experiment.

The response of the system to "ground motion No. 2" would be about 65 percent that of the 1 g earthquake, but about 22 percent higher than that of the 1/2 g earthquake. Depending upon the objective of the experiment, these results might also be satisfactory for interpreting system response.

If the system of interest has multiple frequencies of importance to the overall response, then matching the prototype spectrum at a single point will probably not be satisfactory. The wider the range over

which the system frequencies extend, the wider the range over which the "ground motion" spectrum would be required to approximate the prototype spectrum. This same comment applies if there is an uncertainty range in the fundamental frequency for a single degree of freedom system.

The use of scaled models changes the required simulation requirements. Suppose, for example, that a 1/10th scale of the 2.0 Hz system were to be evaluated. In scaling, assume that the construction materials remain the same and that all linear dimensions in the model are taken as 1/10th those of the protoype system. The resulting natural frequency of the model system would then be 20 Hz or

$$f_m = \frac{f_p}{\lambda} \qquad \text{(III-30)}$$

where

f = frequency

λ = geometric scale factor

and the subscripts m and p refer to model and prototype, respectively.

A perfectly scaled model response would have a peak relative displacement of 1/10th the prototype, a peak relative velocity equal to that of the prototype and a peak acceleration 10 times that of the prototype or

$$D_m = \frac{D_p}{\lambda} \qquad \text{(III-31)}$$

$$V_m = V_p \qquad \text{(III-32)}$$

$$A_m = \lambda A_p \qquad \text{(III-33)}$$

where D, V, and A are spectral values of relative displacement, rela-

tive velocity and absolute acceleration. This type of scaling is sometimes called velocity scaling because velocities in the model and prototype at similar (i.e., scaled) times are the same.

In order to achieve perfectly scaled response in an experiment, it is necessary to also scale the input excitation. Figure III-16 shows the 1 g prototype spectrum of figure III-15 and a perfectly scaled 1/10th scale spectrum of the 1 g prototype. It can be seen in figure III-16 that the model system (20 Hz) has a response to the scaled environment which is related to the prototype system (2 Hz) response in the prototype environment by equations III-31 through III-33. It can also be seen that the model response to "ground motion No. 1" is only about 50 percent that of the model in the scaled prototype environment. Indeed, the accelerations and frequencies in the ground motion environment are too low compared to what would be required for a good simulation of the scaled prototype environment. It is clear that the specification of simulation criteria must account for the system dynamic characteristics, including scaling if smaller models are to be tested, and the effect of the system characteristics upon those aspects of the prototype environment which govern the response.

4. CONCLUSIONS

This section has described various factors which must be considered in establishing simulation criteria which an experimental method must meet to provide reasonable insight into earthquake ground motion effects on engineering systems. The two primary aspects of the problem are

a. Earthquake environment characteristics

b. System characteristics

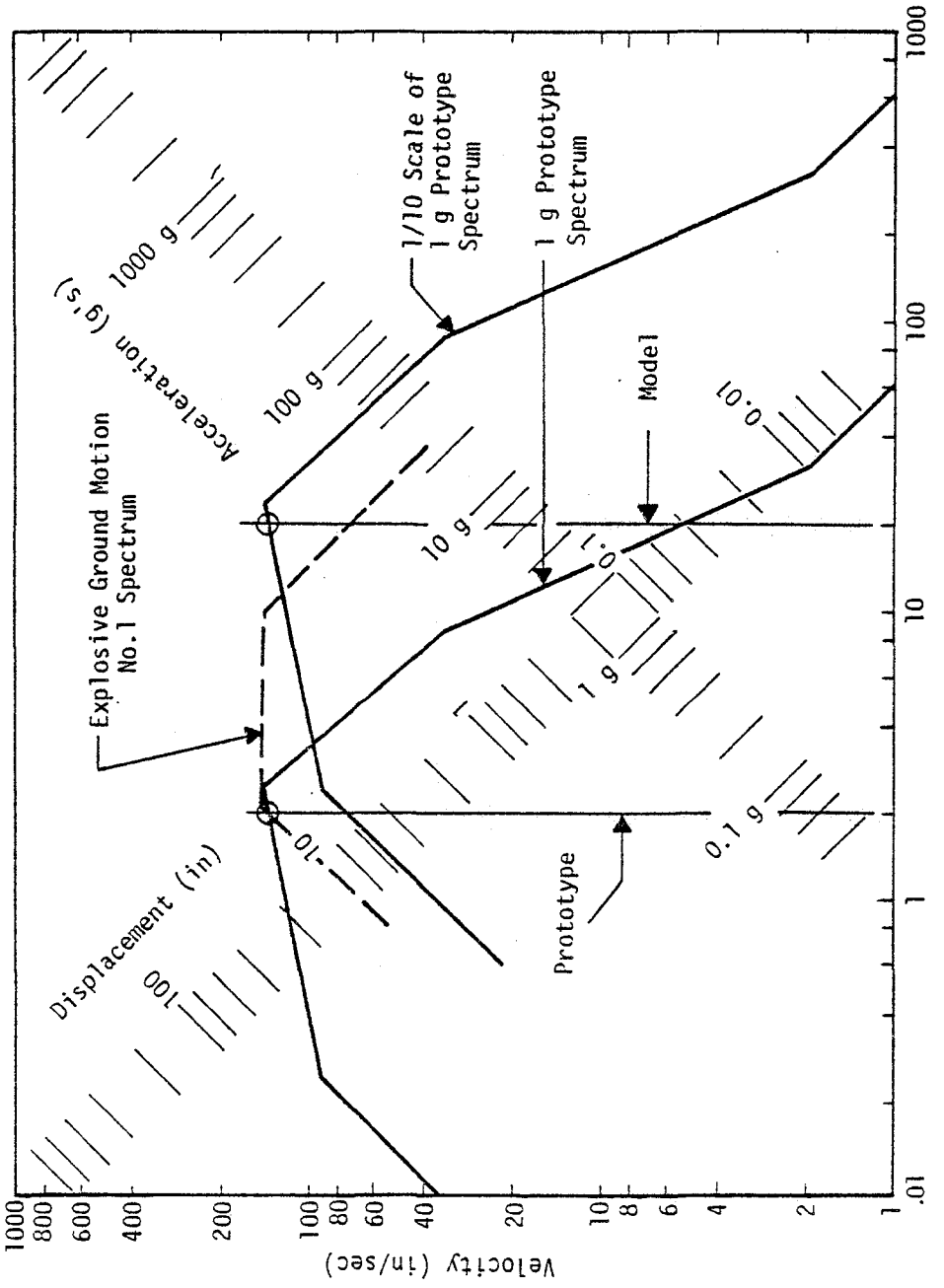

Figure III-16. Effect of Scaling on Response Spectra

The state-of-the-art in understanding earthquake phenomena and for predicting soil stress and motion in a particular location is relatively poor. However, there is sufficient data from past earthquakes so that estimates of peak motion amplitudes and, importantly, shock spectra are possible.

Simulation criteria should be specified in relation to the system of interest. If belowground stresses are important then simulations may be required to reproduce specific earthquake waves and their associated stress fields. If only the ground motion is important then there is flexibility in the methods that can be used to create the ground motion. If the study of basic phenomena, e.g. inelastic soil-structure interaction, is of interest, then a sufficient simulation specification may simply be the development of large soil strains so that the phenomena can be investigated and tested against theory.

In many instances, it appears that a good method for evaluating (and, inversely, designing) the ground motion is through the use of response spectra. If a ground motion produces system response at levels similar to those produced by an earthquake, then the specific details of the motion are important only to the extent that they influence the response spectrum. If modeling is used in simulation experiments, appropriate scaling of both the system and the input environment is required.

5. REFERENCES

III-1 Bolt, B.A., "Elastic Waves in the Vicinity of the Earthquake Source," Chap. 1, and "Causes of Earthquakes," Chap. 2, in Earthquake Engineering, edited by R.L. Wiegel, Prentice-Hall, Inc., Englewood Cliffs, N.J., 1970.

III-2 Bolt, B.A., "Causes of Earthquakes, Crustal Strain, and Plate Tectonics," Lecture I, and "Seismic Waves and Estimation of Strong Motions," Lecture V, Earthquake Resistant Design of Engineering Structures, Short Course, University of California, Berkeley, California, June 19-30, 1972.

III-3 Housner, G.W., "Important Features of Earthquake Ground Motions," Proceedings, 5th World Conference on Earthquake Engineering, Rome, 1973.

III-4 Housner, G.W., "Strong Ground Motion," Chap. 4, in Earthquake Engineering, edited by R.L. Weigel, Prentice-Hall, Inc., Englewood Cliffs, N.J., 1970.

III-5 Ewing, W.M., Jardetzky, W.S. and Press, F., Elastic Waves in Layered Media, McGraw-Hill Book Company, New York, 1957.

III-6 Newmark, N.M. and Rosenbleuth, E., Fundamentals of Earthquake Engineering, Prentice-Hall, Inc., Englewood Cliffs, N.J., 1971.

III-7 Pekeris, C.C. and Lifson, H., "Motion of the Surface of a Uniform Elastic Half-Space Produced by Buried Pulse," J. Acoust. Soc. Am., 29, 1233, 1957.

III-8 Schnabel, P.B. and Seed, H.B., "Accelerations in Rock for Earthquakes in the Western United States," Earthquake Resistant Design of Engineering Structures, Short Course, University of California, Berkeley, California, June 1972.

III-9 Idriss, I.M. and Seed, H.B., "Seismic Response of Horizontal Soil Layers," Journal of the Soil Mechanics and Foundation Division, ASCE, Vol. 94, No. SM4, July 1968.

III-10 Idriss, I.M. and Seed, H.B., "Influence of Soil Conditions on Ground Motions During Earthquakes," Journal of the Soil Mechanics and Foundation Division, ASCE, Vol. 95, No. SM1, January 1969.

III-11 Housner, G.W., "Intensity of Ground Shaking Near the Causative Fault," Proceedings, Third World Conference on Earthquake Engineering, Vol. I, New Zealand, 1965.

III-12 Trifunac, M.D. and Hudson, D.E., "Analysis of the Poicoma Dam Accelerogram - San Fernando, California Earthquake of 1971," Bull. Seism. Soc. of Amer., Vol. 61, pp 1393-1411, Oct. 1971.

III-13 Ambraseys, N.N., "Dynamics and Response of Foundation Materials in Epicentral Regions of Strong Earthquakes," Proceedings, Fifth World Conference on Earthquake Engineering, Rome, 1973.

III-14 Matthiesen, R.B., Howard, G. and Smith, C.B., "Seismic Considerations in Siting and Design of Power Plants," Nuclear Engineering and Design, 25, 3-15, 1973.

III-15 Esteva, L., "Seismic Risk and Seismic Basing Decisions," Seminar on Seismic Design of Nuclear Power Plants, Massachusetts Institute of Technology Press, Cambridge, Mass., 1969.

III-16 Newmark, N.M. and Hall, W.J., "Seismic Design Spectra for Trans-Alaska Pipeline," Proceedings, Fifth World Conference on Earthquake Engineering, Rome, 1973.

III-17 Newmark, N.M., Blume, J.A. and Kapur, K.K., "Seismic Design Spectra for Nuclear Power Plants," Journal of the Power Division, ASCE, Vol. 99, No. PO2, November 1973.

III-18 Esteva, L. and Rosenbleuth, E., "Espectros de Temblores a Distencias Moderadas y Grandes," Bol. Soc. Mex. Ing. Sism., 2(1), 1-18, 1964.

III-19 Trifunac, M.D. and Brady, A.G., "A Study on the Duration of Strong Earthquake Ground Motion," Bull. Seism. Soc. Amer., Vol. 65, No. 3, pp 581-626, June 1975.

III-20 Strong Motion Earthquake Accelerograms, Digitized and Plotted Data, Volume II - Corrected Accelerograms and Integrated Ground Velocity and Displacement Curves, Part A - Accelerograms IIA001 through IIA020, EERL 71-50, Earthquake Engineering Research Laboratory, California Institute of Technology, Pasadena, California, Sept. 1971.

III-21 Meirovitch, L. Analytical Methods in Vibrations, The Macmillan Company, Collier-Macmillan Canada, Ltd., Toronto, 1967.

III-22 Analyses of Strong Motion Earthquake Accelerograms, Volume III - Response Spectra, Part A - Accelerograms IIA001 through IIA020, EERL 72-80, Earthquake Engineering Research Laboratory, California Institute of Technology, Pasadena, California, August 1972.

III-23 Hudson, D.E., "Response Spectrum Techniques in Engineering Seismology," Proceedings of the World Conference on Earthquake Engineering, Berkeley, California, June 1956.

III-24 Crawford, R.E., Higgins, C.J. and Bultmann, E.H., The Air Force Manual for Design and Analysis of Hardened Structures, AFWL-TR-74-102, Air Force Weapons Laboratory, Kirtland AFB, New Mexico, October 1974.

III-25 Analyses of Strong Motion Earthquake Accelerograms, Volume IV - Fourier Amplitude Spectra, Part A - Accelerograms IIA001 through IIA020, EERL 72-100, Earthquake Engineering Research Laboratory, California Institute of Technology, Pasadena, California, August 1972.

III-26 Housner, G.W., "Important Features of Earthquake Ground Motion," Proceedings, Fifth World Conference on Earthquake Engineering, Rome, 1973.

III-27 Cloud, W.K. and Perez, V., "Strong Motion Records and Acceleration," Proc. 4th World Conference on Earthquake Engineering, Santiago, Chile, 1969.

III-28 Mironov, P.S., Shchupletsov, Yu. P., and Pyatunin, B.S., "Seismic Vibrations During Explosions and Problems of Earthquake Safety of Buildings and Structures," Vzryunoye Delo (Moscow) Sbornik, No. 71/28, pp 169-174, 1972, (Translation FTD-HC-23-1571-74, Foreign Technology Division, Air Force Systems Command, Wright-Patterson AFB, Ohio).

III-29 Shamin, V.M., "Seismic Effect of Powerful Explosions," Doklady of the Academy of Sciences, USSR, Earth Science Section, Vol. 185, March-April 1959 (Translated by American Geological Institute).

III-30 Watabe, M., "Comments on the Shaking Table at Tsukuba, Japan," Earthquake Environment Simulation, Final Report and Proceedings of a Workshop on Simulation of Earthquake Effects on Structures.

III-31 Sozen, M.A., "The University of Illinois Earthquake Simulator," Earthquake Environment Simulation, Final Report and Proceedings of a Workshop on Simulation of Earthquake Effects on Structures, National Academy of Engineering, Washington D.C., 1974.

Page Intentionally Left Blank

SECTION IV
ANALYSIS OF DATA

1. INTRODUCTION

Simulation environments will be created by explosive charges in various arrays and, perhaps, in combination with various enhancement techniques. The basic charge configurations are spherical, cylindrical and planar (see figure IV-1) and enhancement techniques may include:

a. Increasing the size of the region affected by using multiple charges in two-dimensional arrays

b. Employing explosives with longer burn times

c. Decoupling explosives by detonating in drums or cavities

d. Focusing energy into a specific region using special arrays

e. Lengthening motion duration in a specific region by sequential firing of charges

f. Emplacement of barriers or trenches in the media to obtain reflections or refractions which tailor the motions or increase durations.

The selection of a charge configuration and appropriate enhancement technique will be dependent upon the simulation criteria for a particular engineering system of interest. Parameters which must be considered include motion amplitudes, frequency content and duration, perhaps as they influence response spectra, as well as the physical dimensions of the structure or desired test area. For example, it is expected that for large structures or where several structures will be

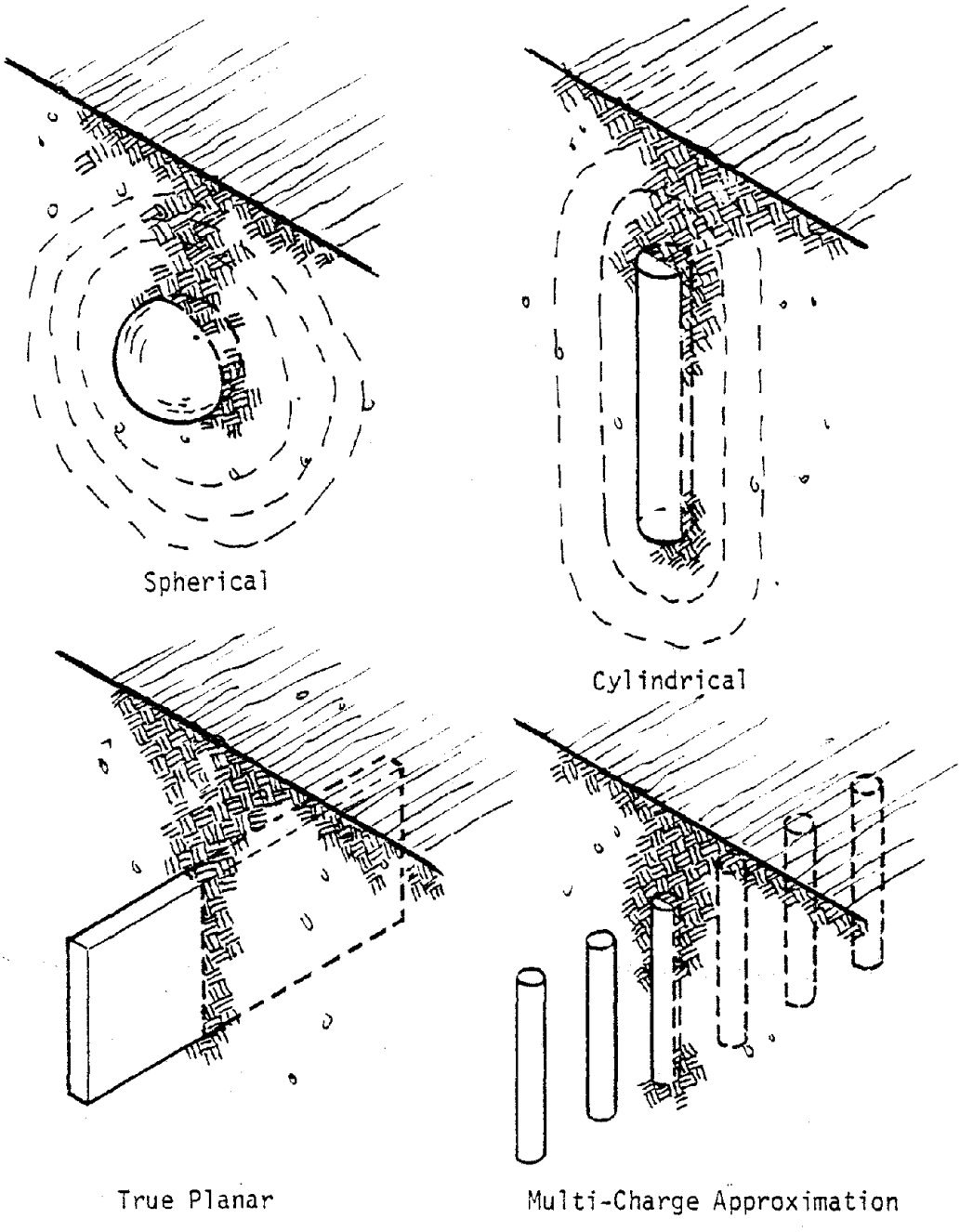

Figure IV-1. Three Classes of Explosive Charge Configuration

tested in the same experiment, a large experimental area with relatively uniform motions would be desired. A planar array whose linear dimension is dependent upon the desired width of the test area may provide an appropriate test geometry for this case.

Available data on the effects of single charges, as well as some of the potential enhancement techniques, have been outlined in Section II. In this section, the data are presented and analyzed to validate or establish scaling laws and to allow identification of data base deficiencies which must be reconciled to allow simulation design with reasonable confidence. First, the importance of dimensional analysis and the applicable scaling laws are presented. Then, spherical, cylindrical and planar data are analyzed to determine their agreement with the scaling laws. Data on enhancement techniques are considered last. Finally, the deficiencies in the data base are described. These deficiencies define the objectives of the numerical calculations presented in Section V.

The analysis in this section concentrates on dry granular materials since most of the available experimental data were taken in these materials and, further, dry alluvial sites are likely candidates for initial simulation experiments. However, some attention is given to scaling terms which account for some of the effects of different materials. These terms can form the basis of the extension of this work to other types of materials.

2. DIMENSIONAL ANALYSIS CONSIDERATIONS

In a large number of physical problems, the phenomena are so

complex that mathematical formulation of the equations for the phenomena is extremely difficult. This is especially true of dynamic problems involving explosive sources in inelastic media. In these cases, it is common practice to evaluate the phenomena experimentally and develop empirical relations from measured response data.

Whether a theoretical or an experimental approach is taken to a problem, the initial steps in the analysis must be, first, a qualitative evaluation of the phenomena and, second, identification of the important physical parameters which control the phenomena. The two approaches depart at this point. The theoretical approach attempts to develop a mathematical model for the problem which will lead to the mathematical relations between the parameters, while the experimental approach attempts to establish the relations by means of experiments in which the governing parameters are varied in a reasonable way.

Experiments are expensive, and it is important to keep the experiment size and the number of parameter variations to a minimum. Further, it is important to have a uniform guide for "scaling" and evaluating experimental results from different experiments so that empirical relations among the parameters can be developed. A useful tool in performing these functions is dimensional analysis. The fundamentals of dimensional analysis are described in a number of references (e.g., refs. IV-1, IV-2 and IV-3). Some of the basic results are reviewed herein and used to develop consistent scaling parameters for various high explosive configurations.

In general, most of the parameters that are dealt with in physical

sciences depend in magnitude upon the scale used to measure them, and are called dimensional quantities. Non-dimensional quantities are independent of the system of measurement. The establishment of units for three physical quantities is ordinarily enough to define the units for any other physical quantity. Mass, length and time or force, length and time* are convenient units usually selected and they are called fundamental or primary units. Other units, for example velocity, may be derived from the fundamental units and these are called derived or secondary units. If force, length and time are selected as fundamental units, the associated dimensions can be written

$$\begin{aligned} &\text{dimension of force} \overset{d}{=} [F] \\ &\text{dimensions of length} \overset{d}{=} [L] \\ &\text{dimensions of time} \overset{d}{=} [T] \end{aligned} \qquad \text{(IV-1)}$$

where $\overset{d}{=}$ indicates dimensional equivalence and the brackets [] indicate the dimensions of the quantity. The dimensions of any physical quantity can be written as a monomial power of the three fundamental units or

$$\text{dimensions of a quantity} \overset{d}{=} [F]^a[L]^b[T]^c \qquad \text{(IV-2)}$$

where a, b and c are exponents. If the quantity is dimensionless then a=b=c=0.

Physical laws are functional relations between the parameters which define the phenomena. Since the phenomena are independent of the system of measurement, the functional relations must be independent of

* In thermodynamic problems a fourth unit, perhaps temperature, is also necessary.

the systems of measurement. Hence, if the relation between the physical parameters governing a particular phenomena is

$$f(A_1, A_2, A_3, \ldots\ldots, A_n) = 0 \qquad \text{(IV-3)}$$

then

$$[A_1]^{a_1}[A_2]^{a_2}\ldots[A_n]^{a_n} \stackrel{d}{=} [F]^0[L]^0[T]^0 \qquad \text{(IV-4)}$$

Equation IV-4 is a statement of dimensional homogeneity and states that the most general term in equation IV-3 must be dimensionless.

Since the functional relation must be independent of the system of units, equation IV-3 can be written as

$$f(\Pi_1, \Pi_2, \Pi_3 \ldots\ldots \Pi_m) = 0 \qquad \text{(IV-5)}$$

where $\Pi_1, \Pi_2, \ldots\ldots \Pi_m$ are dimensionless quantities and are functions of the original parameters. Buckingham's Pi theorem (ref. IV-4) states that if equation IV-3 is complete, then the Π terms of equation IV-5 are independent products of the original parameters A_1 through A_n, are dimensionless in the fundamental dimensions, and that the number of terms in the solution m, is less than the original number of terms, n, by a factor, k, where k usually equals the number of fundamental dimensions, i.e., $m = n - k$. A proof for the theorem is given in reference IV-1.

If the number of fundamental dimensions is 3 (e.g., F, L, T) then the general relation (Eq. IV-5) usually contains 3 terms less than the original relation (Eq. IV-3). This simplification, as well as the formulation of the non-dimensional Π terms, are the main advantage which

dimensional analysis lends to the analysis of a physical problem. If the number of fundamental dimensions equals the number of physical parameters with independent dimensions which govern a phenomena, then the relations will be completely determined to within a constant factor by dimensional analysis (ref. IV-1); i.e., if n - 1 = k, it will only be possible to form a single non-dimensional Π-term from the parameters and the functional relations for k = 3 can be written

$$CA_1^{a_1}A_2^{a_2}A_3^{a_3}A_4^{a_4} = 0 \qquad \text{(IV-6)}$$

or

$$A_1 = CA_2^{m_2}A_3^{m_3}A_4^{m_4} \qquad \text{(IV-7)}$$

where the exponents are determined by the dimensions of A_1 and C must come from theory or experiment. In the most general case, however, dimensional analysis does not yield the functional relation. It must be determined from experiment.

In formulating a dimensional analysis, it is necessary to include all the parameters which may control the phenomena even if they are constant. The derivation of the dimensionless Π-terms may then be determined in any number of ways. Inspection is one approach, but the use of the statement of dimensional homogeneity (Eq. IV-4 provides a systematic approach).

Consider, as an example, the case of a spherical explosion in a homogeneous elastic soil. The parameters listed in table IV-1 are commonly considered important in governing the phenomena (e.g., ref. IV-5). Dimensions of force, length and time are taken as fundamental.

Table IV-1

Some Parameters Determining Explosion Phenomena From a Spherical Source in an Elastic Soil

Parameter	Symbol	Dimensions
1. Dependent		
Peak Soil Stress	σ	F/L^2
Peak Particle Acceleration	a	L/T^2
Peak Particle Velocity	v	L/T
Peak Displacement	d	L
Various Characteristic Times	t	T
2. Independent		
Explosive Energy	E	FL
Range	R	L
Soil Density	ρ	FT^2/L
Dilatational Wave Speed	C	L/T
Poisson's Ratio	ν	--

The equations relating the dependent and independent parameters are

$$\sigma = f_1(E_0, R, \rho, C, \nu) \qquad (a)$$

$$a = f_2(E_0, R, \rho, C, \nu) \qquad (b)$$

$$v = f_3(E_0, R, \rho, C, \nu) \qquad (c) \qquad \text{(IV-8)}$$

$$d = f_4(E_0, R, \rho, C, \nu) \qquad (d)$$

$$t = f_5(E_0, R, \rho, C, \nu) \qquad (e)$$

The dimensional homogeneity of equation IV-8(a) can be expressed

$$F^0L^0T^0 \stackrel{d}{=} [\sigma]^{a_1}[E_0]^{a_2}[R]^{a_3}[\rho]^{a_4}[C]^{a_5}[\nu]^{a_6} \qquad \text{(IV-9)}$$

so that

$$F^0L^0T^0 = \left(\frac{F}{L^2}\right)^{a_1}\left(FL\right)^{a_2}\left(L\right)^{a_3}\left(\frac{FL^2}{L^4}\right)^{a_4}\left(\frac{L}{T}\right)^{a_5} \qquad \text{(IV-10)}$$

where the term involving ν has been eliminated from equation IV-10 since it is already dimensionless and is, therefore, a Π-term. Equation IV-10

leads to the following relations involving the exponents.

$$\begin{aligned} 0 &= a_1 + a_2 + a_4 && \text{(a)} \\ 0 &= -2a_1 + a_2 + a_3 - 4a_4 + a_5 && \text{(b)} \\ 0 &= 2a_4 - a_5 && \text{(c)} \end{aligned} \qquad \text{(IV-11)}$$

Equation IV-11 may be solved in terms of a_2 and a_4 to give

$$F^0L^0T^0 \stackrel{d}{=} [\sigma]^{-a_2-a_4}[E_0]^{a_2}[R]^{-3a_2}[\rho]^{a_4}[C]^{2a_4} \qquad \text{(IV-12)}$$

or rearranging

$$F^0L^0T^0 \stackrel{d}{=} \left[\frac{E_0}{\sigma R^3}\right]^{a_2}\left[\frac{\rho C^2}{\sigma}\right]^{a_4} \qquad \text{(IV-13)}$$

The terms in brackets are dimensionless and a complete set of Π-terms is therefore

$$\begin{aligned} \Pi_1 &= \frac{E_0}{\sigma R^3} && \text{(a)} \\ \Pi_2 &= \frac{\rho C^2}{\sigma} && \text{(b)} \\ \Pi_3 &= \nu && \text{(c)} \end{aligned} \qquad \text{(IV-14)}$$

Π-terms can be multiplied, inverted, squared, or rooted to form new groups of Π-terms. It is convenient to have terms which separate the dependent and independent variables and which are physically meaningful. A new set of Π-terms can be developed as

$$\begin{aligned} \Pi_1' &= \frac{1}{\Pi_2} = \frac{\sigma}{\rho C^2} && \text{(a)} \\ \Pi_2' &= \left(\frac{1}{\Pi_1} \cdot \Pi_2\right)^{\frac{1}{3}} = \frac{(\rho C^2)^{\frac{1}{3}}R}{E_0} && \text{(b)} \\ \Pi_3 &= \nu \end{aligned} \qquad \text{(IV-15)}$$

so that non-dimensional relationship for peak stress can be written

$$\frac{\sigma}{\rho C^2} = f_1\left(\frac{(\rho C^2)^{\frac{1}{3}} R}{E_0^{\frac{1}{3}}}, \nu\right) \qquad \text{(IV-16)}$$

By similar application of the method illustrated above, the relationships for the other variables can be shown to be

$$\frac{a E_0^{\frac{1}{3}}}{(\rho C^8)^{\frac{1}{3}}} = f_2\left(\frac{(\rho C^2)^{\frac{1}{3}} R}{E_0^{\frac{1}{3}}}, \nu\right) \qquad \text{(a)}$$

$$\frac{v}{c} = f_3\left(\frac{(\rho C^2)^{\frac{1}{3}} R}{E_0^{\frac{1}{3}}}, \nu\right) \qquad \text{(b)}$$

$$\frac{(\rho C^2)^{\frac{1}{3}} d}{E_0^{\frac{1}{3}}} = f_4\left(\frac{(\rho C^2)^{\frac{1}{3}} R}{E_0^{\frac{1}{3}}}, \nu\right) \qquad \text{(c)} \qquad \text{(IV-17)}$$

$$\frac{(\rho C^5)^{\frac{1}{3}} t}{E_0^{\frac{1}{3}}} = f_5\left(\frac{(\rho C^2)^{\frac{1}{3}} R}{E_0^{\frac{1}{3}}}, \nu\right) \qquad \text{(d)}$$

It can be seen that the relations previously expressed in equation IV-8 in terms of five independent variables are now expressed in terms of two independent variables. It is important to note that the relations involve three variables and, therefore, the functions must be considered in three-space.

A major advantage of equations IV-17 is that they immediately show how the variables should be scaled to determine if experimental data fit the proposed scaling. Range, for example, should be scaled by the inverse of the cube of energy or yield and, for experiments in different materials, by the cube root of the constrained modulus of the material. Cube root of yield scaling is common, but the material terms are not normally included. It should be noted that range scaling in ground motion literature usually considers charge size in units of weight rather

than energy. Since weight is proportional to chemical energy release for a given type of explosive, the scaling is equivalent, but the range term is no longer non-dimensional. Reference IV-5 has applied this form of scaling to nuclear underground test data in various rocks. The agreement for rocks with widely different seismic velocities (e.g., Tuff vs Granite) is not good and, therefore, it is not clear that the proposed scaling is complete. These relations have been applied to Mole data in different materials and to cylindrical calculations for different elastic materials and have been found inadequate.

In an earlier paragraph it was stated that it is necessary to include all physical parameters which influence the phenomena, even if they are constant. It is possible that the total energy , E_0, may not be sufficient to completely characterize the source. For example, the peak pressure at the source may be an important parameter. As an illustration, consider an explosive source which at detonation is instantaneously converted to an ideal gas which contains the energy of the explosion as internal energy. The source characteristics can be completely categorized by the total mass of explosive, W, the internal energy per unit mass, ε_0, the initial density, ρ_0, and the ratio of specific heats, γ_r. The peak pressure of such an ideal gas source is

$$P_0 = (\gamma_r - 1)\rho_0\varepsilon_0 \qquad \text{(IV-18)}$$

The total explosive energy used to derive equations IV-16 is simple $\varepsilon_0 W$.

If P_0 is included in the dimensional analysis then an additional Π-term

$$\Pi = \frac{P_0}{\rho C^2} \qquad \text{(IV-19)}$$

must be added to the relations expressed by equations IV-16. The relations between the dependent and independent parameters can then be written

$$\frac{\sigma}{\rho C^2} = f_1\left(R\left(\frac{\rho C^2}{E_0}\right)^{\frac{1}{3}}, \frac{P_0}{\rho C^2}, \nu\right) \qquad (a)$$

$$\frac{a}{C^2}\left(\frac{E_0}{\rho C^2}\right)^{\frac{1}{3}} = f_1\left(R\left(\frac{\rho C^2}{E_0}\right)^{\frac{1}{3}}, \frac{P_0}{\rho C^2}, \nu\right) \qquad (b)$$

$$\frac{v}{C} = f_2\left(R\left(\frac{\rho C^2}{E_0}\right)^{\frac{1}{3}}, \frac{P_0}{\rho C^2}, \nu\right) \qquad (c) \qquad \text{(IV-20)}$$

$$d\left(\frac{\rho C^2}{E_0}\right)^{\frac{1}{3}} = f_3\left(R\left(\frac{\rho C^2}{E_0}\right)^{\frac{1}{3}}, \frac{P_0}{\rho C^2}, \nu\right) \qquad (d)$$

$$Ct\left(\frac{\rho C^2}{E_0}\right)^{\frac{1}{3}} = f_5\left(R\left(\frac{\rho C^2}{E_0}\right)^{\frac{1}{3}}, \frac{P_0}{\rho C^2}, \nu\right) \qquad (e)$$

Recombination of Π-terms can yield an alternate set of relations

$$\frac{\sigma}{P_0} = f_1\left(R\left(\frac{P_0}{E_0}\right)^{\frac{1}{3}}, \frac{P_0}{\rho C^2}, \nu\right) \qquad (a)$$

$$\frac{a}{C^2}\left(\frac{E_0}{P_0}\right)^{\frac{1}{3}} = f_2\left(R\left(\frac{P_0}{E_0}\right)^{\frac{1}{3}}, \frac{P_0}{\rho C^2}, \nu\right) \qquad (b)$$

$$\frac{\rho C v}{P_0} = f_3\left(R\left(\frac{P_0}{E_0}\right)^{\frac{1}{3}}, \frac{P_0}{\rho C^2}, \nu\right) \qquad (c) \qquad \text{(IV-21)}$$

$$d\left(\frac{P_0}{E_0}\right)^{\frac{1}{3}} = f_4\left(R\left(\frac{P_0}{E_0}\right)^{\frac{1}{3}}, \frac{P_0}{\rho C^2}, \nu\right) \qquad (d)$$

$$Ct\left(\frac{P_0}{E_0}\right)^{\frac{1}{3}} = f_5\left(R\left(\frac{P_0}{E_0}\right)^{\frac{1}{3}}, \frac{P_0}{\rho C^2}, \nu\right) \qquad (e)$$

There are many other possible formulations, all correct so long as six independent Π-terms are included.

A comparison of equations IV-20 and IV-21 indicates that there is no unique way of scaling range or the dependent variables, as was the case

in equations IV-17 when only a limited source description was included. The functional relationships are multi-variate. They cannot be reduced to two-dimensions, as is often attempted when scaled response parameters are plotted versus some form of scaled range on log-log paper. Even if the explosive type is the same from event to event (i.e., P_o is constant), the relations remain multi-variate.

To the authors' knowledge, the scaling relations expressed by equations IV-20 or IV-21 have not been tested against data. However, it is believed that they should form the basis for extensions of the results herein to new materials. Although actual explosives will not behave as ideal gases, a physical source parameter similar to P_o is expected to be important. Therefore, terms involving P_o, ρ and C are expected to be present in the relations.

For completeness, a corresponding set of relations for cylindrical geometry are

$$\frac{\sigma}{P_o} = f_1\left(R\left(\frac{P_o}{\gamma}\right)^{\frac{1}{2}} , \frac{P_o}{\rho C^2} , \nu\right) \qquad (a)$$

$$\frac{a}{C^2}\left(\frac{\gamma}{P_o}\right)^{\frac{1}{2}} = f_2\left(R\left(\frac{P_o}{\gamma}\right)^{\frac{1}{2}} , \frac{P_o}{\rho C^2} , \nu\right) \qquad (b)$$

$$\frac{\rho C v}{P_o} = f_3\left(R\left(\frac{P_o}{\gamma}\right)^{\frac{1}{2}} , \frac{P_o}{\rho C^2} , \nu\right) \qquad (c) \qquad \text{(IV-22)}$$

$$d\left(\frac{P_o}{\gamma}\right)^{\frac{1}{2}} = f_4\left(R\left(\frac{P_o}{\gamma}\right)^{\frac{1}{2}} , \frac{P_o}{\rho C^2} , \nu\right) \qquad (d)$$

$$Ct\left(\frac{P_o}{\gamma}\right)^{\frac{1}{2}} = f_5\left(R\left(\frac{P_o}{\gamma}\right)^{\frac{1}{2}} , \frac{P_o}{\rho C^2} , \nu\right) \qquad (e)$$

where γ is the lineal energy density and has units FL/L or F. The

relations for a planar charge are

$$\frac{\sigma}{P_o} = f_1\left(R\left(\frac{P_o}{\alpha}\right) , \frac{P_o}{\rho C^2} , \nu\right) \qquad (a)$$

$$\frac{a}{C^2}\left(\frac{\alpha}{P_o}\right) = f_2\left(R\left(\frac{P_o}{\alpha}\right) , \frac{P_o}{\rho C^2} , \nu\right) \qquad (b)$$

$$\frac{\rho C v}{P_o} = f_3\left(R\left(\frac{P_o}{\alpha}\right) , \frac{P_o}{\rho C^2} , \nu\right) \qquad (c) \qquad \text{(IV-23)}$$

$$d\left(\frac{P_o}{\alpha}\right) = f_4\left(R\left(\frac{P_o}{\alpha}\right) , \frac{P_o}{\rho C^2} , \nu\right) \qquad (d)$$

$$Ct\left(\frac{P_o}{\alpha}\right) = f_5\left(R\left(\frac{P_o}{\alpha}\right) , \frac{P_o}{\rho C^2} , \nu\right) \qquad (e)$$

where α is the areal energy density and has units FL/L^2 or F/L.

The data analysis presented in the following is concerned with a common material, dry granular alluvial type soil. In the same material, the scaling relations for the spherical, cylindrical and planar geometries are simplified considerably and reduce to

$$\sigma = F_{1Y}\left(\frac{R}{Y}\right) \qquad (a)$$

$$a \cdot Y = F_{2Y}\left(\frac{R}{Y}\right) \qquad (b)$$

$$v = F_{3Y}\left(\frac{R}{Y}\right) \qquad (c) \qquad \text{(IV-24)}$$

$$\frac{d}{Y} = F_{4Y}\left(\frac{R}{Y}\right) \qquad (d)$$

$$\frac{t}{Y} = F_{5Y}\left(\frac{R}{Y}\right) \qquad (e)$$

where Y is $W^{\frac{1}{3}}$, $\gamma^{\frac{1}{2}}$, or α depending on whether the geometry is spherical, cylindrical, or planar, respectively; and F_{iY} $(i = 1,\ldots,5)$

indicates the relationships are dimensional and dependent on the parameter being considered and the geometry.

In actual problems, there will be many other variables which may be important. Examples are the depth of the charge below the free-surface, the finite length of cylindrical or planar charges, the depth to the target point location, material nonlinearity, material strength and gravity. Inclusion of these terms in the dimensional ánalysis is straightforward, but there is generally insufficient material property data or experimental data or both to allow evaluation of their importance. The relations given in equation IV-24 are the basis for most of the work herein. Other considerations are introduced as required in analysis and/or justified by available data.

3. DATA FROM SPHERICAL EXPLOSIONS

A large base of data from spherical explosions in dry granular media is available from various experiments at Nevada Test Site. Relatively deep burial is of interest for simulation applications, and suitable data is available from the Mole 200 and 400 series, JANGLE HE-3 and TEAPOT ESS. The tests have been reviewed in Section II, and the data is available in reference IV-6.

Horizontal accelerations, velocities and displacements in the Mole 200 and 400 series for scaled depths of burst greater than 0.5 ft/lb$^{\frac{1}{3}}$ are plotted in figures IV-2, IV-3 and IV-4, respectively. The material at the 200 and 400 series sites has been considered the same and, therefore, data from both series have been plotted together. It can be seen in figures IV-2 and IV-3 that the data from the two series scatter together;

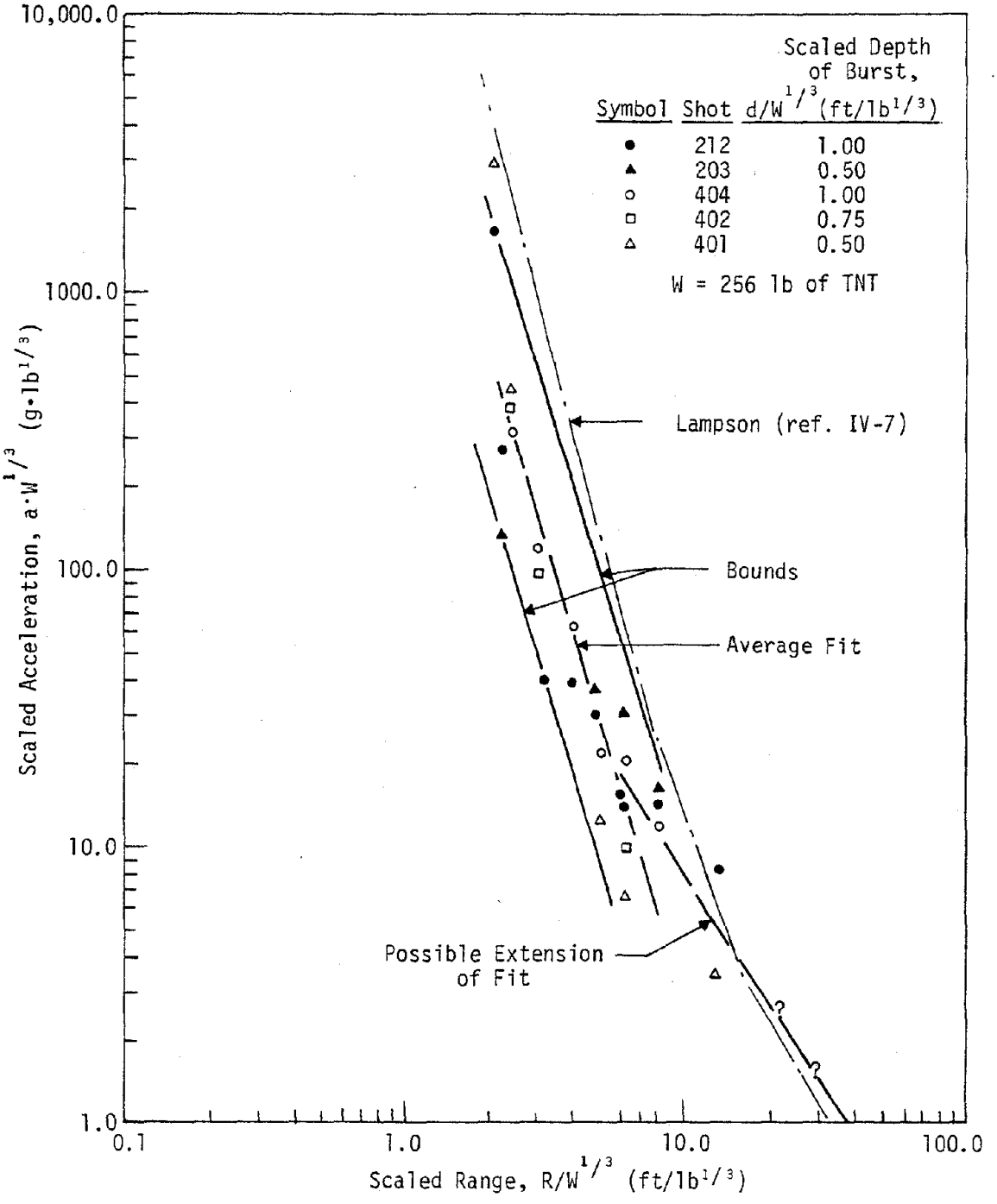

Figure IV-2. Mole Horizontal Accelerations from Deeply Buried Shots in Dry Gravel-Sand Mix

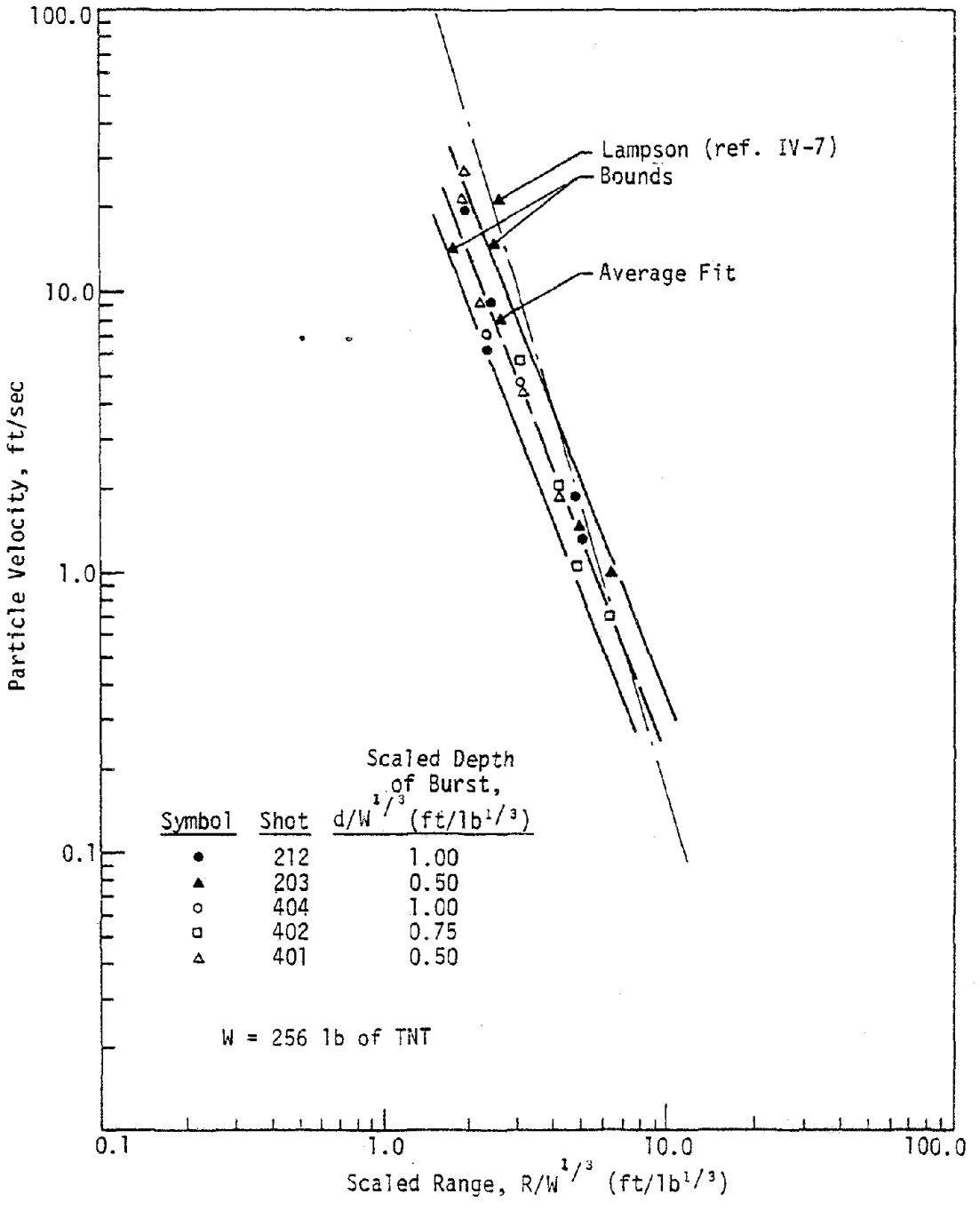

Figure IV-3. Mole Horizontal Velocities from Deeply Buried Shots in Dry Gravel-Sand Mix

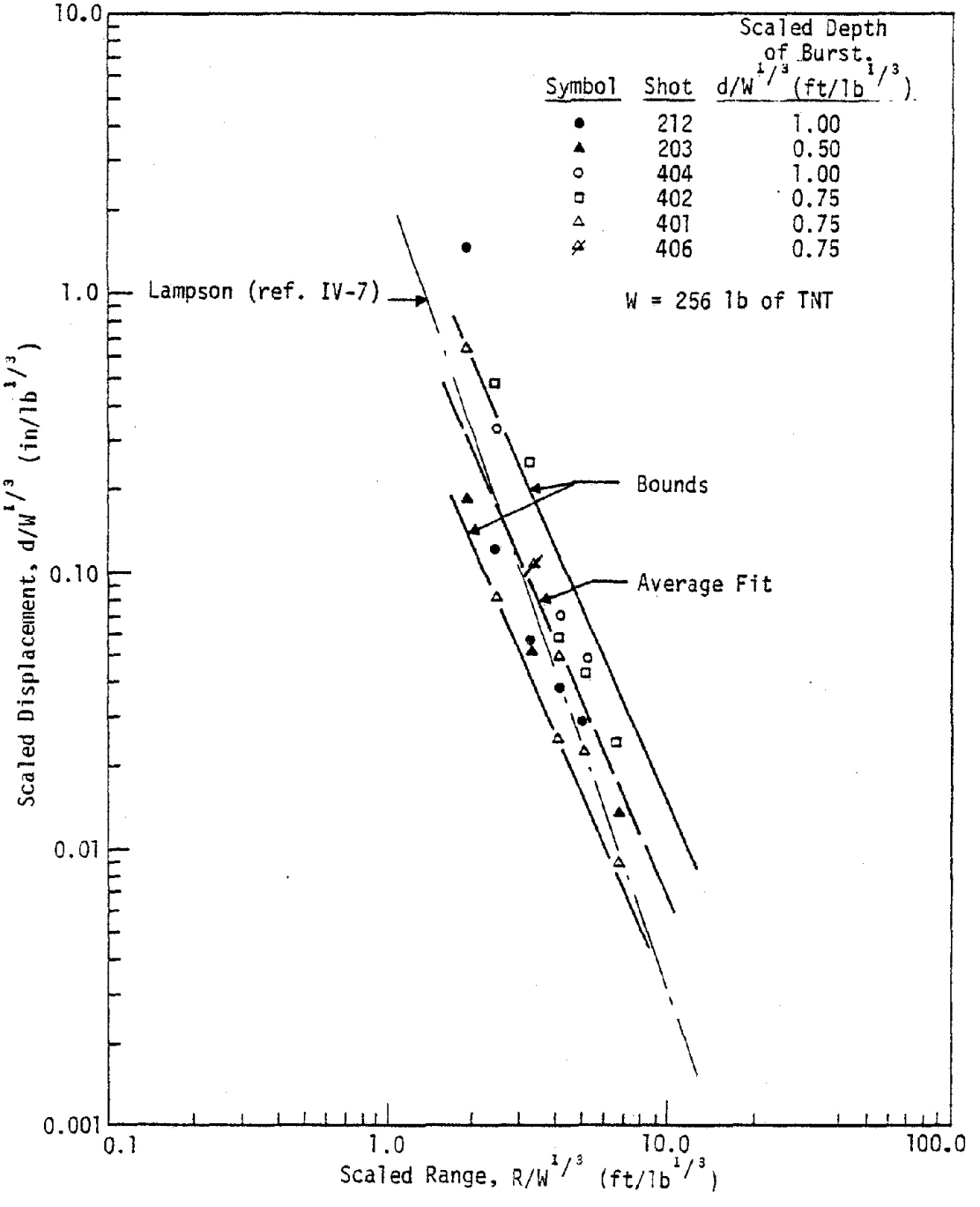

Figure IV-4. Mole Horizontal Displacements from Deeply Buried Shots in Dry Gravel-Sand Mix

hence, the assumption of a common material, at least for acceleration and velocity, has some justification in the data. The displacement data of figure IV-4, however, seems to separate with the 400 series events yielding higher displacements. Measured wave speeds averaged 3600 ft/sec in the 200 series and 2900 ft/sec in the 400 series, indicating the 400 series site was less stiff than the 200 series site. The difference is apparently reflected mostly in the displacement data. Since the wave speed difference was not known prior to the tests and since the difference in the magnitude (about a factor 2) seems too large to be accounted for simply by the difference in wave speeds (a factor of 1.2), the data from both series are treated as a group. The scatter introduced is no greater than has been observed in single well instrumented experiments.

With the assumption stated above, the Mole 200 and 400 series data in dry gravel-sand can be represented by

$$a \cdot W^{\frac{1}{3}} = 6000 \left(\frac{R}{W^{\frac{1}{3}}} \right)^{-3.3} \quad \pm \text{ a factor of } 3.3 \quad (a)$$

$$v = 80 \left(\frac{R}{W^{\frac{1}{3}}} \right)^{-2.6} \quad \pm \text{ a factor of } 1.6 \quad (b) \qquad \text{(IV-25)}$$

$$\frac{d}{W^{\frac{1}{3}}} = 1.45 \left(\frac{R}{W^{\frac{1}{3}}} \right)^{-2.4} \quad \pm \text{ a factor of } 2.1 \quad (c)$$

where

a = acceleration in g's

v = velocity in ft/sec

d = displacement in inches

R = range in feet

W = charge weight in lbs of TNT

The decay exponents show that accelerations decay most rapidly with range; velocities and displacement follow, in that order. However, the decay difference between the velocities and displacements may not be significant within the scatter of the data. There is a tendency for the acceleration data to decay at a reduced slope beyond a scaled range of about 6. There is insufficient data to define the decay slope with any confidence and, hence, the dashed-line in figure IV-2 with a slope of -1.6 is shown with question marks. The reduction in slope suggests that the peak stress beyond this range is approaching an elastic condition. Measurements suggest an average seismic wave speed in the material of 3600 ft/sec and a unit weight of 100 lbs/ft^3 (see Section II). The particle velocity at a scaled range of 6 is about 0.75 ft/sec. If the behavior is near-elastic, radial stress at the range can be estimated by

$$\sigma = \rho C v \qquad \text{(IV-26)}$$

where

σ = stress

ρ = mass density

C = seismic velocity

v = particle velocity

Substitution of the appropriate parameters suggest the radial stress at a scaled range of 6 to be about 60 lb/in^2. This value is consistent with elastic limits in dry granular materials estimated from in-situ material property tests.

Lampson's empirical relations (ref. IV-7), given previously in

equations I-5, I-6 and I-7, are also plotted in figures IV-2, IV-3 and IV-4 for the unit weight and average seismic velocity stated in the previous paragraph. The relations for acceleration and velocity are higher than the data and decay more rapidly. The relation for acceleration shows a tendency toward reduced attenuation and comes into agreement with the small amount of data and the reduced slope which was fitted to the data beyond a scaled range of about 10. Lampson's relation for displacement (fig. IV-4) goes through the data quite well. Although it has a greater attenuation rate than the fit shown, it can probably be considered an equally good fit within the data scatter. This observation indicates that there is significant uncertainty in decay slopes fitted to scattered data. Use of the fits beyond the ranges for which data is available is highly uncertain.

Vertical accelerations measured on the Mole 200 and 400 series are plotted in figure IV-5. As with the horizontal accelerations, the data from the two series scatter together. The vertical data, to a scaled range of about 6, is fit very well by a line having the same decay slope as for the horizontal accelerations (-3.3) but with an amplitude of about 1/3 the horizontal amplitude. The fit equation is

$$a \cdot W^{\frac{1}{3}} = 2000 \left(\frac{R}{W^{\frac{1}{3}}} \right)^{-3.3} \qquad \text{(IV-27)}$$

The data scatter is about the same as for the horizontal data. Beyond a scaled range of 6, the vertical data scatter significantly and suggest little or irregular attenuation. Some vertical accelerations exceed the horizontals. The data suggest a change in the phenomena causing the peak vertical acceleration. While at closer range, peak

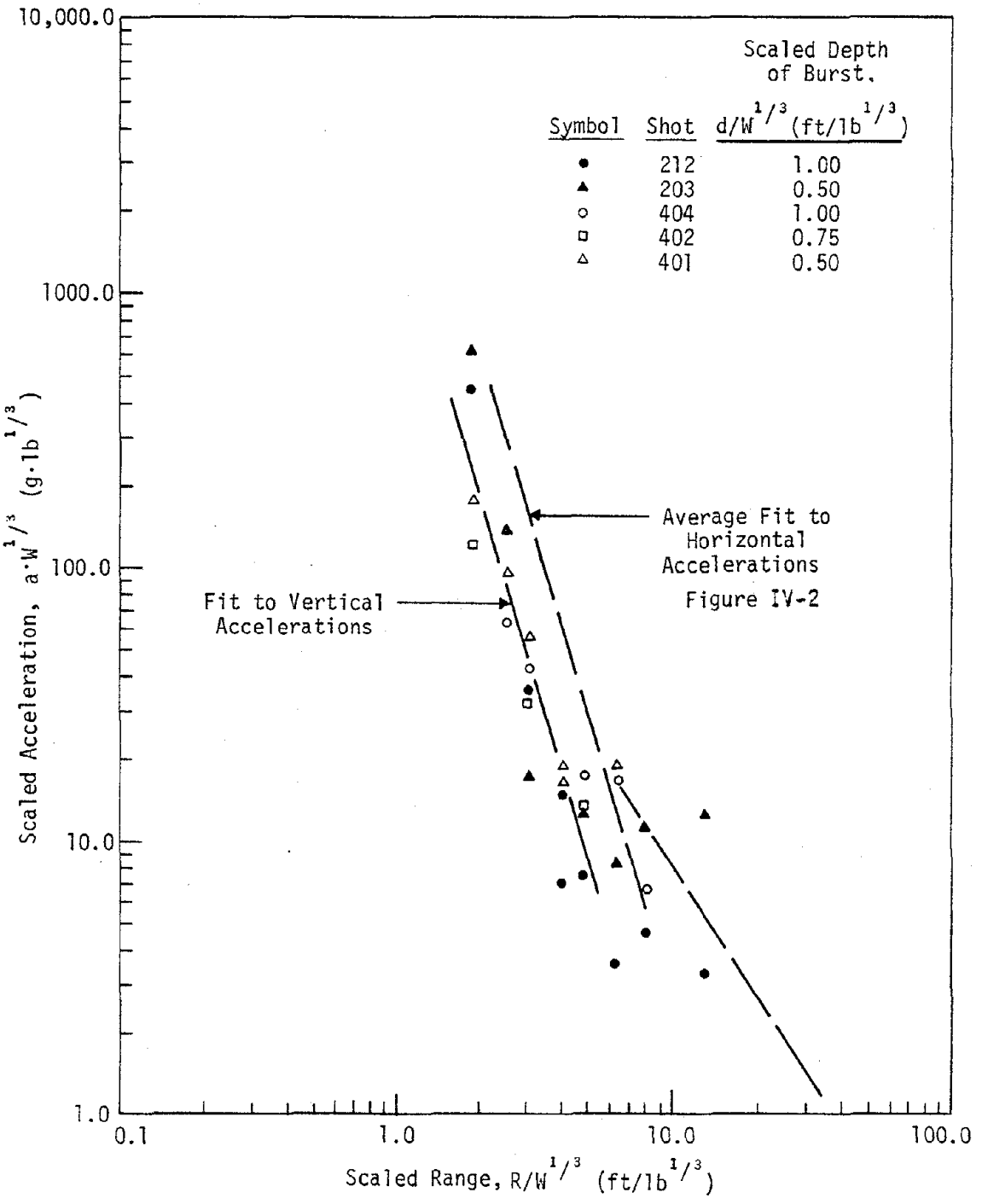

Figure IV-5. Mole Vertical Accelerations from Deeply Buried Shots in Dry Gravel-Sand Mix

vertical and horizontal accelerations occur at the wave front at about the same time, the vertical accelerations at more distant ranges often occur later in the waveform suggesting that they may be due to shear or surface wave phenomena. From a prediction viewpoint, the peak vertical acceleration beyond a scaled range of 6 should be taken equal to the horizontal component. No vertical velocity or displacement data are available from Mole.

Two characteristic times of the 200 and 400 series horizontal velocity pulses, the time from peak outward to peak inward velocity and the duration of the outward velocity phase, are plotted in figure IV-6. The data has been separated into near-surface gage and near-radial gage categories because the data seem to suggest different trends at these locations, especially the outward phase duration. This difference is believed due to shear failure and flow of material near the surface which is not significant at the near-radial positions.

The data for peak outward to peak inward velocity contains considerable scatter and clear trends are not discernable. The near-radial data appear to be decreasing rapidly with range at close ranges (to a scaled range of about 4) and approaching a plateau at greater ranges. This apparent trend is represented by the dashed-line with question marks in figure IV-6(a) (1); the question marks to indicate the tenuous nature of the trend line. The few near-surface gages indicate a similar trend to a scaled range of about 4, but the trend beyond this range cannot be determined due to the absence of data.

The outward phase duration data for near-radial positions separates

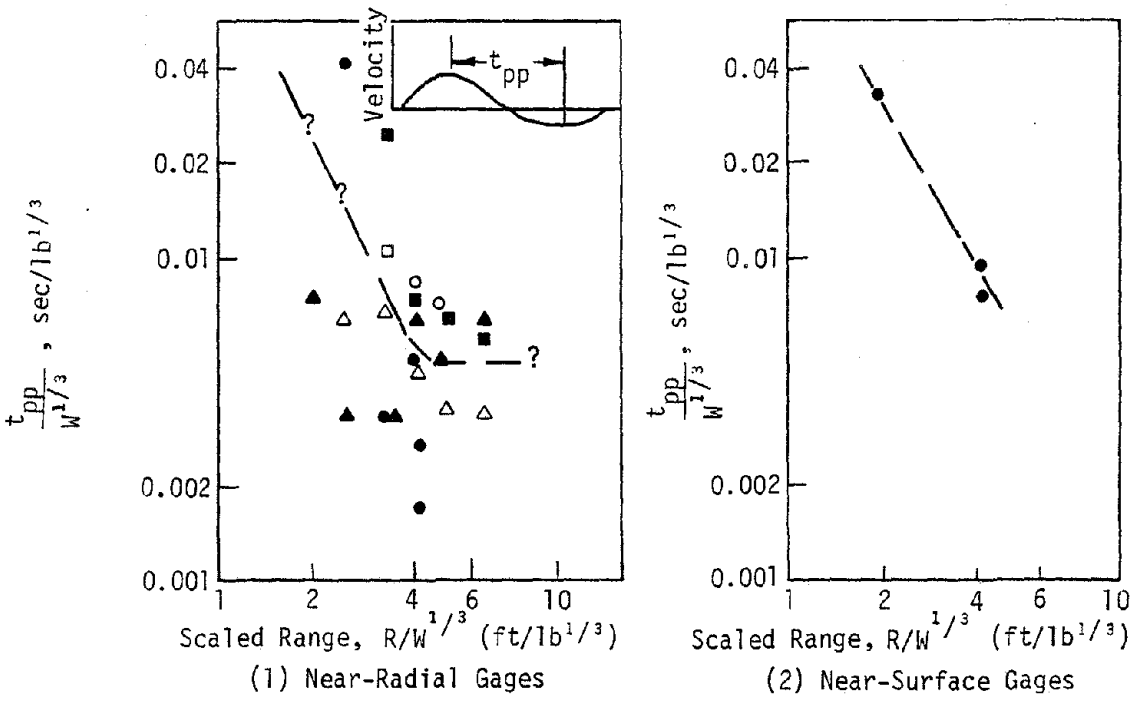

(a) Time from Peak Outward to Peak Inward Velocity

Note: Symbol definitions are the same as on figures IV-2 through IV-5.

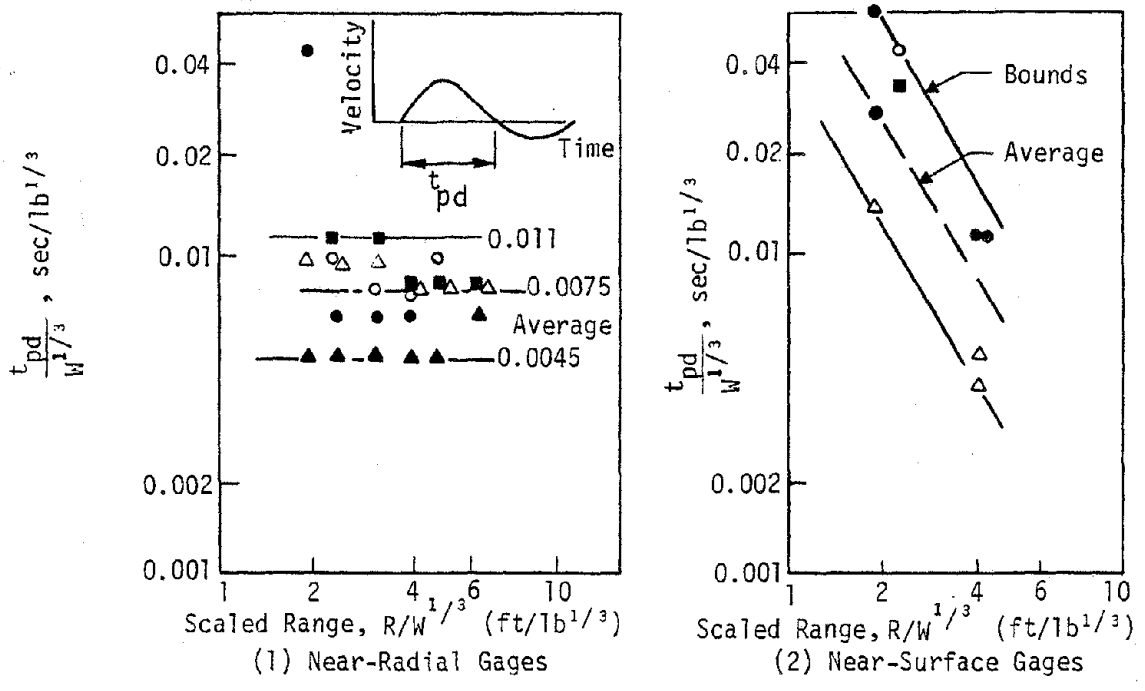

(b) Outward Phase Duration of Horizontal Velocity

Figure IV-6. Characteristic Times of Mole Horizontal Velocity Pulses from Deeply Buried Shots in Dry Gravel-Sand Mix

according to series with the 400 series data being highest. This is consistent with the displacement data which indicates higher displacements in the 400 series. However, for reasons previously outlined for displacements, the data from both series are treated as a single group. The near-radial data from individual tests and the data as a whole do not exhibit a consistent variation with range. Indeed, there appears to be very little variation with range. No variation has been assumed and the data has been averaged to yield

$$\frac{t_{pd}}{W^{\frac{1}{3}}} = 0.0075 \begin{matrix} + \text{ a factor of } 1.5 \\ - \text{ a factor of } 1.7 \end{matrix} \qquad \text{(IV-28)}$$

where

t_{pd} = outward phase duration in seconds

W = explosive weight in lbs

The scatter in this correlation is equal to or less than the scatter for the peak motion amplitude parameters discussed earlier.

The outward phase durations for the near-surface gages contain a clear tendency toward reduced amplitude with increasing range. The average outward phase velocity to a scaled range of 4 is expressed by

$$\frac{t_{pd}}{W^{\frac{1}{3}}} = 0.082 \left(\frac{R}{W^{\frac{1}{3}}}\right)^{-1.7} \pm \text{ a factor of } 2 \qquad \text{(IV-29)}$$

There is no data beyond a scaled range of 4, but the average duration at that range is 0.078 sec/$lb^{\frac{1}{3}}$ which is very close to the duration for the near-radial gages. It is possible that near-surface shear and flow has become less significant at this range and both near-surface and

near-radial gages will behave similarly at scaled ranges beyond 4.

The data of figures IV-2, IV-3, IV-4, IV-5 and IV-6 and the associated equations have been scaled by $W^{\frac{1}{3}}$ (i.e., equations IV-24). Since the data are from charges of the same size (256 lbs), the $W^{\frac{1}{3}}$ scaling cannot be verified by the data. Its use is for convenience in later comparisons. The validity of $W^{\frac{1}{3}}$ scaling in a common material is discussed next.

Figures IV-7, IV-8 and IV-9 compare the bounds and average fits to the Mole 200 and 400 series peak motion data with the data from JANGLE HE-3 and TEAPOT ESS. JANGLE HE-3 had a yield of 2560 lbs of TNT while TEAPOT ESS was a nuclear event with a yield of 1.2 kT of TNT equivalent. Both were at scaled depths of burst 0.5 $ft/lb^{\frac{1}{3}}$. Data from DIP IA at McCormick Ranch (ref. IV-8 and IV-9) are also plotted on the figures but will not be discussed at this time.

Since JANGLE HE-3 and TEAPOT ESS represent experiments having yields of 10 and 9375 times as great as in the Mole series at the same site, it is of interest to evaluate the degree to which $W^{\frac{1}{3}}$ scaling collapses the data. It can be seen in figure IV-7 that the bounds to the Mole horizontal acceleration data contain most of the data from the larger events except the JANGLE HE-3 data beyond a scaled range of about 6. The JANGLE data reaches a constant value at a scaled range of about 4 and maintains this value to a scaled range of about 8 after which it attenuates again at about the same slope as in the near region. The cause of this behavior is not clear. It is not the same as the apparent transition to elastic behavior that occurs in the Mole data nor does it occur in the available TEAPOT data.

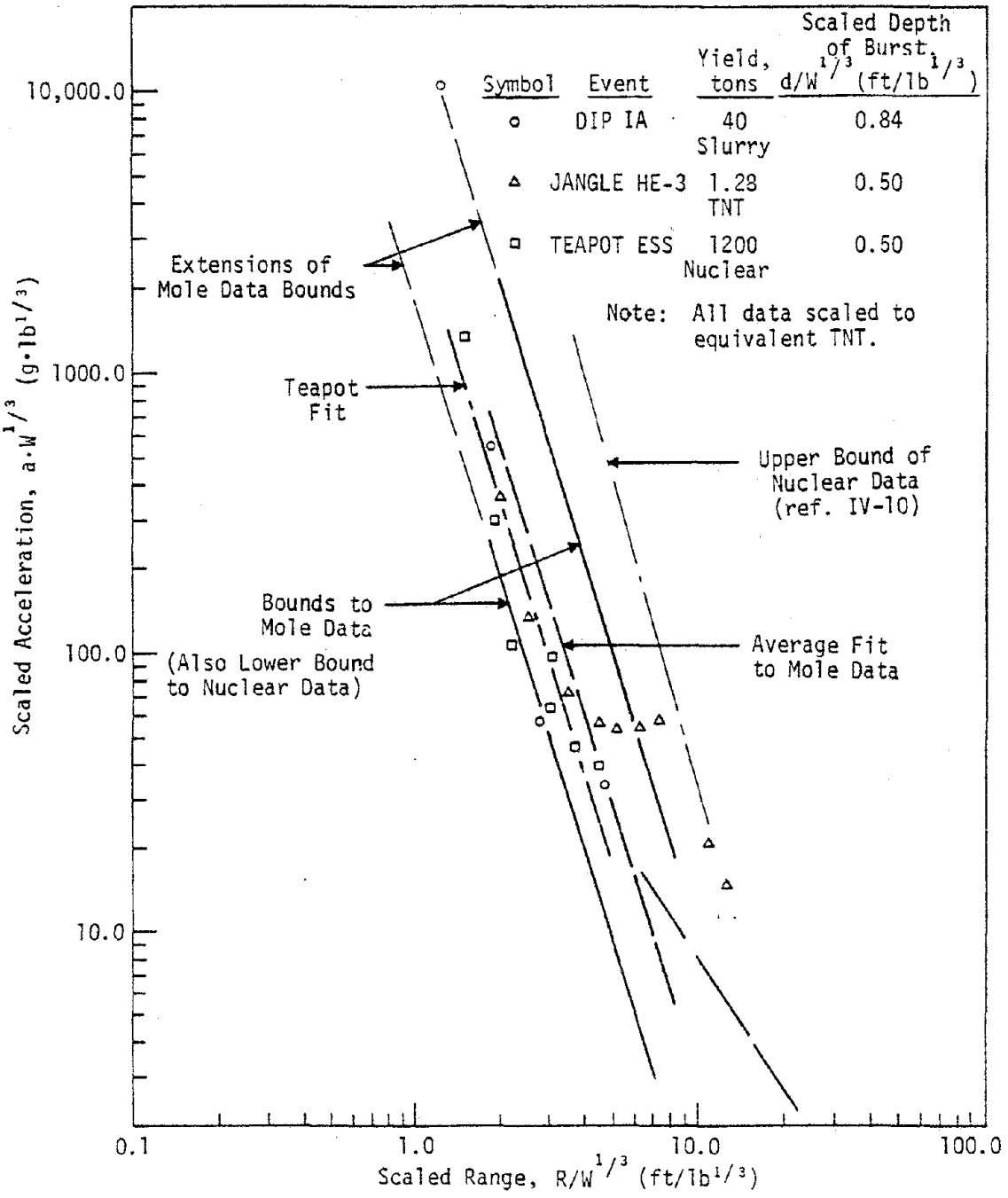

Figure IV-7. Some Horizontal Acceleration Data from Large Events in Dry Alluvium Compared with Mole

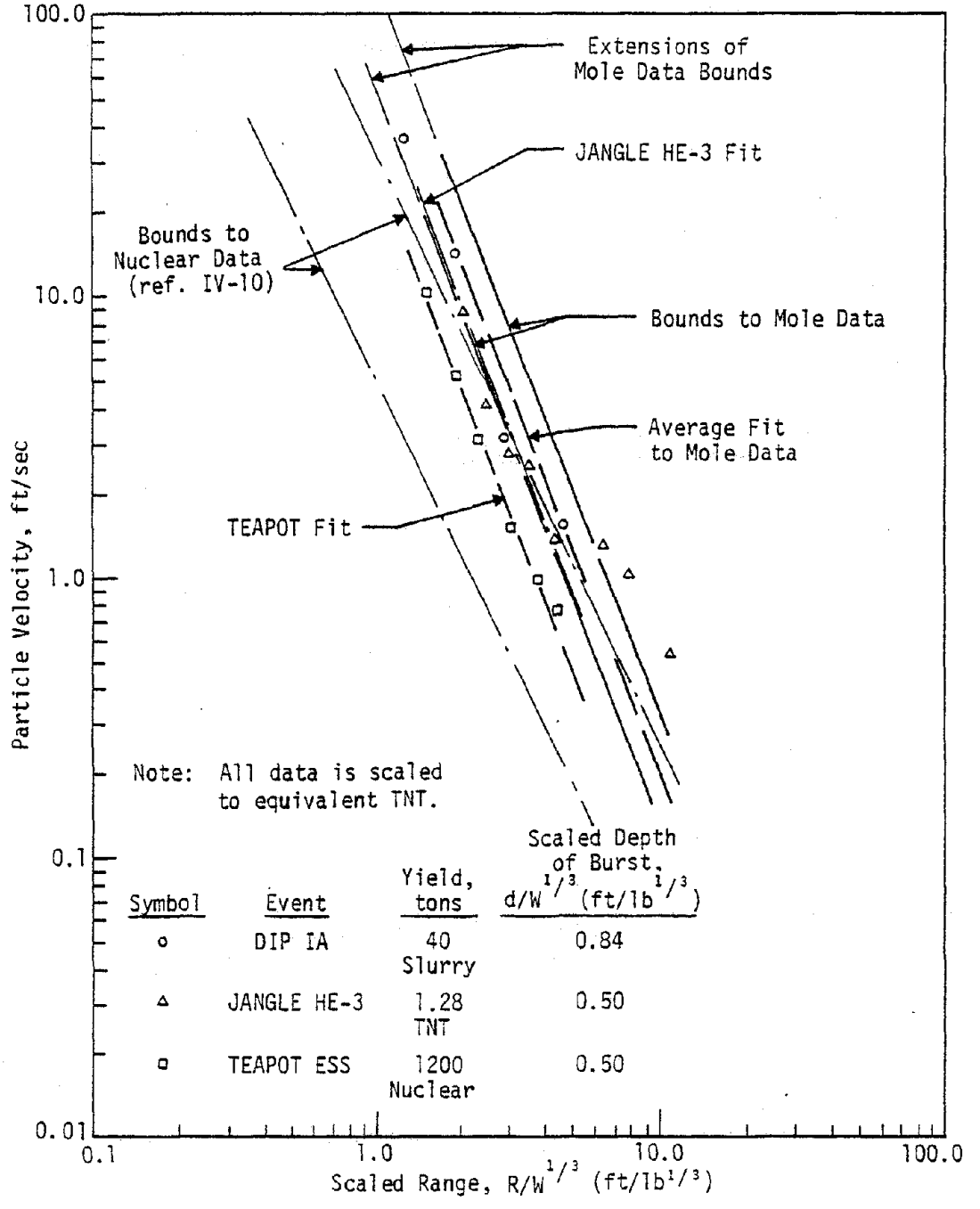

Figure IV-8 Some Horizontal Velocity Data from Large Events in Dry Alluvium Compared with Mole

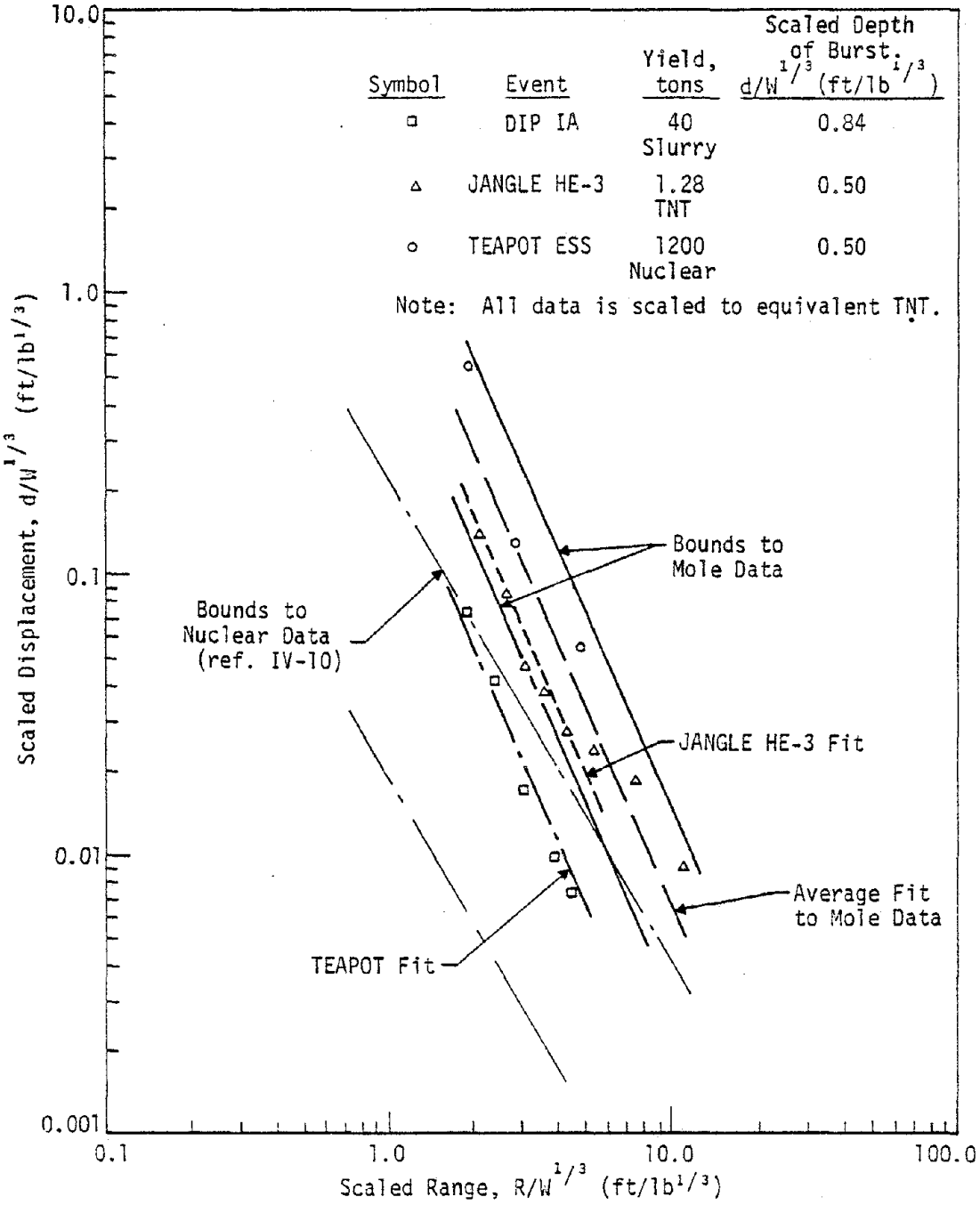

Figure IV-9 Some Horizontal Displacement Data from Large Events in Dry Alluvium Compared with Mole

Bounds to nuclear data in alluvium, which are much larger than the Mole bounds, encompass all of the data. Although most of the TEAPOT and JANGLE HE-3 data lie within the Mole scatter, there is a clear tendency for the data of the larger events to lie below the Mole average. TEAPOT lies the furthest below while JANGLE (to a scaled range of 6) lies in between. This same tendency occurs to a larger extent in the velocity data (fig. IV-8) and the displacement data (fig. IV-9). It is also evident in figures IV-8 and IV-9 that nuclear data in alluvium, represented by the bounds shown, lie well below the Mole bounds. These data all suggest a dependence upon W which is not included in $W^{\frac{1}{3}}$ scaling.

A dependence of ground motion data on gravity has been suggested in the ground motion community for several years but the dependence has not been formalized nor gained general acceptability. The Russians (ref. IV-11), as discussed in Section II, considered gravity scaling in the absence of material property dependence. Such scaling leads to the following expressions for the major ground motion parameters:

$$\frac{\sigma}{(\rho g)^{\frac{3}{4}} E_0^{\frac{1}{4}}} = f_1\left((\rho g)^{\frac{1}{4}}\left(\frac{R}{E_0^{\frac{1}{4}}}\right)\right) \qquad \text{(a)}$$

$$\frac{a}{g} = f_2\left((\rho g)^{\frac{1}{4}}\left(\frac{R}{E^{\frac{1}{4}}}\right)\right) \qquad \text{(b)}$$

$$\left(\frac{\rho}{g^3 E_0}\right)^{\frac{1}{8}} v = f_3\left((\rho g)^{\frac{1}{4}}\left(\frac{R}{E_0^{\frac{1}{4}}}\right)\right) \qquad \text{(c)} \qquad \text{(IV-30)}$$

$$\left(\frac{E_0^{\frac{1}{4}}}{g}\right) d = f_4\left((\rho g)^{\frac{1}{4}}\left(\frac{R}{E_0^{\frac{1}{4}}}\right)\right) \qquad \text{(d)}$$

$$\left(\frac{\rho g^5}{E_o}\right)^{\frac{1}{3}} t = f_5\left((\rho g)^{\frac{1}{4}}\left(\frac{R}{E_o^{\frac{1}{4}}}\right)\right) \qquad \text{(e)}$$

The range in equations IV-30 is scaled by $E_o^{\frac{1}{4}}$ and, hence, gravity scaling is often called fourth root of yield scaling.

It is difficult to believe that relations which exclude material properties will be complete. Indeed, although material property effects are not well defined, available data indicate material differences. Equations IV-21 include dilational wave speed and Poisson's ratio as material property terms. To these, a nondimensional term involving gravity of the form given below can be added

$$\Pi_{11} = \frac{g}{C^2}\left(\frac{E_o}{P_o}\right)^{\frac{1}{3}} \qquad \text{(IV-31)}$$

The appropriate functional relation involving gravity and material properties for the independent variables of equations IV-21 is therefore

$$f_i\left(R\left(\frac{P_o}{E_o}\right)^{\frac{1}{3}}, \frac{P_o}{\rho C^2}, \nu, \frac{g}{C^2}\left(\frac{E_o}{P_o}\right)^{\frac{1}{3}}\right) \qquad \text{(IV-32)}$$

For a common explosive type and a common material, equation IV-32 can be written in dimensional form for the dependent variables as

$$\sigma = f_1\left(\frac{R}{W^{\frac{1}{3}}}, W\right) \qquad \text{(a)}$$

$$aW^{\frac{1}{3}} = f_2\left(\frac{R}{W^{\frac{1}{3}}}, W\right) \qquad \text{(b)}$$

$$v = f_3\left(\frac{R}{W^{\frac{1}{3}}}, W\right) \qquad \text{(c)} \qquad \text{(IV-33)}$$

$$\frac{d}{W^{\frac{1}{3}}} = f_4\left(\frac{R}{W^{\frac{1}{3}}}, W\right) \qquad \text{(d)}$$

$$\frac{t}{W^{\frac{1}{3}}} = f_5\left(\frac{R}{W^{\frac{1}{3}}}, W\right) \qquad \text{(e)}$$

where W is the explosive weight.

Equations IV-33 indicate that each dependent variable is a function of two variables and, therefore, neither $W^{\frac{1}{3}}$ nor $W^{\frac{1}{4}}$ scaling are appropriate if gravity is important. The solution will be a surface in three-space with the dependent variable on one axis, scaled range on a second axis and the amount of explosive on the third axis. It is often observed that ground motion data plots versus range as a straight line on log-log paper. If it is assumed that the solution in log-log three-space is a plane, then solutions of the type below can be sought

$$P = KR^nW^m \qquad \text{(IV-34)}$$

where

P = the dependent variable of interest

K = a constant

n,m = exponents

Fits to the TEAPOT and JANGLE HE-3 peak motion data are shown in figures IV-7, IV-8 and IV-9. The fits to JANGLE HE-3 are limited to scaled ranges less than about 4. The peak motion amplitudes at a scaled range of two as a function of $W^{\frac{1}{3}}$ are plotted in figure IV-10. $W^{\frac{1}{3}}$ is used rather than W for convenience in plotting. It can be seen that the amplitudes are fit fairly well by straight lines, indicating that the differences in energy per unit mass at the source (nuclear VS. TNT) do not appear significant at the depth of burial considered and that equation IV-34 is reasonable. Solutions to equation IV-34 for acceleration, velocity,

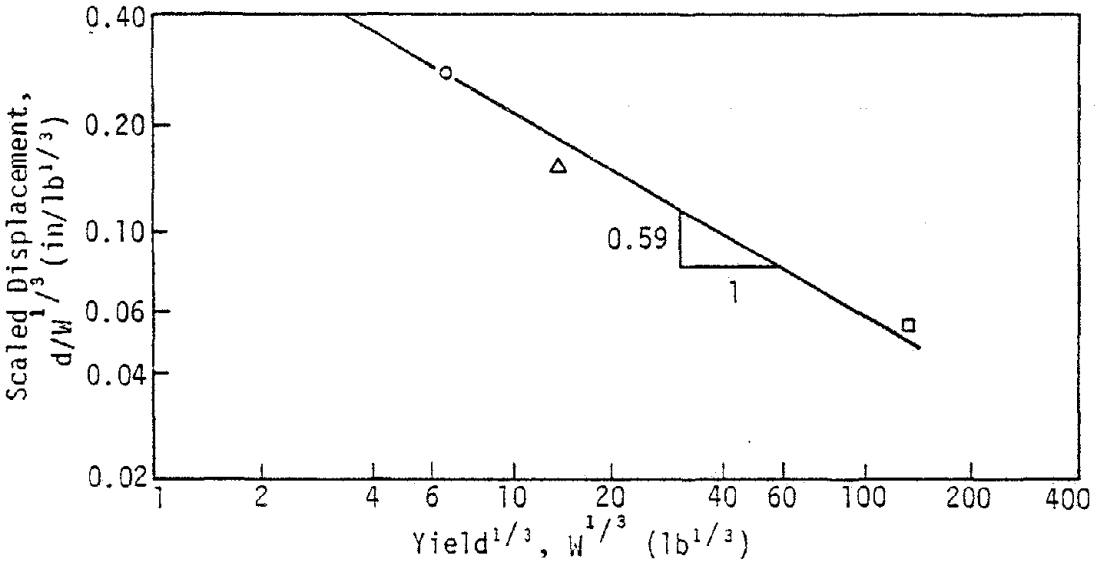

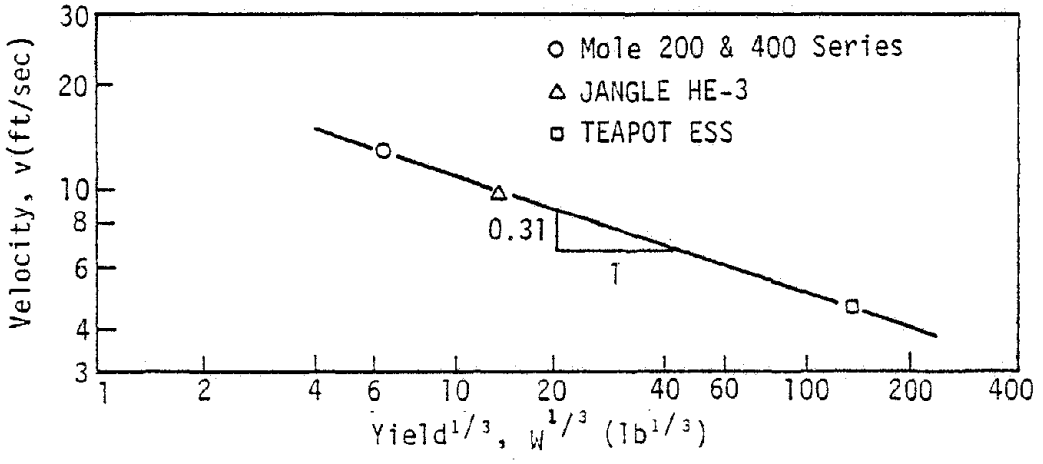

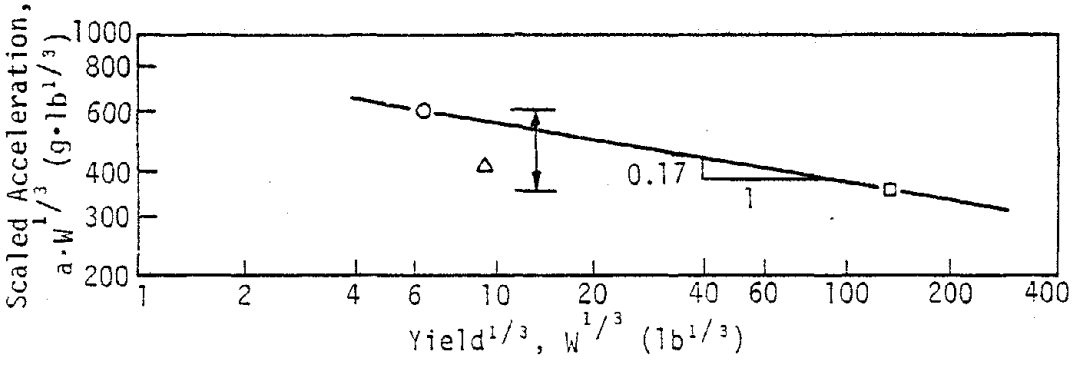

Figure IV-10. Effect of Yield on Peak Ground Motions in Dry Alluvium at Scaled Range, $R/W^{1/3}$ = 2 ft/lb$^{1/3}$

and displacement are:

$$aW^{0.31} = 8150\left(\frac{R}{W^{0.31}}\right)^{-3.3} \qquad (a)$$

$$v = 142.5\left(\frac{R}{W^{0.29}}\right)^{-2.6} \qquad (b) \qquad \text{(IV-35)}$$

$$\frac{d}{W^{0.28}} = 4.32\left(\frac{R}{W^{0.28}}\right)^{-2.4} \qquad (c)$$

where

a = acceleration in g's

v = velocity in ft/sec

d = displacement in inches

R = range in feet

W = explosive yield in lbs of TNT

It can be seen in equations IV-35 that acceleration scales almost by $W^{\frac{1}{3}}$, displacements by almost $W^{\frac{1}{4}}$ with velocity in between. This suggests that gravity has its major influence on displacement.

Characteristic times for JANGLE HE-3 and TEAPOT ESS are compared with Mole 200 and 400 series times in figure IV-11. It can be seen that the trends in the peak to peak times are similar but the data from the different events are separated significantly. TEAPOT ESS data is lowest, Mole highest and JANGLE HE-3 data in between. The peak to peak times decrease rapidly to a scaled range of about four, reach a low and then increase at a lower rate. The outward duration data initially decrease and then increase slightly beyond a scaled range of about four. The amplitude order of the outward phase data is the same as for the peak to peak time data. As in the peak motion data, there appears to be

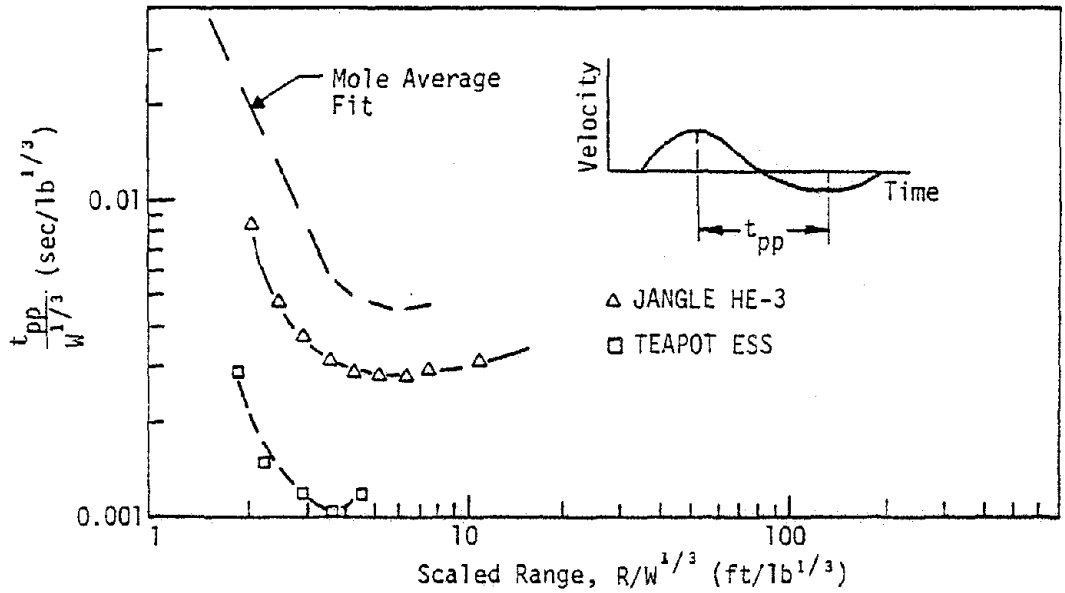

(a) Time from Peak Outward to Peak Inward Velocity

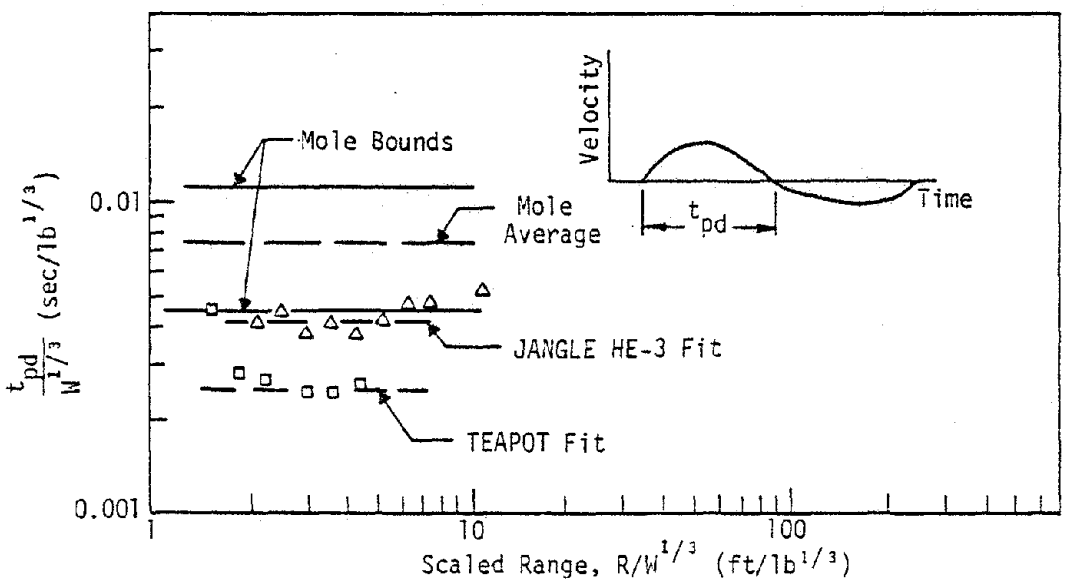

(b) Outward Phase Duration of Horizontal Velocity

Figure IV-11. Characteristic Times of Horizontal Velocity Pulse

a clear dependence of the amplitudes on yield.

Although there is a slight variation of the outward phase duration apparent in the JANGLE HE-3 and TEAPOT data, these data are fit fairly well by average constant fit lines as was used for the Mole data. The constant fits are plotted as a function of yield in figure IV-12. Again, $W^{\frac{1}{3}}$ has been used instead of W for convenience in plotting. Also plotted in figure IV-12 is the peak to peak time at a scaled range of four. Both sets of data are fit fairly well by straight lines. The marked curvature of the peak to peak data indicate that an equation of the form of equation IV-34 cannot be fit to the data. However, peak to peak times can be estimated approximately by

$$t_{pp} = t_{pp}(\text{JANGLE HE-3})\left(\frac{W}{2560 \text{ lbs}}\right)^{0.17} \qquad \text{(IV-36)}$$

The outward phase duration can be estimated by

$$t = 0.018W^{0.17} \qquad \text{(IV-37)}$$

where

t = time in seconds

W = yield in pounds of TNT

Equation IV-37 indicates that the outward phase duration scales approximately by $W^{\frac{1}{6}}$.

4. DATA FROM CYLINDRICAL EXPLOSIONS

The data base for cylindrical explosions is relatively small compared with the spherical base and the planar base to be discussed in the next sub-section. Data of reasonably long duration to relatively

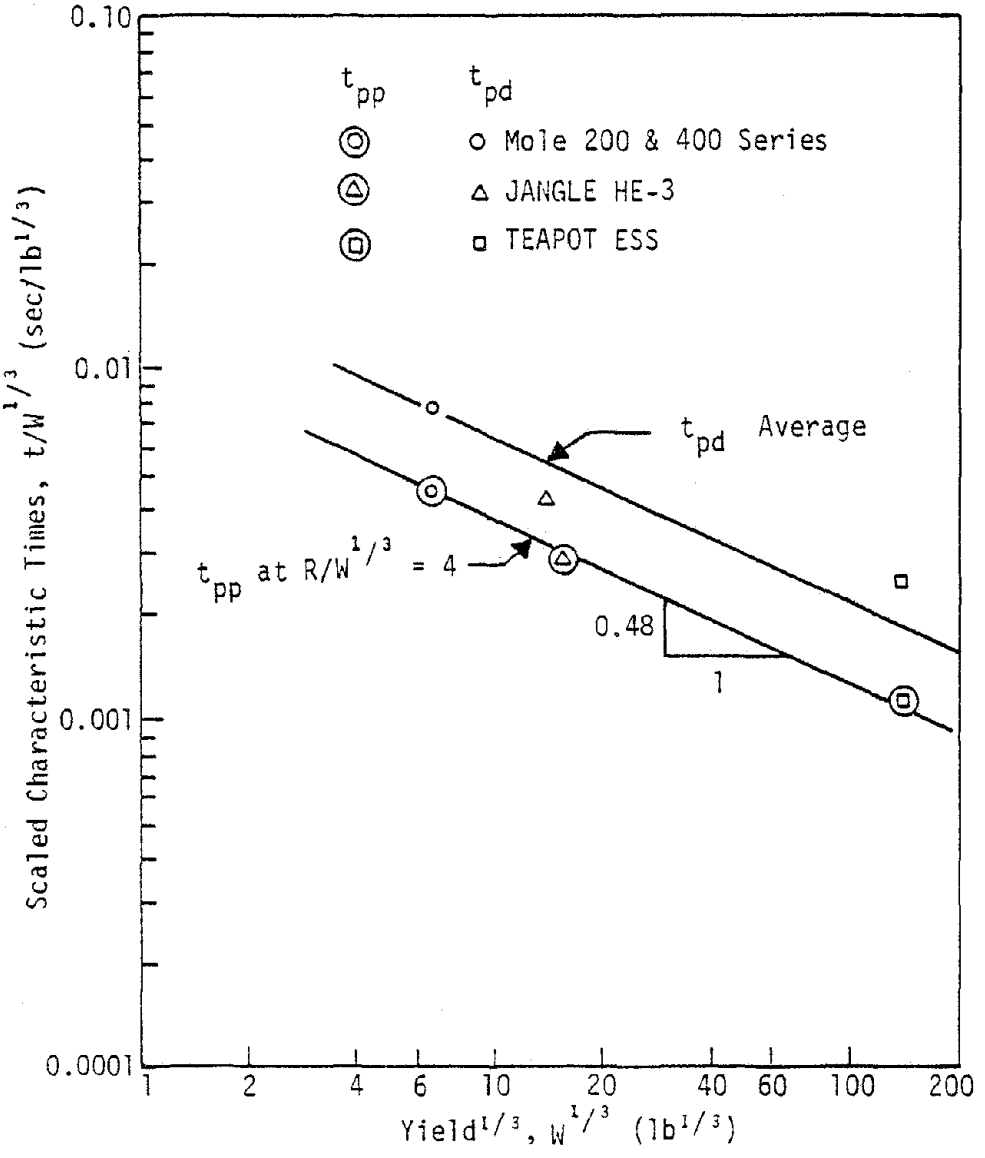

Figure IV-12. Variation of Characteristic Times with Yield in Dry Alluvium

distant ranges are available in dry granular soil only from the University of New Mexico DIHEST Enhancement Program (ref. IV-12). The cylindrical tests were designated Shots 6, 7, 8 and 12. Their pertinent characteristics were given previously in table II-13. Briefly, Shots 6 and 7 were decoupled shots in which PETN primacord was placed in a 3-foot diameter borehole at a loading density of 5 lbs per foot of hole. The PETN was distributed in the borehole for Shot 6, but concentrated on the centerline for Shot 7. Shot 8 used the same loading density but the explosive was placed in a 9-inch diameter borehole and then grouted. The length of explosive for all three shots was 12 feet and there was 6 feet of surcharge above the explosive. Shot 12 was primarily a yield variation on Shot 6. The loading density was 22.9 lbs/ft of PETN and the explosive was distributed in the borehole. However, the explosive length (13.3 feet), depth of surcharge (8 feet) and borehole diameter (4 feet) were not scaled from Shot 6 (lengths would have had to be scaled by $\gamma^{\frac{1}{2}}$ for a complete scaling comparison).

The scaled depths of burst for all events taken as point charges are greater than 0.5 ft/lb$^{\frac{1}{3}}$ (TNT) so that it appears that the depths of burst are sufficient for the shots to be considered deeply buried. Thus, it can be assumed that the unscaled surcharge heights are not important. However, in comparing Shots 6, 7 and 8 with 12, there remains some uncertainty in assessing scaling rules and deriving prediction relations due to unscaled explosive lengths and borehole diameters. These differences, on the other hand, may lead to insight regarding their effects.

Before proceeding with an analysis of the data, it is important to assess anticipated effects of finite borehole lengths. Scaling terms

for cylindrical geometry were derived earlier. It was shown that $\gamma^{\frac{1}{2}}$ scaling is appropriate (Equations IV-22 and IV-24)when the borehole extends infinitely in both directions, i.e., the geometry is completely cylindrical. In any field problem, however, the borehole will always have a finite length. The finite length will produce relief waves which originate at the ends of the borehole at the instant of detonation and propagate into the loaded region. Both the loading waves and the relief or unloading waves in elastic media are shown in figure IV-13. The major loading wave is a compression wave (P-wave) which causes motion away from the explosion and moves away from the borehole with velocity C_p. Along the length of the explosion it has a planar front in cross-section. At the instant of detonation, a compression wave and a shear wave are initiated at the ends of the explosion. In addition, a von Schmidt-like wave (a shear wave connected between the P-wave and S-wave fronts) is also expected to be initiated at the ends. In the region above and below the explosion these waves are loading waves, i.e., they are moving into unloaded material. In the region loaded by the incident P-wave, however, these waves are relief waves. Figure IV-13 shows that the direction of particle motion associated with the waves tends to bring the material back to its initial condition, i.e., the major direction of motion is inward.

At a point at the mid-depth of the explosive, the loading wave will arrive first and cause outward motion. At some later time, the P-relief waves (P') will arrive causing some inward motion (their vertical components will cancel at the mid-depth). The major inward motion will likely occur with the arrival of the SP-relief wave.

In inelastic soil media, the wave pattern will distort somewhat

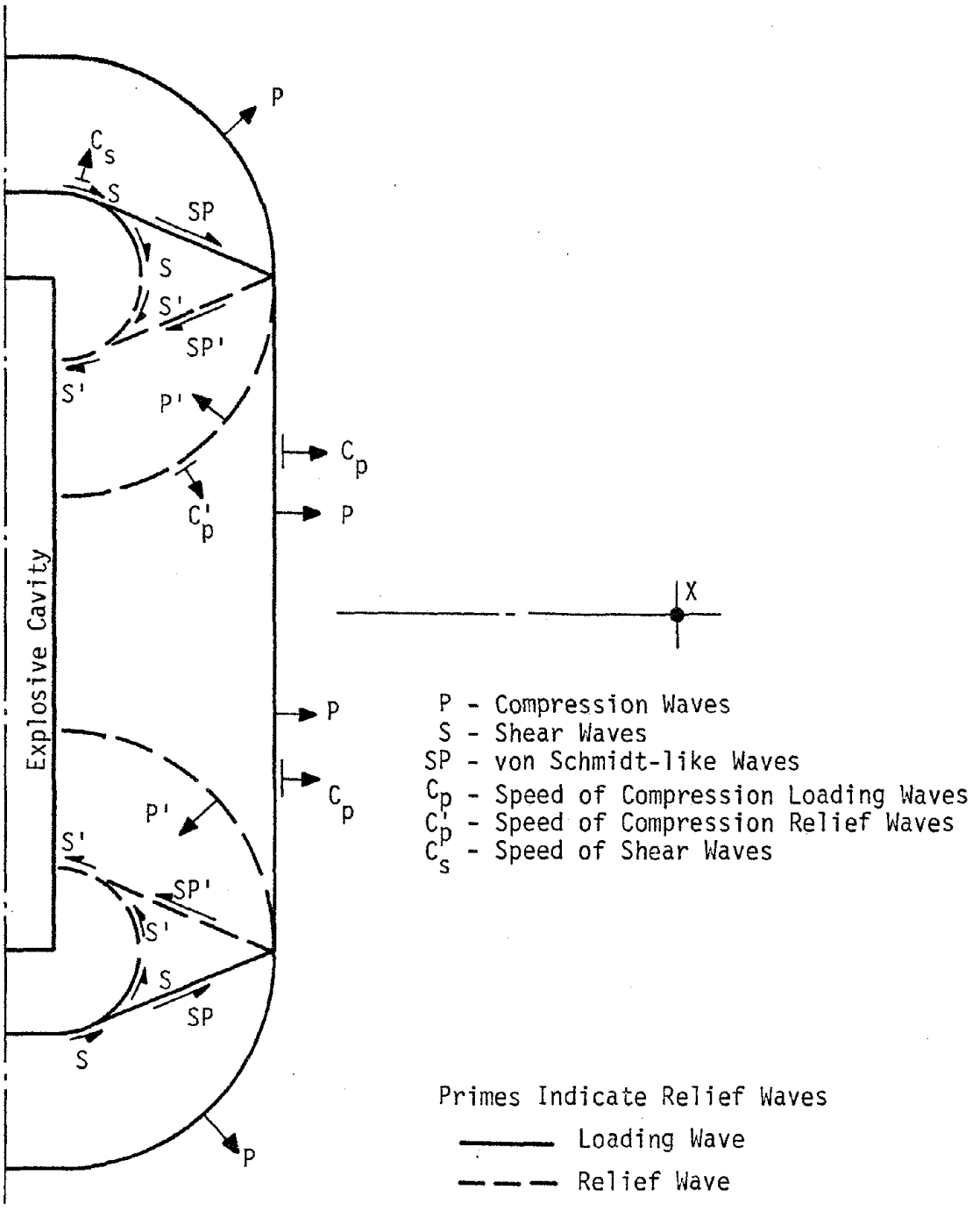

Figure IV-13. Major Wave Fronts From Cylindrical Explosion in Elastic Media

from that of figure IV-13, but the major loading and unloading waves will still exist. In general, the loading wave velocity of the incident P-wave (C_p) will be less than (1/2 to 3/4) that of the P-relief wave due to the inelastic behavior of soils. The P-relief wave velocity will be approximately the seismic velocity. The SP-wave will have a velocity which is controlled by the loading P-wave velocity and the S-wave velocity.

Using ray tracing and geometry, the arrival times of the various waves at a point X (see figure IV-13) at the mid-depth of the explosive are:

$$t_a^P = X/C_p \qquad \text{(IV-38)}$$

$$t_a^{P'} = \left(1/C_p'\right) \sqrt{(H/2)^2 + X^2} \qquad \text{(IV-39)}$$

$$t_a^{S'} = \left(1/C_s'\right) \sqrt{(H/2)^2 + X^2} \quad \text{for } X < (H/2)\sqrt{C_p^2/(C_p^2 - C_s'^2)} \qquad \text{(IV-40)}$$

$$t_a^{SP'} = \left(H/2C_s'\right)\sqrt{2C_p^2 - (C_s'^2 / C_p^2) - (C_s'^2)} + \left(1/C_p\right)\left(X - (H/2)\sqrt{C_p^2/(C_p^2 - C_s'^2)}\right)$$
$$\text{for } X > (H/2)\sqrt{C_p^2/(C_p^2 - C_s'^2)} \qquad \text{(IV-41)}$$

where

t_a^P = time of arrival of peak of loading wave

$t_s^{P'}$ = time of arrival of P-relief wave

$t_a^{S'}$ = time of arrival of S-relief wave

$t_a^{SP'}$ = time of arrival of SP-relief wave

X = range from explosion

C_p = P-loading wave velocity

C'_p = P-relief wave velocity

C'_s = S-relief wave velocity

H = height of explosive

The first relief effect will be due to the P-relief wave. Since it generally travels faster than the loading wave, it will overtake and begin to erode the peak (stress or velocity) beyond some range. Equations IV-38 and IV-39 can be solved simultaneously to determine the range to be

$$R' = (H/2)\sqrt{C_p^2/(C_p'^2 - C_p^2)} \qquad \text{(IV-42)}$$

Where R' = range at which the P-relief wave overtakes the P-loading wave. For a P-loading wave velocity of one-half the relief velocity, R' will be 0.71 H. For three-fourths the relief velocity, R' will be 0.91 H. Beyond R', the attenuation of the peak stress or velocity will approach spherical attenuation. The rate will probably not change instantaneously, but rather will begin to transition to a spherical condition.

Peak acceleration attenuation will be affected in a similar way. Since the peak acceleration occurs shortly before peak velocity, the beginning of the acceleration attenuation change will probably occur at about the same range as the velocity or stress change. However, since peak acceleration is much more sensitive to wave field changes, especially increases in rise time in the velocity time history which will be a major effect of relief, the transition to complete spherical attenuation will probably occur more rapidly.

Peak outward displacement changes will begin to occur at the range at which the peak velocity begins to be eroded by the P-relief wave but

major changes will not start until arrival of the S or SP-relief waves. Because of their low velocities, these waves will probably rarely overtake the peak of the P-loading wave. The major effect of S or SP-relief waves will be to reduce the outward phase duration of the velocity pulse, i.e. tend to pull the particles inward. The time of peak displacement (i.e. the outward phase duration of the velocity pulse) is related in a complex way to the size of the source (yield), Poisson's ratio and the failure behavior of the soil (see, for example, ref. IV-13). Hence, the range at which major S or SP-relief effects occur cannot be simply estimated. However, it is expected that the transition region for displacements will be larger than the transition region for accelerations or velocities.

These anticipated effects are illustrated qualitatively in figure IV-14. All kinematic parameters begin to transition at range R' which corresponds to the range at which the P-relief wave overtakes the P-loading wave. The peak acceleration quickly transitions to spherical attenuation while the peak particle velocities and displacements transition less rapidly. There is generally insufficient data to completely define the transition regions and the individual fits in cylindrical and spherical regions will be extended herein to a single intersection point which defines an effective transition range. These extensions are qualitatively illustrated in figure IV-14 by dashed lines.

All explosions will be influenced by the free-surface after some time which is dependent on their depth of burst. The major effect of the free-surface is expected to be a significant contribution of motion toward the free-surface. This will be particularly important for esti-

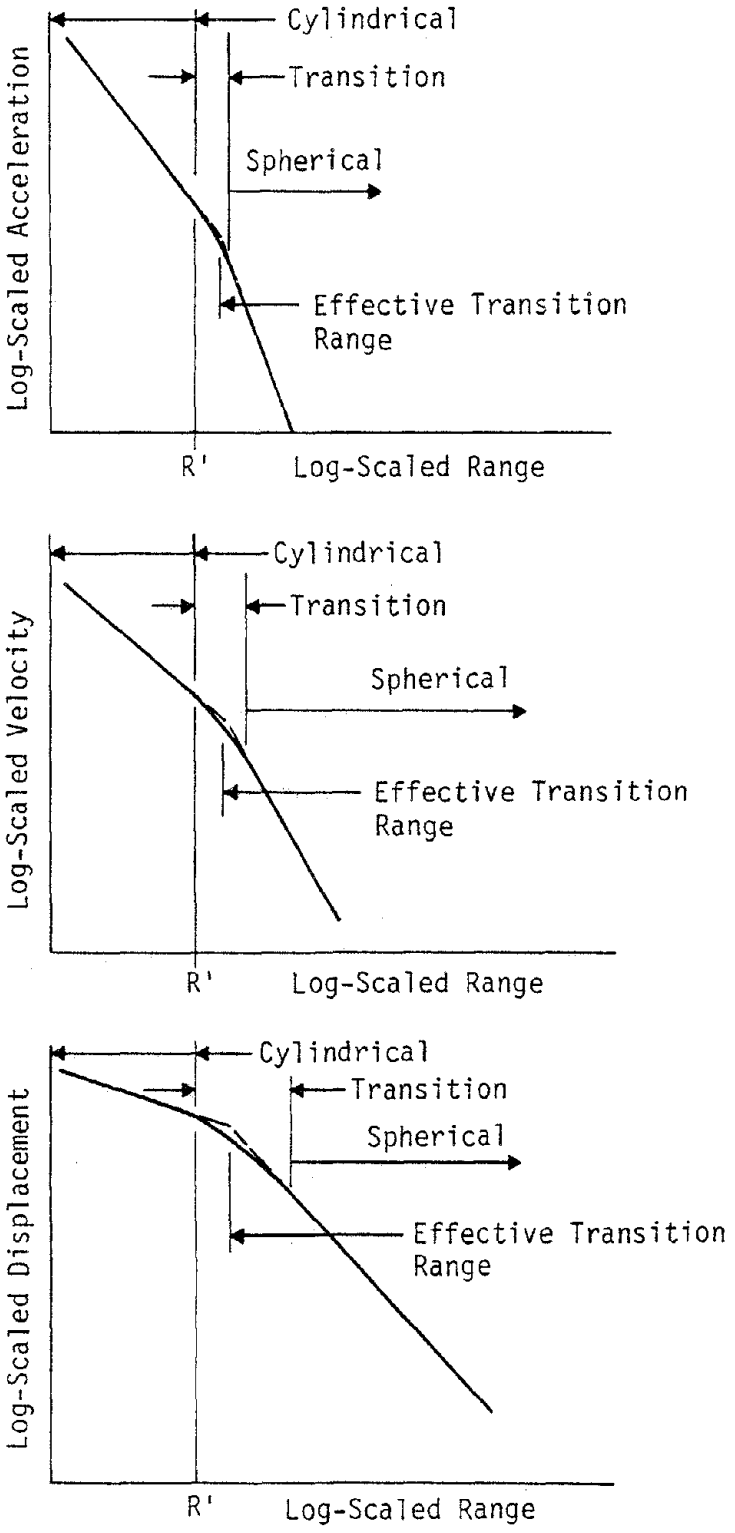

Figure IV-14. Effect of Finite Explosive Length on Peak Ground Shock Attenuation

mating vertical motion components in simulation experiments. The cylindrical experiments of interest here did not contain vertical measurements. Hence, the discussion of free-surface effects is postponed to the subsection dealing with planar arrays where vertical motion data is available for evaluation.

Radial velocity time histories from Shots 6, 7 and 8 were shown previously in figure II-24. Peak radial accelerations, velocities and displacements for these shots as well as Shot 12 are plotted in figures IV-15, IV-16 and IV-17. The data have been scaled by $\gamma^{\frac{1}{2}}$ where γ is the linear charge density. Although the Shot 12 data is sparse and contains significant scatter especially for displacements, the $\gamma^{\frac{1}{2}}$ scaling brings the Shot 12 data (22.9 lbs/ft PETN) into relatively good agreement with Shots 6, 7 and 8 (5 lbs/ft of PETN).

The acceleration data show an attenuation slope of -3.35 from the near region to a scaled range of about 5. This attenuation is comparable to a spherical decay slope (-3.3 for Mole). Hence, the acceleration data do not seem to indicate a cylindrical region. It may be that there is insufficient close-in data to clearly delineate the cylindrical region. The reduced attenuation rate of -2.2 beyond a scaled range of 5 is probably attributable to a transition to more elastic behavior. The particle velocity at scaled range of 5 is about 4 ft/sec.

The velocity data show an initial decay slope of -1.52 to a scaled range of about 3.5 and a decay slope averaging about -2.05 beyond this range. Shot 8 shows a somewhat steeper decay slope but it is not known whether this is data scatter or real and due to the fact that the Shot 8 explosive was grouted at the origin. In any case, the difference is not

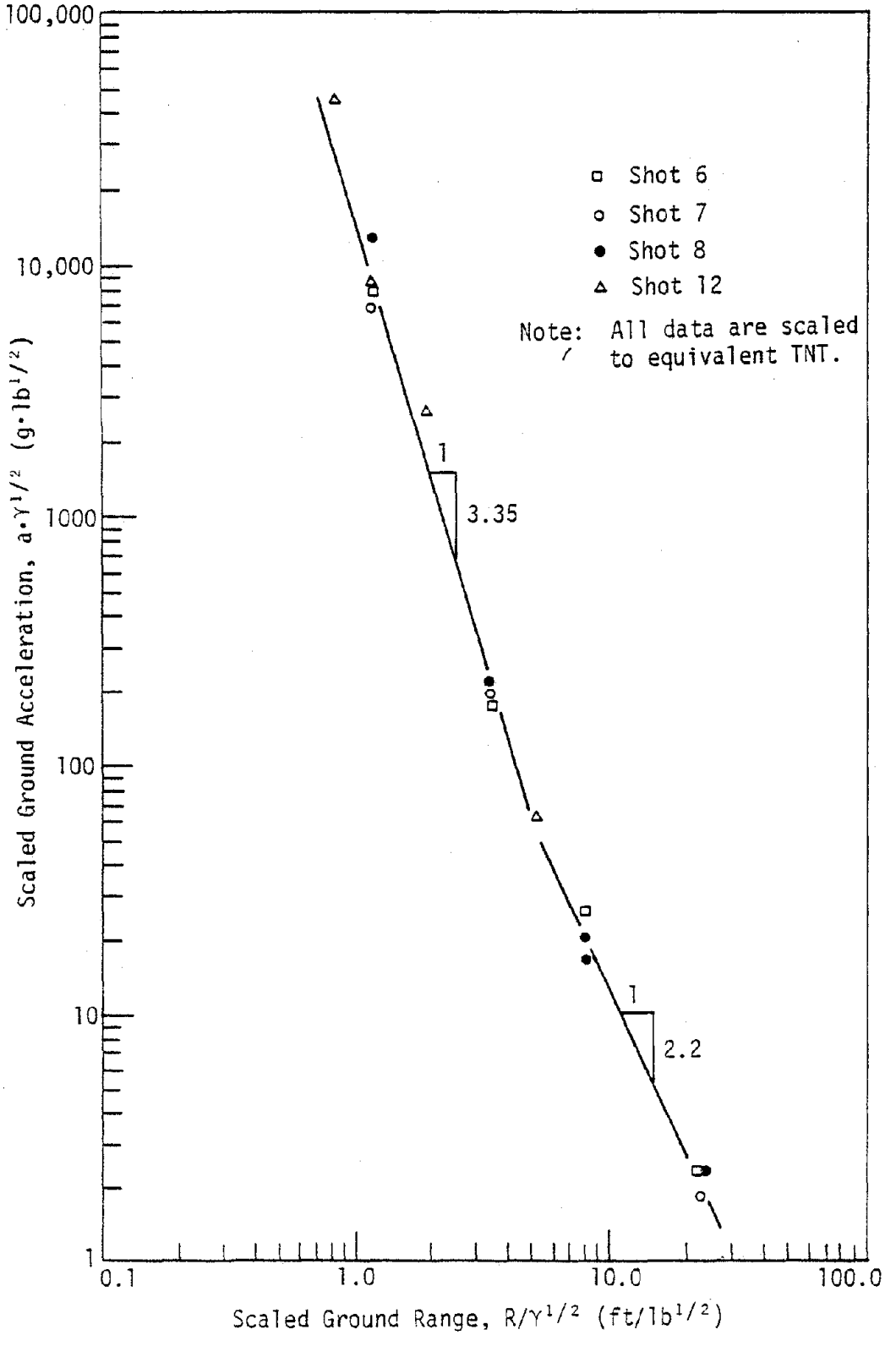

Figure IV-15. Radial Accelerations from Cylindrical Shots at McCormick Ranch

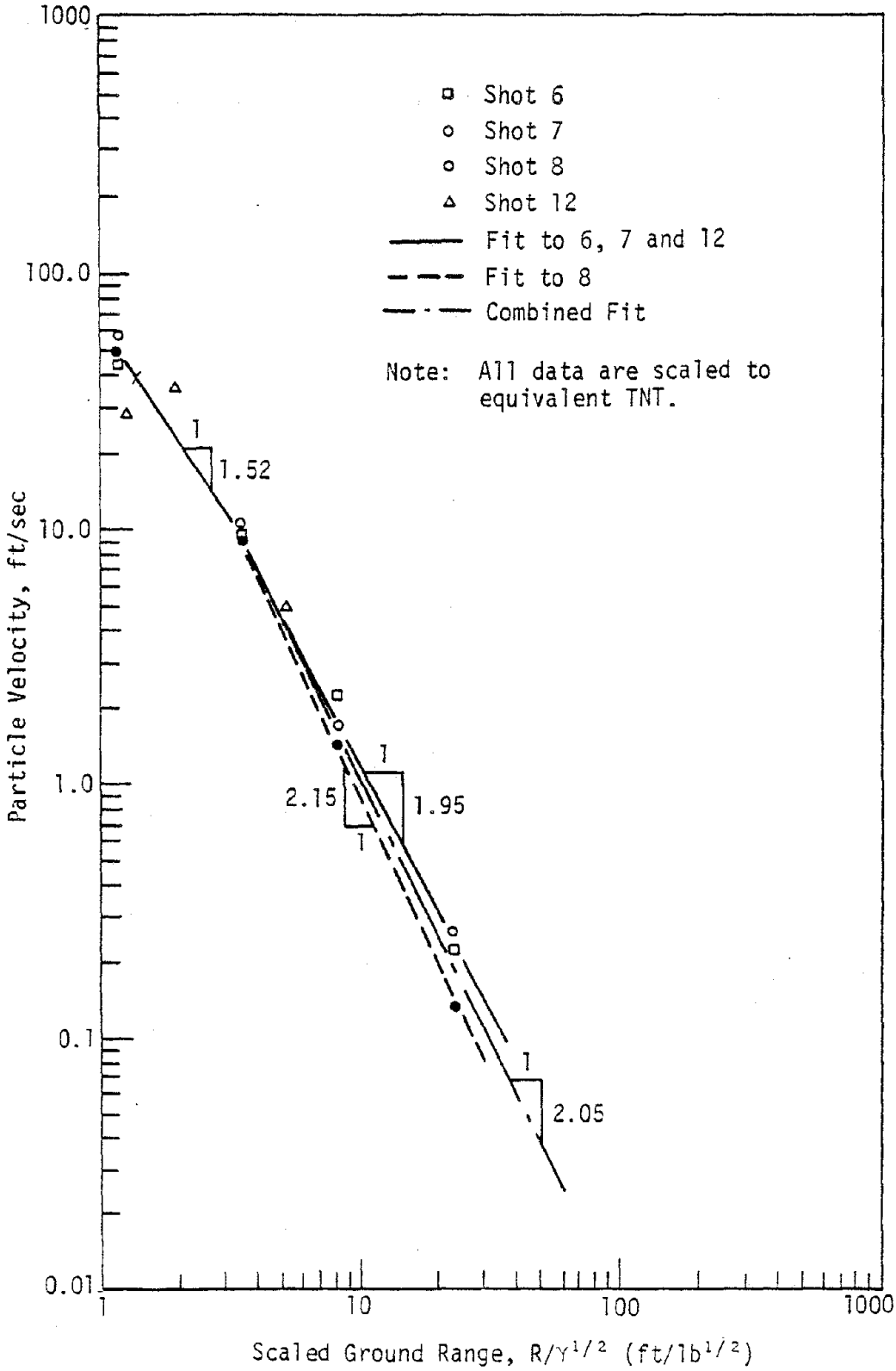

Figure IV-16. Radial Particle Velocities from Cylindrical Shots at McCormick Ranch

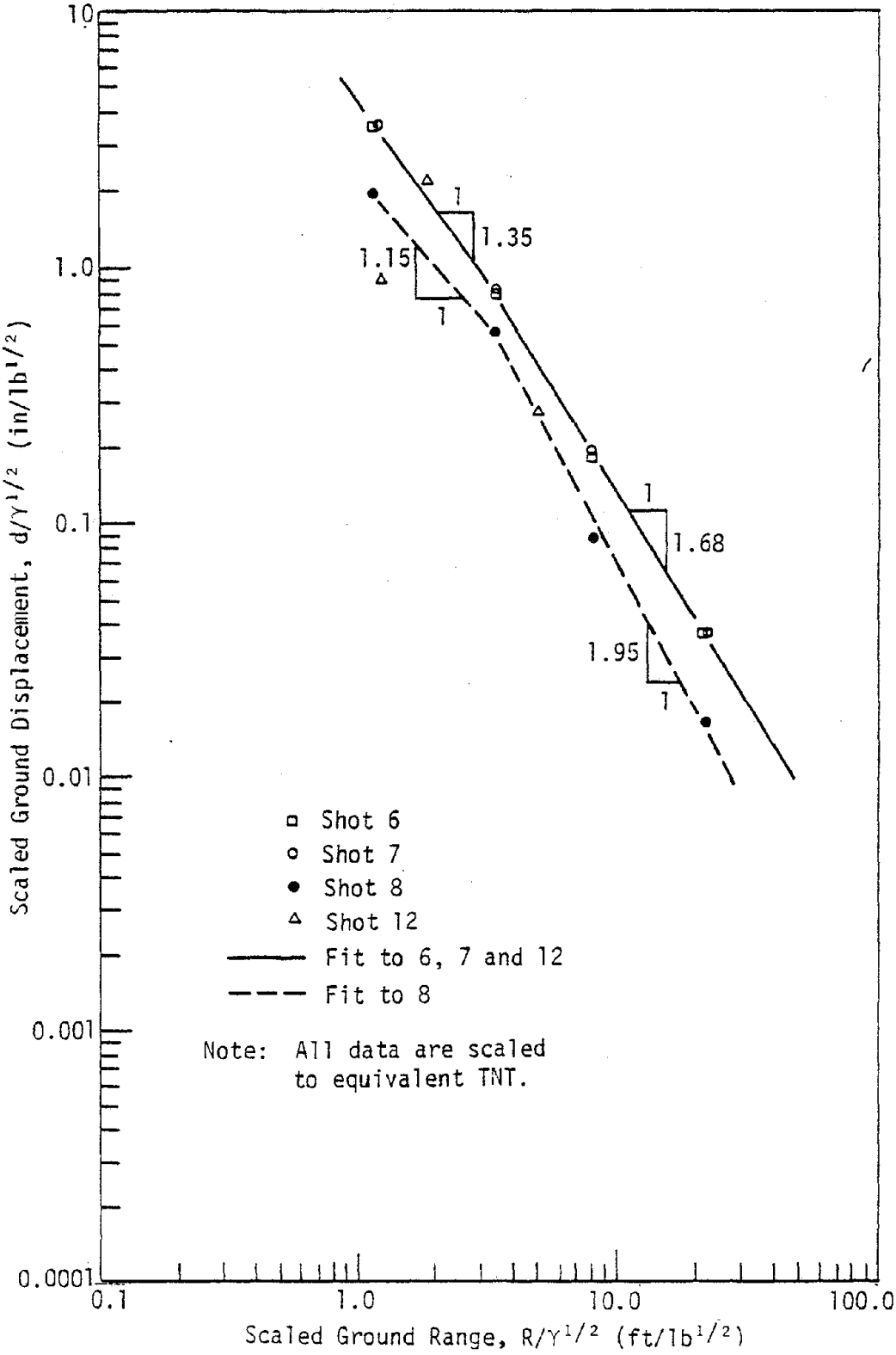

Figure IV-17. Radial Displacements from Cylindrical Shots at McCormick Ranch

major.

The break in slope at the 3.5 scaled range appears to be the effective transition from cylindrical to spherical attenuation. (Mole attenuates at -2.6.) The start of the transition was estimated earlier to be about 0.71 to 0.91 H, depending upon the ratio of the loading to the relief wave speed. These ranges correspond to scaled ranges of 3.3 to 4.2 for Shots 6, 7 and 8 which had an explosive height of 12 feet. The transition in the data agrees well with these estimates and corresponds to a transition range of 0.76 H. There are too few data from Shot 12 to draw any firm conclusions regarding Shot 12's transition. The $\gamma^{\frac{1}{2}}$ scaling does, however, bring the data of Shot 12 within the scatter of the other data.

The displacement data show a definite separation between the data of Shot 8 and those of Shots 6 and 7. Shot 8 displacements are on the order of 50 percent lower than Shots 6 and 7. This separation is apparently due to the method of coupling at the explosive source and indicates that grouted explosives lead to decreased displacements compared with decoupled explosives. Shots 6 and 7 cannot be distinguished within the scatter of the data. The method of explosive dispersal within a borehole, therefore, does not appear to be a significant parameter. The data of Shot 12 is significantly scattered and, therefore, cannot be used for firm conclusions. The $\gamma^{\frac{1}{2}}$ scaling does, however, bring Shot 12 into the vicinity of the other data.

The displacements attenuate initially with a slope of -1.15 to -1.35 to a scaled range of about 3.5. Beyond this range the attenuation becomes -1.68 to -1.95. These latter rates are somewhat lower than the spherical

attenuation rate of -2.4 for Mole. The transition range of 3.5 is about the same as for particle velocity. Actually, it is possible that the transition range for both velocity and displacement is at a nearer range, but this cannot be determined with the available data.

The following relations summarize the variation of peak acceleration, peak velocity and peak displacement with range for decoupled cylindrical shots at McCormick Ranch:

$$a \cdot \gamma^{\frac{1}{2}} = 13{,}700\left(R/\gamma^{\frac{1}{2}}\right)^{-3.4} \text{ for } R/\gamma^{\frac{1}{2}} < 5 \qquad \text{(a)}$$

$$a \cdot \gamma^{\frac{1}{2}} = 1{,}900\left(R/\gamma^{\frac{1}{2}}\right)^{-2.2} \text{ for } R/\gamma^{\frac{1}{2}} > 5 \qquad \text{(b)}$$

$$v = 62\left(R/\gamma^{\frac{1}{2}}\right)^{-1.5} \text{ for } R/\gamma^{\frac{1}{2}} < 0.75\ H/\gamma^{\frac{1}{2}} \qquad \text{(c)}$$

$$v = 53.7\left(H/\gamma^{\frac{1}{2}}\right)^{0.5}\left(R/\gamma^{\frac{1}{2}}\right)^{-2.0} \text{ for } R/\gamma^{\frac{1}{2}} > 0.75\ H/\gamma^{\frac{1}{2}} \qquad \text{(d)} \qquad \text{(IV-43)}$$

$$d/\gamma^{\frac{1}{2}} = 4.5\left(R/\gamma^{\frac{1}{2}}\right)^{-1.4} \text{ for } R/\gamma^{\frac{1}{2}} < 0.75\ H/\gamma^{\frac{1}{2}} \qquad \text{(e)}$$

$$d/\gamma^{\frac{1}{2}} = 4.25\left(R/\gamma^{\frac{1}{2}}\right)^{0.3}\left(R/\gamma^{\frac{1}{2}}\right)^{-1.7} \text{ for } R/\gamma^{\frac{1}{2}} > 0.75\ H/\gamma^{\frac{1}{2}} \qquad \text{(f)}$$

where

a = acceleration in g's

v = velocity in ft/sec

d = displacement in inches

R = range in feet

γ = lineal charge density in lbs/ft of TNT

H = height of charge in feet

The relationships for acceleration and velocity (Equations IV-43(a), (b), (c) and (d)) also apply to coupled charges but displacements for coupled charges will be about 50 percent lower.

Figure IV-18 shows an idealized velocity time history from a cylindrical explosion with selected characteristic times designated thereon. The characteristic times selected are the outward velocity phase, t_{pd}, the time from peak outward to peak inward velocity, t_{pp}, and the duration of the first motion cycle, t_T. Available data (see figure II-24) indicate that a second outward phase may occur, but there is insufficient data to define its occurrence and characteristics. However, it has been indicated by a dashed line.

The scaled characteristic times for Shots 6, 7, 8 and 12 are plotted as a function of scaled range in figure IV-19. The data from Shots 6 and 7 scatter together further reinforcing the conclusions from the peak data that the dispersal of explosive within the source cavity is unimportant. The data from both shots can, therefore, be treated as a single set.

The peak to peak times and the duration of the first motion cycle for Shots 6, 7 and 12 show no variation with range while the data from Shot 8 seem to increase markedly between scaled ranges of 3.5 to 8 and remain constant thereafter. It is not known whether this trend is related to the grouted coupling at the source or due to data uncertainties. For lack of a clear understanding of the cause, t_{pp} and t_T data with range for Shot 8 have been averaged to obtain mean characteristic times for comparison with Shots 6, 7 and Shot 12. The averages are shown in figure IV-19.

As described earlier in the discussion of qualitative effects of finite explosive length, the explosive height is expected to play an important role in both attenuation of peaks and in waveforms. The S

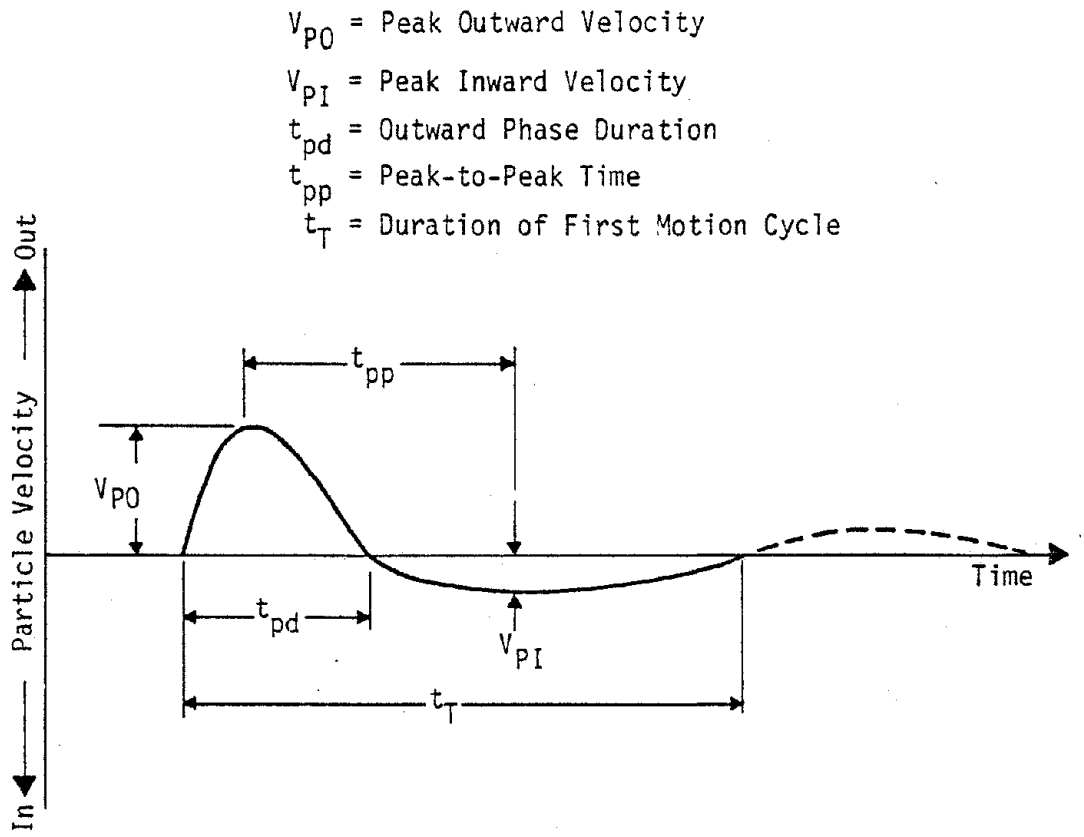

Figure IV-18. Idealized Particle Velocity Time History from Cylindrical or Planar Explosion of Finite Dimensions

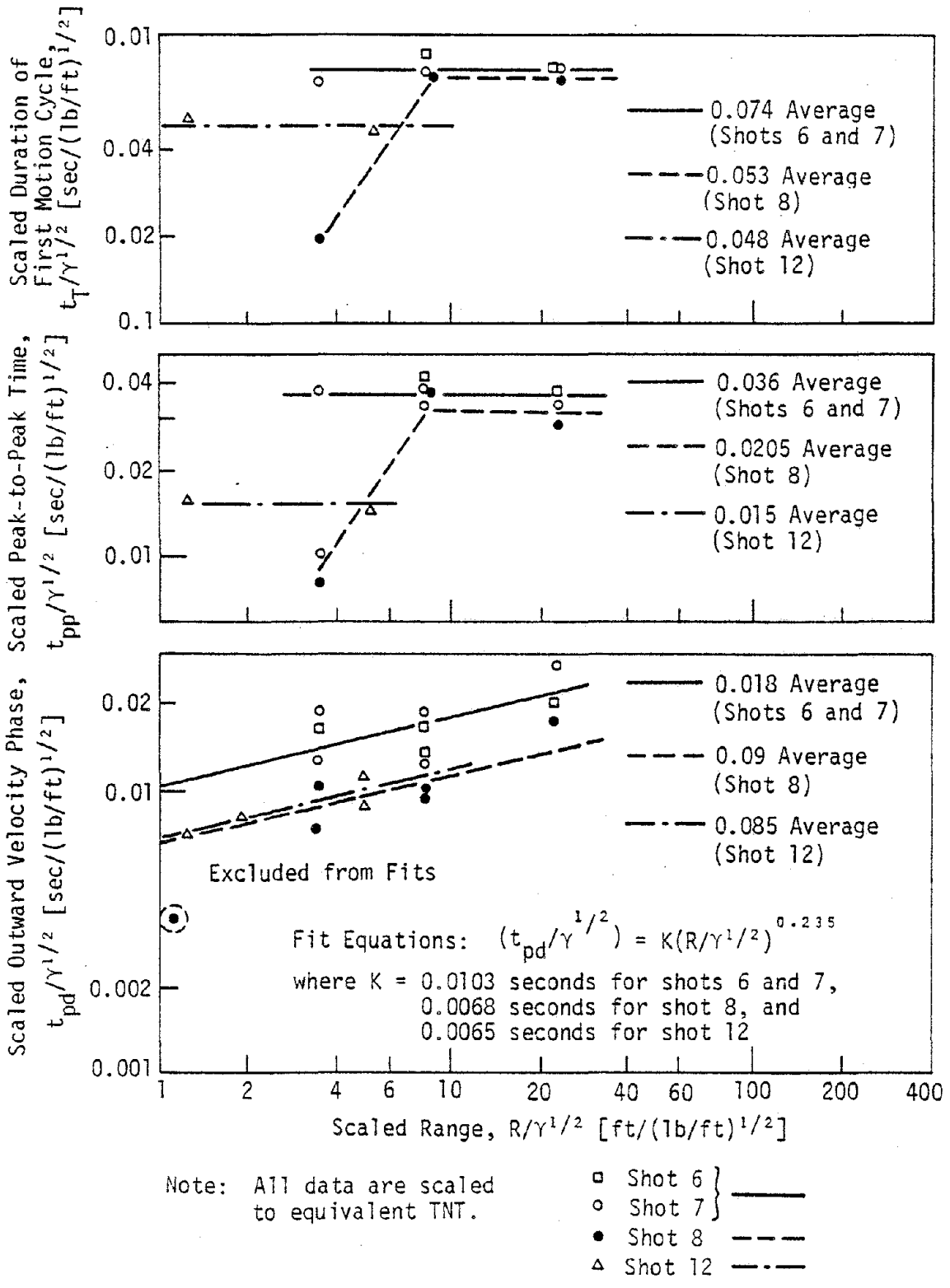

Figure IV-19. Scaled Characteristic Times Versus Scaled Range for Cylindrical Charges

or SP-relief arrivals, for example, are expected to cause a significant reversal in the outward velocity. It seems necessary then to include both the amplitude of the source (reflected in γ) and the source height (H) in scaling characteristic times. An appropriate scaling term including H is $H/\gamma^{\frac{1}{2}}$. (This term has already been used in equation IV-43.)

The average values for t_{pp} and t_T and the value of t_{pd} at a scaled range of $R/\gamma^{\frac{1}{2}} = 1$ are plotted versus $H/\gamma^{\frac{1}{2}}$ for the various shots in figure IV-20. The data show a clear trend of increasing characteristic time with increasing explosive height. Straight-line fits have been made to the data of Shots 6 and 7 and Shot 12, but these fits are highly uncertain due to the few data points. The Shot 8 data has not been included in the fits due to the source difference of Shot 8. As noted previously, grouting of the explosive at the source seems to decrease characteristic times.

An important part of the cylindrical velocity waveform is the amplitude of the peak inward velocity, V_{PI}. Figure IV-21 plots the ratio of the peak inward velocity to the peak outward velocity versus range scaled by the explosive height. The data contain significant scatter, but show a definite trend toward increasing relative magnitude of the inward component with increasing range. A linear fit to the data is

$$\frac{V_{PI}}{V_{PO}} = 0.10 + 0.112\ (R/H) \qquad \text{(IV-44)}$$

where

V_{PI} = peak inward velocity

V_{PO} = peak outward velocity

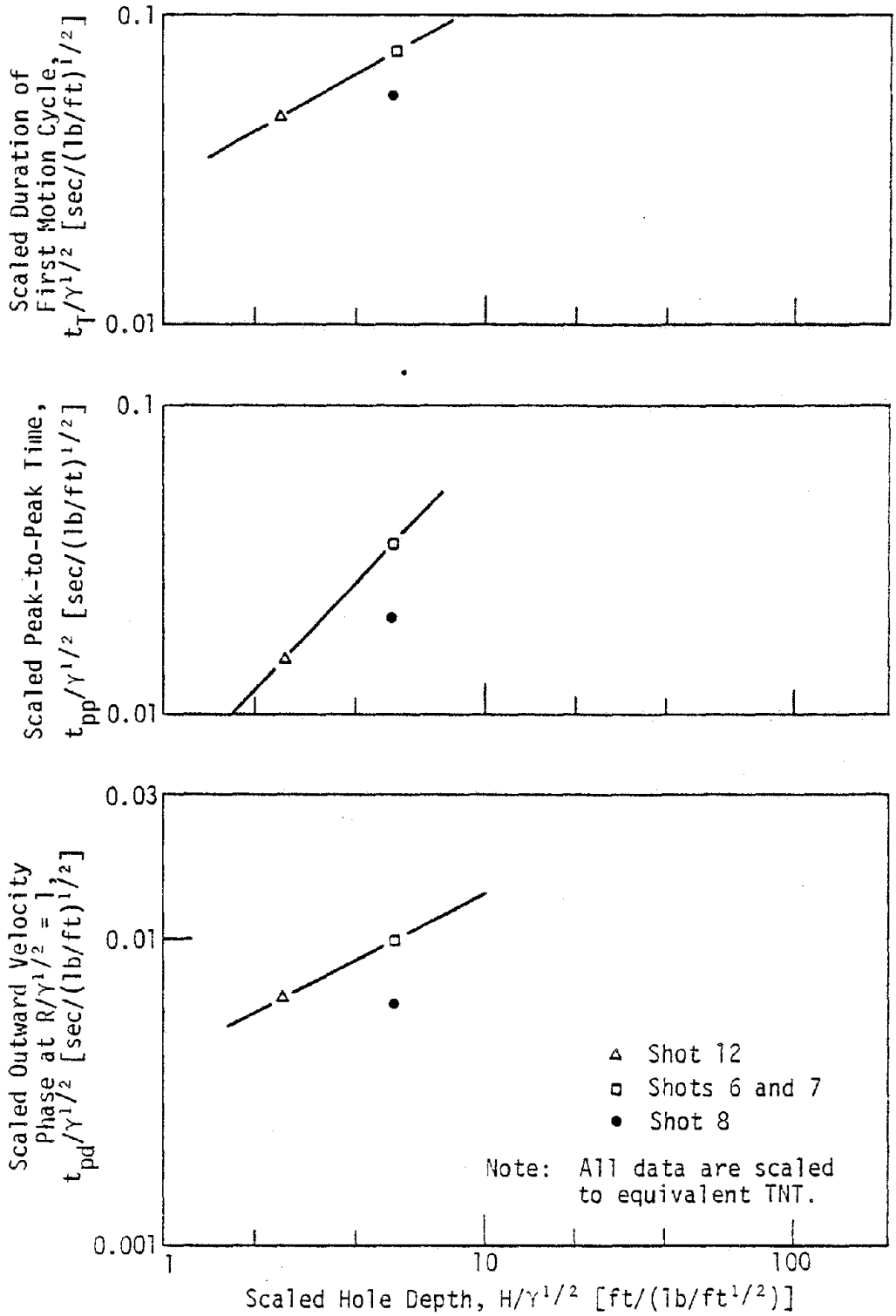

Figure IV-20. Scaled Characteristic Times Versus Scaled Explosive Height for Cylindrical Charges

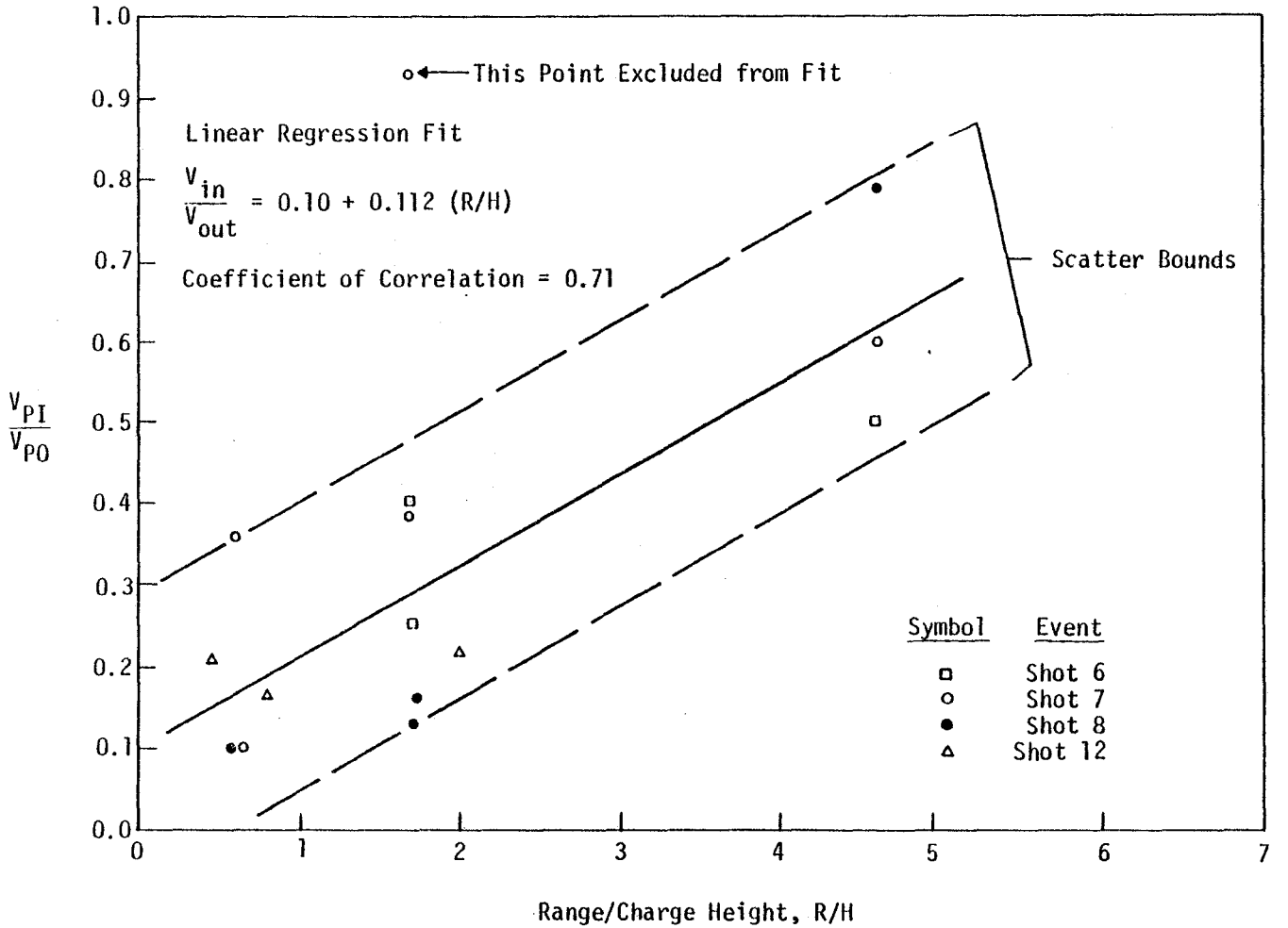

Figure IV-21. Ratio of Peak Inward Velocity to Peak Outward Velocity as Function of Scaled Range for Cylindrical Data

R = range

H = explosive height

The correlations for peak amplitudes, characteristic times and the ratio of peak inward to peak outward velocity which have been presented can be combined with the idealized waveform of figure IV-18 to construct waveform predictions for the first motion cycle from cylindrical explosions in dry granular media. The later parts of the waveform are uncertain due to a sparsity of data. Some data indicate a second outward pulse which is shown dashed in figure IV-18. Its definition is uncertain but, roughly, its amplitude is about one-half the peak inward velocity of the first cycle and its duration is about the same as the inward phase duration of the first cycle.

The rise time to the peak outward velocity increases with range in soils. This increase in rise time is a major contributor to acceleration attenuation. The rise time as a function of range can be estimated approximately by (ref. IV-10).

$$\Delta t_r \simeq \frac{1}{3}\frac{R}{C_i} \text{ to } \frac{R}{C_i} \qquad \text{(IV-45)}$$

where

Δt_r = rise time to peak velocity

R = range

C_i = seismic velocity

5. DATA FROM PLANAR EXPLOSIONS

A relatively large base of data in dry granular soil exists from seven (7) experiments conducted at The University of New Mexico's

McCormick Ranch Test Site. The experiment characteristics are given in table IV-2. Table IV-3 presents some characteristics of the experiments scaled by the areal loading density, α.

The Mini-SIMQUAKE experiment contained two arrays fired with a time delay. The measured ground motion from the back array (fired first) is unambiguous planar array data prior to arrival of the pulse from the front array. Upon arrival of the front array pulse, the motions result from the superposition of effects from the two arrays. However, the amplitudes of the back array effects are relatively small at the time of the second pulse arrival and, therefore, the front array (second pulse) effects are assumed to be independent planar array effects in later analyses. Two additional planar experiments, SIMQUAKE IA and SIMQUAKE IB, were recently performed at McCormick Ranch, but the data from these events have not been sufficiently reduced for use in this analysis.

As with cylindrical charges, it is important to anticipate the phenomenological effects which would be expected to occur in planar experiments due to finite charge extent. The appropriate scaling parameter for planar charges is the areal charge density, α, where the charge extends infinitely in both directions. However, the finite extent of planar charges leads to waves which propagate from the boundaries of the charge. The conditions are similar to those shown in figure IV-13 and explained for a cylindrical charge. The waves initiated at the boundary are loading waves in the region above and below the charge and relief waves in the region loaded directly by the charge. There are two sets of boundary waves in the planar case, however. One set from the top and bottom of the array and a second set from the ends of the array. Usually, the array

Table IV-2

Characteristics of Planar Events

Geometry				Explosive					
Event	Length (ft)	Height (ft)	Surcharge (ft)	Type	Total Weight (lbs)	Equivalent TNT Weight* (lbs)	Placement	Areal Charge Density, α(lbs/ft^2 TNT)	Reference
DEP[1] SHOT 1	12	4	4	PETN	48	64.3	Continuous	1.34	IV-12
DEP SHOT 3	20	6.7	6	PETN	133	178	16 holes	1.34	IV-12
DEP SHOT 9A	40	13.3	8	PETN	2133	2858	11 holes	5.37	IV-12
DEP SHOT 13	40	13.3	8	PETN	533	714	11 holes	1.34	IV-12
DIP IIA[2]	208	35	30	AN SLURRY	80,000	110,000	29 holes	15.11	IV-14
DIP VA	1136	204	60	AN SLURRY	72,000	99,300	16 holes	0.43	IV-8
MSQ[3]-BACK ARRAY	40	15	5	PETN	347	465	12 holes	0.78	IV-15
MSQ-FRONT ARRAY	40	15	5	PETN	232	174	16 holes	0.29 (0.52 design)‡	IV-15

1. DIHEST Enhancement Program
2. DIHEST Improvement Program
3. MINI-SIMQUAKE

*1 lb PETN = 1.34 lbs TNT
1 lb AN Slurry = 1.38 lbs TNT
See appendix A

‡Some holes failed to fire

Table IV-3

Some Scaled Characteristics of Planar Events

Event	α (lbs/ft^2 TNT)	$\frac{H}{\alpha}$	$\frac{L}{\alpha}$	$\frac{S}{\alpha}$	$\gamma = \alpha H$ (lbs/ft^2 TNT)	$\frac{S}{\gamma^{1/2}}$	$\frac{L}{H}$
DEP SHOT 1	1.34	3.0	9.0	3.0	5.36	1.73	3
DEP SHOT 3	1.34	5.0	14.9	4.5	9.0	2.0	3
DEP SHOT 9A	5.37	2.5	7.5	1.5	71.4	0.95	3
DEP SHOT 13	1.34	9.9	29.8	6.0	17.8	1.90	3
DIP IIA	15.11	2.3	13.8	2.0	529	1.30	6
DIP VA	0.43	474	2642	140	88	6.40	5.6
MSQ-BACK	0.78	19.2	51.3	6.4	11.7	1.46	2.7
MSQ-FRONT ARRAY	0.29	51.7	137.9	17.2	4.4	2.38	2.7

length is several times the array height and the waves from the top and bottom of the array are the first to provide relief, with the waves from the ends arriving some time later. Along the centerline, perpendicular to the array, attenuation of peak motion parameters is expected to occur as shown in figure IV-22. At ranges near the array, the relief effects do not affect peak parameters and the attenuation is planar and due only to inelastic effects. Beyond some range, which can be estimated by the methods described for cylindrical charges, relief waves from the array top and bottom begin to overtake the loading waves and cause the attenuation rates to approach cylindrical conditions. Finally, at some greater range, relief waves from the ends of the array overtake the loading waves and a transition to spherical attenuation might be expected. As for the cylindrical case discussed earlier, the transition regions for the parameters of acceleration, velocity and displacement are expected to be different with the accelerations transitioning over a short range, the displacements over a longer range and the velocities somewhere in between.

Most engineering systems for which ground motion simulation is required are located at or near the ground surface. Explosive arrays, due to the need for enhanced coupling, will be buried. The loading phenomena in the near-surface region is, therefore, very important. In the previous discussion of cylindrical explosions, it was noted that the loading waves above the explosive consist of an incident P-wave, S-wave, and a von Schmidt-like wave which is linked between the P- and S-waves. Upon encountering the free-surface, these waves will reflect and cause some changes in amplitudes near the surface compared with amplitudes near the center of the array, especially for vertical motions.

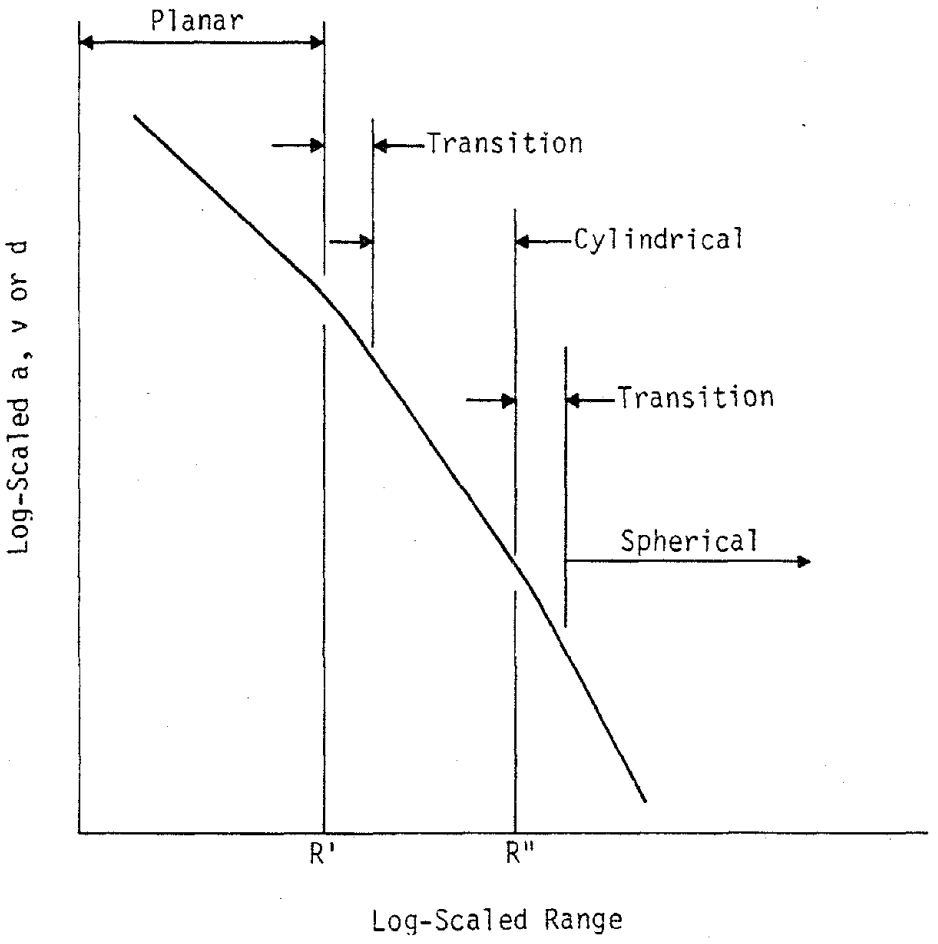

Figure IV-22. Effect of Finite Array Dimensions on Peak Ground Shock Attenuation

The incident waves and their free-surface reflections are shown in figure IV-23. The arrows on the wave fronts indicate the direction of motion associated with each wave upon its arrival. The major outward horizontal motion may not be contained within the incident P-wave only, but is thought to be spread between the incident P-wave and the incident SP-wave. A small vertical component is associated with the incident P-wave, but the major vertical motions may not occur until later. The SP-wave and S-wave from the base of the array will contribute upward motion while the S-wave from the array top will contribute downward motion. The directions of motion associated with the waves reflected at the free-surface indicate enhancement of the vertical component of motion, but a lesser effect upon the horizontal components. The free-surface reflections causing upward motion will ultimately penetrate into the deeper materials and give an upward component of motion to the entire field, including the centerline at the mid-depth of the array which, because of symmetry, would have no vertical motion in the absence of a free-surface. Although the phenomena described are difficult to assess, some understanding of the phenomena, the directions of motion associated with the wave fronts and estimates of the arrival times of the various waves can aid in interpreting the measured data.

Peak horizontal accelerations, velocities and displacements measured on planar events are shown in figures IV-24, IV-25 and IV-26. For Mini-SIMQUAKE, the motions at arrival of the front array pulse result from a superposition of back and front array effects. It is possible to estimate the incremental effects of the acceleration and velocity from the records, but this is not possible for the front array displacements. Hence, front array displacements are not plotted. All data have been scaled appropriately by the areal charge density, α (Eqs. IV-24). The different explo-

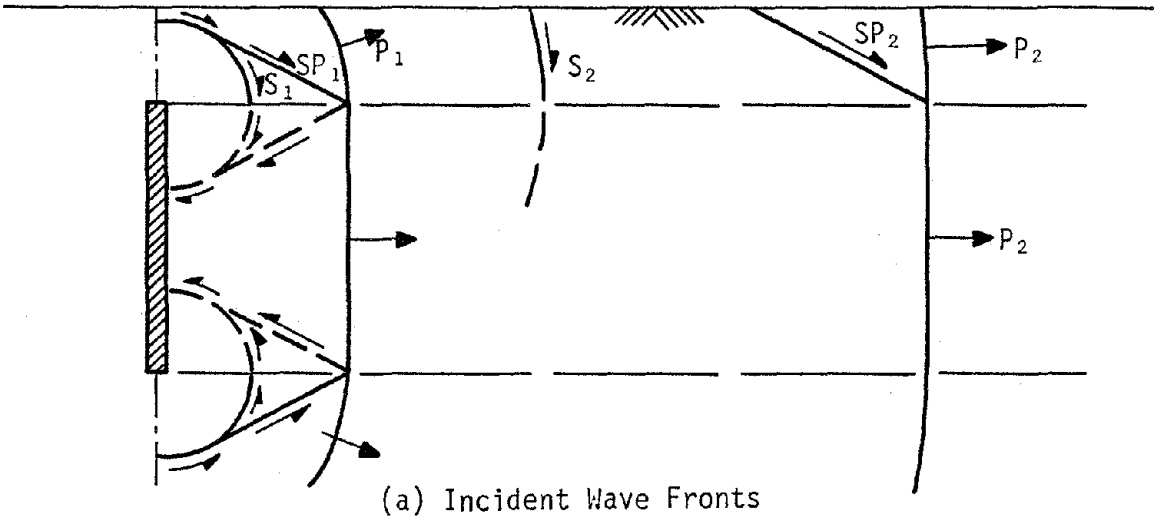

(a) Incident Wave Fronts

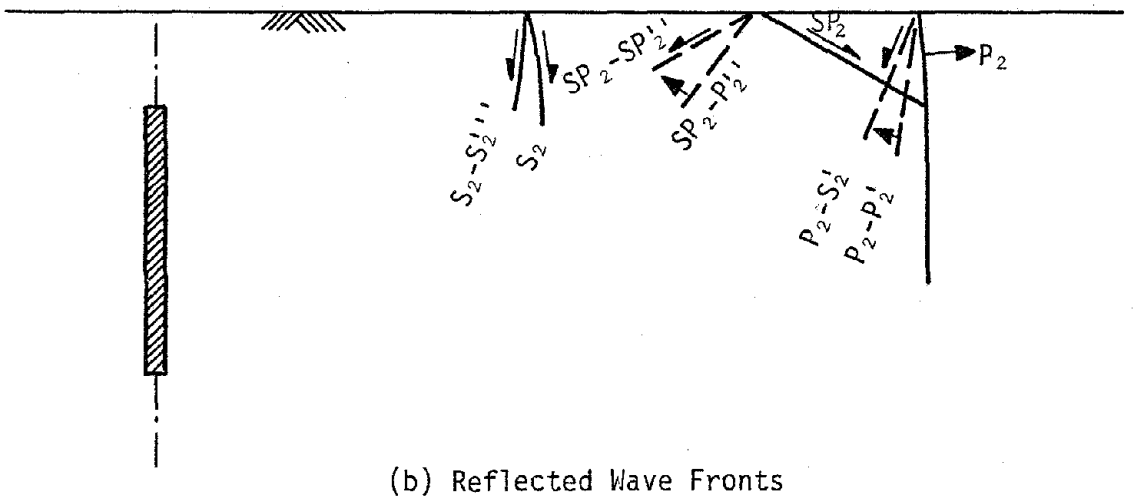

(b) Reflected Wave Fronts

Notation: Subscripts 1 and 2 refer to two different times

P - Incident P-Wave
S - Incident S-Wave
SP - Incident von Schmidt-like Wave
P-P' - Reflected P Due to Incident P
P-S' - Reflected S Due to Incident P
SP-P'' - Reflected P Due to Incident SP
SP-SP'' - Reflected SP Due to Incident SP
S-S''' - Reflected S Due to Incident S

Figure IV-23. Incident and Reflected Wave Fronts Near Surface

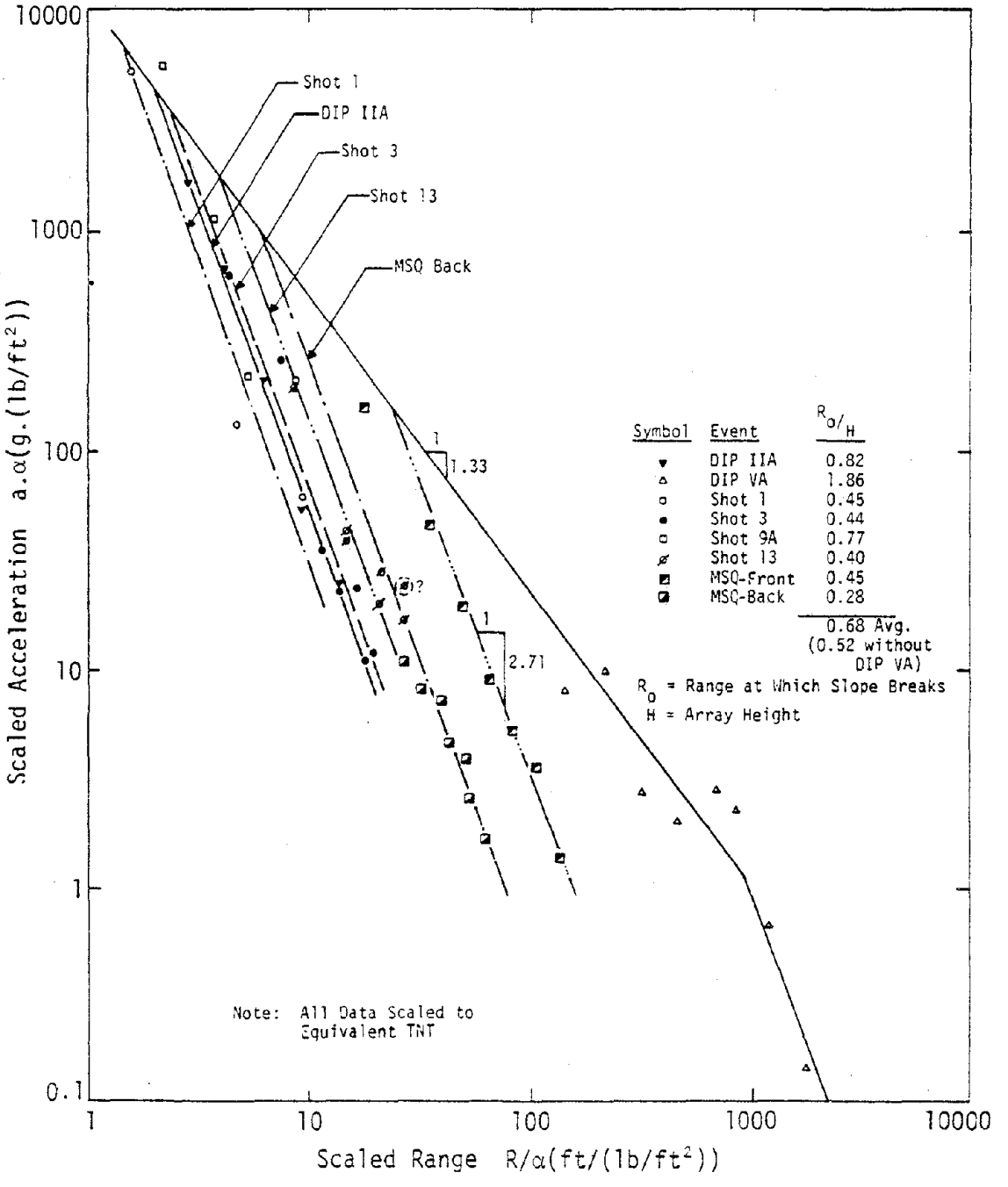

Figure IV-24. Peak Horizontal Acceleration Versus Range on the Centerline of Planar Events

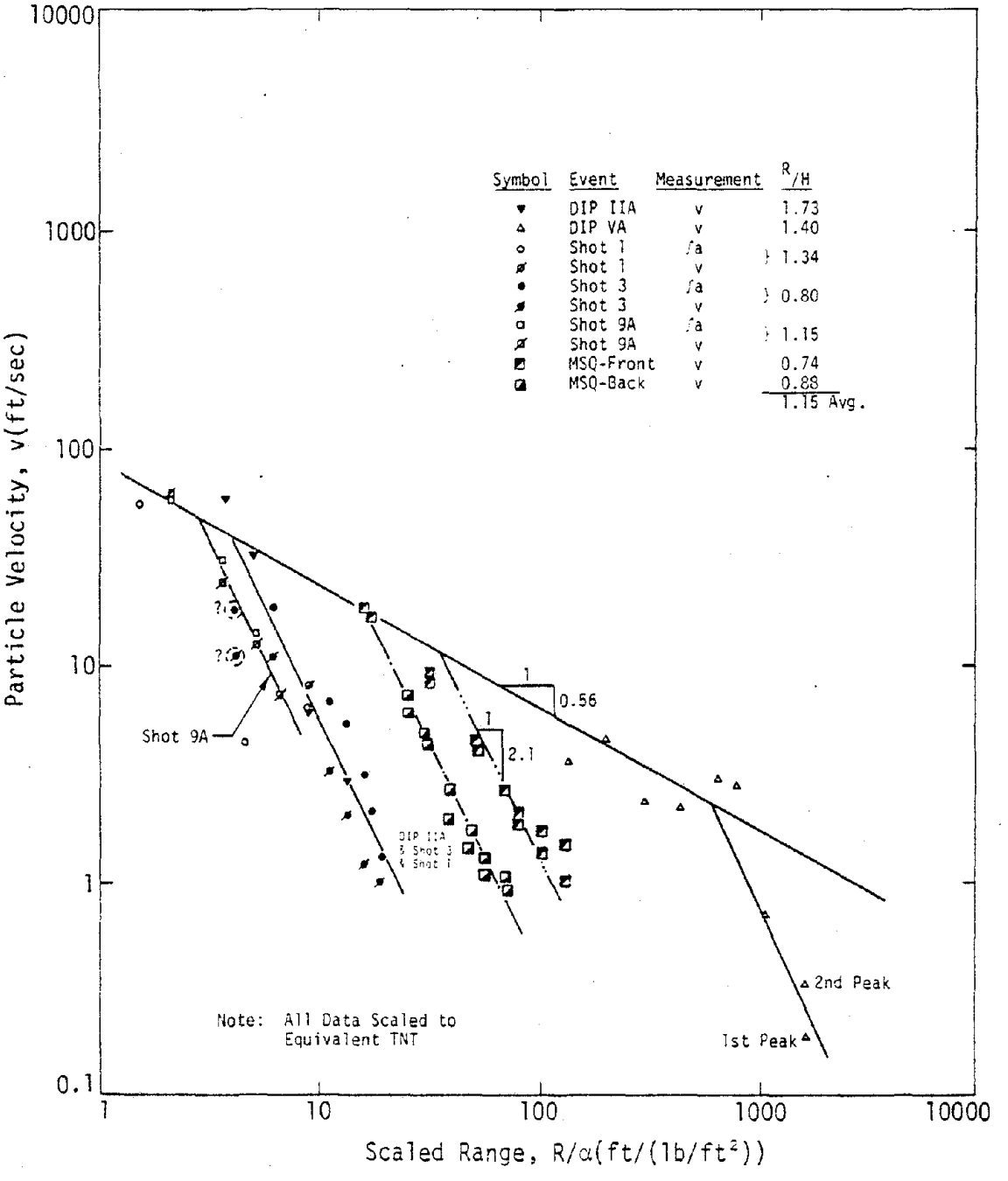

Figure IV-25. Peak Horizontal Velocity Versus Range on the Centerline of Planar Events

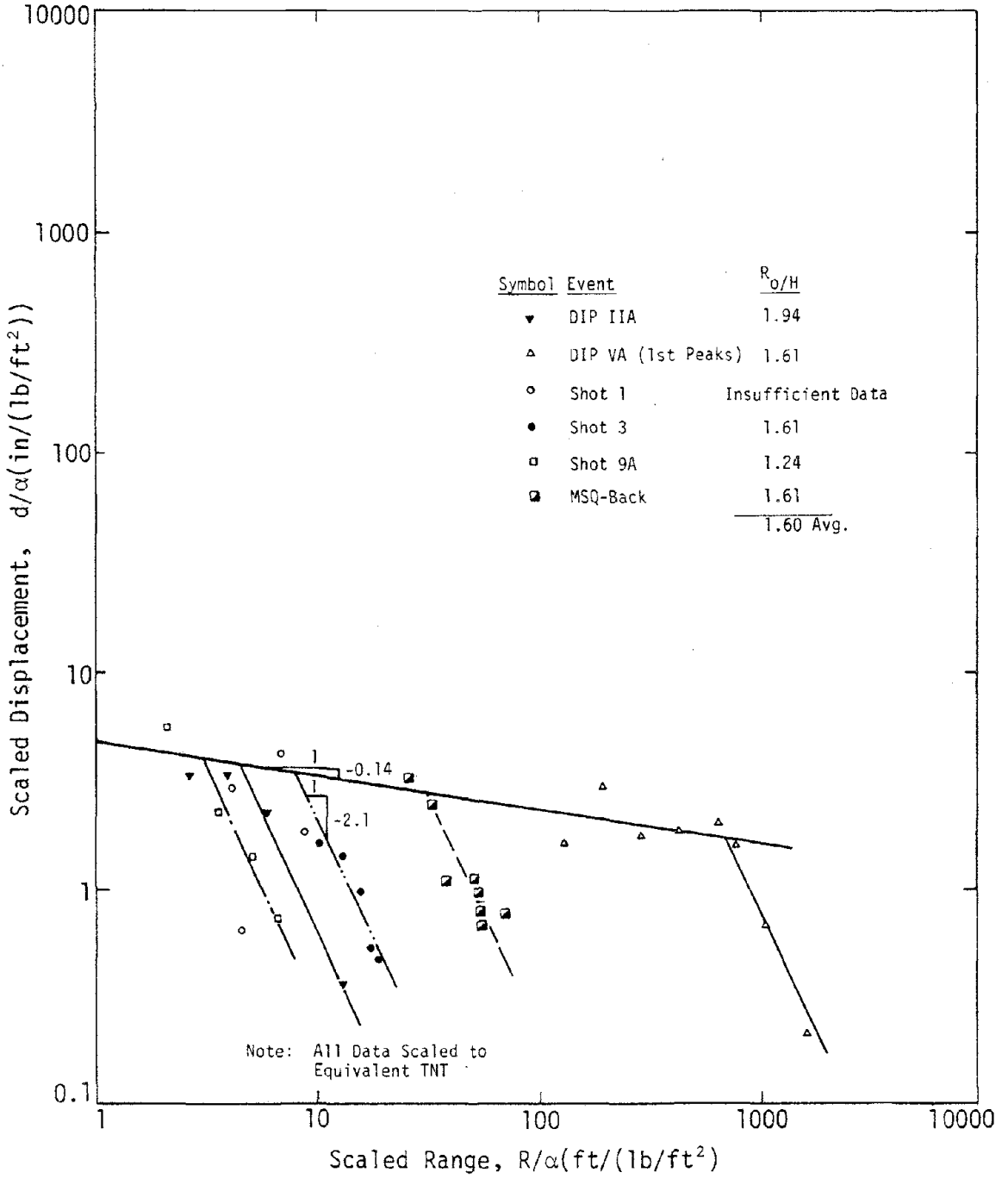

Figure IV-26. Peak Displacement Versus Range on the Centerline of Planar Events

sives in the various events have all been equated to TNT using the equivalency factors of Appendix A.

The acceleration measurements on DIP IIA were of poor quality and there were no accelerations measured on DIP VA. Accelerations for these events were estimated from the peak particle velocity and the rise time to peak particle velocity by the relation

$$a_{max} = K \frac{v_{max}}{\Delta t_r} \qquad \text{(IV-46)}$$

where

a_{max} = maximum acceleration

v_{max} = maximum particle velocity

Δt_r = rise time to peak particle velocity

K = a constant, usually taken equal to 2

Equation IV-46 is an empirical relation from reference IV-10. A value of 2 for K corresponds to the assumption of a parabolic rise to peak velocity.

Equation IV-46 is compared with measured accelerations on cylindrical Shots 6, 7, 8 and 12, where good acceleration measurements were available, in table IV-4. With the exception of the high acceleration levels near the explosions and a few other data, equation IV-46 using a K value of 2 gives results within 15 percent of the measurements. Since data scatter in a well instrumented experiment is commonly a factor of 2 and often a factor of 4, equation IV-46 is considered satisfactory for estimating accelerations where measurements are not available.

The acceleration data of figure IV-24 are all fit very well with an attenuation slope of -2.71. The fact that the fit lines are in different

Table IV-4

Comparison of Measured Peak Accelerations with Accelerations Estimated by Equation IV-46

	Range (ft)	A Measured	A Estimated	% Difference	K
Shot 6	3	3000	1732	-42	3.41
	9	67	73	+ 9	1.84
	21	10	9.3	- 7	2.15
	59	0.9	0.97	+ 8	1.86
Shot 7	3	2600	2252	-13	2.31
	9	74	81	+ 9	1.83
	21	6.3	5.8	- 8	2.17
	59	0.7	0.6	-14	2.33
Shot 8	3	4000	2019	-50	3.96
	9	85	74	-13	2.30
	21	7.8	7.4	- 5	2.11
	59	0.9	1.27	+41	1.42
Shot 12	7	1200	1863	+55	1.29
	10.5	400	310	-23	2.58
	28	13	12.4	- 5	2.10

Avg. k 2.24

Avg. K excluding close-in measurement 2.06
Avg. K for close-in measurements 2.74

positions reflects the fact that the scaled array height was different from event to event, i.e., the scaled transition range varied from event to event. The attenuation rate of -2.71 apparently reflects cylindrical attenuation after relief waves from the top and bottom of the array have overtaken the P-loading wave. The cylindrical and spherical data showed spherical attenuation rates of -3.3 to -3.4. The -2.71 rate, therefore, is consistent with what might be expected cylindrically. Unfortunately, there is little data on most of the events in the planar region. Only DIP VA contains what appears to be planar data and these data, along with the very close-in data of Shot 1 and Shot 9A, have defined the estimate of planar behavior shown with an attenuation slope of -1.33. Given this planar fit, the transition ranges were derived from the intersection of the cylindrical fits with the planar fit and these ranges are tabulated in figure IV-24. They range from 0.28 to 1.86 times the height of the array (H). The value of 1.86 for DIP VA appears spurious compared with the other data, perhaps due to the large data scatter in the experiment. Elimination of this data point reduces the upper limit to 0.82 H and yields an average of 0.52 H.

Given a value of 0.52 H for the break from planar to cylindrical attenuation, a break to spherical attenuation might be expected at 0.52 times the length of the array (L). There are very few data in this region and such a break is not evident. It may be that reduced attenuation due to a transition to elastic behavior may be compensating for the increased attenuation due to spherical behavior at the more distant ranges.

The particle velocity data of figure IV-25 show behavior similar to the acceleration data. The apparent cylindrical attenuation is -2.1 and the

apparent planar attenuation -0.56. The effective transition range for velocity ranges from 0.74 to 1.73 H with 1.15 H being the average. Extrapolating this transition range to the array lengths (1.15L), no data would be expected to be in the spherical region (i.e. all data is within 1.15L).

The displacements shown in figure IV-26 also exhibit similar behavior. The planar attenuation is estimated to be -0.14, the cylindrical attenuation -2.1 and the average transition range 1.6 H. As with velocities, no data is expected to be in the spherical region. The fact that the cylindrical attenuation rate for displacement is the same as the attenuation rate for velocities (-2.1) is consistent with the data for cylindrical charges (-2.0 for v, -1.9 for d) and spherical charges (-2.6 for v and -2.4 for d). This characteristic suggests, as noted for the spherical data, that there is very little change in the duration of the outward velocity phase with range beyond the near region.

The peak horizontal kinematic parameters on the centerline of the planar events at McCormick Ranch can be represented by the following fit equations:

$$a\alpha = 10{,}150\left(\frac{R}{\alpha}\right)^{-1.33} \quad \text{for } \frac{R}{H} \leq 0.52 \quad \text{(a)}$$

$$a\alpha = 4119\left(\frac{H}{\alpha}\right)^{1.38}\left(\frac{R}{\alpha}\right)^{-2.71} \quad \text{for } \frac{R}{H} > 0.52 \quad \text{(b)}$$

$$v = 81.8\left(\frac{R}{\alpha}\right)^{-0.56} \quad \text{for } \frac{R}{H} \leq 1.15 \quad \text{(c)} \qquad \text{(IV-47)}$$

$$v = 101.4\left(\frac{H}{\alpha}\right)^{1.54}\left(\frac{R}{\alpha}\right)^{-2.1} \quad \text{for } \frac{R}{H} > 1.15 \quad \text{(d)}$$

$$\frac{d}{\alpha} = 4.6\left(\frac{R}{\alpha}\right)^{-0.14} \quad \text{for } \frac{R}{H} \leq 1.6 \quad \text{(e)}$$

$$\frac{d}{\alpha} = 11.7\left(\frac{H}{\alpha}\right)^{1.96}\left(\frac{R}{\alpha}\right)^{-2.1} \qquad \text{for } \frac{R}{H} > 1.6 \qquad (f)$$

where

a = acceleration in g's

v = velocity in ft/sec

d = displacement in inches

α = areal charge density in lbs/ft^2 of equivalent TNT

R = range in feet

H = array height in feet

These equations are applicable to range less than about 1 to 1.5 L where L is the length of the array.

In the previous analysis of spherical data it was shown that gravity effects are important in interpreting the data. In the spherical data, yields ranged from 256 lbs to 1.2 kT (a range in $W^{\frac{1}{3}}$ of about a factor of 21). The planar events have areal charge densities ranging from 0.29 lb/ft^2 to 15.11 lbs/ft^2 in equivalent TNT (a difference of about a factor of 52). It, therefore, might be expected that gravity would be influential in the planar data. However, the variations in parameters from event to event (array heights, lengths, surcharge heights) do not permit an analysis of gravity effects. For example, it would be desirable to have two experiments with a significantly different α but the same scaled array dimensions to investigate gravity. An attempt was made to include gravity in the planar analysis by extrapolating the gravity terms from the spherical data analysis, but the results did not improve the data fits or consistency beyond that for the analysis presented. It may be that gravity is leading to the large spread in the effective transition

ranges for the various events, but this scatter cannot be removed with the currently available data.

An idealized horizontal velocity pulse from a planar experiment is the same as that shown in figure IV-18 for a cylindrical experiment. The characteristic times of outward phase duration, peak to peak time and duration of the first motion cycle for data on the centerline of the planar experiments are plotted versus scaled range in figures IV-27, IV-28, and IV-29, respectively. There appears to be no consistent or significant variation in these times with range. For outward phase duration, this observation is consistent with the fact that peak velocity and peak displacement have the same decay rate in the cylindrical region. Given the absence of consistent range variations within the data scatter, the scaled characteristic times for each experiment have been averaged. These averages are plotted versus scaled array height $\left(\frac{H}{\alpha}\right)$ in figure IV-30. It can be seen that there is a rapid increase in characteristic time with increasing array height to scaled array height of about 8, beyond which the times seem to approach an asymptote.

The magnitude of the peak inward velocity in the first motion cycle as a proportion of the peak outward velocity $\left(\frac{V_{PI}}{V_{PO}}\right)$ versus the ratio of range to charge height $\left(\frac{R}{H}\right)$ is plotted in figure IV-31. Although there is significant data scatter, this form of correlation $\left(\frac{V_{PI}}{V_{PO}} \text{ vs } \frac{R}{H}\right)$ minimizes the scatter and produces a more consistent trend than alternate correlations that were attempted. This seems to imply that the range and array height play the dominant roles in determining the inward velocity magnitudes. The trend is toward increasing inward component with increasing range. A linear fit to the data is

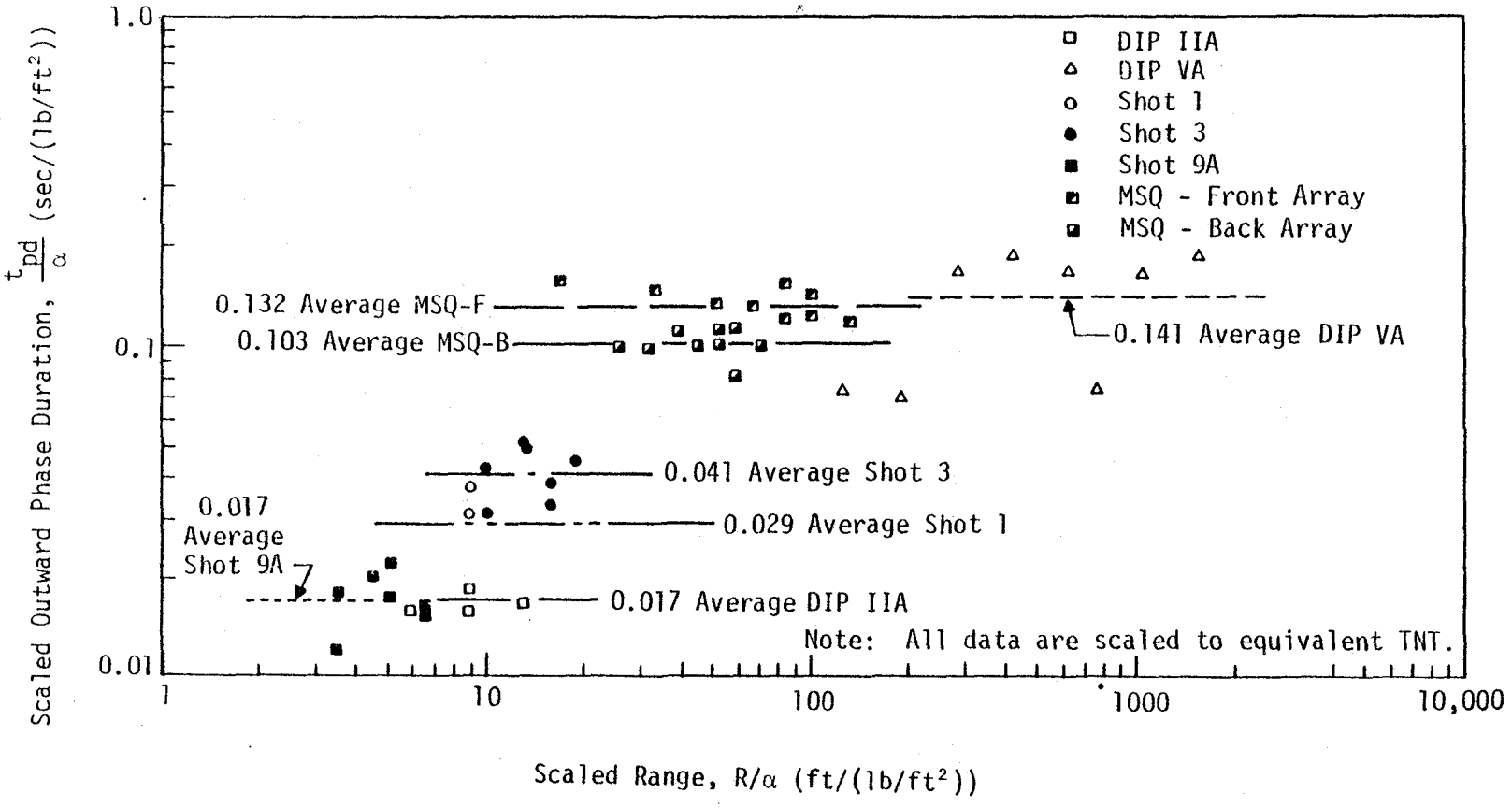

Figure IV-27. Variation of Outward Phase Duration on Centerline Horizontal Velocities with Range for Planar Events

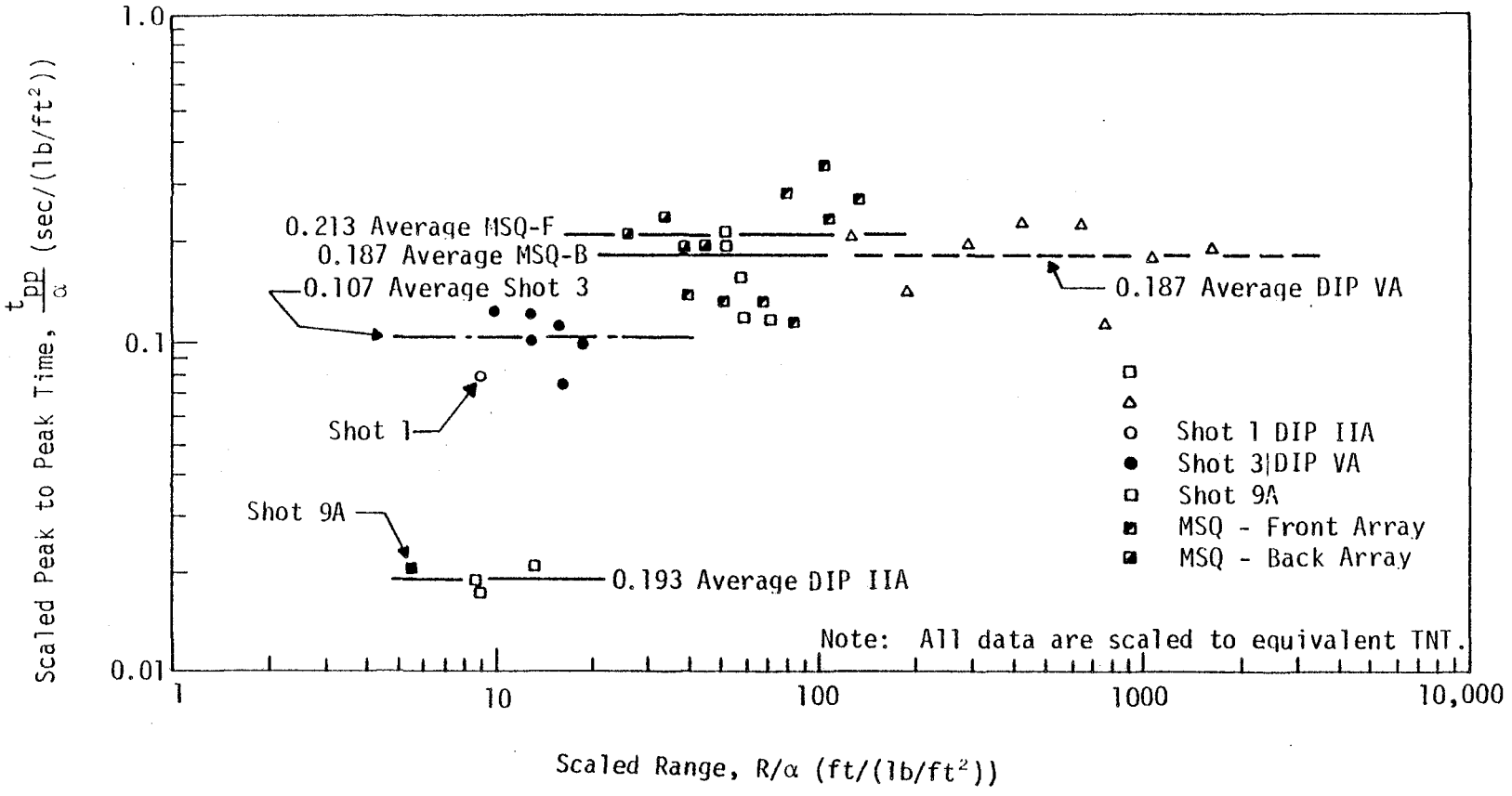

Figure IV-28. Variation of Peak-to-Peak Characteristic Time on Centerline Horizontal Velocities with Range for Planar Events

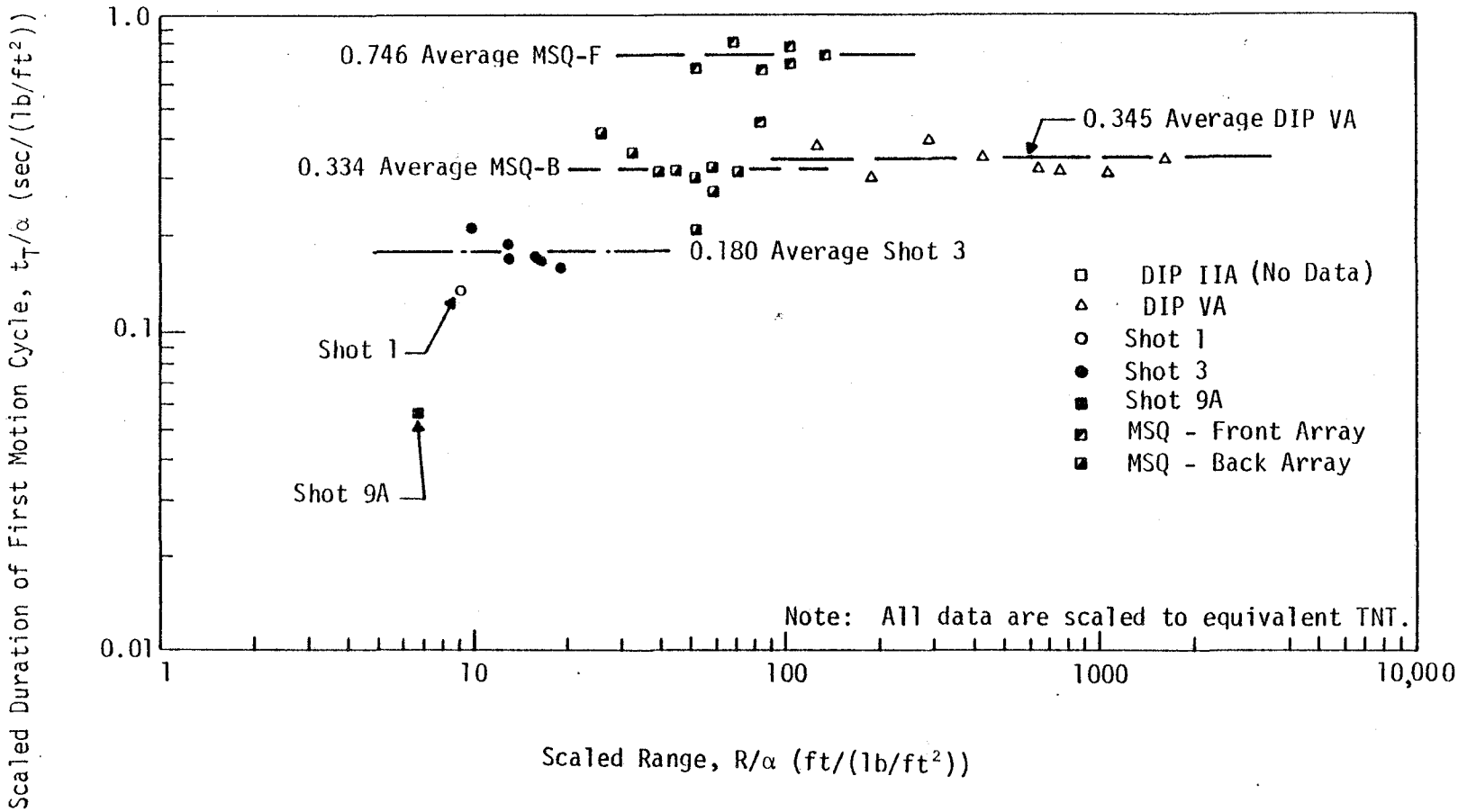

Figure IV-29. Variation of Duration of First Motion Cycle on Centerline Horizontal Velocities with Range for Planar Events

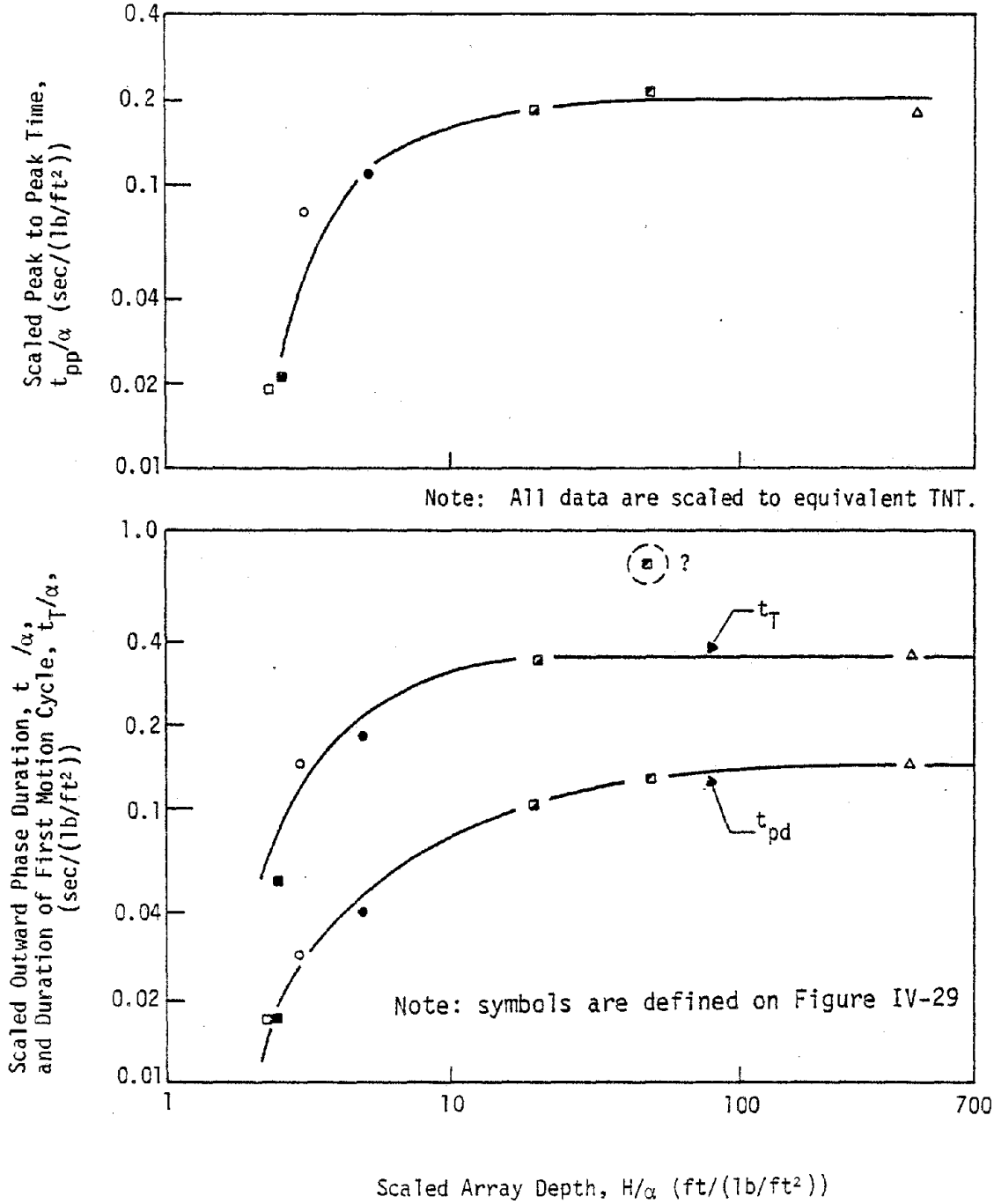

Figure IV-30. Variation of Centerline Characteristic Times with Array Height

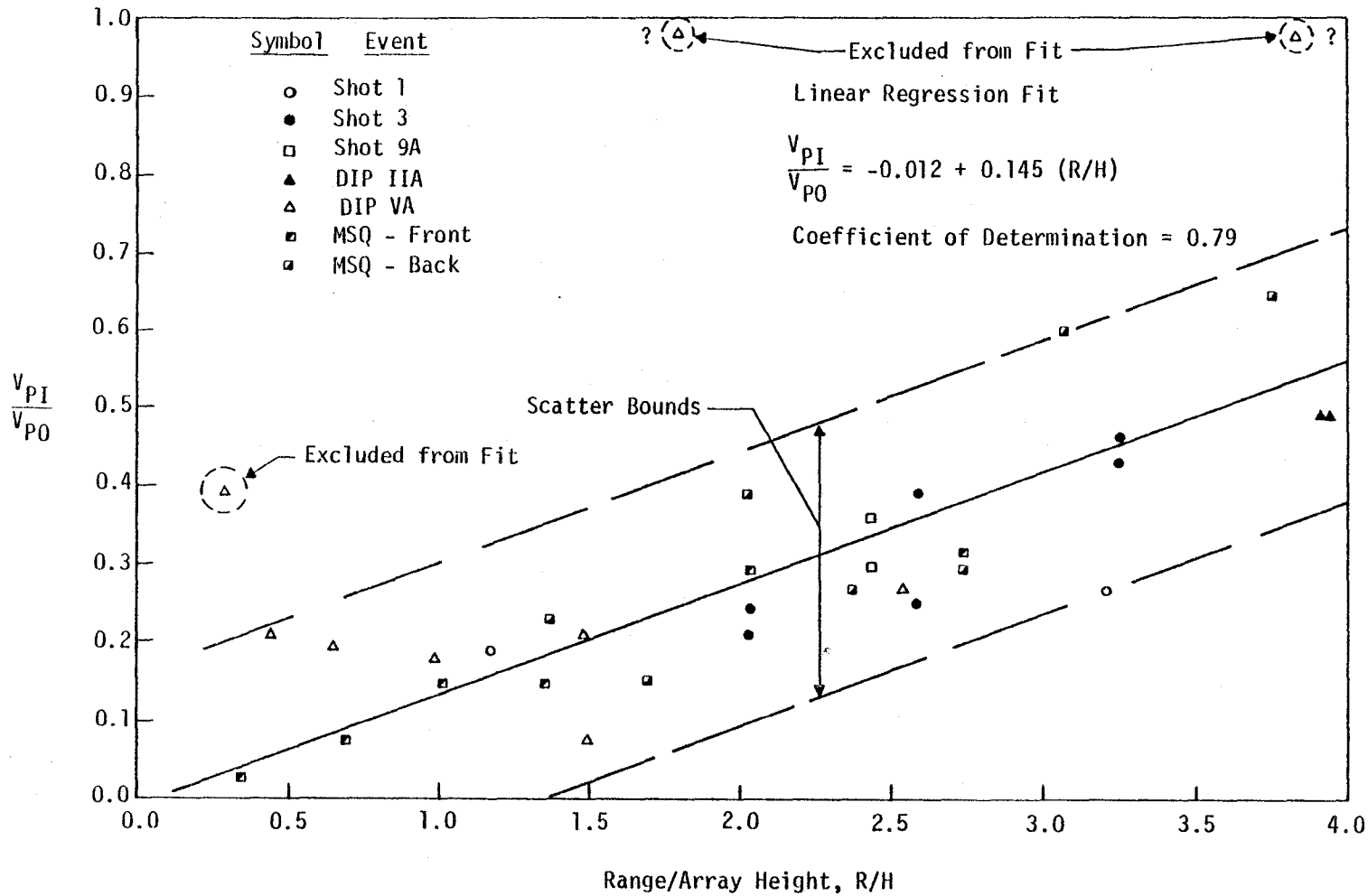

Figure IV-31. Ratio of Peak Inward to Peak Outward Velocity as Function of Range for Planar Events

$$\frac{V_{PI}}{V_{PO}} = -0.012 + 0.145\left(\frac{R}{H}\right) \qquad \text{(IV-43)}$$

where

V_{PI} = peak inward velocity

V_{PO} = peak outward velocity

R = range

H = array height

The correlations for peak amplitudes, characteristic times and the ratio of peak inward to peak outward velocity which have been presented, can be combined with the idealized waveform of figure IV-18 to construct waveform predictions for the first motion cycle from planar experiments in dry granular soil. As for cylindrical events, the waveform beyond the first cycle is uncertain due to absence of data. However, a second outward pulse will probably occur. A rough estimate can take its amplitude to be about one-half the inward amplitude and its duration to be about the same as the inward phase duration of the first cycle. The rise time of the first outward velocity as a function of range can be estimated by equation IV-45.

The previous discussion and correlations are concerned with ground motion behavior on the centerline and at the mid-depth of the array. In most of the events conducted, this position was the most heavily instrumented and most susceptible to analysis. Earthquake simulation applications, however, will be concerned primarily with facilities at or near the ground surface. In addition, large facilities may extend well off of the centerline and, also, it may be necessary to site some facilities off center to make maximum use of the available test area. Hence,

it is necessary to understand motion variations with depth and with cross-range. Depth and cross-range variations can be investigated partially from data from DIP IIA and, to a lesser extent, from DIP VA.

Figure IV-32 plots the variations in the peak particle velocity with depth. The data is normalized by the value of the measured peak particle velocity at or nearest to the mid-depth. For DIP IIA, the nearest measurement was at 40 feet while the array mid-depth was at 47.5 feet. The data for DIP IIA scatter significantly and there is no consistent variation with depth. Overall, it appears that the peak horizontal velocity on DIP IIA can be taken constant with depth and equal to the peak horizontal velocity on the centerline. The scatter is about ± 50 percent and this scatter is consistent with the scatter at the mid-depth in a single well instrumented experiment.

The data for DIP VA, with the exception of one point, lie below the mid-depth value both above and below the mid-depth. This is inconsistent with DIP IIA and it is not known whether this behavior is real or due to an erroneously high measurement at the mid-depth position. Since DIP IIA data are more numerous, of better quality and at amplitude levels closer to those required for strong earthquake simulation, it is recommended that the DIP IIA trend of no variation with depth be tentatively used for prediction pending calculations or more data. This trend is consistent with the qualitative observation in the earlier discussion of phenomena that free-surface effects will be most dominant in vertical motion components.

Figure IV-33 plots the variations in peak horizontal accelerations as

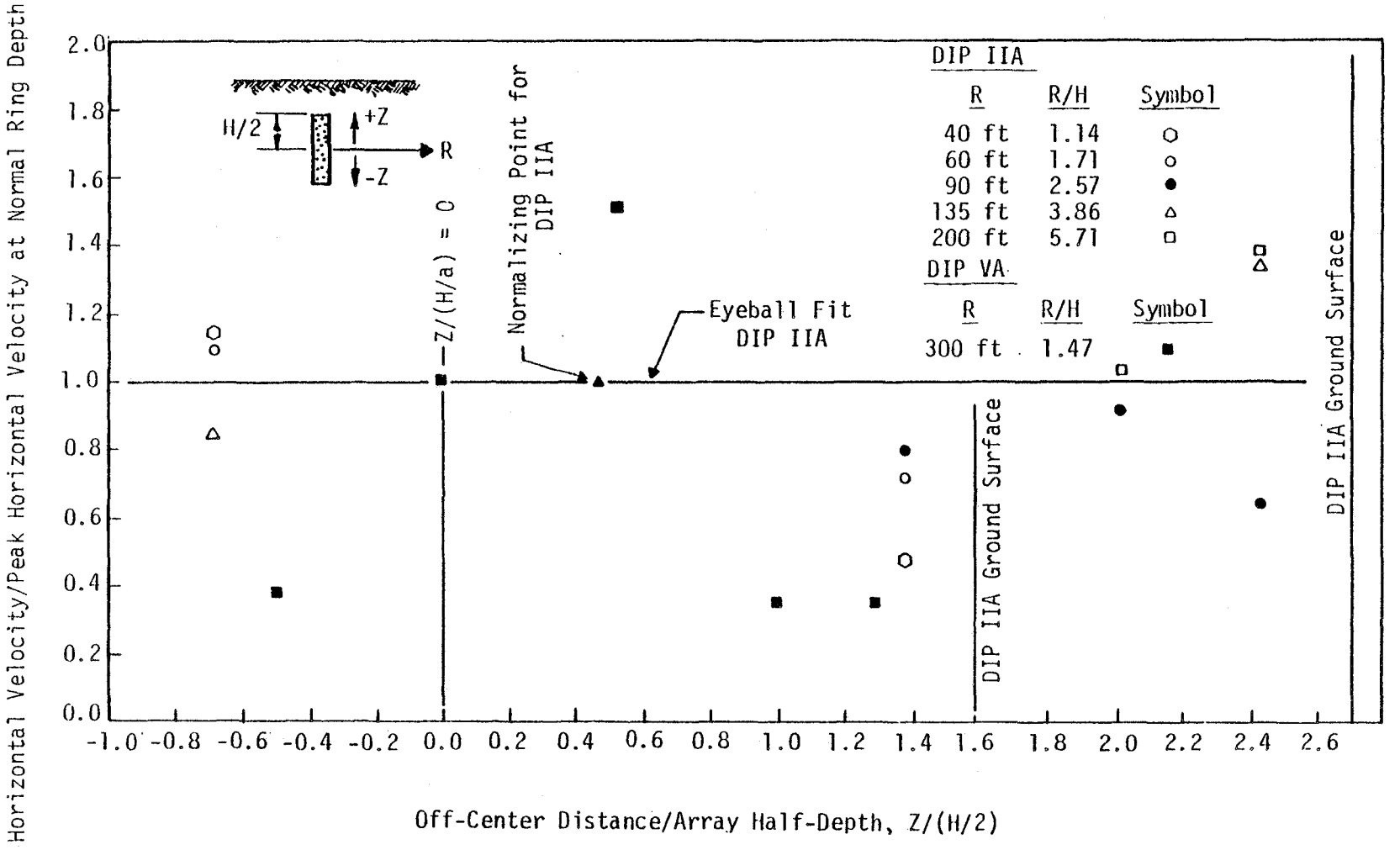

Figure IV-32. Variation of Peak Horizontal Velocity with Depth on Planar Events

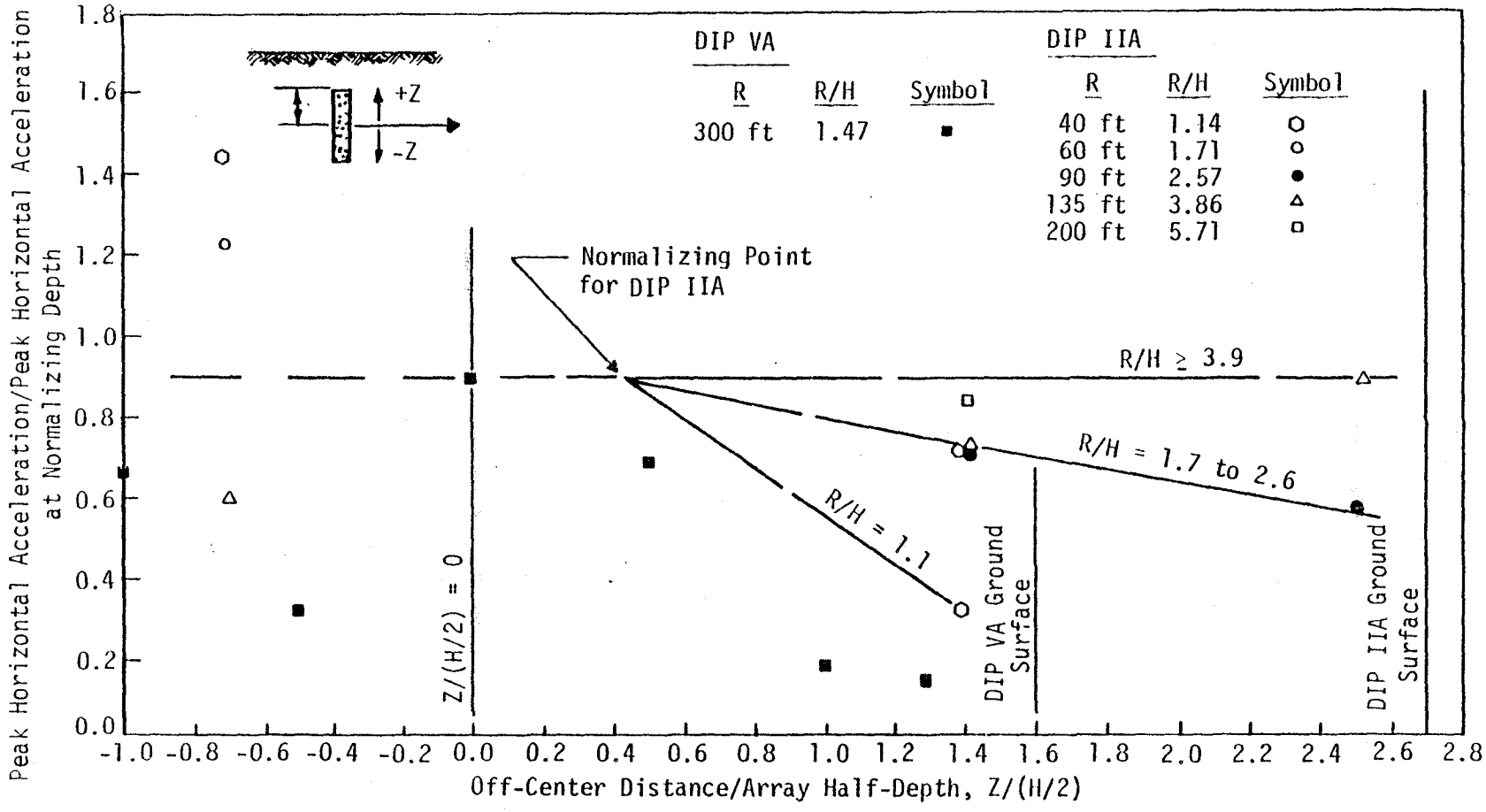

Figure IV-33. Variation of Peak Horizontal Acceleration with Depth on Planar Events

a function of depth. The data is scattered considerably and the discernment of trends is tenuous at best. Below the mid-depth the trend is not clear at all and it has been assumed that there is no significant variation of the peak with depth to the depth of the array bottom. Above the mid-depth there appears to be a trend of decreasing acceleration with increasing height, especially above the top of the array. This trend is consistent with the spreading wavefronts above the array and relief toward the free-surface (figure IV-23). The variation seems to be related to the range (scaled by H). Near to the array the decrease in acceleration is rapid while beyond a scaled range of about 4 there seems to be no variation with depth. These trends are based on DIP IIA. DIP VA shows a similar trend, but the sparsity of data and scatter do not allow quantitative assessment of the trend.

The variation in peak horizontal displacement as a function of depth on DIP IIA and DIP VA is shown in Figure IV-34. Displacement variations are a complex function of range and depth. In the near region, displacements are influenced greatly by shear failure in the soil. The existence of the free-surface causes enhancement of outward displacement due to the lack of confinement. In this region, there is little or no inward velocity phase. With increasing range shear failure effects diminish and, hence, free-surface effects also become less predominant. This trend is evident in the DIP IIA data where there is almost a factor of 2 increase of near-surface displacement above the mid-depth displacement at a scaled range ($\frac{R}{H}$) of about 4, but only about a 50 percent increase at a scaled range of about 6. Unfortunately, there are too few data to substantiate that the DIP IIA trends are general trends and that $\frac{R}{H}$ scaling is appropriate. Indeed, the DIP VA data (low for what is suspected to be

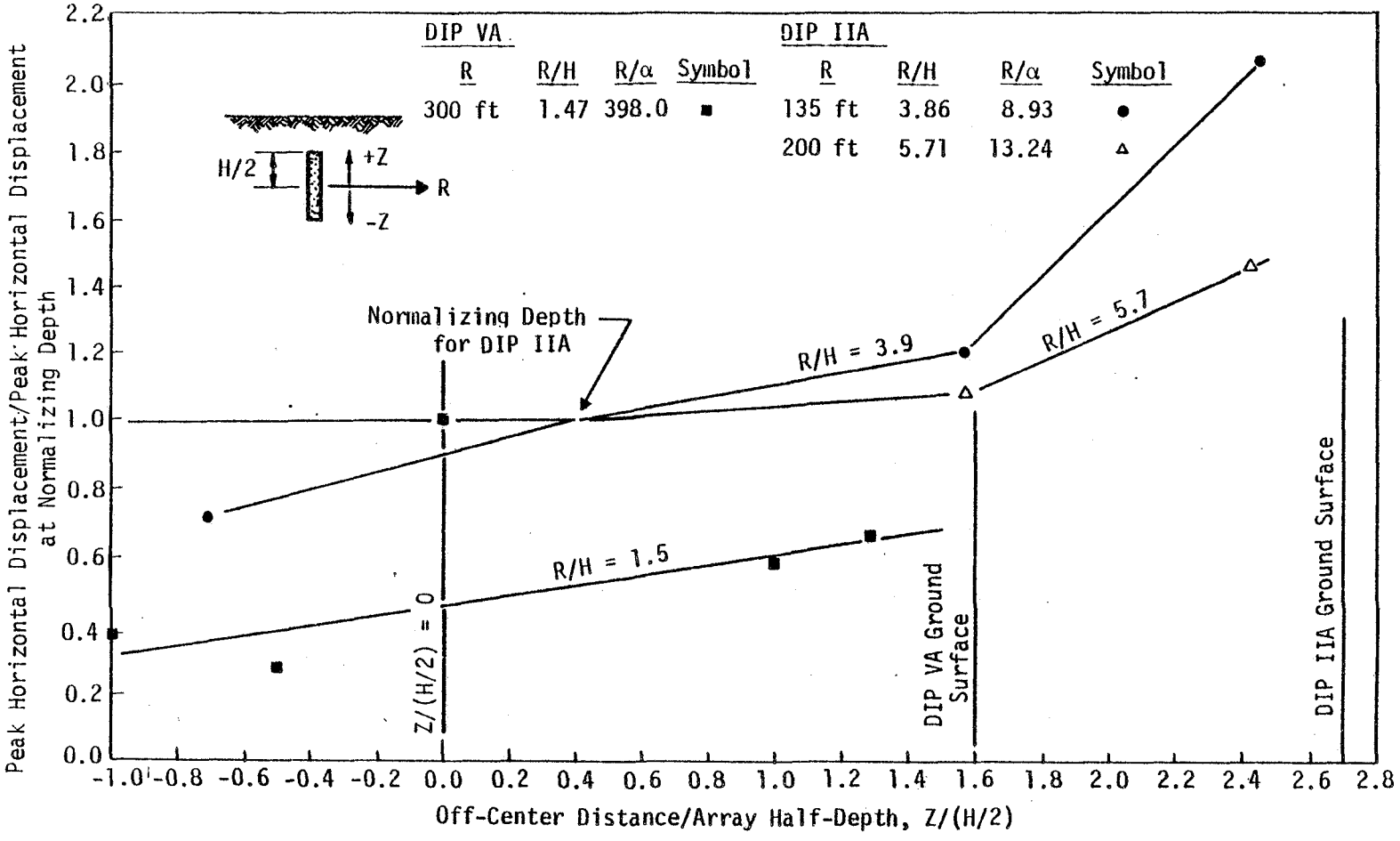

Figure IV-34. Variation of Peak Horizontal Displacement with Depth on Planar Events

an erroneously high measurement at the mid-depth) does not show as marked an increase in the near-surface region at a scaled range of 1.5. $\frac{R}{\alpha}$ scaling does not provide adequate correlation either.

Increase in horizontal displacement near the free-surface implies an increase in the outward phase duration of the horizontal velocity pulse. This trend is evident in figure IV-35 which plots the variation of the outward velocity phase duration as a function of depth. At and below the mid-depth there is little variation, but the duration clearly increases as the surface is approached. The increase appears to be greater near the source, but a general correlation involving the scaled range and the depths as related to array characteristics and free-surface location cannot be ascertained from the available data. However, figures IV-34 and IV-35 do provide information which can provide a crude guide to variations.

The variation of peak horizontal velocity with cross-range on DIP IIA and DIP VA is shown in figure IV-36. There seems to be no variation within the data scatter in the middle one-third of the array. Beyond the middle third the amplitude decreases and the amount of the decrease seems to be related to range scaled by the array width. Near to the array $\left(\frac{R}{L} = 0.2\right)$ the data indicates no variation. Between $\frac{R}{L} = 0.2$ and $\frac{R}{L} = 0.3$ there seems to be a rapid decrease in relative amplitude with cross-range while beyond $\frac{R}{L} = 0.3$ there is a gradual increase in relative amplitude. The DIP VA data off the array center is considerably lower than at the center even within the center third, but the data seem to be about constant. The low amplitude may be due to an erroneously high amplitude value at the center as was suggested in the previous discus-

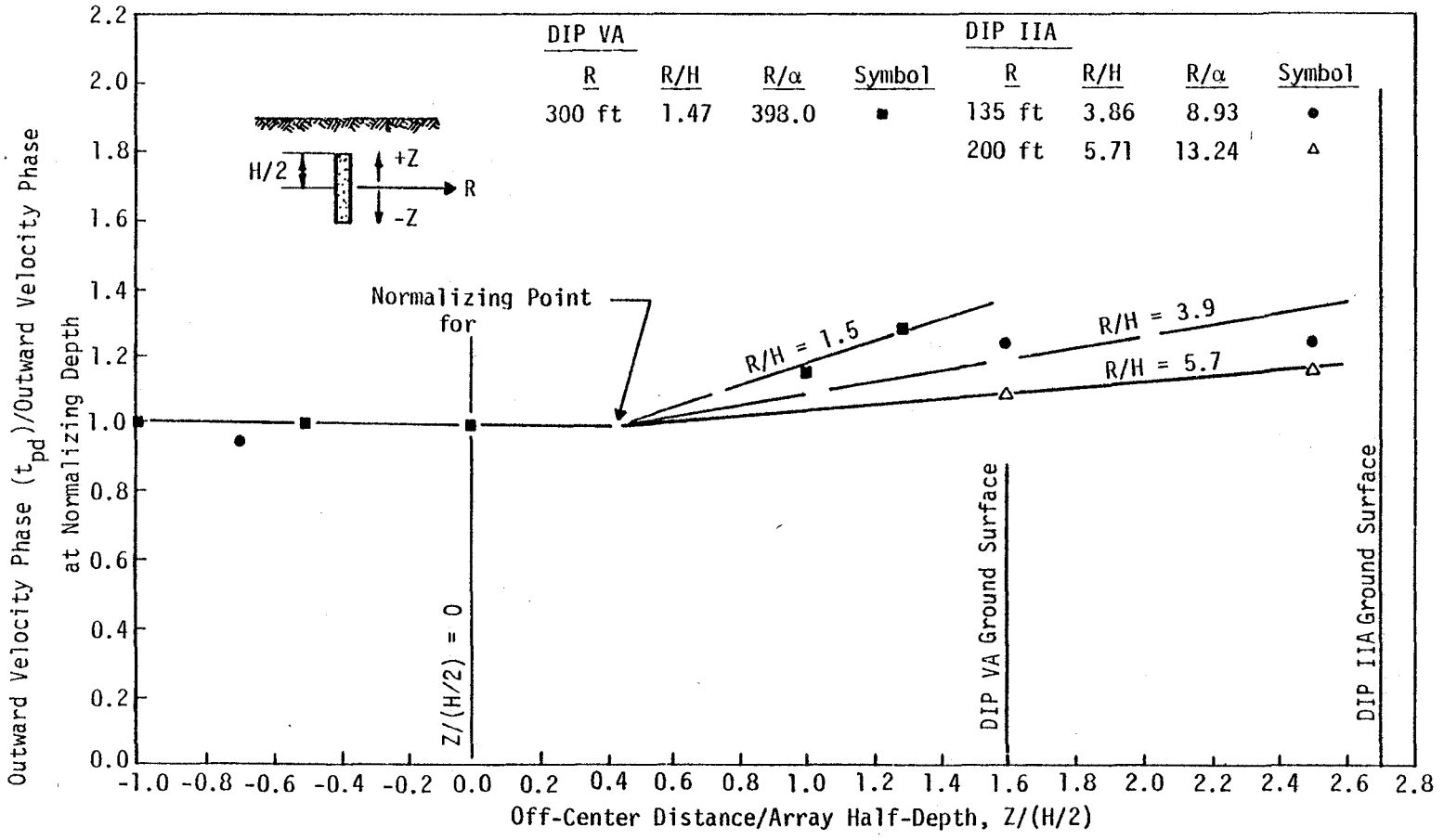

Figure IV-35. Variation of Outward Velocity Phase Duration with Depth on Planar Events

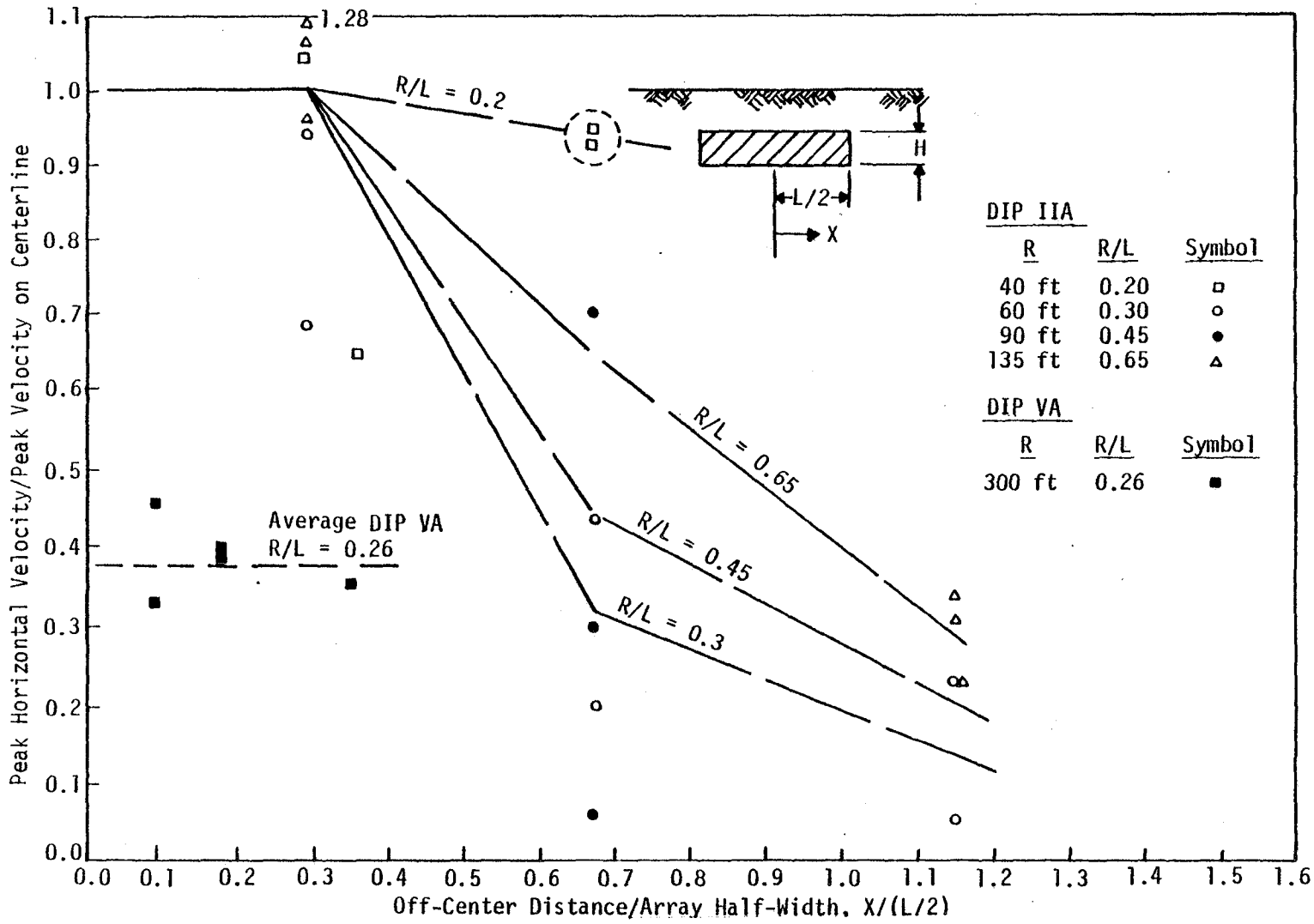

Figure IV-36. Variation of Peak Horizontal Velocity with Cross-Range on Planar Events

sion of variations with depth. The fact that they are constant in the center third is consistent with the DIP IIA data. There are no DIP VA data beyond the middle third of the array.

Figure IV-37 presents cross-range data on peak horizontal acceleration. As with velocity, there is considerable scatter, but the trends are the same as those for velocity. The few data available on displacement variations with cross-range are shown in figure IV-38. Data in DIP IIA are only available at one range and the variation with cross-range is about the same as for horizontal velocity, i.e., little variation within the center third of the test area and attenuation to about 50 percent of the on-center amplitude at the array edge. The DIP VA data is all located within the center third and shows no significant cross-range variation therein (excluding the suspect center measurement). For prediction purposes, it appears that displacement variations can be taken similar to the velocity variations of figure IV-35.

Vertical response as a function of range in the near-surface region will be very important for earthquake simulations. As described previously, the vertical response will be strongly influenced by the free-surface and, indeed, ultimately will destroy symmetry on the array mid-depth and give the entire field an upward motion component. Unfortunately, vertical data of adequate quality only exist on DIP IIA and even those are few in number. Hence, it is not possible to relate vertical response to various scaling parameters with any level of confidence. The material which follows simply presents the data and suggests possible phenomenological causes.

Figures IV-39, IV-40, and IV-41 present vertical and horizontal velocity

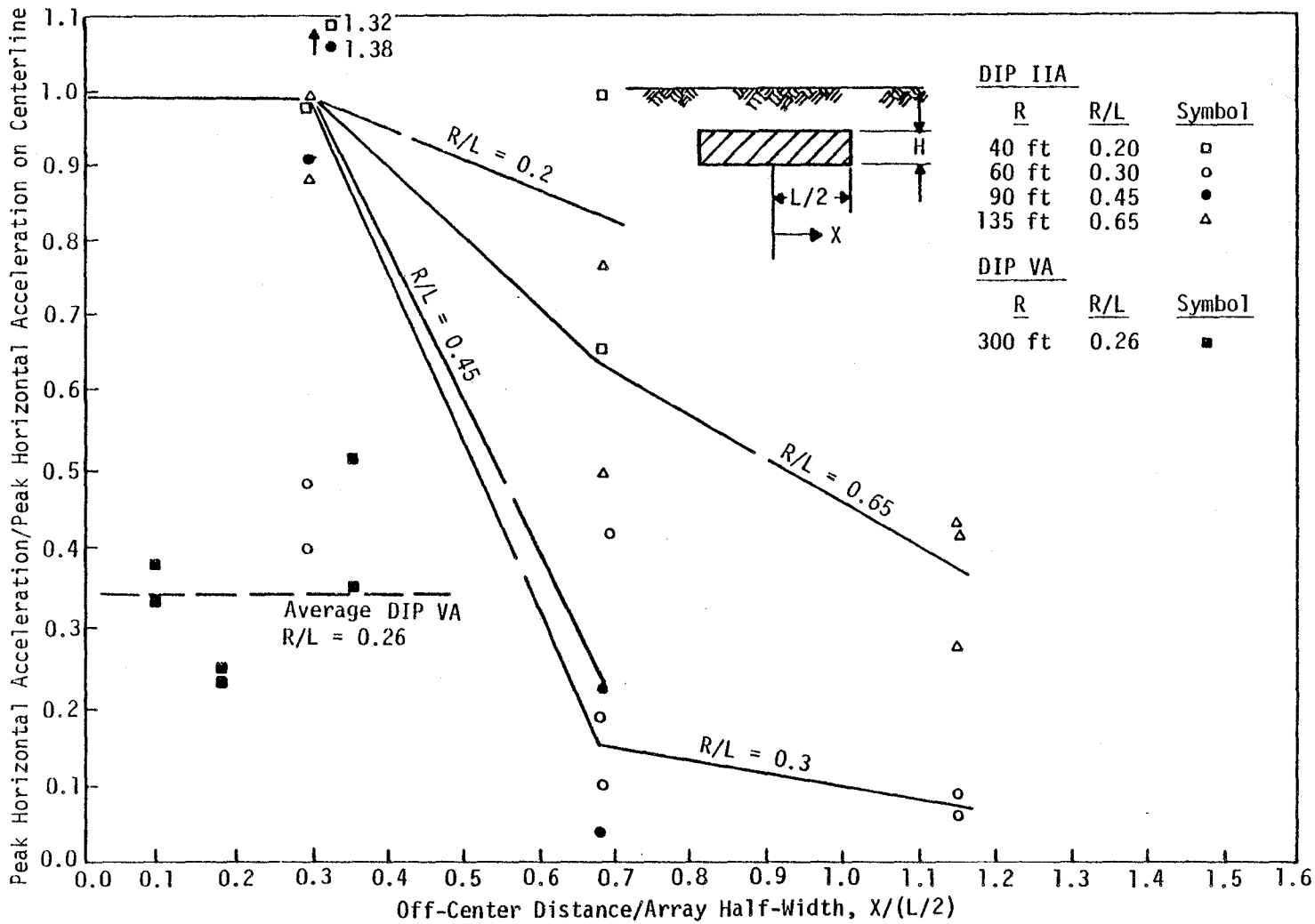

Figure IV-37. Variation of Peak Horizontal Acceleration with Cross-Range on Planar Events

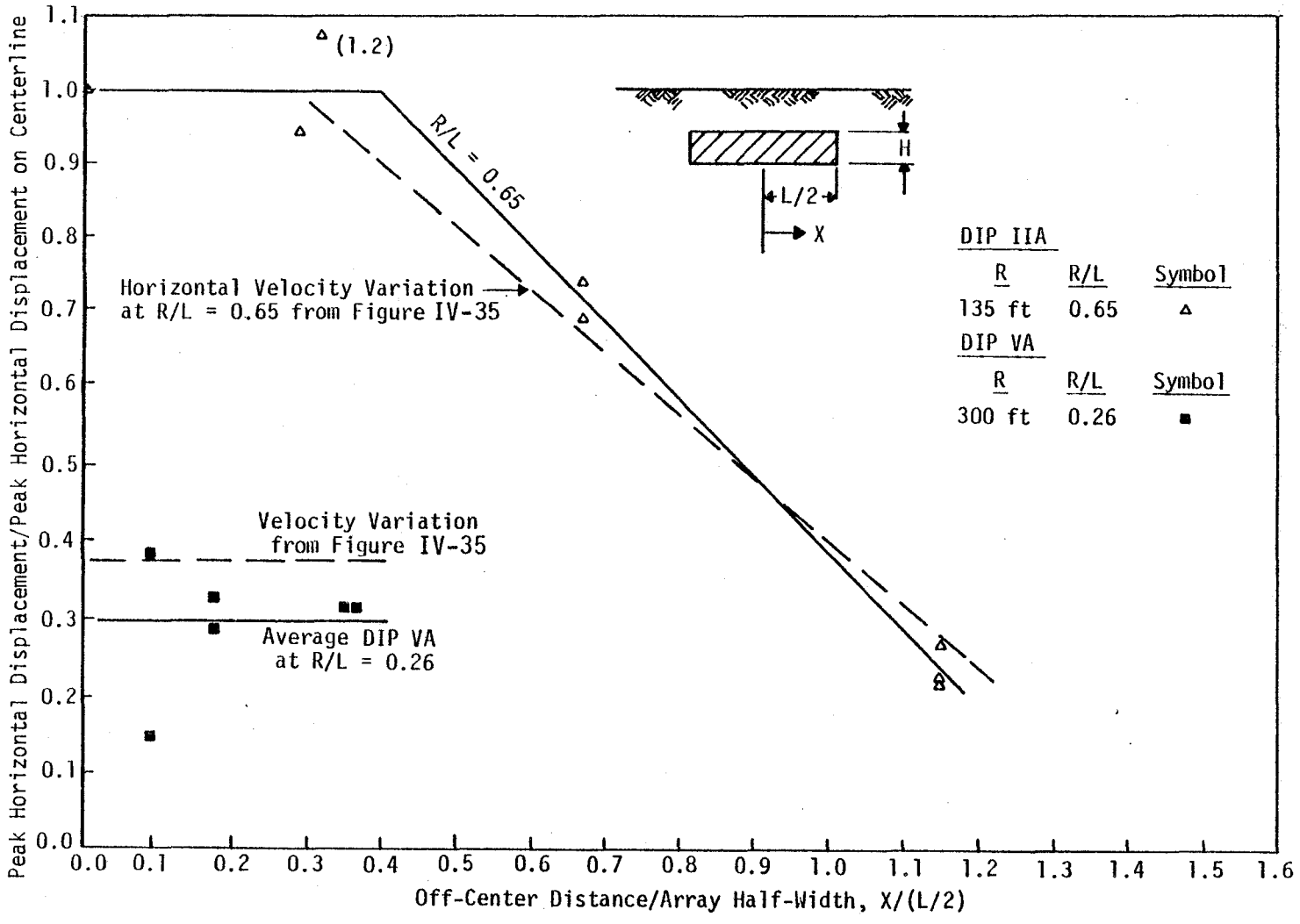

Figure IV-38. Variation of Peak Horizontal Displacement with Cross-Range on Planar Events

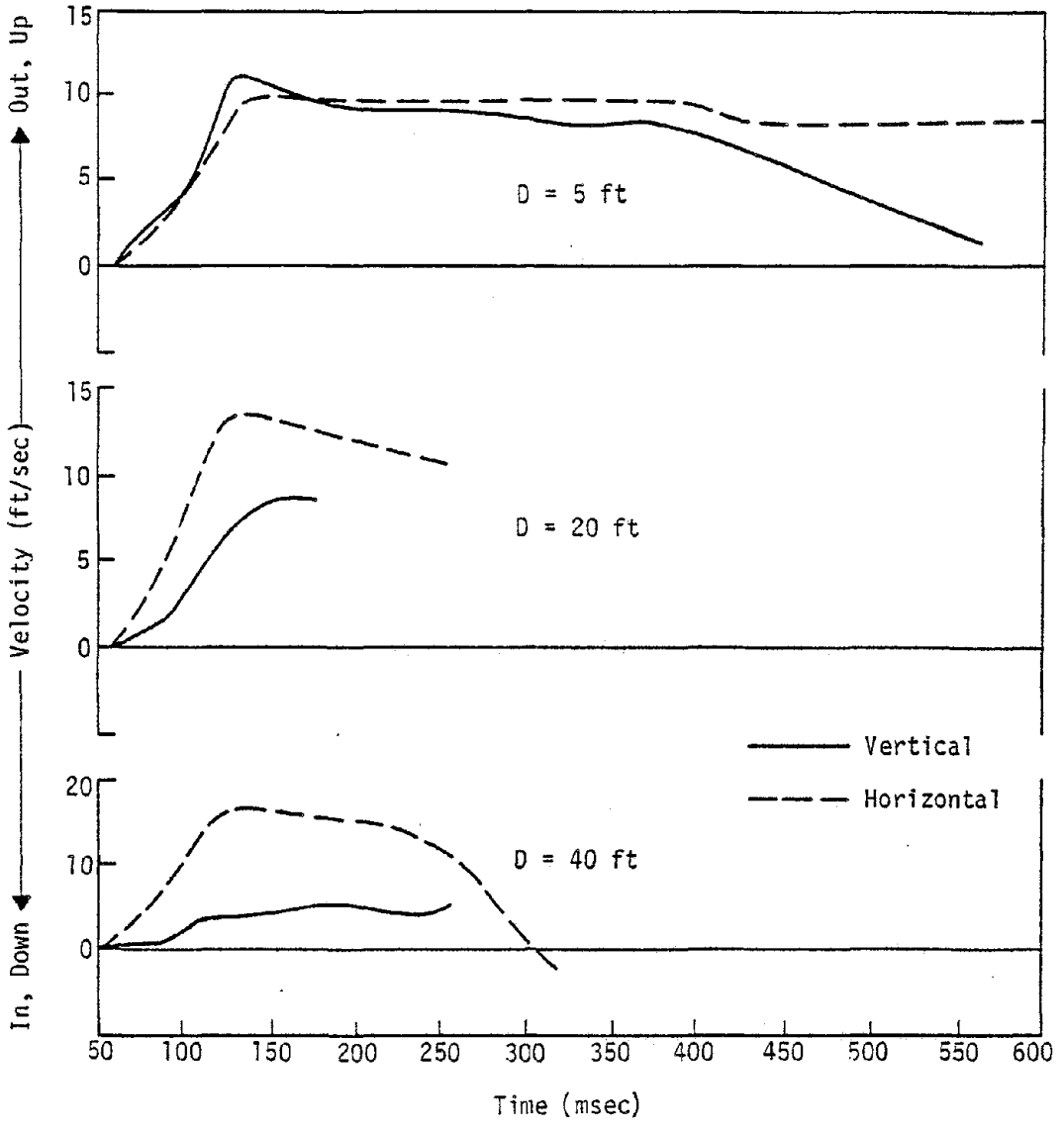

Figure IV-39. Vertical and Horizontal Velocity Time Histories on DIP IIA at 90-Foot Range

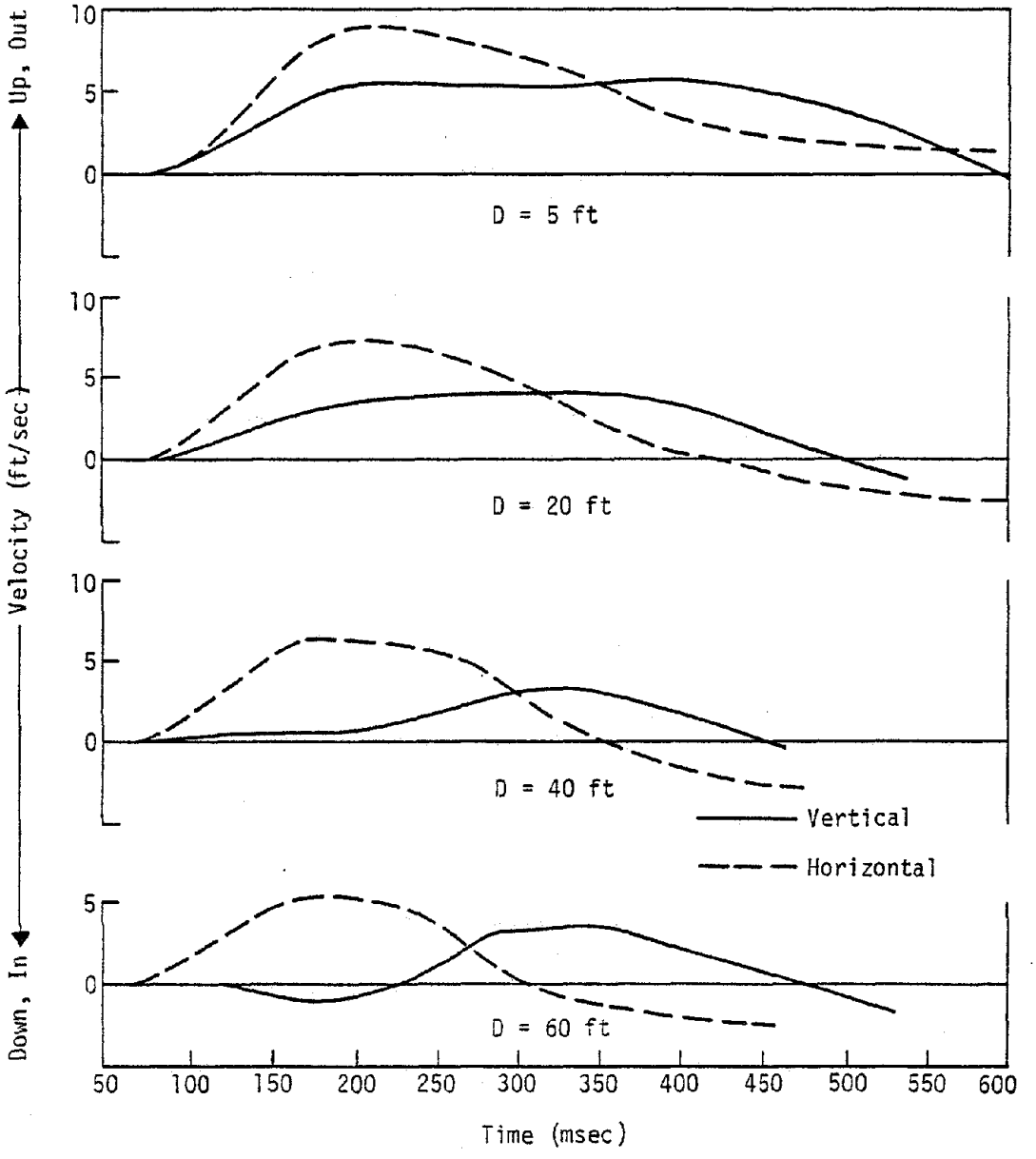

Figure IV-40. Vertical and Horizontal Velocity Time Histories on DIP IIA at 135-Foot Range

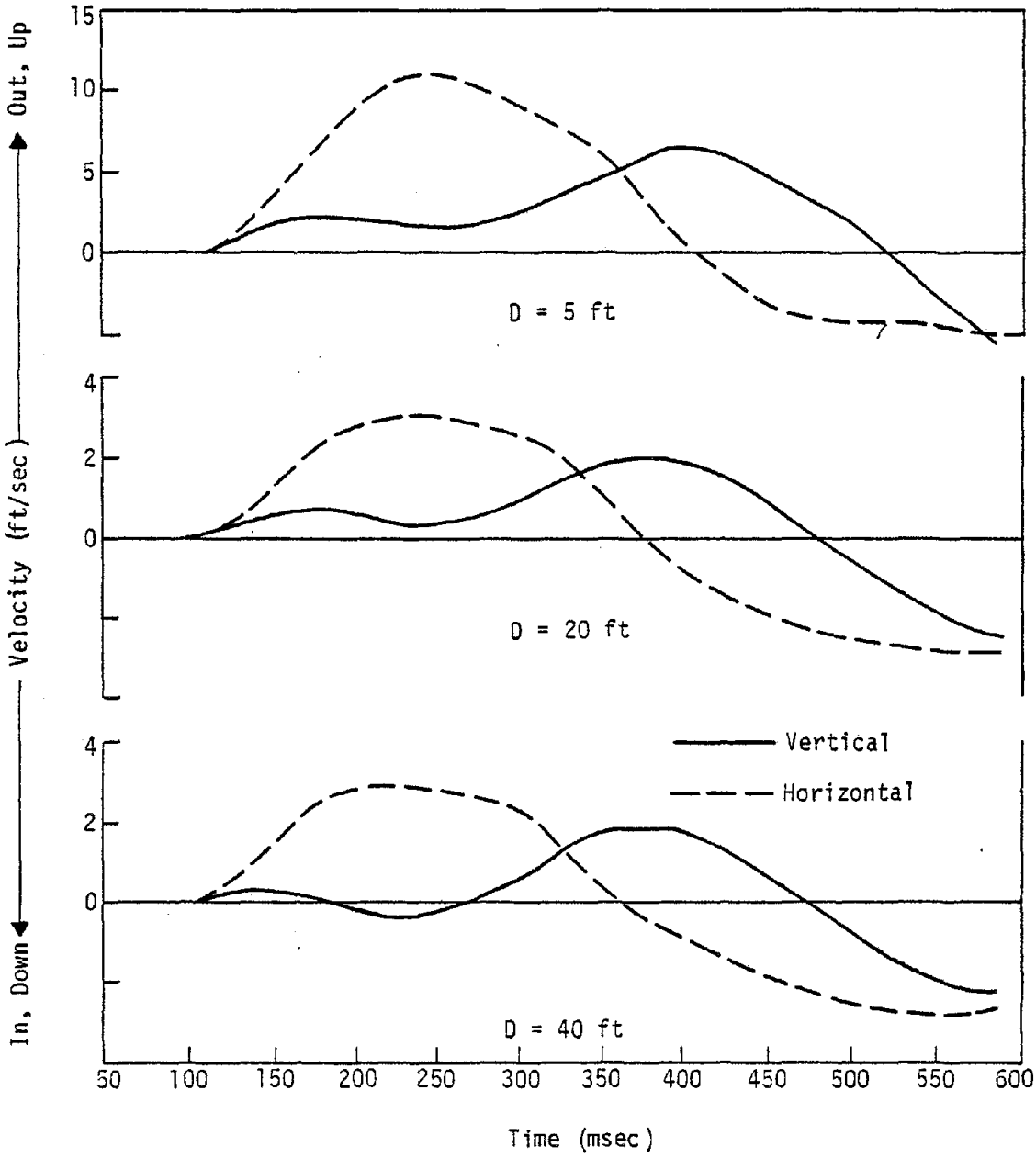

Figure IV-41. Vertical and Horizontal Velocity Time Histories on DIP IIA at 200-Foot Range

waveforms at various depths at the 90, 135 and 200-foot ranges, respectively, on DIP IIA. At the 90-foot range the vertical waveforms are similar in gross shape to the horizontal waveforms and, near the surface, the vertical velocity is about equal to the horizontal. At the 135-foot range, and, especially at the 200-foot range, the vertical waveform in the near-surface region begins to develop two distinct upward bumps. They are subtle at 35 feet, but quite distinct at 200 feet. In addition, the upward velocity phase duration at these ranges exceeds the outward velocity phase duration. It is believed that these phenomena are due to the separation of the incident P, SP and S-waves in the near-surface region as previously illustrated in figure IV-23. Estimates of the wave arrival times in DIP IIA support this hypothesis as do the directions of motion associated with major features of both the vertical and horizontal waveforms. For example, at 200 feet the first motion is up and out, consistent with the incident P-wave direction of motion. The vertical motion then begins to reverse while the horizontal motion continues outward, consistent with SP motion. Finally, the vertical motion is upward again at about the same time as the outward horizontal motion reaches a peak and begins to reverse. This may be the SP effects from the array bottom.

It appears that the vertical waveform may be decomposed into two waveforms of shape similar to the idealized horizontal waveform of figure IV-17, out of course, with different amplitudes and different time characteristics. This is illustrated in figure IV-42. Although it is possible to describe a credible hypothesis for the observed vertical waveform features and suggest a possible decomposition of the waveform, the few data from DIP IIA are inadequate for quantification of the phenomena or

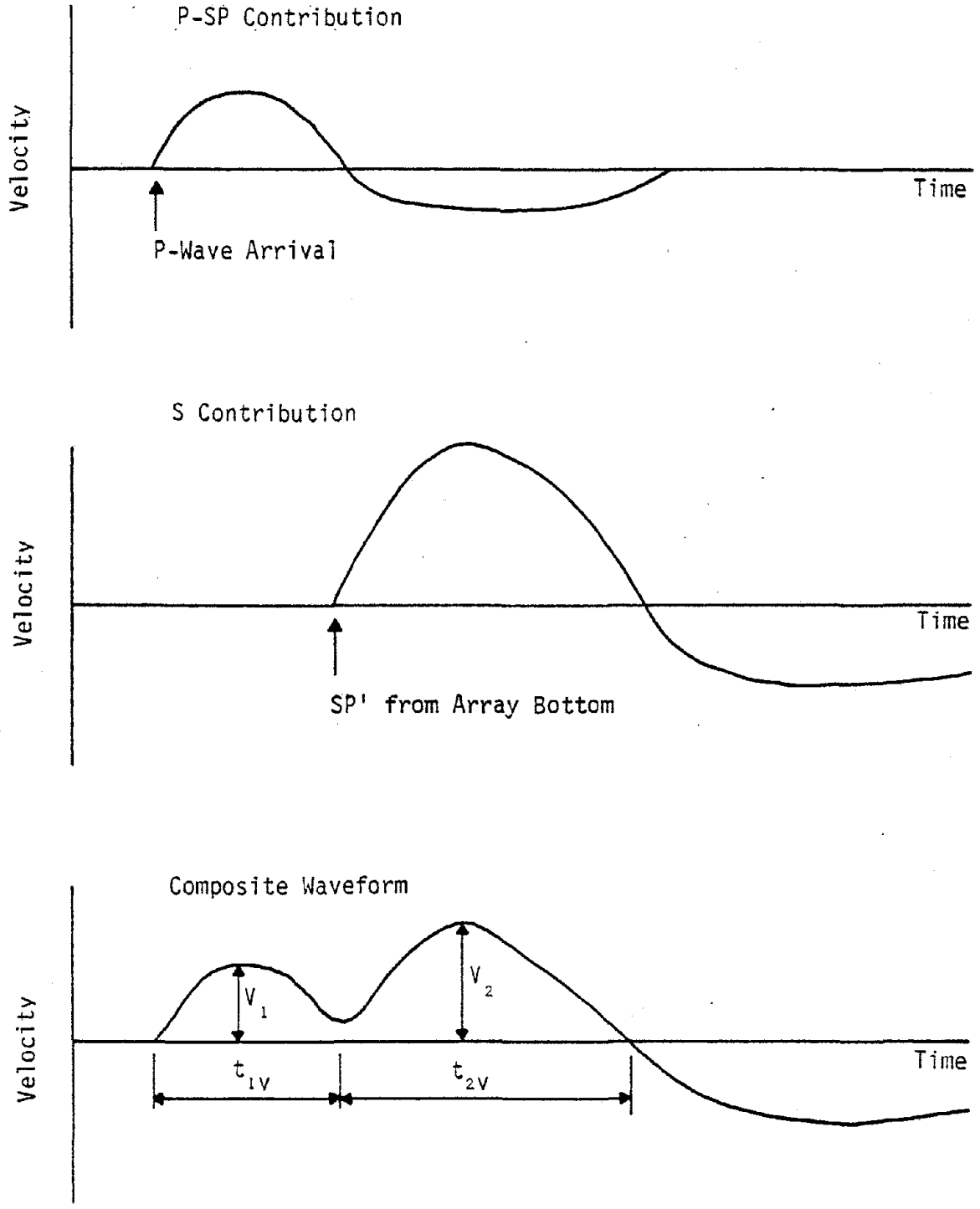

Figure IV-42. Possible Decomposition of Vertical Velocity Into P-SP and SP'-Wave Contributions

the development of a general prediction. The DIP IIA data can, however, provide a rough guide to the waveform characteristics. Table IV-5 lists the characteristics designated in the composite waveform of figure IV-42 for the 135 and 200-foot ranges on DIP IIA. The 90-foot range data do not explicitly contain the double "bump" characteristic and, therefore, are not included. The time and amplitude characteristics of the composite waveform (V_1, V_2, etc) contain the influence of P, SP and S-wave components combined, but V_1 and t_{1V} can be used as a very rough indicator of the characteristics of the P-SP contributions as can V_2 and t_{2V} for the S contribution. It appears from the data of table IV-5 that t_{1V} and t_{2V} can be taken, on the average, as about 0.5 and 1.0, respectively, times the outward phase duration of the horizontal velocity pulse, t_{pd}. Little can be concluded with regard to V_1 and V_2 except that they appear to attenuate at different rates. V_1 diminishes in amplitude much more rapidly than V_2.

In general, V_2 is the peak upward vertical velocity. Peak upward velocities and peak upward accelerations on DIP IIA are given in table IV-6. Except at the very near-surface (5-foot depth) at the 90-foot range, the peak vertical upward velocity near the surface can be taken as about 60 percent of the peak horizontal. The ratio at the 40-foot depth is only 40 percent, but this depth lies near the array mid-depth. The peak vertical acceleration can be estimated quite well as about 45 percent of the peak horizontal.

The cross-range variations of peak vertical acceleration, velocity and displacement are shown in figures IV-43, IV-44, and IV-45, respectively. Within the scatter of the data the vertical cross-range variations are

Table IV-5

Characteristic Parameters of Vertical Velocity Waveforms on DIP IIA

Range (ft)	Depth (ft)	t_{pp}^{*}(ms)	t_{1V}^{**}(ms)	t_{2V}(ms)	t_{1V}/t_{pd}	t_{2V}/t_{pd}	V_1 (ft/sec)	V_2 (ft/sec)	V_1/V_2
135	5	--	230	300	--	--	5.5	6.0	0.92
	20	340	200	210	0.60	0.62	3.5	4.0	0.88
	40	280	130	255	0.82	0.91	0.5	3.5	0.14
	60	235	120	300	0.51	1.28	1.3	3.5	0.37
200	5	300	140	270	0.47	0.90	2	6.5	0.31
	20	280	140	245	0.50	0.88	0.7	2.0	0.35
	40	265	120	250	0.45	0.94	0.3	1.8	0.17
					Avg. 0.56	Avg.0.92			

* t_{pd} = outward phase duration of horizontal velocity

** Refer to figure IV-42 for remainder of nomenclature definition

Table IV-6

Variation of Peak Vertical Motion Parameters with Range on DIP IIA

5' Depth

Range(ft)	R/α	V_V(ft/sec)	V_V/V_H	A_V(g)	A_V/A_H
90	6.0	13.0	1.24	10.0	1.09
135	8.9	5.7	0.66	2.0	0.43
200	13.2	6.5	0.59	2.48	0.47
			Avg.0.63 (Excludes 90ft)		Avg.0.45 (Excludes 90ft)

20' Depth

Range(ft)	R/α	V_V(ft/sec)	V_V/V_H	A_V(g)	A_V/A_H
60	4.0	15	0.63	19.4	0.45
90	6.0	8.5	0.65	5.1	0.47
135	8.9	4.0	0.57	1.62	0.42
200	13.2	2.0	0.67	0.62	0.44
			Avg.0.63		Avg.0.45

40' Depth

Range(ft)	R/α	V_V(ft/sec)	V_V/V_H	A_V(g)	A_V/A_H
40	2.7	23.5	0.42	104	0.60
60	4.0	9.5	0.30	15	0.33
90	6.0	5	0.30	6.2	0.04
135	8.9	3.2	0.51	1.25	0.25
200	13.2	1.8	0.62	0.98	0.65
			Avg.0.43		Avg.0.45

V_V = vertical velocity
V_H = horizontal velocity
A_V = vertical acceleration
A_H = horizontal acceleration

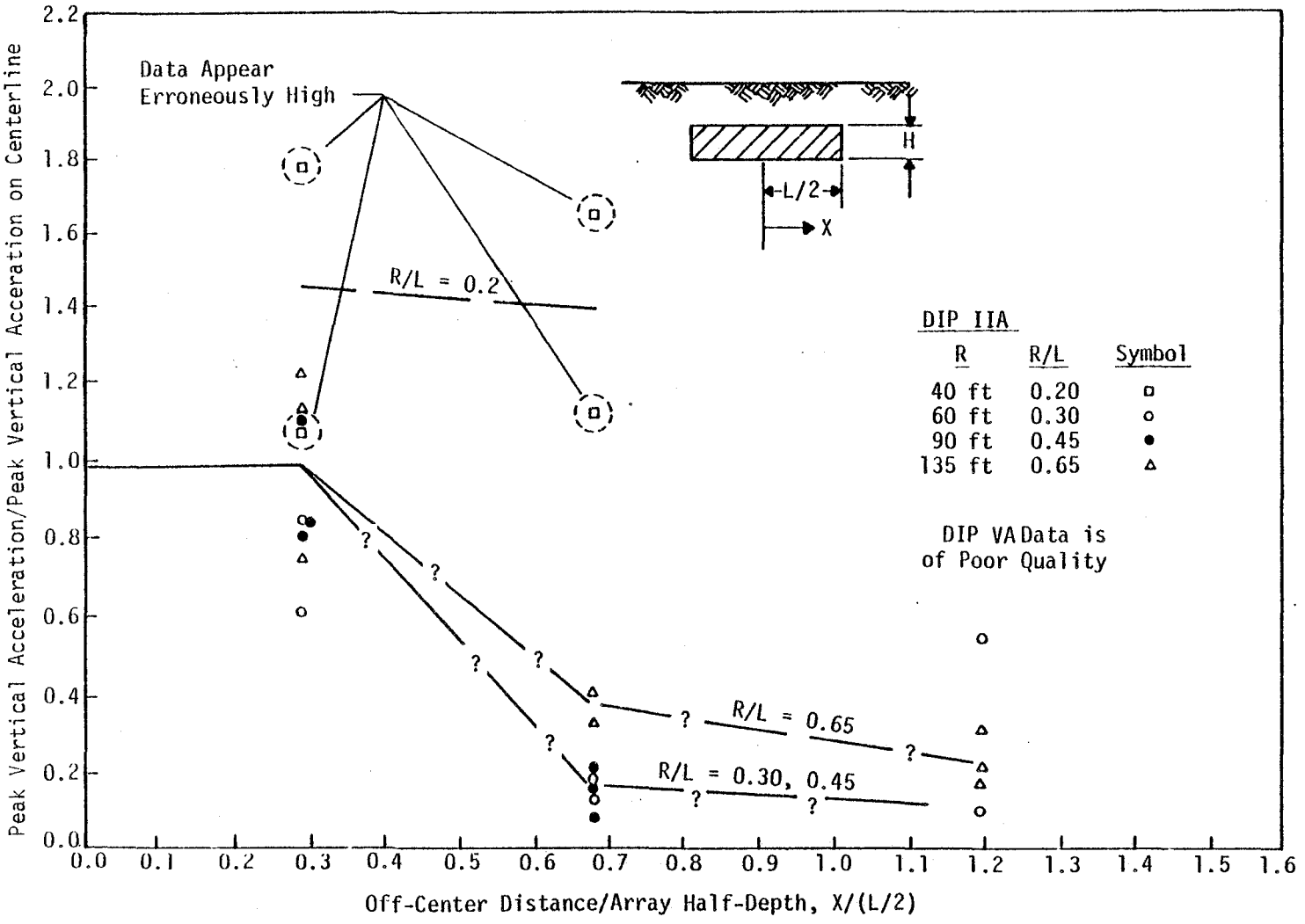

Figure IV-43. Variation of Peak Vertical Acceleration with Cross-Range on Planar Events

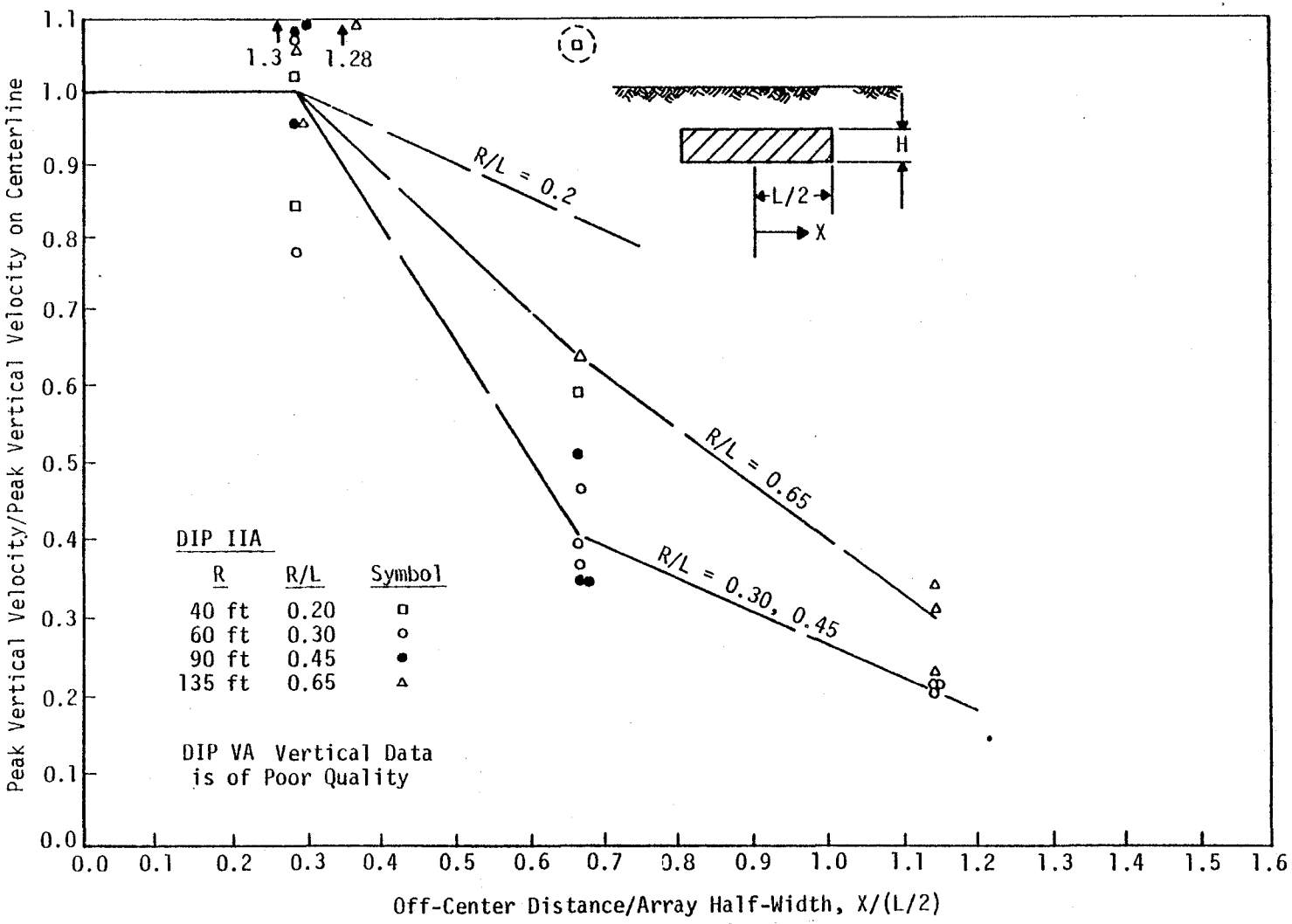

Figure IV-44. Variation of Peak Vertical Velocity with Cross-Range on Planar Events

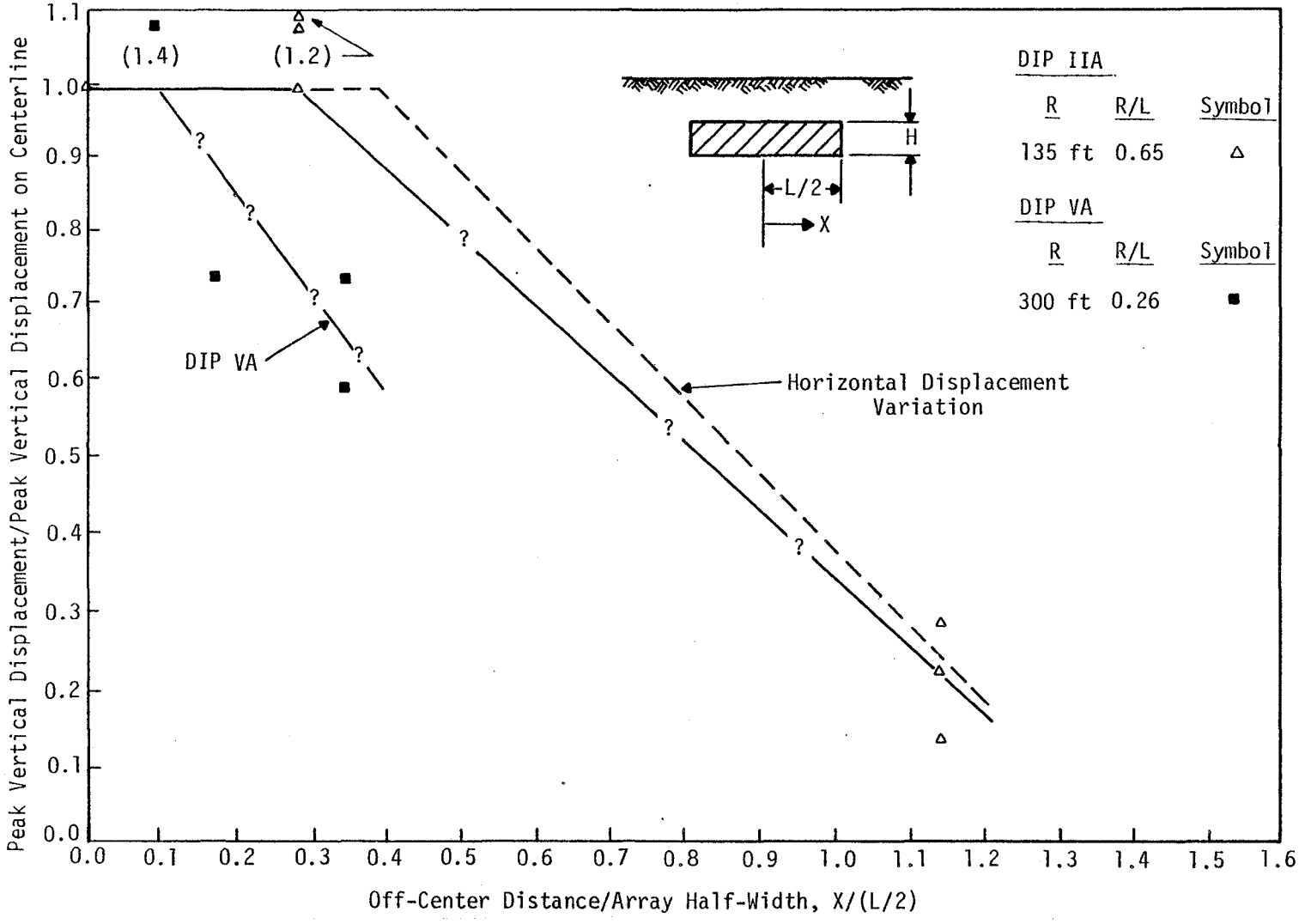

Figure IV-45. Variation of Peak Vertical Displacement with Cross-Range on Planar Events

the same as those described previously for the horizontal components.

6. DATA FROM ENHANCEMENT EXPERIMENTS

The general objective of enhancement is to alter the ground motions from explosions so that their amplitudes, frequency content and durations more closely approximate those of earthquakes. The use of a planar explosive array is an enhancement technique in this sense in that it allows the introduction of the parameter of array height for additional control of motion attenuation, frequency content and duration. There are other potential methods and they are addressed here.

Enhancement techniques for which some data are available include

a. Focused Explosive Arrays
b. Explosives with Longer Burn Times
c. Decoupling of Explosives
d. Relief Trenches and Shock Barriers
e. Multiple, Time Sequenced Detonations

Each of these concepts and sources of available data have been outlined in Section II. Numerical calculations involving relief trenches and shock barriers are discussed in Section VI.

The potential value of focused arrays for increasing ground motion parameters in a limited region was investigated by the University of New Mexico at the McCormick Ranch Test Site (ref. IV-12). While it was hoped that focusing would enhance time durations and displacements, it was found that stresses and accelerations were enhanced more than velocities and displacements. Some results comparing Shot 3 (unfocused) and Shot 5 (focused) were previously given in table 14. Displacements were only increased an average of 34 percent while accelerations were increased

by over a factor of 2. Data from Shot 9A (unfocused) and Shot 10 (focused) showed similar results. The data from these events are significantly scattered and there are insufficient data for detailed empirical analysis beyond the general observations described above. Since focusing seems to have its greatest effect upon acceleration and only affects a limited region, its use in earthquake ground motion simulation seems limited. Therefore, further analysis is not performed herein. Since the focusing effect seems to be primarily a geometric phenomena it probably is susceptible to analysis with calculations, should earthquake simulation applications be identified in the future.

The use of explosives with longer burn times to extend the duration of the source was investigated by UCLA (refs. IV-16 and IV-17). Dynamites with detonation rates ranging from 6400 to 20,800 ft/sec were investigated. It was found that no significant difference in the measured peak motion amplitudes or time histories occurred. Hence, it appears that varying explosive burn times is not a significant means of altering ground motions.

Decoupling of explosives was investigated in the University of New Mexico studies (ref. IV-12) and is currently under investigation by Stanford Research Institute. In the University of New Mexico studies, decoupling was obtained by suspending PETN primacord in cylindrical cavities. Intimate coupling was obtained by grouting the primacord in place. Direct coupling comparisons were available from the results of Shots 6, 7 and 8, and have been described in the previous paragraphs dealing with cylindrical explosion data. Within the variations of the parameters investigated, no obvious increase in velocity or acceleration was apparent

from decoupling. Decoupled displacements, however, were about twice as high as those in the event where the explosive was grouted in place. There is insufficient data to analyze the effect quantitatively. However, the observation indicates a significant potential of decoupling. The effect should be investigated with further experiments and may be analyzable with calculations.

The decoupling research at SRI is now in progress and results are not yet available. It is understood, however, that their research is concerned with the containment of the explosion in a mechanical device which allows control of explosive gas venting. The objective is to reduce peak pressure and initial acceleration and increase time duration at the source.

Enhancement methods with greatest potential for immediate or near-term applications for earthquake ground motion simulation are the use of multiple explosions and the use of relief trenches or shock barriers in the medium. It appears from the analyses previously presented that the use of two-dimensional arrays allows a wide range of control over motion attenuation, frequency content and duration through variations in explosive loading density, array dimensions and target range. The number of cycles of motion and total motion duration, however, are limited in a single event and may not be sufficient for tests on some engineering structures. Significant acceleration cycles seem to be limited to about 4 and the corresponding velocity cycles to about 2. The use of multiply sequenced explosions appears to be a viable way of extending the number of cycles and the total duration. In Section II, the use of sequenced explosions by UCLA and by the Russians was described.

The result of both research programs indicated the feasibility of using multiple explosions. The available data from their experiments, however, does not allow quantitative analysis. In addition, the resulting motion amplitudes, although significant, were relatively low compared with current strong earthquake design levels. To obtain high level motion amplitudes while using explosive arrays of practical size, it appears necessary to place the explosive arrays as near to each other as possible. In addition, it will be important to predict the motion amplitudes and time histories to insure the experiment design meets requirements. The University of New Mexico recently conducted an experiment, called Mini-SIMQUAKE (ref. IV-15), to investigate these requirements on a relatively small scale. An elevation of the experiment is shown in figure IV-46. The objective of the experiment was to verify, on a small scale, the technical feasibility of sequentially firing two relatively close arrays containing relatively large amounts of explosive and to obtain ground motion data to aid in understanding the environment produced by multiple arrays.

The multiple array concept of UNM requires that the explosive arrays be fired from back to front so that each pulse is traveling through material which has not been cratered or seriously disturbed. Because of motion attenuation with distance, back arrays must be loaded with more explosives than arrays nearer the target point to maintain the same motion amplitude at the target. Obviously, the closer arrays can be placed to each other the less the amount of required explosives. However, with decreased array separation, unfired arrays will be severely loaded by the pulses from the previously fired arrays and there is

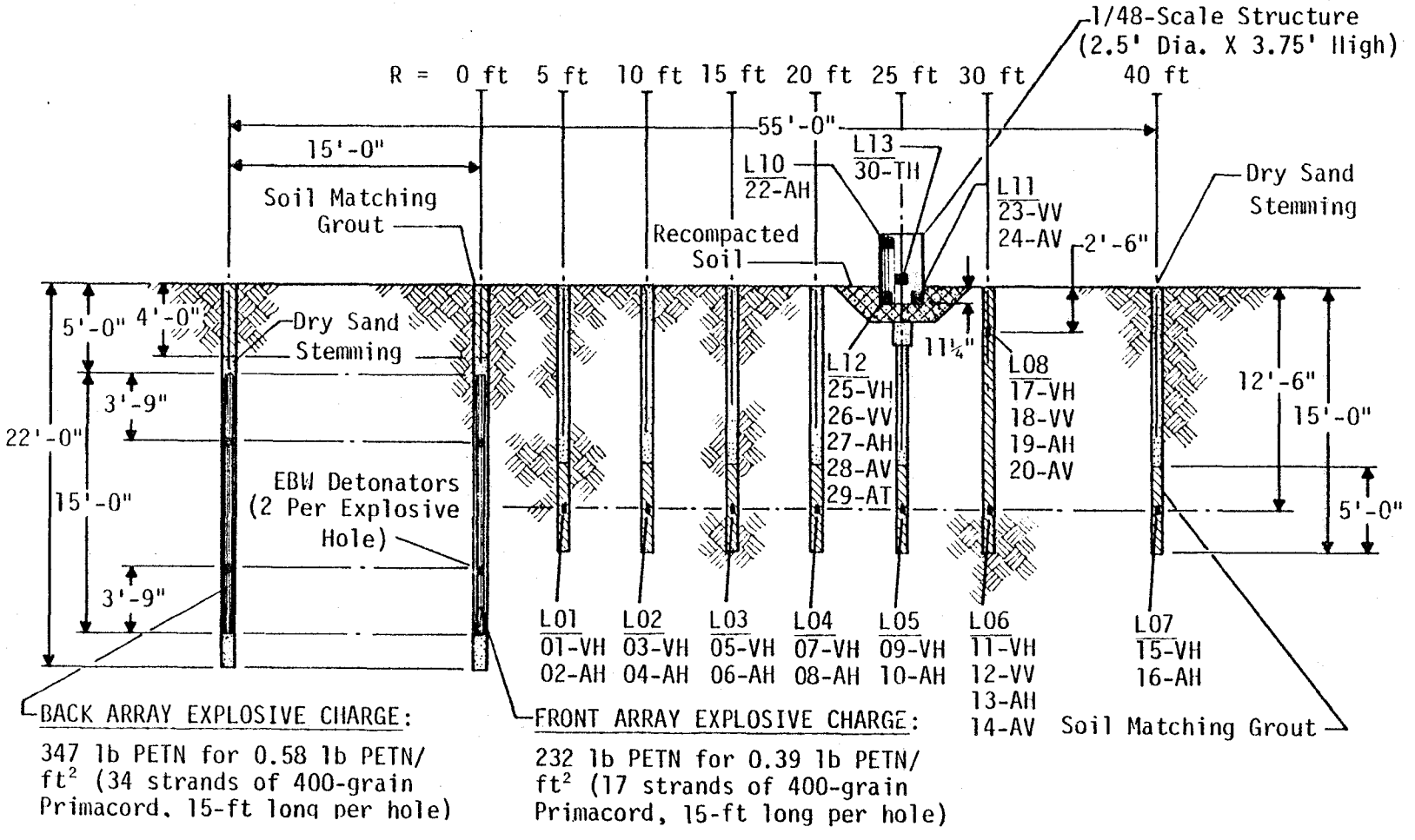

Figure IV-46. Elevation - Mini-SIMQUAKE (ref. IV-15)

technical concern about maintaining the integrity of the explosive and firing system of unfired arrays.

Mini-SIMQUAKE demonstrated that it is possible to closely space arrays of large amounts of explosive, but that the spacing must be carefully designed and special attention must be given to protection of the firing system. In addition, the experiment provided important data on rectangular explosive arrays both individually and in multiply sequenced experiments. The data was included in the planar array analysis presented previously, under the assumption that the arrays did not interact. The interaction of the arrays and a potential method for estimating effects is discussed below.

The most obvious method for estimating the effects of a multiple array experiment is the use of linear superposition. In linear superposition, the contribution of each array is estimated individually and then summed according to the array time phasing to obtain the combined result. Linear superposition for the horizontal velocity at the 30-foot range at the array mid-depth on Mini-SIMQUAKE is compared with the measured data in figure IV-47. The time delay between the arrays was set at 300 msec because the correlations for planar arrays indicated the duration of the back array (first) pulse would be about that amount. The predictions of figure IV-47 are based upon the correlations previously presented for single arrays and the pulse shape is fitted with straight lines. The back array arrival time was estimated from the site seismic velocity (1600 ft/sec). The front array arrival time was estimated as the range divided by the seismic velocity plus the 300 msec firing delay between arrays.

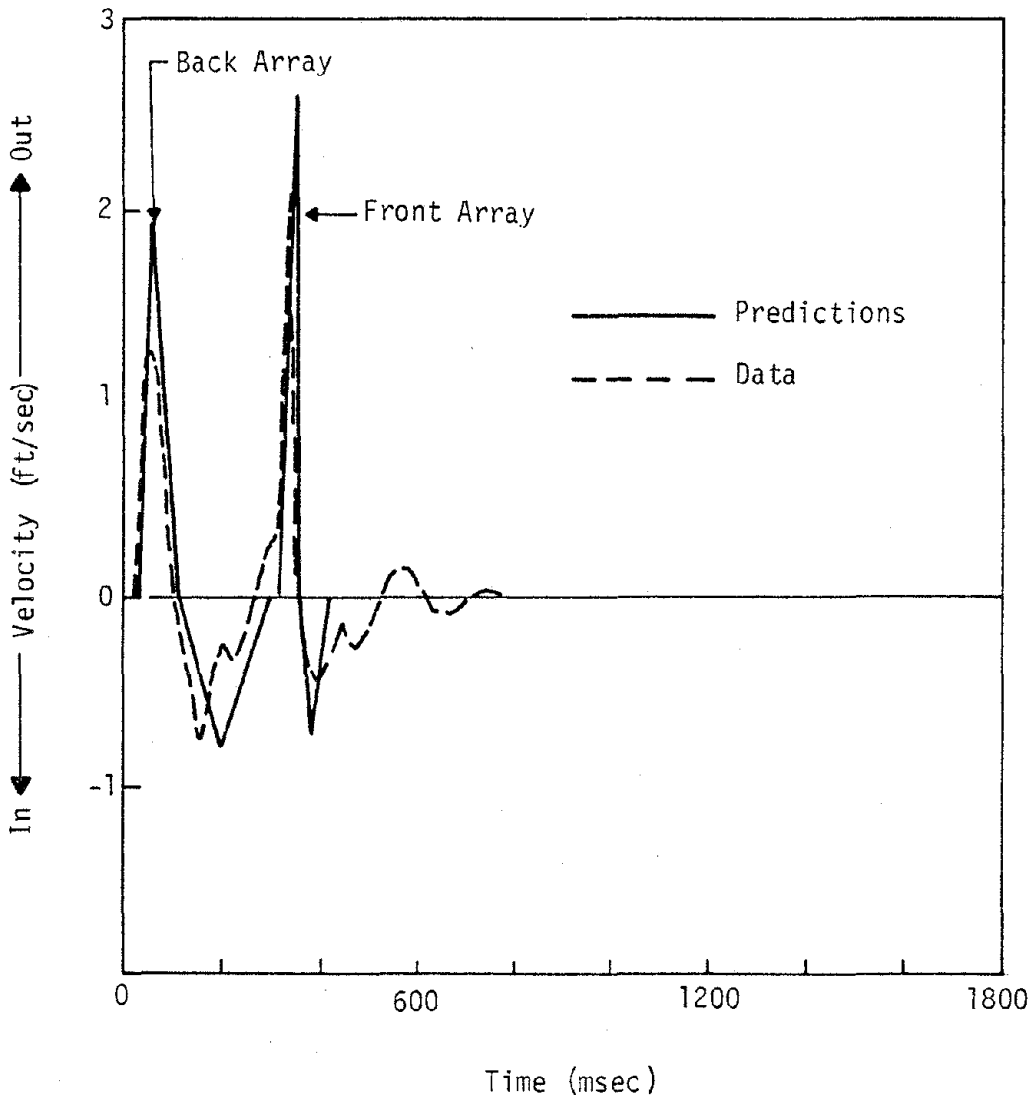

Figure IV-47. Comparison of Horizontal Velocity Prediction and Measurement on Mini-SIMQUAKE at 30-Foot Range

Several conclusions are evident from figure IV-47. First, the planar array correlations for velocity amplitudes are in good agreement with the data. Second, the characteristic time estimates for the back array pulse are in good agreement with the data. The outward phase duration prediction for the front array pulse is also in good agreement with the data, but the inward pulse and later oscillations are not predicted as well. Third, while it was assumed prior to the test that each array would generate a single significant velocity pulse, the data from the back array indicate that a second velocity cycle is beginning when the front array pulse arrives. This is the first set of planar array data to late times available, and it appears that two significant velocity cycles may be achievable from a single array. The fact that back array pulse motion was still in progress when the front array pulse arrived may be the cause of the late time disagreement between the prediction and the experiment. In general, the comparison between prediction and experiment is good and indicates that linear superposition appears to be a reasonable way of estimating combined effects. Of course, further data would be desired to substantiate this conclusion.

The use of relief trenches and relief holes as a means of increasing displacements and lengthening motion durations was also investigated by UNM (ref. IV-12) and briefly described in Section II. A relief trench effectively provides a free-surface from which the incident wave reflects and travels back into the initially loaded region. The reflected wave, in turn, might be expected to cause a second outward motion pulse. The use of relief holes was investigated because of the cost and difficulty associated with constructing a relief trench to relatively large

depth.

Figures IV-48 and IV-49 show measured horizontal velocity in time histories on Shots 9 and 13. The characteristics of these shots were given previously in table IV-13 and figure IV-25, and measured amplitude data in figure IV-26. It can be seen in figure IV-48 that the effect of relief is to greatly increase the time duration of the outward velocity phase at all ranges and significantly increase the velocity amplitude at ranges near the trench. Figure IV-49 shows similar effects on the trench side, but lesser effects on the hole relieved side.

DIP IIIA (ref. IV-18) was a larger test of boundary relief than Shots 9 and 13 and its characteristics were given previously in table IV-15 and figure IV-34. As in Shot 13, one side of the event was trenched while the other was relieved with drill holes. The velocity and displacement data from DIP IIIA are compared with predictions using equation IV-47 (no enhancement) in figure IV-50. Acceleration data were few and of poor quality and could not be compared. It can be seen in figure IV-50 that the velocity data scatters about the prediction except at ranges near the trench where the trench data is higher than the prediction and the hole relieved data by about 30 to 50 percent. The trench and hole relief displacements are markedly higher than the predictions at all ranges.

Velocity time history predictions for DIP IIIA were developed by superimposing an initial pulse prediction based upon the planar array correlations of previous paragraphs and a reflected pulse from the trench or relief holes. The measured data at two ranges are compared with no

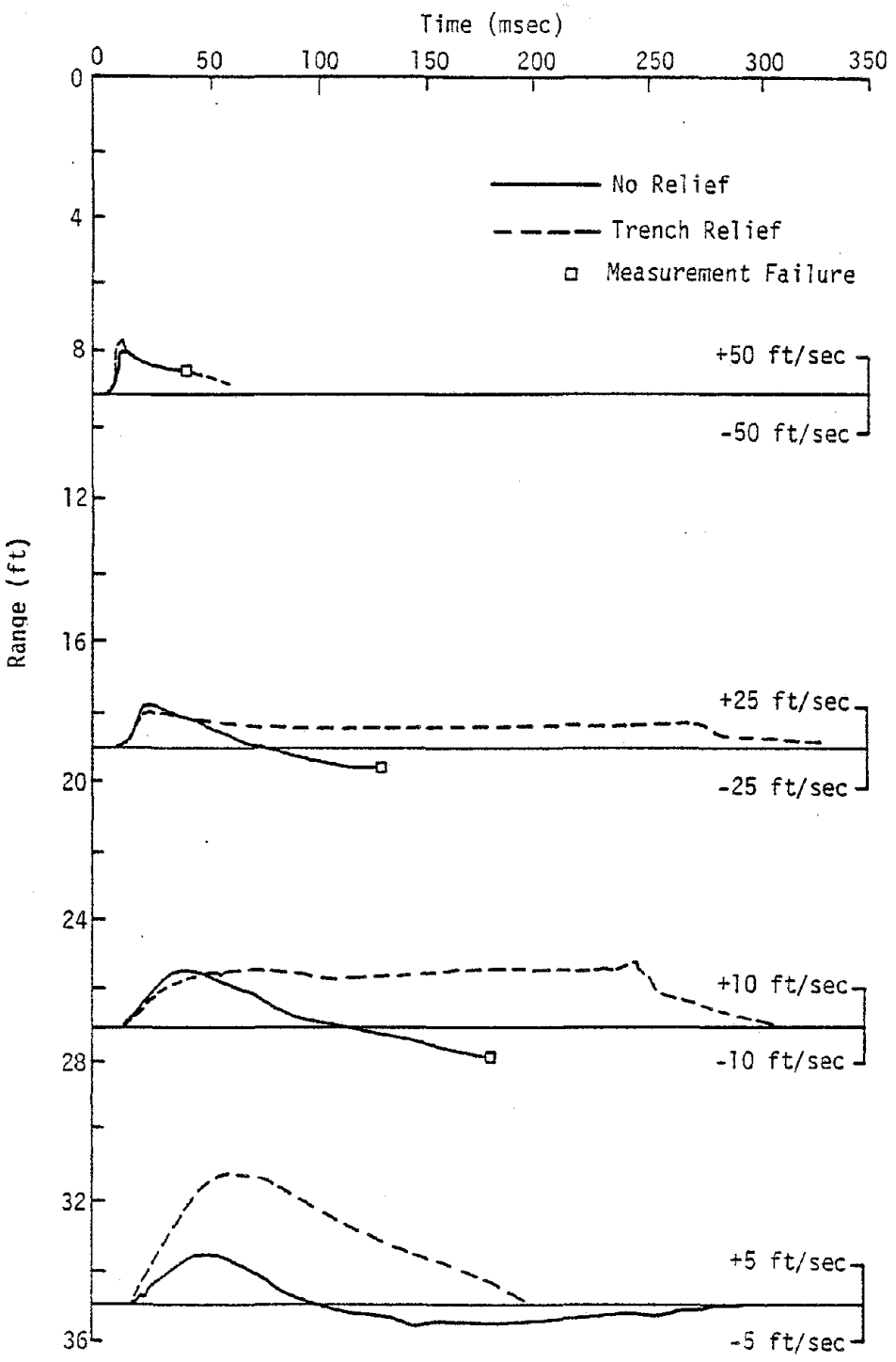

Figure IV-48. Shot 9 Horizontal Velocity Time Histories

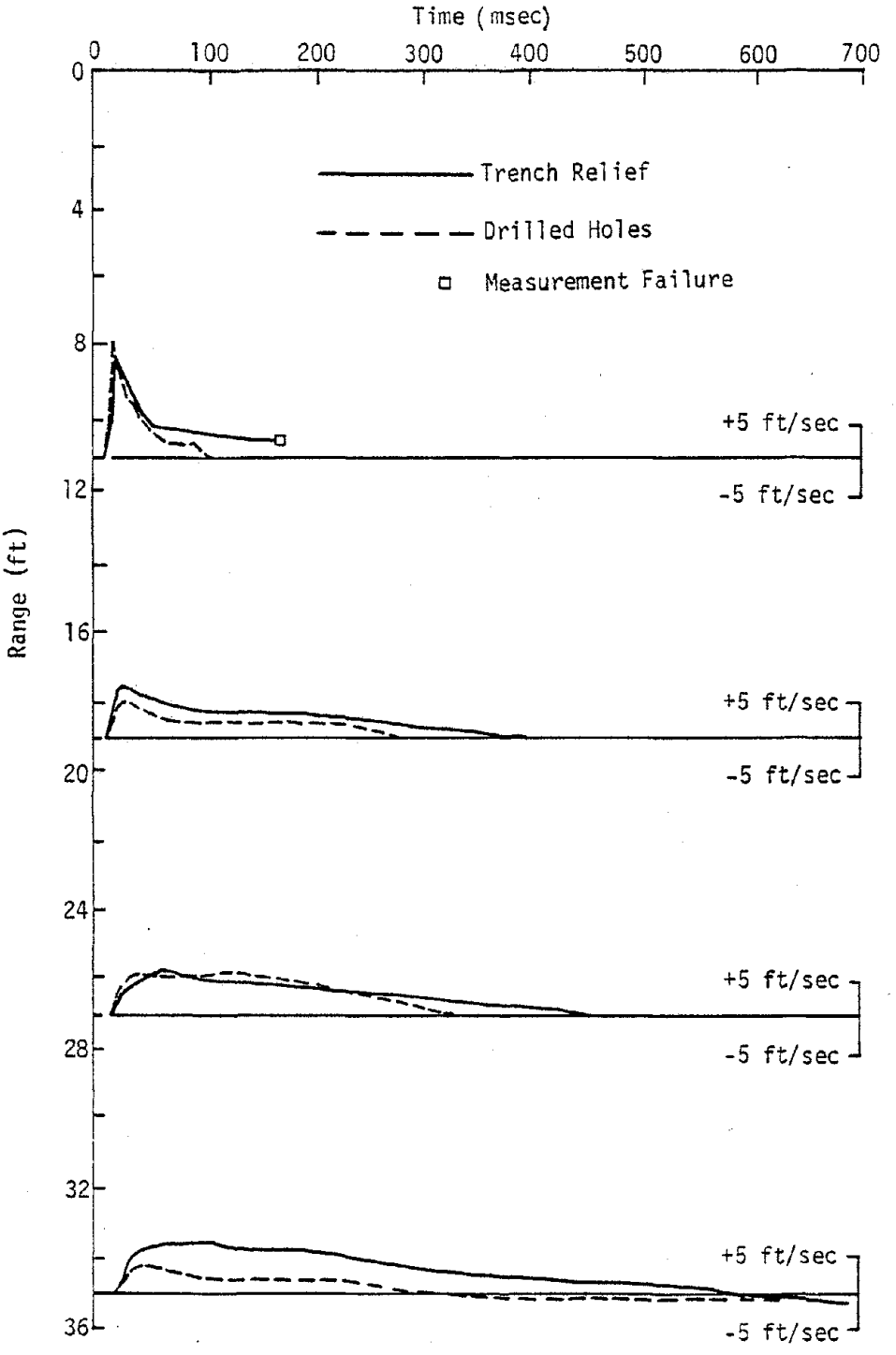

Figure IV-49. Shot 13 Horizontal Velocity Time Histories

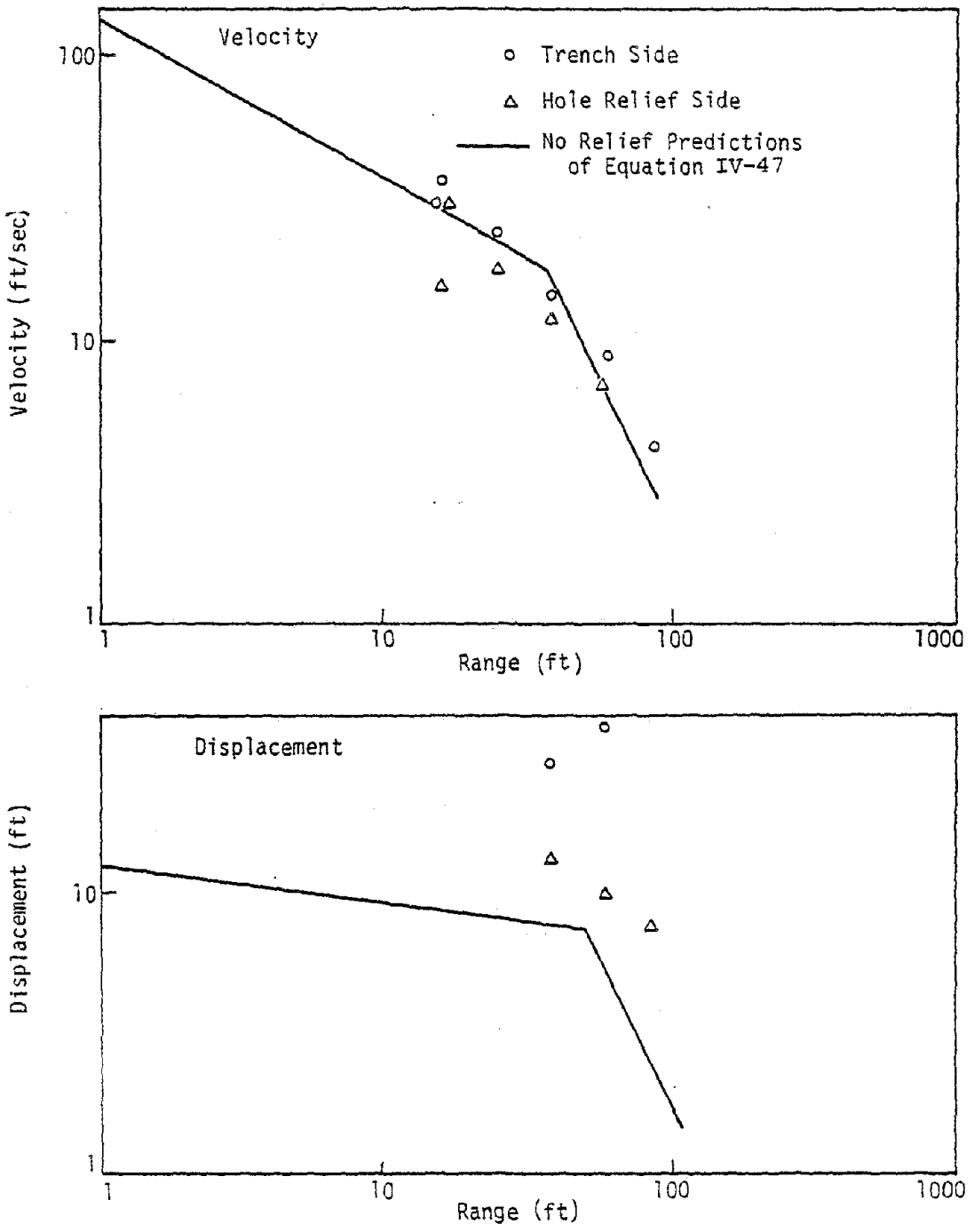

Figure IV-50. Horizontal Velocities and Displacements on Centerline of DIP IIIA

relief time history predictions in figure IV-51. Peak outward velocity amplitude agreement is reasonable and probably within the scatter that might be expected in a single experiment. Waveform agreement for the hole-relief data is also reasonable at the 39-foot range. However, at the 61-foot range, the outward velocity pulse on the hole-relief side seems to have a rounder peak which leads to a larger displacement. The trench data have a very long outward phase and do not agree well with the no-relief prediction.

The predicted velocity time history at the 100-foot range trench location (also shown in figure IV-51) was used to estimate a reflected pulse which could be combined with the initial pulse for a better estimate of the relief effect. There are too few data to estimate the reflection details and its attenuation as it propagates back into the test area. It was assumed that simple reflection occurred and no attenuation took place as the pulse propagated. The simple reflection predictions are compared with the measurements in figure IV-52. It can be seen that the reflection broadens the predicted pulse at both ranges. At the 61-foot range, this brings the prediction into good agreement with the hole-relief data and at the 39-foot range broadens the pulse so that it is similar in shape to the hole-relief data initially. At neither range, however, does the prediction even crudely approximate the trench-relief data. It appears that the use of a relief trench causes extensive shear flow which leads to outward velocities of very long duration. This phenomena cannot be approximated with a simple reflection assumption. Simple reflection does, however, seem to predict the hole relief effect although additional data are required to improve the prediction

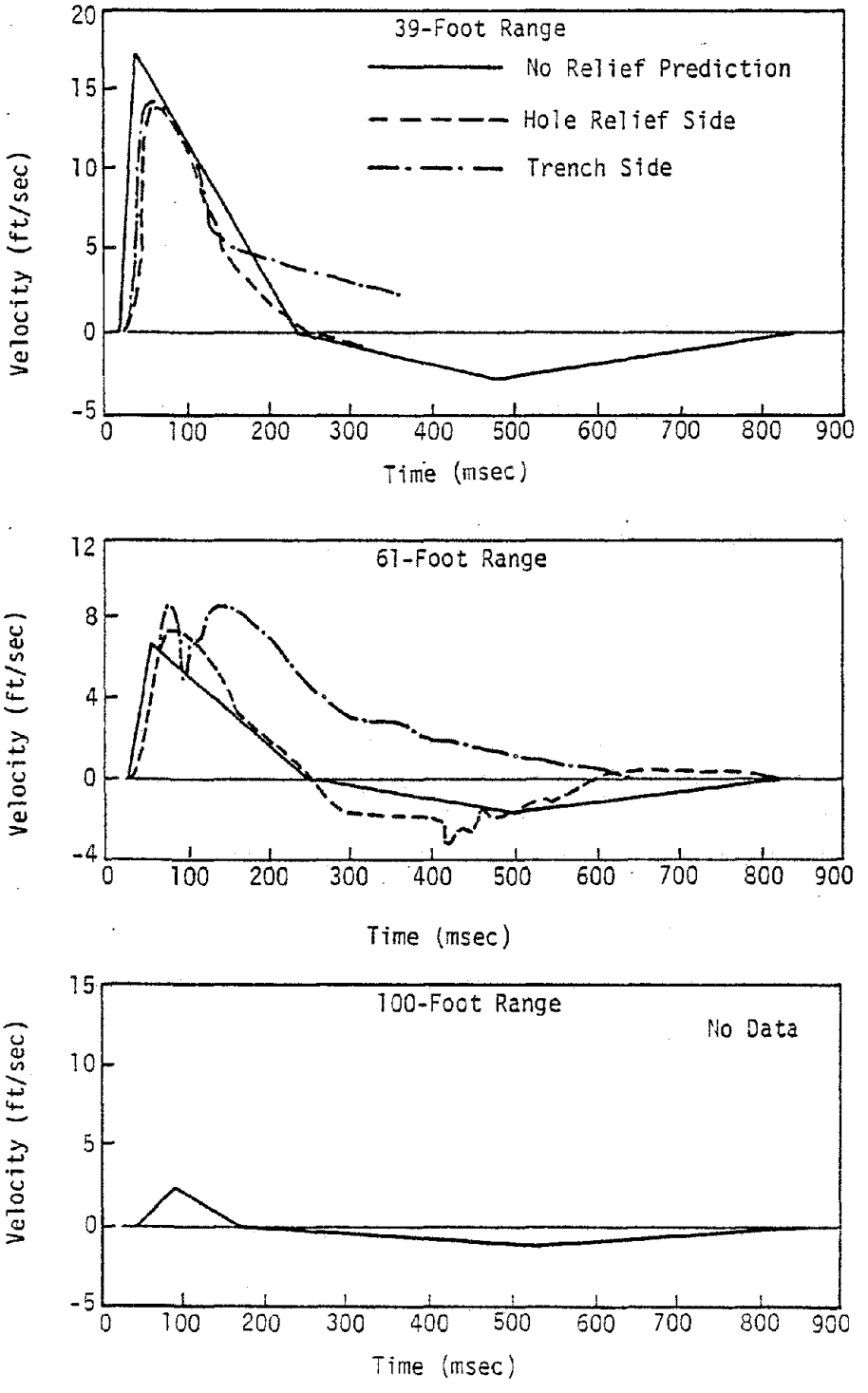

Figure IV-51. Some DIP IIIA Velocity Time Histories Compared with Predictions Assuming No Relief

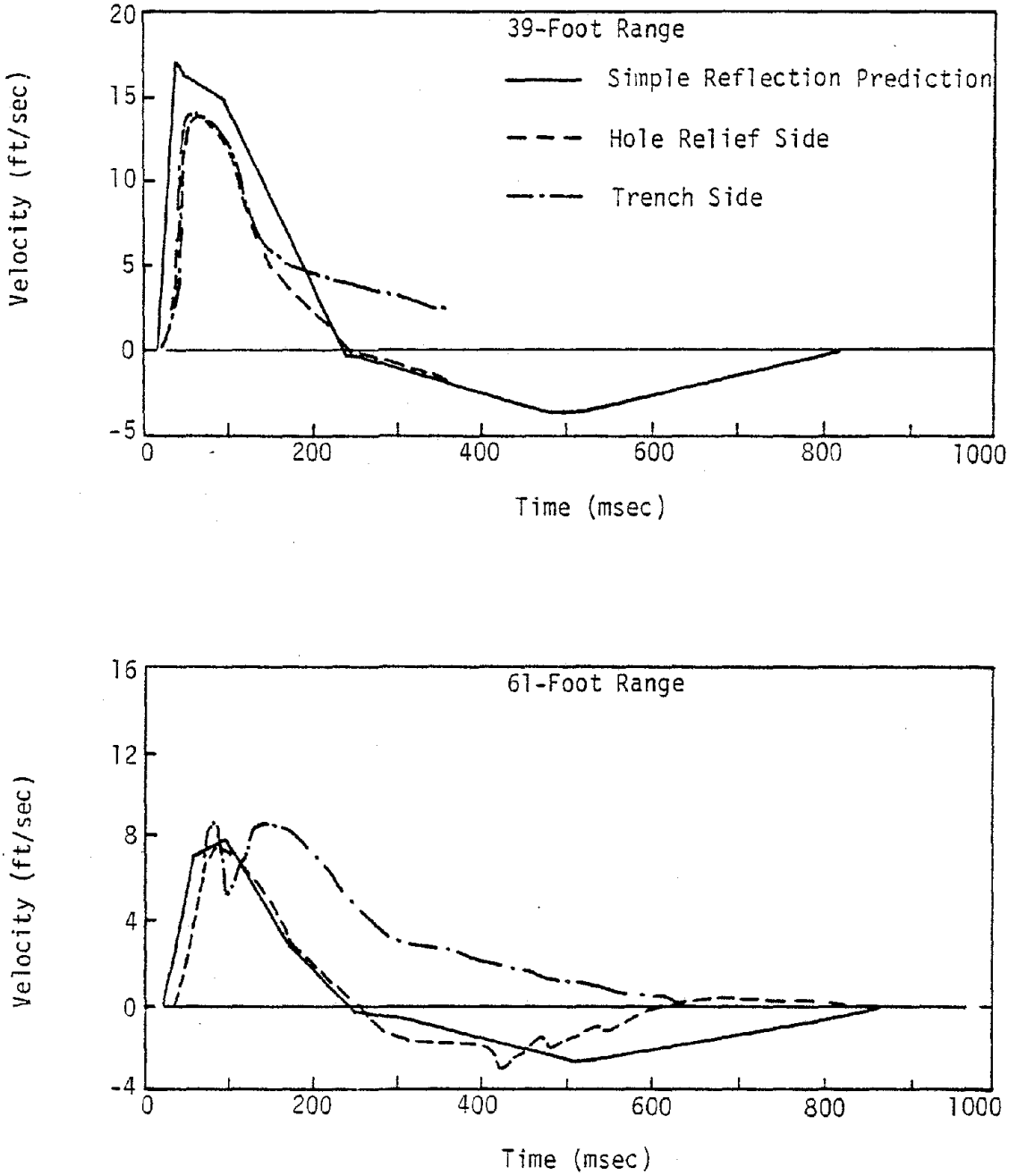

Figure IV-52. Some DIP IIIA Velocity Time Histories Compared with Predictions Assuming Simple Reflection from Relief Region

of the reflection and, especially, its attenuation. It appears that relief holes do cause a relief reflection, but the support between holes limits the large outward shear flow caused when a complete open trench is used.

While relief trenches enhance velocities and displacements and cause little effect upon accelerations, the use of strong reflecting barriers or shock shields in the media might be expected to reduce accelerations and cause lesser effect upon velocities and displacements. The motions of geologic media beneath rigid masses which are acted upon by shock inputs are discussed in reference IV-10 in connection with structure-media interaction for nuclear loads. The one-dimensional response of a rigid mass on elastic soil to a triangularly decaying shock is shown in non-dimensional form in figure IV-53. It can be seen that an increase in the mass of the block will cause a decrease in the peak velocity of the block (and soil immediately beneath the block) and a lengthening of the duration of the motion of the block. The peak acceleration of the mass and soil (represented by the initial slope of the velocity-time histories) also decreases. Peak acceleration of soil not shielded by a rigid mass would theoretically be infinite while the peak acceleration with a rigid shield is simply the peak pressure (P_m) divided by the mass per unit area of the rigid shield. These theoretical results suggest that it may be possible to achieve a substantial decrease in peak acceleration without causing a major drop in velocity.

Reference IV-19 presents results of shock tube experiments with shock shields designed to reduce the loads delivered to buried structures in nuclear problems. The problem is basically the same as that

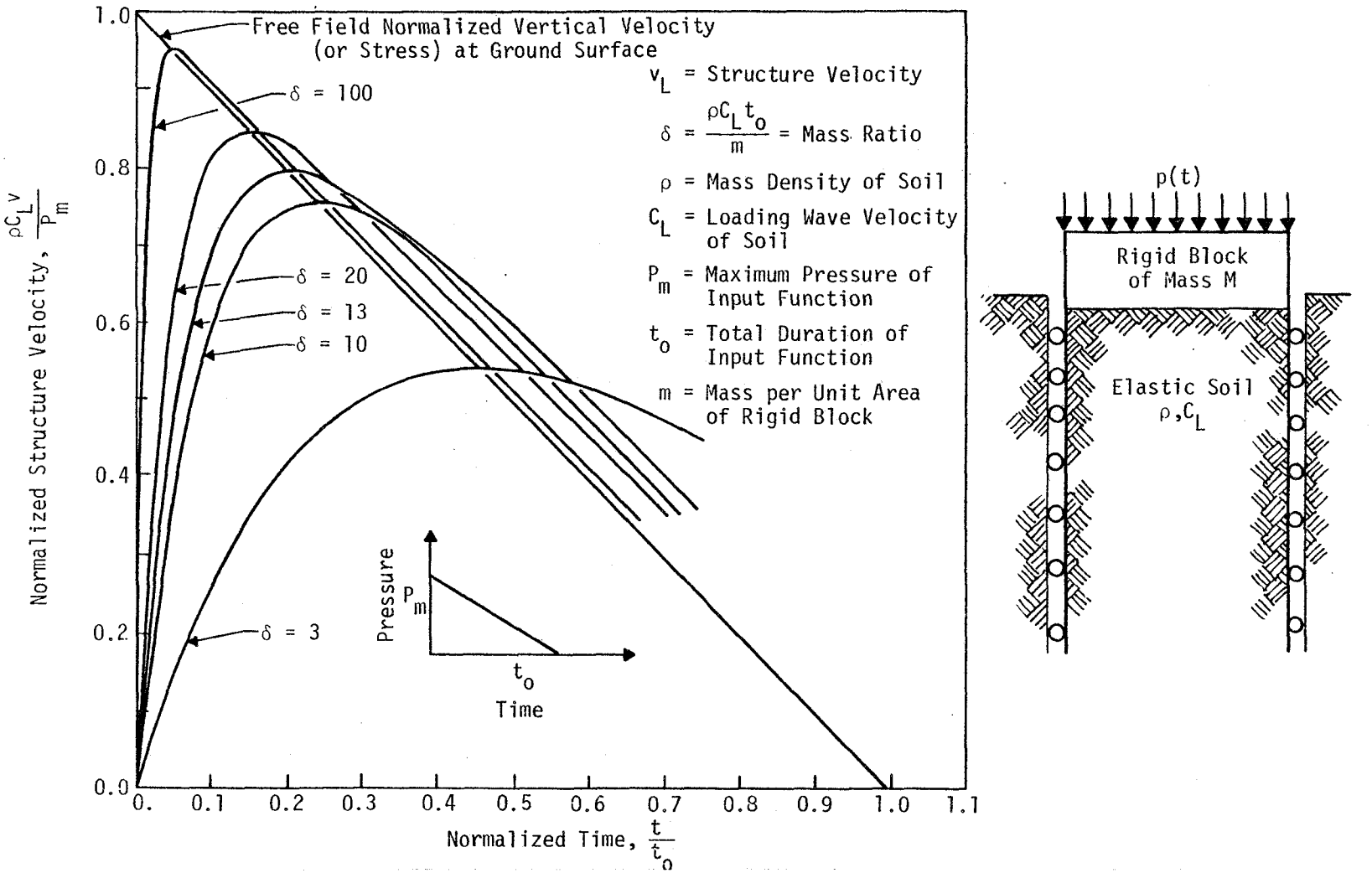

Figure IV-53. Normalized Response of Rigid Mass on Elastic Soil-Triangular Decaying Input Pressure (ref. IV-10)

described above, and some acceleration results are presented in figure IV-54. It can be seen that a 2-foot thick concrete shock shield at the surface reduces peak accelerations on the order of a factor of 2 to 3. Velocity measurements on the same experiments indicate a reduction of peak velocity of about 20 to 30 percent.

The solution for the peak velocity and the time of peak velocity for the problem shown in figure IV-53 is (ref. IV-10).

$$\frac{\rho C_L v_m}{P_m} = 1 - \tau_m \qquad \text{(a)}$$

$$\tau_m = \frac{1}{\delta} \ln(\delta + 1) \qquad \text{(b)} \qquad \text{(IV-49)}$$

$$\delta = \frac{\rho C_L t_o}{m} \qquad \text{(c)}$$

where

P_m = maximum pressure of the input function

ρ = mass density of soil

C_L = loading wave velocity of the soil

v_m = maximum velocity of mass

τ_m = normalized time at which maximum velocity occurs = t_m/t_o

t_o = total duration of input pressure function

This solution may be used to determine if the acceleration reduction of figure IV-54 is predictable by the simple one-dimensional theory. The idealized input pressure time history for the shock shield experiments is shown in figure IV-55. It appears that the early time behavior may be represented by a triangular pulse with duration, t_o, of 0.004 seconds.

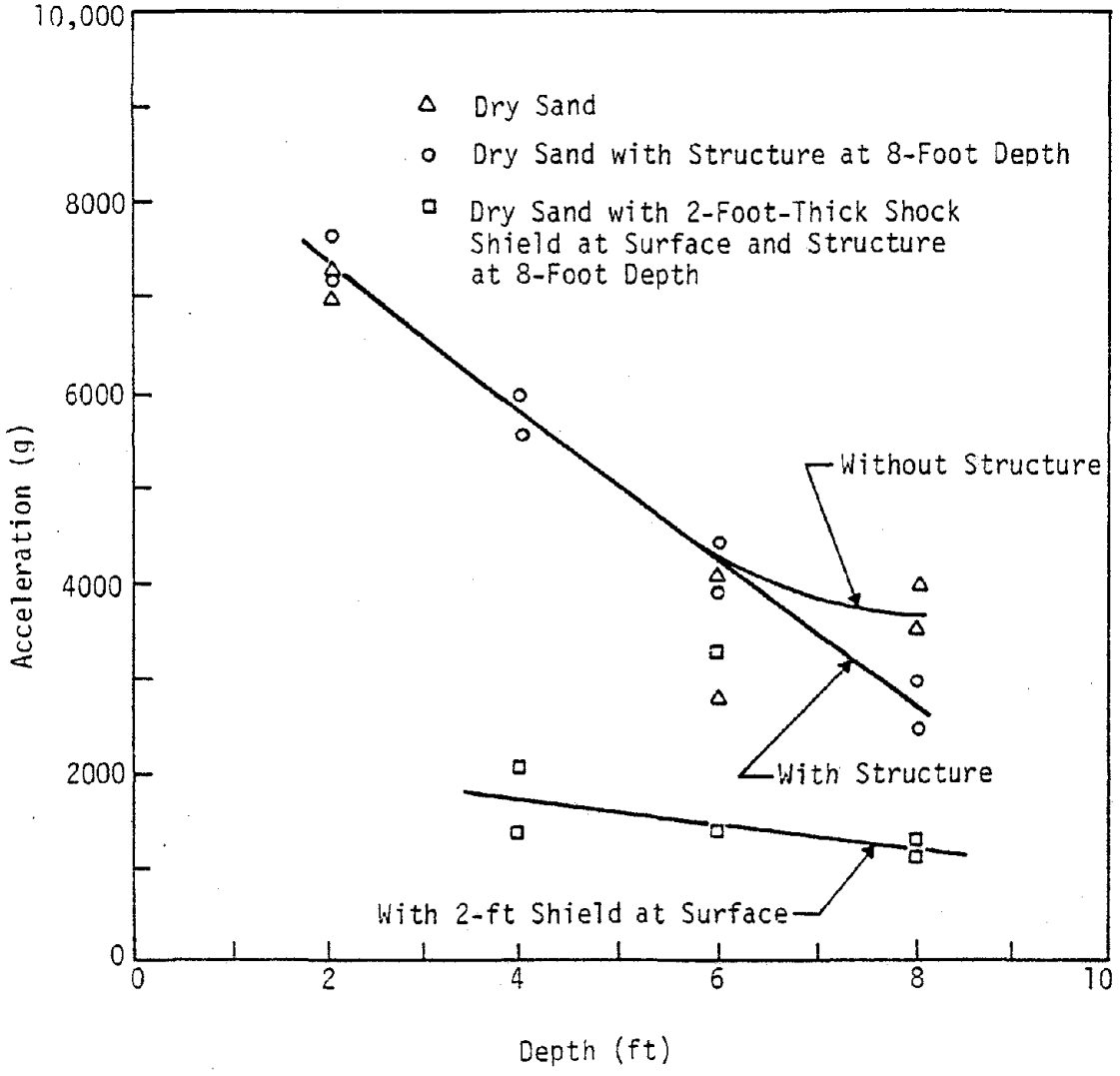

Figure IV-54. Effect of Shock Shield Upon Peak Accelerations (ref. IV-19)

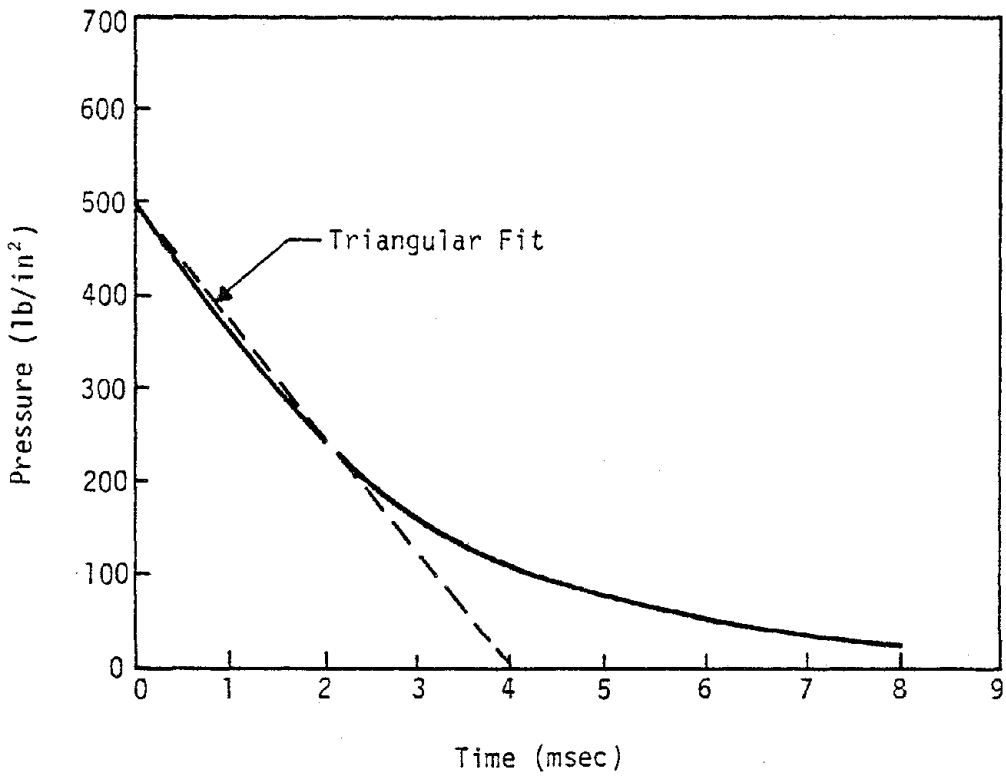

Figure IV-55. Input Pressure Time History for Shock Shield Experiments of Reference IV-19

The soil used in the shock shield studies was Ottawa sand and reference IV-19 gives its mass density, ρ, as 3.48 lb-sec^2/ft^4 and its uniaxial secant modulus associated loading wave velocity C_L, as about 1500 ft/sec. Taking the weight density of concrete to be 150 lb/ft^3, the mass ratio, δ, can be computed to be about 2.2. The normalized time of peak velocity is then 0.53 and the normalized peak velocity 0.47. Using equation IV-46 to compute acceleration, the peak acceleration of the mass would be

$$a = 2\,\frac{v_m}{\Delta t_r} = 2\,\frac{0.47\left(\frac{P_m}{\rho C_L}\right)}{0.53\ t_o} = 1.77\,\frac{P_m}{\rho C_L t_o} \qquad \text{(IV-50)}$$

In the absence of the mass, the peak acceleration near the surface can be estimated by assuming a 1 millisecond rise time (ref. IV-10), so that

$$a = 1.15\,\frac{P_m}{\rho C_L \left(\frac{0.001}{0.004}\right) t_o} = 4.60\,\frac{P_m}{\rho C_L t_o} \qquad \text{(IV-51)}$$

Hence, near the surface, the introduction of a 2-foot shock shield would be expected to reduce peak acceleration to about 38 percent the free-field value. A similar reduction might be expected to occur at depth. There are no acceleration measurements near the surface for the 2-foot shock shield, but the measurements at 4, 6 and 8 feet in figure IV-54, show accelerations with the shock shield to be about 30 to 34 percent of those without the shock shield. This result suggests that the simple one-dimensional theory seems adequate for estimating acceleration.

It should be noted that although the relative acceleration amplitudes seem to be predicted quite well, absolute acceleration computed

by the relations above are well below the measurements of reference IV-19. Indeed, the acceleration measurements seem to be exceedingly high for the input pressure of 500 lb/in^2. The cause of this discrepancy is not known. However, the relative differences shown by the data and by the analysis are believed to be correct.

There appears to be a practical limitation to the use of shock shields for large experiments which may require explosives to extend to several tens of feet. The construction of a concrete shock shield in front of such a large array would appear to be quite costly. It may be possible, however, to construct a smaller shield in the vicinity of the structure of interest at a more practical cost. Should shock shields appear potentially useful in the future, then further analysis to reconcile the acceleration discrepancy noted above, and additional data will be necessary to further verify design procedures.

7. SUMMARY OF CONCLUSIONS FROM DATA ANALYSIS AND MAJOR UNCERTAINTIES

a. General

Previous paragraphs have presented basic data and empirical analyses of data on dry silts and sands with potential application to the simulation of earthquake-like ground motions. Where possible within the data, an attempt was made to quantify relations which can be used for design and prediction of experiments. Emphasis was given to peak amplitude parameters and characteristic times as well as to complete velocity waveforms. Although there is a substantial amount of data available, many of the proposed relationships and especially the waveforms, are subject to considerable uncertainty. The major uncertainties

are summarized below and these uncertainties provide the basis for the theoretical calculation program described in the next section.

b. Spherical Correlations

A gravity scaling term was required to explain the response in the spherical experiments over a wide range of yields. Displacements and characteristic times of the horizontal velocity pulse were especially affected. This aspect of the analysis is unique compared to previous investigations and it would be desirable to have expanded experimental and theoretical verification. Due to a lack of sufficient data, there are also significant uncertainties associated with the vertical near-surface motion components in spherical experiments.

c. Cylindrical Correlations

The cylindrical data appeared to manifest a transition from cylindrical to spherical behavior which was related to the finite height of the explosive. Additional verification of the attenuation rates and the location of the transition region is required. In addition, more information on characteristic times, the overall horizontal waveform, especially late time features, vertical components and the variation of the motion components with range and depth is needed.

d. Planar Correlations

The planar data seemed to manifest a transition from planar to cylindrical behavior which, as with the cylindrical data, was related to the finite height of the explosive. This behavior requires additional verification before high confidence in the qualitative and quantitative

relations presented can be achieved. In addition, as with the spherical and cylindrical cases, much more information is required on characteristic times, vertical components, waveforms and their variations with range and depth. Cross-range variation information is also needed.

e. Enhancement

The available data on enhancements are generally only sufficient to indicate trends and potential uses. Much more quantitative information over a greater range of parameters is required before the full value of enhancement can be evaluated, and enhancement design can be accomplished. The possible exception is the use of multiple explosions which definitely appears feasible and analyzable based upon available data. Decoupling requires further data and calculations. Calculations on use of relief procedures and shock shields are presented in Section VI. Additional data is required to substantiate results of these calculations.

8. REFERENCES

IV-1 Sedov, L.I., Similarity and Dimensional Methods in Mechanics, Academic Press, New York and London, 1959.

IV-2 Baker, W.E., et al, Similarity Methods in Engineering Dynamics, Sparton Books, Hayden Book Company, Inc., Rochelle Park, N.J., 1973.

IV-3 Murphy, G., Similitude in Engineering, The Ronald Press Co., New York, 1950.

IV-4 Buckingham, E., Model Experiments and the Forms of Empirical Equations, Spring Meeting, American Society of Mechanical Engineers, June 1915.

IV-5 Hendron, A.J., Scaling of Ground Motions From Contained Explosions in Rock for Estimating Direct Ground Shock from Surface Bursts on Rock, Technical Report No. 15, Omaha District Corps of Engineers, Omaha, Nebraska, January 1973.

IV-6 Sachs, D.C. and Swift, L.M., Small Explosion Tests, Project Mole, Vols. I and II, Final Report AFSWP-291, Stanford Research Institute, Menlo Park, California, December 1955.

IV-7 Lampson, C.W., "Explosions in Earth," in Effects of Impact and Explosion, Summary Technical Report of Division 2, National Defense Research Committee, Vol. I, Washington, D.C., 1946.

IV-8 Simmons, K.B., DIHEST Improvement Program Tests DIP IVA and DIP VA, AFWL-TR-74-238, Air Force Weapons Laboratory, Kirtland AFB, New Mexico, April 1975.

IV-9 Seusy, E., Private Communication, Air Force Weapons Laboratory, Kirtland AFB, New Mexico, January 1977.

IV-10 Crawford, R.E., Higgins, C.J. and Bultman, E.H., The Air Force Manual for Design and Analysis of Hardened Structures, AFWL-TR-74-102, Air Force Weapons Laboratory, Kirtland AFB, New Mexico, October 1974.

IV-11 Kuzmina, N.V. et al, "Seismic Effect of Eruptive Explosions in Nonrock Coherent Ground," Problems in Engineering Seismology, Edited by S.V. Medvedev (Translation from Russian), Consultants Bureau, New York, 1966.

IV-12 Simmons, K.B., Soil DIHEST Motion Enhancement Techniques, AFWL-TR-72-233, Air Force Weapons Laboratory, Kirtland AFB, New Mexico, September 1973.

IV-13 Bratton, J.L., Fedock, J. and Higgins, C.J., An Evaluation of the Parameters Affecting Cylindrical Wave Propagation in Geologic Materials, AFWL-TR-77-184, Air Force Weapons Laboratory, Kirtland AFB, New Mexico, August 1977.

IV-14 Schlater, D.R., DIHEST Improvement Program Test DIP IIA, Data Report, AFWL-TR-72-35, Air Force Weapons Laboratory, Kirtland AFB, New Mexico, April 1972.

IV-15 Higgins, C.J., Simmons, K.L., Pickett, S. and Crawford, R.E., Quick-Look Report on Mini-SIMQUAKE, A Small Explosive Test Designed to Simulate Earthquake-Like Ground Motions, Univeristy of New Mexico Report to the Electric Power Research Institute, Palo Alto, California, May 1977.

IV-16 Bleiweis, P.B., et al, "Simulation of Strong Motion Earthquake Effects on Structures Using Explosive Blasts," Nuclear Engineering and Design, Vol. 25, pp. 126-149, 1973.

IV-17 Chrostowski, J. et al, Simulating Strong Motion Earthquake Effects on Nuclear Power Plants Using Explosive Blasts, UCLA-34P193-1-, UCLA-ENG-7119, Nuclear Energy Laboratory and Earthquake Engineering and Structures Laboratory, School of Engineering and Applied Science, University of California at Los Angeles, February 1972.

IV-18 Schlater, D.R., DIHEST Improvement Program Test DIP IIIA, Data Report, AFWL-TR-74-16, Air Force Weapons Laboratory, Kirtland AFB, New Mexico, April 1974.

IV-19 Kvammen, A., An Experimental Investigation of Shock Shields, AFWL-TR-69-65, Air Force Weapons Laboratory, Kirtland AFB, New Mexico, December 1969.

Page Intentionally Left Blank

SECTION V
NUMERICAL CALCULATIONS

1. METHODOLOGY AND ASSUMPTIONS

The empirical analyses of the previous section resulted in approximate relations between the major experiment parameters (yield, geometry, etc) and various aspects of the ground motion environment. The level of confidence in the relations varies depending upon the amount of available data. There are remaining uncertainties regarding many parameters especially transition ranges, characteristic times, and vertical motion components. These uncertainties can only be resolved by additional data or theoretical analysis. Theoretical solutions to these problems, which must consider inelastic material behavior, are not available and their development appears beyond the current state-of-the-art. Field experiments, on the other hand, are quite expensive and several would be required to allow an adequate variation in parameters.

The use of finite difference or finite element calculations as a source of numerical experiments is an alternate to field experiments. The calculation output can be viewed as measured data from an experiment and analyzed by the same methods used to analyze field data. This approach suggests that calculations can substitute for experiments on a one-to-one basis at only a fraction of the cost of field experiments. In addition, numerical calculations are not limited by the relatively few instrument locations practical in actual experiments and do not con-

tain the large random measurement scatter encountered in the field.

The use of numerical calculations was the approach selected in this study to aid in resolving some of the uncertainties associated with the empirical correlations. The same empirical or semi-empirical concepts derived from phenomenological evaluations and dimensional analysis were applied to the numerical output. The scaled results, in turn, were used to evaluate the relationships between the calculated ground motions and the major input variables.

Although calculations are known to have quantitative limitations due to finite zone size, input source and material property uncertainties and geometry limitations (e.g. when two-dimensional models are used for three-dimensional problems), calculations are qualitatively correct for the problem modeled and do provide correct relative quantitative variations as input parameters are varied. The relationships derived from calculational results can be empirically modified to adjust for their limitations by using the available measured data.

The major parameters selected for evaluation with calculations were:

(a) Nondimensional scaling terms relating source characteristics to motion parameters in spherical, cylindrical and planar geometry.

(b) Attenuation rates in inelastic silts and sands in spherical, cylindrical and planar geometry.

(c) The effect of source coupling on motion amplitude in cylindrical geometry.

(d) The relation between finite cylindrical and planar charge size and the transition range for ground motion parameters.

(e) Peak Vertical response in the near-surface region of planar events.

The evaluations were limited to dry granular material since most available data are in such material and dry alluvial sites are prime candidates for initial simulation tests.

2. THE CODES USED

The problems of interest are all, ultimately, two or three-dimensional. Spherical explosions will be influenced by the free-surface after some time and become two-dimensional. Cylindrical explosions will also be influenced by the free-surface and, in addition, will be influenced by the finite length of explosive, both effects causing two-dimensional effects. Planar explosions will be influenced in a similar manner by the free-surface and finite explosive height, but, in addition, will be influenced ultimately by the finite width of explosive, leading to three-dimensional effects. In spite of the ultimate two or three-dimensional nature of the problems, a lesser number of dimensions can be used to analyze many of the effects of interest. One-dimensional spherical, cylindrical or planar geometry can be used to evaluate scaling terms and the effect of material nonlinearity on scaling. Two-dimensional calculations can be used to evaluate the effect of finite explosive height and free-surface effects in cylindrical or planar problems. In assessing three-dimensional effects, it is often possible to infer the difference between two and three-dimensions from the difference between one and two-dimensions. Only one and two-dimensional calculations were performed in this study. Three-dimensional calculations may be desirable in the future to verify some of the conclusions herein should such calculations appear

practical.

The one-dimensional calculations were made with the WONDY IV code (ref. V-1). WONDY IV is a wave propagation code which solves the finite difference analogs to the one-dimensional differential equations of motion in Lagrangian coordinates. The geometry can be spherical, cylindrical or rectangular (planar). In all cases, motion is restricted to one direction but, in cylindrical and spherical geometry, appropriate circumferential strains are included. The artificial viscosity method is used to maintain stability in the vicinity of strong stress gradients.

WONDY IV has the ability to handle any equation-of-state desired by the user. In addition, there are several equations-of-state included in the code including an ideal gas, and an ideally elastic-plastic-hydrodynamic material. The equations-of-state used in the calculations were the ideal gas and a special non-linear, plastic equation-of-state for soils. The soil equation-of-state and the specific parameters for the material of interest are described in a later paragraph. WONDY IV can be initiated by boundary conditions (e.g. pressures), initial conditions or both. Input conditions in this study are also explained in a later paragraph.

Output from WONDY IV can be obtained in either printed or plotted form. Plotted form is the most convenient, and plots of stress and velocity versus time and stress path at each target point of interest were obtained for this study. Typical plotted output for a target point in a spherical problem is given in Appendix D.

The two-dimensional code used was TOODY II (ref. V-2), which solves

finite difference analogs to the two-dimensional Lagrangian equations of motion. The code may be used under either rectangular (plane strain) or axisymmetric conditions. Both WONDY IV and TOODY II were written at Sandia Laboratories. As a result, both codes contain similar features with regard to input, output, boundary condition and equation-of-the-state options. Further details on WONDY IV and TOODY II, including mathematical development, assumptions and input instructions can be found in references V-1 and V-2, respectively.

3. ASSUMED EXPLOSIVE SOURCE

The detonation process involves the conversion of explosive material to gases and condensates in a very short period of time and with the release of large amounts of chemical energy. After detonation, the chemical energy resides in the explosion products in the form of internal energy. This internal energy is manifested physically through high pressure and temperature in the explosion products and, possibly, vaporized material from the surrounding medium. The products exert pressure on the surrounding material which, in-turn, expands allowing the pressure to drop until an equilibrium condition between the pressure and the surrounding medium is reached or, if the explosion is near the surface, the explosion vents to the atmosphere.

The explosion process was approximated in some of the calculations with an ideal gas model. This model assumed that the explosive material was instantaneously converted to an ideal gas containing the available energy of detonation. The initial volume of the gas was taken as the initial volume of the cavity containing the explosive. Both the gas and the surrounding soil were modeled in the calculations and their

behavior was calculated simultaneously in the code. The ideal gas equation-of-state is especially simple and is given by

$$pv^{\gamma} = \text{constant} \qquad \text{(V-1)}$$

where

p = pressure

v = specific volume

γ = ratio of specific heats

The pressure is given by

$$p = (\gamma - 1)\rho\varepsilon \qquad \text{(V-2)}$$

where

ρ = initial density

ε = initial energy per unit mass (specific energy)

and the sound speed is given by

$$c = \sqrt{\gamma(\gamma - 1)\varepsilon} \qquad \text{(V-3)}$$

Equations V-1, V-2, and V-3 may be used to establish the initial conditions in the cavity from the initial values of energy and density.

The explosives of interest are TNT, PETN, AN slurry and ANFO. Average values used for density and available energy for these explosives are given in table V-1. The values were selected as representative values from the ranges given in Appendix A. A ratio of specific heats, γ, of 1.32 was used for all explosives. Although γ is known to vary from explosive to explosive and to be a function of temperature and pressure, little is known about its actual value and variation for the explosives

considered here. The range of γ is fairly limited, however, (about 1.2 to 1.4) and the value of 1.32 for PETN when used in equation V-2 yields values for peak pressure which are in excellent agreement with an empirical relation for peak pressure given in reference V-3. The empirical relation, derived from numerous HEST experiments, relates the peak pressure in a cavity to the total amount of PETN in the cavity and is

$$P_o = 22.5 + 4297\ \gamma_c \qquad \text{(V-4)}$$

where

P_o = peak pressure lb/in^2

γ_c = PETN charge density in lbs/ft^3

Table V-1

Representative Explosive Properties For Use in Ideal Gas Source Models

Explosive	Density lb/ft^3	(gm/cc)	Available Energy ft-lb/lb	(cal/gm)
TNT	93.7	(1.5)	1.42×10^6	(1010)
PETN	81.1	(1.3)	1.91×10^6	(1360)
AN Slurry	93.7	(1.5)	1.99×10^6	(1420)
ANFO	58.1	(0.93)	1.25×10^6	(890)

The ideal gas source model was used in most one-dimensional calculations and a few of the initial two-dimensional cylindrical calculations. The use of this model in the two-dimensional calculations caused serious calculation problems however. The problems were associated with severe zone distoration at the bottom and top of the explosive cavity. Figure V-1 shows the deformed mesh in the region of the explosive cavity after about 20 msec in the first attempt at a two-dimensional cylindrical

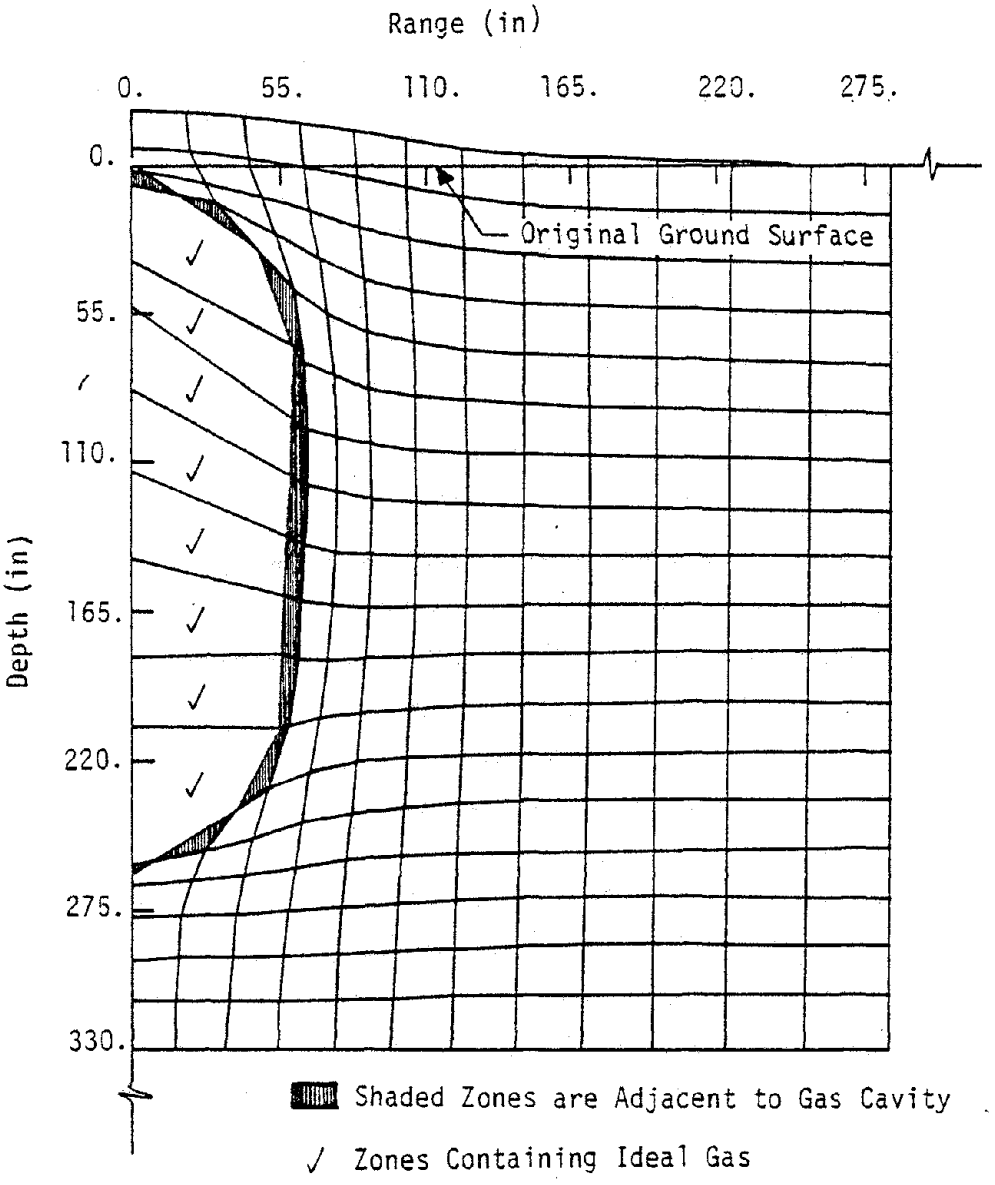

Figure V-1. Deformed Mesh at 21 Milliseconds in Region of Explosive Cavity In the First Cylindrical Simulation of Shot 7

simulation of Shot 7. It can be seen that there is severe zone distortion adjacent to the gas cavity.

The original size of the zones adjacent to the cavity was approximately that of the zone in the bottom left-hand corner of the figure. The zones on the radial boundary of the cavity are crushed to about 25 percent of their original width in the deformed configuration. Worst distortion from a computation viewpoint occurs in the soil zones at the bottom and top of the cavity. In these zones, the zone boundaries have crossed each other and the total area of each zone is approaching zero. This condition causes the computation time step to become exceedingly small so that the overall computation cannot proceed. This severe distortion and its effect on computation time is a problem inherent in calculations involving large deformations with a Lagrangian code. In addition to zone distortion, the Lagrangian mesh, which locks the zones together, inhibits the expansion of the gas toward the free-surface and prevents venting of the explosion. Venting is known to be the major release of the explosive pressures at late times.

Attempts were made to alleviate the zone distortion and to enhance the gas expansion by implementing slide lines in the calculations. Figure V-2 shows the deformed mesh of a cylindrical calculation where slide lines were used between the cavity region and the adjacent soil. It can be seen that distortion in the zones above and below the cavity is reduced and that a plug of soil above the cavity has moved upward significantly relative to the adjacent soil, thereby enhancing gas expansion. Although these results are in the direction desired, the zoning is complicated, the amount of gas expansion is still too small for a good venting approx-

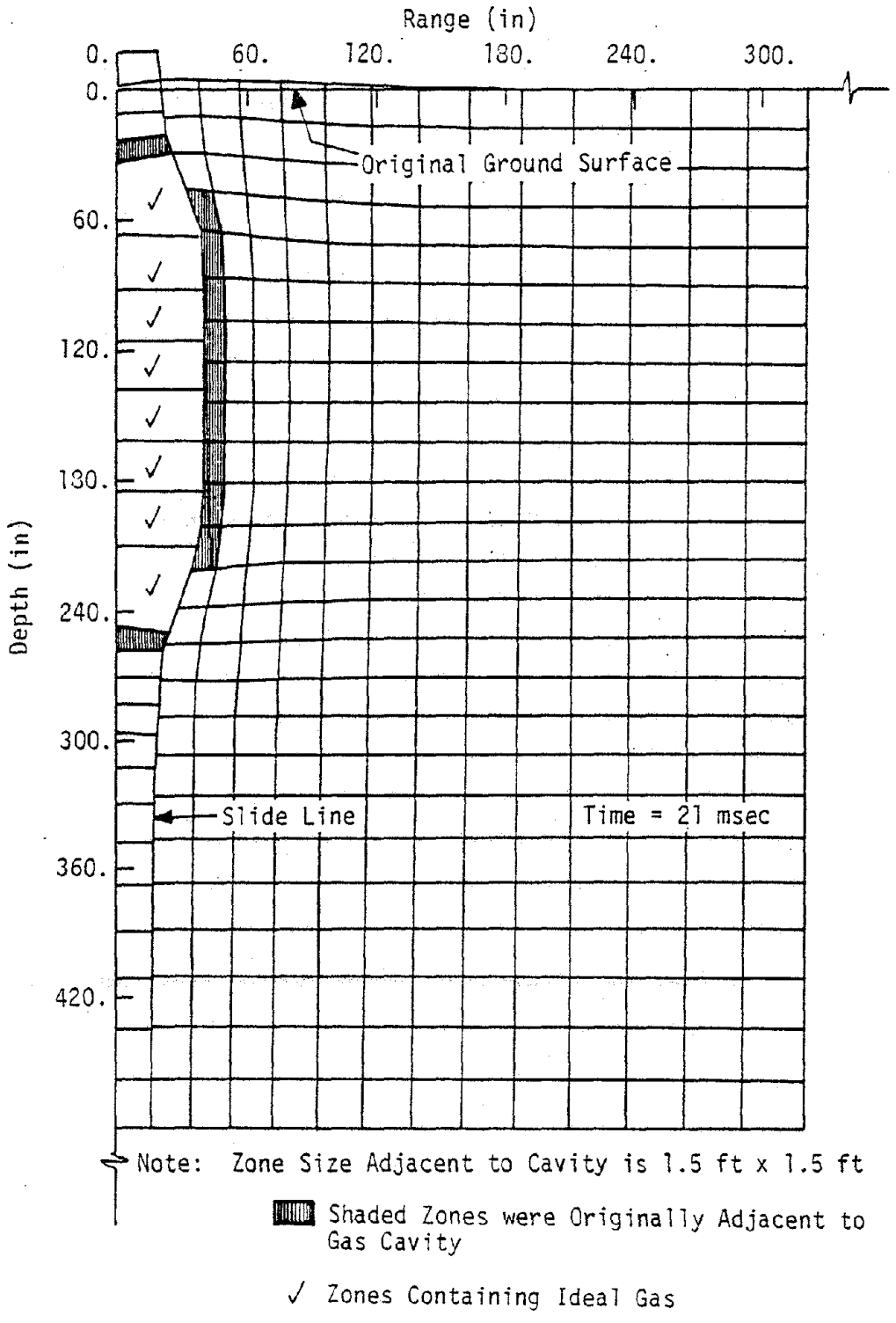

Figure V-2. Use of Slide Lines to Reduce Mesh Deformation and Enhance Gas Expansion Toward The Free-Surface

imation and the required time step is too small for long time, production calculations.

A second attempt was made to enhance gas expansion while minimizing zone distortion by zoning the soil above the explosion into a trapezoidal plug separated from the adjacent soil by slide lines, as shown in figure V-3. It was hoped that the plug would behave as a pseudo-crater and give a better approximation to venting. The assumption here, as with the previous slide line approach, was that the behavior at ranges of interest would be sensitive to the overall gross behavior at the source rather than specific details. The pseudo-crater approach did little to enhance venting compared with the vertical slide line approach (fig. V-2) and, in addition, required more complex zoning and larger computation times. Also, zone boundary interference along the inclined slide line caused numerical problems.

The various approaches to modeling the explosion in two-dimensions using an ideal gas in a cavity led to two significant conclusions:

(a) Zoning complications and/or zoning distortions were such that long computation times would be required for the parametric variations required in this study.

(b) None of the zoning approaches gave an adequate approximation of explosion venting to the atmosphere.

Cavity pressure-time histories computed with the various ideal gas approaches are compared with each other and with a one-dimensional cylindrical calculation for the same soil properties in figure V-4. The two-dimensional results shown are from the cavity mid-depth but it was found that there was no distinguishable variation of pressure with loca-

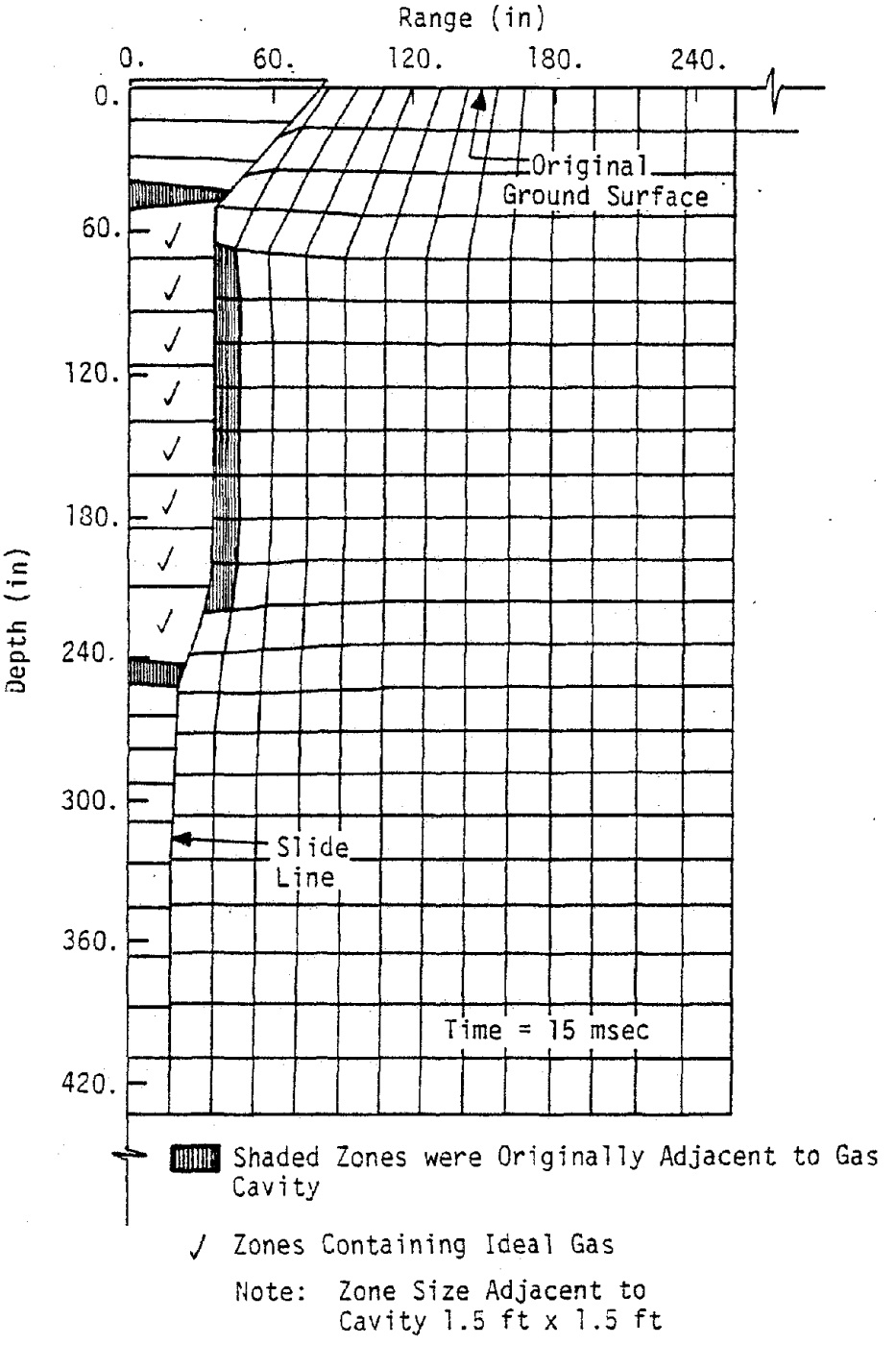

Figure V-3. Use of Pseudo-Crater and Slide Lines to Reduce Mesh Deformation and Enhance Gas Expansion Toward The Free-Surface

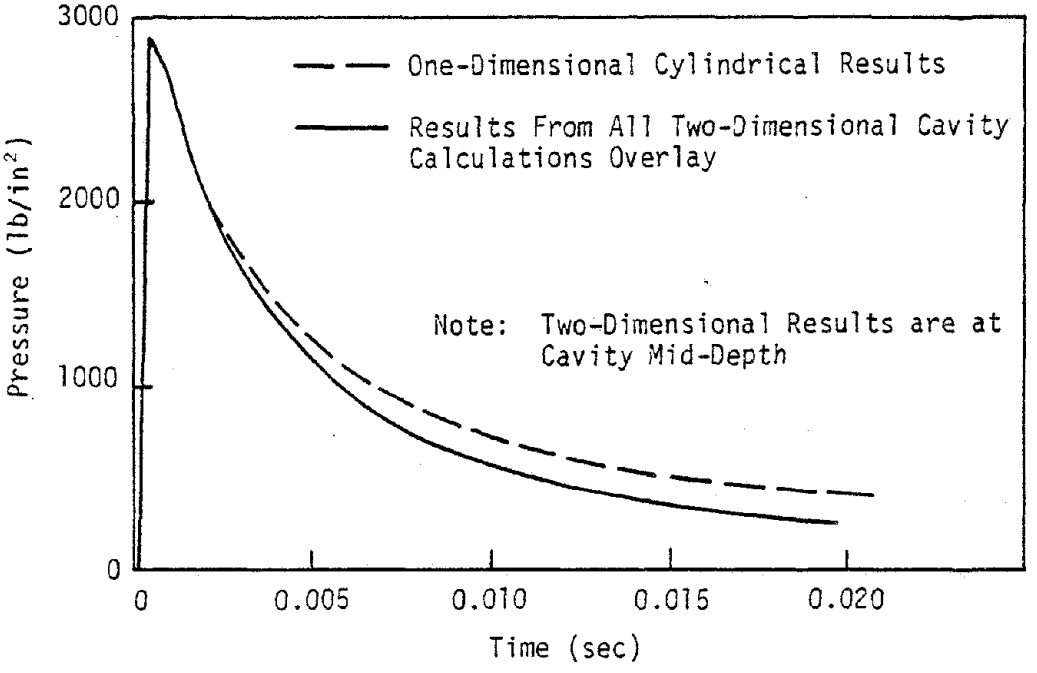

Figure V-4. Variation of Cavity Pressure-Time History with Cavity Treatment

tion in the cavities. The mid-depth results, therefore, may be taken as representative of any location in the cavity. The cavity pressures computed in two-dimensions were about the same regardless of cavity treatment. The two-dimensional pressures, however, were somewhat lower than the one-dimensional pressures at late times(i.e., the pressures decay more rapidly in two-dimensions than one-dimension). The difference between the one and two-dimensional calculations, however, are not considered significant within the uncertainty of the assumptions inherent in the derivation of the ideal gas properties for the explosion to start with.

Since the prime objective of the calculations was to obtain insight into ground motion behavior at intermediate to far ranges as a function of major source changes, and because of the complexity and high cost of detailed source modeling, two-dimensional sources were approximated in the parametric calculations by a pressure-time history applied over the region in which the original explosive was in contact with the soil. The pressure-time history was derived by modifying one-dimensional ideal gas calculations to account for explosive venting. As noted above, the differences between one and two-dimensional behavior were found small within the overall uncertainty of approximating the source.

The atmospheric venting modifications assumed that venting would begin at the top of the explosive region after the wave initiated at the top of the explosion has propagated to the surface, reflected, and then penetrated back to the top of the explosion. At this time all of the soil above the explosion would be in a state of spall and moving upward at a high velocity. Venting was assumed complete after

a rarefaction wave in the gas, initiated at the top of the cavity at the start of venting, had propagated through the cavity and then returned to the surface. The wave speed in the soil was taken as the wave speed of the peak stress, approximated as three-quarters the seismic velocity because of the high stresses near the explosion. The rarefaction wave speed in the gas was estimated by (ref. V-4)

$$C_r = C_o\left(\frac{\tilde{p}(\tilde{p} + 6)}{6\tilde{p} + 1}\right)^{\frac{1}{2}} \qquad \text{(V-5)}$$

where

C_r = rarefaction velocity in gas

C_o = ambient speed of sound in gas

$\tilde{p} = \frac{p}{p_a}$

p = gas pressure at time of start of venting

p_a = atmospheric pressure

The input pressure to a two-dimensional cylindrical simulation of Shot 7 is shown in figure V-5. The two-dimensional ideal gas pressure-time history (used since it was available) was assumed to go linearly to zero starting at the time of arrival of the reflection from the surface and ending when a rarefaction wave had transited the cavity and returned to the surface. The overall pressure-time history was then approximated by a simple overall fit of the form

$$p(t) = P_o e^{-\frac{at}{t_o}}\left(1 - \frac{t}{t_o}\right) \qquad \text{(V-6)}$$

where

p = pressure

P_o = peak pressure

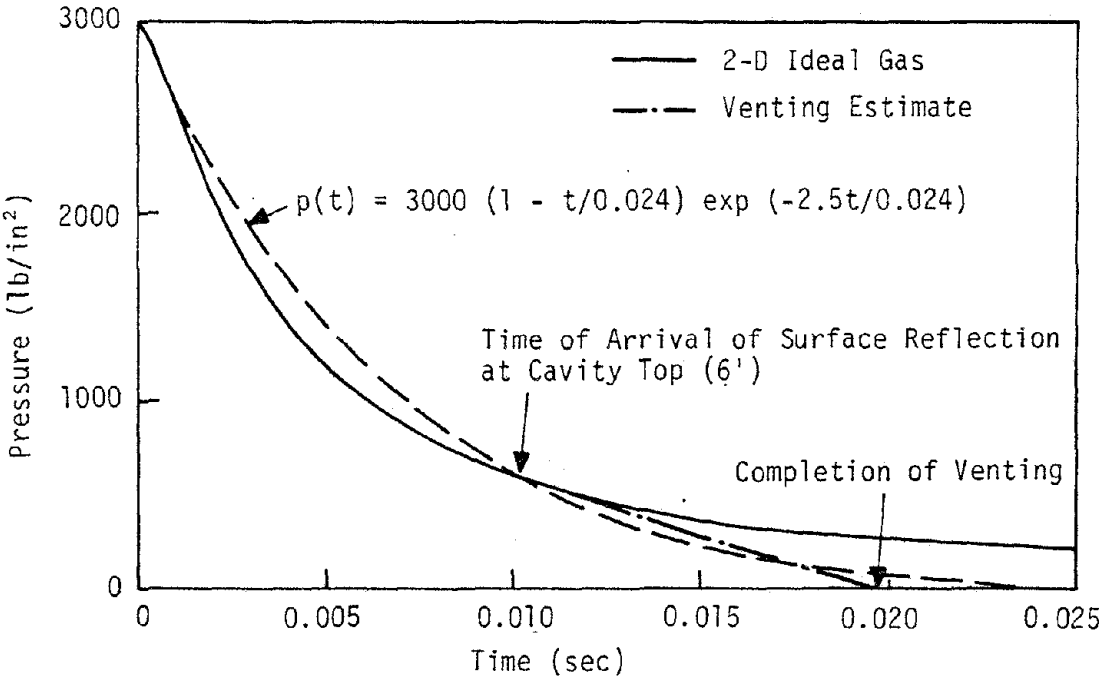

Figure V-5. Simple Pressure-Time History Approximation For Cylindrical Shot 7

t_o = duration coefficient

a = decay coefficient

The pressure-time fit of figure V-5 was applied as a pressure boundary condition over the physical length of the explosive. The deformed mesh at 140 milliseconds in this calculation is shown in figure V-6. The grid did not include the zones above and below the cavity because of instabilities which remained, even using a pressure-time history, in the zones immediately above and below the cavity. The effect of the material in this area was approximated by applying a pressure above and below the cavity region equal to the pressure in the adjacent soil zone. This procedure eliminated the instabilities and allowed the calculation to proceed to the time of interest with a reasonable amount of computer time.

An additional approximation was required in formulating the input pressure-time histories for the planar calculations. Planar explosive arrays in the field are generally created by placing explosives in closely spaced boreholes. At distances from the array on the order of twice the borehole spacing, the ground motion behavior is governed largely by the average effect of all of the boreholes. This average effect has been expressed in Section IV by the areal charge loading density, α. In the planar calculations, the array was also approximated by an areal loading rather than the effect of individual boreholes. In order to estimate a pressure-time history from a planar array, it was necessary to estimate an effective cavity volume. The combined volume of typical boreholes would have been so small that the selection of practical zone sizes would have been impossible. Hence, the cavity volume was chosen so that reasonable zone sizes could be selected. It will be shown later

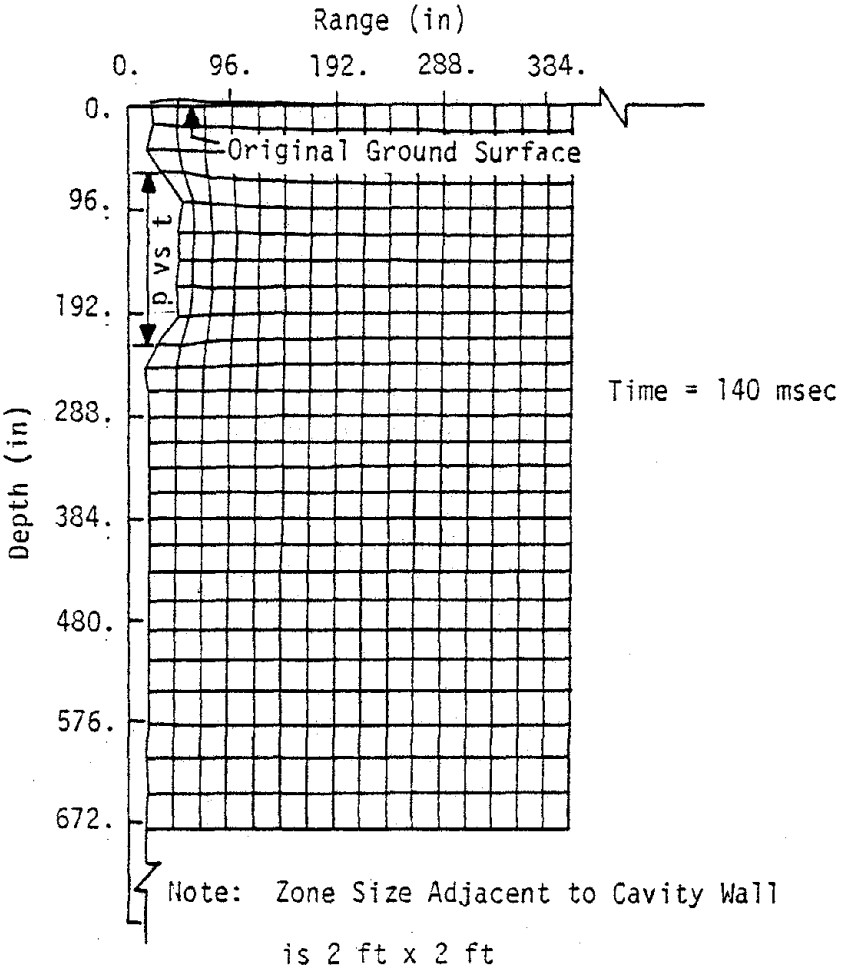

Figure V-6. Deformed Mesh at 140 Milliseconds Using Applied Pressure Approximation For Explosion

that ground motions have some sensitivity to cavity volume but, so long as cavity volume is scaled properly, the relative effects of the major input variables are obtainable with this assumption.

The assumptions described above, which take the real explosion and translate it to a simple pressure time-history input, are major and are subject to significant uncertainty. However, they were necessary to enable practical calculations to the late times of interest to earthquake simulation. In spite of the assumptions, the resulting pressure-time histories do preserve the essential features of the explosion yield and areal size. As a result, although the precise quantitative behavior in the resulting calculations may be uncertain because of these assumptions, the relative quantitative behavior as a function of parameter variations is believed to be correct.

4. ASSUMED MATERIAL PROPERTIES

The parametric calculations were performed using a nonlinear, inelastic material model consisting of a unique, piece-wise linear, hysteretic hydrostat to define pressure-volume behavior and a multilinear failure surface of the Mohr-Coulomb type to limit deviatoric stresses. The hydrostat, shown in figure V-72, relates the pressure, p, to the excess compression, μ, in both loading and unloading. The pressure is defined as the average of the three normal stresses acting on a material element, i.e.,

$$p = 1/3\ \sigma_{ii} \qquad \text{(V-7)}$$

(summation notation implied)

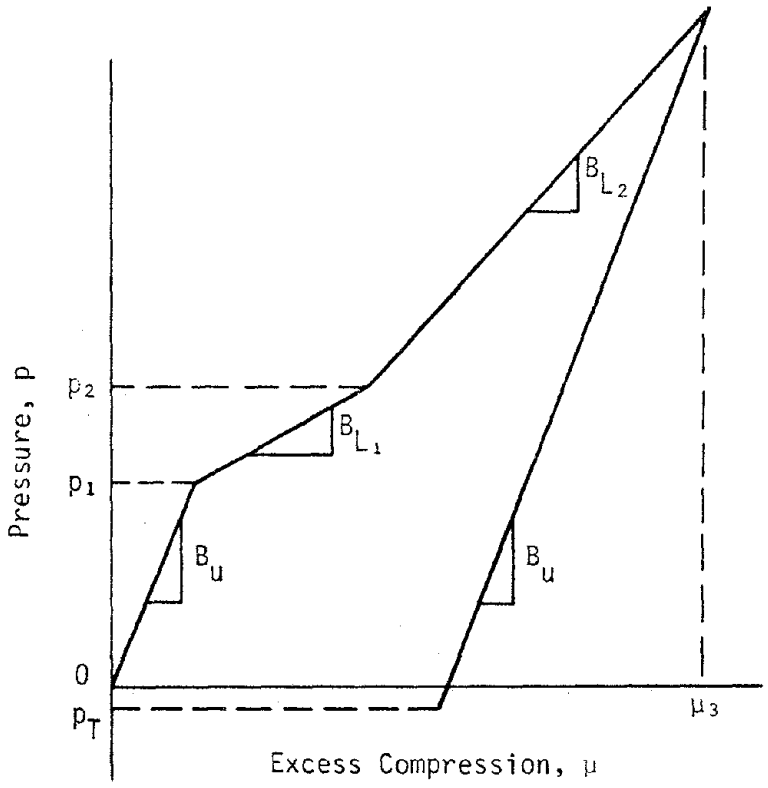

(a) Hydrostat

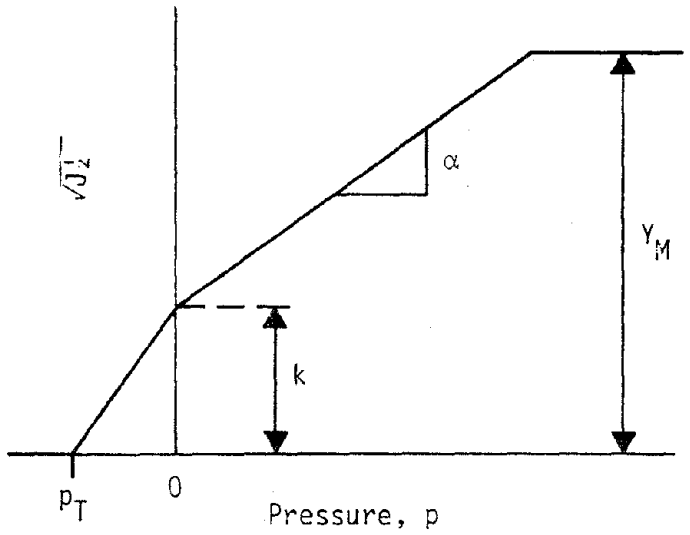

(b) Failure Surface

Figure V-7. Soil Constitutive Model Used in Calculations

where

p = pressure

σ_{ii} $(i=1,2,3)$ = normal stresses defined as positive in compression

The excess compression is defined by

$$\mu = \left(\frac{\rho}{\rho_o} - 1\right) \tag{V-8}$$

where

ρ = current density

ρ_o = initial density

and is simply the spatial (Eulerian) volumetric strain. The hydrostat is defined by linear segments with bulk moduli, B_{L1}, B_{L2}, etc. As many segments as necessary to define the material of interest may be used. The unloading-reloading modulus, B_u, is ordinarily taken as equal to the initial loading modulus.

The incremental deviatoric stress components are computed by

$$\dot{\sigma}'_{ij} = 2G\dot{\varepsilon}'_{ij} \tag{V-9}$$

where

$\dot{\sigma}'_{ij}$ = deviatoric stress increments

G = local shear modulus

$\dot{\varepsilon}'_{ij}$ = deviatoric strain increments

The local shear modulus, G, is estimated from

$$G = \frac{3}{2}\left(\frac{1 - 2\nu}{1 + \nu}\right) B \tag{V-10}$$

where

B = local bulk modulus

ν = Poisson's ratio which may be different in loading and unloading

The total deviatoric stresses, σ'_{ij}, at a particular time are limited by a failure envelope.

The failure envelope, shown in figure V-7b, is the Drucker-Prager generalization (ref. V-5) of the Mohr-Coulomb failure envelope. The envelope relates the limiting values of the square root of the second invariant of the stress deviator tensor, $\sqrt{J'_2}$, to the pressure. $\sqrt{J'_2}$ is defined by

$$\sqrt{J'_2} = (1/2\sigma'_{ij}\sigma'_{ij})^{\frac{1}{2}} \qquad \text{(V-11)}$$

where σ'_{ij} = deviatoric stress components. The failure envelope is usually derived from the standard triaxial test where $\sqrt{J'_2}$ is computed from the stress deviator by

$$\sqrt{J'_2} = \frac{1}{\sqrt{3}} (\sigma_1 - \sigma_3) \qquad \text{(V-12)}$$

where

σ_1 = vertical stress in the triaxial test

σ_3 = confining stress in the triaxial test.

and the corresponding pressure is

$$p = \frac{1}{3} (\sigma_1 + 2\sigma_3) \qquad \text{(V-13)}$$

The failure envelope may have any number of linear segments, although only two segments are commonly used. At low to intermediate pressures,

$\sqrt{J_2'}$ is linearly related to p by

$$\sqrt{J_2'} = k + \alpha p \tag{V-14}$$

where k and α are coefficients. The coefficients are related to conventional triaxial parameters by

$$\alpha = \frac{2\sqrt{3}\ \sin\phi}{3 - \sin\phi} \tag{V-15}$$

$$k = \frac{2c}{\sqrt{3}\left(\frac{1}{\cot\phi} - \frac{1}{3}\tan\phi\right)} \tag{V-16}$$

where

ϕ = angle of internal friction

c = cohesion intercept

At high pressures, the failure envelope is usually taken as constant (sometimes called the von Mises limit). Computed values of the deviator stresses, σ'_{ij}, from equation V-9 are checked against the failure envelope to determine if an admissable stress state exists. If $\sqrt{J_2'}$ is less than or equal to the failure value at the corresponding pressure, the computed values are accepted without modification. If $\sqrt{J_2'}$ is greater than the failure value, the deviator stresses are corrected to force them to lie on the failure envelope. This correction is performed using a nonassociated flow rule in which the pressure is held constant.

Ordinarily, laboratory or field data on hydrostatic behavior are not available. Available information usually consists of seismic velocity data and/or laboratory uniaxial strain data. Uniaxial response can be converted to an estimate of hydrostatic response through Poisson's

ratio and the failure surface. In the uniaxial test, the radial stress is related to the axial stress, prior to failure, by

$$\sigma_r = \frac{\nu}{1 - \nu} \sigma_a \tag{V-17}$$

where

σ_r = radial stress

σ_a = axial stress

ν = Poisson's ratio

The pressure is then

$$p = \frac{1}{3}\left(\frac{1 + \nu}{1 - \nu}\right) \sigma_a \tag{V-18}$$

The excess compression is

$$\mu = \frac{\varepsilon_z}{1 - \varepsilon_z} \tag{V-19}$$

where ε_z = axial strain.

Equations (V-18) and (V-19) relate the uniax to the hydrostat up to the point of failure. At each stage of use of these equations the failure surface must be checked. $\sqrt{J_2'}$ in the uniaxial test is

$$\sqrt{J_2'} = \frac{1}{\sqrt{3}}\left(\frac{1 - 2\nu}{1 - \nu}\right) \sigma_a \tag{V-20}$$

Starting with the value of pressure at which the failure surface is encountered, the relation between $\sqrt{J_2'}$ and p on the failure surface must be used to compute the pressure. The most direct procedure involves, first, selecting a value for p and, second, determining the corresponding value of $\sqrt{J_2'}$ from the failure envelope. The corresponding uniaxial stress is then

$$\sigma_a = \frac{2\sqrt{3}}{3} \sqrt{J_2'} + p \qquad \text{(V-21)}$$

The uniaxial strain which corresponds to this value of uniaxial stress may then be used to compute the excess compression associated with the selected value of p.

The baseline material selected for the parametric calculations was dry McCormick Ranch silty sand. Most existing simulation data are from McCormick Ranch and the site is a prime candidate for additional earthquake simulation experiments. Soil data for the site are available from references V-6, V-7, and V-8 and recent unreported tests performed by CERF.

The site, above about 75 feet, consists mainly of silty, clayey fine sand (classification SM and SC) with light cementation throughout. There are some gravel and hard caliche lenses as well as a few layers of plastic silts and clays but these conditions occur seldom and the site is quite uniform overall. Air-bailed, dry drill holes remain open without support in this material but undisturbed samples are difficult to obtain. The soil below 75 feet is a clean uniform sand. Most simulation tests have been performed above this material and, therefore, its properties have not been determined. The ground water table at the site is below 500 feet.

A representative seismic profile for the site is given in table V-2. The seismic velocity gradually increases from 1300 to 2200 ft/sec from the surface to 14 feet and then remains 2200 ft/sec to a depth of 85 feet, indicating the relative uniformity of the upper silty sand. The increase in seismic velocity at 85 feet is probably associated with the

uniform sand layer. The data of reference V-7 indicate that the average dry unit weight in the upper 50 feet is about 102 lbs/ft^3 and the average moisture content about 6.5 percent. These values combine to give an average total unit weight of 109 lbs/ft^3.

Table V-2

Representative Seismic Profile for McCormick Ranch Test Site (ref. V-6)

Depth(ft)	Seismic Velocity(ft/sec)
0-3	1300
3-14	1750
14-85	2200
85-260	3750
260 and Below	6100

Two alternative estimates of the uniaxial strain response of the silty sand are shown in figure V-2. Reference V-6 recommends a composite uniaxial stress-strain curve for the upper 65 feet of material based upon laboratory uniaxial tests. This recommendation (laboratory-based) was taken as one alternative. A second alternative was considered because recent analyses of in-situ material property test data (e.g., ref. V-9) indicate that laboratory derived stiffness properties may be too soft. These analyses suggest that seismic behavior may persist to a stress level of about 100 lb/in^2 and that stiffness may remain higher than indicated by laboratory data to very high stresses.

The second alternative model was derived by assuming a seismic modulus (taking 1650 ft/sec as an average velocity in the upper material) to the 100 lb/in^2 stress level and then softening the model to correspond to a modulus based upon one-half the seismic velocity. This latter assumption is based upon long standing empirical correlations which

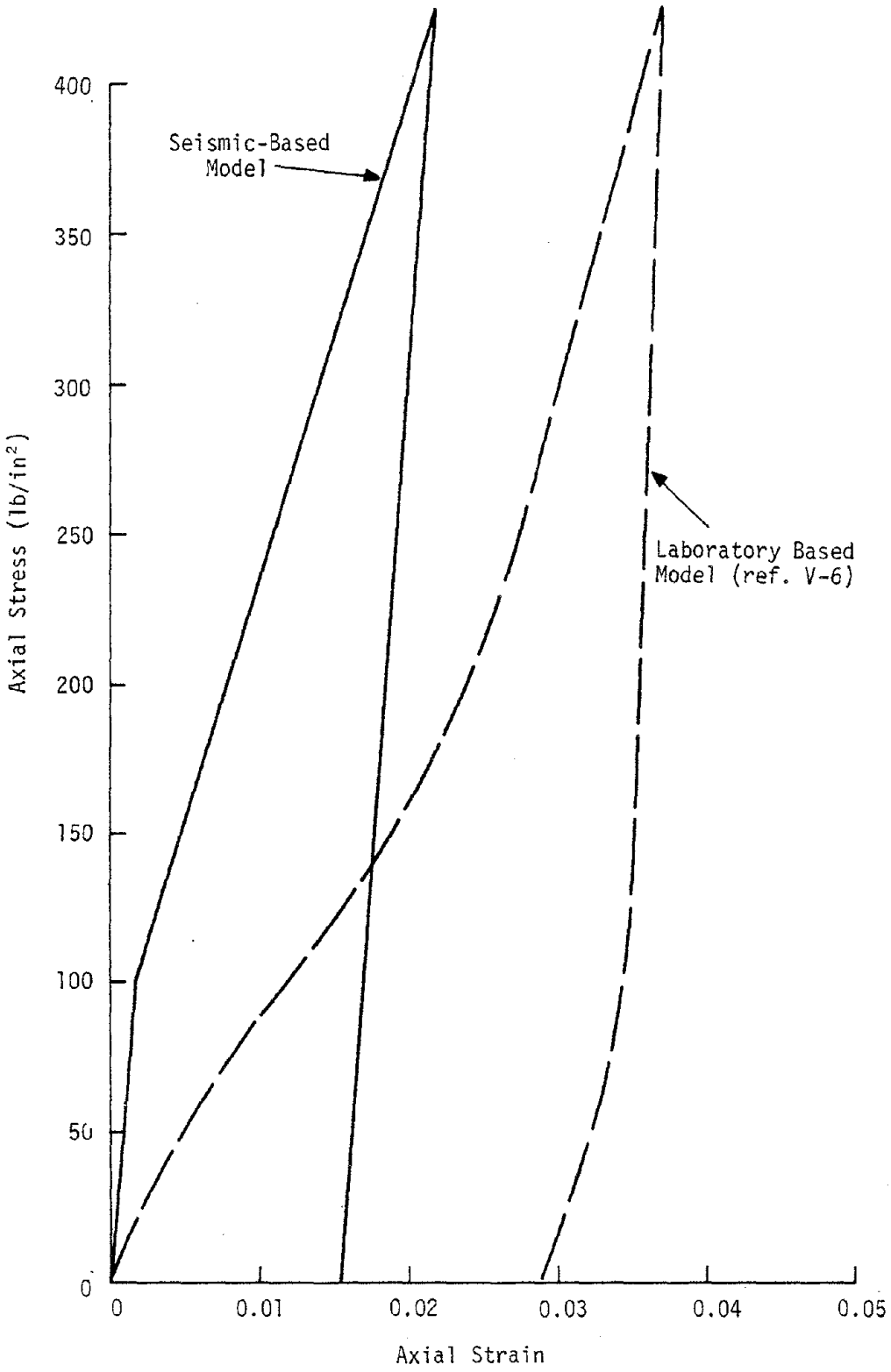

Figure V-8. Alternate Uniaxial Stress-Strain Models

indicate the effective loading wave speed at intermediate stress levels (300 to 1000 lb/in^2) is about one-half the seismic velocity (e.g., ref. V-10). Unloading is assumed to occur at the seismic modulus.

It can be seen in figure V-8 that the seismic-based model is significantly stiffer than the laboratory model in loading but they have similar unloading stiffnesses. The seismic-based model was used in most of the parametric calculations, although one cylindrical calculation was performed with the laboratory model to obtain some insight into the effect of material property changes.

Failure data was available from triaxial tests reported in reference V-8 and recent unreported results from CERF. All tests were performed on recompacted samples at various conditions of density and moisture. As a result, there is some uncertainty in interpreting in-situ behavior of the soil. Figure V-9 presents the data in terms of $\sqrt{J_2'}$ versus p and several alternative fits of the failure envelope. Alternate A was a direct fit of the data from reference V-8. It was found that cylindrical calculations of Shot 7 using this fit did not give sufficient inward motion compared with the data. Several additional calculations were performed with varying failure surfaces to obtain better agreement of the calculated inward to outward particle velocity ratio with the Shot 7 data. The fit designated alternate B gave the best agreement when the ideal gas source was used. Alternate C gave the best agreement when a pressure-time input including a venting estimate was used. The major difference between alternates B and C and alternate A is the intercept on the $\sqrt{J_2'}$ axis. Alternates B and C indicate significant cohesion at zero pressure. This is believed due to cementation and other

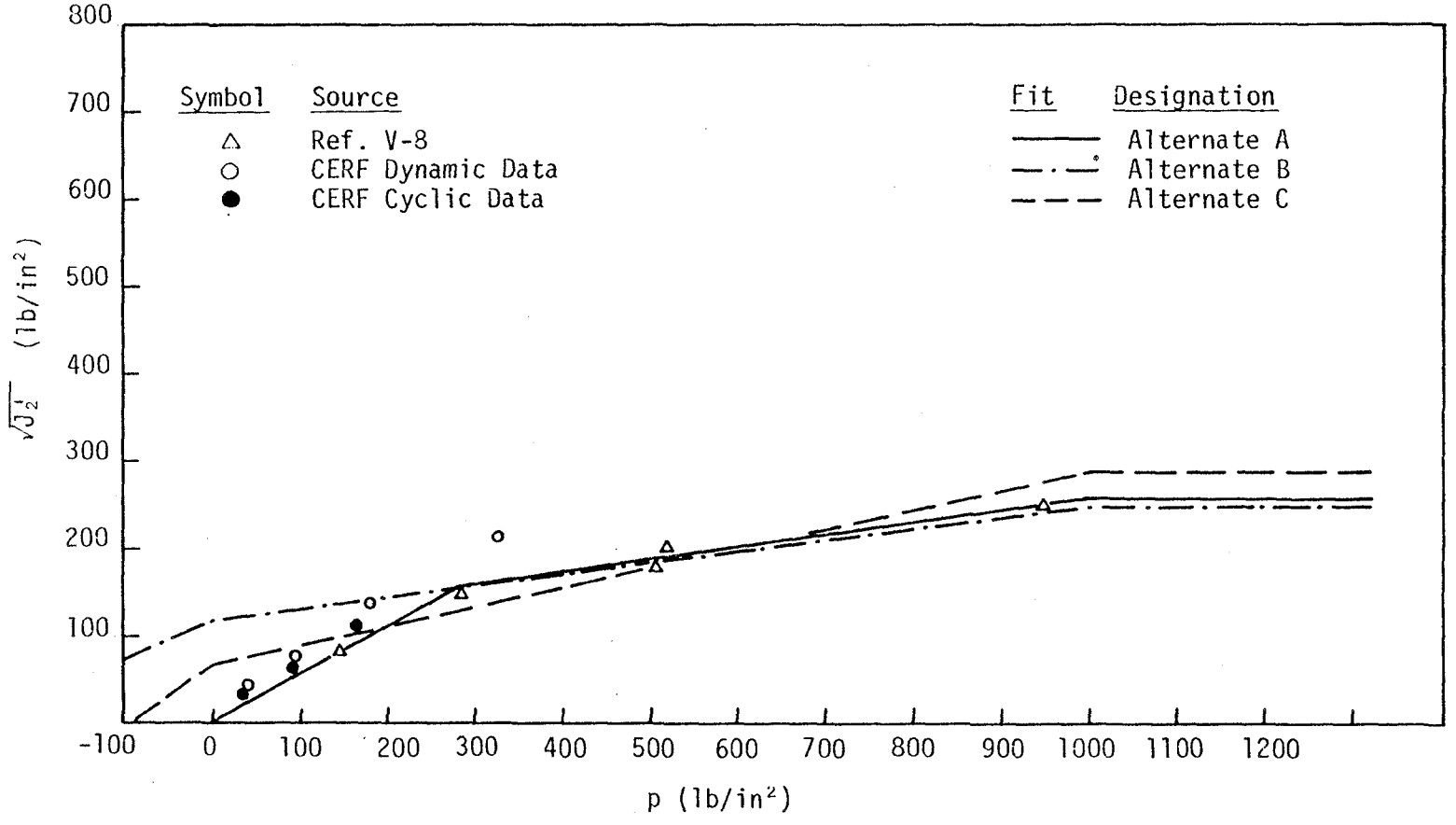

Figure V-9. Triaxial Failure Data for McCormick Ranch and Alternate Fits to the Failure Envelope

long term in-situ conditions which are lost during sampling and recompaction for laboratory tests.

Some of the early cylindrical parametric calculations used alternates A and B. However, alternate C was finally selected as the best fit and was used for most of the calculations. This fit includes a tensile pressure cutoff of - 100 psi. This tensile cutoff is probably somewhat large for the site materials but was required in order to maintain stability in the calculations. Tension models currently available are inadequate, and instability and large oscillations occur when tensile failure occurs. Fortunately, large tensions are not encountered in the calculations at most ranges of interest. Therefore, this condition is believed to have little influence upon interpretations of the calculations.

As mentioned earlier, the material model for the calculations requires input in terms of a hydrostat and a yield surface. The alternate uniaxial fits of figure V-8 were converted to hydrostats assuming a Poisson's ratio of 0.3 and using the alternate A fit to the failure data. The hydrostats are shown in figure V-10. The hydrostats are relatively insensitive to failure surface variations within the range considered and therefore these hydrostats were not changed when other yield surfaces (alternates B and C) were used in calculations.

Most of the parametric calculations used the seismic-based hydrostat and the alternate C yield surface since these were finally chosen as the best representation of the in-situ material. However, the laboratory-based data and/or the alternate B and C failure envelopes were

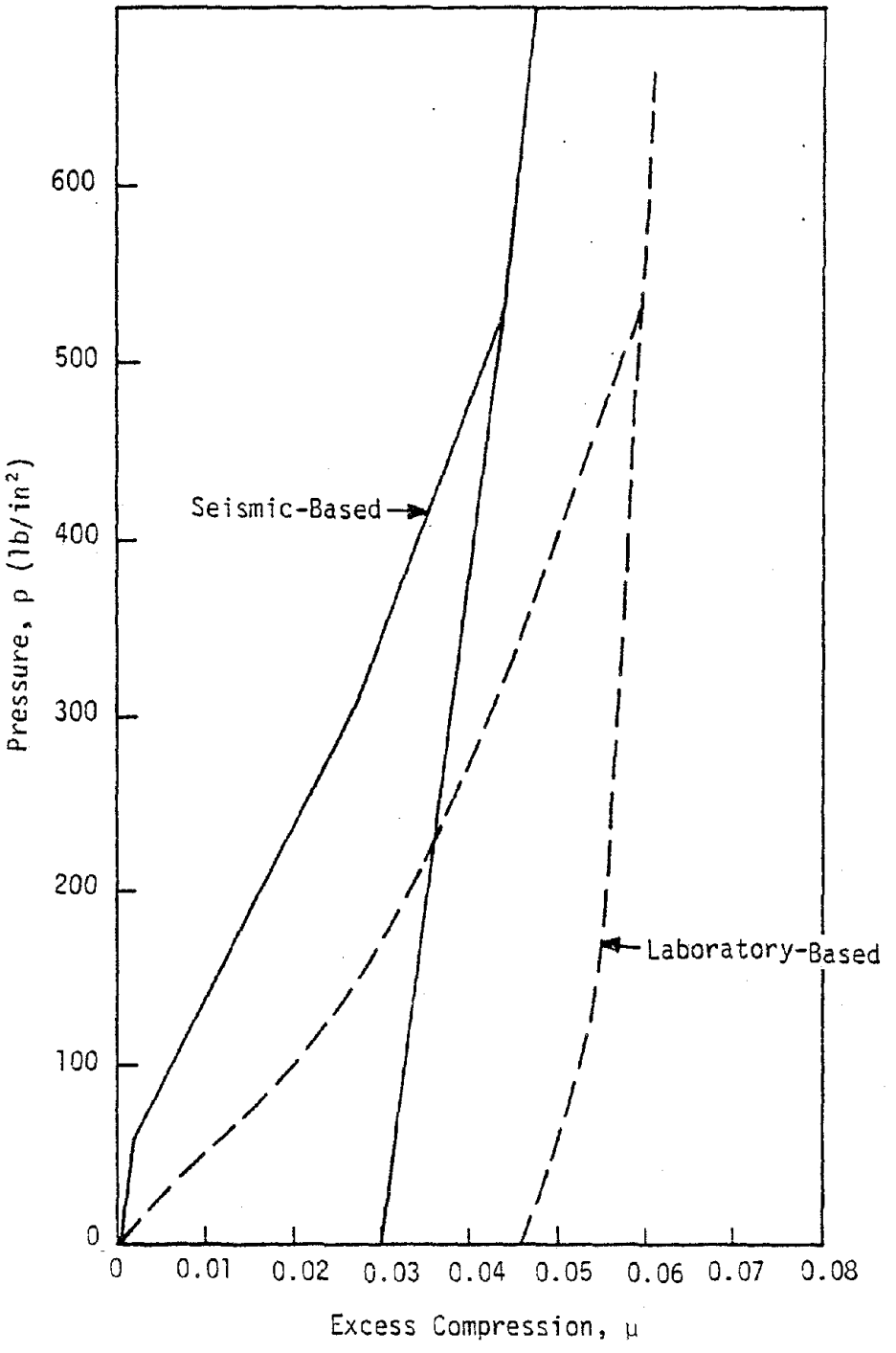

Figure V-10. Alternate Hydrostatic Models

used in some of the early cylindrical parametric variations. Table V-3 shows the four main material property combinations which were used and designates them as alternates 1 through 4. The designation will be referred to later when calculation results are presented.

Table V-3

Main Material Property Combinations
Used In Calculations

Alternate	Hydrostat	Failure Surface
1	Seismic	A
2	Laboratory	A
3	Seismic	B
4	Seismic	C

In addition to the majority of calculations which used inelastic material models, three cylindrical elastic calculations were performed for a preliminary estimate of proper material property scaling in the presence of elastic property variations. The elastic parameters used in these calculations are given in table V-4. The variations designated elastic 1, 2, and 3 correspond roughly to unit weights and elastic loading wave speeds of dry soil, wet soil, and soft rock, respectively.

5. CALCULATION SET-UP

Calculations of three general types were performed in this study, namely spherical, cylindrical, and planar. Spherical calculations were performed in one-dimensional geometry while cylindrical and planar calculations were performed in both one-dimensional and two-dimensional geometry. The main purpose of the spherical calculations was to deter-

mine whether standard scaling rules derived assuming elastic behavior were applicable to nonlinear materials. In addition, it was desired to evaluate attenuation rates for comparison with far-field cylindrical and planar data.

The cylindrical calculations were designed to aide in resolving scaling questions, cylindrical attenuation rates, the effect of finite charge length, and off-centerline motion variations. In addition, the cylindrical configuration was used to develop calculation procedures, to observe the effect of limited material property variations and the effect of source coupling.

Table V-4

Elastic Parameters Used In Material Property Scaling Calculations

Identifier	Unit Weight (lbs/ft^3)	Elastic Wave Speed, C (ft/sec)	Poisson's Ratio, ν
Elastic 1	109	825	0.3
Elastic 2	115	2750	0.3
Elastic 3	140	8000	0.3

The planar geometry was of interest because of its apparent near-term applicability to simulation. In the planar case, attenuation rates, the effect of array height, and off-centerline variations were investigated. In addition, the effect of the free-surface and the vertical response in the near-surface region were evaluated.

Over 36 calculations were performed in this program. Table V-5 summarizes the main calculations, their characteristics, and the individual

calculation objectives. A calculation identifier, consisting of a number, a letter, and another number, is assigned to each calculation for reference in later paragraphs. The first number refers to the number of dimensions in the calculation (1 = one-dimensional, 2 = two-dimensional). The letter refers to the geometry (S = spherical, C = cylindrical, P = planar). The second number is a sequential number in the calculation sequence.

Not all of the calculations summarized in table V-5 are treated in the discussions which follow. Those calculations which have "calculation procedure" as their objective were used to establish initial insight into important parameters and to guide the selection of zone sizes, calculation times, and loading conditions (e.g., the pressure versus time loadings described earlier). Their results are not explicitly presented. Some cylindrical material property variations (i.e., alternates 5, 6, and 7) were intermediate steps in the selection of a best estimate of in-situ properties. The results of these calculations provide no new information beyond other calculations and are also not presented. Most one-dimensional calculations were performed with an ideal gas explosive model. A few were performed with a pressure input to determine differences from the ideal gas model and to provide a baseline for comparison with the two-dimensional calculations. All two-dimensional calculations, except a few early "calculation procedure" runs, used a pressure input.

Figure V-11 shows typical configurations for the two-dimensional calculations. For efficiency, the effect of array height on the ground motion parameters on the centerline were determined in symmetric cal-

Table V-5

Summary of Calculations
(a) Spherical Calculations

Calculation No.	W* (lbs)	r_o* (ft)	Zone Size Data			Calculation Time (sec)	Material Property Alternate	Calculation Objectives, Additional Information
			Zoning Type**	Radial	Vertical			
1S1	80.4	2.75	A	6-24(248	--	0.150	4	Yield Scaling
1S2	107200	30	A	120-480(4830)	--	1.0	4	Yield Scaling

(b) Cylindrical Calculations

Calculation No.	γ* (lbs/ft)	r_o* (ft)	Zone Size Data			Calculation Time (Sec)	Material Property Alternate	Calculation Objectives
			Zoning Type**	Radial	Vertical			
1C1	0.27	1	A	3-24(400)**	--	0.150	1	Calculation Procedure
1C2	1.34	1	A	3-24(400)	--	0.150	1	Calculation Procedure
1C3	6.70	1	A	3-24(400)	--	0.150	1	Coupling Variation
1C4	6.70	1.5	A	3-24(400)	--	0.150	1	Coupling Variation, Material Property Variation
1C5	35.8	2.0	A	3-24(400)	--	0.250	1	Calculation Procedure
1C6	6.7	1.5	A	6-24(400)	--	0.150	2	Material Property Variation
1C7	6.7	1.5	A	6-24(400	--	0.150	4	Material Property Variation
1C8	6.7	1.5	A	6-24(400)	--	0.150	5	Material Property Variation
1C9	6.7	1.5	A	6-24(400)	--	0.150	6	Material Property Variation

* See footnotes at end of table.

Table V-5

Summary of Calculations (Cont.)
(b) Cylindrical Calculations (Cont.)

Calculation No.	γ * (lbs/ft)	r_o^* (ft)	Zone Size Data			Calculation Time (sec)	Material Property Alternate	Calculation Objectives, Additional Information
			Zoning Type**	Radial	Vertical			
1C10	6.7	1.5	A	6-24(400)**	--	0.150	3	Yield Scaling, Material Property Variation
1C11	6.7	0.25	A	3-24(400)	--	0.150	1	Coupling Variation
1C12	1.34	0.5	A	3-24(400)	--	0.150	3	Yield Scaling
1C13	30.2	2.0	A	3-24(400)	--	0.250	3	Yield Scaling
1C14	6.7	1.5	A	6-18(150)	--	0.150	Elastic 1	Material Property Scaling
1C15	6.7	1.5	A	6-36(272)	--	0.150	Elastic 2	Material Property Scaling
1C16	6.7	1.5	A	6-72(475)	--	0.150	Elastic 3	Material Property Scaling
1C17	6.7(P)	1.5	A	6-24(400)	--	0.150	3	P vs t Comparison, Material Property Variation
1C18	6.7(P)	1.5	A	6-24(400)	--	0.150	4	P vs t Comparison, Material Property Variation
1C19	6.7(P)	1.5	A	6-24(400)	--	0.150	7	P vs t Comparison, Material Property Variation
2C1	6.7	1.5	B	18(15)-52(114)	18(24)-45(105)	0.040	1	Calculation Procedure, No Relief Condition
2C2	6.7	1.5	B	18(15)-52(114)	18(24)-45(105)	0.080	1	Calculation Procedure, Plug Relief Condition
2C3	6.7	1.5	B	18(15)-51(125)	18(24)-44(102)	0.080	1	Calculation Procedure, Crater Relief Condition
2C4	6.7(P)†	1.5	B	24(60)-69(232)	24(30)-69(202)	0.150	4	Array Height Variation, Symmetric, H-12 ft
2C5	6.7(P)	1.5	B	24(60)-69(232)	24(30)-69(202)	0.150	4	Array Height Variation, Symmetric, H-48 ft
2C6	6.7(P)	1.5	B	24(60)-69(232)	24(72)-61(202)	0.150	4	Array Height, Variation, Symmetric, H-96 ft
2C7	6.7(P)	1.5	B	24(60)-69(232)	24(30)-69(202)	0.150	4	Free Surface Effects, H=12 ft, S=6 ft

* See footnote at end of table

Table V-5

Summary of Calculations (Cont.)
(c) Planar Calculations

Calculation No.	α* (lbs/ft)	t/2* (ft)	Zone Size Data			Calculation Time (sec)	Material Property Alternate	Calculation Objectives Additional Information
			Zoning Type	Radial	Vertical			
1P1	14.74	10	A	120-480(4830)**	--	1.0	4	Yield Scaling
1P2	3.58	2.5	A	30-120(800)	--	2.5	4	Yield Scaling
2P1	3.58(P)	2.5	C	60(200)-300(600,1100)	30(25)-300(500,825)	1.0	4	Array Height Variation Symmetric, H=10 ft
2P2	3.58(P)	2.5	C	60(200)-300(600,1600)	60(100)-300(500,1300)	0.8	4	Array Height Variation, Symmetric, H=40 ft
2P3	3.58(P)	2.5	C	60(200)-300(600,1600)	60(100)-300(500,1300)	1.0	4	Array Height Variation, Symmetric, H=80 ft
2P4	3.58(P)	2.5	C	60(200)-300(600,1600)	60(100)-300(500,1300)	1.0	4	Array Height Variation, Symmetric, H=160 ft
2P5	3.58(P)	2.5	C	60(200)-300(600,1600)	60(100)-300(500,1300)	1.0	4	Free-Surface Effects, H=40 ft, S=20 ft
2P6	3.58(P)	2.5	C	60(200)-300(600,1600)	60(100)-300(500,1300)	1.0	4	Free-Surface Effects, H=40 ft, S=40 ft

Table V-5
Summary of Calculations (Cont.)

Footnotes:

* W = total explosive weight in equivalent TNT for spherical charges
γ = lineal charge density in equivalent TNT per unit length for cylindrical charges
α = areal charge density in equivalent TNT per unit area for planar charges
r_o = cavity radius for spherical or cylindrical charges
t/2 = cavity half-width for planar charges
H = array height in two-dimensional calculations
S = surcharge height in two-dimensional calculations with a free-surface

** Zoning Type A: ΔX_i, inches - ΔX_f, inches (X_f, feet). See figure V-12a

Zoning Type B: ΔX_i or ΔY_i, inches (X_1 or Y_1, feet) - ΔX_f or ΔY_f, inches (X_2 or Y_2, feet). See figure V-12b

Zoning Type C: ΔX_i or ΔY_i, inches (X_1 or Y_1, feet) - ΔX_f or ΔY_f, inches (X_2 or Y_2, X_3 or Y_3, feet). See figure V-12b

† (P) = equivalent pressure-time history

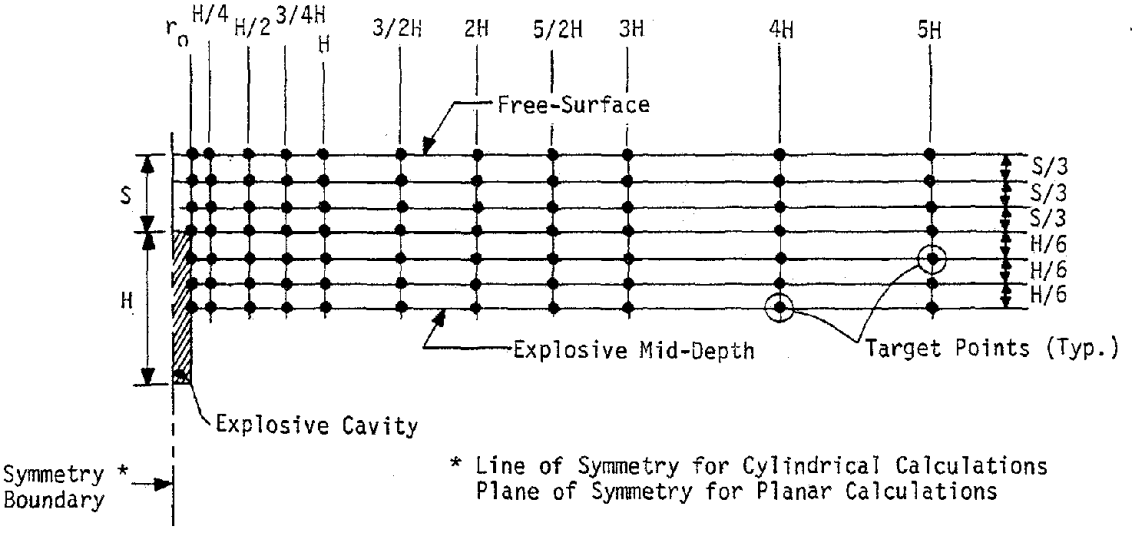

b) Configuration for Calculation Including the Free-Surface

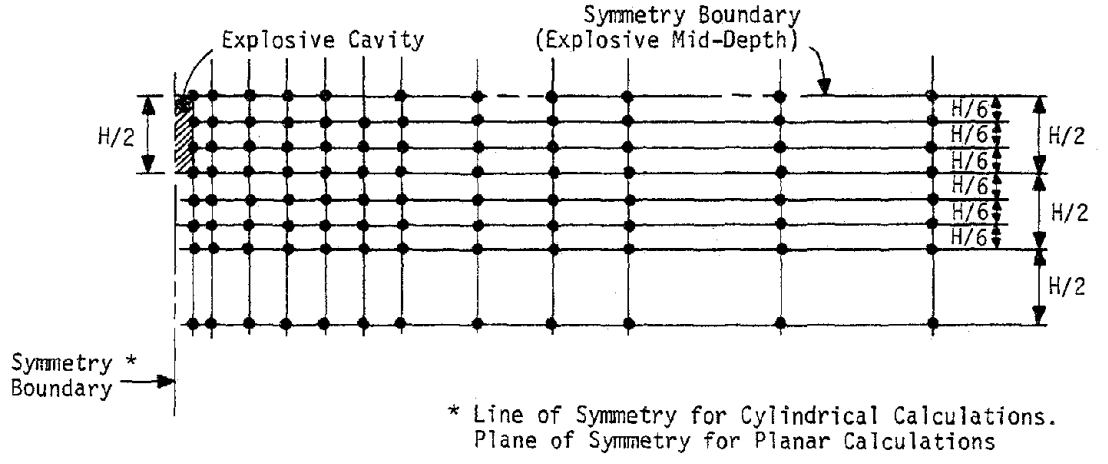

a) Configuration for Symmetric Calculation

Figure V-11. Typical Calculation Configurations and Target Points

culations (fig. V-112), where the mid-depth of the explosive was taken as a plane of symmetry. Off-centerline behavior and vertical behavior due to the free surface was ascertained by a more limited number of free-surface calculations (fig. V=116).

The zoning configurations used are shown in figure V-12. Zone size, in both one and two-dimensions, was finest near the source and then allowed to grow with increasing range and depth. Three zoning types were used. In one dimension, the zones grew in a cubic fashion in a manner described in reference V-1. This zoning is designated type A. In two dimensions, type B zoning held the zones in a region adjacent to the explosive source (bounded by X_1, Y_1 in figure V-12b) constant in size. Zones beyond this region were then allowed to grow arithmetically to the boundaries of the calculation (bounded by X_2, Y_2 in figure V-12b). In several planar calculations, where it was necessary to zone to very large ranges, arithmetic zone size increases would have led to unusually large zone aspect ratios. In these cases, the arithmetic zone size increase was stopped at some range and depth (X_2, Y_2) and constant zoning was again used to the problem boundaries (X_3, Y_3). The boundaries of the calculations were set so that spurious boundary reflections did not affect calculation results during the time of interest.

Zone sizes were selected in relation to the explosive loading, and as a compromise between calculation accuracy and efficiency. Initial one-dimensional cylindrical calculations with a lineal charge density of 6.7 lbs/ft of TNT were performed with very fine zoning (ΔX_i = 3 inches). A small parametric study indicated that an initial 6 inch zone size gave sufficient accuracy and this size was used for several cylindrical

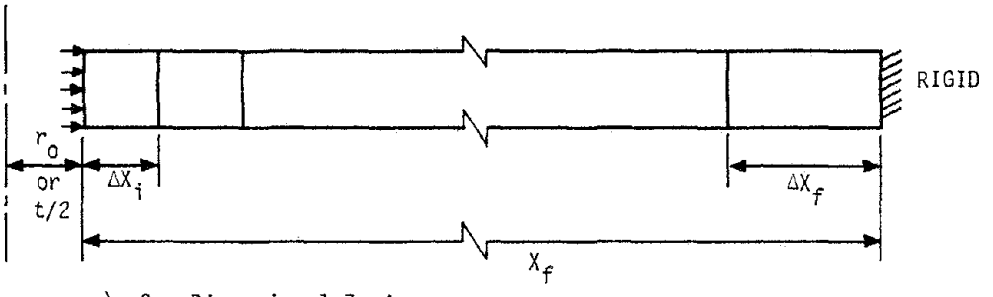

a) One-Dimensional Zoning

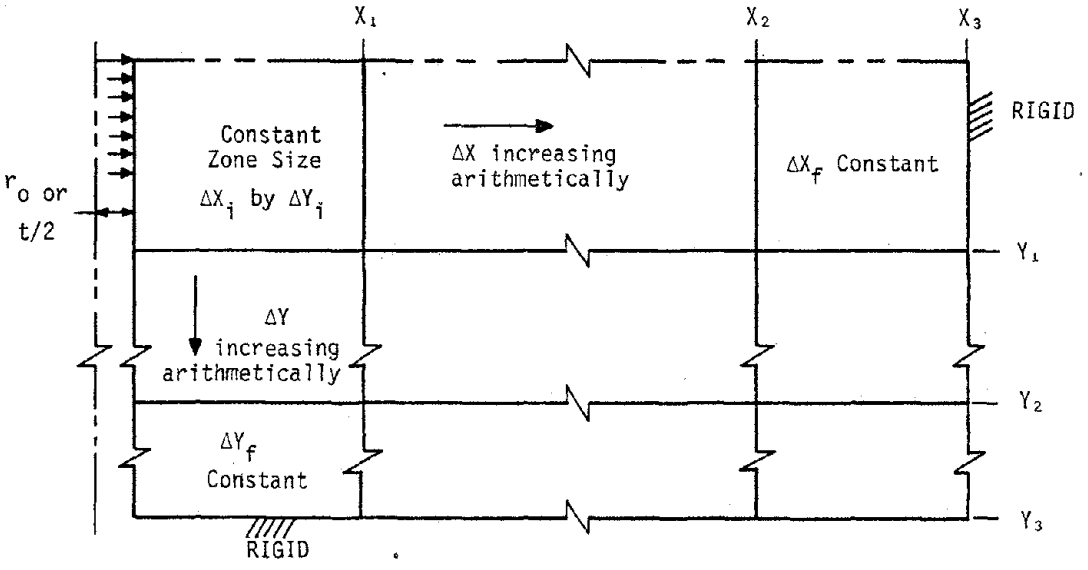

b) Two-Dimensional Zoning

Figure V-12. Zoning Configurations

calculations. In two-dimensions, these zone sizes would have been impractical. A 2-foot zone size was finally selected for the two-dimensional calculations. It was found that in the region of one-dimensional motion, except very near the source, the 2-foot zone size gave agreement with the one-dimensional results that would have been well within the scatter of a well instrumented experiment. In the two-dimensional planar calculations much larger zone sizes were necessary to allow calculations to the large ranges of interest. Here the amplitude results, especially near the source, are probably attenuated because of the large zoning. However, the comparative quantitative results between calculations are believed correct.

6. SPHERICAL RESULTS

Two spherical calculations were performed to verify the applicability of standard $W^{\frac{1}{3}}$ scaling for ground motions in inelastic media, as has been suggested by Crowley (ref. V-11), and to obtain information on spherical attenuation rates. The yields in the two calculations were 80.4 and 107,200. lbs of equivalent TNT, corresponding to a yield difference of greater than three orders of magnitude. The explosions were approximated by an ideal gas approximation and the cavity radii for the two calculations were in scaled proportion.

The calculated velocity and corresponding displacement time histories at a range of about 147 feet from the 107,200. lb source are shown in figure V-13. The velocity has a finite rise time due to the nonlinear loading behavior of the soil. The velocity time history has a large outward phase, a smaller inward phase and, finally, a second outward phase before settling down to zero. The total motion endures for about 0.75 sec.

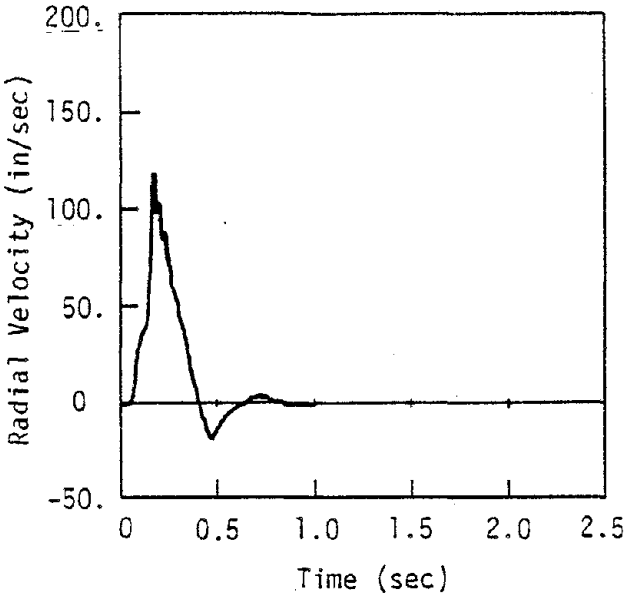

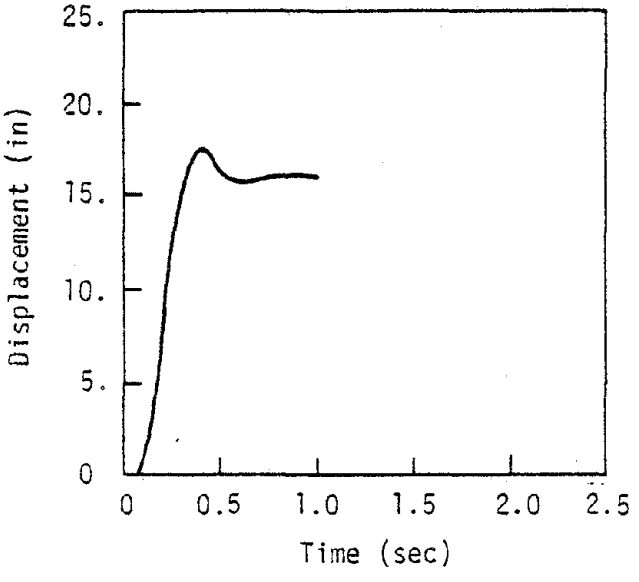

Figure V-13. Calculated Velocity Time History and Its Integration at the 147-Foot Range From a Spherical Explosion of 107,200 lbs of TNT (Calculation 1S2)

Peak radial accelerations, particle velocities and displacements, scaled by $W^{\frac{1}{3}}$, are plotted in figures V-14, V-15, and V-16, respectively. Since accelerations are poorly calculated in finite difference codes, the accelerations were estimated from the peak velocity and rise time to peak velocity using equation IV-46 from Section IV. The scaling results indicate that $W^{\frac{1}{3}}$ scaling does an excellent job of collapsing the calculated results. The acceleration attenuation rate is about -3.5 to a scaled range of about 5, after which the attenuation rate lessens to about -1.6. Velocity attenuates at -2.4 to a scaled range of about 5.6 and then at -1.6. The particle velocity at the range corresponding to the attenuation break is 1.8 ft/sec and this corresponds (using equation IV-26) to a radial stress of about 70 lb/in^2. The elastic limit of the material model was 100 lb/in^2. The break in the attenuation slope of both the accelerations and velocities is, therefore, associated with the transition to elastic behavior.

The displacements attenuate at -2.3, slightly smaller than the velocity attenuation rate, beginning at a scaled range of about 1. The lesser attenuation evident in figure V-16 at nearer ranges is probably due to severe shear failure from the high stresses near the source. The displacements do not exhibit a change in attenuation rate at more distant ranges. The reason for this is evident in the data for the outward duration of the particle velocity which are plotted in figure V-17. These data also scale well. At near ranges, the outward duration attenuates very slowly. The small attenuation of -0.09 accounts for the difference between the velocity and displacement attenuation rates in the inelastic region. At a scaled range of about 6, the outward phase duration begins

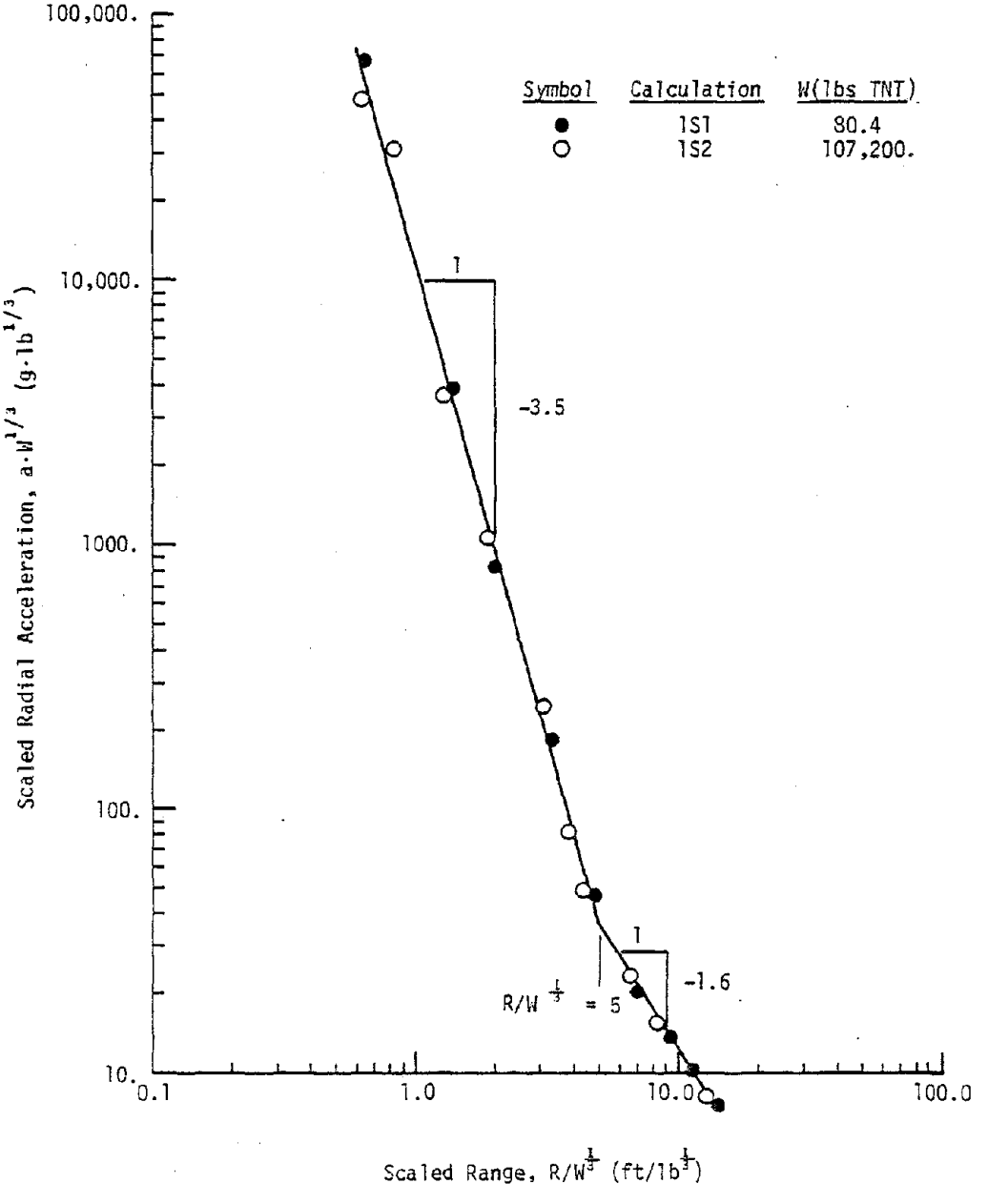

Figure V-14. Radial Accelerations in Spherical Geometry

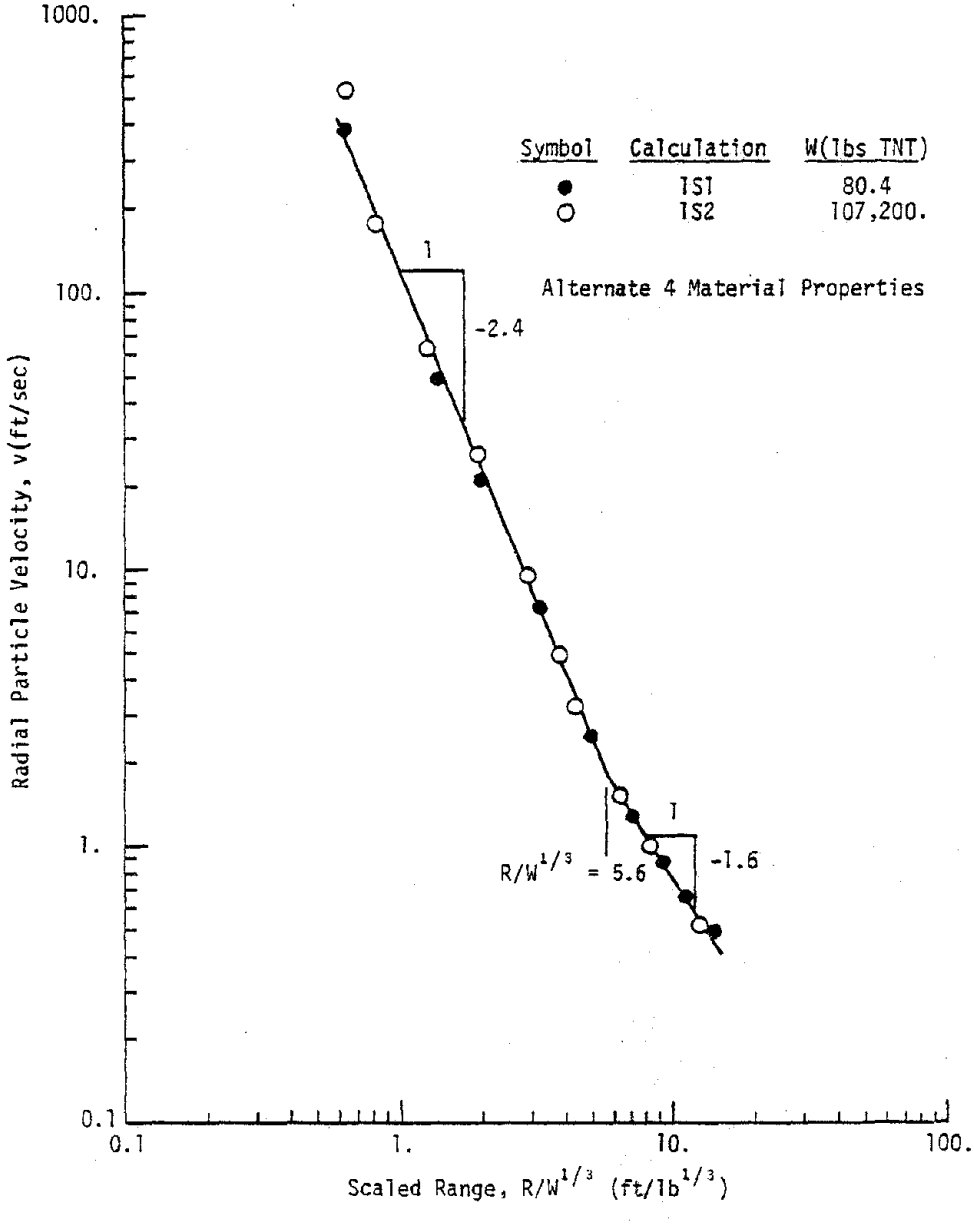

Figure V-15. Radial Particle Velocities in Spherical Geometry

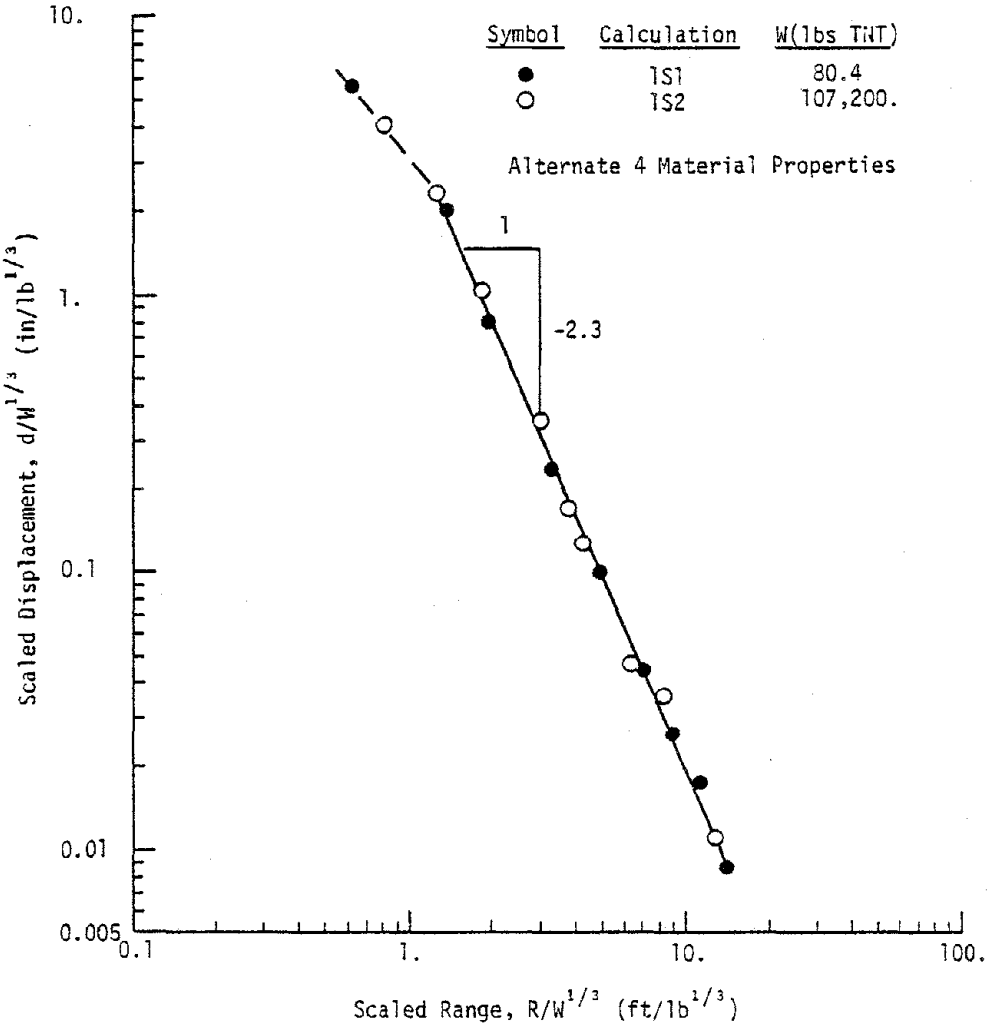

Figure V-16. Radial Displacements in Spherical Geometry

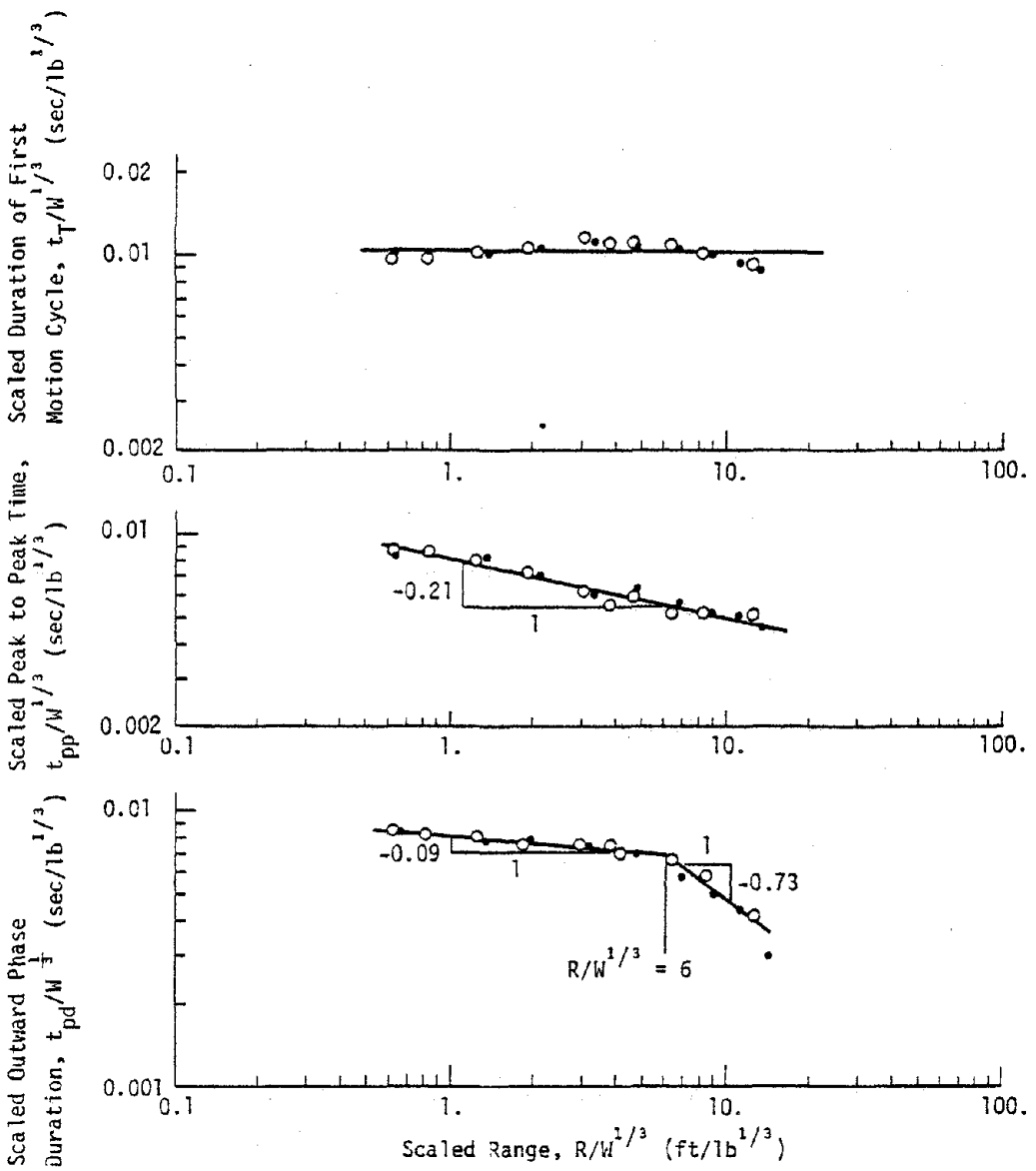

Symbol	Calculation	W(lbs TNT)
•	1S1	80.4
o	1S2	107,200

Alternate 4 Material Properties

Figure V-17. Velocity Characteristic Times in Spherical Geometry

to attenuate at -0.73. This increased attenuation combines with the reduced attenuation of the particle velocity so that there is essentially no effect on displacement attenuation.

At ranges nearer than about 5 ft/lb$^{\frac{1}{3}}$, the calculated ground motions are fit very well by

$$aW^{\frac{1}{3}} = 11{,}200\ (R/W^{\frac{1}{3}})^{-3.5} \qquad (a)$$

$$v = 120\ (R/W^{\frac{1}{3}})^{-2.4} \qquad (b) \qquad (V\text{-}22)$$

$$d/W^{\frac{1}{3}} = 4.0\ (R/W^{\frac{1}{3}})^{-2.3} \qquad (c)$$

where

a = acceleration in g's

v = particle velocity in ft/sec

d = displacement in inches

R = range in feet

W = yield in lbs of equivalent TNT

7. CYLINDRICAL RESULTS

a. Introduction

The cylindrical calculations were designed to evaluate six areas:

(1) The effect of sources coupling

(2) Yield scaling in cylindrical geometry

(3) Elastic material property scaling

(4) Effects of inelastic material property variations

(5) The effect of finite explosive height

(6) Free-surface effects

In each case, the effect of the specific parameters on radial acceleration, velocity, and displacement and their time histories was of interest. As mentioned earlier, cylindrical geometry was of interest because planar array effects are expected to approach cylindrical behavior at some range away from the array, and some cylindrical data are available for comparison with calculations. The first four areas were addressed with one-dimensional calculations. The fifth and sixth areas involve two-dimensional effects and, therefore, were evaluated with two-dimensional calculations.

b. Source Coupling

In the initial one-dimensional cylindrical calculations (1C1 through 1C5), the source yield was varied but little attention was given to the dimension of the cavity radius. The radius was simply selected to be a convenient value. It was found that the results of these calculations did not scale well. After evaluation of these calculations, it was determined that cavity radius, which is a factor in source coupling, played a significant role in some ground motion effects away from the charge.

Variation of the cavity radius for a given amount of explosive causes a variation in the initial energy per unit mass in the cavity and, hence, a variation of the peak pressure in the ideal gas source (see equation V-2). Peak pressure, therefore, was determined to be an important scaling parameter when using an ideal gas source.

Three calculations (1C3, 1C4, and 1C11) were used to obtain insight into the effect of cavity radius. In those calculations, the total amount of explosive was held constant at 6.7 lbs/ft of TNT (5.0 lbs/ft

of PETN) while values of 1.5, 1.0, and 0.25 feet were used for the cavity radius. These variations resulted in cavity pressures of about 3000, 6800, 110,000 lb/in^2, respectively. The 1.5-foot cavity radius corresponds to the condition of experimental Shots 6 and 7 discussed in Section IV.

The radial accelerations, velocities, and displacements as a function of range under the three coupling conditions are shown in figures V-18, V-19, and V-20. The accelerations and velocities are peak values while the displacements are the values when the particle velocity has decayed to one-half its peak. This distinction was necessary because the alternate 1 material properties did not result in an inward velocity phase and the displacement continued to increase with time. This was the prime reason for evaluating and using better in-situ material models for later calculations.

The acceleration and velocity results at ranges nearer than about 15 feet separate significantly as a function of cavity radius. At 15 feet and beyond, however, the effect of cavity radius cannot be detected. The displacements separate as a function of cavity radius at all ranges. This is a result of a frequency content difference in the particle velocity time history as a function of cavity radius. At a given range in these calculations the displacements are proportional to the cavity radius to about the 1/3 power although this result should not be used as a general relation without further evaluation.

The cavity radius variations were performed to develop insight into the effect of source coupling details. Although further calculations

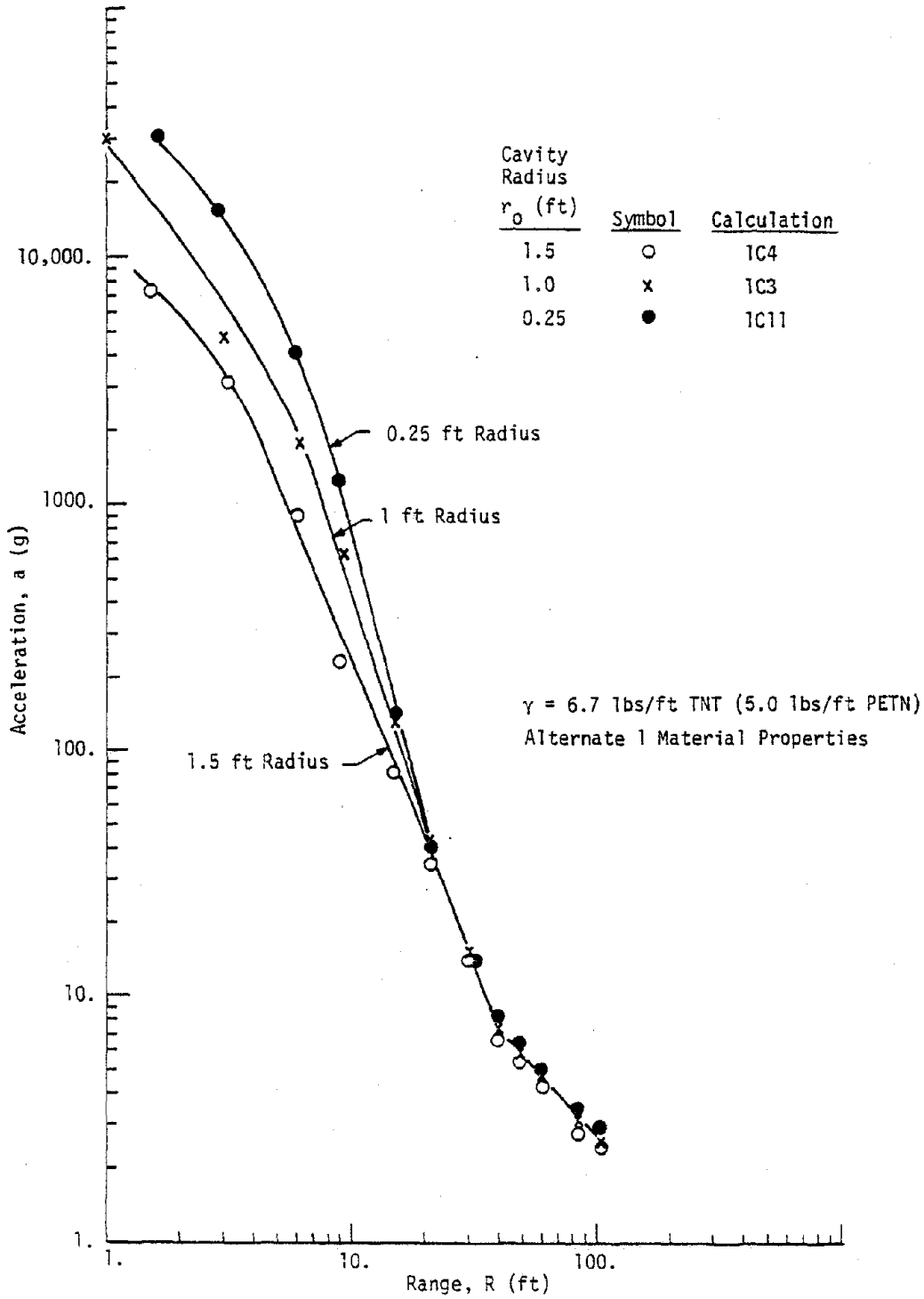

Figure V-18. Effect of Source Coupling on Radial Acceleration in One-Dimensional Cylindrical Geometry

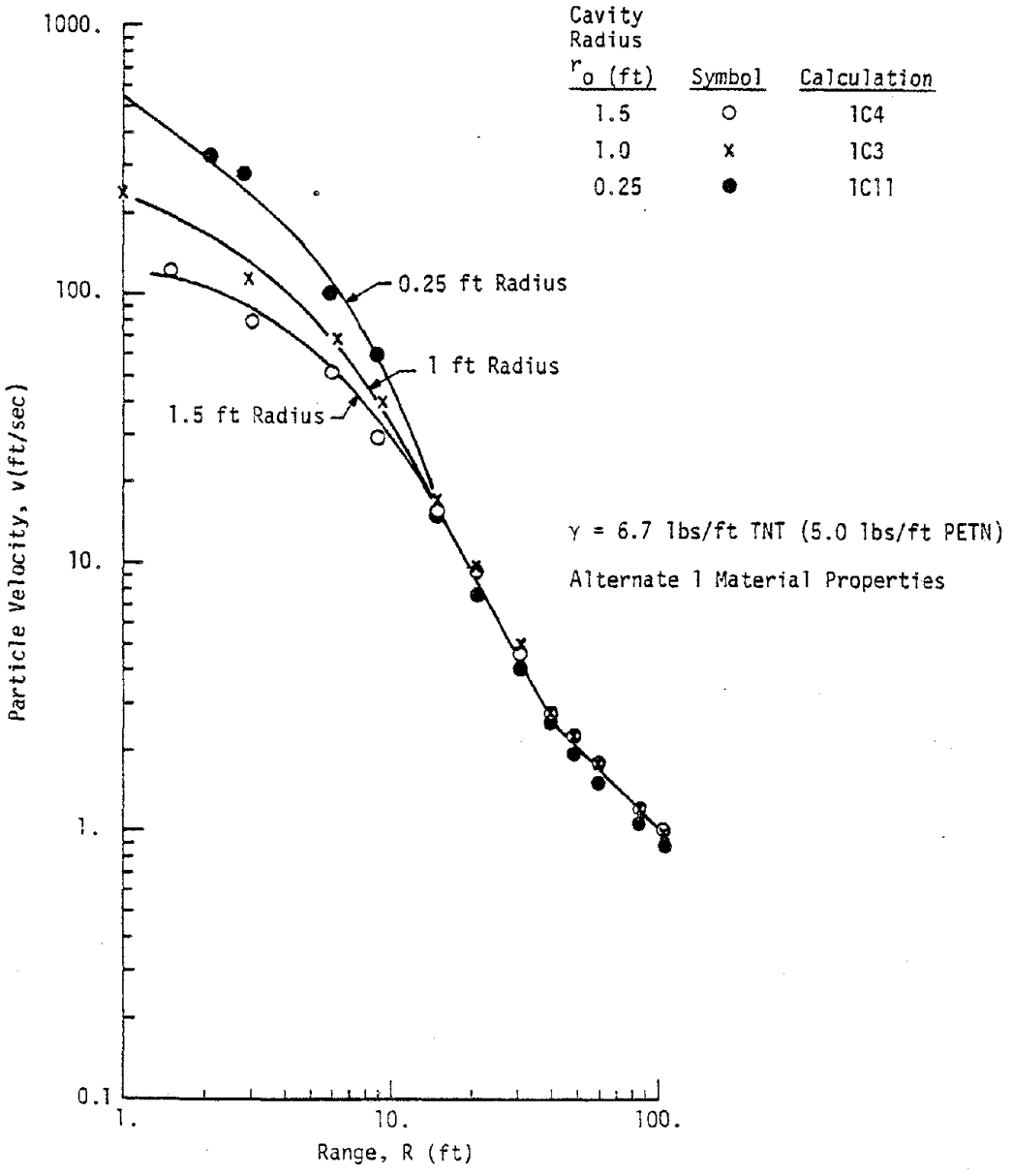

Figure V-19. Effect of Source Coupling on Radial Velocity in One-Dimensional Cylindrical Geometry

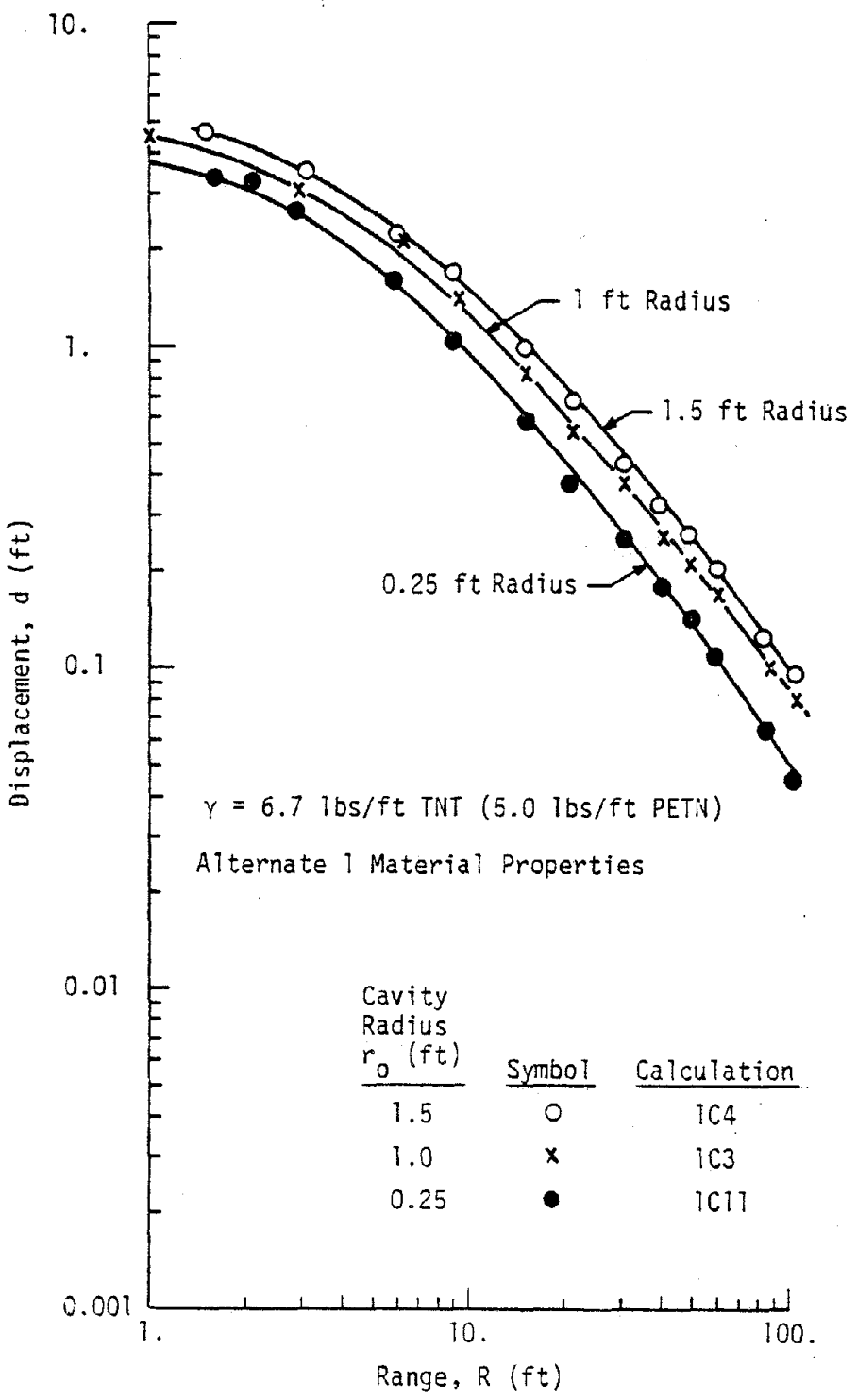

Figure V-20. Effect of Source Coupling on Radial Displacement in One-Dimensional Cylindrical Geometry

and analysis would be required to reach firm quantitative relations, the limited results obtained lead to several important conclusions:

(1) A source term related to cavity radius or, equivalently, source pressure is important for ground motion scaling. In order to remove this effect when using an ideal gas approximation for different yields in a common geology, it is necessary to change the cavity dimensions so that $r_o/W^{\frac{1}{3}}$, $r_o/\gamma^{\frac{1}{3}}$, or t/α, depending on geometry, remains constant. This results in the pressure at the source remaining constant. In actual physical problems involving a common solid explosive, this effect is automatically taken care of since the explosive yield is proportional to the explosive volume and the detonation pressure remains constant. Detonation pressure differences, however, may lead to some uncertainty when scaling results from different explosives. It is common to use a single factor to relate the energy equivalency of different explosives, and this is the approach used herein. It is likely that a second factor related to the explosive detonation pressure may also be important but this effect has not yet been accounted for in the ground motion community.

(2) The effect of cavity radius or peak pressure on accelerations and particle velocities diminishes with increasing range. This suggests that source approximations similar to those used herein, where large cavity dimensions were necessary to allow practical zoning, may be usable for direct quantitative predictions at intermediate to far ranges. Absolute quantitative predictions of displacements will probably be high due to the large source volume.

(3) Variations of source coupling in the field by placing the explosive in different sized cavities may be a viable way of altering the displacements and, as a result, the frequency content of ground motion

for simulation purposes. Accelerations and velocities at intermediate to far ranges, however, may not be changed much.

c. Yield Scaling

Three one-dimensional cylindrical calculations (1C10, 1C12, 1C13) with different lineal charge densities, γ, were conducted to evaluate $\gamma^{\frac{1}{2}}$ scaling and to determine cylindrical attenuation rates in dry alluvial materials. An ideal gas source and alternate 3 material properties were used in the calculations. In view of the coupling effects noted in the previous discussion, the scaled cavity radius, $r_o/\gamma^{\frac{1}{2}}$, was held approximately constant from calculation to calculation. A typical velocity time history and its integration are shown in figure V-21. The velocity has a finite rise time due to the nonlinear loading behavior of the soil. The velocity has a large outward phase, a smaller inward phase and, finally, an additional two motion cycles of relatively small amplitude. The motion duration is about 0.11 sec.

Calculated peak accelerations, velocities, and displacements, scaled appropriately by $\gamma^{\frac{1}{2}}$, are plotted versus scaled range in figures V-22, V-23, and V-24. It can be seen that $\gamma^{\frac{1}{2}}$ scaling does a very good job of collapsing the data for a variation in γ of over a factor of 22. The small variations in the calculated results at the close-in ranges are probably due to the small differences in the scaled cavity radii.

The relations between the kinematic parameters and range are curved lines, but when fit with straight lines on log-log paper, as is commonly done with field data, the data suggest distinct regions with different attenuation rates. Accelerations attenuate at a rate of -1.55 to a

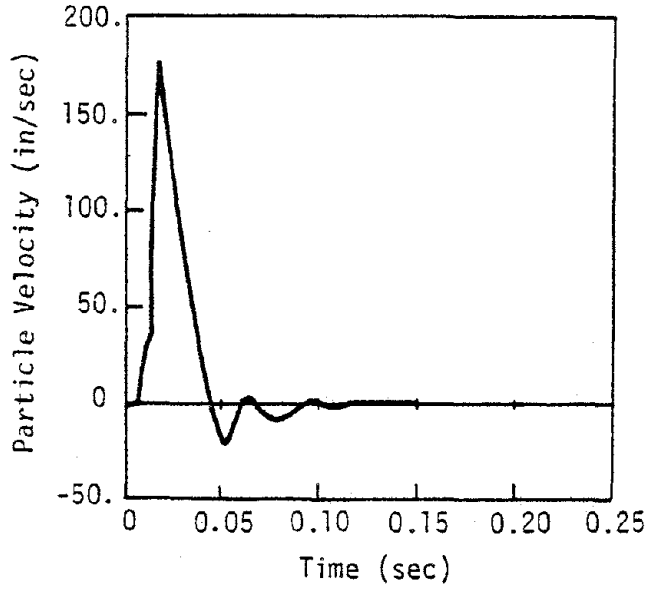

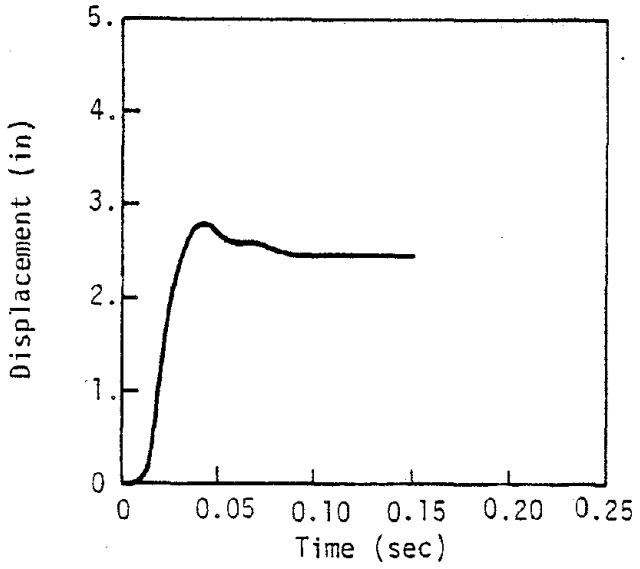

Figure V-21. Calculated Velocity Time History and Its Time History at the 15-Foot Range From a Cylindrical Explosion of 6.7 lbs/ft of TNT In a 1.5-Foot Diameter Cavity (Calculation 1C10)

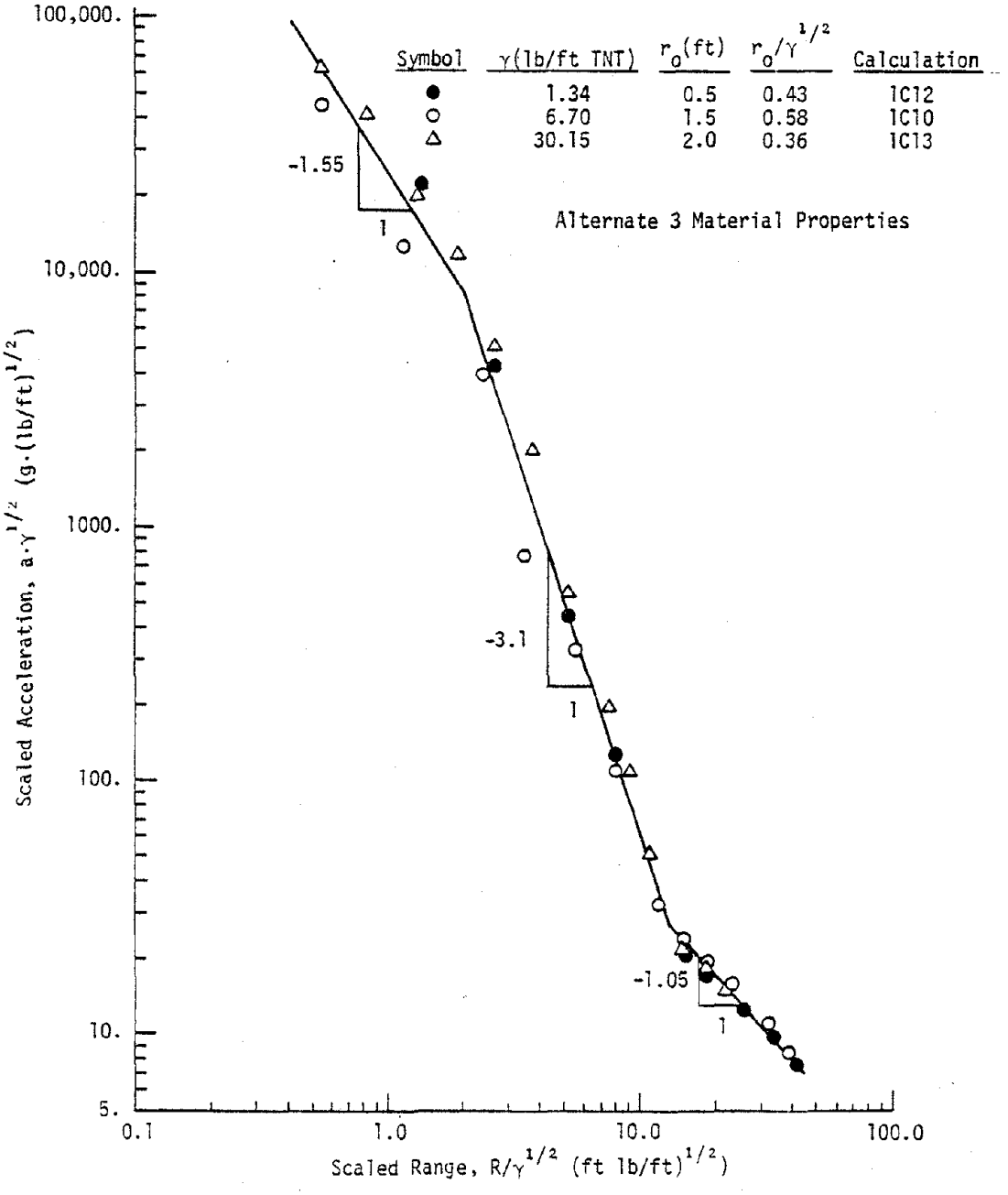

Figure V-22. Scaled Acceleration Versus Scaled Range in One-Dimensional Cylindrical Geometry

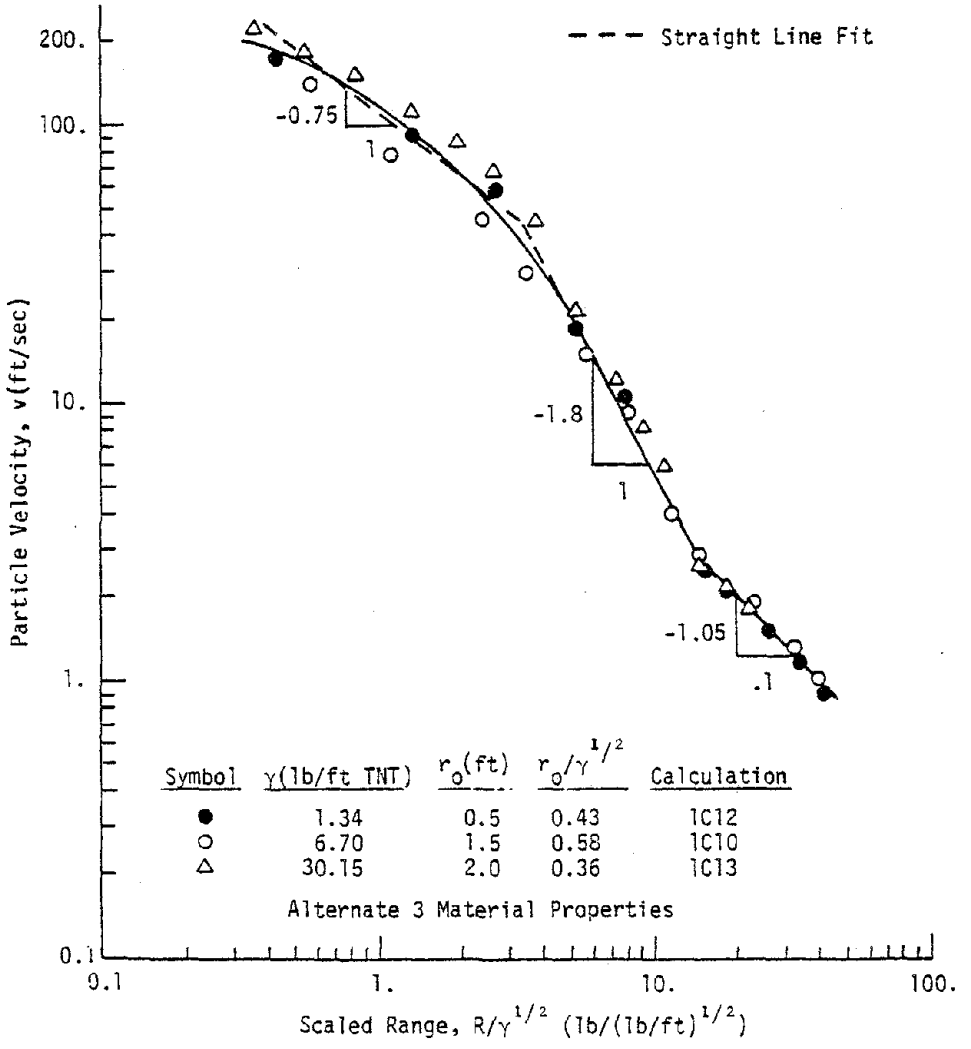

Figure V-23. Radial Particle Velocity Versus Scaled Range in One-Dimensional Cylindrical Geometry

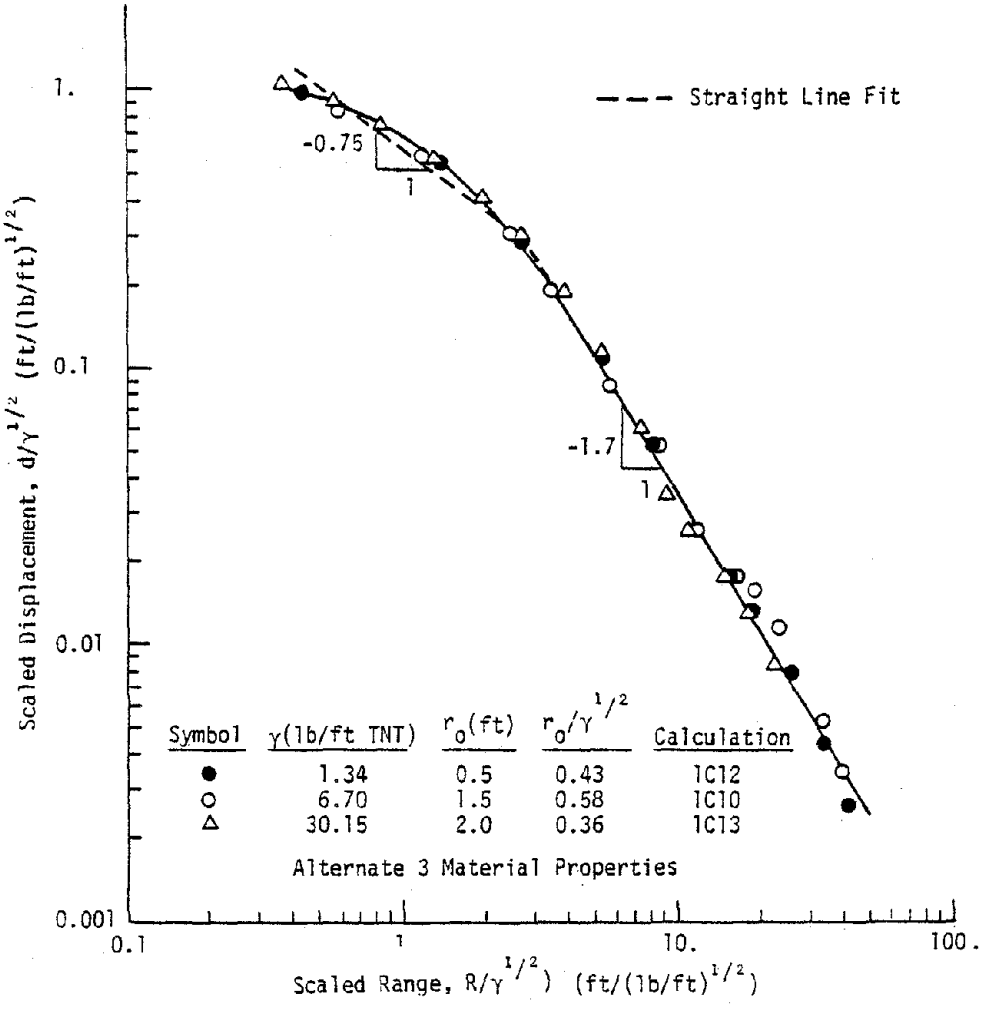

Figure V-24. Scaled Displacement Versus Scaled Range in One-Dimensional Cylindrical Geometry

scaled range of about 2 and then attenuate at -3.1. Finally, at a scaled range of about 15 the attenuation drops to about -1.05. Velocities show a similar trend. Initial attenuation is at -0.75 to a scaled range of about 3 after which it becomes about -1.8. At a scaled range of about 14, the attenuation rate decreases to -1.05. The low initial attenuation rates appear to be due to highly plastic behavior near the source. The change which occurs at $R/\gamma^{\frac{1}{2}} = 14$ corresponds to the transition to elastic behavior.

Displacements show a similar trend in the close-in and intermediate regions (attenuation at -0.75 to a scaled range of about 3 then at -1.7) but no elastic transition is evident. This can be explained in the behavior of the outward velocity phase duration. Scaled characteristic times, defined as shown previously in figure IV-18, are shown in figure V-25. They also scale very well with $\gamma^{\frac{1}{2}}$. The outward velocity phase initially attenuates at 0.08 which is about the difference between the particle velocity and displacement attenuation rates. At a scaled range of about 20 the attenuation rate increases to 0.08. This increased attenuation compensates for the decreased particle velocity attenuation in this region so that there is little effect upon displacement attenuation.

The peak outward to peak inward velocity characteristic time varies in a complex way but the variation can be fit approximately by a line having an attenuation rate of -0.20. The total duration of the first outward cycle remains about constant with range.

Figure V-26 plots the ratio of the peak inward particle velocity to the peak outward particle velocity as a function of scaled range on

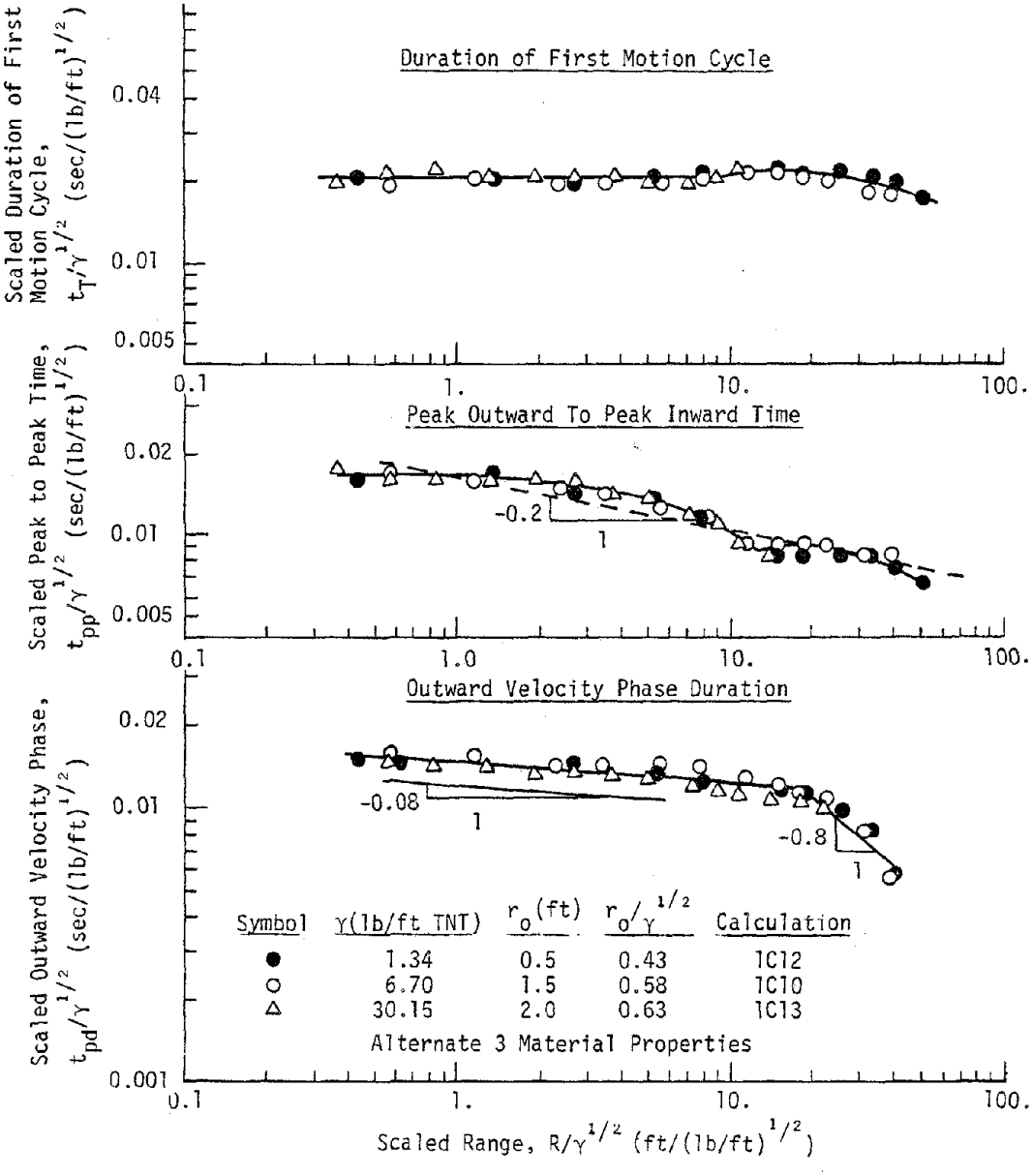

Figure V-25. Scaled Characteristic Times Versus Scaled Range in One-Dimensional Cylindrical Geometry

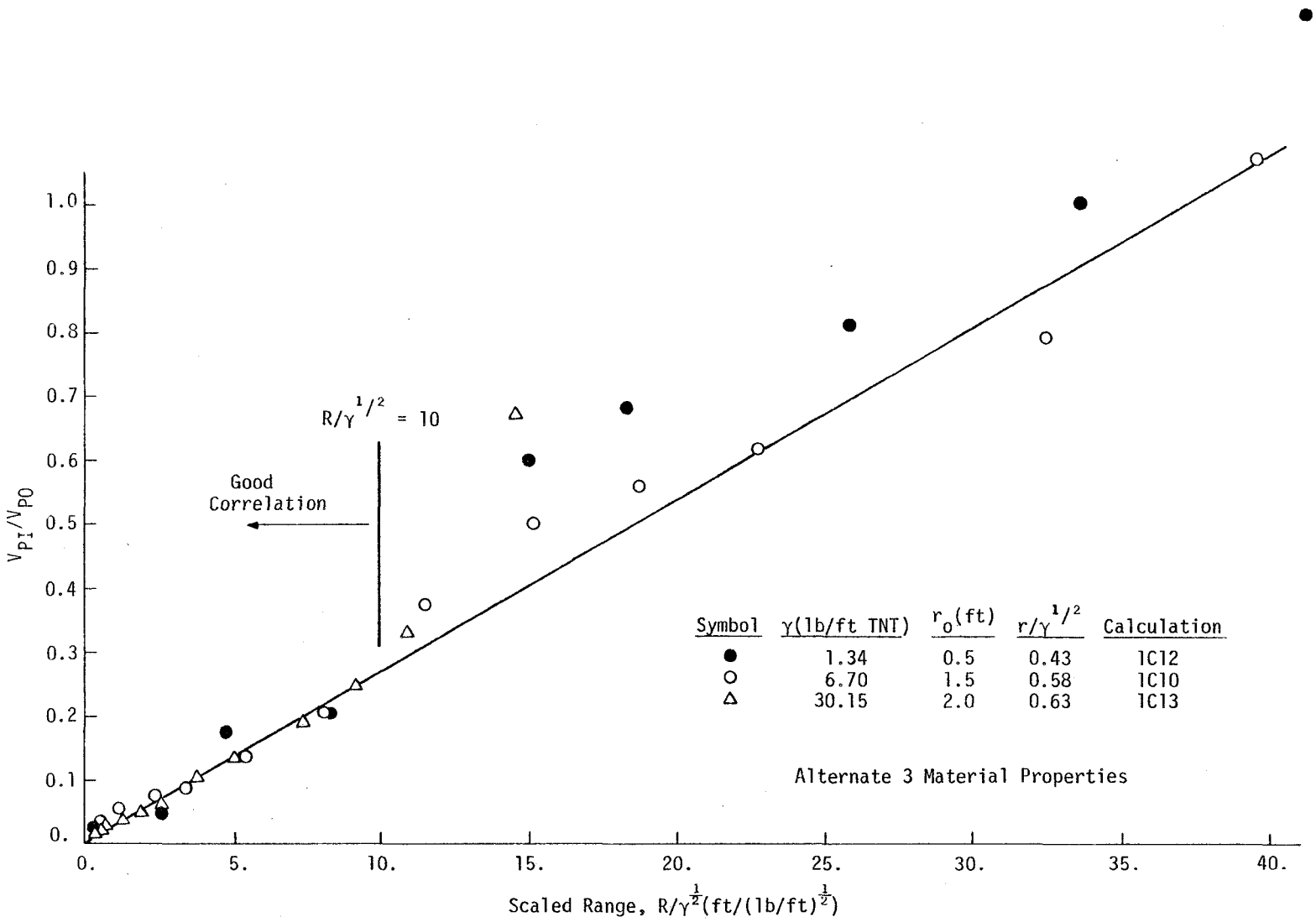

Figure V-26. Ratio of Peak Inward to Peak Outward Particle Velocity Versus Scaled Range (Linear Paper)

linear paper. The data from the three calculations collapse quite well to a scaled range of about 10 beyond which the correlation is not as good. Figure V-27 shows the same data on log-log paper. Here the data collapses well beyond a scaled range of 10. It appears that the relation between the inward to outward velocity ratio and scaled range is complex and cannot be reduced to a single scaling rule.

d. Elastic Material Property Scaling

Although a single material, McCormick Ranch silty sand, was of main interest in this study, a limited number of one-dimensional elastic calculations were performed to evaluate the effect of varying elastic properties on scaling. The calculations utilized the same input (6.7 lbs/ft of TNT equivalent in a 1.5 foot radius cavity) but varied the densities and wave speeds in a purely elastic model of the soil. The elastic parammeters were summarized earlier in table V-4.

It was found that the scaling proposed in reference V-12 and expressed for spherical geometry in equation IV-17 did not work but that the scaling expressed in equation IV-21 was needed to collapse the data. Equation IV-21 assumes that source pressure is a governing parameter. The result is that scaling terms which reduce the results to a two axis problem (i.e., scaled motion versus scaled range) cannot be derived explicitly. The results of the calculations were analyzed empirically, and it was found that simple scaling terms were present. The terms were:

$$\text{Radial Stress} \quad : \quad \frac{\sigma}{P_o} \qquad \text{(a)}$$

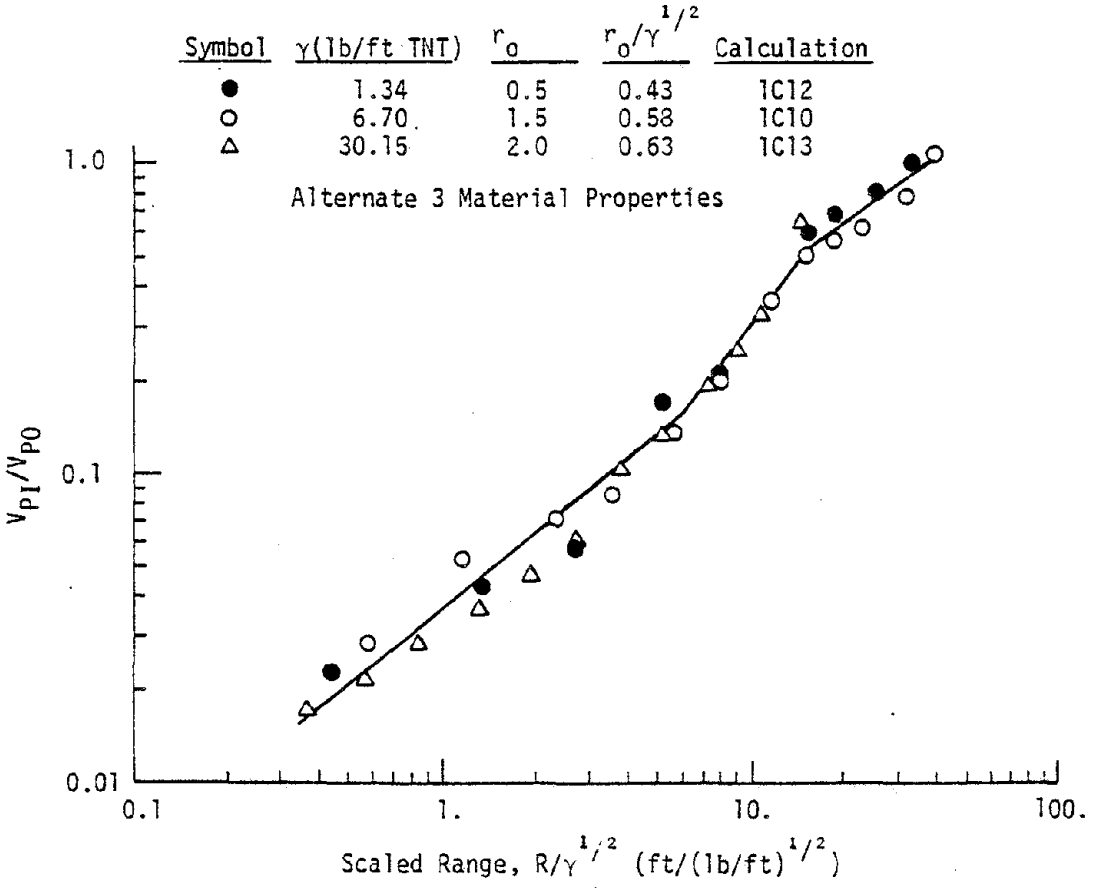

Figure V-27. Ratio of Peak Inward to Peak Outward Particle Velocity Versus Scaled Range (log-log paper)

$$\text{Radial Velocity} : \frac{\rho C v}{P_o} \qquad (b)$$

$$\text{Radial Displacement} : \frac{\rho C^2 d}{\gamma^{\frac{1}{2}}} \qquad (c) \qquad \text{(V-23)}$$

$$\text{Range} : \frac{R}{\gamma^{\frac{1}{2}}} \qquad (d)$$

where

σ = radial stress

v = radial particle velocity

d = radial displacement

ρ = material mass density

C = material elastic dilatational wavespeed

γ = lineal charge density

P_o = peak source pressure

It is interesting that these terms are precisely those which are implied by a closed form solution to the response of elastic material to a spherical ideal gas loading (ref. V-13) but they have never been used before to analyze empirical or calculational data.

The correlations which result from these terms are shown for radial stress, radial velocity, and radial displacement in figures V-28, V-29, and V-30, respectively, The P_o term has been dropped in these figures because it is constant in the three problems. This of course would be the case in the field where a common explosive is used. It can be seen that the calculated results are collapsed very well by the scaling terms of equation V-23. Similar scaling terms of acceleration and characteristic times are believed derivable in a similar way but further calculations will be necessary before they can be well defined. It is believed that the terms of equation V-23 should form the starting point for

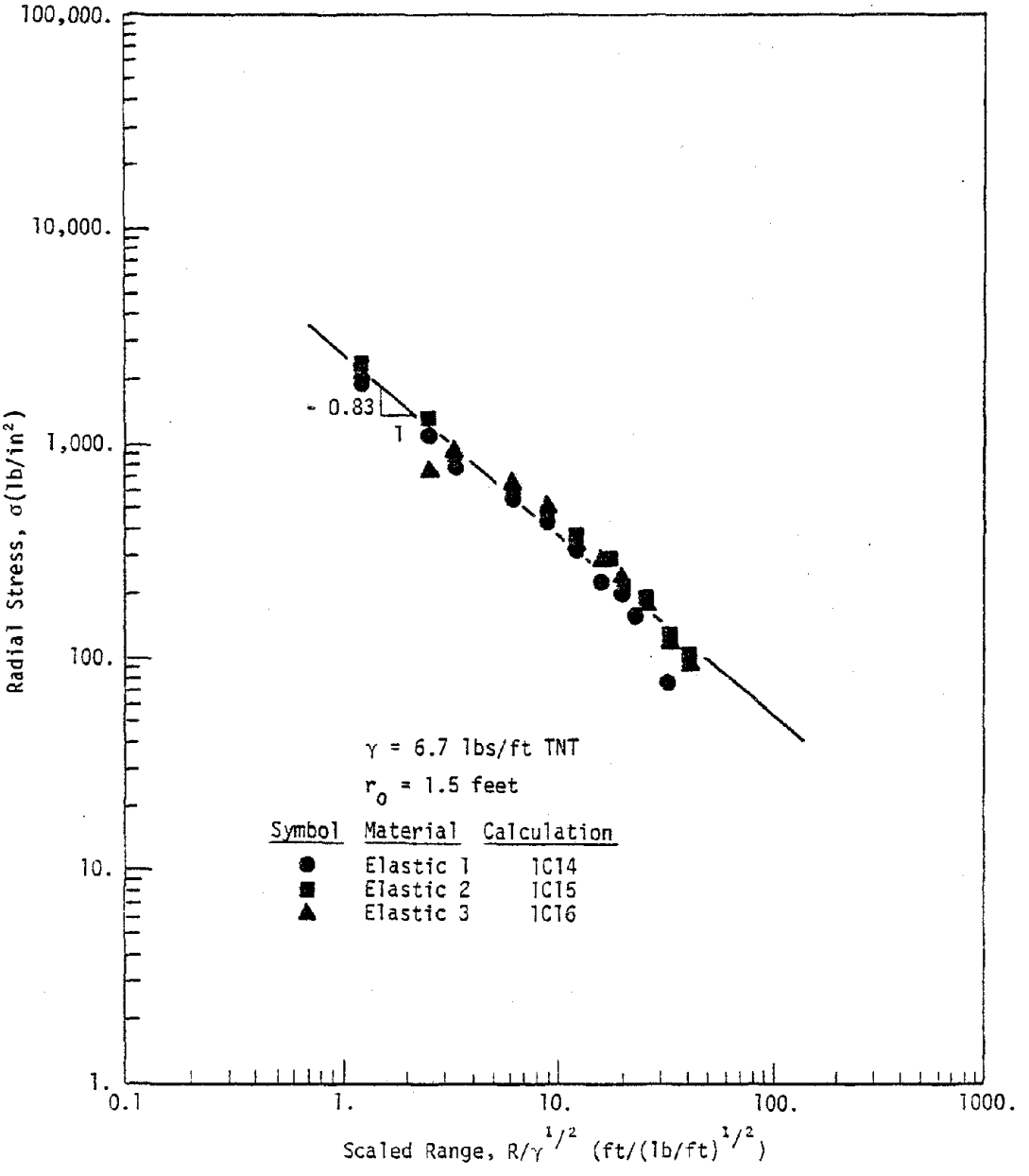

Figure V-28. Radial Stress Versus Scaled Range in Different Elastic Materials

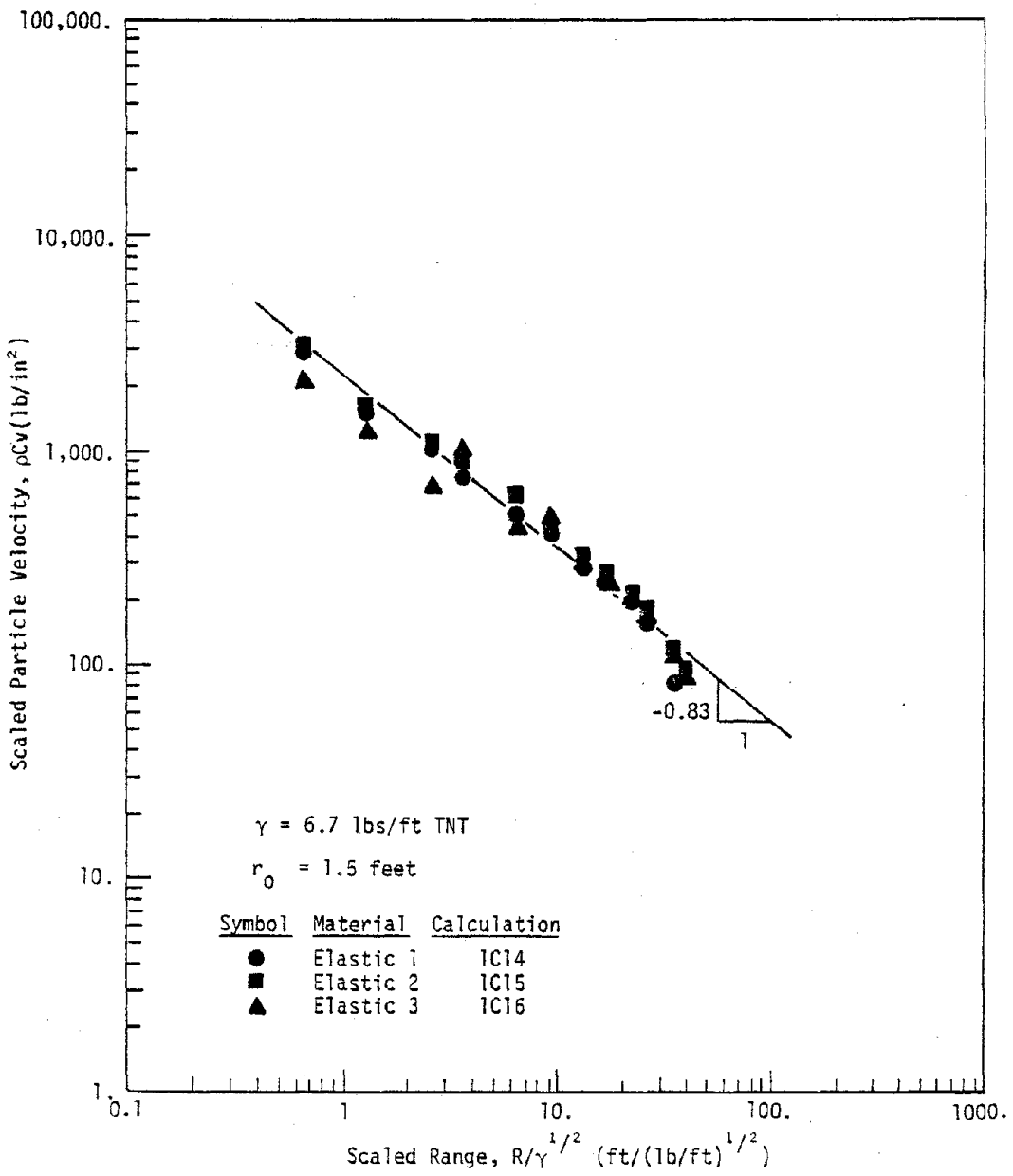

Figure V-29. Scaled Radial Particle Velocity Versus Scaled Range in Different Elastic Materials

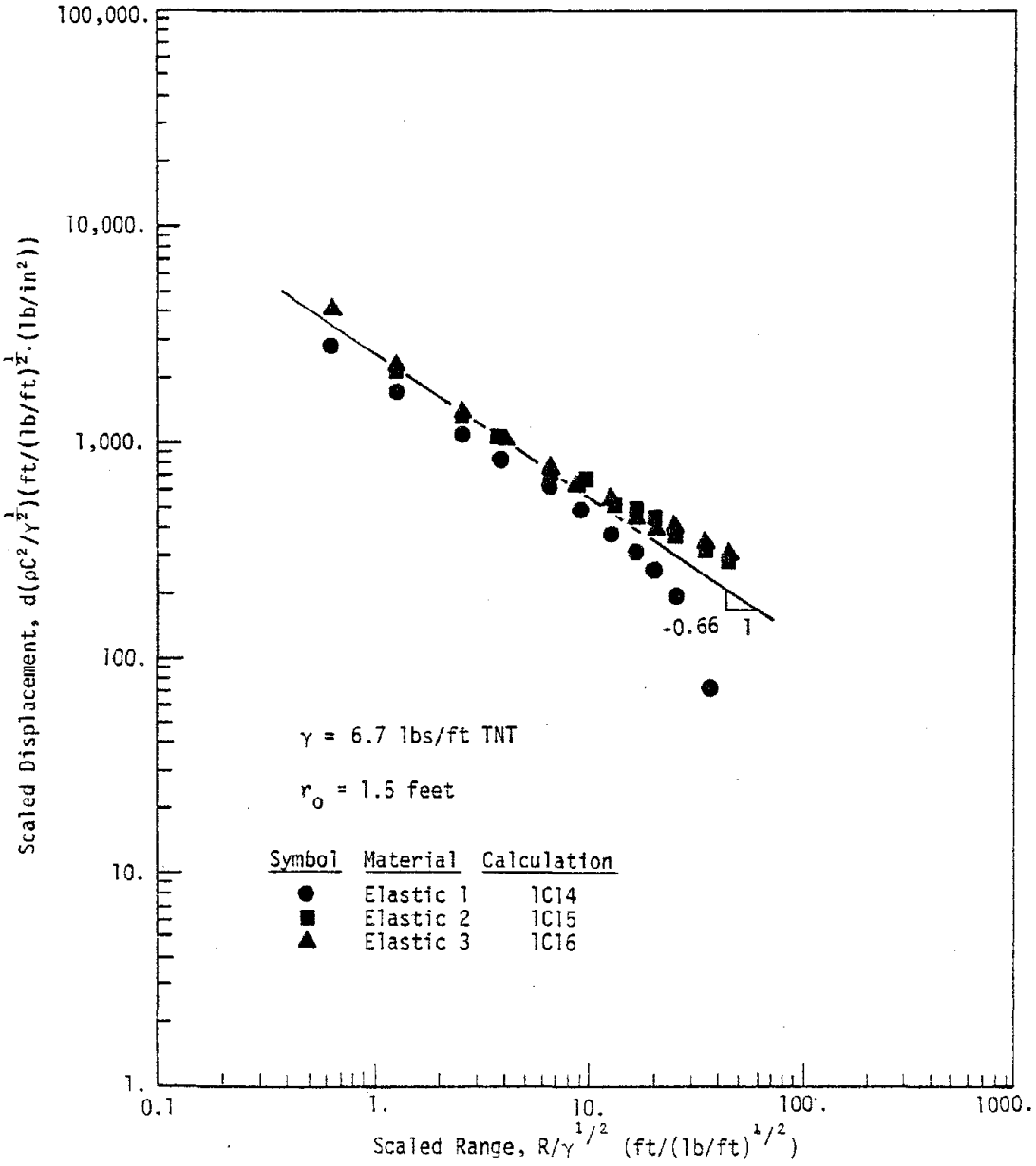

Figure V-30. Scaled Displacement Versus Scaled Range in Different Elastic Materials

future extensions of simulation to different materials.

e. Effects of Inelastic Material Variations

In the course of establishing a best estimate of material properties for McCormick Ranch soils, several one-dimensional cylindrical problems were calculated with varying material properties. The number of calculations is not sufficient to derive quantitative relations between specific properties and response. However, the results of the calculations yield some qualitative insight into inelastic material property effects.

All of the calculations were run using an ideal gas source with 6.7 lbs/ft of equivalent TNT (5 lbs/ft of PETN) in a 1.5-foot radius cavity (the Shot 6 and 7 experimental configuration). The results presented here are for the four material property options previously summarized in table V-3. The options allow a view of response change for a constant yield surface with two different hydrostat stiffnesses, and for a constant hydrostat with three different yield surfaces.

Peak radial stresses for the four material property conditions are plotted in figure V-31. Peak radial stress versus range for alternates 1, 3, and 4, which all used the seismic-based hydrostat, is effectively the same. The radial stress for alternate 2, which had a softer and more hysteretic hydrostat based on laboratory data, attenuates at a significantly higher rate. The failure surface does not seem to play a significant role in controlling radial stresses.

Peak radial velocities versus range are plotted in figure V-32. Velocities separate on the basis of hydrostat, with very little apparent

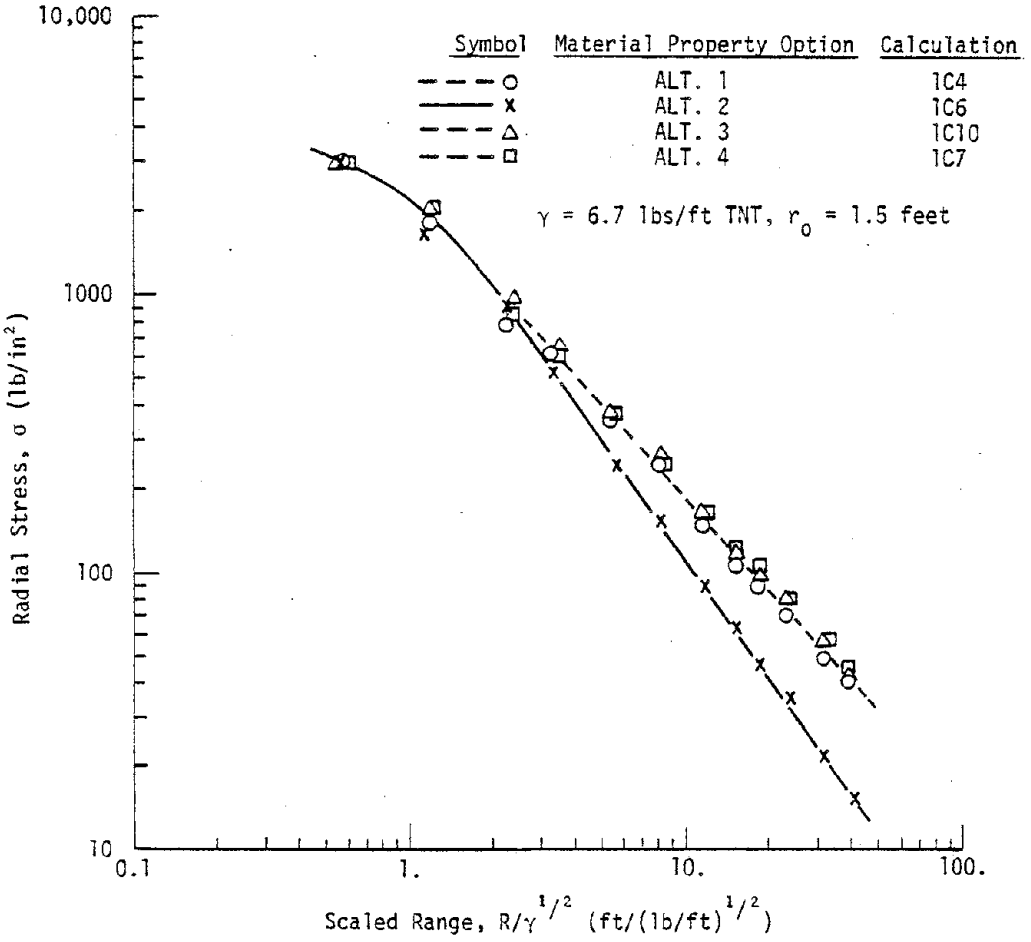

Figure V-31. Effect of Inelastic Material Properties on Radial Stress in One-Dimensional Cylindrical Geometry

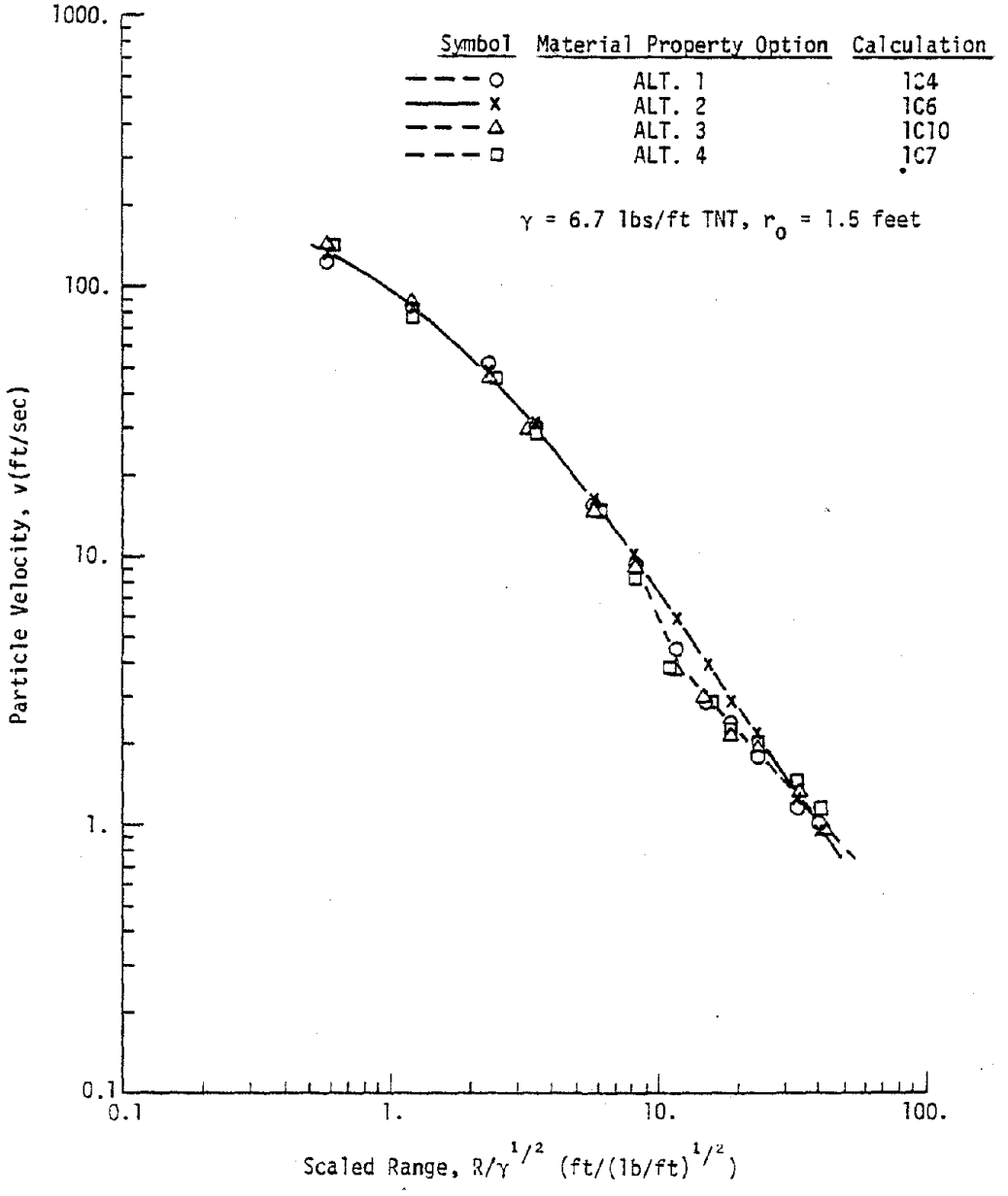

Figure V-32. Effect of Inelastic Material Properties on Radial Particle Velocity in One-Dimensional Cylindrical Geometry

yield surface effect. This result is similar to that for stresses. The amplitude difference between the two hydrostat conditions is reduced, however, compared to the stress differences. In a set of experimental data the differences would probably not be considered significant. It appears that the large hysteresis in the laboratory-based hydrostat is causing a larger stress attenuation but the softer modulus is leading to higher corresponding particle velocities. The result is that the particle velocities are not far different from those which occur for the seismic-based hydrostat.

Peak radial accelerations are given in figure V-33. The accelerations in the softer hydrostat material (alternate 2) remain higher than in the seismic-based hydrostat cases beyond a scaled range of about 4, partially because of somewhat higher particle velocities in this region, but also because of a smaller rise time to peak particle velocity. The seismic-based hydrostat is a softening type in which the secant and tangent moduli decrease with increasing stress. This causes rise time to increase with range. The laboratory-based hydrostat is a stiffening type in which moduli increase with increasing stress. This condition leads to the propagation of shocks or steep velocity gradients without a significant change in rise time with range.

Displacements, shown in figure V-34, are strongly influenced by both failure surface and the hydrostat differences. The differences in peak displacements between alternates 1 and 3, which used the same hydrostat but different failure envelopes, is about a factor of five. The difference between alternates 1 and 2 which used the same failure envelope but different hydrostats is about 50 percent. The differences between

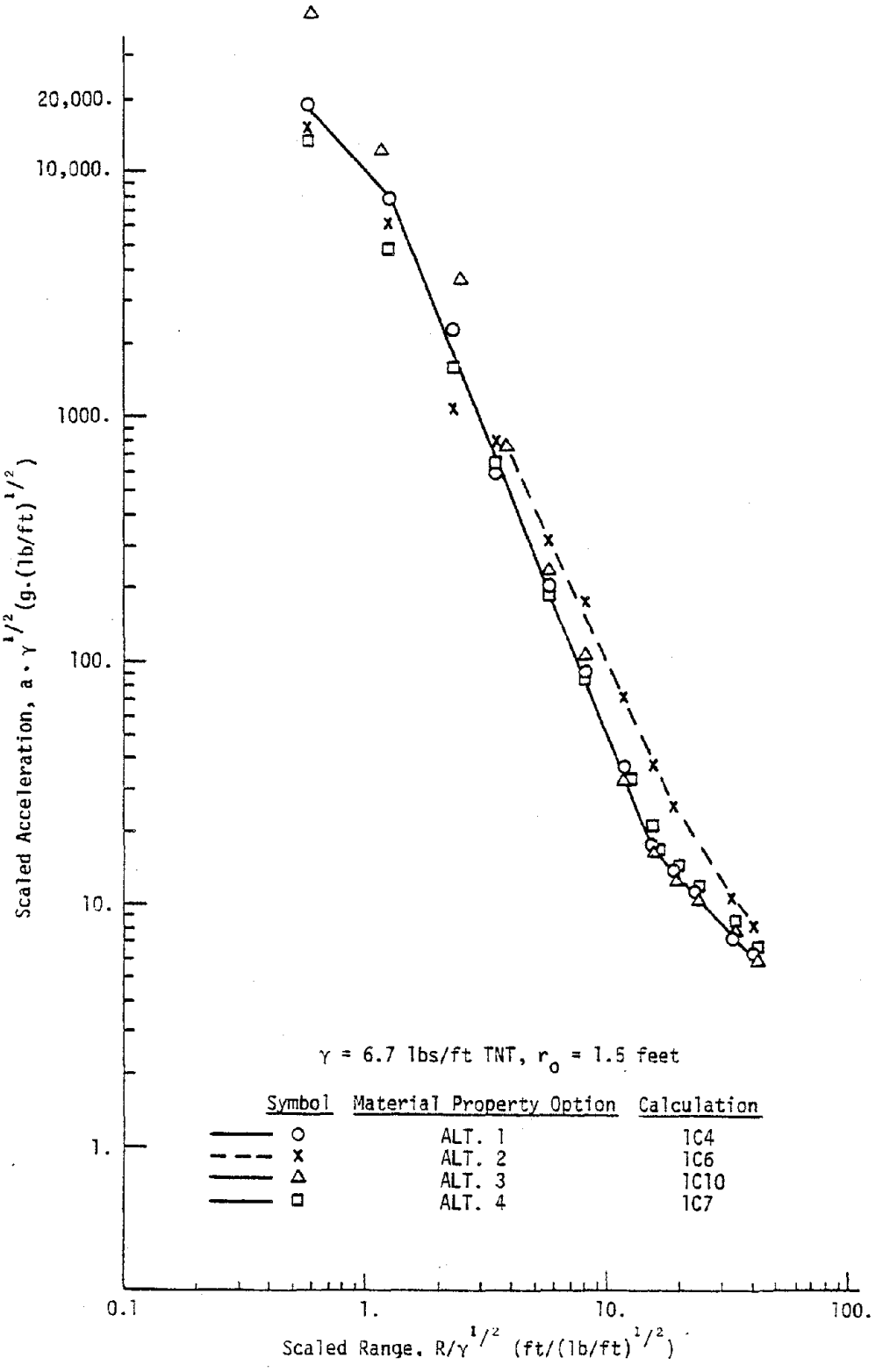

Figure V-33. Effect of Inelastic Material Properties on Radial Acceleration in One-Dimensional Cylindrical Geometry

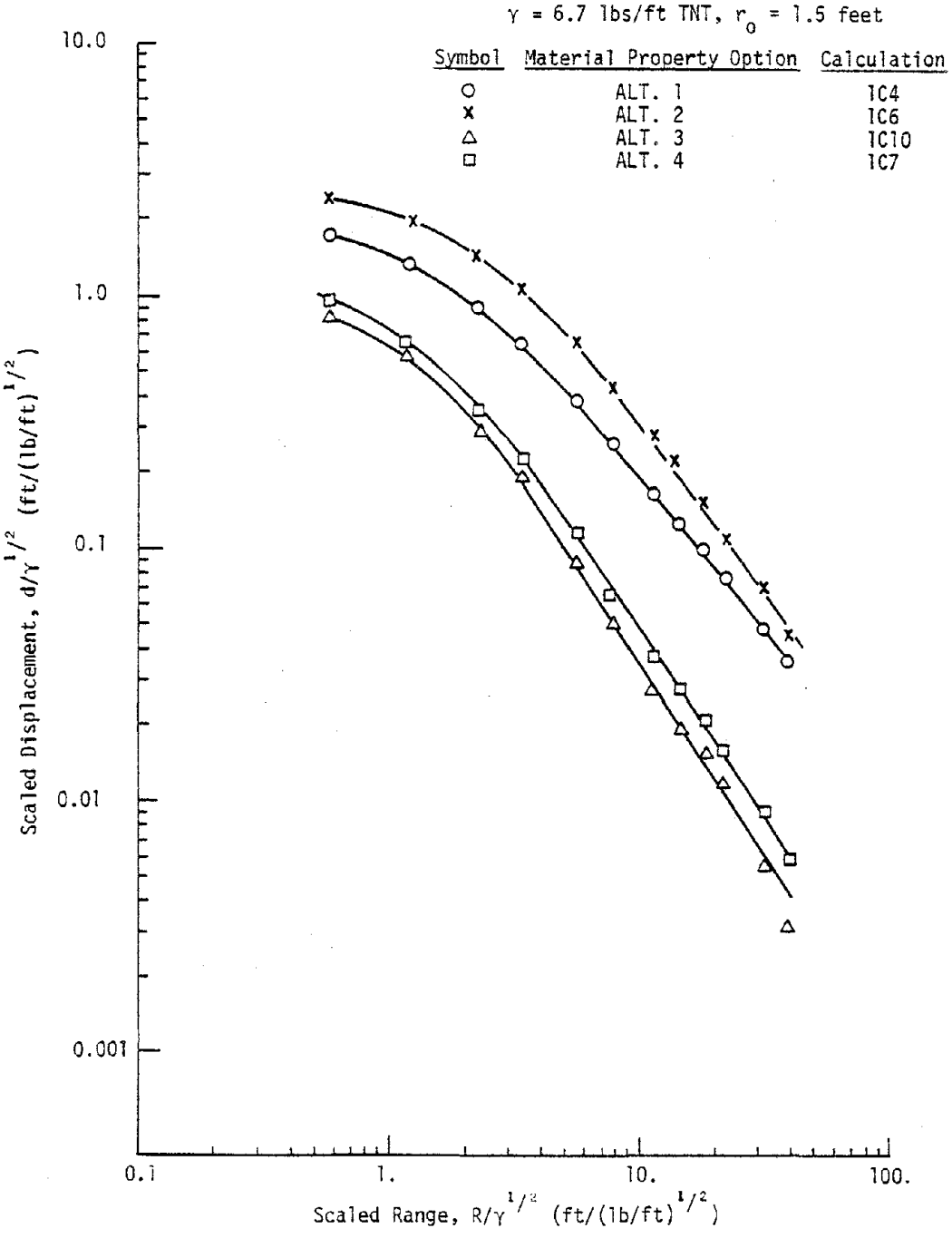

Figure V-34. Effect of Inelastic Material Properties on Radial Displacement in One-Dimensional Cylindrical Geometry

alternate 1, 3, and 4 behavior, which all used the same seismic-based hydrostat, appear due to the influence of the failure surface on the outward phase duration of the velocity pulse. Figure V-35 shows comparisons of calculated velocity time histories at about the 15-foot range in each of the calculations. The rise to peak velocity and the peak velocity for the seismic-based hydrostat cases (alternates 1, 3, and 4) are all about the same. The velocity decay, however, is substantially different. Alternate 1 decays very slowly and has a large outward phase duration. Alternate 4 has a much shorter outward phase duration while that of alternate 3 is somewhat larger than alternate 4, but still much less than alternate 1.

Figure V-36 displays the failure envelopes associated with alternates 1 and 3 (the cases having the longest and shortest outward phase durations) and the stress paths experienced by these materials, at the 15-foot range. The major difference in the stress paths occurs on unloading from the peak pressure. The unloading is controlled by the failure envelopes. Deviatoric stresses in the alternate 3 material remain high during unloading while those in the alternate 1 material decay as required by the failure envelope. It appears that the slope of the failure surface has the major effect on the outward phase duration. The failure surface for alternate 4 has a slope intermediate between alternates 1 and 3 and this is consistent with the intermediate outward phase duration result for alternate 4. Although these calculations indicate a clear relationship between failure envelope and outward phase duration, a larger number of calculations would be required to develop a quantitative correlation.

The effect of the hydrostat on the velocity time history can also

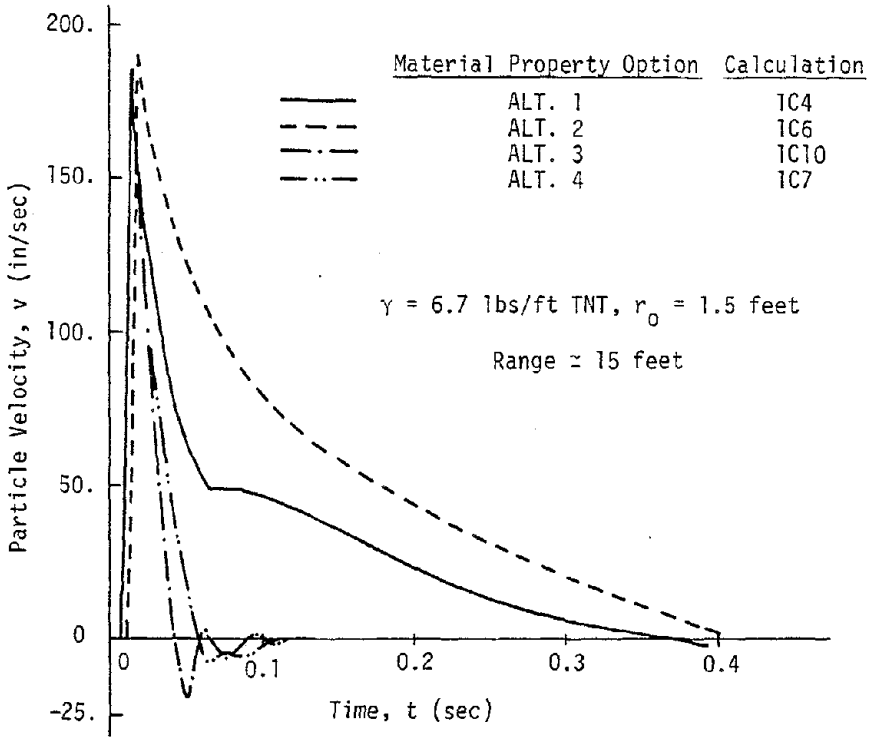

Figure V-35. Effect of Inelastic Material Properties on Particle Velocity Time Histories in One-Dimensional Geometry

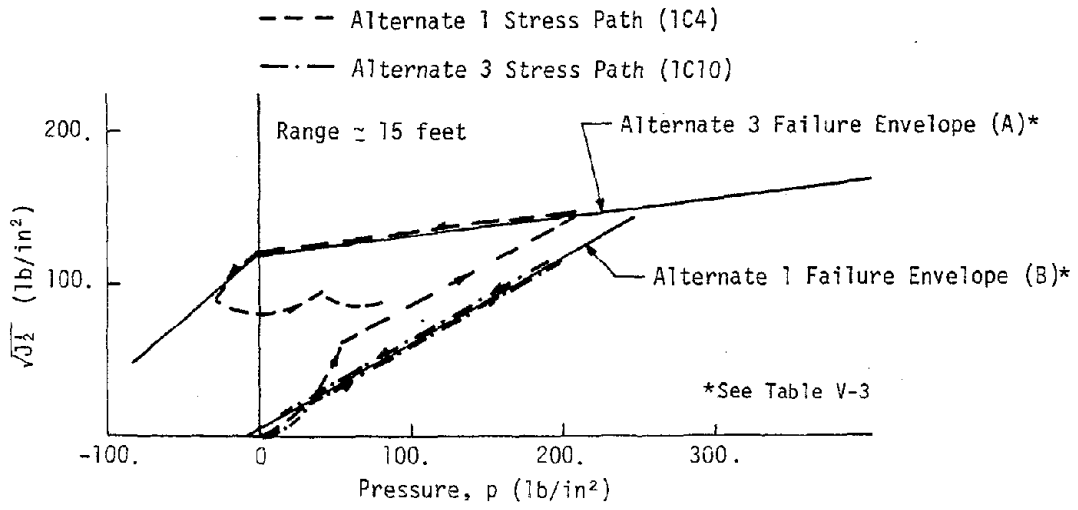

Figure V-36. Effect of Failure Envelope Upon Stress Paths in One-Dimensional Cylindrical Geometry

be observed in figure V-36. Alternates 1 and 2 used the same failure envelope but different hydrostats. Alternate 2, associated with the softer laboratory-based hydrostat, arrives later and achieves a somewhat higher peak velocity. Although it's outward phase duration is on the order of that of alternate 1, it maintains significantly higher velocities throughout its time history. As with failure surface effects, the qualitative observations cannot be quantified without additional parametric calculations.

The observed differences between the various calculations with different material properties were used in selecting alternate 4 as a best estimate of in-situ properties. Although precise quantitative relations were not derived, the material properties were varied iteratively in a trial and error process to achieve reasonable agreement with the measured data of cylindrical Shot 7. Arrival time, the ratio of inward to outward velocity and outward phase duration were given main emphasis in determining agreement.

f. Effects of Finite Explosive Length

The effects of finite explosive length in cylindrical geometry were investigated with three two-dimensional calculations in which the explosive length was taken as 12 feet, 48 feet, and 96 feet (2C4, 2C5, 2C6). The input was a pressure-time history applied over the region of the explosive. The input pressure was derived from that produced by an ideal gas equivalent of 6.7 lbs/ft of TNT in a 1.5-foot radius cavity, modified for venting by the method described previously. These input conditions, combined with the 12-foot explosive length, correspond to the experimental

conditions for Shots 6 and 7. The calculations were performed with a plane of symmetry at the mid-depth of the explosive so that free-surface effects were not present.

Figure V-37 compares radial accelerations at the explosive mid-depth in the explosive length variations with those calculated in one-dimension (1C18) with the same pressure time input. The comparisons indicate that the finite explosive results coincide with the one-dimensional results to a transition range, R_0, which is about 0.6 times the explosive length. Beyond this range the accelerations from the finite length explosions attenuate more rapidly. The attenuation rate depends upon the stress region. The 12-foot results begin to attenuate more rapidly at a scaled range of about 2.3 ft/(lb/ft)$^{\frac{1}{2}}$ which is well in the inelastic region. The attenuation rate in this region is -3.6 which is in good agreement with the spherical results shown previously (fig. V-14). The attenuation rate beyond a scaled range of about 7 is -1.75 and this is in good agreement with spherical results in the elastic region.

The 48-foot results transition to spherical behavior and elastic behavior at about the same scaled range so that only the elastic attenuation rate is exhibited. The 96-foot results coincide closely with the one-dimensional results at all ranges. Extrapolating from the 12-foot and 48-foot results, which exhibit a transition at 0.6 H, the transition for the 96-foot calculation should be at a scaled range of about 22 ft/(lb/ft)$^{\frac{1}{2}}$. Since this range is at the last calculated range, no transition is evident in the results.

Although free-surface effects will be discussed later, figure V-37

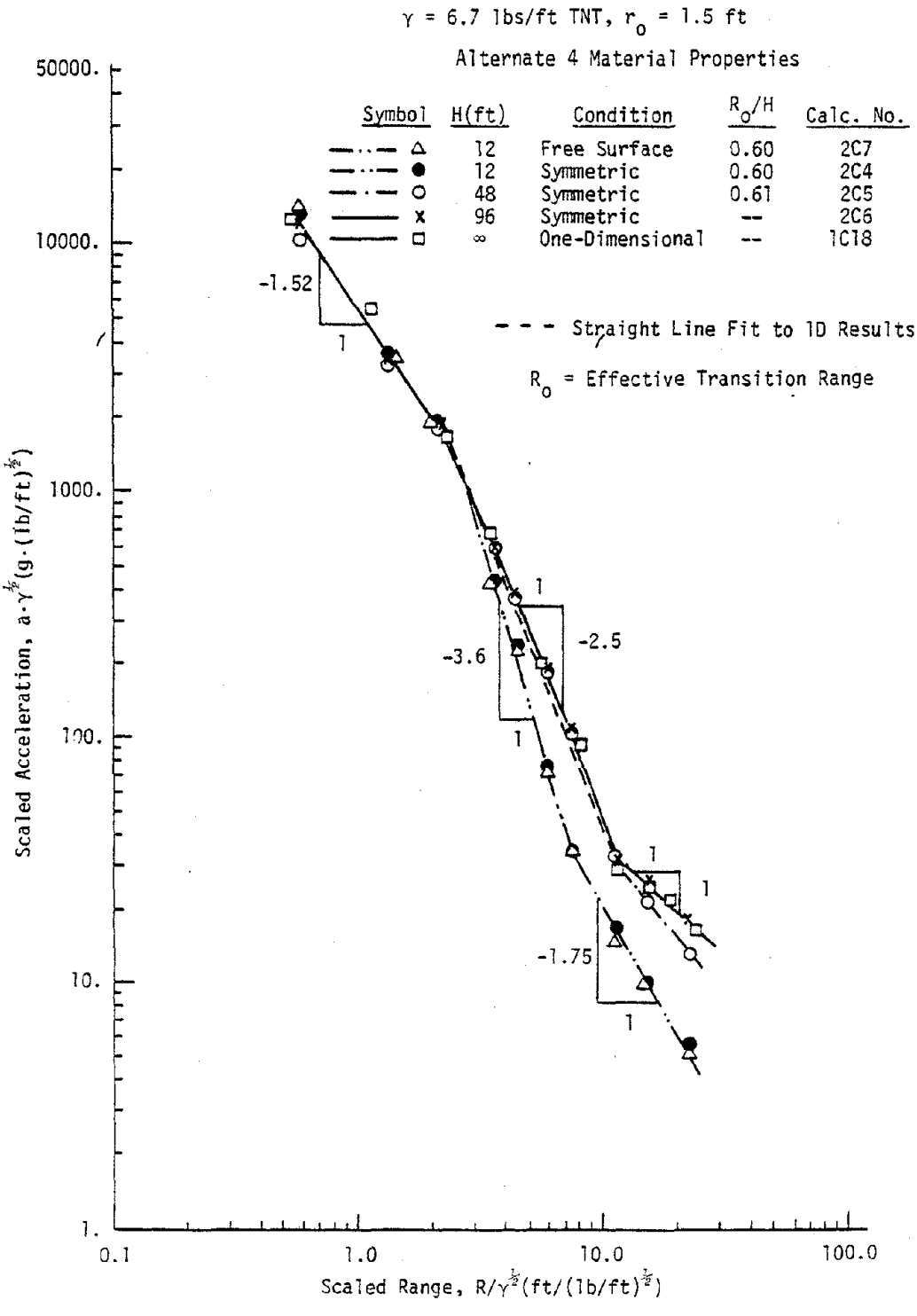

Figure V-37. Effect of Explosive Length on Radial Acceleration at Explosive Mid-Depth in Cylindrical Geometry

shows a comparison between 12-foot explosive length results in the symmetric calculation (2C4) and a free-surface calculation (2C7). There is no apparent effect of the free-surface on the peak radial accelerations at the explosive mid-depth. This supports the validity of the use of symmetric calculations for evaluating radial mid-depth behavior.

The radial particle velocity results, shown in figure V-38, are similar to those for acceleration. The effective transition range for velocity is about 0.6 H. Beyond this range the velocities attenuate at an inelastic rate of -2.7 and an elastic rate of -1.75, both of which are in good agreement with the spherical results given earlier (fig. V-15). The agreement between the 12-foot symmetric and free-surface results is also good.

Radial displacement results (fig. V-39) transition to spherical attenuation at about 0.55 H. The spherical attenuation rate is -2.5 and there is no apparent transition to elastic behavior. The spherical attenuation rate and the absence of an elastic transition is in good agreement with the spherical results shown in figure V-16.

The radial accelerations, velocities, and displacements at the mid-depth can be fit by the following relations:

$$a\gamma^{\frac{1}{2}} = 5370\ (R/\gamma^{\frac{1}{2}})^{-1.52} \qquad R/\gamma^{\frac{1}{2}} \leq 2.5\ \text{ft/(lb/ft)}^{\frac{1}{2}} \quad \text{(a)}$$

$$a\gamma^{\frac{1}{2}} = 15737\ (R/\gamma^{\frac{1}{2}})^{-2.5} \qquad 2.5\ \text{ft/(lb/ft)}^{\frac{1}{2}} < R/\gamma^{\frac{1}{2}} \leq 0.6\ H/\gamma^{\frac{1}{2}} \quad \text{(b)}$$

$$a\gamma^{\frac{1}{2}} = 8972\ (H/\gamma^{\frac{1}{2}})^{1.1}\ (R/\gamma^{\frac{1}{2}})^{-3.6} \qquad R/\gamma^{\frac{1}{2}} > 0.6\ H/\gamma^{\frac{1}{2}} \quad \text{(c)} \qquad \text{(V-24)}$$

$$v = 110\ (R/\gamma^{\frac{1}{2}})^{-0.75} \qquad R/\gamma^{\frac{1}{2}} \leq 3.2\ \text{ft/(lb/ft)}^{\frac{1}{2}} \quad \text{(d)}$$

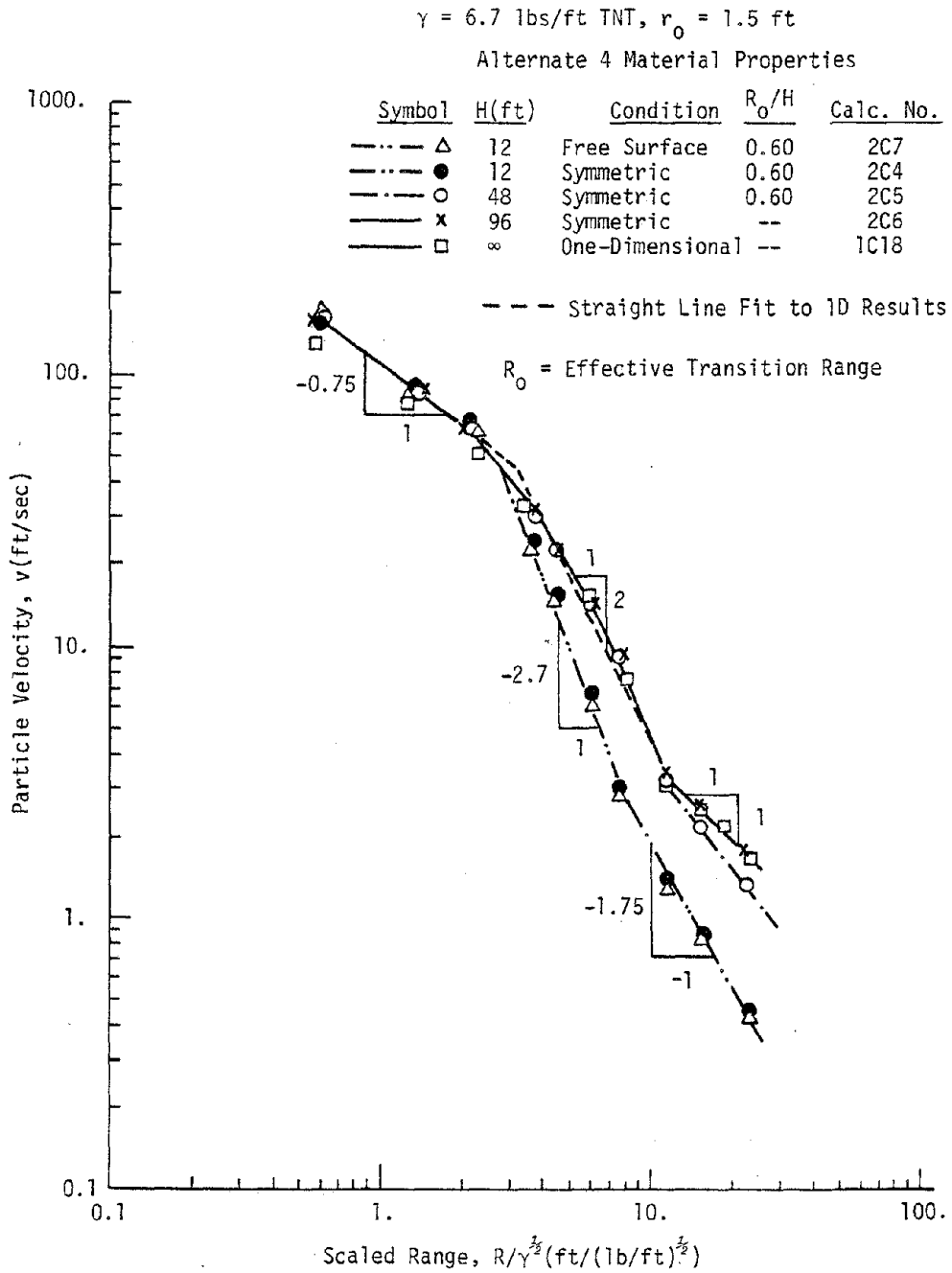

Figure V-38. Effect of Explosive Length on Radial Velocity at Explosive Mid-Depth in Cylindrical Geometry

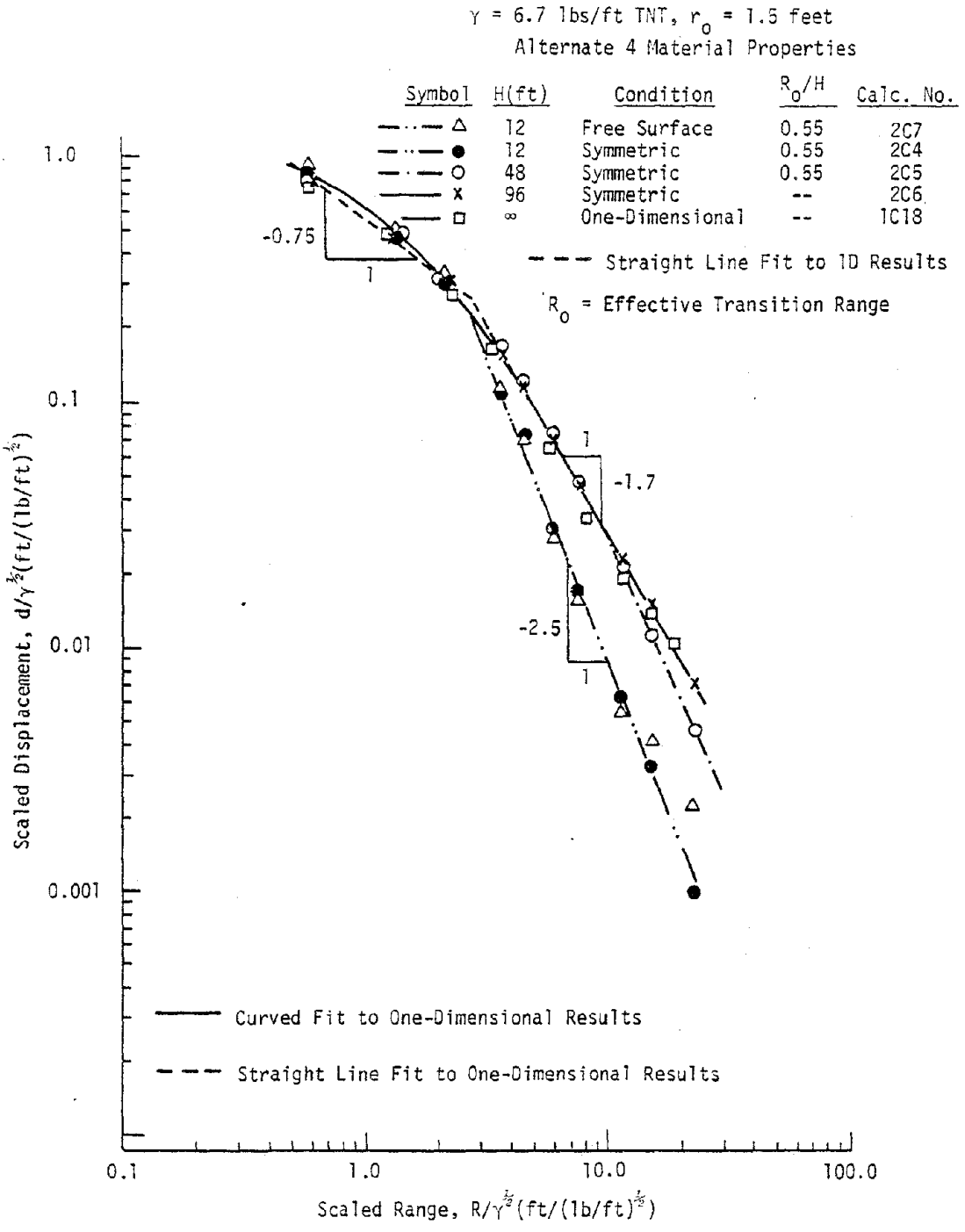

Figure V-39. Effect of Explosive Length on Radial Displacement at Explosive Mid-Depth in Cylindrical Geometry

$$v = 460\ (R/\gamma^{\frac{1}{2}})^{-2} \qquad 3.2 < R/\gamma^{\frac{1}{2}} \leq 0.6\ H/\gamma^{\frac{1}{2}} \quad \text{(e)}$$

$$v = 322\ (H/\gamma^{\frac{1}{2}})^{0.7}(R/\gamma^{\frac{1}{2}})^{-2.7} \qquad R/\gamma^{\frac{1}{2}} > 0.6\ H/\gamma^{\frac{1}{2}} \quad \text{(f)}$$

$$d/\gamma^{\frac{1}{2}} = 0.56\ (R/\gamma^{\frac{1}{2}})^{-0.75} \qquad R/\gamma^{\frac{1}{2}} \leq 2.8 \quad \text{(g)} \quad \text{(V-24)}$$

$$d/\gamma^{\frac{1}{2}} = 1.6\ (R/\gamma^{\frac{1}{2}})^{-1.7} \qquad 2.8 < R/\gamma^{\frac{1}{2}} \leq 0.55\ H/\gamma^{\frac{1}{2}} \quad \text{(h)}$$

$$d/\gamma^{\frac{1}{2}} = 1.0\ (H/\gamma^{\frac{1}{2}})^{0.8}\ (R/\gamma^{\frac{1}{2}})^{-2.5} \qquad R/\gamma^{\frac{1}{2}} > 0.55\ H/\gamma^{\frac{1}{2}} \quad \text{(i)}$$

where

a = acceleration in g's

v = velocity in ft/sec

d = displacement in feet

R = range in feet

γ = lineal charge density in lbs/ft of TNT

H = height of explosive in feet

Figure V-40 presents the scaled characteristic times of the velocity waveform as a function of scaled range. The characteristic times are the same as those defined on figure IV-18. The 12-foot characteristic times are about 75 to 80 percent of those for the 48-foot, 96-foot and one-dimensional calculations, which all scatter together. The duration of the first outward motion cycle does not vary with range. The outward velocity phase is constant with range to a scaled range of about 9 beyond which it decreases rapidly. As noted for previous calculations, this increased attenuation combines with decreased peak velocity attenuation in the elastic region so that displacement attenuation is not affected. The peak to peak times decrease with range at an average attenuation rate of -0.2.

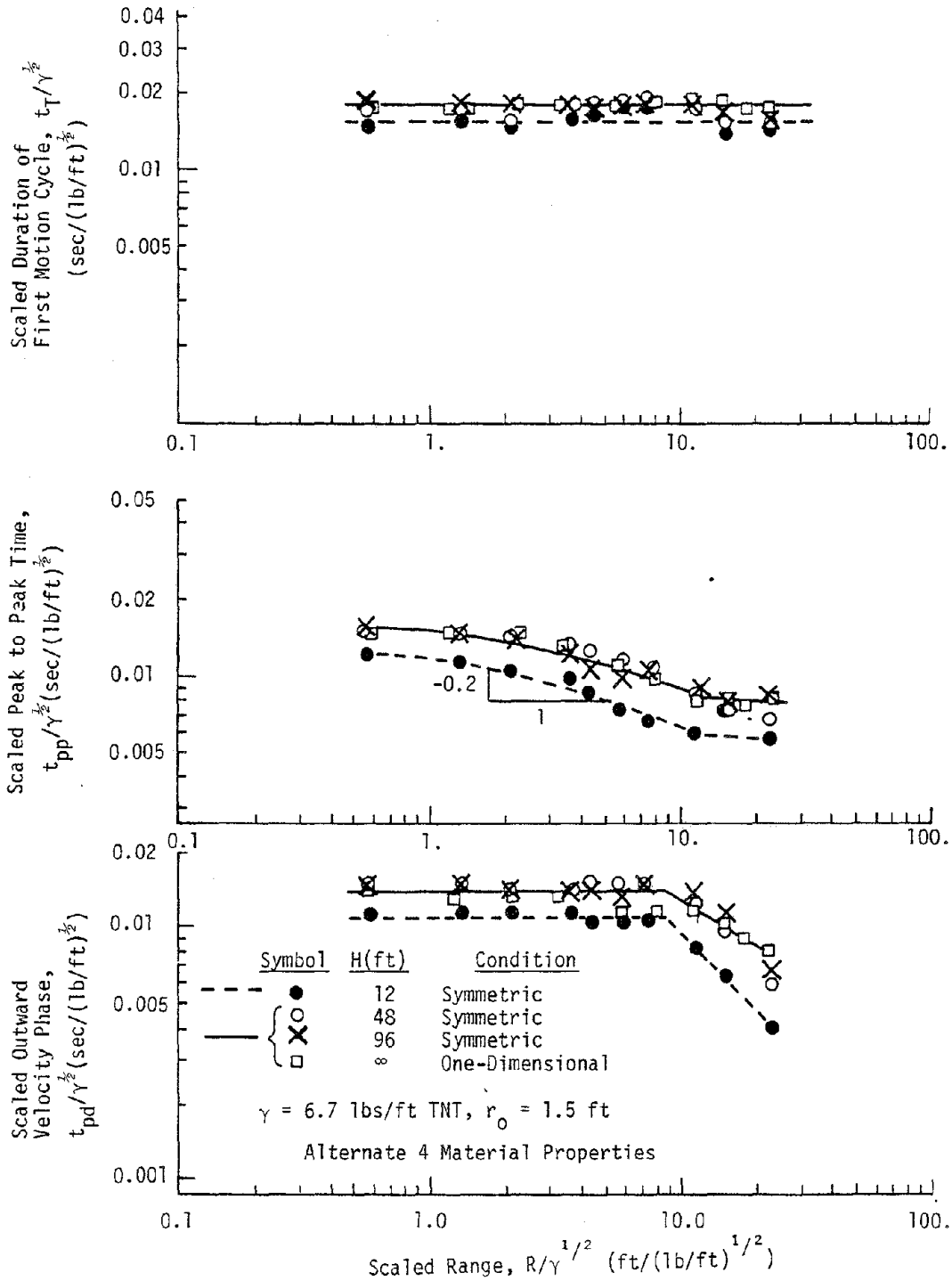

Figure V-40. Variation of Radial Velocity Characteristic Times with Range at the Explosive Mid-Depth in Cylindrical Geometry

The difference between the characteristic times in the 12-foot calculation and those in the other calculations can be interpreted from the calculated waveforms and the wave structure shown previously in figure IV-13. Figure V-41 compares particle velocity waveforms from the three symmetric calculations at three different ranges. The velocity waveform at a given range consists of the basic one-dimensional waveform (including its inward component) as modified by the P- and SP-relief waves. The time at which these reliefs take effect is dependent upon the explosive height, H. What is thought to be the SP-relief in the 48-foot and 96-foot calculations is identified in figure V-41. These effects occur so late in time that the relief has little or no effect upon the first motion cycle at most ranges. The amplitude of the peak velocity in the first cycle is reduced by the P-relief wave, but the characteristic times in the first cycle do not appear to be much affected. Hence, the 48-foot and 96-foot times agree closely with the one-dimensional times. The SP-relief wave in the 12-foot calculation, however, arrives during the decay from the peak velocity in the first motion cycle. In this calculation, therefore, it does affect the characteristic times and leads to the shortened times evident in figure V-40.

Characteristic times as a function of explosive height, are shown in figure V-40. At an $H/\gamma^{\frac{1}{2}}$ of 20 ft/(lb/ft)$^{\frac{1}{2}}$ and above the times are not dependent on H and they correspond to the one-dimensional characteristic times. For scaled explosive heights below 20 ft/(lb/ft)$^{\frac{1}{2}}$ the times decrease. The data from the single 12-foot calculation is not sufficient to develop a strong correlation below this scaled height. However, the break point is a function of soil wave speeds. Times will be affected when the SP-relief arrival time coincides with or is earlier than the

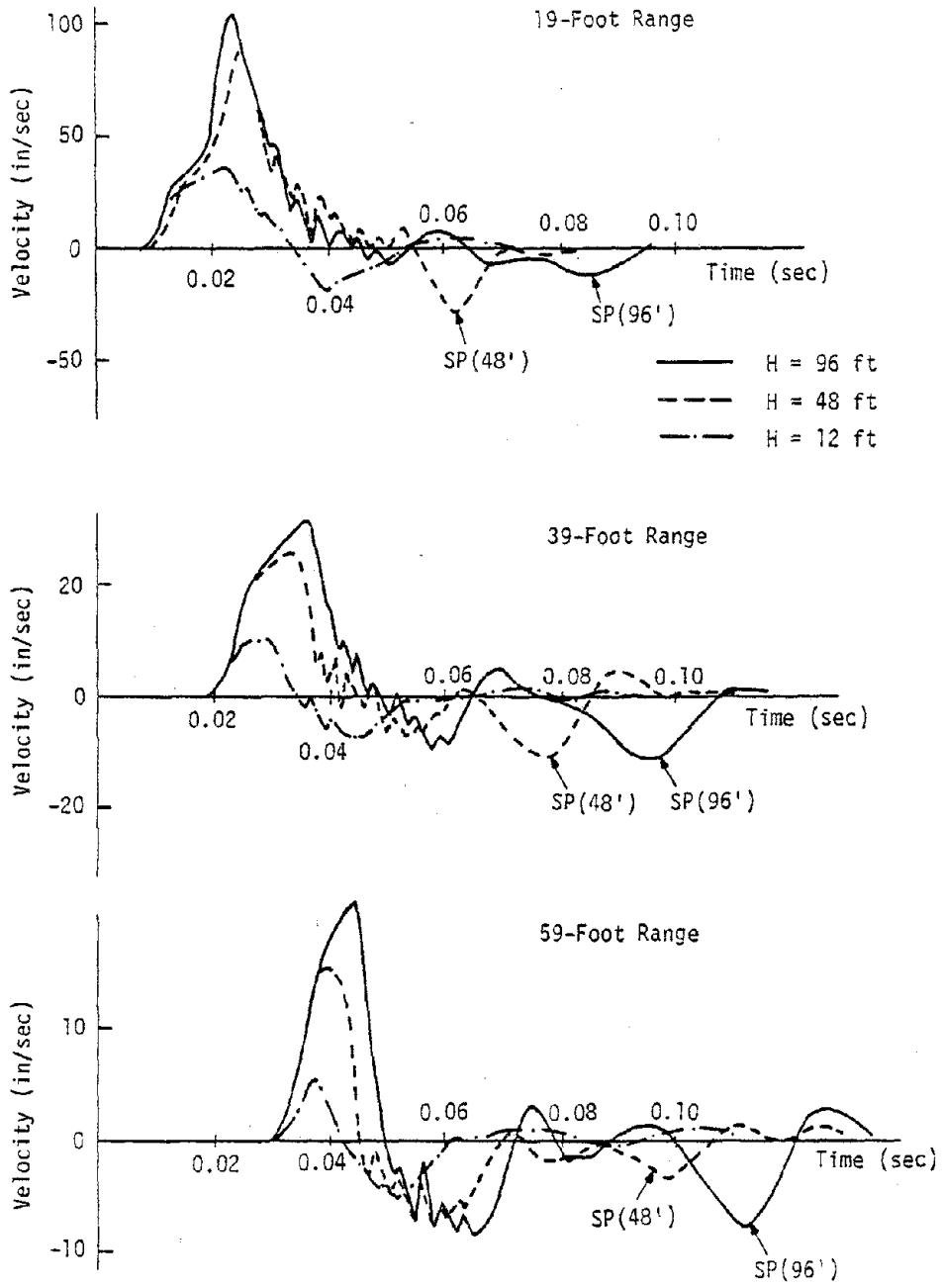

Figure V-41. Comparison of Velocity Time Histories from Two-Dimensional Cylindrical Symmetric Calculations

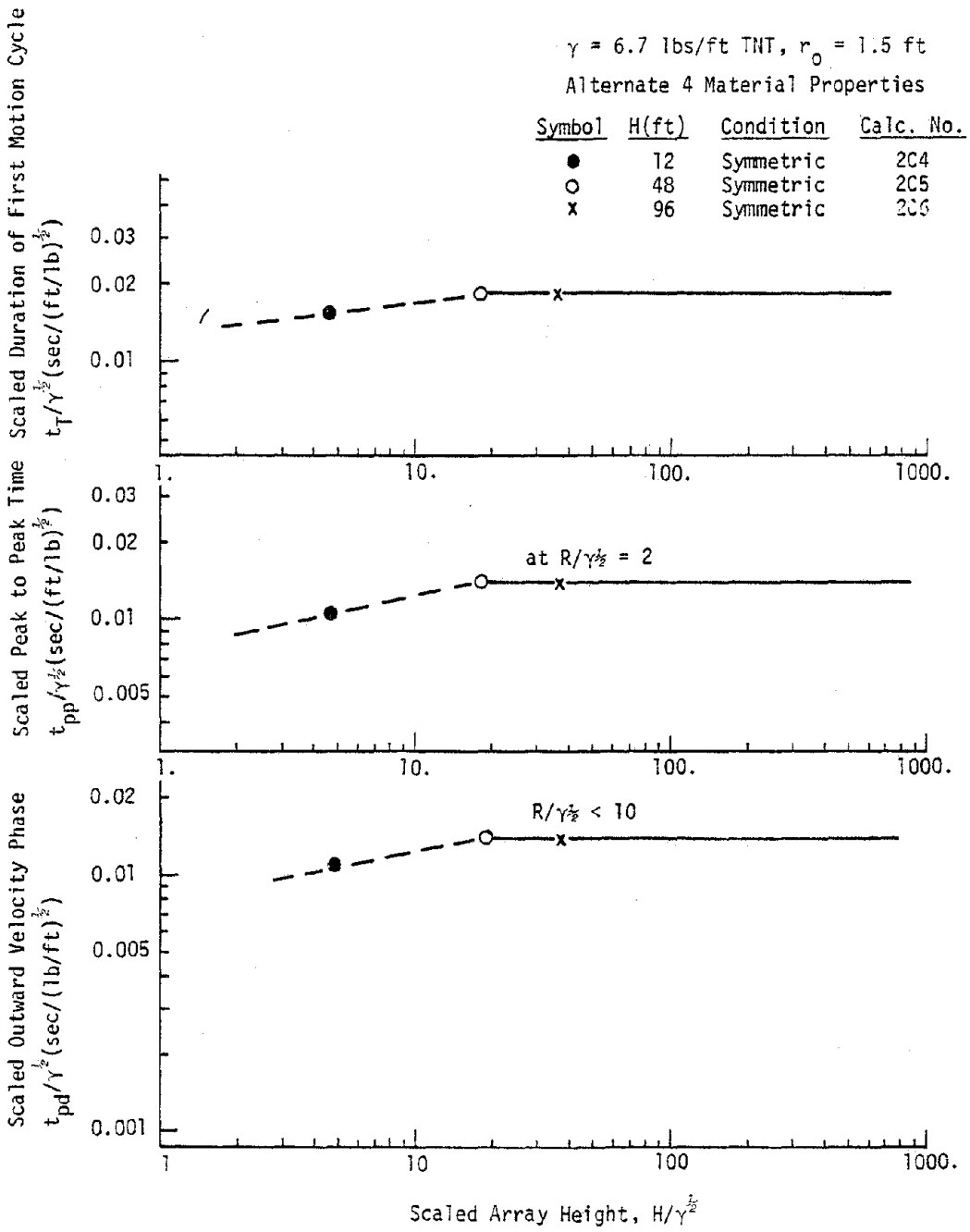

Figure V-42. Effect of Explosive Height on Radial Velocity Characteristic Times in Cylindrical Geometry

outward phase duration in one-dimension. The outward phase duration can be written for scaled ranges less than about 10 as

$$t_{pd} = K\gamma^{\frac{1}{2}} \qquad \text{(V-25)}$$

where

t_{pd} = outward phase duration

γ = lineal charge density

K = a constant

The time between the initial compression arrival and the SP-relief arrival

$$t_{sp} - t_a = \frac{H}{2} \frac{\sqrt{C_p^2 - C_s^2}}{C_p C_s} \qquad \text{(V-26)}$$

where

t_{sp} = time of SP-relief arrival

t_a = time of initial compression arrival

H = explosive height

C_p = P-wave speed

C_s = S-wave speed

Taking C_s to be approximately one-half C_p, the scaled array height at which t_{pd} and $(t_{sp} - t_a)$ are equal is

$$\frac{H}{\gamma^{\frac{1}{2}}} = 0.87K\, C_p \qquad \text{(V-27)}$$

Using the P-wave speed of the calculations (1650 ft/sec) and the value of K from figure V-39 (0.014 sec/(lb/ft)$^{\frac{1}{2}}$), the transition scaled array height is 20.1 ft/(lb/ft)$^{\frac{1}{2}}$. This value was selected as the break point for the dashed fits of figure V-42.

Figure V-43 presents the ratios of the peak inward velocity to the peak outward velocity in the first motion cycle as a function of scaled range. The 48-foot and 96-foot results scatter together and are fit reasonably well with a straight line over all ranges. The ratios for the 12-foot calculation are much larger than those of the 48 and 96-foot calculations everywhere. This is apparently due to strong inward SP effects arriving during the inward portion of the first motion cycle, as described above in relation to characteristic times. Within the two-dimensional results, the differences are consistent. The 48-foot and 96-foot results, however, are inconsistent with the one-dimensional ratios from the calculation with pressure versus time input. It would be expected the two-dimensional ratios would exceed the one-dimensional ratios due to decreased outward and increased inward amplitudes, both due to P-relief. The results show the inverse. This is believed to be caused by the formulation of the pressure-time input at times after venting is assumed to occur. The pressure was held at zero in the one-dimensional calculation while the pressure was held at the overburden stress in the two-dimensional calculation. This latter assumption is believed to be a more correct representation of field conditions.

Results presented to this point are for locations at the mid-depth of the explosive. In general, radial motions at off-center positions decrease. Off-center variations in the three symmetric calculations were collapsed very well when range and off-center distance were scaled by the explosive height (R/H and Z/(H/2)). Fits to the off-center peak motion amplitudes, as a proportion of the peak mid-depth amplitudes, are plotted as functions of the scaled off-center distance in figures V-44,

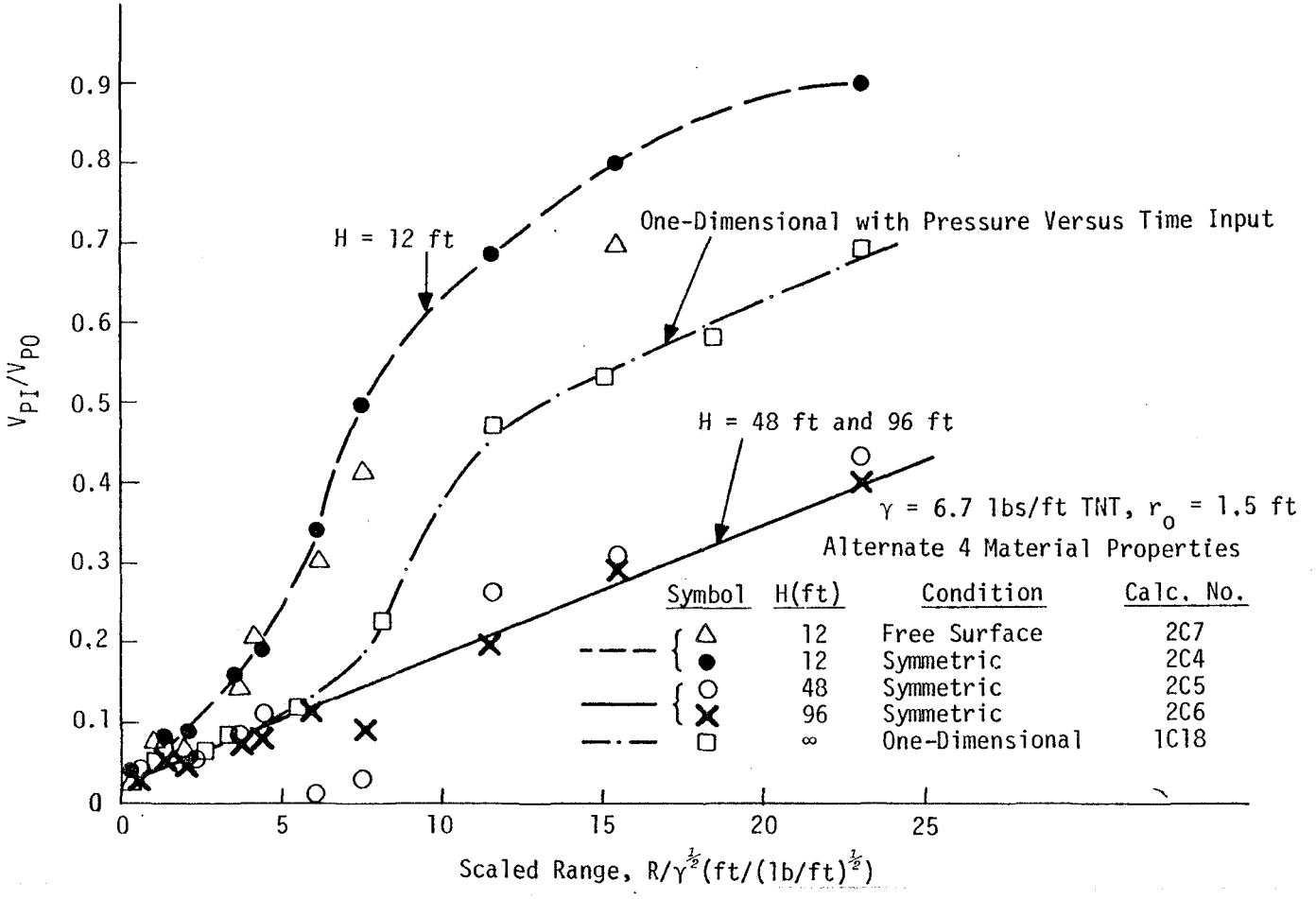

Figure V-43. Ratio of Peak Inward to Peak Outward Radial Velocity in Two-Dimensional Cylindrical Calculations

V-45, and V-46. The off-center particle velocity outward phase duration variations are plotted in figure V-47. These off-center results are not applicable to realistic field problems because of the influence of the free-surface. However, they are thought to be representative of cross-range variations which might be expected in planar events.

g. Free-Surface Effects

Free-surface effects in cylindrical geometry were evaluated with a calculation (2C7) for a 12-foot long cylindrical charge buried 6 feet to the charge top. The calculations utilized the same input and material properties as used in the 12-foot symmetric calculation (2C4). Although a single calculation cannot be used to derive high confidence general relations for free-surface effects, the calculated results provide an indication of free-surface trends.

Peak motion amplitudes at the explosive mid-depth were compared with corresponding quantities in the symmetric calculation previously in figures V-37, V-38, and V-39. The mid-depth results in the two calculations were in very good agreement. There are differences, however, for target locations between the mid-depth and the free-surface. The differences increase as the free-surface is approached. The cause of the differences are free-surface reflections which affect the free-surface region immediately upon arrival of the incident wave, and also affect greater depths at later times as they penetrate downward into the material.

The nature of the differences between symmetric and free-surface behavior is illustrated in figure V-48 which compares radial velocity-

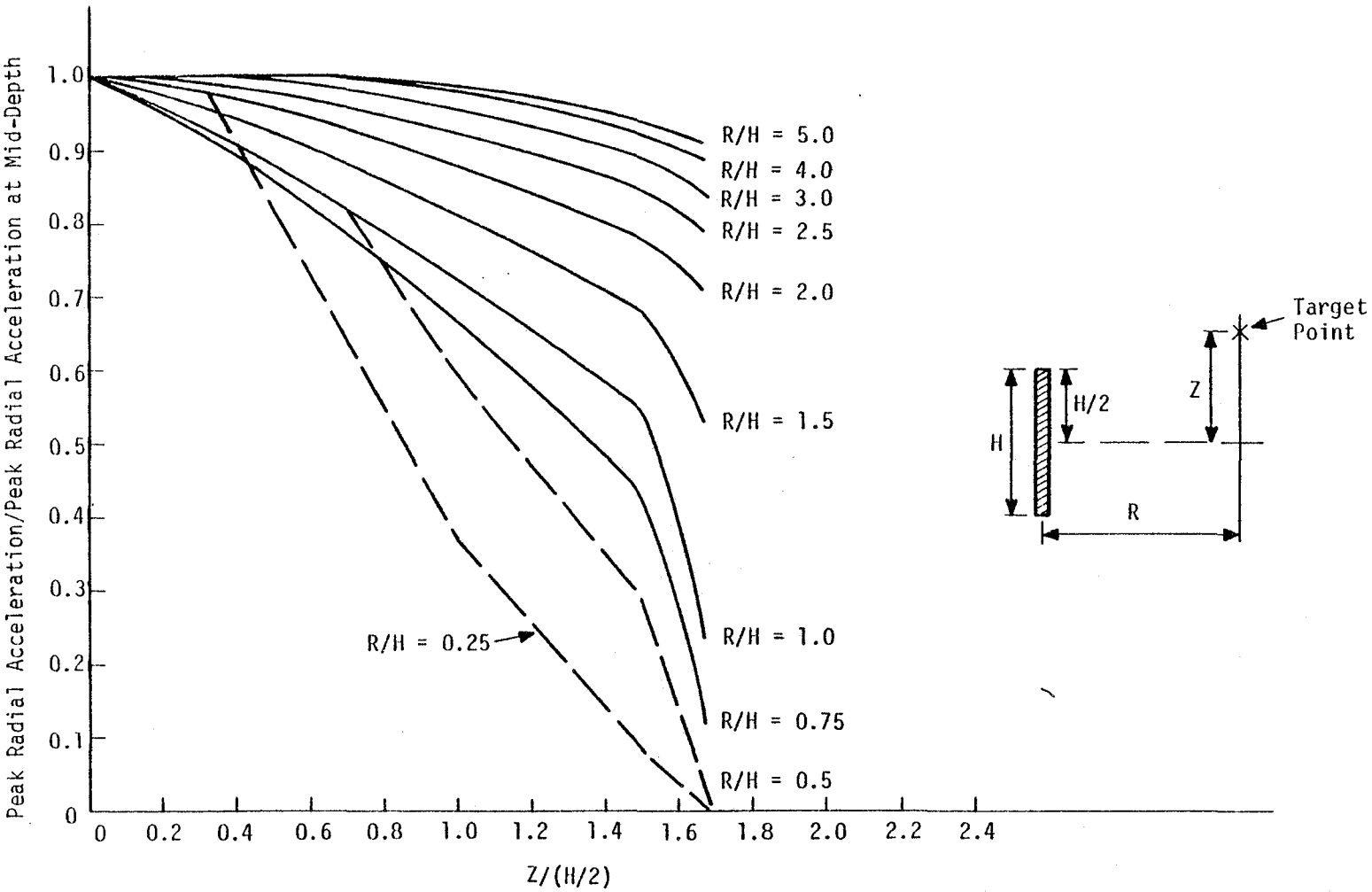

Figure V-44. Variation of Peak Radial Acceleration with Off-Center Distance in Cylindrical Geometry

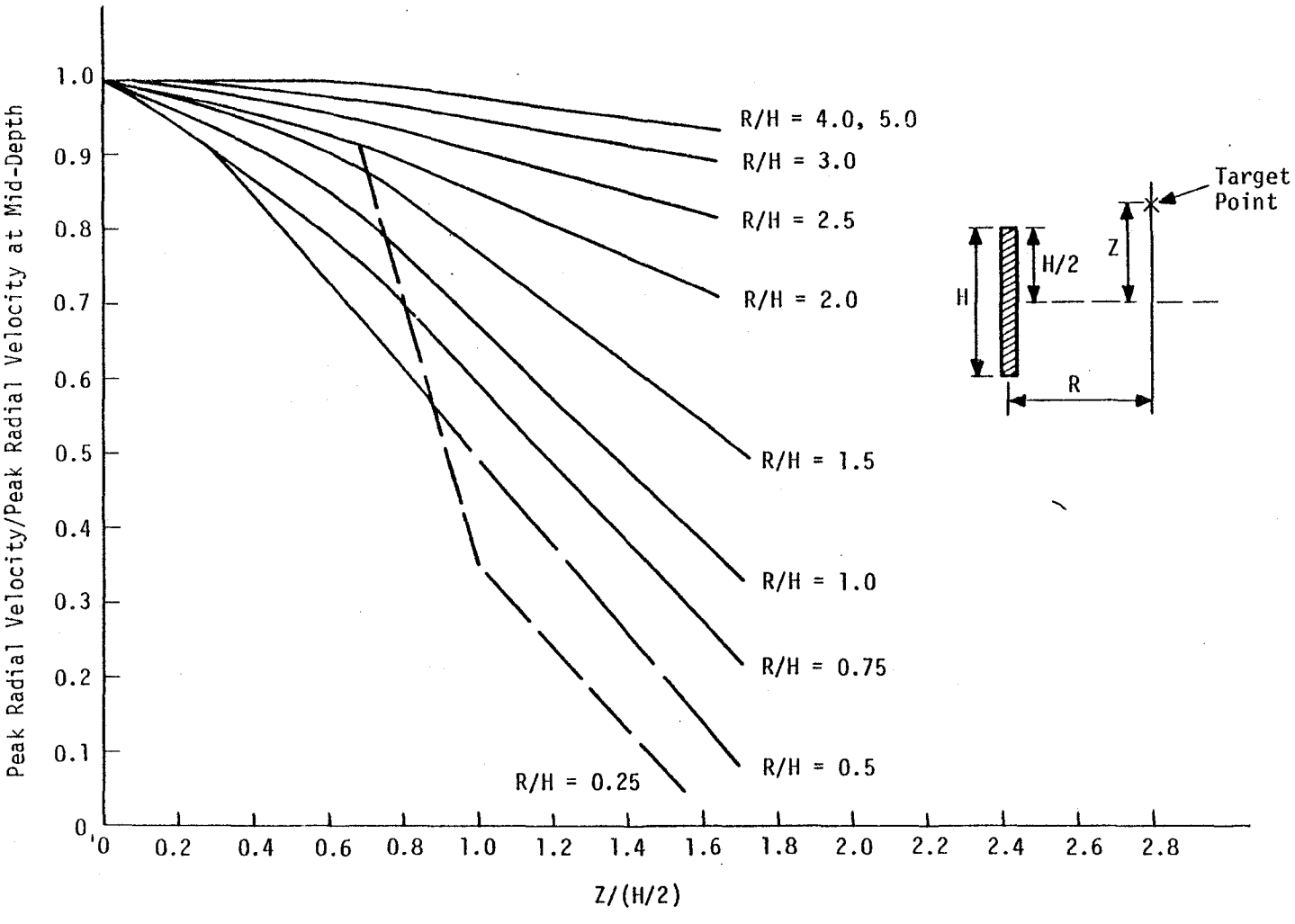

Figure V-45. Variation of Peak Radial Velocity with Off-Center Distance in Cylindrical Geometry

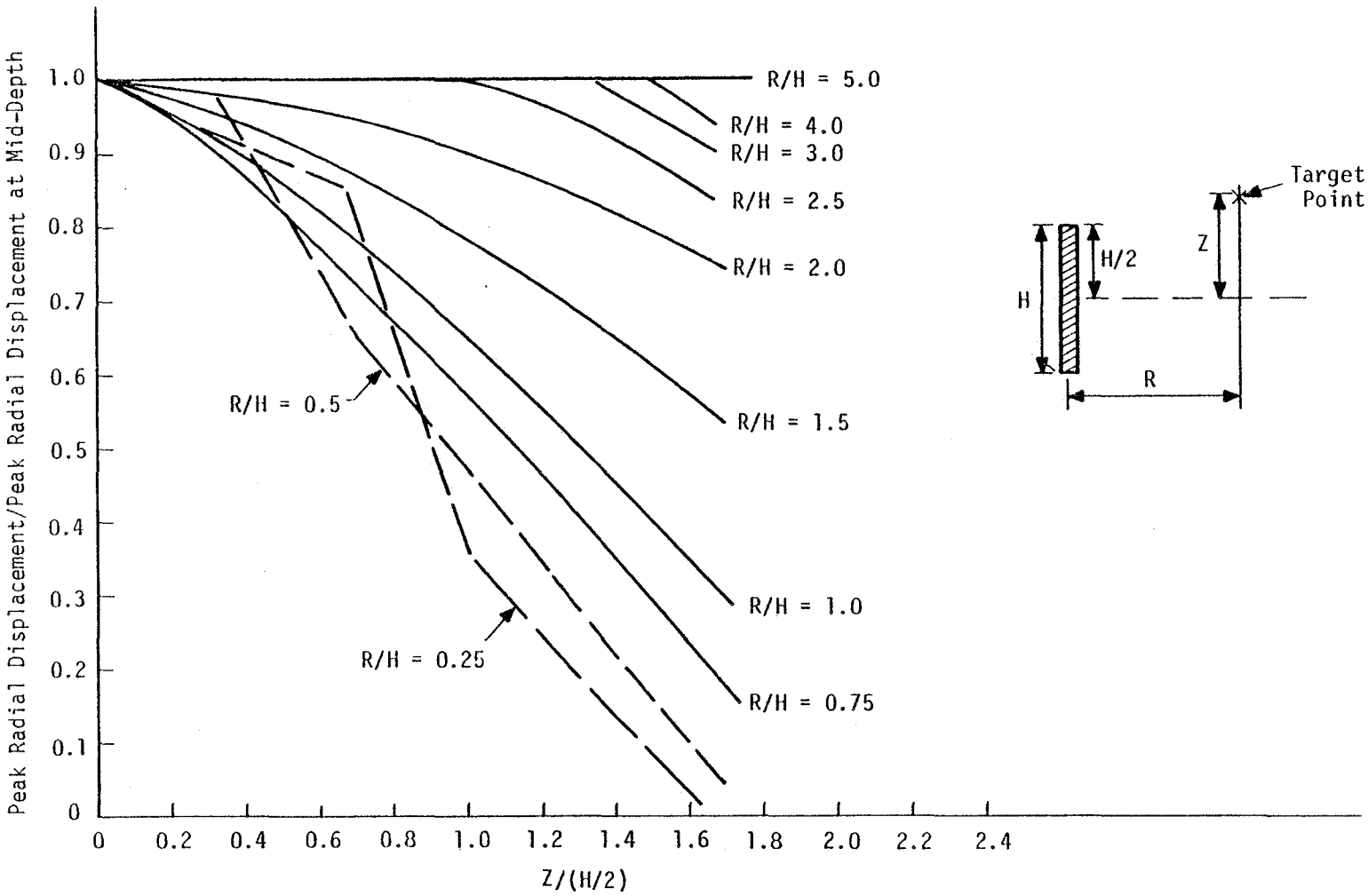

Figure V-46. Variation of Peak Radial Displacement with Off-Center Distance in Cylindrical Geometry

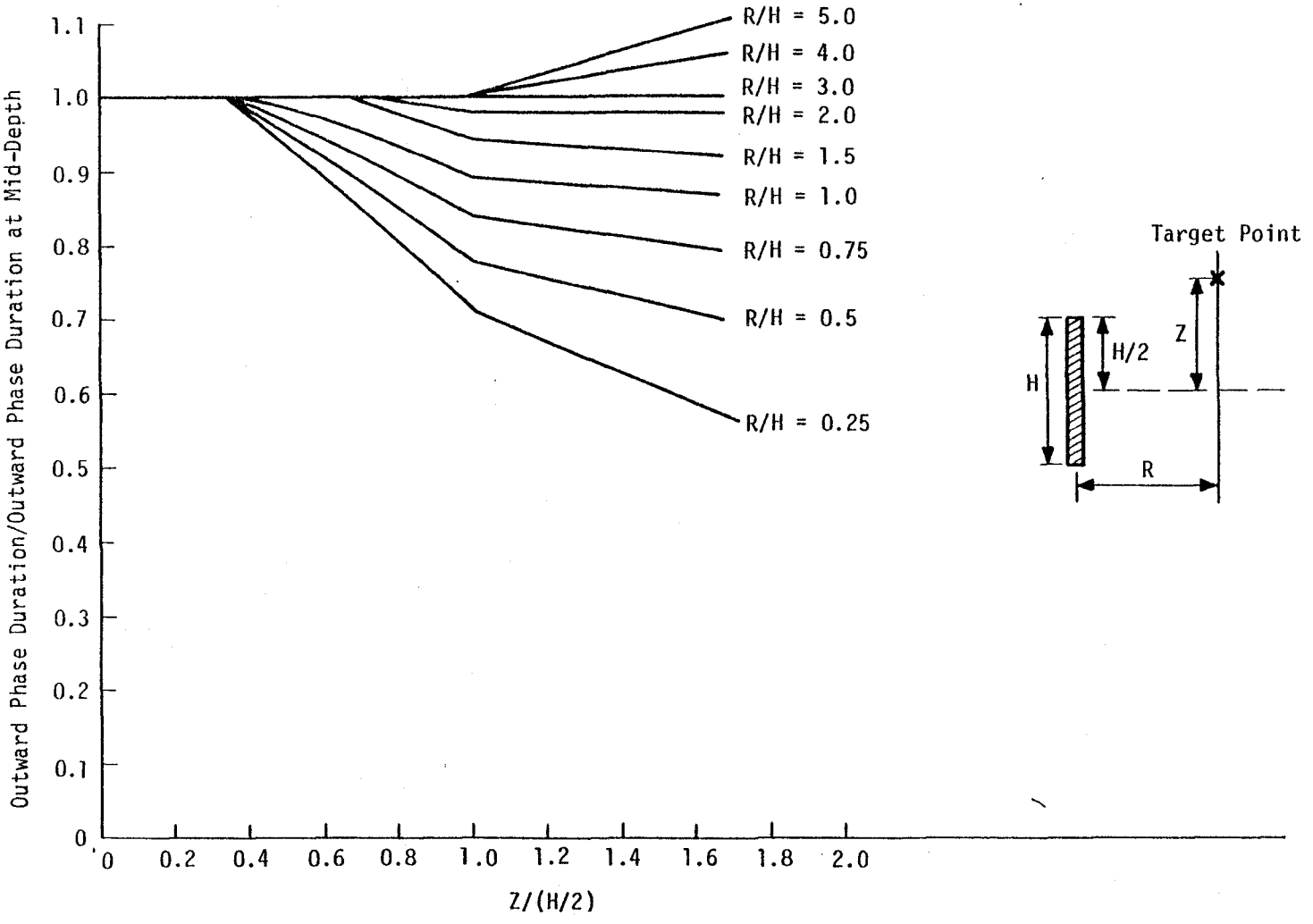

Figure V-47. Variation of Particle Velocity Outward Phase Duration with Off-Center Distance in Cylindrical Geometry

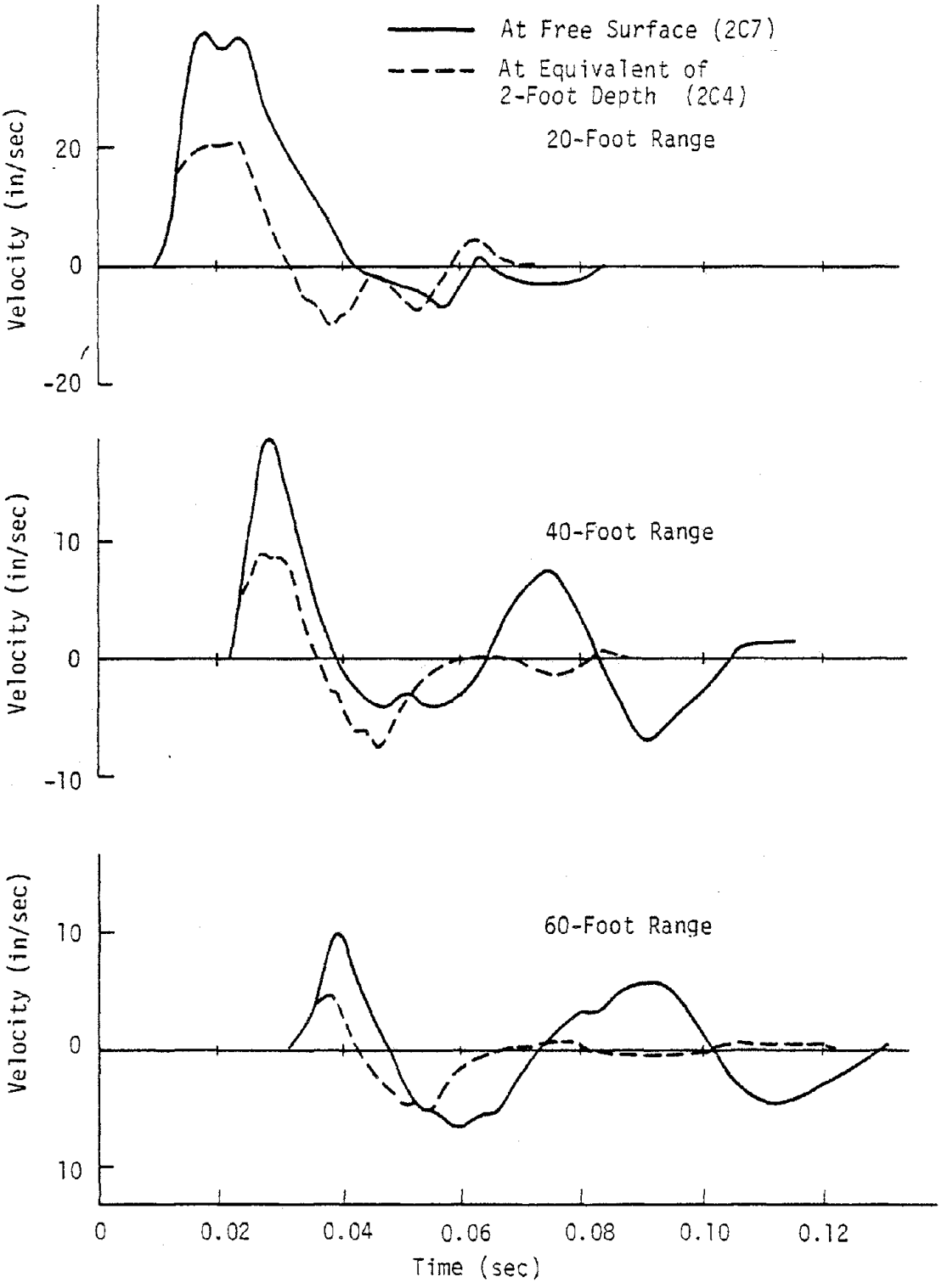

Figure V-48. Effect of Free-Surface on Near-Surface Radial Particle Velocities in Cylindrical Geometry

time histories at the free-surface with those at the nearest corresponding off-center location in the symmetric calculation. The initial velocity amplitudes in the free-surface calculations are about double those in the symmetric calculation. In addition, the characteristic times (a measure of frequency) are longer and the late time oscillation amplitudes are larger in the free-surface results.

Off-center (in the direction of the free-surface) velocity amplitude variations in the free-surface calculation are shown in figure V-49. At ranges near the source ($R/H < 1$), the velocity amplitudes decrease with off-center distance. At greater distances, however, the amplitudes increase as the free-surface is approached. At all ranges, the off-center amplitudes are larger than in the symmetric calculation. The off-center amplitudes in the free-surface calculation as a proportion of the amplitudes at the corresponding off-center distance in the symmetric calculation are plotted in figures V-50, V-51, and V-52. Off-center velocity outward phase duration is plotted in a similar manner in figure V-53. In general, the amplitudes at off-center positions in the presence of a free-surface are equal to or less than twice the amplitude at the corresponding position in a symmetric calculation. Although the results given in figures V-50 through V-53 are for a single free-surface calculation, they can provide a guide to extending symmetric calculation results to free-surface cases.

8. PLANAR RESULTS

a. Yield Scaling

Two one-dimensional planar calculations (1P1, 1P2) with different

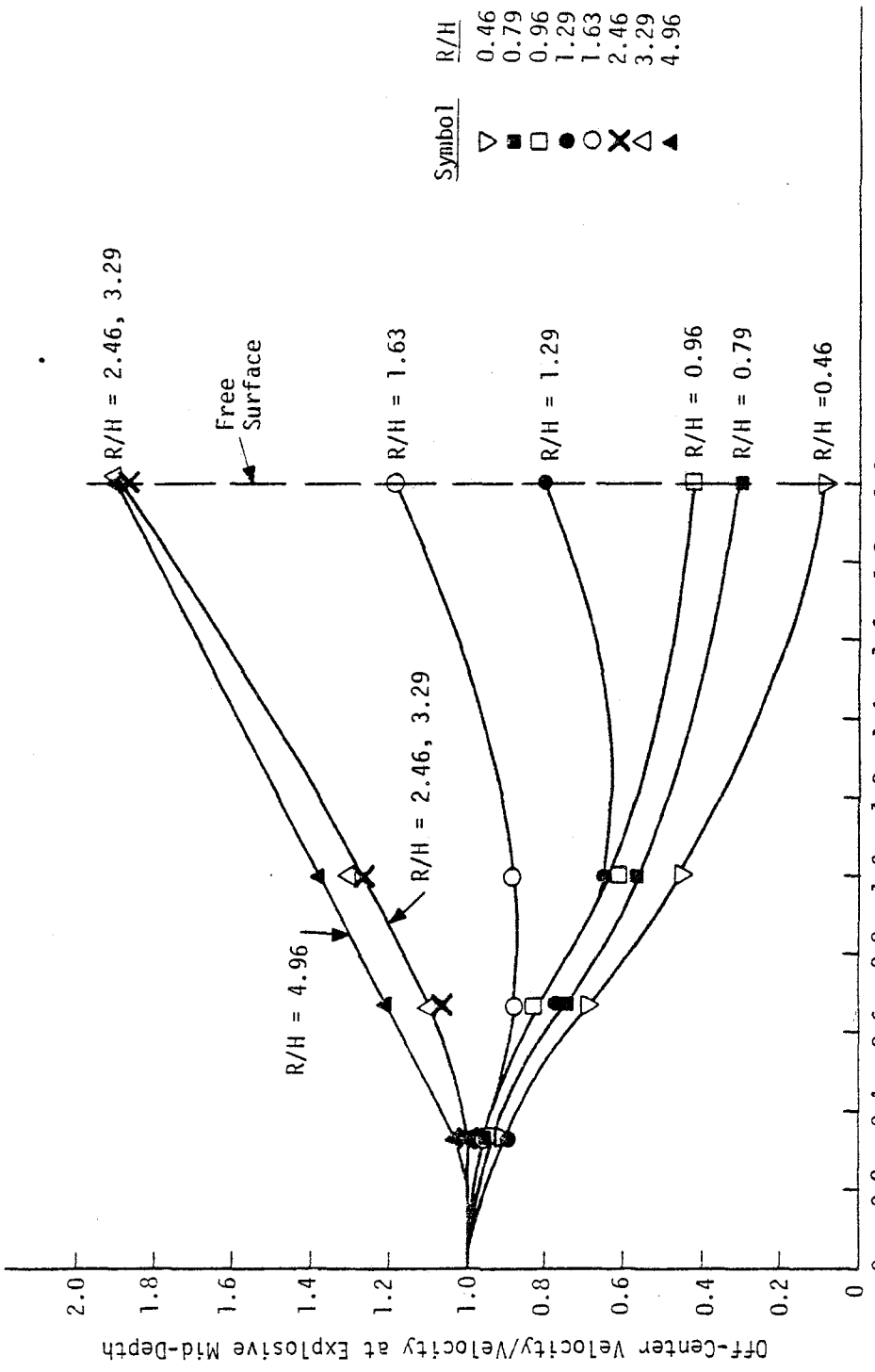

Figure V-49. Effect of Free-Surface on Peak Radial Velocity in Cylindrical Geometry

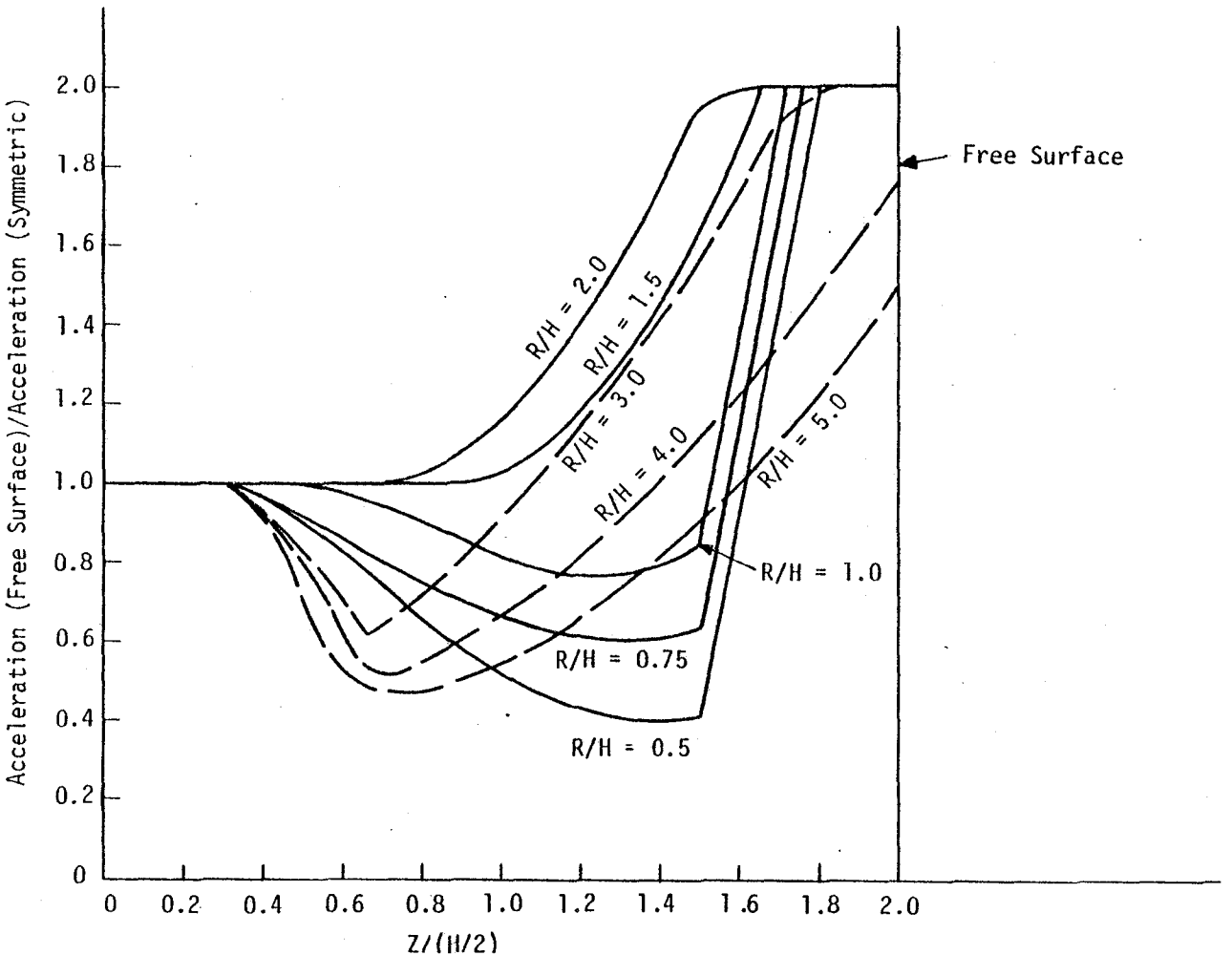

Figure V-50. Variation of Radial Acceleration with Off-Center Distance in Cylindrical Calculation with a Free-Surface

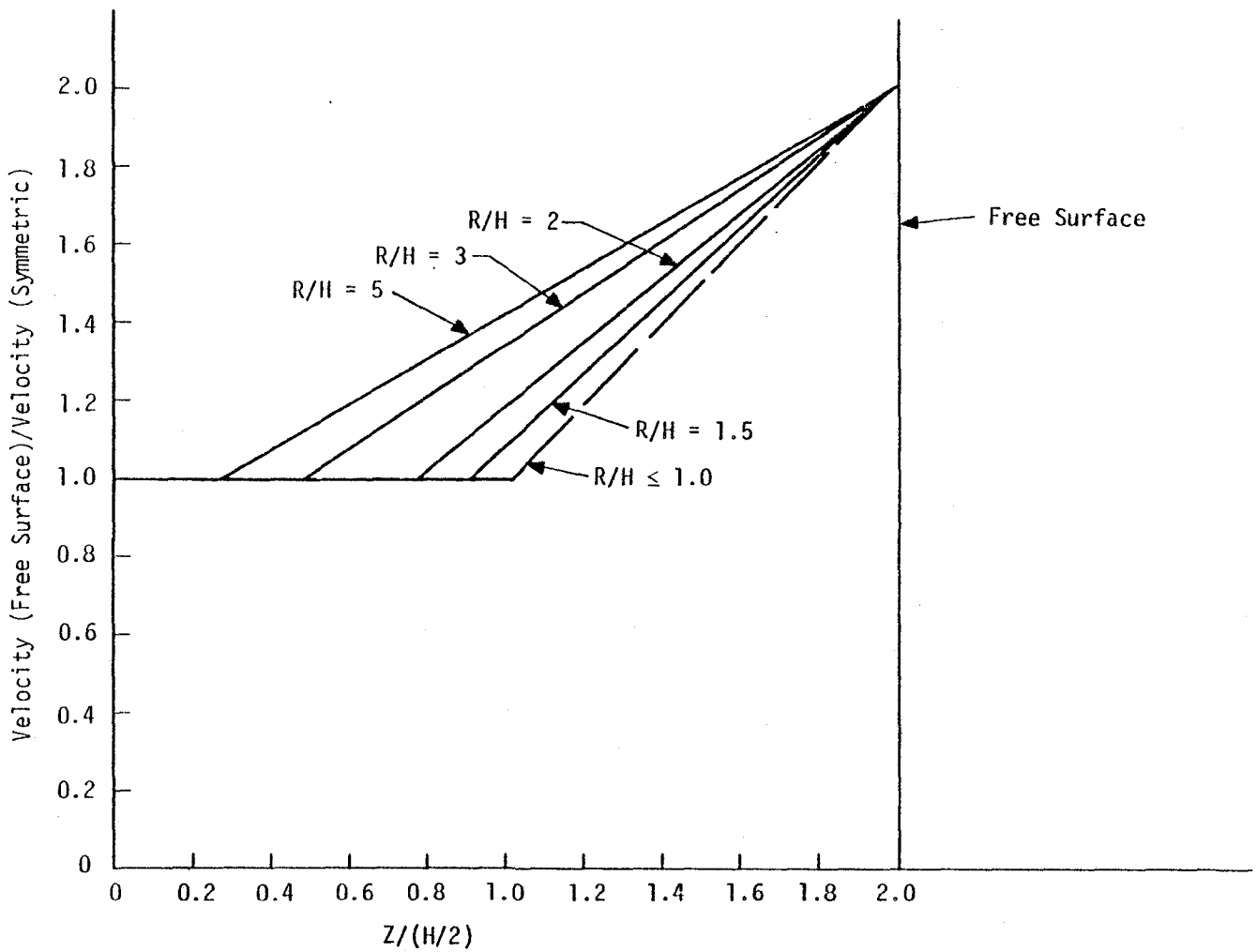

Figure V-51. Variation of Radial Velocity with Off-Center Distance in Cylindrical Calculation with a Free-Surface

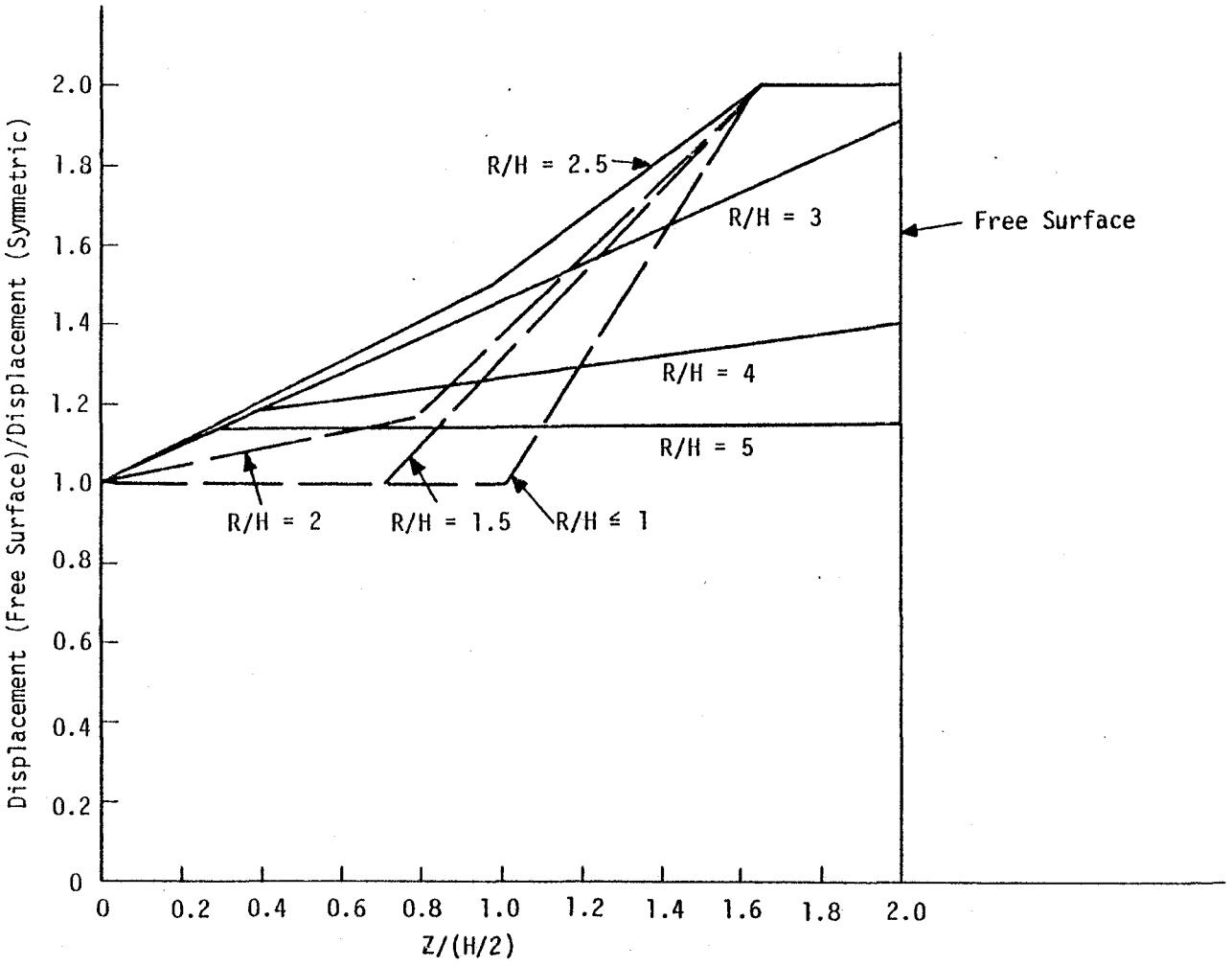

Figure V-52. Variation of Radial Displacement with Off-Center Distance in Cylindrical Calculation with a Free-Surface

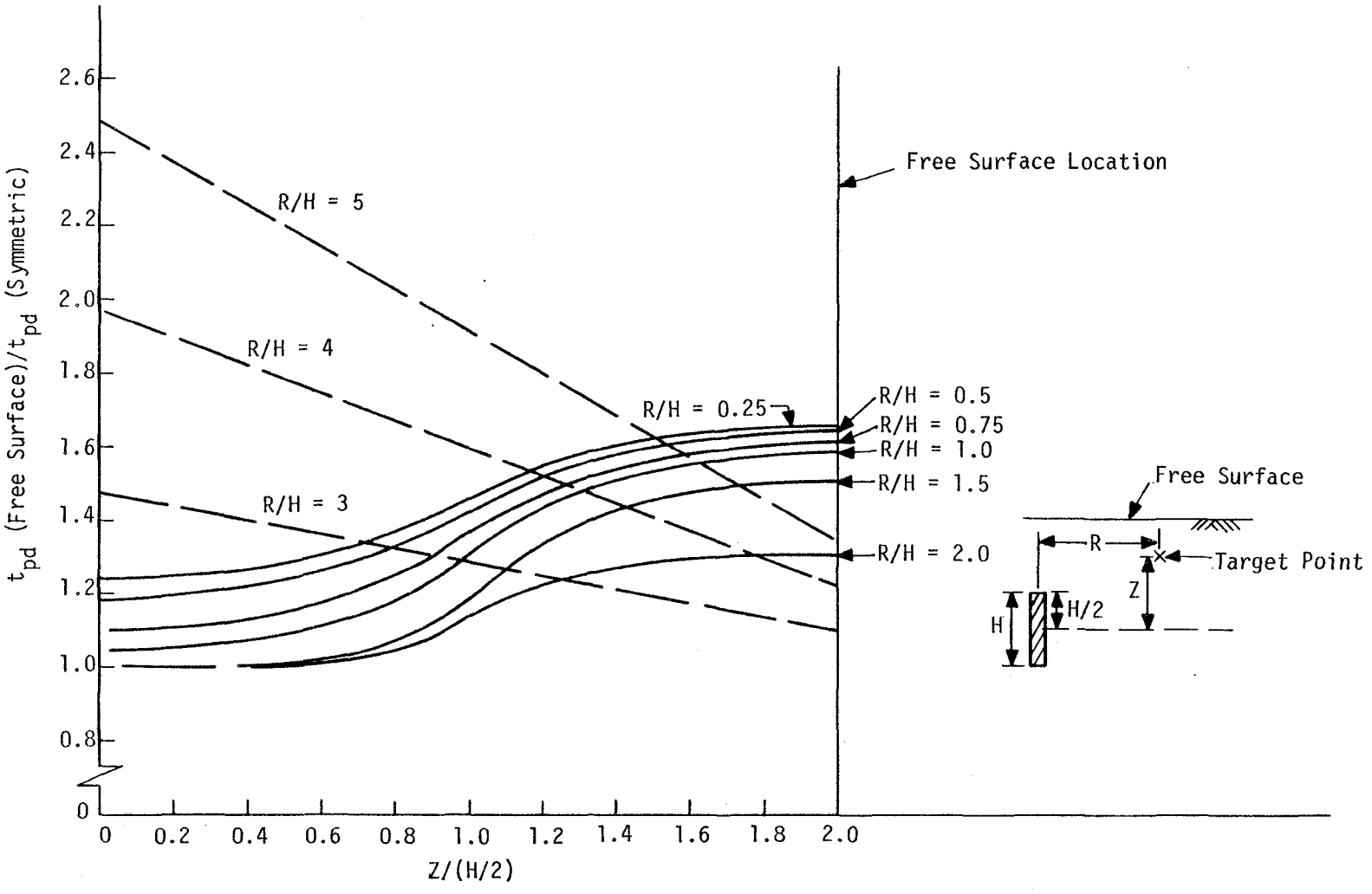

Figure V-53. Variation of Particle Velocity Outward Phase Duration With Off-Center Distance in Cylindrical Calculation with a Free-Surface

areal charge densities, α, were conducted to evaluate α scaling and to determine planar attenuation rates in dry alluvial materials. An ideal gas source was used in these calculations and the scaled cavity width, t/α, was held approximately constant to avoid source coupling differences. A typical velocity-time history and its integration are shown in figure V-54. The velocity exhibits a small elastic precursor which is associated with the elastic portion of the loading hydrostat. The velocity then jumps to its peak value and decays. The velocity does not exhibit an inward phase and this is a characteristic feature of the behavior of hysteretic materials in one-dimensional uniaxial geometry (see e.g. ref. V-10). Because of the absence of an inward velocity phase, the displacement continues to increase with time.

Calculated peak accelerations and velocities, scaled appropriately by α, are plotted versus scaled range in figures V-55 and V-56. It can be seen that α scaling does a very good job of collapsing the data. The linear fits for accelerations and velocities exhibit two distinct regions. An increase in the attenuation rates for accelerations and velocities occurs at a scaled range of about 20 ft/(lb/ft^2). Calculated stresses indicate this range corresponds to a transition from inelastic behavior involving both the nonlinear hysteretic hydrostat and the yield surface to inelastic behavior involving only the hydrostat. The elastic region is never encountered in the range considered in the calculations because of the low planar attenuation rates. The accelerations attenuate initially at -0.89. Beyond a scaled range of 20, the attenuation rate is -1.6. If a single line is fit to all of the data the resulting attenuation rate is -1.19. The corresponding attenuation rates for particle

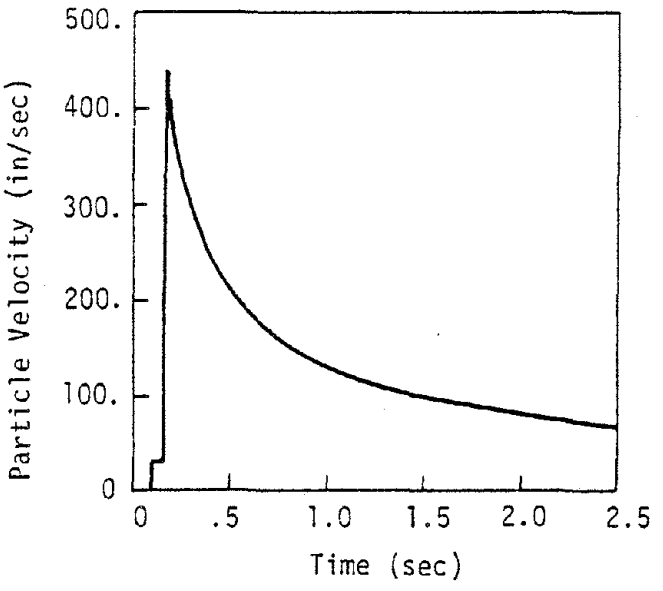

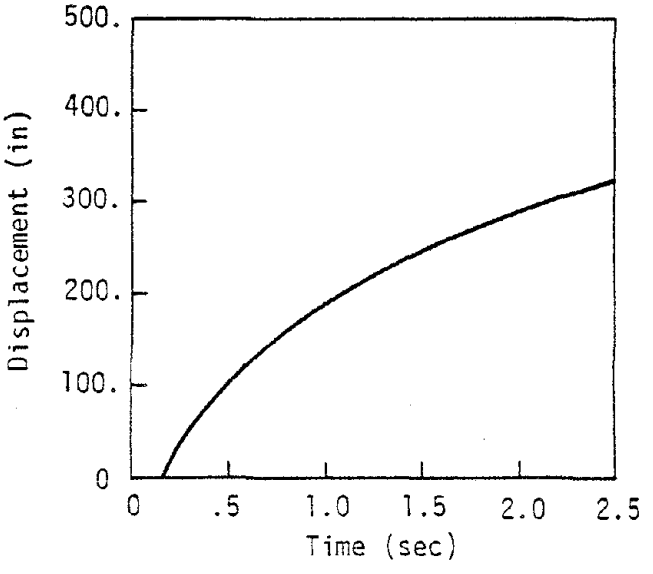

Figure V-54. Calculated Velocity Time History and Its Integration at the 27-Foot Range from a Planar Explosion of 3.58 lbs/ft of TNT in a 5-Foot Wide Cavity (1P2)

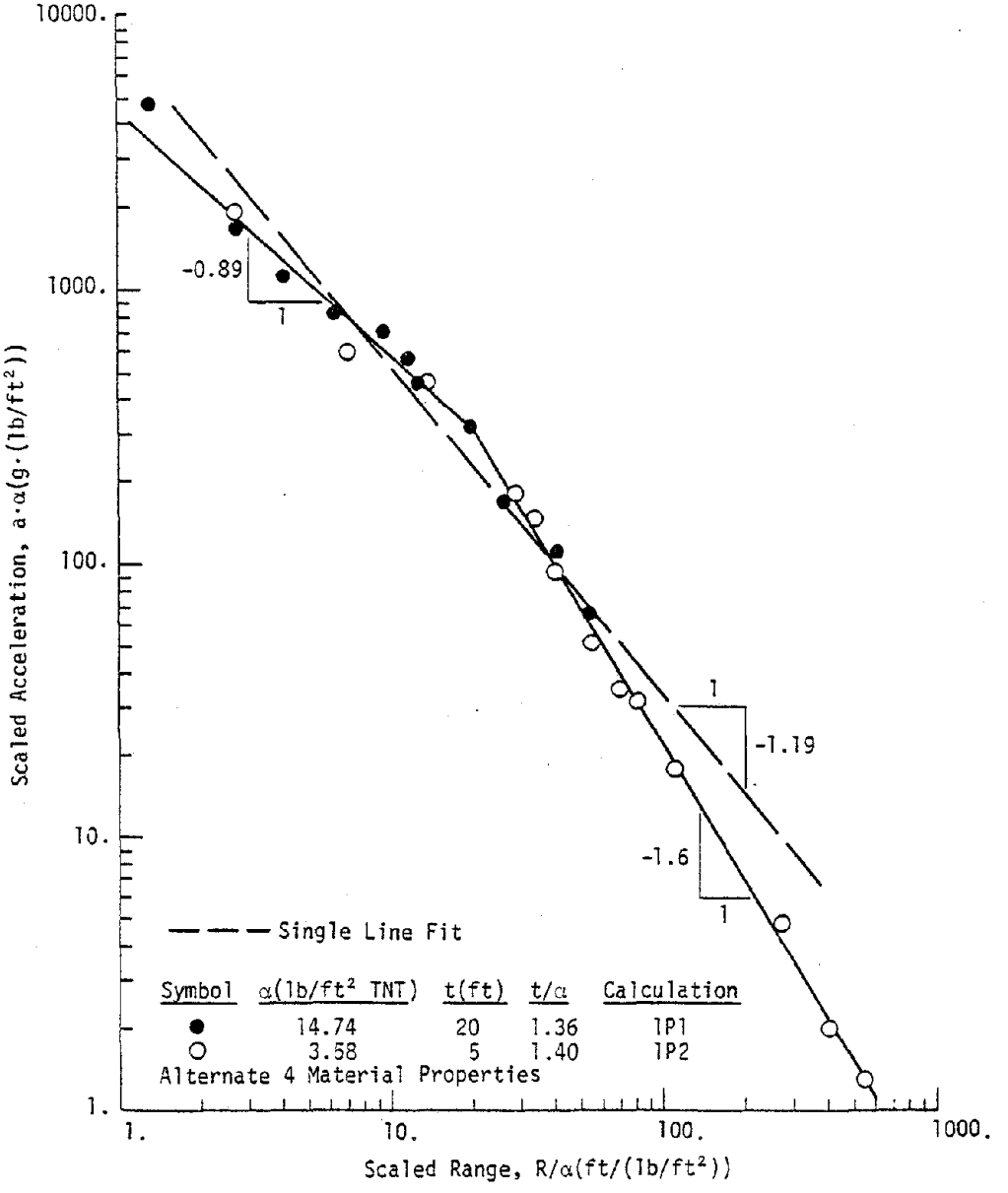

Figure V-55. Scaled Peak Acceleration Versus Scaled Range in One-Dimensional Planar Geometry

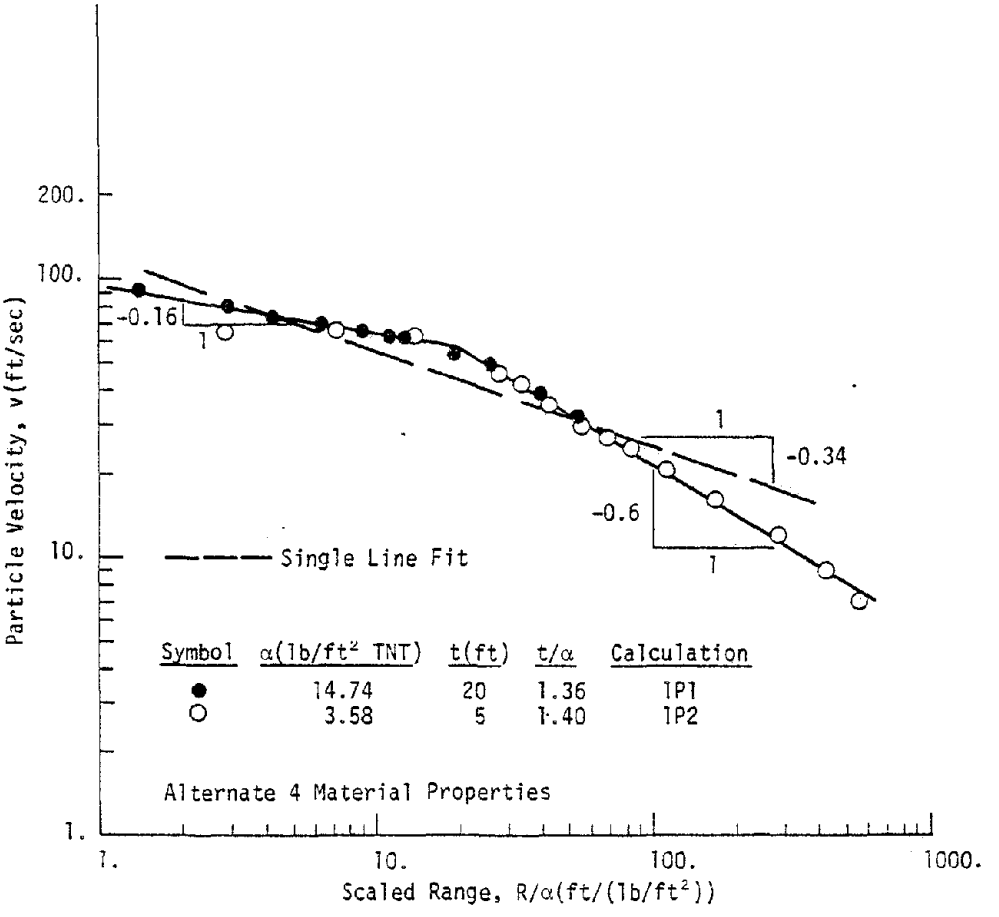

Figure V-56. Peak Particle Velocity Versus Range in One-Dimensional Planar Geometry

velocity are -0.16, -0.6, and -0.34.

The times at which the velocities decayed to one-half their peak values and the displacements at those times were used to evaluate α scaling for characteristic times and displacements. The results for times are shown in figure V-57 while those for displacements are shown in figure V-58. Both of these quantities scale well using the areal charge density α.

b. Effect of Array Height

The effects of array height in planar explosions were investigated with four two-dimensional calculations in which the array height was taken as 10, 40, 80, and 160 feet (2P1, 2P2, 2P3, 2P4). The input was a pressure-time history applied over the region of the explosive. The input pressure was derived from that produced by an ideal gas equivalent of 3.58 lbs/ft^2 of TNT in a 5-foot wide cavity, modified for venting by the method described previously. The calculations were performed in planar geometry with a plane of symmetry at the mid-depth of the explosive so that free-surface effects were not present.

Figure V-59 compares horizontal accelerations at the explosive mid-depth in the array height variations with those calculated in one-dimension. The comparisons indicate that the finite array height results coincide closely with the one-dimensional results to a transition range, R_o, which is related to the array height. While in cylindrical geometry (fig. V-36) the transition range was a constant proportion of the explosive length (0.6 H), the transition range in the planar calculations varies with array height.

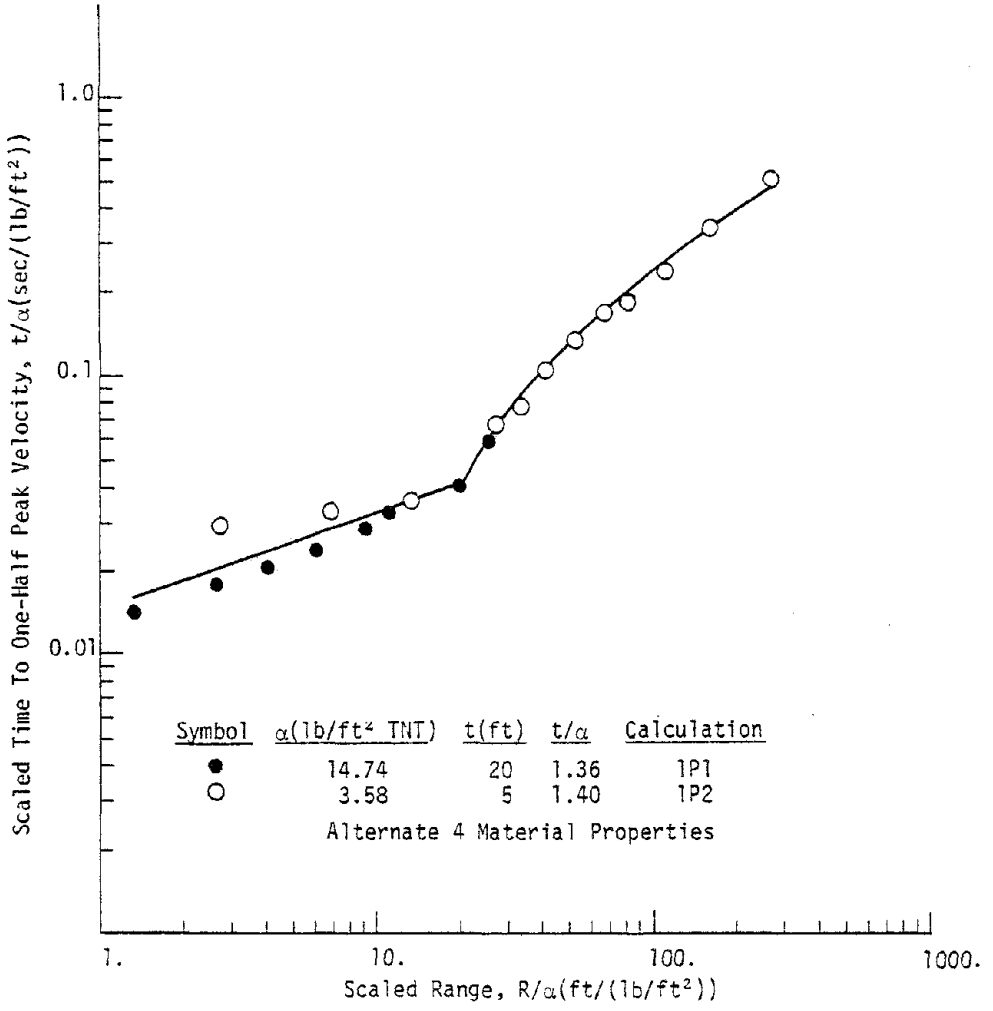

Figure V-57. Scaled Time to One-Half Peak Velocity Versus Scaled Range in One-Dimensional Planar Geometry

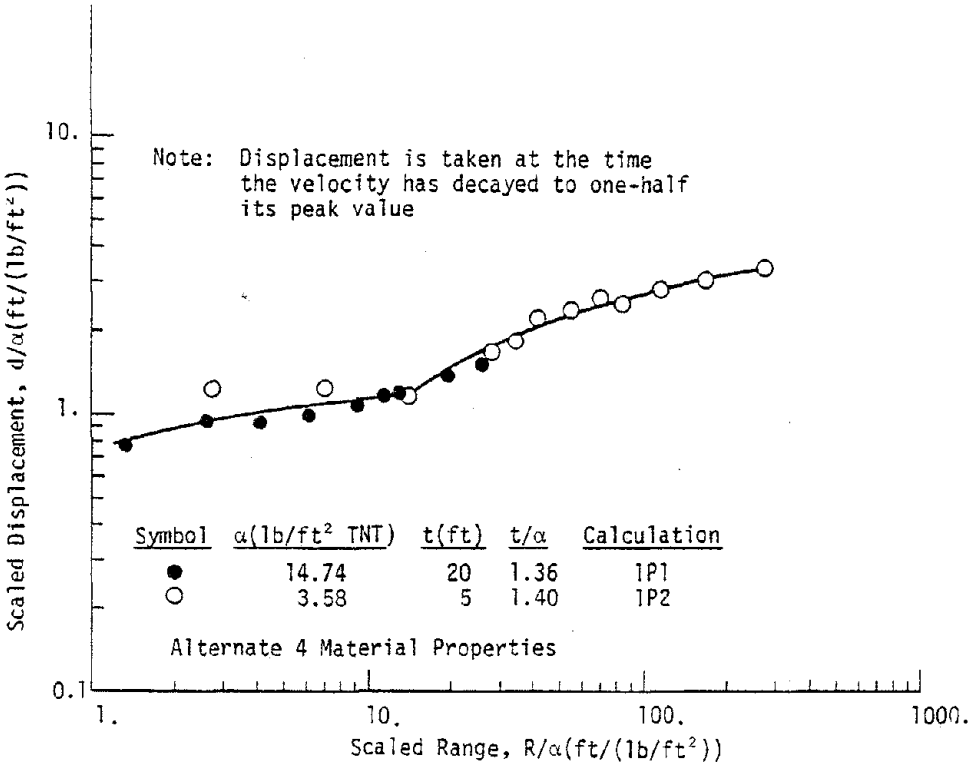

Figure V-58. Scaled Displacement Versus Scaled Range in One-Dimensional Planar Geometry

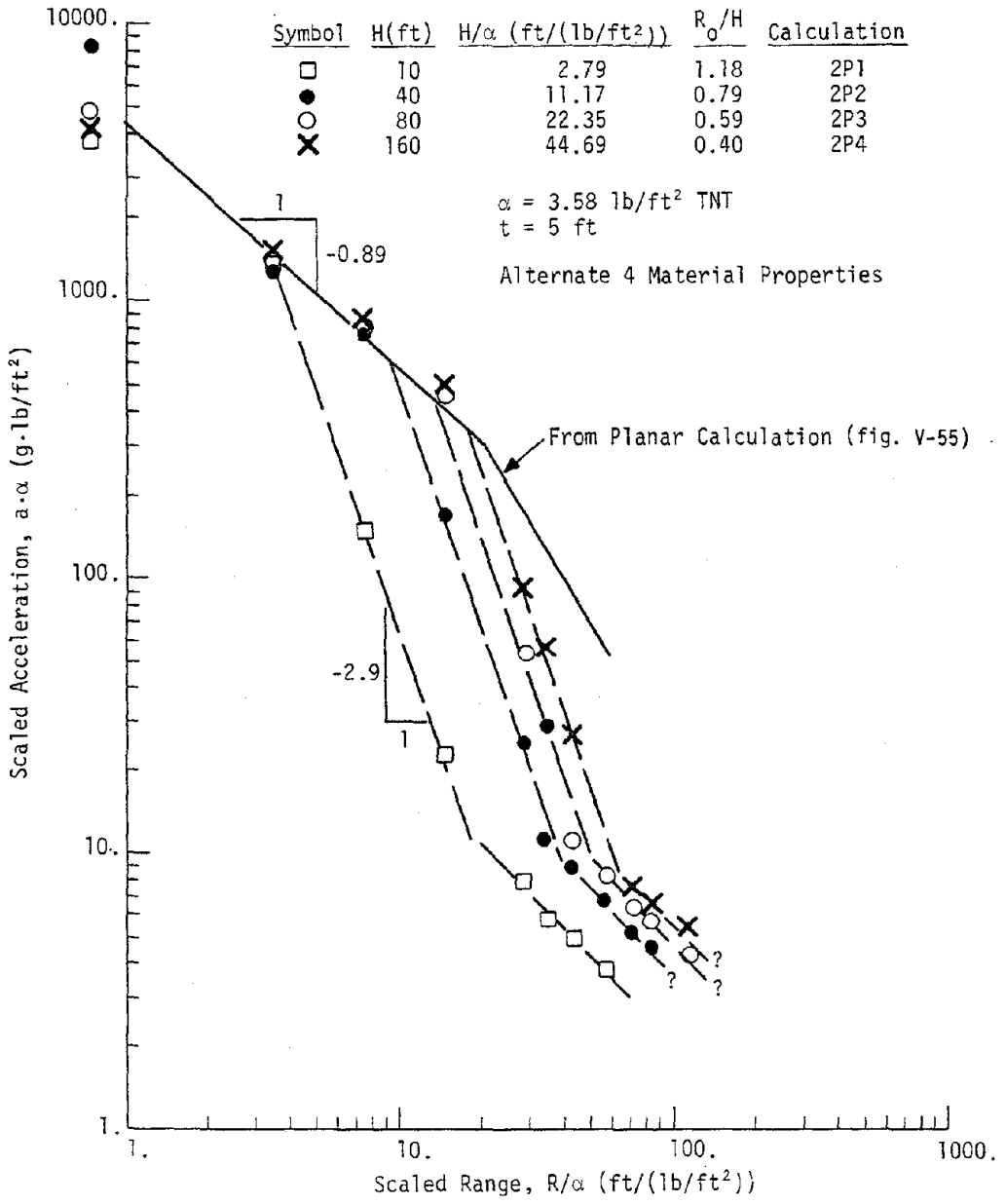

Figure V-59. Effect of Array Height on Horizontal Accelerations in Two-Dimensional Planar Geometry

The initial acceleration attenuation rate, prior to the transition, is -0.89 which is the planar attenuation rate. Beyond the transition range, the attenuation rate is -2.9 and this corresponds fairly well with the one-dimensional cylindrical attenuation rate of -2.5 (fig. V-37). At scaled accelerations below about 10 g·lb/ft^2, the attenuation rate decreases due to a transition to elastic behavior. There is some uncertainty in acceleration estimates from the calculations in this region, but the attenuation rate is believed similar to elastic velocity attenuation.

The horizontal particle velocity results, shown in figure V-60, do not exhibit a sharp transition from planar to cylindrical behavior. The actual ranges at which the velocities depart from planar behavior are in the range 0.4 to 0.75 times the array height. Straight line fits to the velocities intersect the planar relation at ranges of 1.54 to 0.54 times the array height.

Beyond the transition range, velocities attenuate at about -2.1. The attenuation rate becomes about -0.95 for velocities below about 3 ft/sec. This reduced attenuation corresponds to the elastic range. These attenuation rates are in good agreement with the one-dimensional cylindrical rates (fig. V-38).

Horizontal displacements, shown in figure V-61, also exhibit a variable transition range which depends upon the scaled array height. The attenuation rate, prior to transition, is about -0.12. After transition, the rate is -1.82 which is in good agreement with the one-dimensional cylindrical attenuation rate of -1.7 (fig. V-39). As in spherical and cylindrical geometry, no elastic transition is apparent.

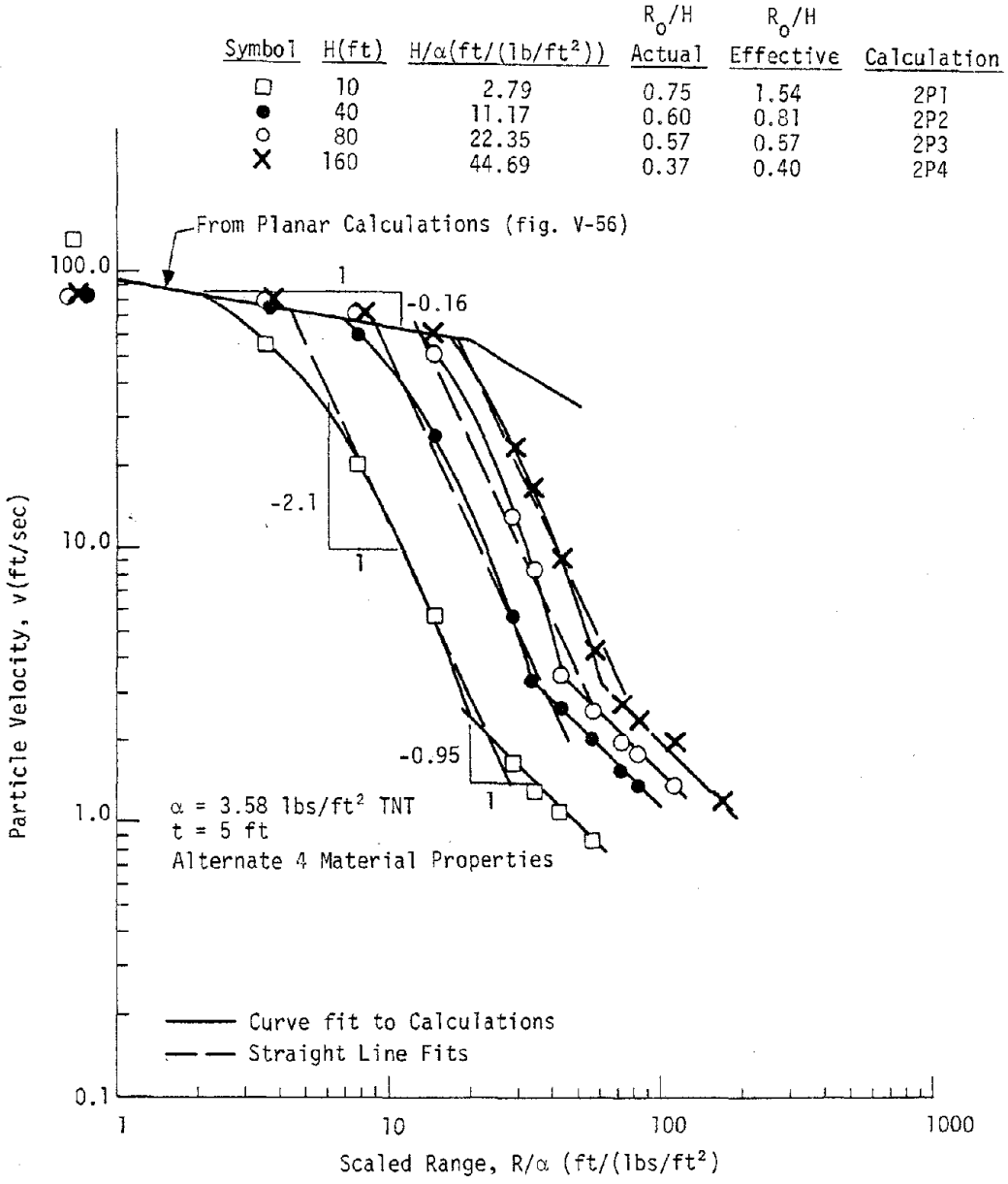

Figure V-60. Effect of Array Height on Horizontal Velocities in Two-Dimensional Planar Geometry

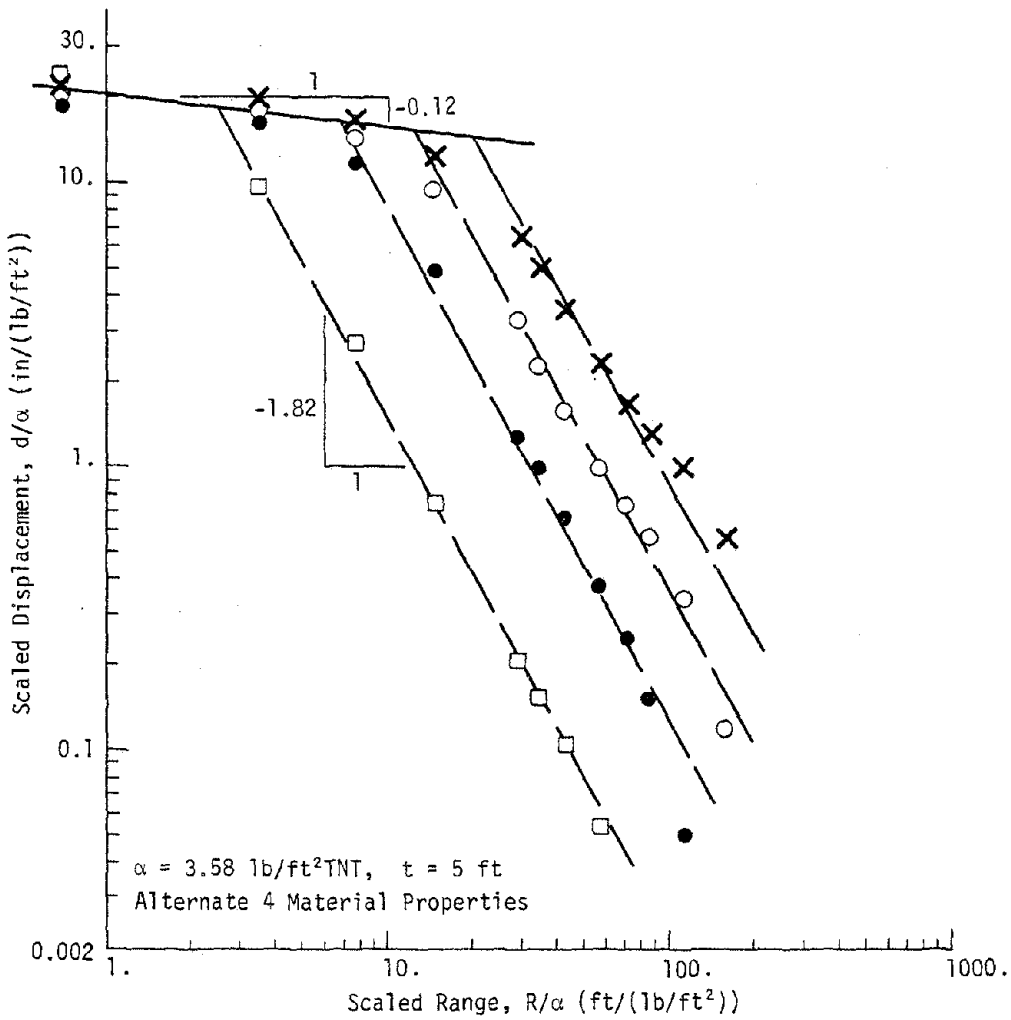

Symbol	H(ft)	H/α(ft/(lb/ft²))	R_o/H	Calculation
□	5	2.79	0.88	2P1
●	40	11.17	0.61	2P2
○	80	22.35	0.55	2P3
×	160	44.69	0.45	2P4

Figure V-61. Effect of Array Height on Horizontal Displacements in Two-Dimensional Planar Geometry

The transition ranges for accelerations, velocities, and displacements are plotted as a function of scaled array height in figure V-62. The variations are fit well by the following relations:

$$\text{acceleration:}\quad R_o/H = 2.0\,(H/\alpha)^{-0.40} \qquad \text{(a)}$$

$$\text{velocity}\quad :\quad R_o/H = 2.6\,(H/\alpha)^{-0.48} \qquad \text{(b)} \qquad \text{(V-28)}$$

$$\text{displacement:}\quad R_o/H = 1.15\,(H/\alpha)^{-0.25} \qquad \text{(c)}$$

where

R_o = transition range in feet

H = array height in feet

α = areal charge density in lb/ft^2 of TNT

Using equation V-28, the horizontal accelerations, velocities and displacements at the mid-depth of planar arrays can be fit by the following relations:

$$a\cdot\alpha = 4400\,(R/\alpha)^{-0.89} \qquad \text{for } R/\alpha \leq 2.0\,H/\alpha)^{0.6} \qquad \text{(a)}$$

$$a\cdot\alpha = 17{,}772\,(H/\alpha)^{1.21}\,(R/\alpha)^{-2.9} \qquad \text{for } R/\alpha > 2.0\,(H/\alpha)^{0.6} \qquad \text{(b)}$$

$$v = 94\,(R/\alpha)^{-0.16} \qquad \text{for } R/\alpha \leq 2.6\,(H/\alpha)^{0.52} \qquad \text{(c)}$$

(V-29)

$$v = 600\,(H/\alpha)(R/\alpha)^{-2.1} \qquad \text{for } R/\alpha > 2.6\,(H/\alpha)^{0.52} \qquad \text{(d)}$$

$$d/\alpha = 21\,(R/\alpha)^{-0.12} \qquad \text{for } R/\alpha < 1.15\,(H/\alpha)^{0.75} \qquad \text{(e)}$$

$$d/\alpha = 26.6\,(H/\alpha)^{1.28}\,(R/\alpha)^{-1.82} \qquad \text{for } R/\alpha > 1.15\,(H/\alpha)^{0.75} \qquad \text{(f)}$$

where

a = acceleration in g's

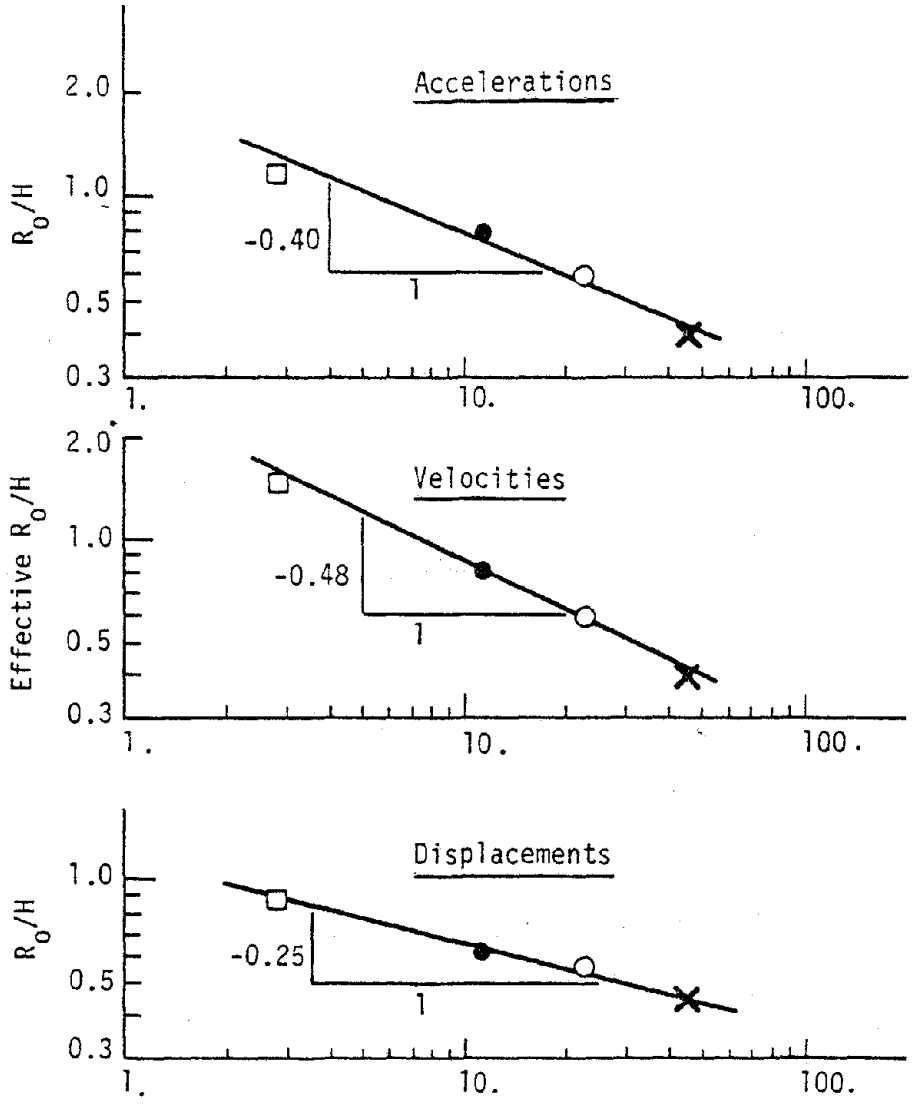

Symbol	H(ft)	H/α (ft/(lb/ft^2))	Calculation
□	10	2.79	2P1
●	40	11.17	2P2
○	80	22.25	2P3
×	160	44.69	2P4

α = 3.58 lb/ft^2 TNT, t = 5 ft
Alternate 4 Material Properties

Figure V-62. Correlation Between Scaled Array Height and Effective Transition Range in Two-Dimensional Planar Geometry

v = velocity in ft/sec

d = displacement in inches

R = range in feet

H = array height in feet

α = areal charge density in lb/ft^2

Figure V-63 compares calculated velocity time histories at the array mid-depth for three different array heights. The results contain some numerical noise but this does not detract significantly from the results or waveform interpretations. Amplitude differences at the more distant ranges are exhibited by the need for different scales for the different calculations. The array height differences are evident in the characteristic times of the waveforms. The outward phase duration increases as the array height increases. This is due to later arrival of the P-relief and SP-relief effects as the array height increases. These relief effects are the cause of the inward component of motion in planar geometry because, as described earlier, one-dimensional planar motion contains no inherent inward motion component.

The very late time parts of the waveform are suspect because after the inward peak, the motion approaches zero as an asymptote rather than enter a second outward phase. It is possible, as described earlier, that this is due to a shortcoming of the input loading conditions, especially treatment of the origin above and below the array. This feature of the time history makes it difficult to estimate the total duration of the first motion cycle.

Scaled characteristic times of the velocity waveforms are plotted

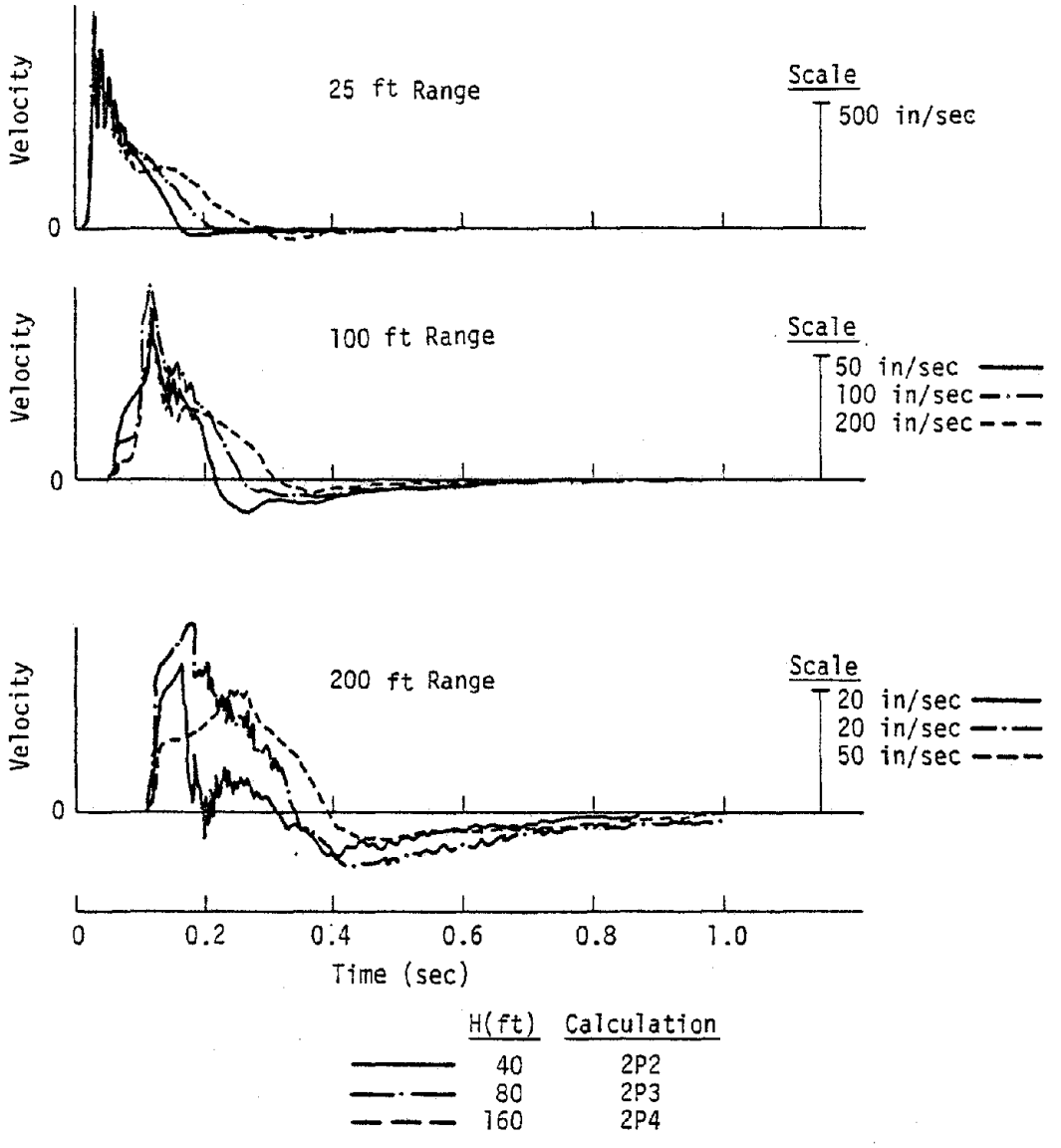

Figure V-63. Comparison of Velocity Time Histories from Two-Dimensional Planar Symmetric Calculations

as a function of scaled range in figure V-64. The outward phase durations and peak to peak times are about constant with range over a large region. In addition, the scaled amplitudes increase with increasing array height. Beyond some range, the characteristic times deviate from constant behavior. The times for the 10-foot array height begin to decrease while the times in the 40, 80, and 160-foot array height calculations increase. These deviations from constant values begin to occur at about the range of the elastic transition. The difference between the 10-foot calculation and the larger array height calculations is a real phenomena in the calculations but its interpretation is uncertain. The difference may be due to the relative phasing of the P-relief and SP-relief waves. In the 10-foot calculation, the two relief waves arrive within about the same time period and their effect is in essence a single relief effect at all ranges. In the larger array calculations, the two relief effects are more separated in time and the SP-relief is the major cause of the inward motion. In the elastic region, the SP-relief seems to travel at a lower wave speed than the initial front, perhaps because the SP-relief is inelastic, and this leads to increased outward scaled durations and peak to peak times. This interpretation is somewhat tenuous because of the complexity of the stress field and, perhaps, combined elastic and inelastic material behavior at these ranges. Uncertainties in the material model formulation also enter the problem at this stage. Fortunately, main interest is in the intermediate region where confidence in the interpretation is better.

Although the total duration of the first motion cycle is uncertain, due to what is thought to be input boundary behavior, an attempt was made

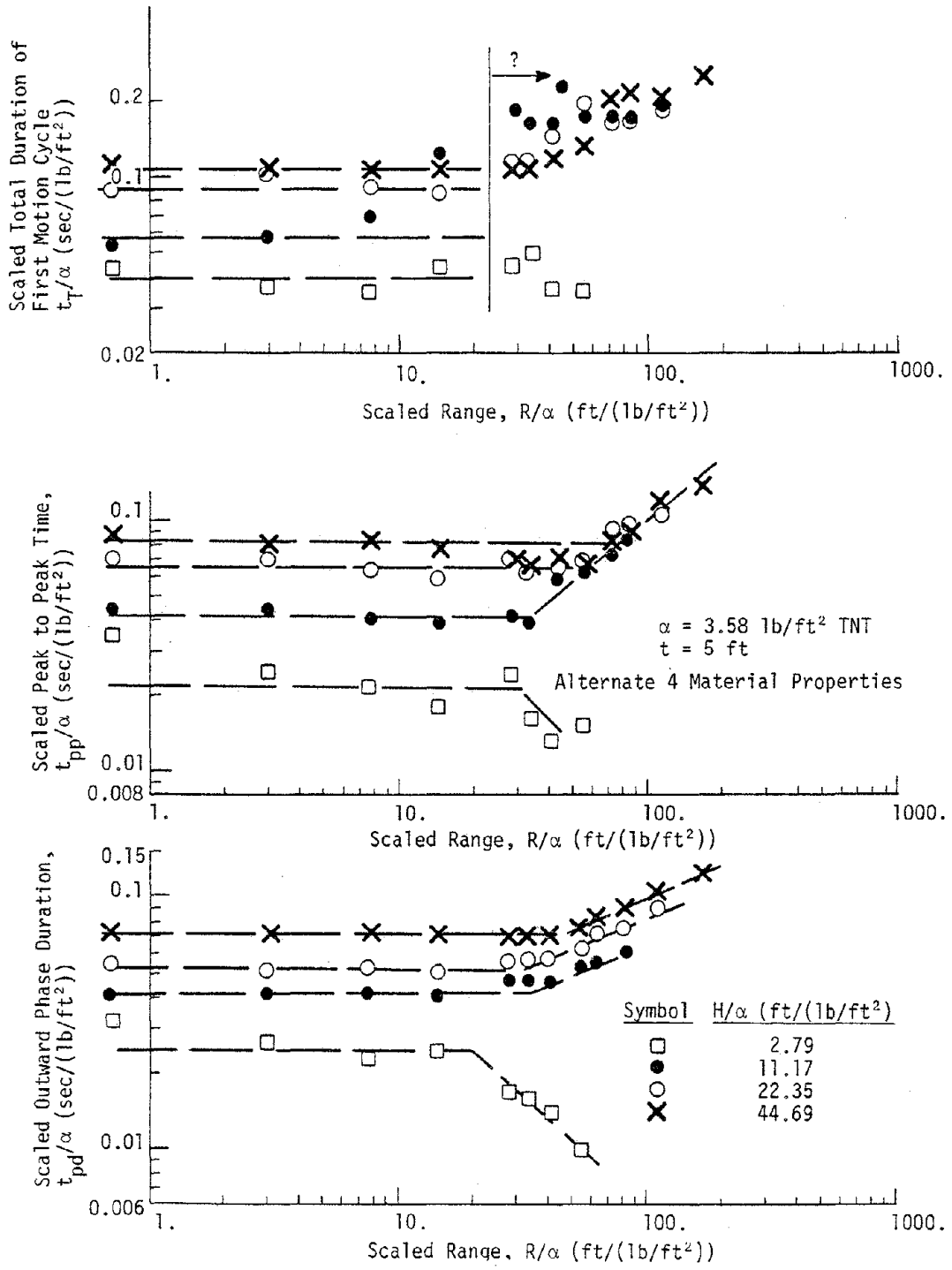

Figure V-64. Variation of Horizontal Velocity Characteristic Times with Range at the Array Mid-Depth in Two-Dimensional Symmetric Planar Geometry

to interpret the duration at the near to intermediate ranges by extrapolating the inward part of the waveforms through zero. These results are also shown in figure V-64. They indicate behavior which is similar to that of the outward phase durations and the peak to peak times, i.e., constant total duration in the near to intermediate region and amplitude increase with increasing array height. Although relative, the trends indicated are believed correct because extrapolation through zero was conducted in a consistent manner. However, there is uncertainty in the absolute values.

The constant values of the scaled characteristic times in the near and intermediate regions are plotted as functions of scaled array height in figure V-65. The time relationships can be fit well by straight lines on log-log paper which have the following equations

$$t_{pd}/\alpha = 0.017\ (H/\alpha)^{0.35} \qquad \text{(a)}$$

$$t_{pp}/\alpha = 0.014\ (H/\alpha)^{0.46} \qquad \text{(b)} \qquad \text{(V-30)}$$

$$t_T/\alpha = 0.026\ (H/\alpha)^{0.37} \qquad \text{(c)}$$

where

t_{pd} = outward velocity phase duration in sec

t_{pp} = peak outward to peak inward time in sec

t_T = duration of the first motion cycle in sec

H = array height

α = areal charge density in lbs/ft^2 of TNT

Figure V-66 presents the ratios of the peak inward to the peak outward velocity as a function of range scaled by the square root of the

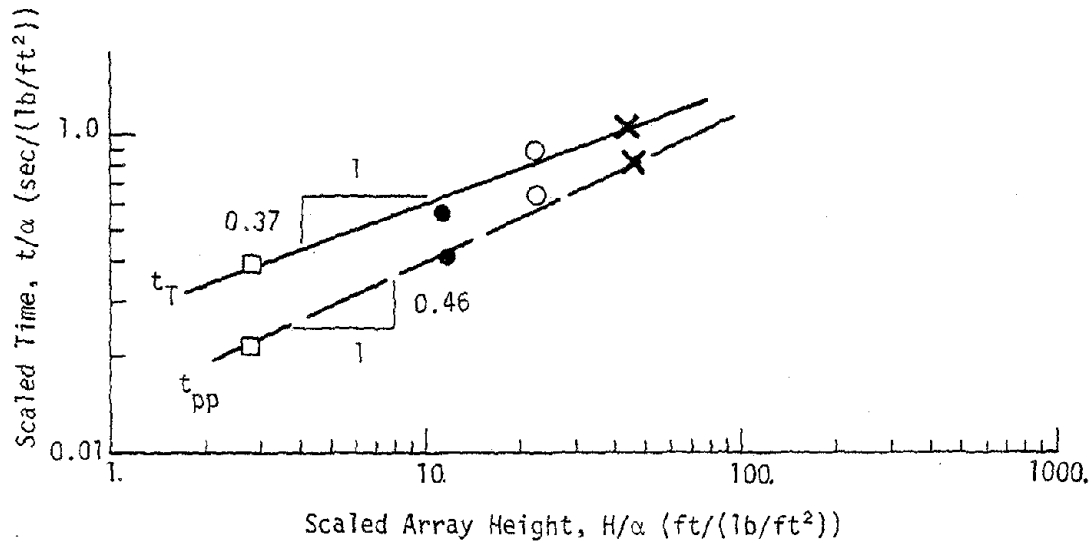

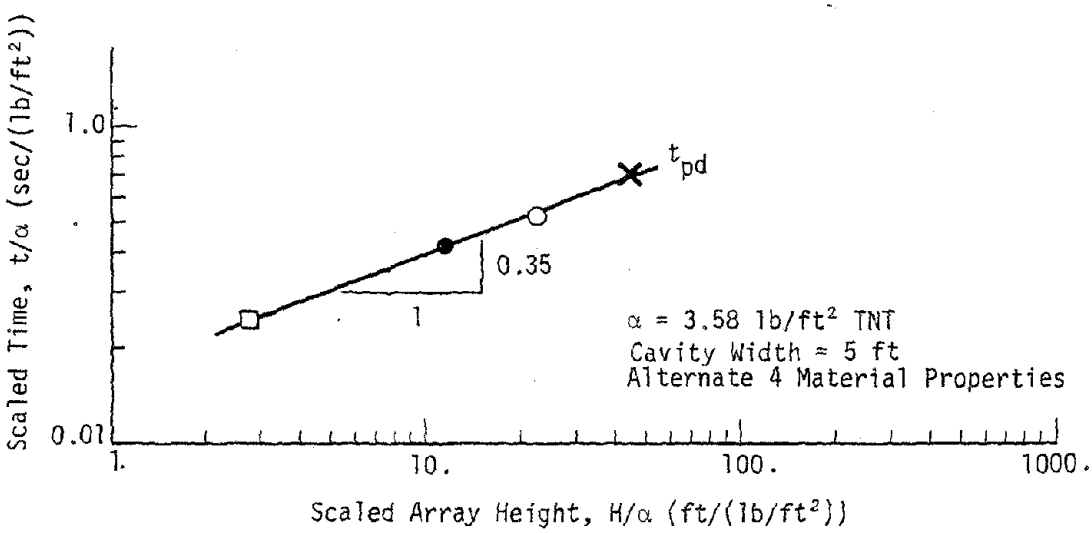

Figure V-65. Effect of Array Height on Horizontal Velocity Characteristic Times in Planar Symmetric Geometry

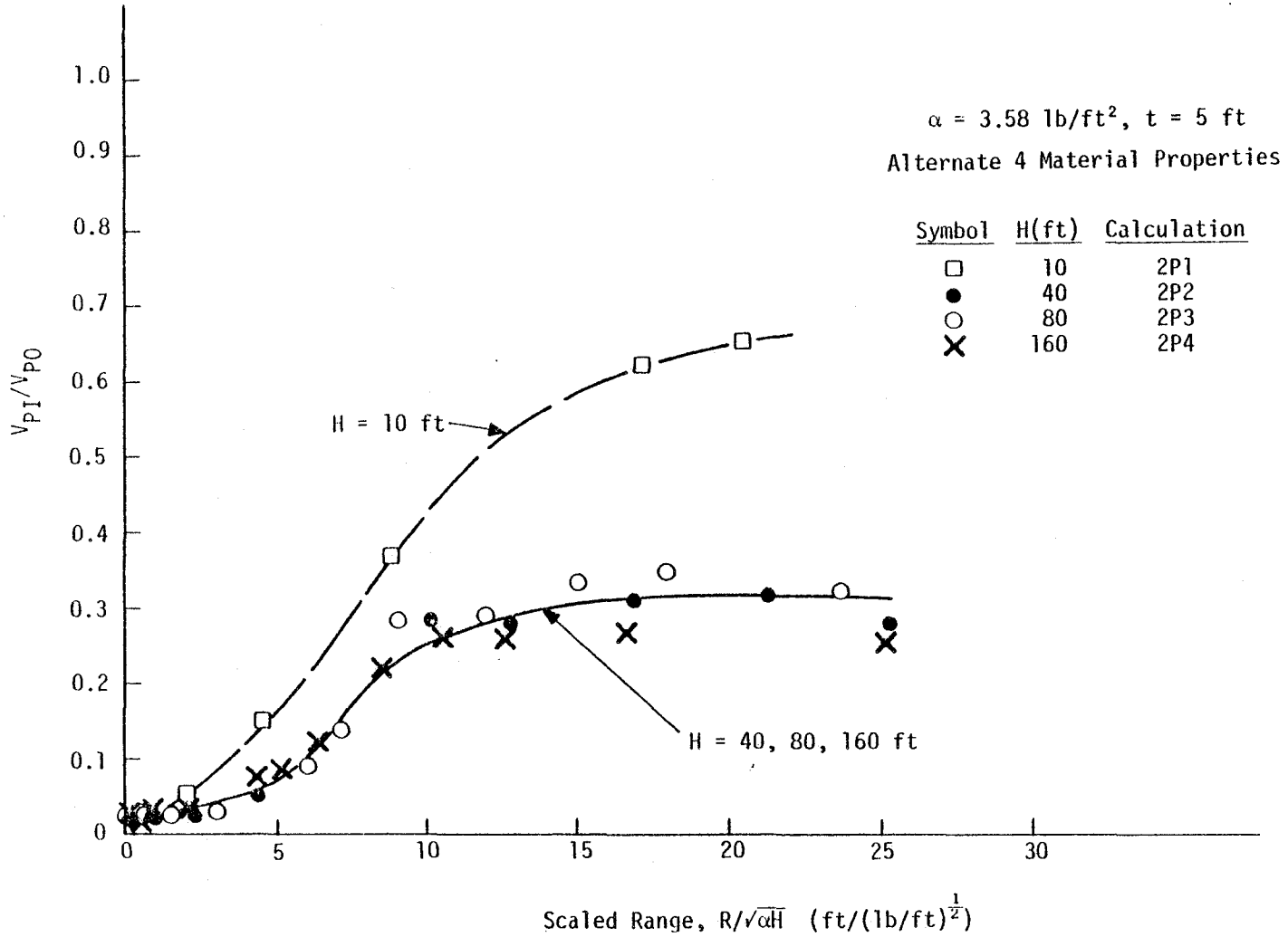

Figure V-66. Ratio of Peak Inward to Peak Outward Horizontal Velocity in Two-Dimensional Planar Symmetric Geometry

product of the array height and the areal charge density. This form of correlation produced the best collapse of the results for all except the 10-foot calculation. The term αH is an effective lineal charge density for the array. The 10-foot calculation contains higher ratios of inward to outward velocities because of the relative phasing of the P-relief and SP-relief effects mentioned previously. In the larger array calculations, the two relief effects are separated in time and the SP-relief provides the major inward component. In the 10-foot calculations, the P-relief and SP-relief effects occur in the same time period and seem to cause a relatively greater inward amplitude. Most practical applications will probably involve large array heights and, therefore, the correlations for the 40, 80, and 160-foot arrays have more applicability.

As with cylindrical geometry, horizontal motions at locations off the array mid-depth will diminish. Off-center variations in the calculation were collapsed reasonably well when the range and off-center distance were scaled by the array height. Fits to the off-center motion amplitudes, as a proportion of the peak mid-depth amplitudes, are plotted as functions of the scaled off-center distance in figures V-67, V-68, and V-69. The off-center variations of the outward velocity phase duration are shown in figure V-70. These results will be used as the basis for estimating off-center behavior in the presence of a free-surface in the following discussion.

Free-surface effects in planar geometry were evaluated with two calculations for a 40-foot high array with a 3.58 lb/ft^2 TNT areal charge density. One calculation utilized a 20-foot surcharge height above the

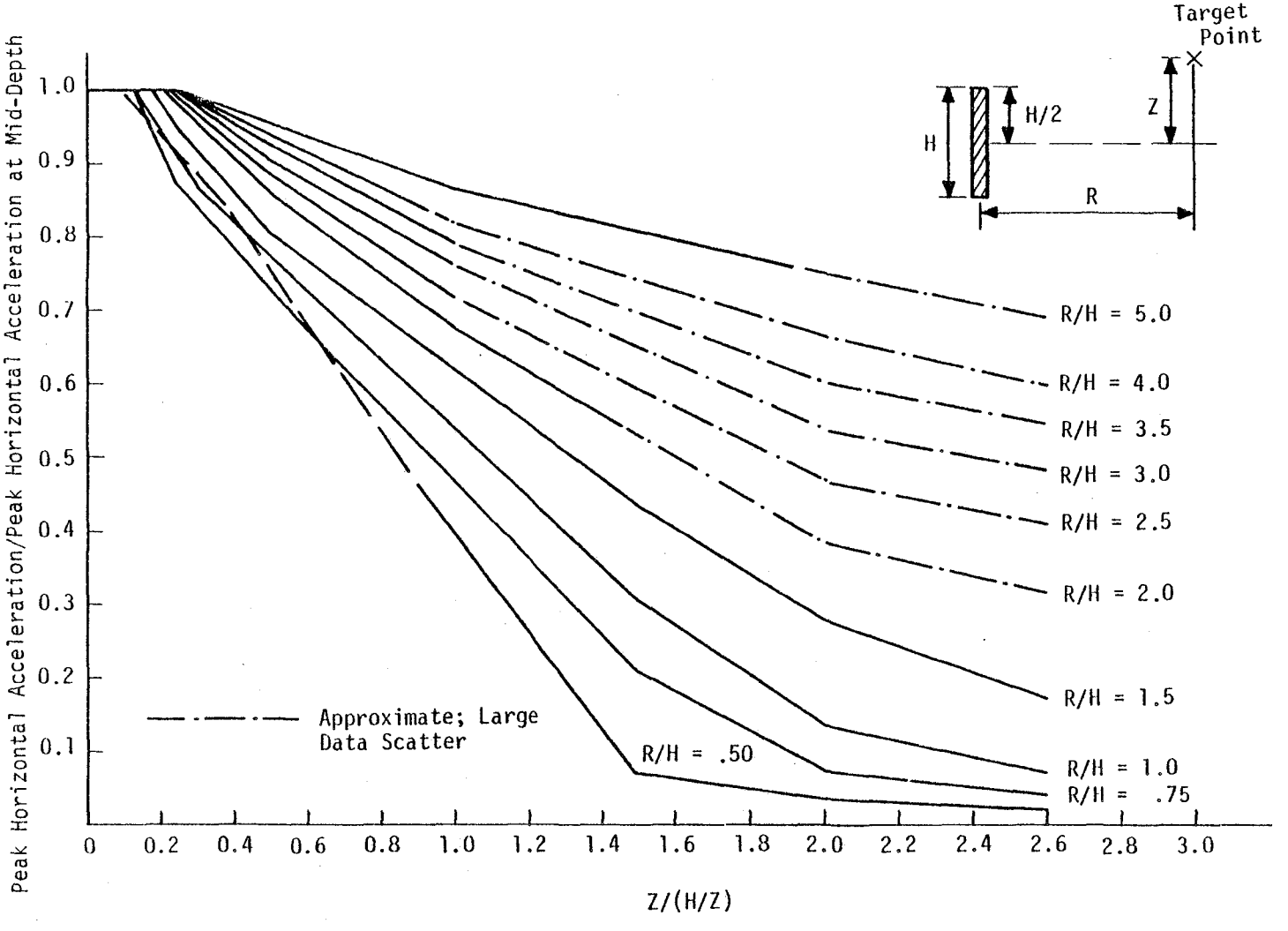

Figure V-67. Variation of Peak Horizontal Acceleration with Off-Center Distance in Planar Symmetric Geometry

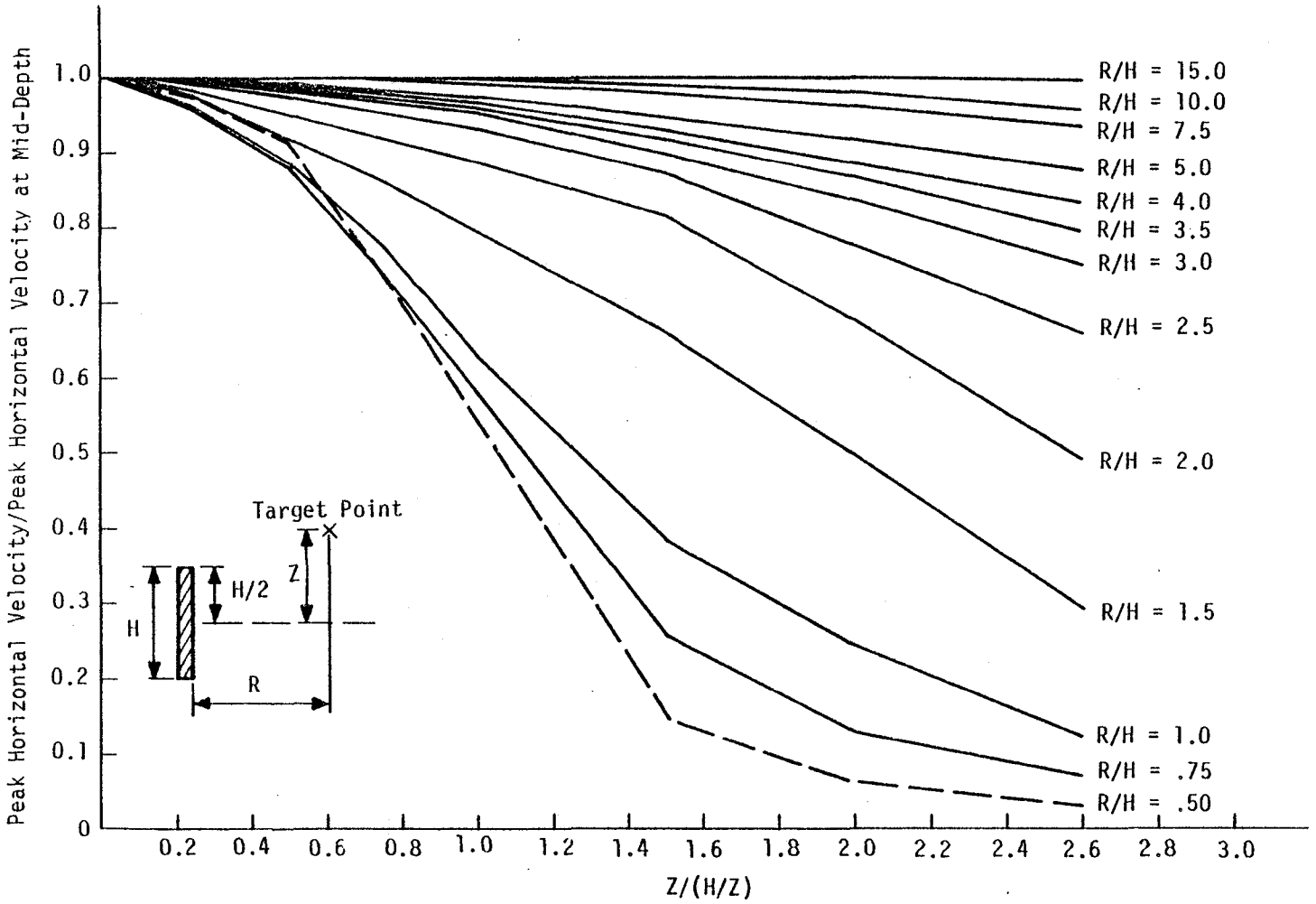

Figure V-68. Variation of Peak Horizontal Velocity with Off-Center Distance in Planar Symmetric Geometry

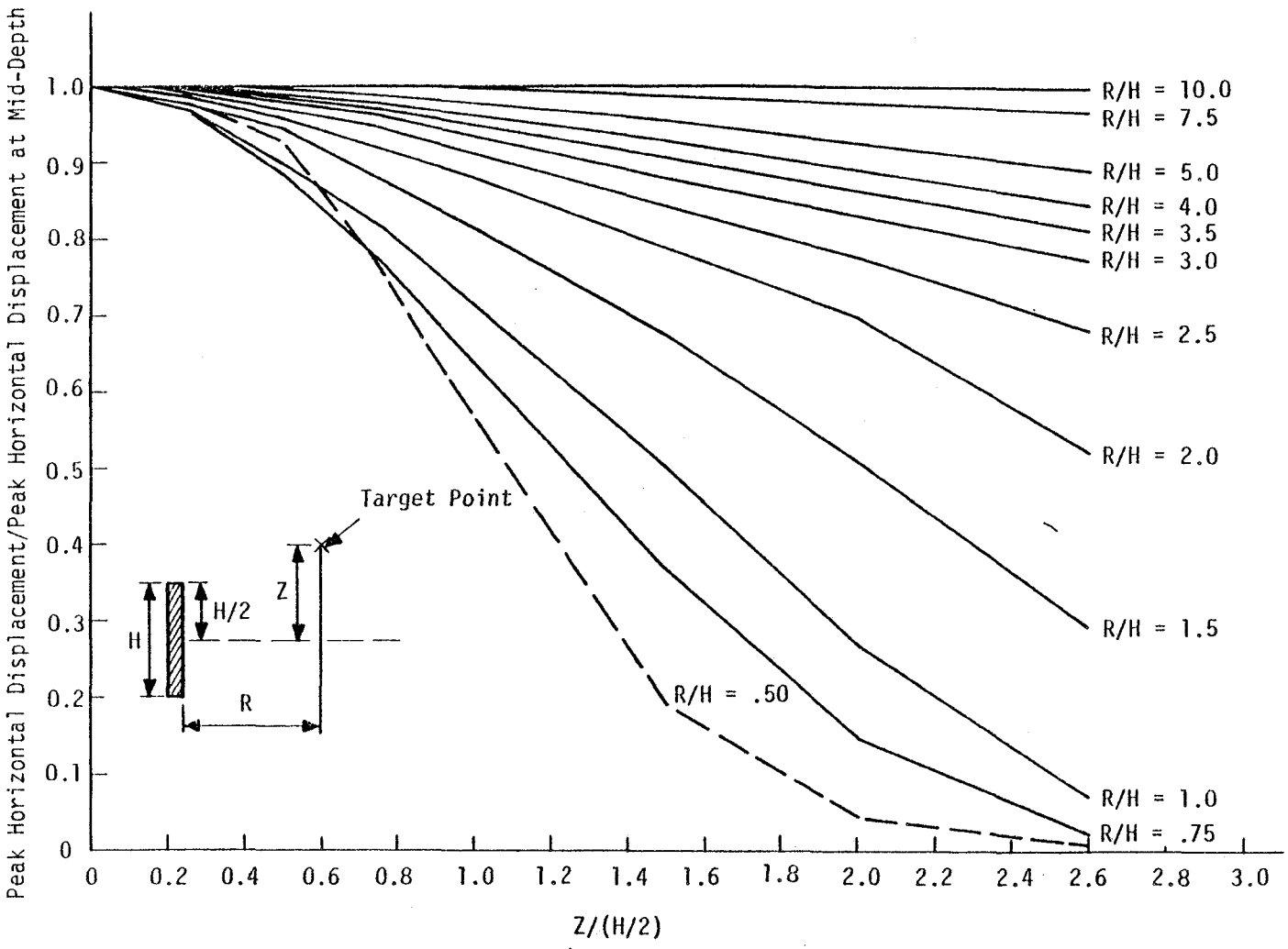

Figure V-69. Variation of Peak Horizontal Displacement with Off-Center Distance in Planar Symmetric Geometry

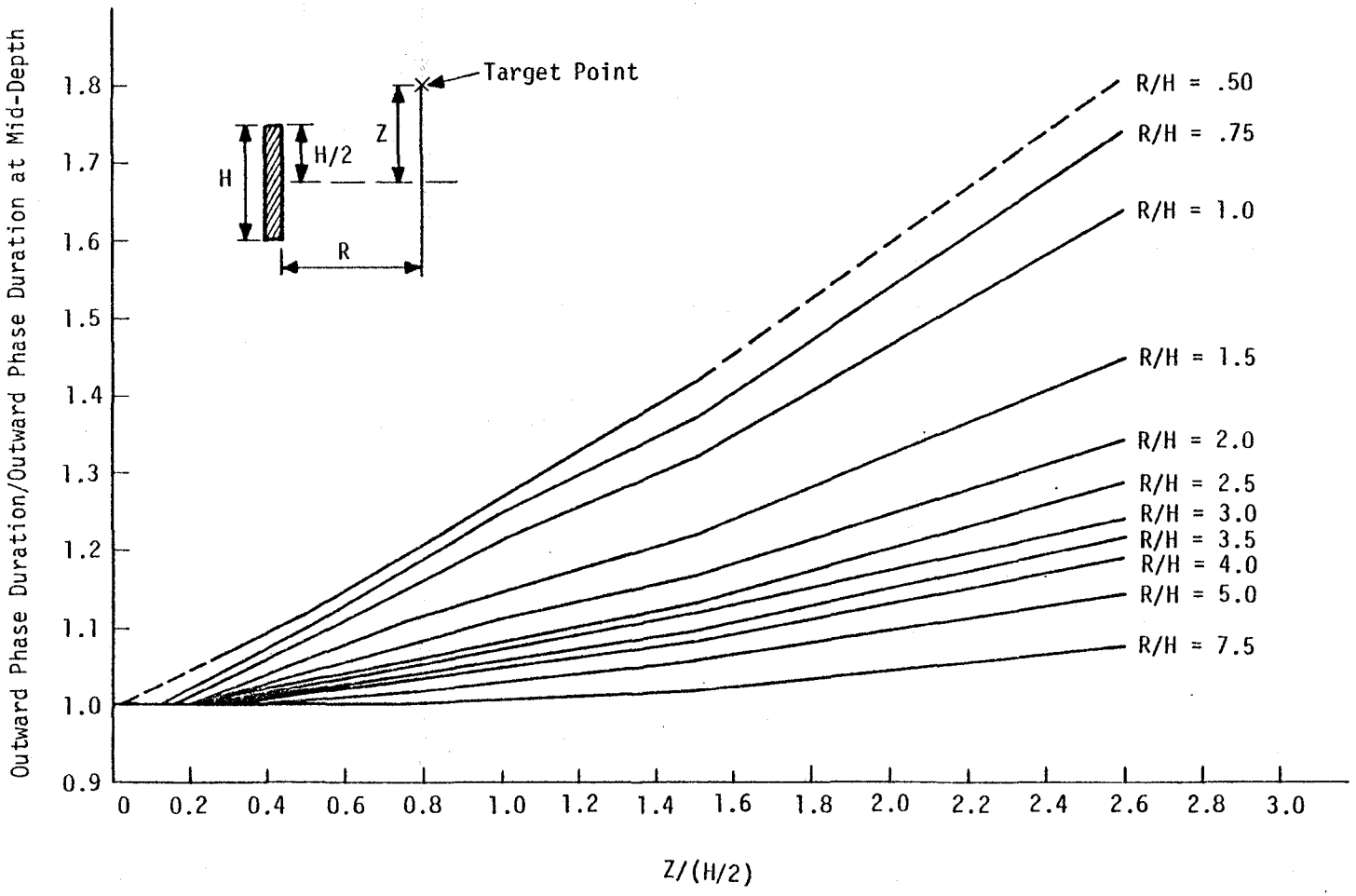

Figure V-70. Variation of Particle Velocity Outward Phase Duration with Off-Center Distance in Planar Symmetric Geometry

explosive (2P5) while the second calculation utilized a 40-foot surcharge (2P6).

The nature of free-surface effects upon horizontal velocity is illustrated in figure V-71 which compares some velocity time histories at the free-surface with corresponding time histories at the same off-center distance in the 40-foot symmetric calculation (2P2). The peak velocity amplitudes are about double those in the symmetric calculations. In addition, the characteristic times are larger. The combination of larger peak velocities and larger outward durations leads to significantly larger outward displacements in the presence of a free-surface.

Figure V-72 plots fits to the average ratios of horizontal acceleration and horizontal velocity to the corresponding quantities at the same off-center distance in the symmetric calculations, as a function of range scaled by the array height. The ratios are plotted for two depths, the free-surface and the array centerline. It can be seen that accelerations at the array centerline are unaffected by the free-surface. The accelerations at the free-surface, however, are about double those at the corresponding off-center distance in the symmetric calculations. This is due to the free-surface reflection. Horizontal velocities at the surface are also doubled due to reflection. The velocities at the array centerline are unaffected out to some range but they then increase and, finally, double at a value of R/H of about 4.5. The velocities on the centerline are affected at a nearer range in the 20-foot surcharge case than in the 40-foot surcharge case. This apparently is due to faster penetration of the reflection to the centerline in the 20-foot case.

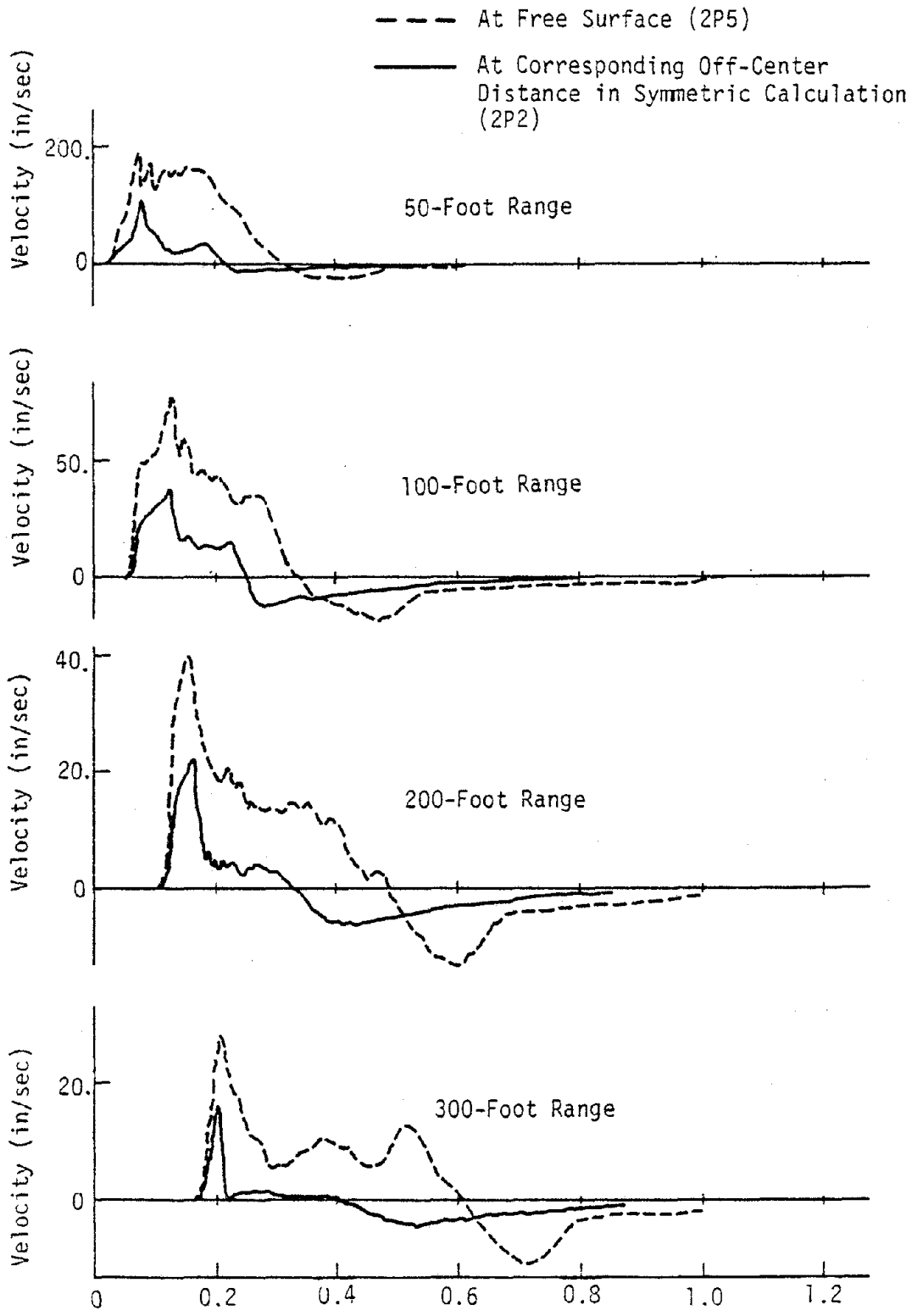

Figure V-71. Effect of Free-Surface on Near-Surface Horizontal Particle Velocities in Planar Geometry

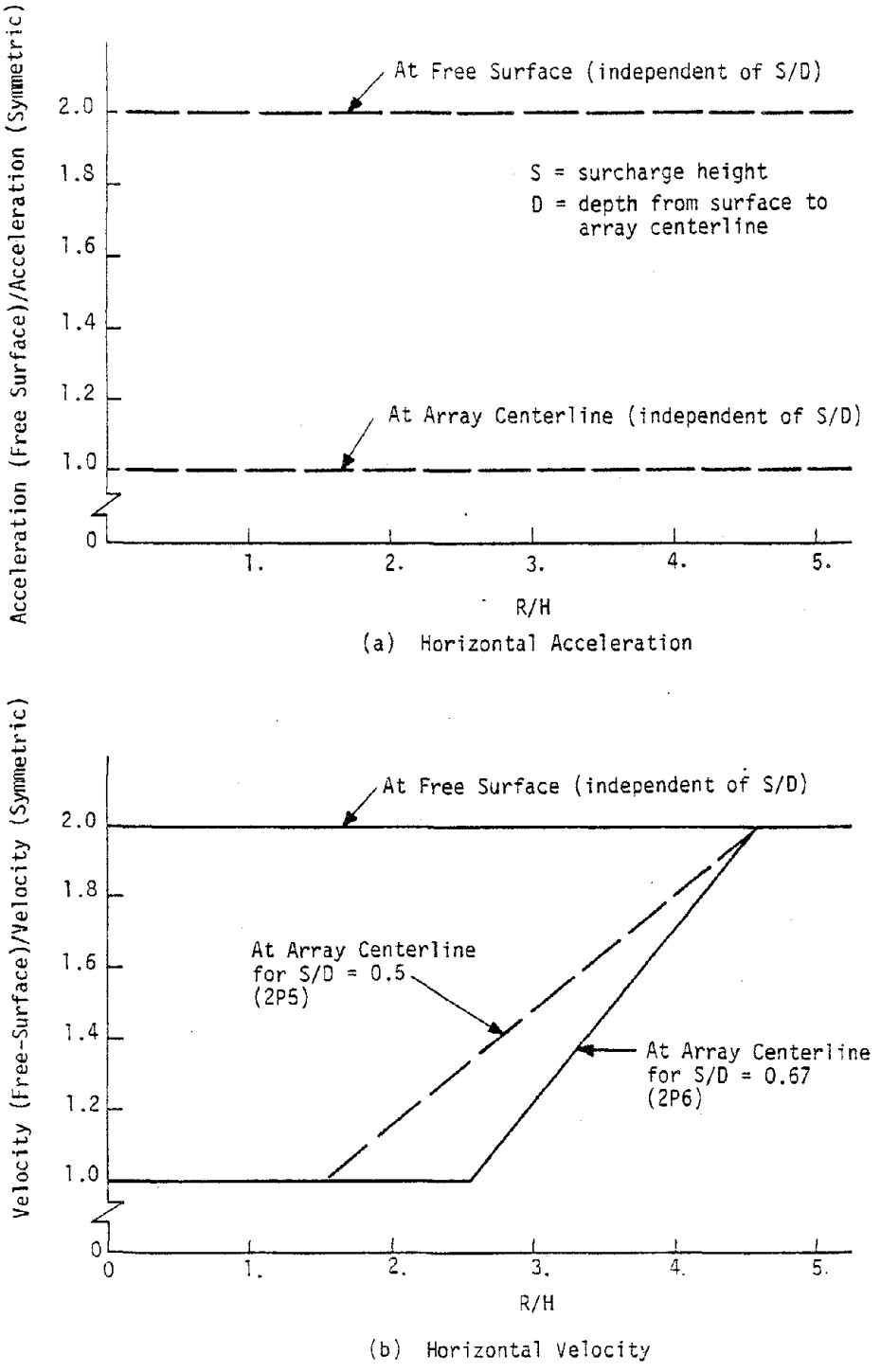

Figure V-72. Effect of the Free-Surface on Horizontal Acceleration and Velocity in Planar Geometry

Ratios for displacements and outward phase durations as a function of scaled range are shown in figure V-78. Displacement ratios at both the surface and centerline increase with range to a scaled range of about 4 after which they seem to remain about constant. Calculation results did not extend far into this region, and, hence, the calculation fits are uncertain as indicated by the question marks in figure V-73a. At both the free-surface and the centerline, the ratio is approximately independent of surcharge height. The outward phase durations at the surface increase with increasing range while they initially decrease and then increase again at the centerline. The outward phase duration behavior is complex and not readily interpretable.

The results of the free-surface calculations indicate significant complexity in the variations of motion and characteristic time amplitudes with depth between the surface and the array centerline. The variations shown previously for the cylindrical case in figures V-50 through V-53 are typical of the complexity, but the actual numerical values of the ratios and their variations are different in the two planar free-surface calculations. Many more calculations would be required to define the variations in general terms. Fortunately, the ratios at the free-surface in the planar calculations seem to be relatively independent of surcharge depth over fairly large ranges, and these ratios are probably adequate for simulation design. If accurate estimates at depth are required then specific two-dimensional calculations should be performed.

Some vertical time-histories at the surface in the 20-foot surcharge calculation are shown in figure V-74. Horizontal velocities are

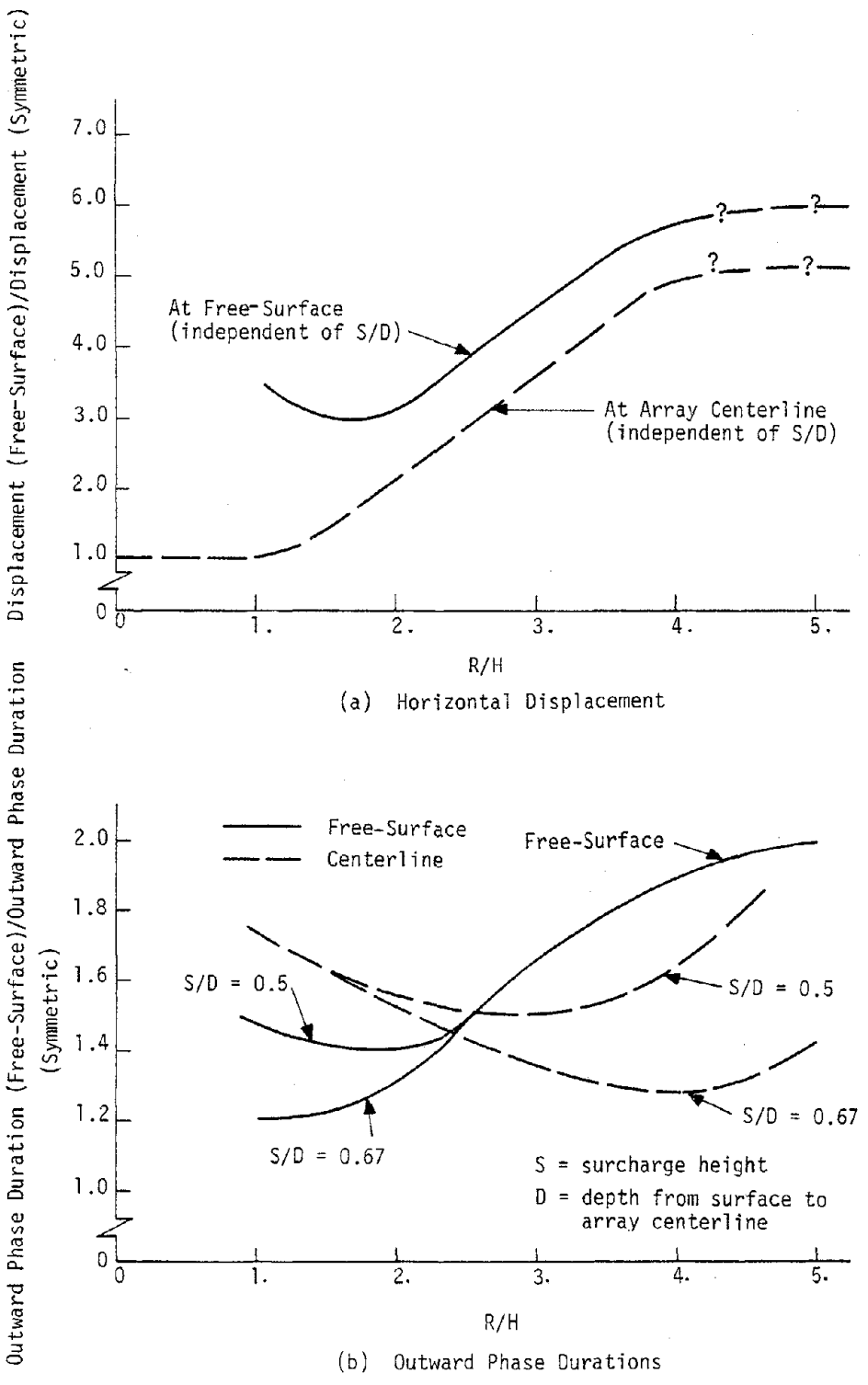

Figure V-73. Effect of the Free-Surface on Horizontal Displacement and Velocity Outward Phase Duration in Planar Geometry

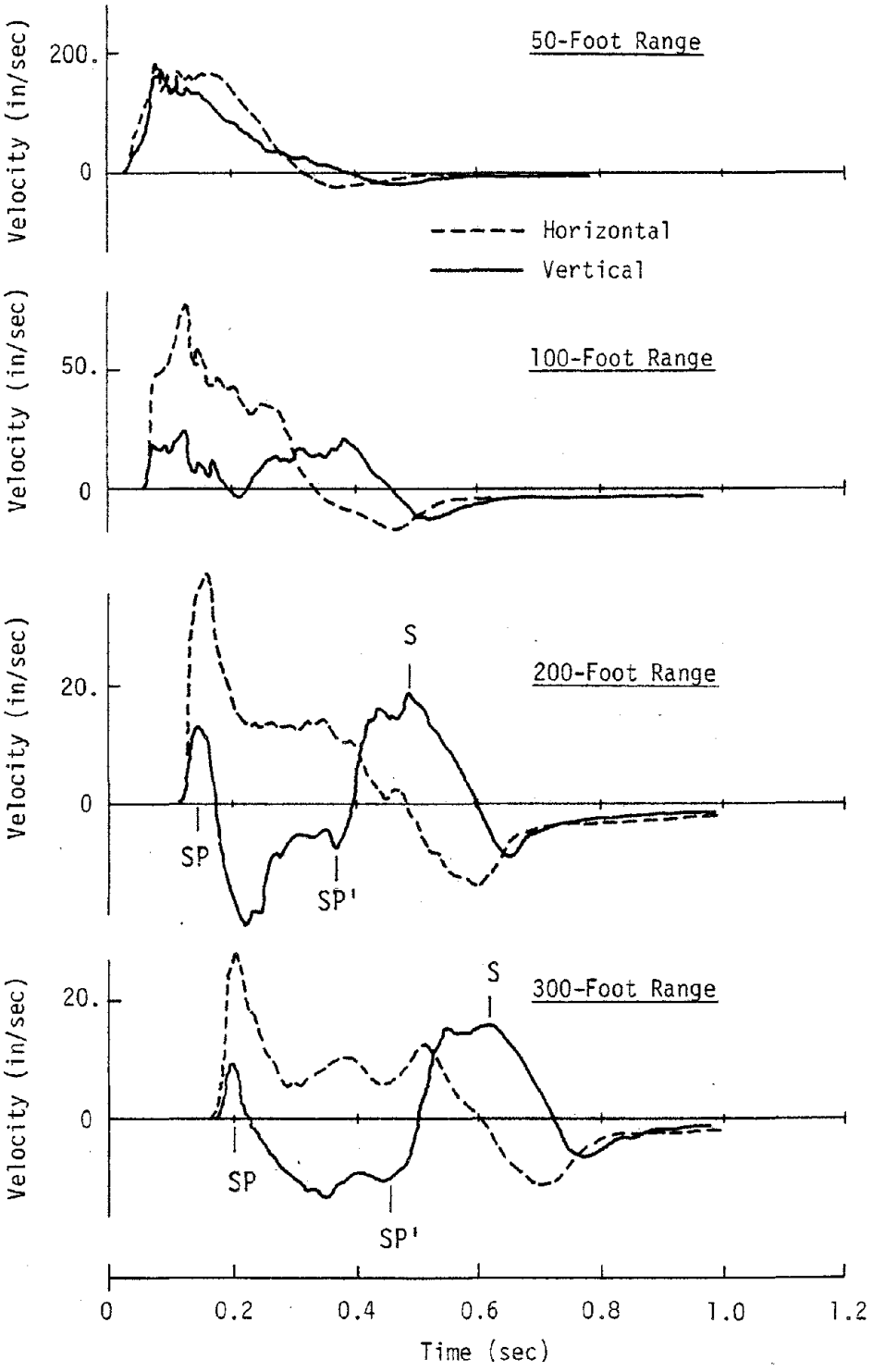

Figure V-74. Some Vertical and Horizontal Velocity Time Histories at the Surface in a Planar Calculation with 20 Feet of Surcharge (2P5)

also shown so that the relative behavior of the vertical and horizontal components can be observed. At the 50-foot range, the vertical and horizontal wave shapes are similar and the peak velocities are about the same. This target location is in the region of strong compression behavior and both the horizontal and vertical motions are due primarily to the incident compression wave. At the farther ranges, the vertical velocity begins to develop a more oscillatory character. At these ranges the wave structure, containing P-waves, SP-waves, and S-waves, becomes complex. The approximate arrivals of the SP-wave from array top (SP), the SP-wave from the array bottom (SP') and the S-wave from the array top (S) are marked at the more distant ranges in figure V-74. Inelastic wave speeds of about one-half the seismic speeds were used. The SP arrival reverses the initial upward motion and causes downward motion while the horizontal motion is still outward. The SP'-wave from the array bottom causes the second upward motion and the major reversal of the outward horizontal motion. The S-wave from the array top causes the late time downward vertical velocity. Other wave arrivals cannot be discerned at the time histories. In general, the major frequency content of the vertical velocity is about 1.5 to 2 times that of the horizontal component. The qualitative behavior of the vertical velocities seems to be in agreement with the wave structure proposed in figures IV-13 and IV-23, as well as the few vertical data from DIP IIA.

Figure V-75 presents ratios of the peak vertical to peak horizontal accelerations and velocities as a function of range scaled by the depth of burst (depth from surface to array mid-depth). This type of scaling resulted in the best collapse of the results of the two calculations.

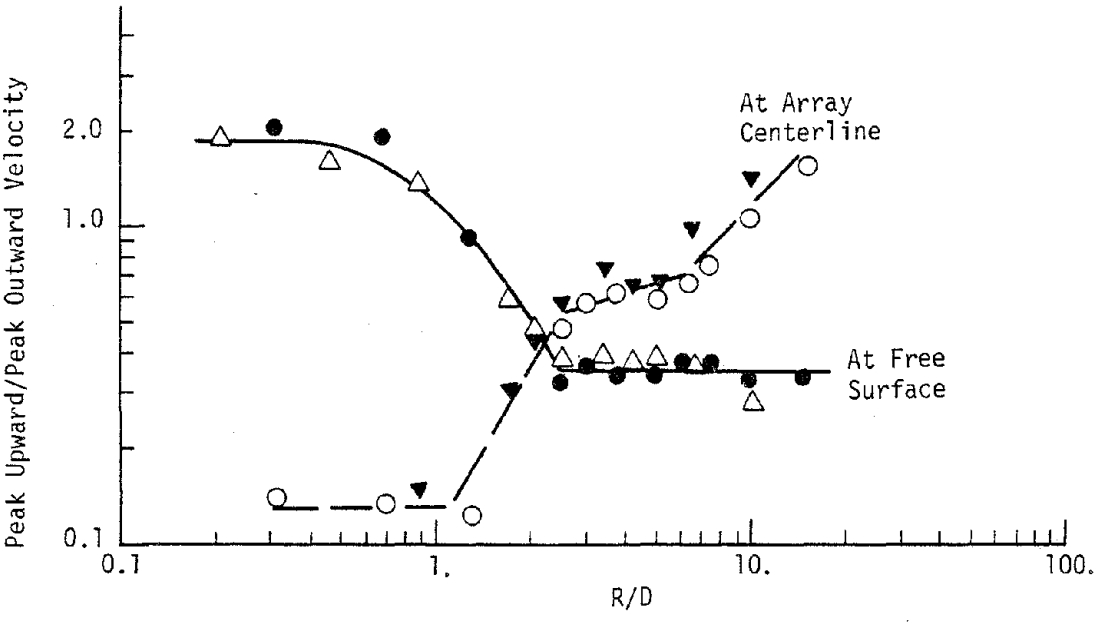

(b) Velocities

Surface	Centerline	S(ft)	D(ft)	Calc. No.
●	○	20	40	2P5
△	▼	40	60	2P6

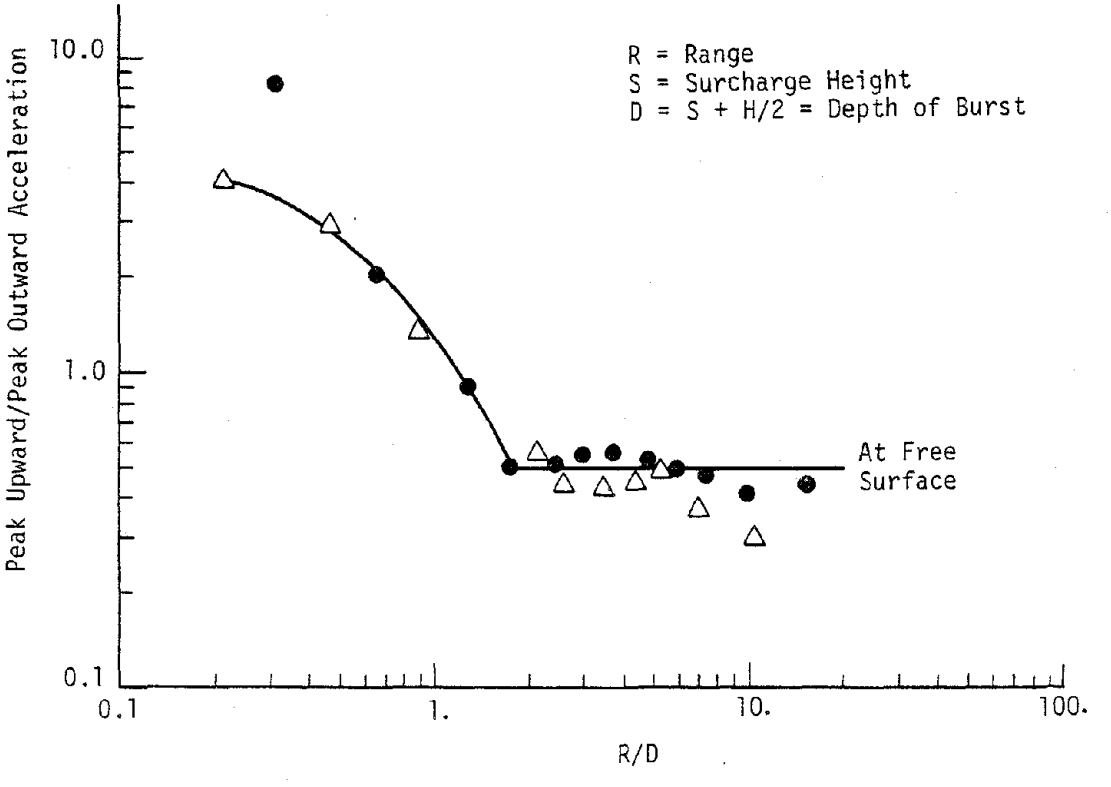

(a) Accelerations

Figure V-75. Ratios of Peak Vertical to Peak Horizontal Accelerations and Velocities in Planar Free-Surface Calculations

Acceleration ratios are given only at the surface because centerline accelerations could not be estimated easily due to the waveform complexity. Velocity ratios are given both at the surface and at the array centerline. The acceleration ratios at the surface decrease with range to a scaled range of about 1.8. Beyond this range the ratio is about constant. The velocity ratios at the surface behave similarly although the constant ratio is not reached until a scaled range of about 2.5.

In the near region the peak vertical motion is caused by the initial P-wave directed at the surface at near normal incidence. As a result, the ratio of vertical to horizontal motion exceeds 1. At more distant ranges, the peak vertical motion is caused initially by the incident P-wave, but at further ranges, by the incident S-wave from the array top. At these ranges, the incident P and S-wave fronts are traveling almost parallel to the ground surface. It is in this region that the ratios of vertical to horizontal acceleration and velocity are about constant. The constant ratios (0.5 for acceleration, 0.35 for velocity) are probably associated with some material property, perhaps Poisson's ratio, but material property variations would be required to determine the material property relationship.

Figure V-76 presents the ratios of peak vertical to peak horizontal displacements as a function of unscaled range*. Unscaled range is used because the calculation results agree best under this condition. Scaling by depth of burst only spreads the ratios from the two calculations.

---

*Range should be scaled by the areal charge density, α, in extrapolating to other charge densities.

Note: See Figure V-75 for definition of symbols

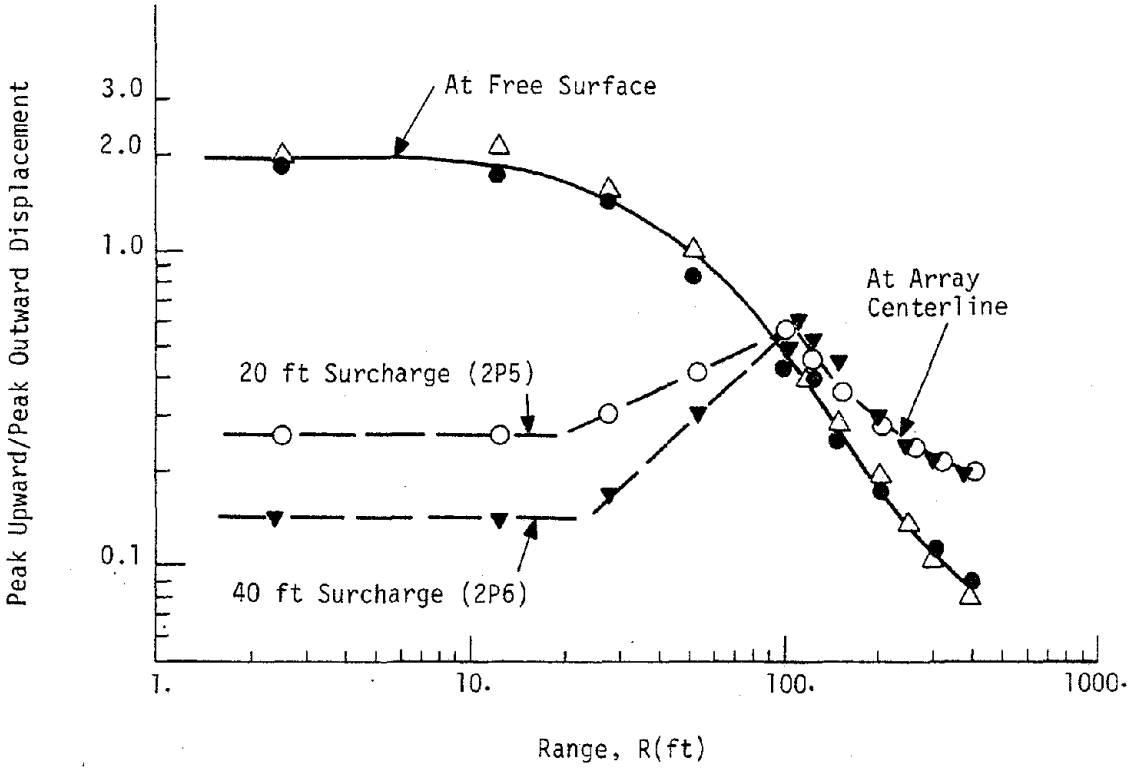

Figure V-76. Ratios of Peak Vertical to Peak Horizontal Displacements in Planar Free-Surface Calculations

This result places some uncertainty on the depth of burst scaling for accelerations and velocities. It may be that acceleration and velocity results are fortuitous and that the two surcharge heights considered are not sufficiently different to allow assessment of the proper scaling.

The displacement ratios at the surface are relatively constant to a range of about 10 feet after which they decrease continually. At the array centerline, the ratios are initially constant, although different in the two calculations. They then increase and finally collapse together at a higher value than at the surface at about 100 feet. Beyond this range, the centerline displacement ratios of the two calculations are about the same and they decrease at a lesser rate than at the surface.

9. SUMMARY OF CONCLUSIONS FROM NUMERICAL CALCULATIONS

a. General

The calculations were designed to aid in resolving some uncertainties on several important aspects of the ground motion environment created by various potential simulation configurations. Specific objectives included evaluation of yield scaling in inelastic material, source coupling effects, inelastic attenuation rates in various explosive geometries, the effects of finite explosive size in cylindrical and planar geometry, free-surface effects and some aspects of material property scaling. Main conclusions in these areas are outlined below.

b. Yield Scaling

The one-dimensional spherical, cylindrical, and planar calculations,

using a highly inelastic soil model, indicated that yield scaling using $W^{\frac{1}{3}}$, $\gamma^{\frac{1}{2}}$ or α, depending on geometry, can be used with confidence in inelastic materials. If such scaling cannot collapse data in apparently similar materials then material property differences or gravity effects must be investigated.

c. Source Coupling

One-dimensional cylindrical calculations with different cavity radii gave significantly different results for velocities and accelerations near the source. At greater distances, the differences diminished. The displacements were different, however, over all ranges. The larger the cavity radius, the larger the displacement. These results indicate that a source parameter, in addition to yield, is an important part of scaling. That parameter appears to be source pressure or, equivalently, source specific energy. This conclusion is reinforced by the elastic material property scaling results discussed below. The coupling results also suggest that it may be possible to control motion frequency content by varying the source cavity size.

d. Attenuation Rates

The one-dimensional results indicated that velocities attenuate only slightly faster than displacements. This implies, and the calculations verify, that the outward phase duration attenuates at a relatively low rate with range. This is true for all characteristic times. The attenuation rate information is valuable because it aids in interpreting the transition phenomena in different geometries.

e. Effects of Finite Explosive Size

The two-dimensional cylindrical calculations indicated that the motion field undergoes a transition from cylindrical to spherical behavior at a range which is approximately 0.6 times the array height. The attenuation rates for the various motion parameters after the transition were the same as the attenuation rates in spherical geometry.

The two-dimensional planar calculations indicated a transition from planar to cylindrical behavior at a range which varied with array height. This result is different from the data interpretation of Section IV and provides a means of improving predictions. The planar results also indicated that the attenuation rates of the motion parameters after the transition are indeed cylindrical attenuation rates. Characteristic times exhibited a relation to array height which differed markedly from the relation implied by the data and, this too, will significantly improve planar prediction capability.

f. Free-Surface Effects

The two-dimensional cylindrical and planar calculations provide qualitative insight into the effect of the free-surface on horizontal and vertical motion components. The quantitative results can be used as a guide for estimates of effects but scaling with parameters such as surcharge height and/or depth of burst is somewhat uncertain. Additional calculations will be required to reduce this uncertainty.

g. Material Property Scaling

One-dimensional cylindrical calculations with three different elas-

tic models indicated that current material property scaling using only yield as a source parameter is inadequate. Proper scaling terms can be developed, however, if the source pressure is included in the dimensional analysis. The proper terms for velocity and displacement were derived based upon an "empirical" analysis of the calculation results.

10. REFERENCES

V-1 Lawrence, R.J. and Mason, D.S., WONDY IV - A Computer Program for One-Dimensional Wave Propagation with Rezoning, SC-RR-71-0284, Sandia Laboratories, Albuquerque, New Mexico, August 1971.

V-2 Bertholf, L.D. and Benzley, S.E., TOODY II - A Computer Program for Two-Dimensional Wave Propagation, SC-RR-68-41, Sandia Laboratories, Albuquerque, New Mexico, November 1968.

V-3 Bratton, J.L. and Mitchell, N.R., "A Summary of Parameters for Designing and Predicting the Airblast Environment of HEST Experiments," Proceedings of the Eric H. Wang Symposium on Protective Structures Technology, Air Force Weapons Laboratory, Kirtland AFB, New Mexico, 21-23 July, 1970.

V-4 Glass, I.I. and Hall, J.G., Handbook of Superseismic Aerodynamics, Section 18, NAVORD Report No. 1488, Vol. 6, 1969.

V-5 Drucker, D.C. and Prager, W., "Soil Mechanics and Plastic Analysis or Limit Design," Quarterly of Applied Mechanics, p. 157, 1952.

V-6 Triandafilidis, G.E., Calhoun, D.E. and Abbott, P.A., Simulation of Airblast-Induced Ground Motions at McCormick Ranch Test Site, Vol. I, Project SILT PILE, AFWL-TR-68-27, Air Force Weapons Laboratory, Kirtland AFB, New Mexico, October 1968.

V-7 Schlater, D.R., DIHEST Improvement Program Test, DIP IA, Data Report, AFWL-TR-71-120, Air Force Weapons Laboratory, Kirtland AFB, New Mexico, January 1972.

V-8 Mazanti, B.B., and Holland, C.N., Study of Soil Behavior Under High Pressure, Report 1: Response of Two Recompacted Soils to Various States of Stress, Vols. 1-3, S-70-2, U.S. Army Waterways Experiment Station, Vicksburg, Miss., 1970.

V-9 Bratton, J.L., and Higgins, C.J., "Measuring Dynamic In-Situ Geotechnical Properties," to be presented at ASCE Earthquake Engineering and Soil Dynamics Conference, Pasadena, California, June 19-21, 1978.

V-10 Crawford, R.E., Higgins, C.J. and Bultmann, E.H., The Air Force Manual for Design and Analysis of Hardened Structures, AFWL-TR-74-102, Air Force Weapons Laboratory, Kirtland AFB, New Mexico, October 1974.

V-11 Crowley, B.K., "Scaling Criteria for Rock Dynamic Experiments," Proceedings, Symposium on Engineering With Nuclear Explosives, American Nuclear Society and USAEC, Conf-700101 (Vol. 1), Las Vegas, Nevada, May 1970.

V-12 Hendron, A.J., Scaling of Ground Motions From Contained Explosions in Rock for Estimating Direct Ground Shock From Surface Bursts on Rock, Technical Report No. 15, Omaha District Corps of Engineers, Omaha, Nebraska, January 1973.

V-13 Cooper, H.F., Jr., Generation of an Elastic Wave By Quasi-Static Isentropic Expansion of a Gas in a Spherical Cavity; Comparison Between Finite Difference Predictions and the Exact Solution, AFWL-TR-66-83, Air Force Weapons Laboratory, Kirtland AFB, New Mexico, September 1966.

Page Intentionally Left Blank

SECTION VI
ENHANCEMENT CALCULATIONS

1. INTRODUCTION

Existing experimental data on enhancement techniques were analyzed in Section IV. The techniques which appear to have the greatest potential usefulness in earthquake ground motion simulation are:

- Multiple, time sequenced explosions
- Decoupled explosions
- Shock barriers
- Relief Trenches

The available multiple, time sequenced explosion data indicate that linear superposition of single explosion motions, according to relative time phasing, is a good means of estimating combined effects. The decoupled charge data, as well as the source coupling calculations of Section V, suggest coupling variations may be a viable way of altering the amplitudes and the frequency content of explosive ground motions. Hence, feasibility of both of these methods in earthquake ground motion simulation is well supported at this time. Further experimental data will be required for the development of improved prediction methods.

The data on shock barriers and relief trenches, however, are from very high motion amplitude regimes which are much higher than those of interest in earthquakes. As a result, further investigation into their effects is

necessary for an improved feasibility evaluation. This section applies simple analytical methods and a few numerical calculations for a limited improved assessment of the use of shock barriers and trenches as enhancement methods.

2. SHOCK BARRIERS

A shock barrier is defined as a stiff, massive emplacement between the explosive source and the test area. The energy reflected from the barrier, as well as the increased time required to move the barrier compared with the free-field soil, diminishes the amplitudes of the motions transmitted to the test area.

A solution for the one-dimensional response of a rigid mass on elastic soil to a triangular decaying shock was outlined in Section IV. The theoretical solution (fig. IV-53) suggested that it was possible to decrease peak accelerations without significantly decreasing peak velocity. The results of shock tube experiments substantiated this conclusion. The closed form solution is for a shock input and the rise times in the shock tube experiments were very short. This condition will not occur under general explosive loads. Hence, it is of interest to evaluate behavior under more applicable pulse shapes. The response of a rigid barrier (fig. VI-1) under a parabolic load (fig. VI-2) is considered. The parabolic load was chosen because it closely approximates the rise to peak stress in actual soil motion data and can be readily analyzed. The solution method follows that given in reference VI-1.

The soil particle velocity behind the structure is equal to the velocity of the structure. Hence, the stress on the rear of the barrier

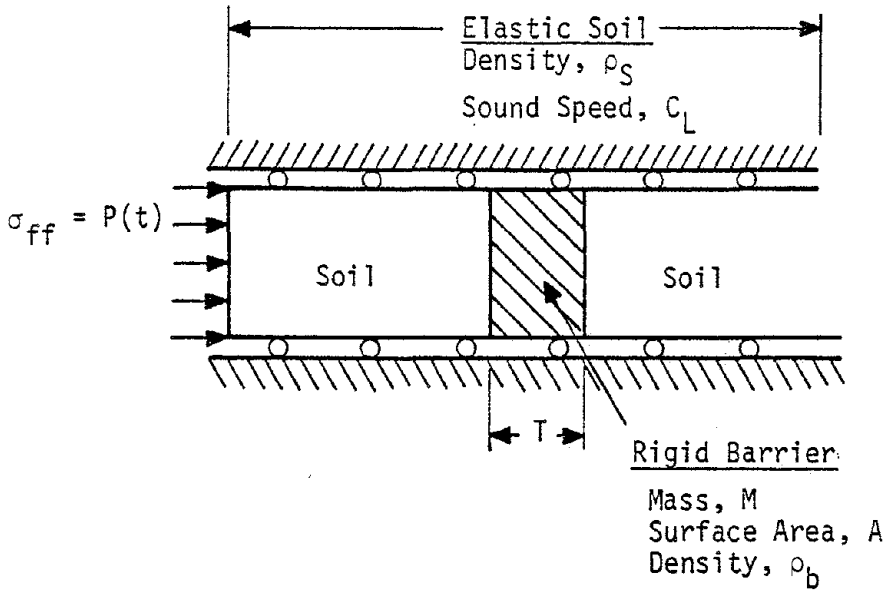

Figure VI-1. One-Dimensional Representation of Rigid Barrier

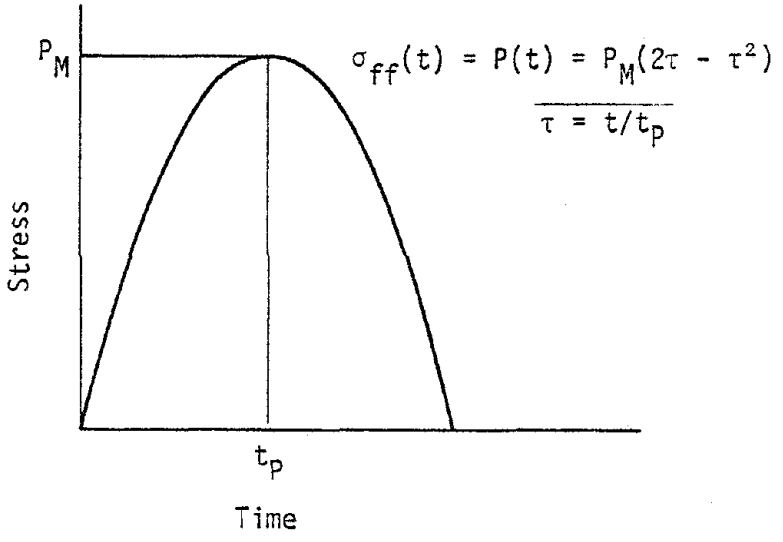

Figure VI-2. Quadratic Pressure Loading Parameters

is

$$\sigma_r(t) = \rho_S C_L \, v(t) \qquad \text{(VI-1)}$$

where

σ_r = stress on rear of the barrier

ρ_S = mass density of the soil

C_L = loading (compressional) wave velocity of the soil

v = barrier velocity

The stress on the incident barrier face is twice the free-field value (since the barrier is rigid) less an amount related to the barrier velocity, i.e.,

$$\sigma_i(t) = 2\sigma_{ff}(t) - \rho_S C_L \, v(t) \qquad \text{(VI-2)}$$

where

σ_i = stress on incident face

σ_{ff} = incident free-field stress

From conservation of momentum, the equation of motion for the rigid barrier, neglecting shear, is:

$$M\dot{v}(t) + 2\rho_S C_L A v(t) = 2A\sigma_{ff}(t) \qquad \text{(VI-3)}$$

where

M = mass of rigid barrier

$v(t)$ = velocity history of barrier

$\dot{v}(t)$ = time derivative of velocity, i.e., acceleration

A = surface area of rigid barrier

For the stress history (fig. VI-2) given by

$$\sigma_{ff}(t) = P(t) = P_M(2\tau - \tau^2) \qquad \text{(VI-4)}$$

where

P_M = maximum incident free-field stress

τ = normalized time, t/t_p

t_p = time to peak pressure

the closed form solution to the differential equation (eq. VI-3) is

$$v(\tau) = \frac{P_M}{\rho_S C_L}\left[\frac{2\tau}{\delta} - \frac{2}{\delta}\left(1 + \frac{1}{\delta}\right)\left(1 - e^{-\delta\tau}\right) + 2\tau - \tau^2\right] \qquad \text{(VI-5)}$$

where

$$\delta = \frac{2\rho_S C_L A t_p}{M} = \frac{2\rho_S C_L t_p}{M/A} = \frac{2\rho_S C_L t_p}{\rho_b T} \qquad \text{(VI-6)}$$

ρ_b = mass density of barrier

T = thickness of barrier

The acceleration of the barrier is

$$a(t) = \dot{v}(t) = \frac{2P_M}{\rho C_L t_p}\left[\left(1 + \frac{1}{\delta}\right)\left(1 - e^{-\delta\tau}\right) - \tau\right] \qquad \text{(VI-7)}$$

Equations VI-5 and VI-7 are plotted in normalized form in figure VI-3. It can be seen that as the mass of the barrier increases (δ decreases) under a specific set of soil and loading conditions, the peak velocity and peak acceleration of the barrier decrease, while the rise time to the peaks increases. These changes would also occur in the soil motion behind the barrier. For a given δ, there is a larger percentage decrease in peak acceleration than in peak velocity. It is of interest to quantify these changes in order to obtain physical estimates of barrier sizes.

The non-trivial root of the equation for acceleration (eq. VI-7)

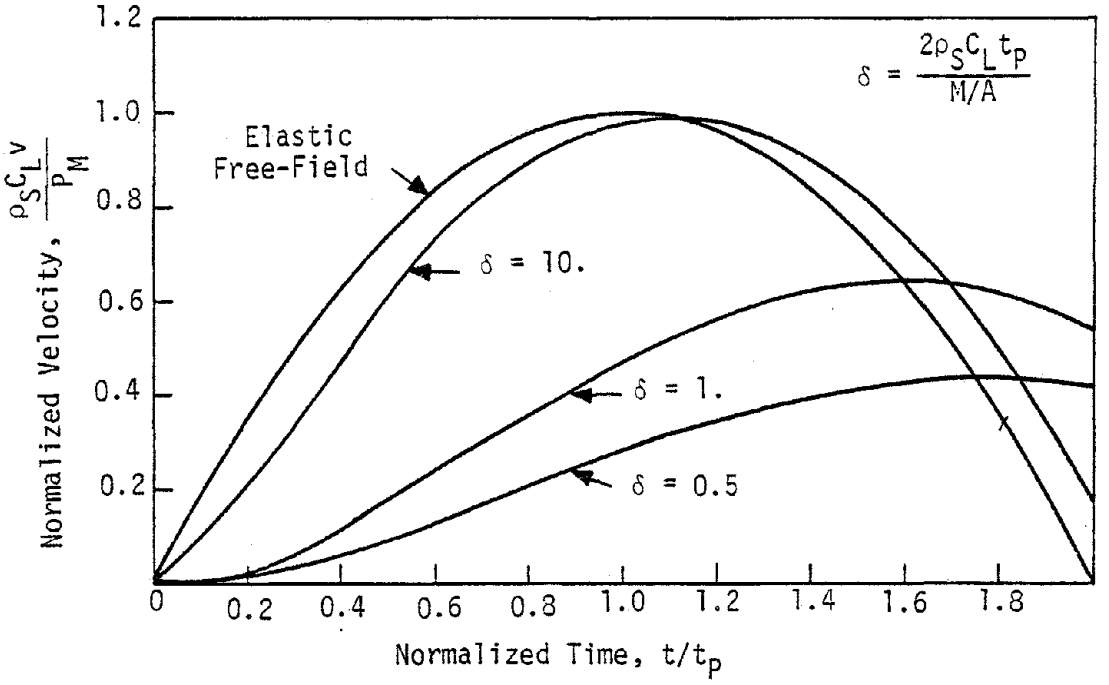

a) Normalized Velocity

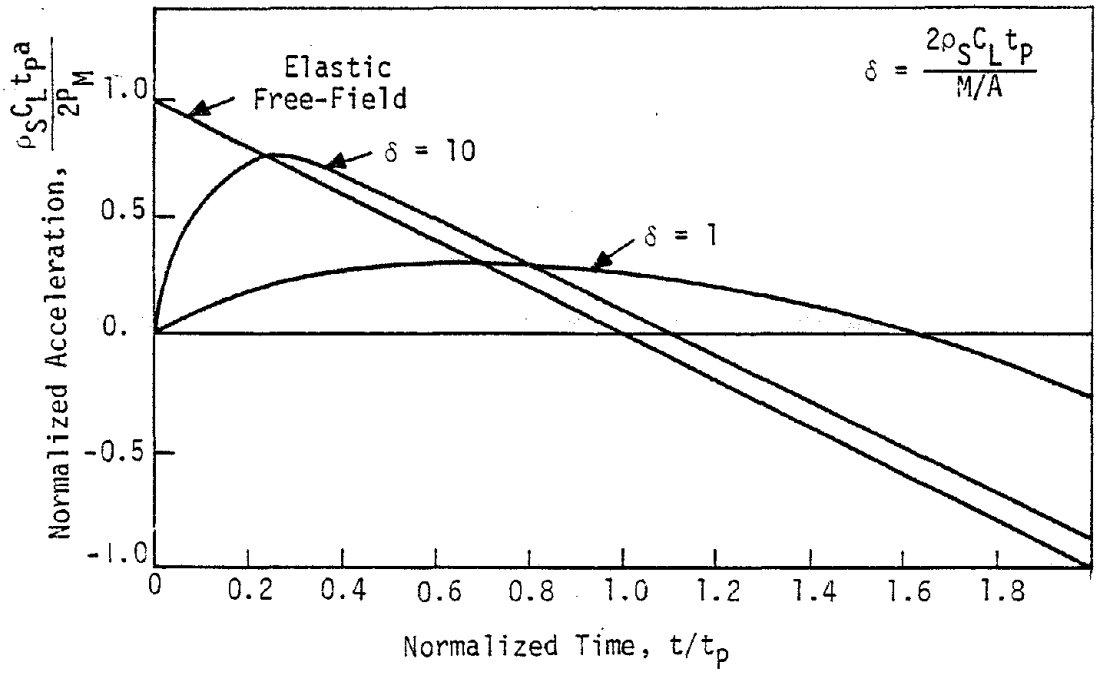

b) Normalized Acceleration

Figure VI-3. Normalized Response of Buried Rigid-Mass, Shock Barrier

$$a(\tau) = \left(1 + \frac{1}{\delta}\right)\left(1 - e^{-\delta\tau}\right) - \tau = 0 \qquad \text{(VI-8)}$$

is the time of peak barrier velocity. Substituting this into the equation for velocity (eq. VI-5) would give peak velocity, v_p, as a function of the normalized material parameter δ. Since equation VI-8 is transcendental, peak velocity was determined numerically. The resulting relation between δ and peak velocity is given in figure VI-4.

The time to peak acceleration is determined from the root of the time derivative of acceleration given by:

$$\dot{a}(t) = (\delta + 1)e^{-\delta\tau} - 1 = 0 \qquad \text{(VI-9)}$$

The root to equation VI-9, or time of peak acceleration is

$$\tau_p = \frac{1}{\delta} \ln(\delta + 1) \qquad \text{(VI-10)}$$

The normalized peak acceleration as a function of the normalized material parameter is therefore

$$a_p = 1 - \frac{1}{\delta} \ln(\delta + 1) \qquad \text{(VI-11)}$$

Peak acceleration as a function of δ is also plotted in figure VI-4. The normalized peak parameters (a_p and v_p) are also the ratios of the structure peak parameter to the corresponding free-field parameter (a_p^S/a_p^{ff} and v_p^S/v_p^{ff}). It can be seen that for a given set of soil, loading, and barrier parameters, peak acceleration is decreased substantially more than peak velocity.

The following set of parameters, which might be representative of a concrete barrier, a silty sand under low stress conditions, and the input

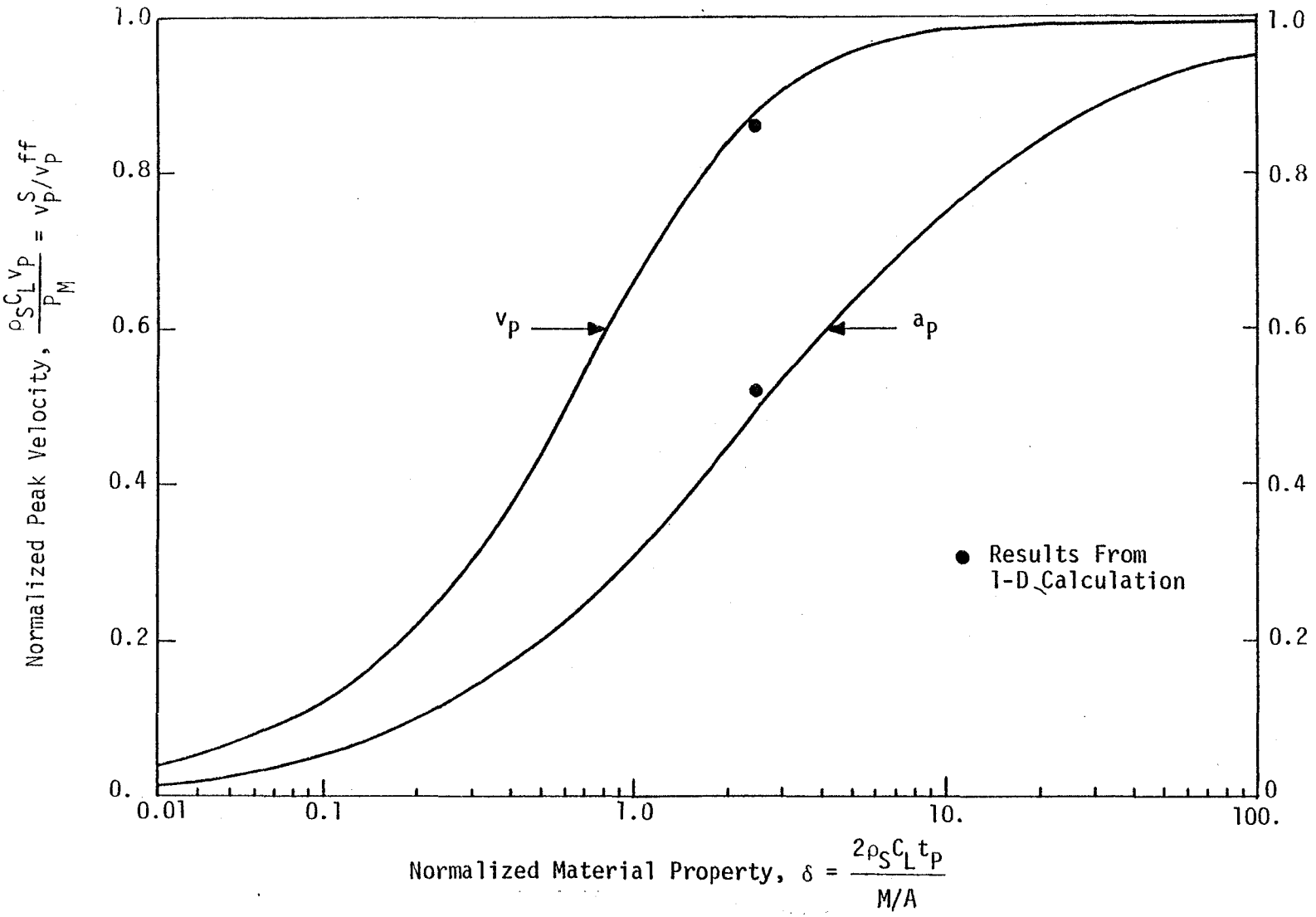

Figure VI-4. Normalized Peak Velocity and Acceleration for Rigid Barrier Under Parabolic Load

from a credible planar simulation experiment are considered.

$\rho_S = 109$ lb/ft^3	Soil data
$C_L = 1650$ ft/sec	
$\rho_b = 150$ lb/ft^3	Barrier data
$t_p = .100$ sec	Input free-field stress data
$P_M = 100$ psi	

The input free-field particle velocity under these conditions is about 2.6 ft/sec while the free-field acceleration is 1.6 g. The particle velocity is in the range of what might be expected in a strong earthquake but the acceleration is too high. A 50 percent reduction in peak acceleration requires a δ of 2.4. The corresponding reduction in peak velocity is only about 15 percent. The thickness of concrete required for this 50 percent reduction in peak acceleration can be calculated from equation VI-6 as:

$$T = \frac{2\rho_S C_L t_p}{\rho_C \delta} = \frac{2(109/32.2)(1650)(.100)}{(150/32.2)(24)} = 100 \text{ ft} \qquad \text{(VI-12)}$$

A 100 ft thick barrier is required to reduce peak acceleration by a factor of 2 - clearly impractical. The rise time to peak pressure (t_p) is the controlling variable for the problem. In the case of incident shocks relatively smaller barriers are required. For example, rise times of .001 to .010 sec would require barriers of 1 to 10 feet thick, respectively, for 50 percent reductions in acceleration. In the case of incident waves with rise times on the order of those expected in large explosive experiments, shock barriers appear impractical.

A one-dimensional, elastic shock barrier calculation was done using WONDYIV (ref. VI-2) to confirm the analytical results. A 10-ft thick

concrete barrier located at a range of 30 to 40 feet from the loading source was modeled with the same parameters used above in equation 9, except a rise time to peak pressure (t_p) of .010 sec was used. The resulting δ was 2.4.

The velocity and acceleration histories in front of and behind the barrier are shown in figure VI-5. The early time motion is as expected from theoretical analysis except for slight pulse spreading due to artificial viscosity. The ratios of the average peak velocity and acceleration behind the barrier to the average peaks in front of the barrier are plotted in figure VI-4. The agreement with the theoretical values is very good. The small differences are due primarily to artificial viscosity.

The one-dimensional shock barrier analyses discussed above indicate that, although the concept is valid conceptually, it would be impractical to use them in large-scale simulation experiments.

3. ONE-DIMENSIONAL RELIEF TRENCH AND TRENCH SCREEN CALCULATIONS

Relief trenches are used behind a test area to reflect loading waves from the explosive source back into the test area, thereby altering frequency content and inducing multiple cycles of motion as the waves reflect between the free trench boundary and the crater and loosened material caused by the explosion. Shots 9 and 13 of the UNM DIHEST Enhancement program (ref. IV-3) and the DIP IIIA experiment (ref. IV-4), in which relief was provided by both open trenching and pseudo-trenching by a series of drilled holes, have been discussed in Section IV.

Trench screens in front of a test area are designed to reduce the motion in the region behind the trench. Experimental investigation of

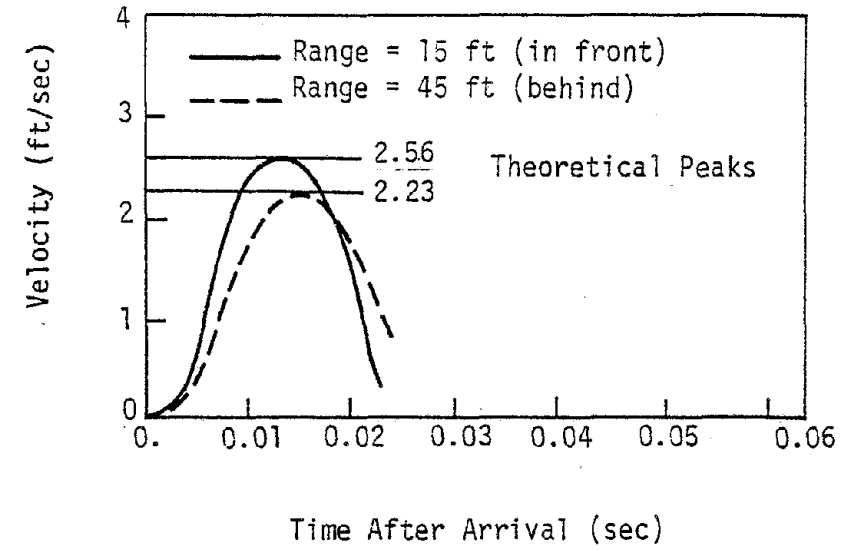

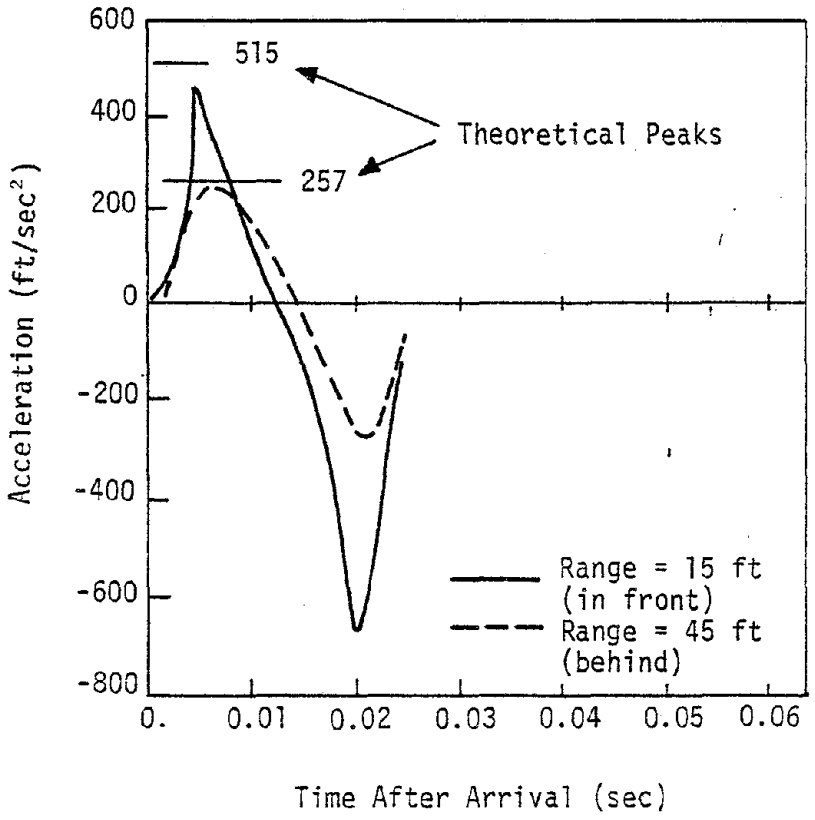

Figure VI-5. Early Time Waveform Comparisons In Front of and Behind Barrier From One-Dimensional Finite Difference Calculation

open trench screens has been primarily concerned with reducing Rayleigh wave displacements (ref. VI-5, VI-6). Bentonite slurry filled trenches have also been used (ref. VI-7).

The response of a one-dimensional soil column with boundary conditions approximating those of an open trench and of a trench backfilled with low density, highly compressible material are discussed in this paragraph. Calculations were performed using the finite element code HONDO (ref. VI-8). The objectives of the calculations were as follows:

a. To examine the effects of soil nonlinearity on the motions of the free-field and to provide a basis for comparison with the calculations involving trench relief.

b. To examine the effects of an open relief trench with the object of extending the duration of the ground motions.

c. To examine the effects of a compressible layer as a means of providing a screened zone beyond the trench, primarily with the object of reducing the particle accelerations.

d. To provide some basis for the design of two-dimensional numerical calculations.

The one-dimensional models used in the calculations are shown in figure VI-6. The applied pressure-time history is the same as discussed in Section V (fig. V-5).

The soil volumetric strain vs. mean stress corresponds to that of McCormick Ranch sand and is shown in figure VI-7. The soil failure surface, also corresponding to that of McCormick Ranch sand is also shown in figure VI-7. The dashed curves in each case are those used for the properties of the compressible backfill materials.

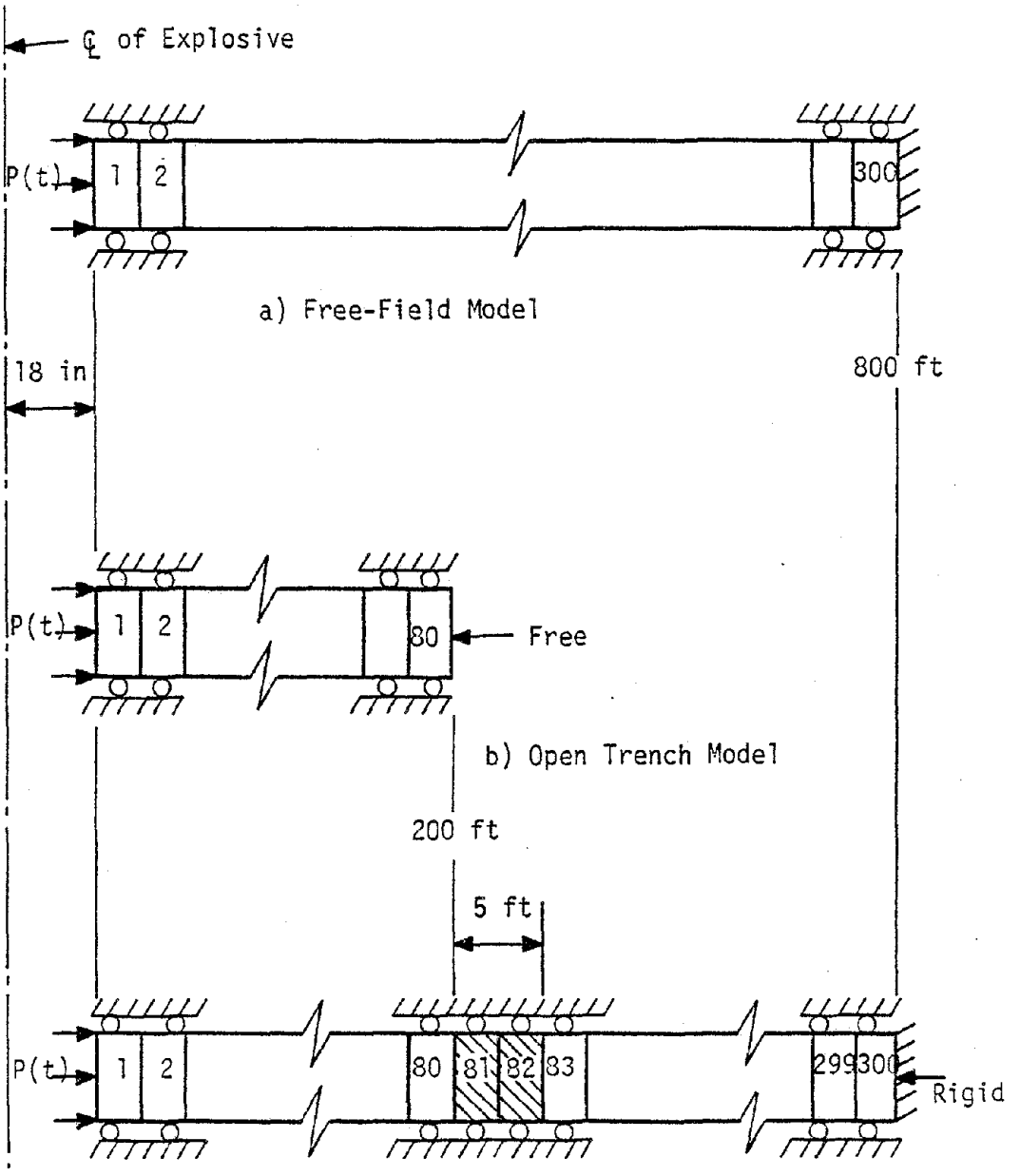

c) Psuedo-Trench Model

Figure VI-6. One-Dimensional Finite Element Models

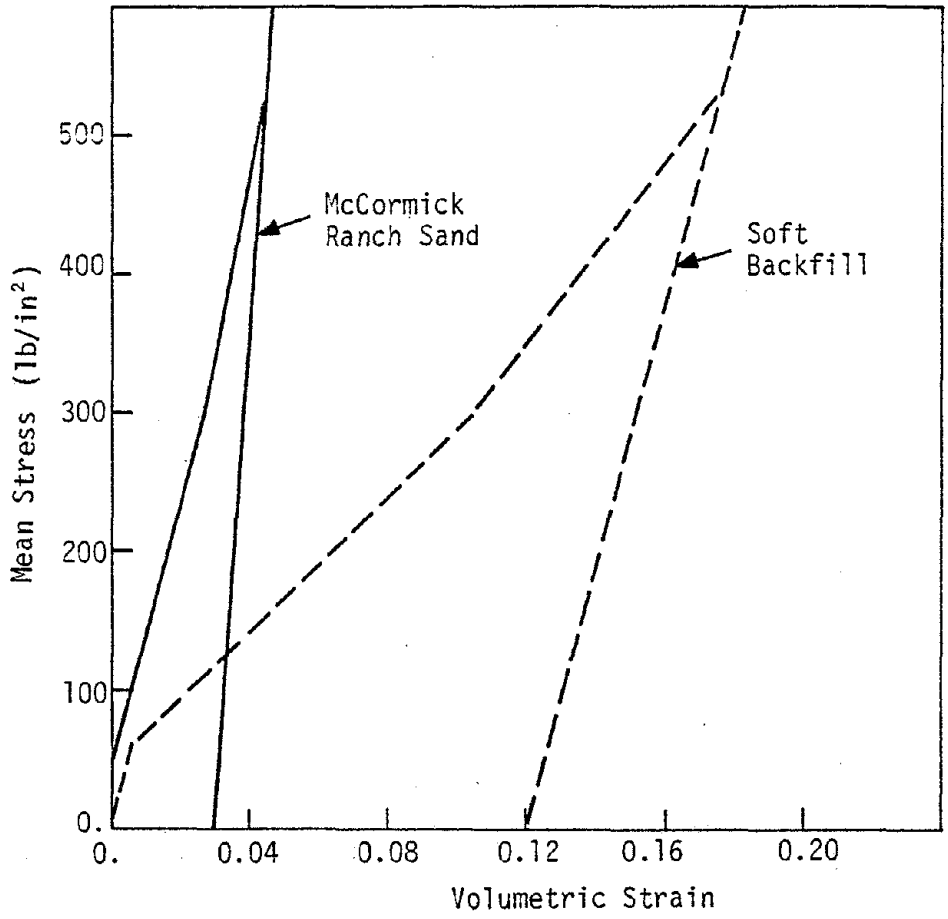

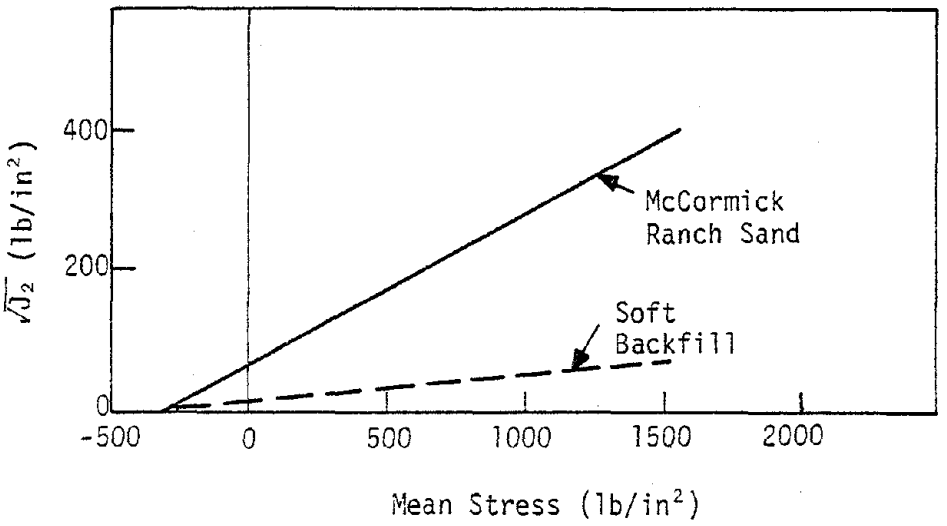

Figure VI-7. Soil Material Properties for One-Dimensional Psuedo-Trench Calculation

Attenuation of peak particle accelerations and velocities with range for each of the models is shown in figure VI-8. Particle accelerations, particle velocities and displacements of the relief models normalized with respect to the free-field motions are shown in figures VI-9. It can be seen that in the open trench model particle accelerations are decreased by approximately 20 percent at the trench boundary while the accelerations at ranges less than 150 feet correspond to those of the free-field. Particle velocities at the trench face are approximately 1.6 times the velocities of the free-field, while at ranges of less than 150 feet the velocities are approximately those of the free-field. Displacements at all ranges are greater than those of the free-field by factors of 1.8 to 2.9.

Examining the effects of a compressible backfill, it can be seen that accelerations at the face of the trench, and for a distance of approximately 50 feet ahead of the trench are greater than those of the free-field. Behind the trench, particle accelerations are lower than those of the free-field with a maximum reduction of 38 percent occurring at a range of 250 feet. Particle velocities are essentially those of the free-field except for increases of approximately 22 percent at ranges of 200 and 550 feet. Displacements are essentially those of the free-field at all ranges.

Velocity-time histories at points ahead of and behind the trench are shown in figure VI-10. It can be seen from the figure that the primary effects of the open trench are to increase the positive phase duration and to produce secondary peaks in velocity from reflections off the free boundary at the trench face. Smaller secondary peaks are produced by reflections off the face of the backfilled trench while the velocities away from these peaks are unaffected with no change in duration of the outward

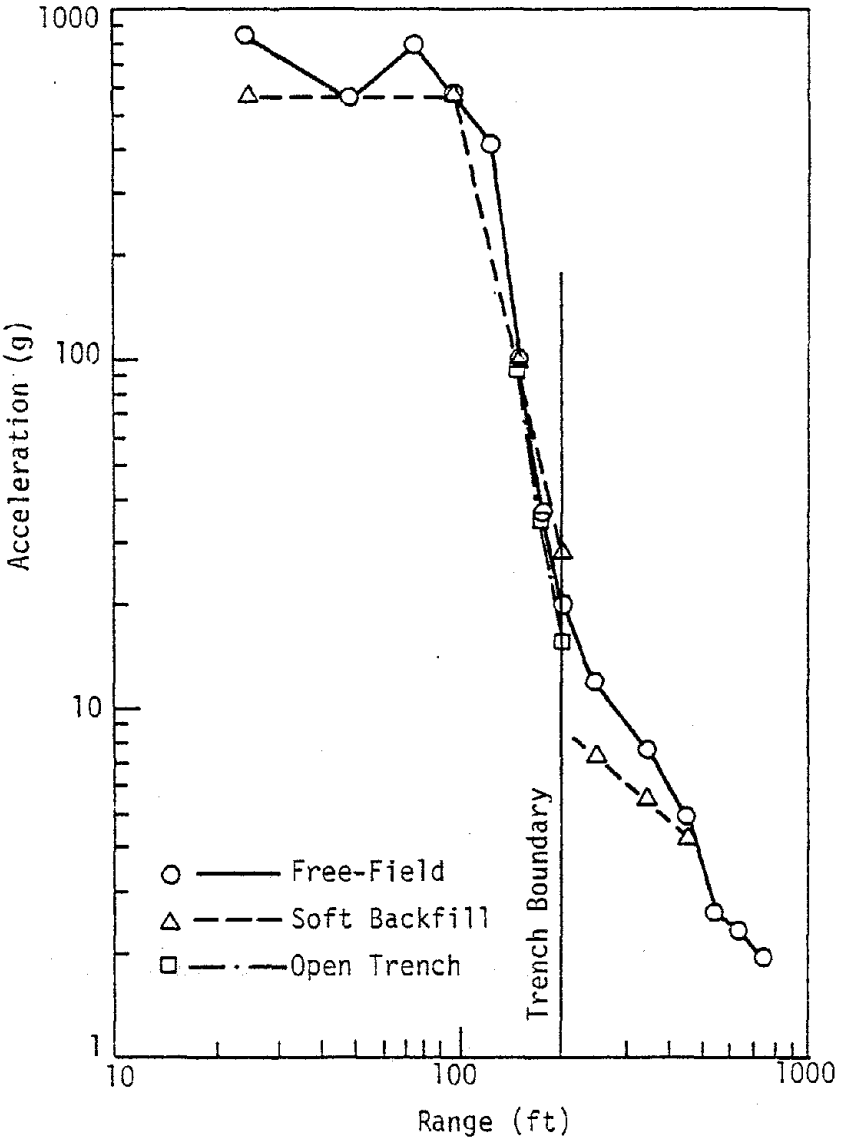

a) Peak Acceleration

Figure VI-8. Peak Particle Acceleration and Velocity from One-Dimensional Finite Element Calculations

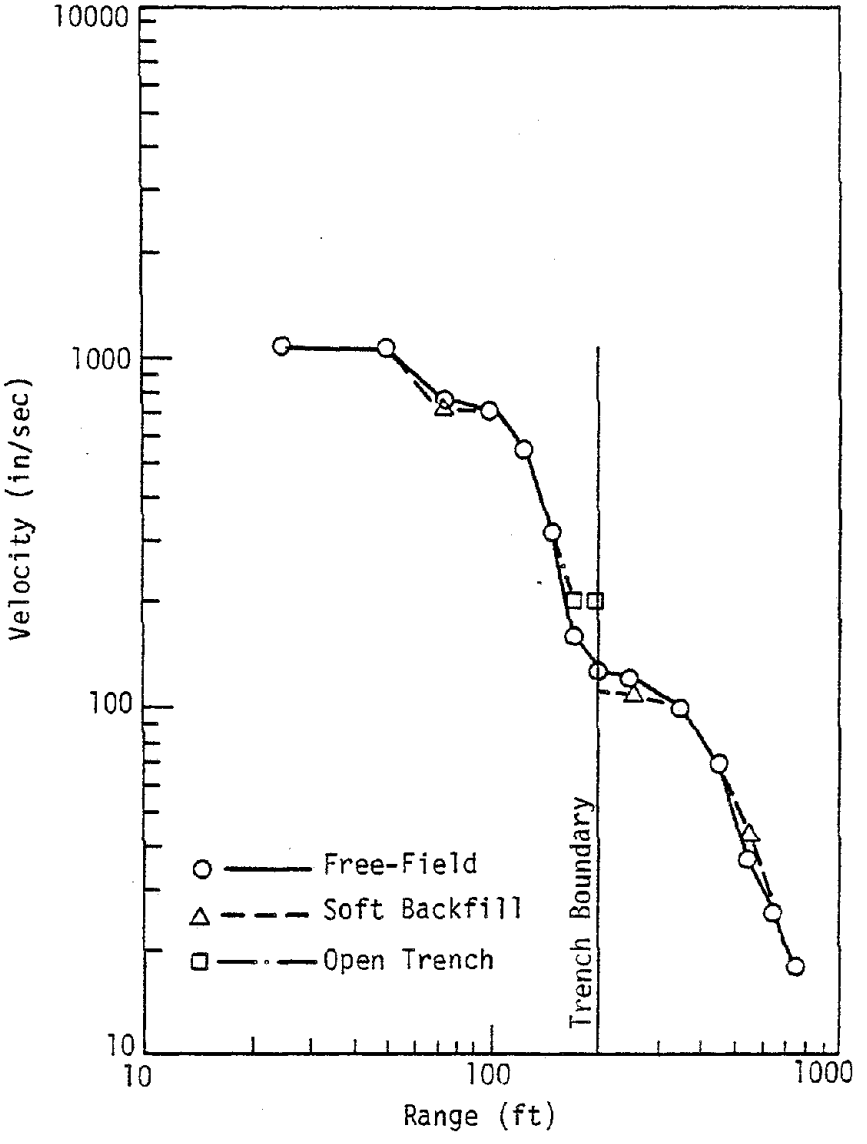

b) Peak Velocity

Figure VI-8 (cont.) Peak Particle Acceleration and Velocity from One-Dimensional Finite Element Calculations

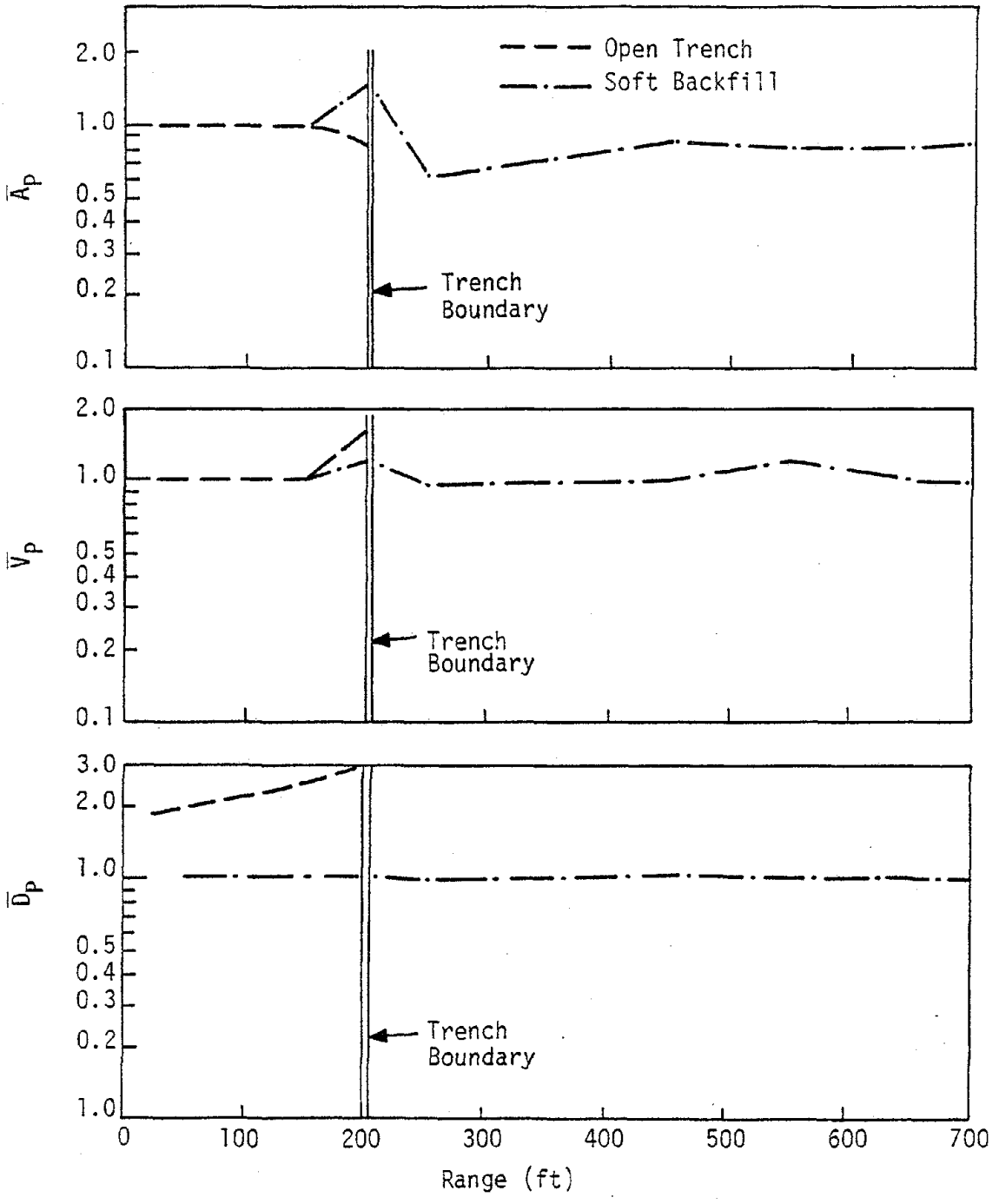

Figure VI-9. Normalized Peak Acceleration ($\bar{A}_p$), Velocity ($\bar{V}_p$), and Displacement ($\bar{D}_p$) for One-Dimensional Calculations

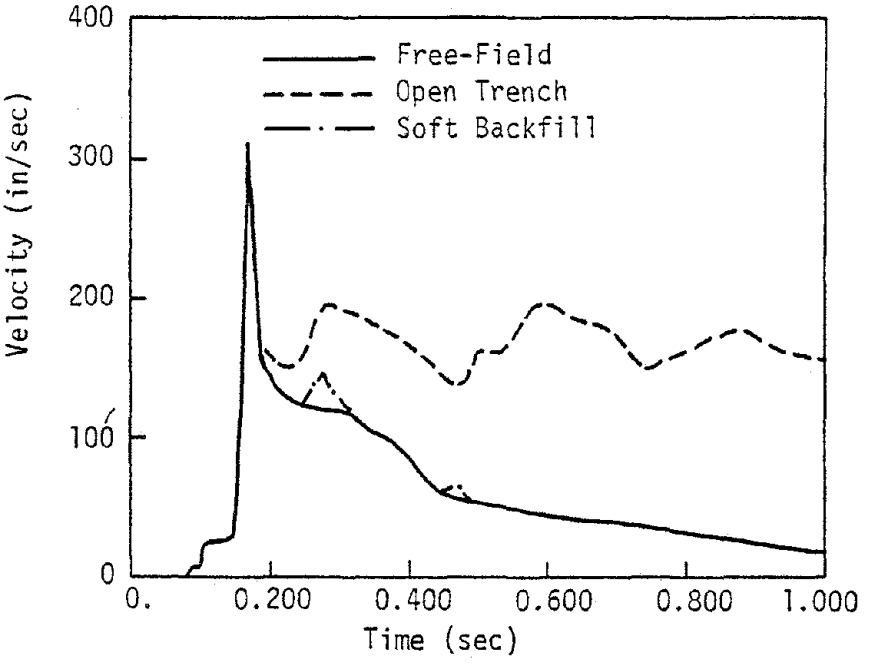

a) 150 ft Range

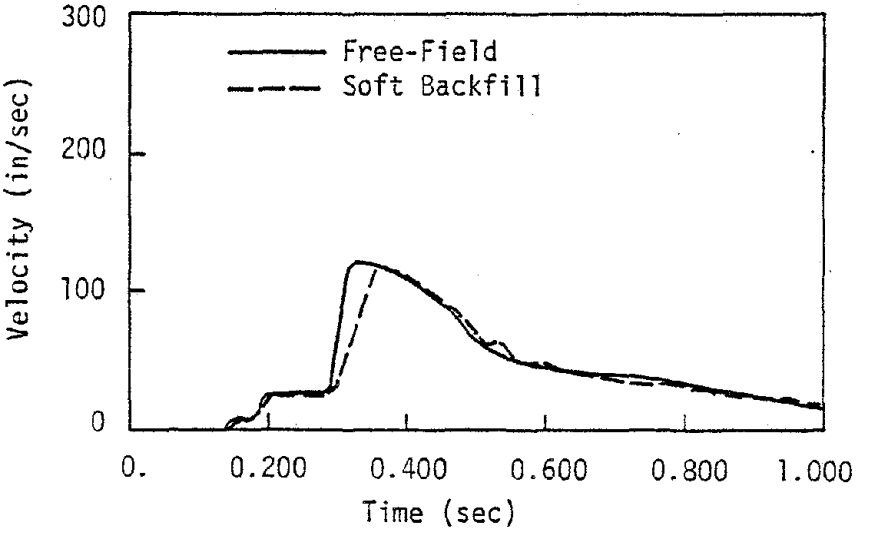

b) 250 ft Range

Figure VI-10. Representative Velocity History Comparisons for One-Dimensional Calculations

motion of the free-field. At a range of 250 feet the primary effect of the soft backfill is to increase the rise time in velocity resulting in a decrease in acceleration.

In the one-dimensional models the trenched region is assumed to extend infinitely in the second and third coordinate directions. The result of such a model should be expected to be an upper bound on the motions in a two-dimensional model where the dimensions of the trench in the plane of motion are finite. We might, therefore, expect somewhat smaller reductions in accelerations and velocities. However, we might expect the reductions in accelerations and velocities to maintain a similar ratio, i.e., velocities would be reduced to a lesser extent than corresponding accelerations.

4. TWO-DIMENSIONAL TRENCH CALCULATIONS

An open trench will eliminate the penetration of direct waves from near-surface explosive sources into the region beyond the trench. Motion in the region behind the trench is caused, in a general sense, by waves which diffuse into the region from the trench boundaries. These diffused waves are generated as the direct waves pass and interact with the boundaries. During the interaction, individual waves will produce a full range of wave types. An idealized view of the primary wavefronts generated by a planar compressional wave (P-wave) at a trench boundary is shown in figure VI-11. Since the P, S and SP waves all have different characteristics and wavespeeds, the energy contained in a single wave in the free-field will spread in time as the diffused waves enter the screened region. In addition, the amplitudes will attenuate geometrically. The spreading and attenuation would be expected to lower motion amplitudes behind the trench, as well as alter the frequency content and duration of the motion.

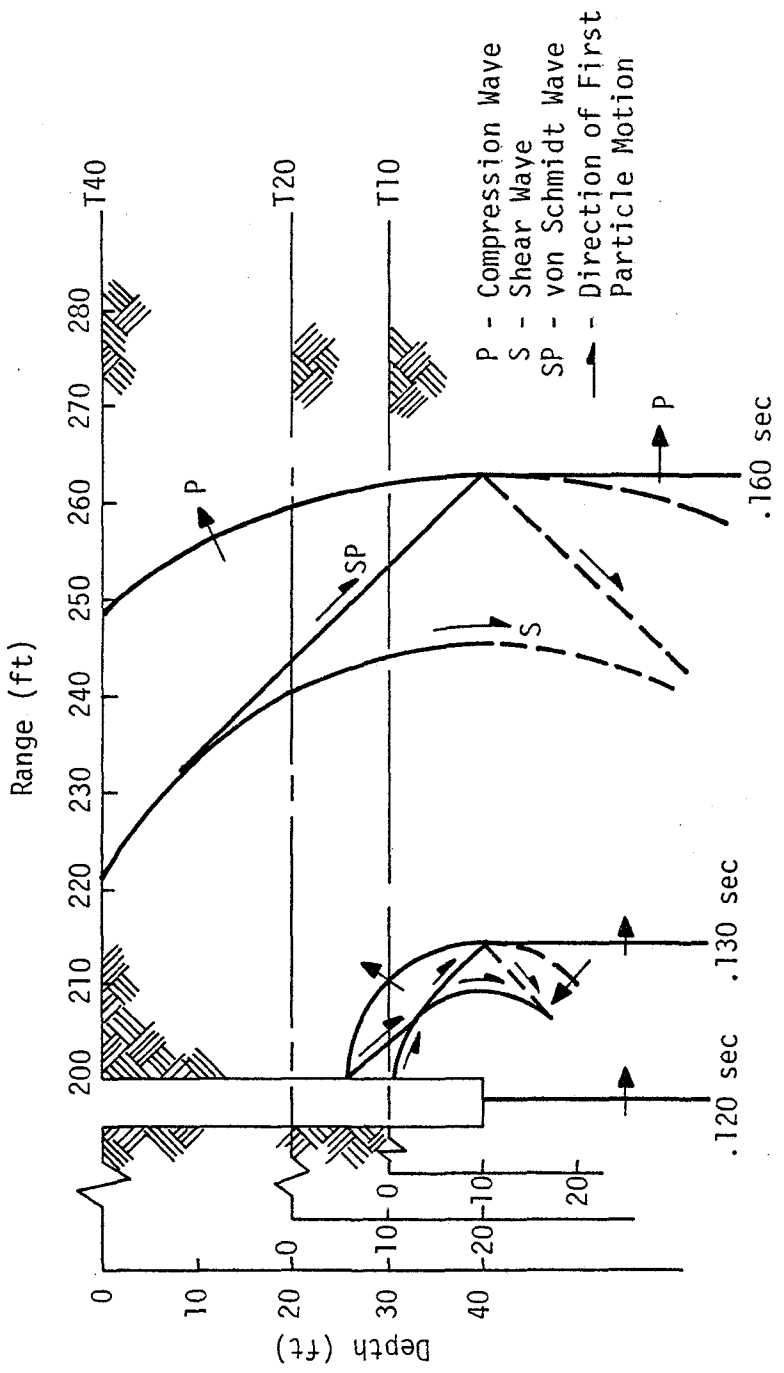

Figure VI-11. Idealized Primary Wavefronts Initiated at the Bottom of a Trench Assuming Planar Incident Wave

The amount of effect will be dependent on trench size since the amount of spreading and geometric attenuation is related to the location of the point of interest with respect to the trench boundaries.

Two-dimensional trench calculations were performed using TOODYII (ref. VI-9) to evaluate these two-dimensional effects, primarily screening effects. The baseline problem for free-field behavior without a trench is calculation 2P5 which was used in the analysis of free-surface effects in Section V. The explosive source was located from 20 to 60 feet in the ground. The assumed material model was for McCormick Ranch silty-sand. A code description and specific calculational values are discussed in detail in Section V.

Three calculations were performed in which the trench depth was 10 ft, 20 ft and 40 ft. These calculations are designated T10, T20, and T40. Each trench was five feet wide (one zone width) and located from 195 to 200 ft from the explosive source. The configurations of the three trench calculations are shown in figure VI-12. It can be seen in the figure that the 10-ft trench is completely above the explosive source, the 20-ft trench extends to the top of the explosive and the 40-ft trench extends to the mid-depth of the explosive.

Figure VI-13 shows vertical velocity histories for all calculations at three ranges (R), one in front of the trench (R = 150 ft) and two behind the trench (R = 220 and 250 ft); and at two depths (D) (the surface and 20 ft). Vertical velocity histories are generally not affected much in qualitative character by the wave interaction with the trench. In front of the trench there is a slight increase in downward motion (peak B) and late time upward motion (peak C) due to the reflections from the

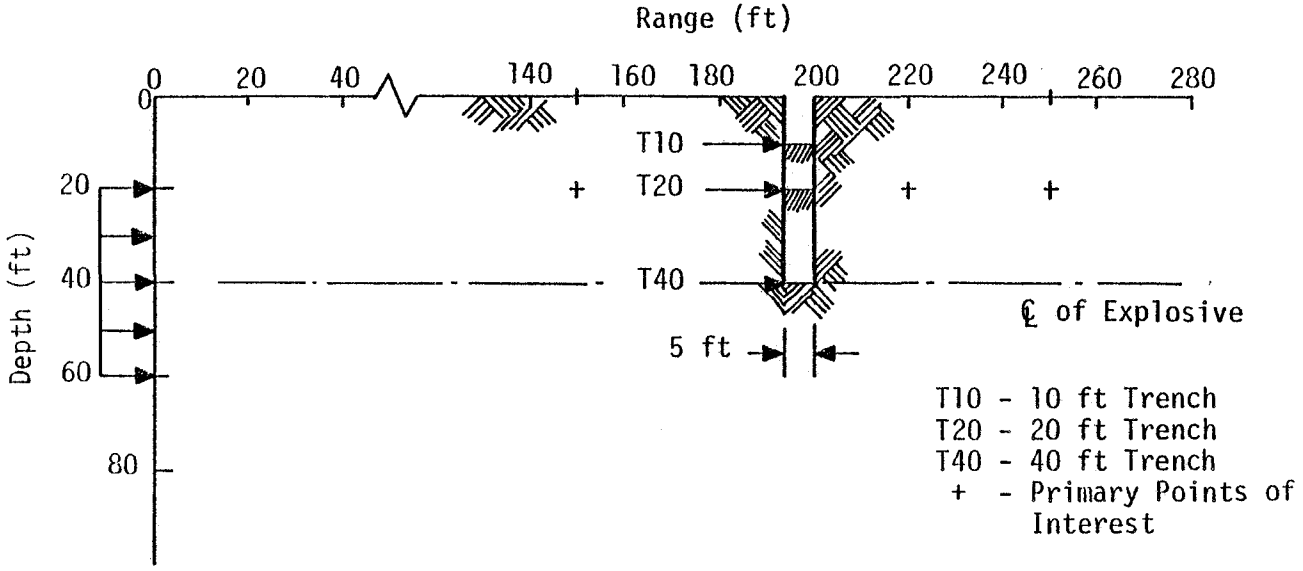

Figure VI-12. Trench Calculation Configurations

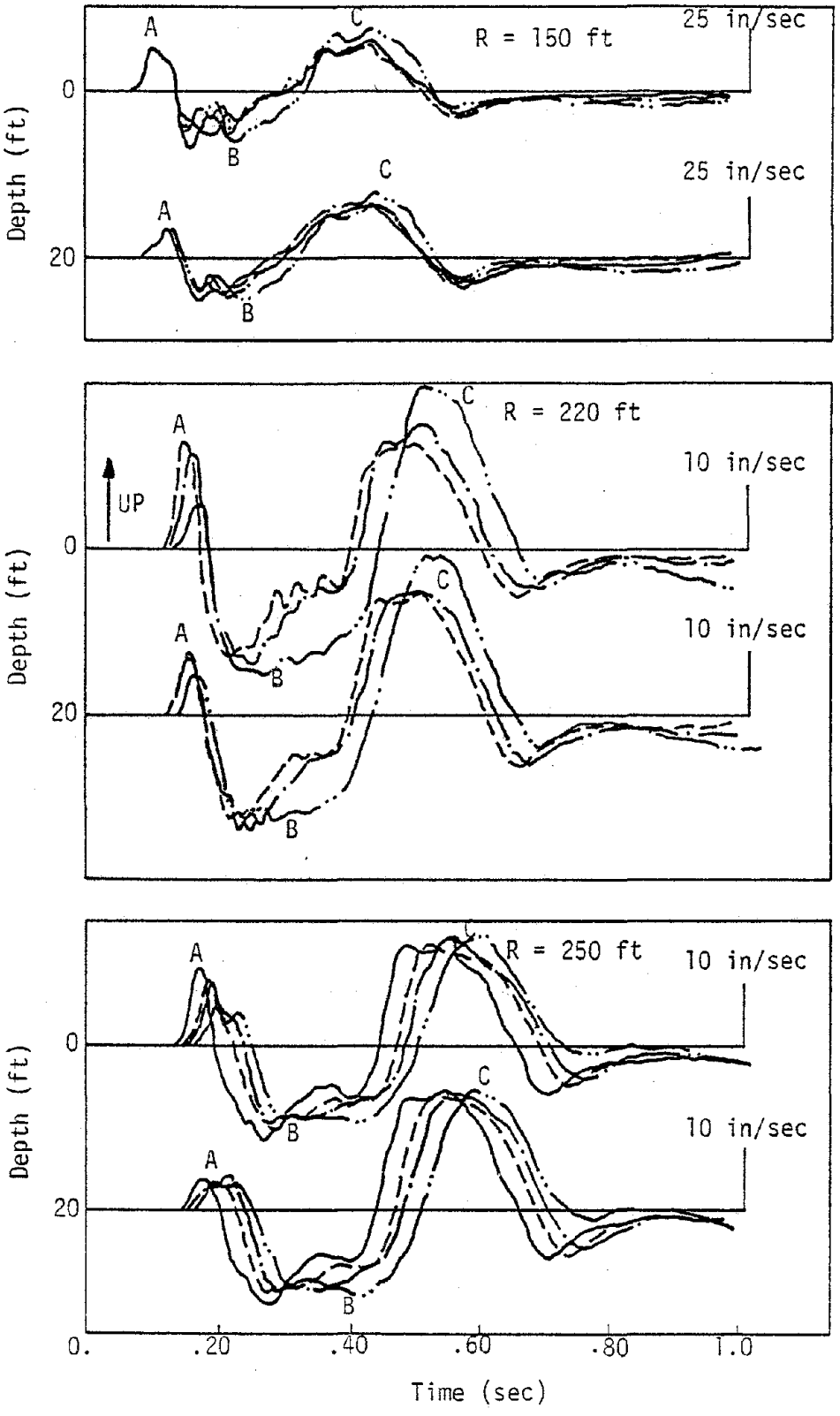

Figure VI-13. Vertical Velocity History Comparisons of Trench Screening Calculations

trench.

Behind the trench, the initial upward motion (peak A) decreases as the trench depth increases. The late downward motion (peak B) and peak upward motion (peak C) increases as the trench depth increases. In these cases, the largest percentage increases occur nearer to the trench (the 220-ft range). There is also a time shift in the vertical time histories behind the trench as a result of the longer times required for the ground motions to penetrate the screened region.

Horizontal velocity time histories are shown in figure VI-14 at the locations described above for the vertical histories. The horizontal components exhibit significant character changes with increasing trench depth. In front of the trench, the peak outward and inward amplitudes, and the outward pulse duration increases with increasing trench depth. This is due to relief reflections at the trench. This effect causes the relief trench enhancement in the region between the explosive source and the trench. A second cycle of motion due to later interaction of the reflected waves with the source is not exhibited, however. Hence, these calculations do not support relief trenches as a contributor to enhanced oscillatory motion.

On the other hand, the screening effect in the region behind the trenches is dramatic. The initial outward velocity, which is the peak outward velocity in the absence of a trench, exhibits a marked decrease with increasing trench depth. Peak outward acceleration decreases at an even greater rate. The character of the waveform also changes. In particular, the late time outward motion becomes more predominant with increasing trench depth. In the 40-ft trench calculation, the late time

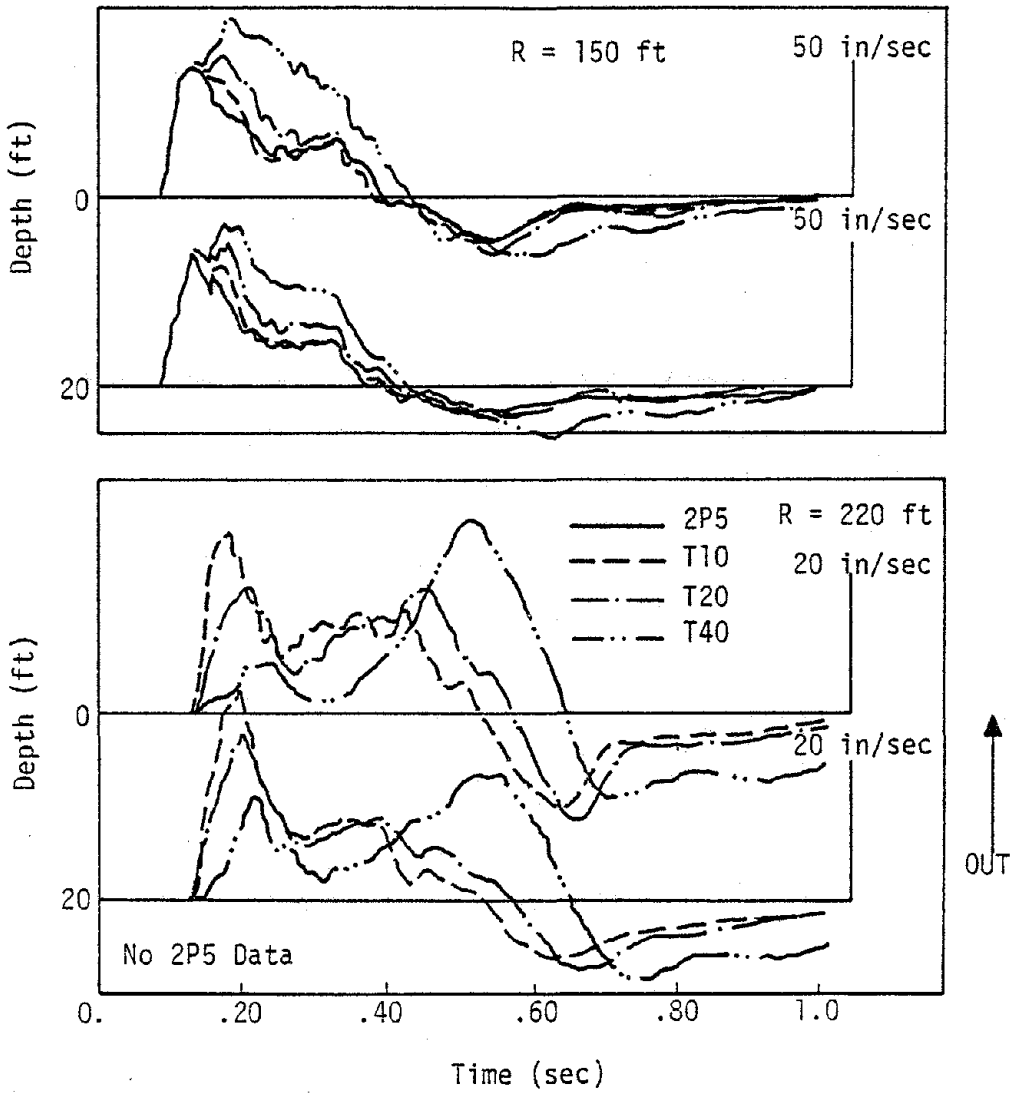

Figure VI-14. Horizontal Velocity History Comparisons of Trench Screening Calculations

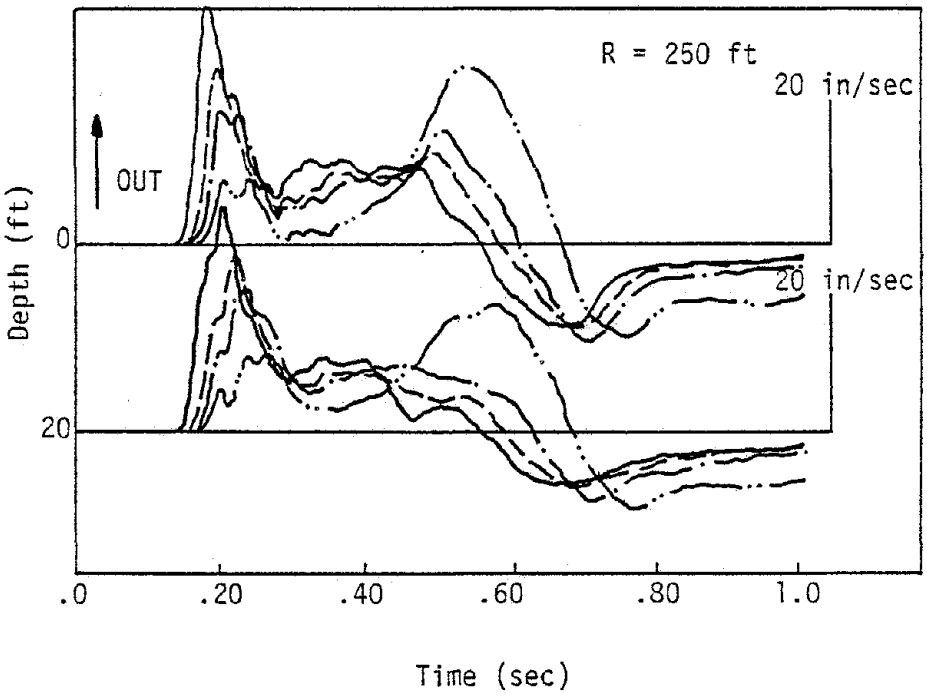

Figure VI-14 (cont.) Horizontal Velocity History Comparisons of Trench Screening Calculations

peak outward velocity reaches or exceeds the peak outward velocity in the 20-ft trench calculation. The peak velocity, however, never does reach the peak achieved in the untrenched calculation. The breakup of waves interacting with the trench boundary, especially the generation of shear waves with associated shear wave speeds, appears to cause the retardation of the large outward motion.

Peak horizontal acceleration, velocity and displacement versus range at the ground surface in the untrenched and trenched calculations are plotted in figures VI-15, VI-16 and VI-17. Peak horizontal acceleration in front of the trench is unaffected but there is a marked reduction behind the trench. At the 250-ft location the reduction ranges from about 45 percent for the 10-ft trench to 80 percent for the 40-ft trench.

Peak outward velocity (fig. VI-16) is also reduced but not as much as acceleration. The 10-ft trench reduction is only about 20 percent. The 40-ft trench behavior indicates the enhancement of the late time horizontal motion. The V_1 parameter is the initial outward velocity and it is reduced about 70 percent. The late time outward velocity, designated V_2, is only reduced about 30 percent.

Peak outward displacement (figure VI-17) in front of the trench is increased due to the free-surface reflection at the trench (i.e., an increased velocity and outward phase duration as previously discussed with respect to the waveforms). The peak displacements behind the trench are not affected however. It appears that, although the waveform character and velocity amplitudes change, the ultimate displacement achieved at the surface is unchanged by a trench.

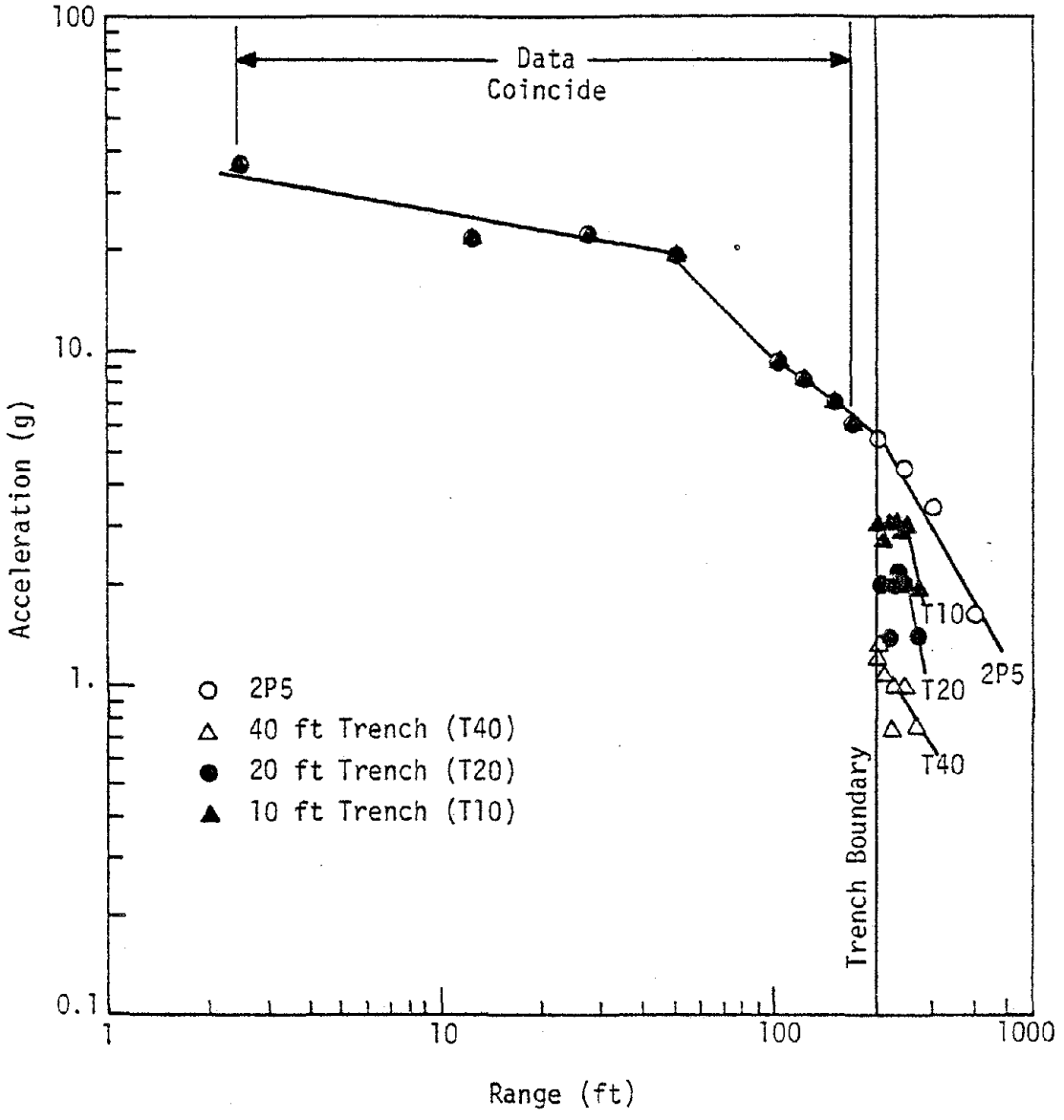

Figure VI-15. Effect of Trench Screening on Peak Outward Acceleration at Ground Surface

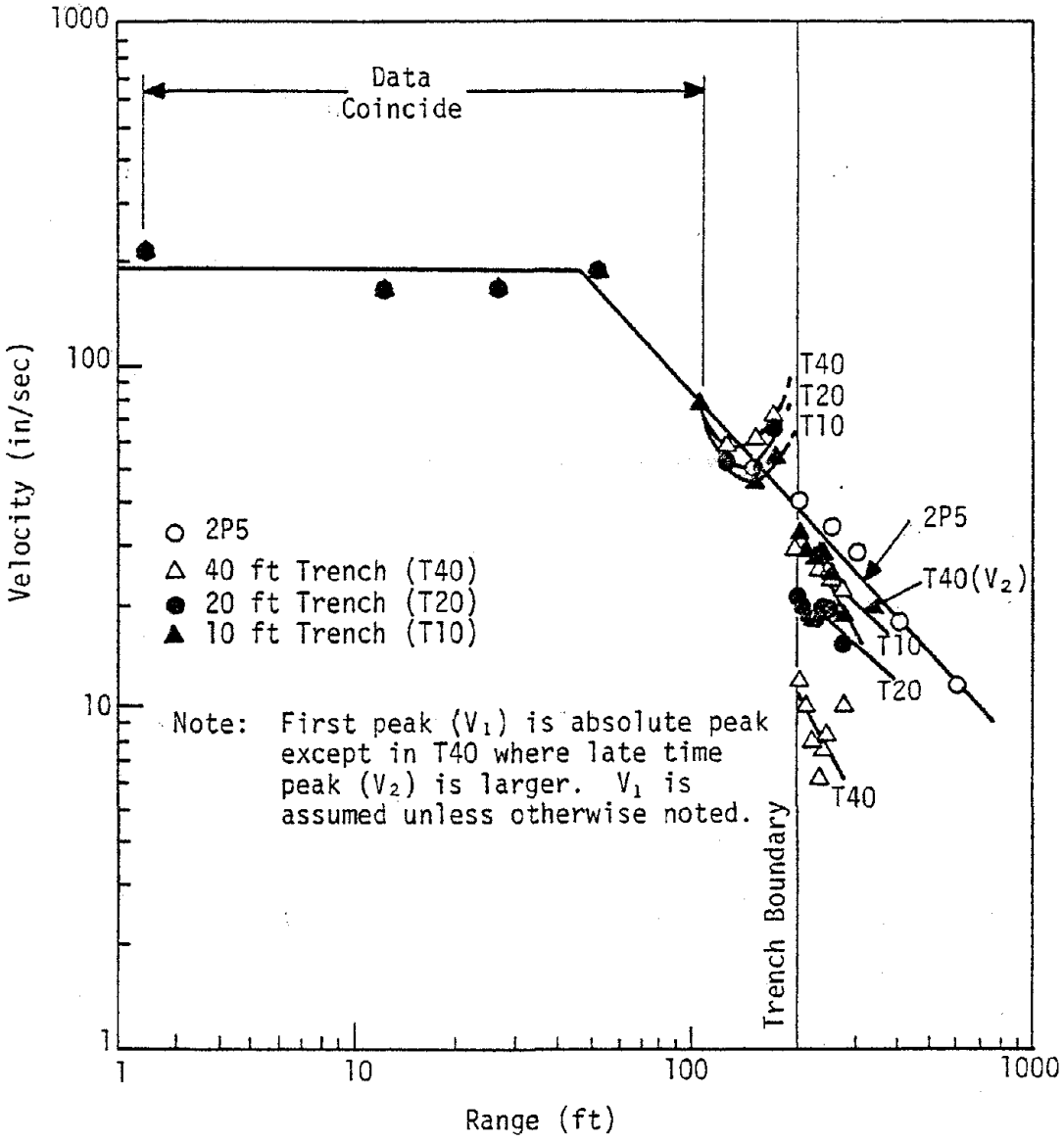

Figure VI-16. Effect of Trench Screening on Peak Outward Velocity at the Ground Surface

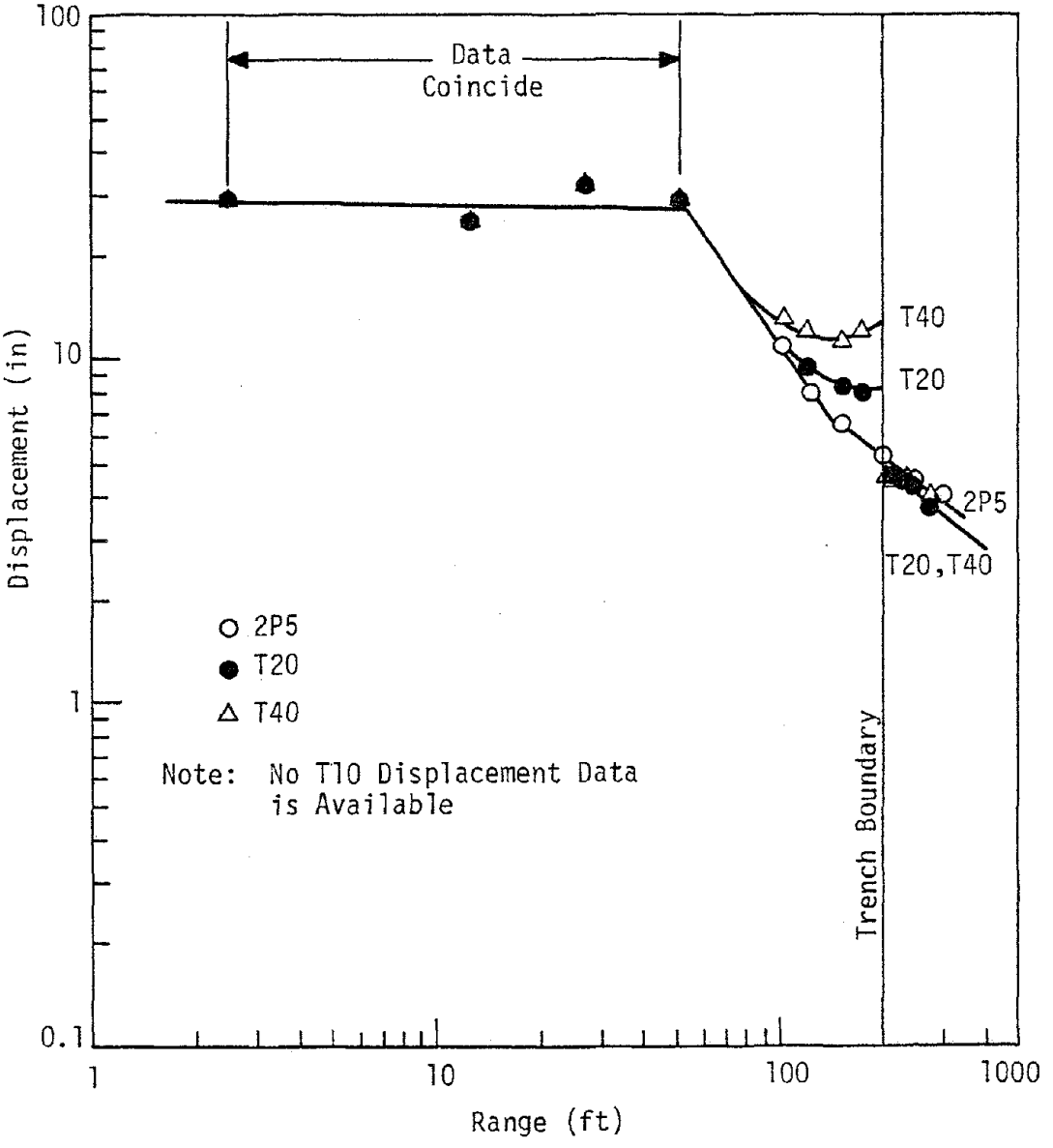

Figure VI-17. Effect of Trench Screening on Peak Outward Displacement at Ground Surface

The changes in peak horizontal acceleration and velocity evident in figures VI-15 and VI-16 were normalized by dividing the trenched amplitude by the corresponding amplitude at the same free-field location in the untrenched calculation. A normalized value of unity implies that the value of a component is the same as the free-field value in the absence of a trench. Normalized peak horizontal components were relatively constant over the range 0 to 50 feet behind the trench at a given depth and for a given trench height. They did vary with depth, however. Average normalized peak horizontal acceleration ($\overline{A}_H$) and velocity ($\overline{V}_H$) are shown as a function of depth in figure VI-18a. $\overline{A}_H$ is about 60, 40, and 20 percent of the free-field value at the surface for the 10-ft, 20-ft and 40-ft trenches, respectively. These values approach unity or the free-field value with depth then seem to decrease again. The decrease is suspect since it is expected that the amplitudes should continuously approach the untrenched conditions with increasing depth. The ratios are based on interpolated untrenched amplitudes in some cases. Interpolation errors may be the cause of the suspect trend.

The first peak outward velocity is shown as a solid line in figure VI-18b for the 10, 20 and 40-ft trenches. For the 10 and 20-ft cases this is also the absolute peak. The dashed line is the second and absolute peak for the 40-ft trench. The first and second peaks approach each other with depth in the 40-ft calculation. $\overline{V}_H$ is 75 percent, 50 percent and 25 percent the free-field value at the surface for the 10, 20 and 40-ft trenches, respectively. These values approach unity with depth. The second or absolute peak for the 40-ft trench shows a different trend. It is 80 percent the free-field value at the surface then decreases with depth.

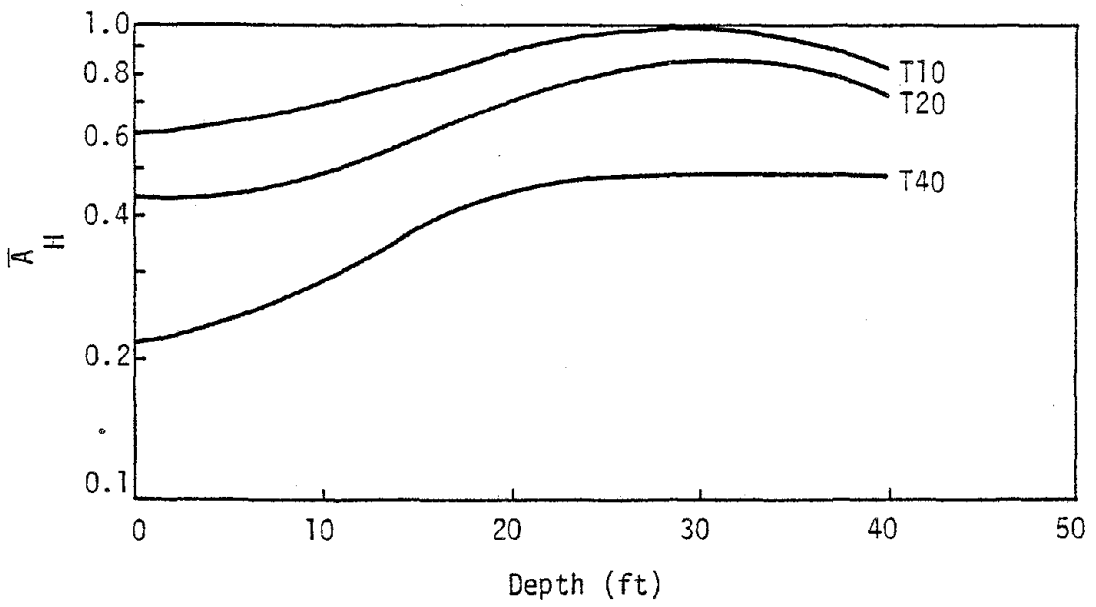

a) Normalized Peak Horizontal Acceleration ($\bar{A}_H$) Versus Depth in Region 50 ft Behind the Trench

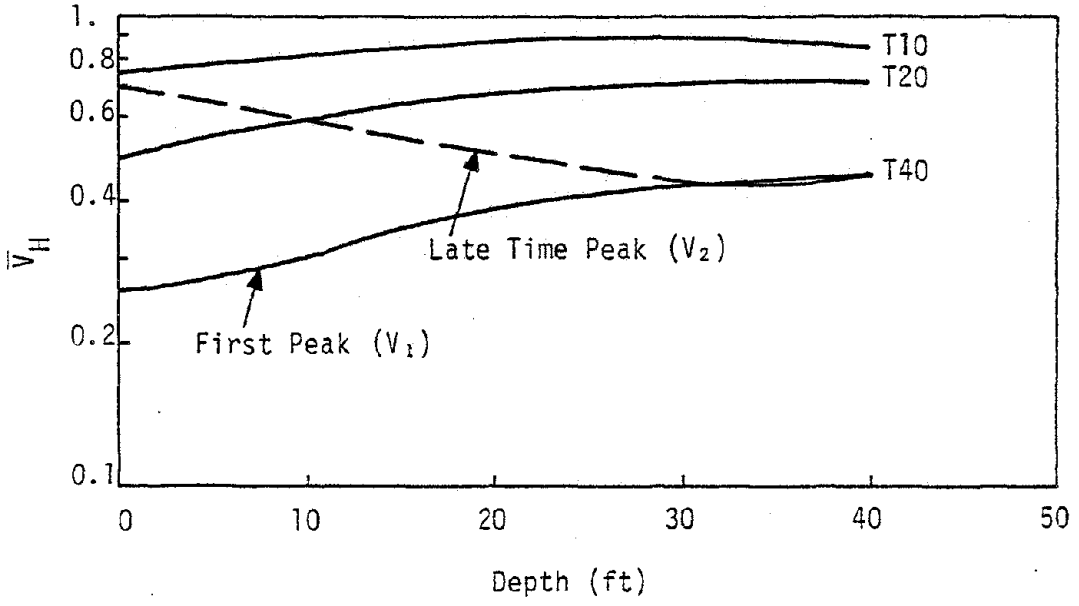

b) Normalized Peak Horizontal Velocity ($\bar{V}_H$) Versus Depth in the Region 50 ft Behind the Trench

Figure VI-18. Normalized Peak Horizontal Acceleration and Velocity in the Trench Calculations

Normalized peak vertical components are shown in figure VI-19. They were relatively constant with depth and varied slightly with range within a given trench calculation. Therefore, average normalized peak vertical acceleration ($\overline{A}_V$) and velocity ($\overline{V}_V$) are plotted as a function of distance behind the trench in figure VI-19. $\overline{A}_V$ is from 10 to 20 percent greater than the free-field value directly behind the trench where the initial P-wave from the bottom of the trench is propagating vertically. $\overline{A}_V$ then decreases to 90 percent, 80 percent and 60 percent the free-field value for the three trench calculations at 50 ft behind the trench. $\overline{V}_V$ for the 40-ft trench is 40 percent greater than the untrenched value directly behind the trench and approaches the free-field value with range. $\overline{V}_V$ for the 10 and 20-ft trenches is essentially unity or very near the free-field value at all ranges.

Attempts to collapse all of the trench results by normalizing range and depth by trench depth to obtain more general relationships were unsuccessful. Hence, the normalized peaks are plotted versus absolute range and depth.

The qualitative effects of trenching are obvious from the calculations, i.e., there is a marked decrease in acceleration, a lesser decrease in velocity and no change in displacement for the horizontal components. Vertical components are not affected as much. The phenomena, however, are quite complex. Additional calculations and new experimental work will be required to enable development of quantitative predictive relations for trench effect.

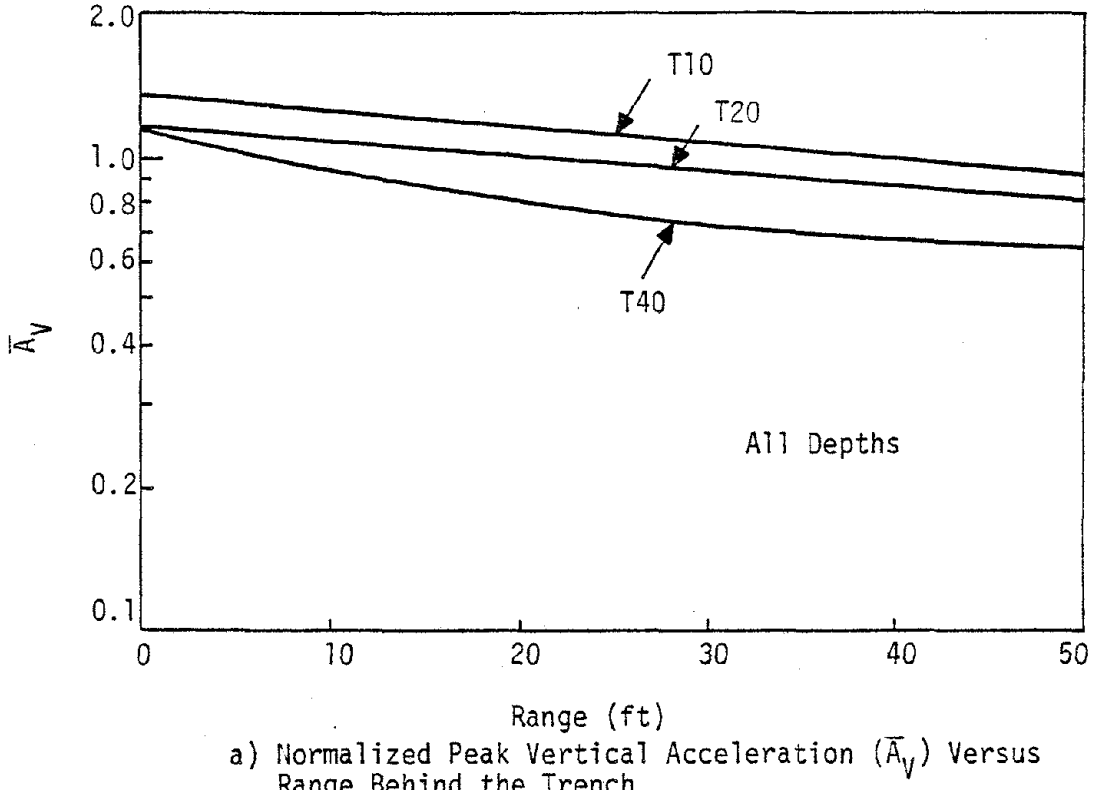

a) Normalized Peak Vertical Acceleration ($\bar{A}_V$) Versus Range Behind the Trench

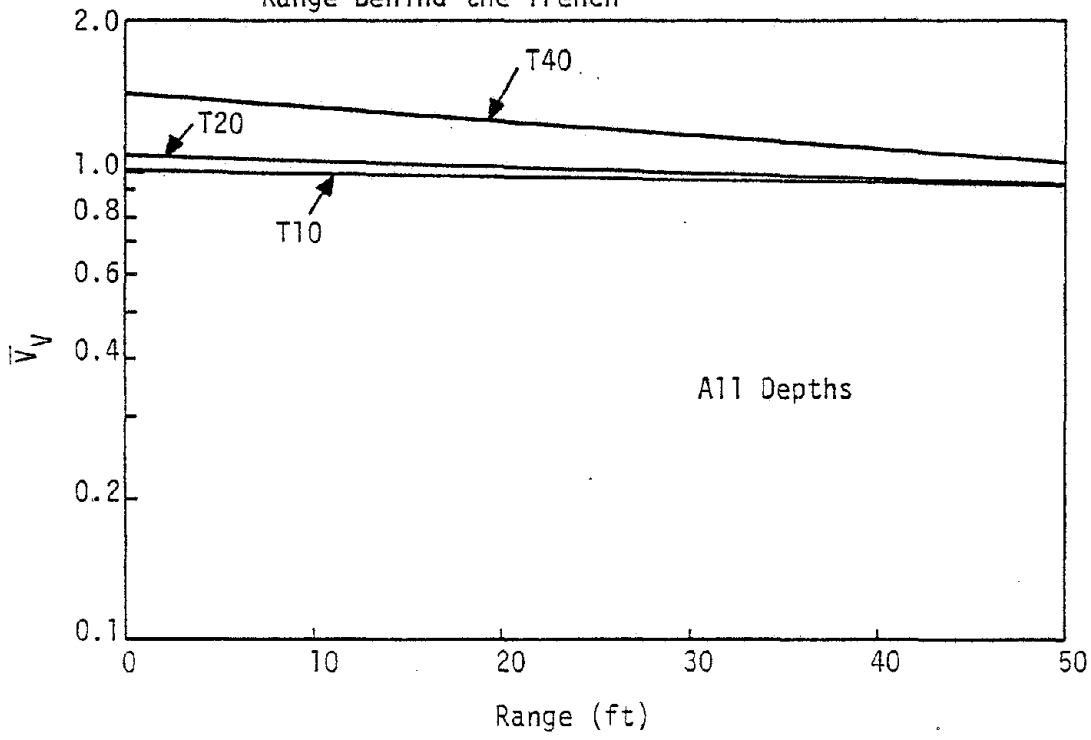

b) Normalized Peak Vertical Velocity ($\bar{V}_V$) Versus Range Behind the Trench

Figure VI-19. Normalized Peak Vertical Acceleration and Velocity in the Trench Calculations

5. CONCLUSIONS

Simple analytical methods and a limited number of numerical calculations were used to provide additional insight into the use of shock barriers and trenches as enhancement methods in earthquake ground motion simulation. The major conclusions are as follows:

a. The use of shock shields to reduce horizontal accelerations in large experiments appears to be impractical because of the large shield masses required. This result is due to the relatively long rise times which occur in the input ground motions. However, it may be practical in small scale experiments where small model structures are used.

b. The use of trenches as relief boundaries does not appear to induce additional motion cycles compared with the motion from a unenhanced explosion. This conclusion is evident from both one- and two-dimensional results.

c. The use of trenches or pseudo-trenches (in the form of closely spaced drill holes) to screen a region behind the trench appears to be a very practical method of reducing horizontal accelerations. Horizontal velocities are reduced to a lesser extent and displacements are unchanged. This trend is the desired trend for earthquake ground motion simulations. Further calculations and field experiments to quantify trench screening effects are strongly recommended.

6. REFERENCES

VI-1 Crawford, R.E., Higgins, C.J. and Bultman, E.H., The Air Force Manual for Design and Analysis of Hardened Structures, AFWL-TR-74-102, Air Force Weapons Laboratory, Kirtland AFB, New Mexico, October 1974.

VI-2 Lawrence, R.J. and Mason, D.S., WONDYIV - A Computer Program for One-dimensional Wave Propagation with Rezoning, SC-RR-71-0284,

Sandia Laboratories, Albuquerque, New Mexico, August 1971.

VI-3 Simmons, K.B., Soil DIHEST Motion Enhancement Techniques, AFWL-TR-72-233, Air Force Weapons Laboratory, Kirtland AFB, New Mexico, September 1973.

VI-4 Schlater, D.R., DIHEST Improvement Program Test DIP IIIA, Data Report, AFWL-TR-74-16, Air Force Weapons Laboratory, Kirtland AFB, New Mexico, April 1974.

VI-5 Woods, R.D. and Richard, F.E., "Screening of Elastic Surface Waves by Trenches," Proc. Int'l Symp. on Wave Propagation and Dynamic Properties of Earth Materials, Albuquerque, New Mexico, August 23-25, 1967, pp. 275-284.

VI-6 Richart, F.E., Jr., Hall, J.R., Jr. and Woods, R.D., Vibrations of Soils and Foundations, Prentice-Hall, Inc., 1970, pp. 244-262.

VI-7 Dolling, H.J., "Schwingungsisolierung von Bauwerken durch tiefe, aug geeignite Weise stabilisierte Schlitze," (Vibration Isolation of Building by Deep, Suitably Stabilized Slits), Sonderdruck aus VDI-Berichte 88, s. 3741, 1965.

VI-8 Key, S.W., HONDO-A Finite Element Computer Program for the Large Deformation Dynamic Response of Axisymmetric Solids, Sandia Laboratories Report No. SLA-74-0039, April 1974.

VI-9 Bertholf, L.D. and Benzky, S.E., TOODYII - A Computer Program for Two-Dimensional Wave Propagation, SC-RR-68-41, Sandia Laboratories, Albuquerque, New Mexico, November 1968.

SECTION VII
SYNTHESIS OF DATA AND CALCULATIONS

1. INTRODUCTION

The empirical analyses of Section IV resulted in interpretations of the ground motion environments from spherical, cylindrical and planar explosions, and empirical estimates of the relationships between the motion characteristics and the major explosion parameters. Several uncertainties remained at the end of the analyses, particularly with regard to scaling in inelastic material, attenuation rates in the various geometries, the effects of array size, and vertical response in the near-surface region. The calculations, presented in Sections V and VI, were designed to reduce these uncertainties.

Results from the two sources are synthesized in this section. For unenhanced experiments the relationships evident in the calculations are taken as fundamentally correct in form and in relative quantitative behavior for the material and geometries modeled. However, they may be different in their absolute quantitative behavior compared with the field data due to material model inadequacies, finite zoning, and explosive input assumptions. The main approach in this section is to empirically modify the relationships from the calculations so that they yield quantitative results comparable to those measured in the field. The resulting relations provide the basis for predicting future unenhanced simulation experiments in dry alluvial materials with a reasonable level of confidence.

Data on enhancement techniques are quite limited, and only a limited number of enhancement calculations were performed in this study. Although this information provides good insight into the qualitative effects and usefulness of the various techniques in simulation, the quantitative prediction of effects remains uncertain. Only tentative recommendations can be made in this section.

2. SPHERICAL RESULTS

The calculated spherical results demonstrated the applicability of $W^{\frac{1}{3}}$ scaling in inelastic materials in the absence of gravity. The relations for the motion parameters (eq. V-22) gave excellent attenuation rate agreement with the empirical relations for Mole (fig. IV-25), but the amplitudes in the calculations were higher than the Mole averages. Accelerations were about 90 percent higher, velocities about 50 percent higher and displacements about 175 percent higher. The accelerations and velocities were, however, within the Mole data scatter. The calculated velocity outward phase durations and peak to peak times (fig. V-17) agreed well with the Mole averages at near-radial positions (fig. VI-6). The differences between the Mole data and the calculations may lie in material property differences. The calculations utilized a seismic velocity of 1650 ft/sec while the Mole site seismic velocity was 2900 to 3000 ft/sec. Future analyses of this difference, should spherical charges be used in simulation, may lead to a synthesis of those results in terms of material properties. In the interim it is recommended that the Mole empirical relations, modified to account for gravity, be used for radial motion estimates in dry alluvial materials. These relations (eq. IV-35) are repeated below for convenience.

$$aW^{0.31} = 8150(R/W^{0.31})^{-3.3} \quad (a)$$

$$v = 142.5(R/W^{0.29})^{-2.6} \quad (b) \qquad \text{(VII-1)}$$

$$d/W^{0.28} = 4.32(R/W^{0.28})^{-2.4} \quad (c)$$

where

a = acceleration in g's

v = velocity in ft/sec

d = displacement in inches

W = charge weight in lbs of TNT

The velocity and acceleration relations should be used only to the range at which the velocity has decayed to a value corresponding to the elastic stress limit. This limit can be estimated to be about 100 lb/in^2 and equation IV-26 can be used to estimate the corresponding velocity. The elastic attenuation rate for acceleration and velocity can be taken as -1.6.

Characteristic time estimates can be made using the calculated results shown in figure V-25 since they are in agreement with Mole but do not contain the large data scatter of the field data. Figure IV-10 can be used to adjust these times for gravity effects.

3. CYLINDRICAL RESULTS

Figures VII-1, 2, and 3 compare predicted accelerations, velocities, and displacements, based upon the calculated results with the fits to the cylindrical motion data for Shots 6, 7, and 8 (figs. IV-15, 16 and 17). These shots had a scaled array height of 4.64 ft/(lb/ft)$^{\frac{1}{2}}$. The

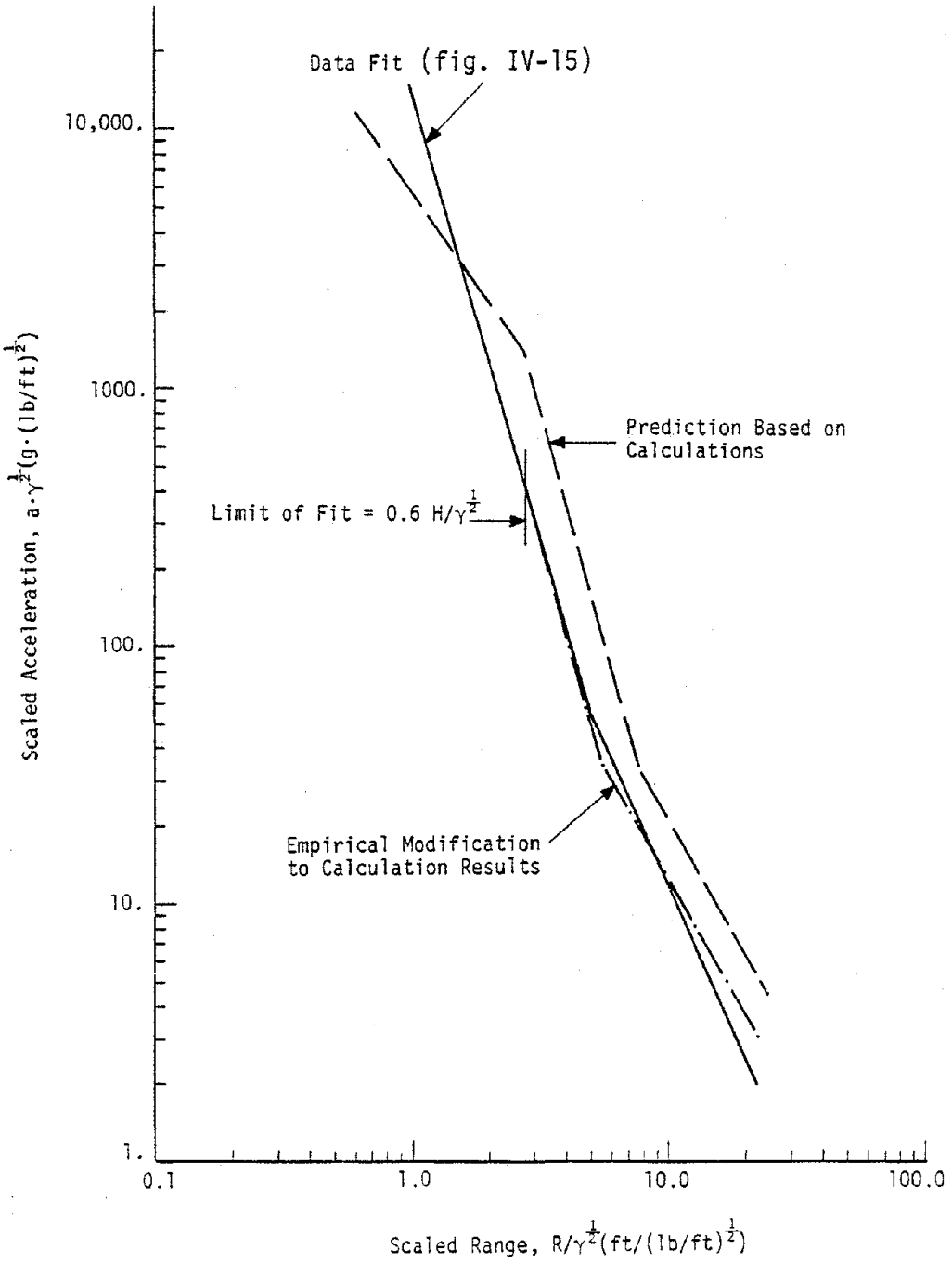

Figure VII-1. Cylindrical Accelerations Predicted from Calculations Compared with Data

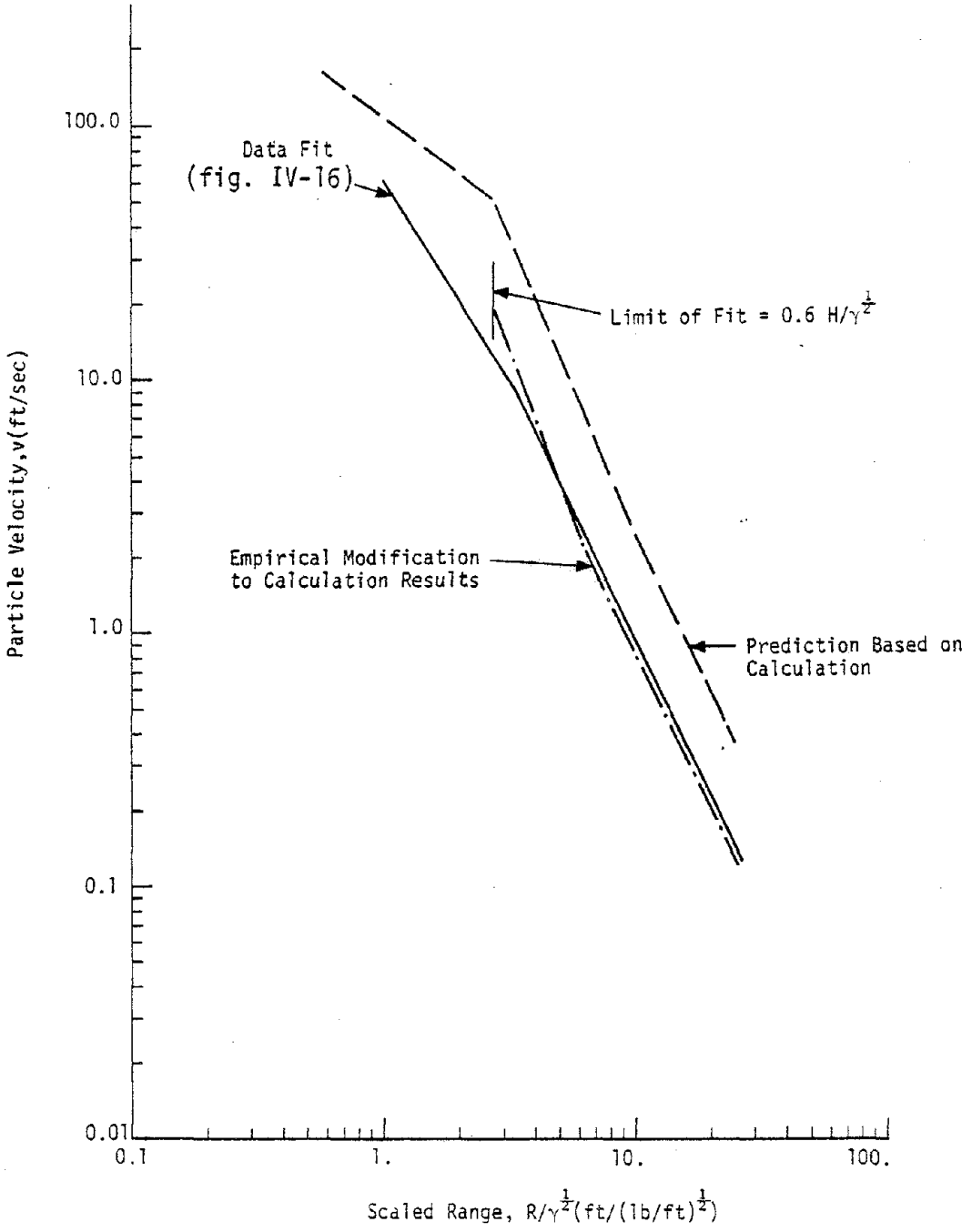

Figure VII-2. Cylindrical Velocities Predicted from Calculations Compared with Data

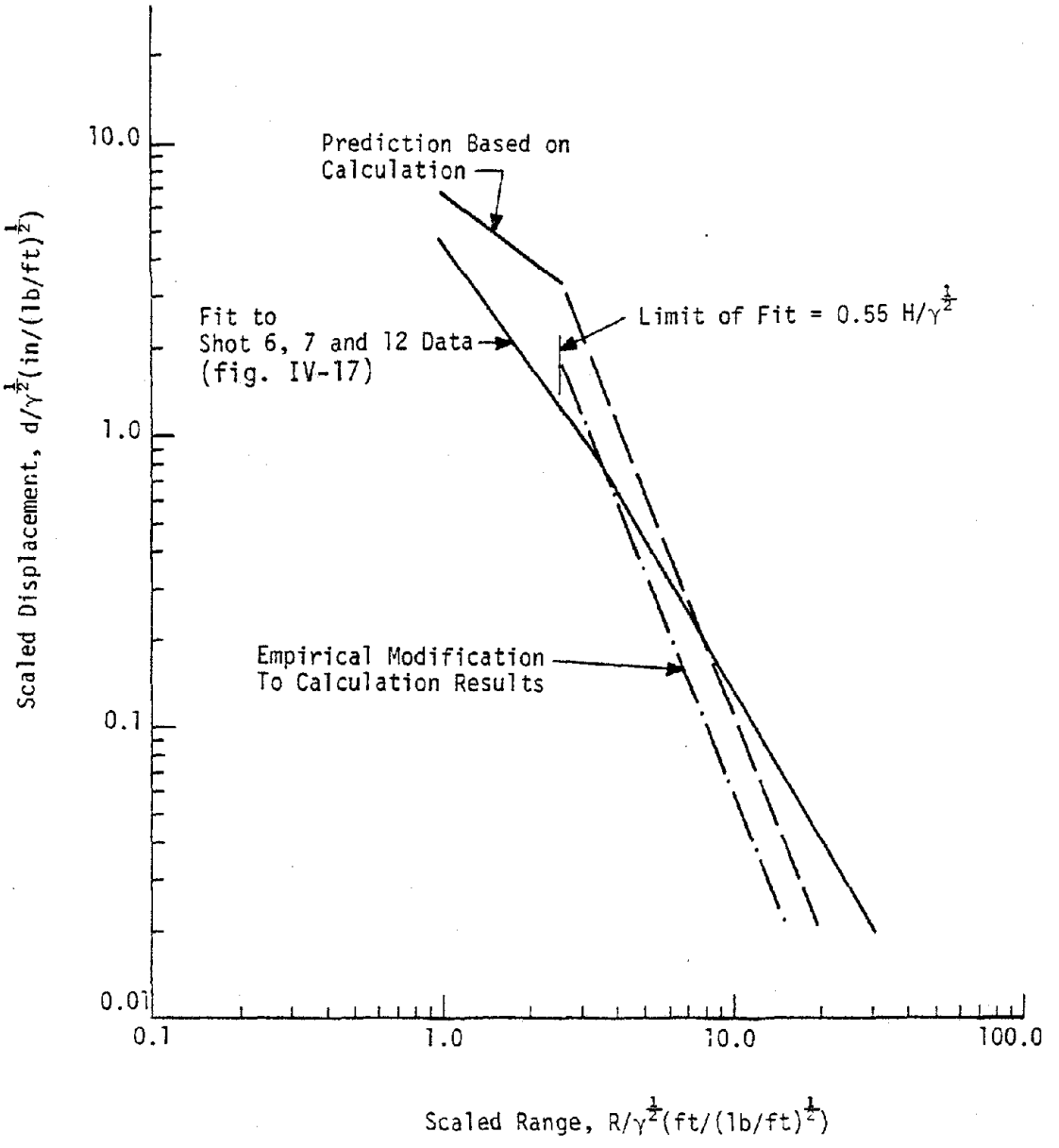

Figure VII-3. Cylindrical Displacements Predicted from Calculations Compared with Data

calculated accelerations and velocities in the near-region ($R/\gamma^{\frac{1}{2}}$ < about 3 ft/(lb/ft)$^{\frac{1}{2}}$) have a lower slope than the data. Beyond this region, however, the calculated results have attenuation rates in very good agreement with the data but the absolute amplitudes are high by a factor of 2.5. These differences are consistent with an in-situ material having a higher shear strength at high confining pressures than used in the model.

The calculated displacements have a different slope than the data over all ranges. Calculated amplitudes are higher at near ranges but lower at more distant ranges. The experimental displacement results are anomalous because the spherical and planar data, as well as the spherical, planar and cylindrical calculations, all indicate that the attenuation rate for displacements is just slightly less than that for velocities. The cylindrical data is at odds with this result. This difference may be due to velocity baseline errors which, in turn, significantly affect displacements. Baseline problems are evident in the original data.

Simulation applications will involve particle velocities below about 10 ft/sec. This velocity is in the intermediate region where velocity and acceleration results are in good agreement with the data in terms of attenuation behavior and the transition range from cylindrical to spherical behavior (0.6 $H/\gamma^{\frac{1}{2}}$ in calculations vs. 0.75 $H/\gamma^{\frac{1}{2}}$ in data). In this region and beyond, the calculation relations for acceleration and velocity can be empirically modified to give good agreement with the experimental results. The recommended relations are

$$a\cdot\gamma^{\frac{1}{2}} = 3000(H/\gamma^{\frac{1}{2}})^{1.1}\ (R/\gamma^{\frac{1}{2}})^{-3.6} \quad \text{for } R/\gamma^{\frac{1}{2}} > 0.6\ H/\gamma^{\frac{1}{2}} \quad \text{(a)} \qquad \text{(VII-2)}$$

$$v = 105(H/\gamma^{\frac{1}{2}})^{0.7}\ (R/\gamma^{\frac{1}{2}})^{-2.7} \quad \text{for } R/\gamma^{\frac{1}{2}} > 0.6\ H/\gamma^{\frac{1}{2}} \quad \text{(b)} \qquad \text{(VII-2)}$$

where

a = acceleration in g's

v = velocity in ft/sec

H = explosive height in feet

R = range in feet

γ = lineal charge density in lbs/ft

These equations apply to the range at which the elastic limit is reached. As in the spherical case, the elastic limit for radial stress can be taken as about 100 lb/in^2. Equation IV-26 can be used to estimate the corresponding particle velocity. Beyond the range corresponding to this velocity the attenuation rate should be decreased to -1.75 for both velocities and accelerations.

An empirical modification for displacement is somewhat uncertain because of the significant attenuation differences between the calculations and the data. Prior to attempting a modification, characteristic times are reviewed since peak displacement is related to the peak velocity and the velocity outward phase duration. In both the data and the calculations the duration was relatively constant with range to the elastic transition range, but the durations did vary with the array height. The variations of the average characteristic times with array height in the calculations are compared with the measured averages in figure VII-4. Although the data is scattered, the calculation results are significantly lower than the data. The differences are most likely due to material model inadequacies. Recommended empirical modifications for the

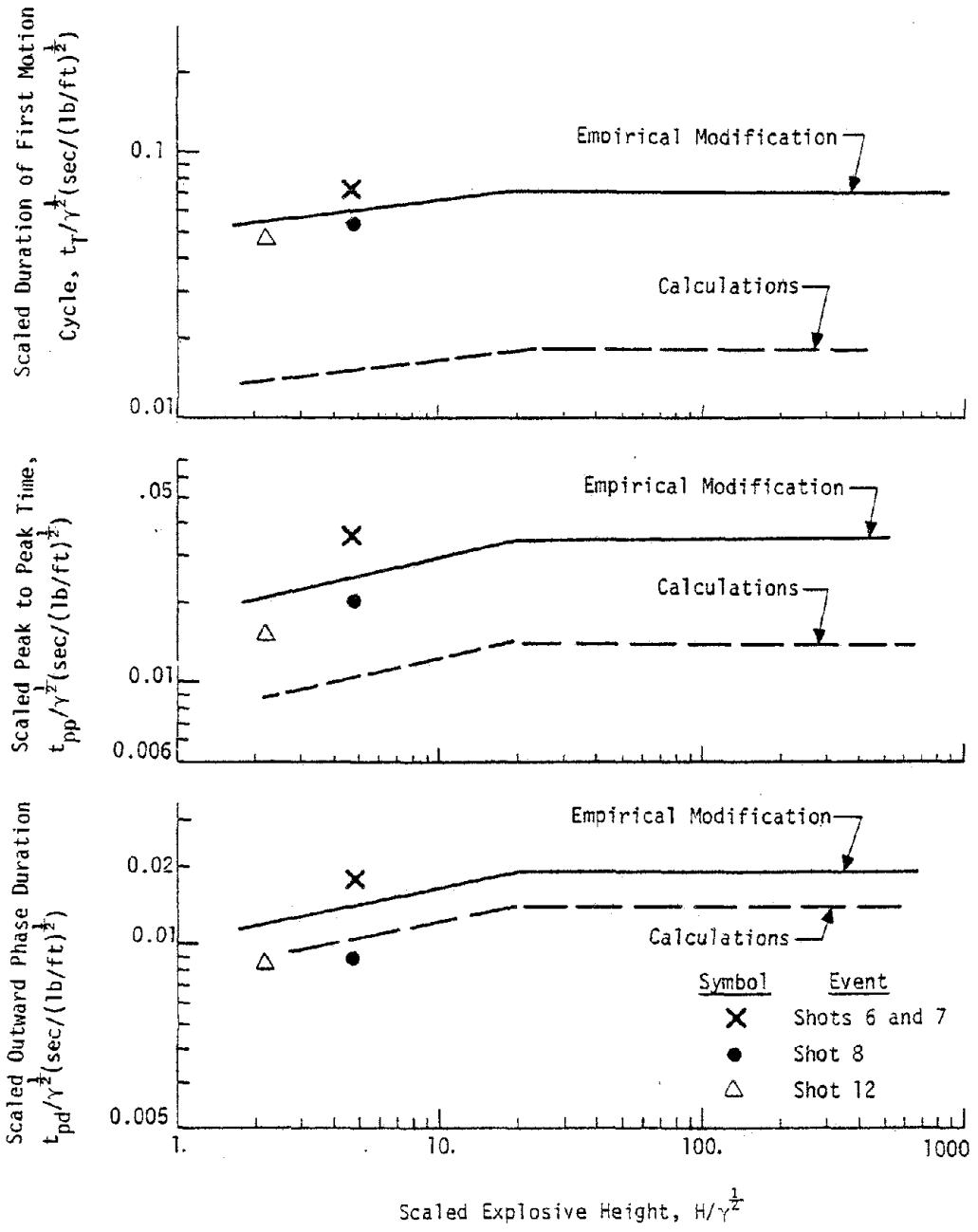

Figure VII-4. Cylindrical Characteristic Times from Calculations Compared with Data

characteristic times which pass through the data are shown as solid lines in figure VII-4.

The empirical modification for the scaled outward phase duration results in an increase of the calculated relationship of about a factor of 1.4. The empirical modification previously stated for particle velocities resulted in a decrease of calculated velocities of about a factor of 2.5. These two modifications imply a decrease of displacements by a factor of about 1.8. The calculated displacement relation modified by this factor is shown in figure VII-3. It is in good agreement with the data at the nearer ranges but is lower at greater ranges. At the present time, the modified calculation fit is recommended. This recommendation is based upon the consistency of the velocity and displacement attenuation slopes in spherical and planar data as well as a suspicion that there are some baseline trend problems in the cylindrical displacement data. The recommended relation for displacements beyond the transition range is

$$d/\gamma^{\frac{1}{2}} = 6.6\ (H/\gamma^{\frac{1}{2}})^{0.8}\ (R/\gamma^{\frac{1}{2}})^{-2.5} \quad \text{for } R/\gamma^{\frac{1}{2}} > 0.55\ R/\gamma^{\frac{1}{2}} \qquad \text{(VII-3)}$$

where d = displacement in inches and the other variables are defined as in equation VII-2.

Figure VII-5 compares the ratios of the peak inward to peak outward velocities in the calculations with those of the data. The comparison indicates that the inward components in the calculations are higher than in the data. This ratio appears to be strongly dependent on the material behavior, as indicated in figure V-35. The difference here is apparently due to some inadequacy in the calculation material model.

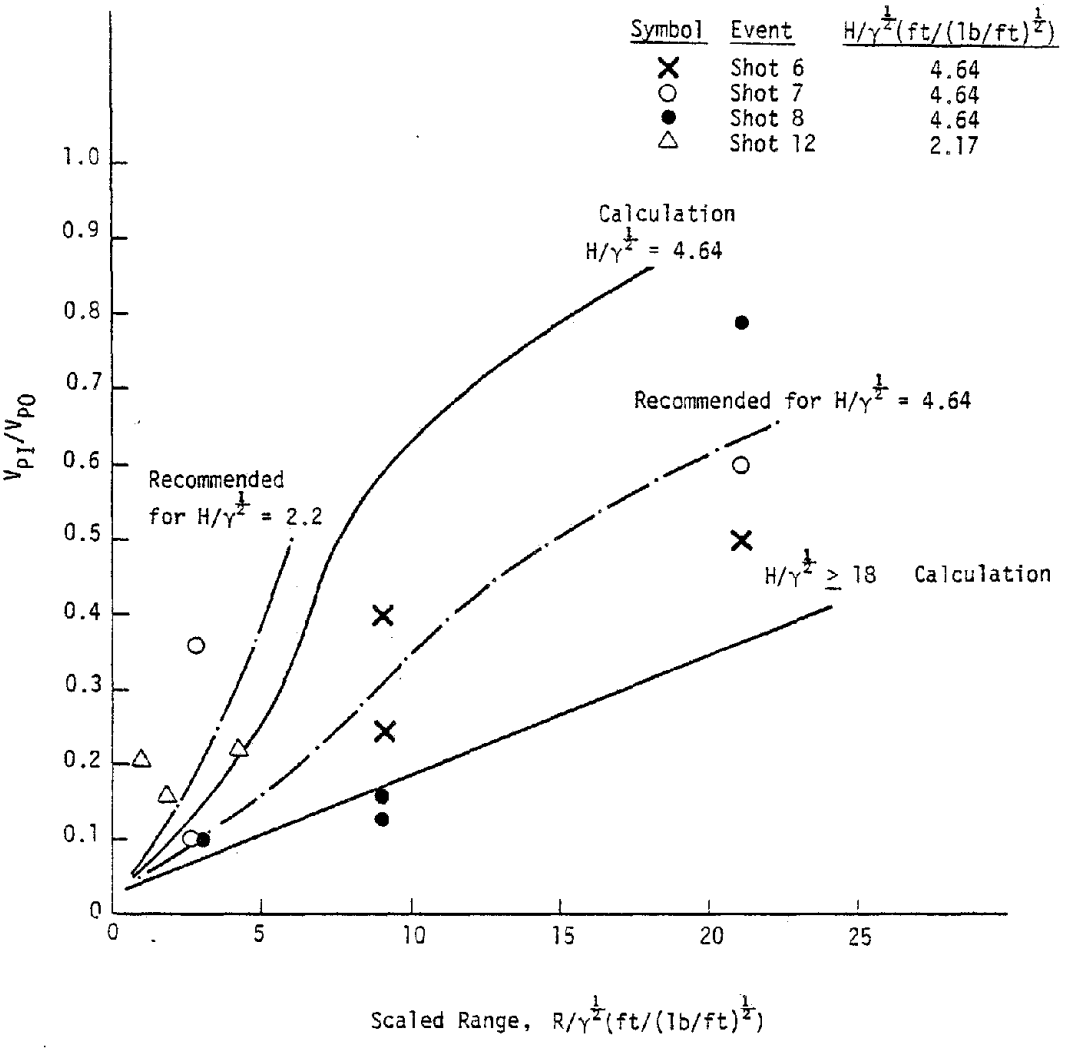

Figure VII-5. Calculated Ratios of Peak Inward to Peak Outward Velocity in Cylindrical Geometry Compared with Data

Recommended fits for the two array height cases for which data are available are shown in figure VII-5. There are insufficient data available to generalize these fits, but the fits given and the trends evident in the calculation results can provide a guide for estimating inward motion components.

There are no cylindrical data available for evaluation of off-center and free-surface effects. The normalized fits to the calculated results shown previously in figures V-44 through V-47 for off-center variations under symmetric conditions, and figures V-50 through V-53 under free-surface conditions are recommended at the current time.

4. PLANAR RESULTS

Planar results on the centerline are evaluated by comparing predictions based on the planar calculations with the measured data from DIP IIA and Mini-SIMQUAKE (MSQ). These events contain good data and span a wide range of areal charge densities and scaled array heights. DIP IIA had a charge density of 15.11 lb/ft^2, while the charge densities for the MSQ back and front arrays were 0.78 and 0.29 lbs/ft^2, respectively. All charge densities are in equivalent TNT. The scaled array heights for these events are 2.32, 19.2 and 51.7 $ft/(lb/ft^2)$, respectively.

Figures VII-6, 7 and 8 compare predicted centerline accelerations, velocities and displacements using equation V-29 with the measured data. The predictions for accelerations are higher than the data by a factor of about 1.5 for DIP IIA and MSQ-F, and by a factor of about 3 for MSQ-B. The predictions for velocity are high by a factor of about 1.8

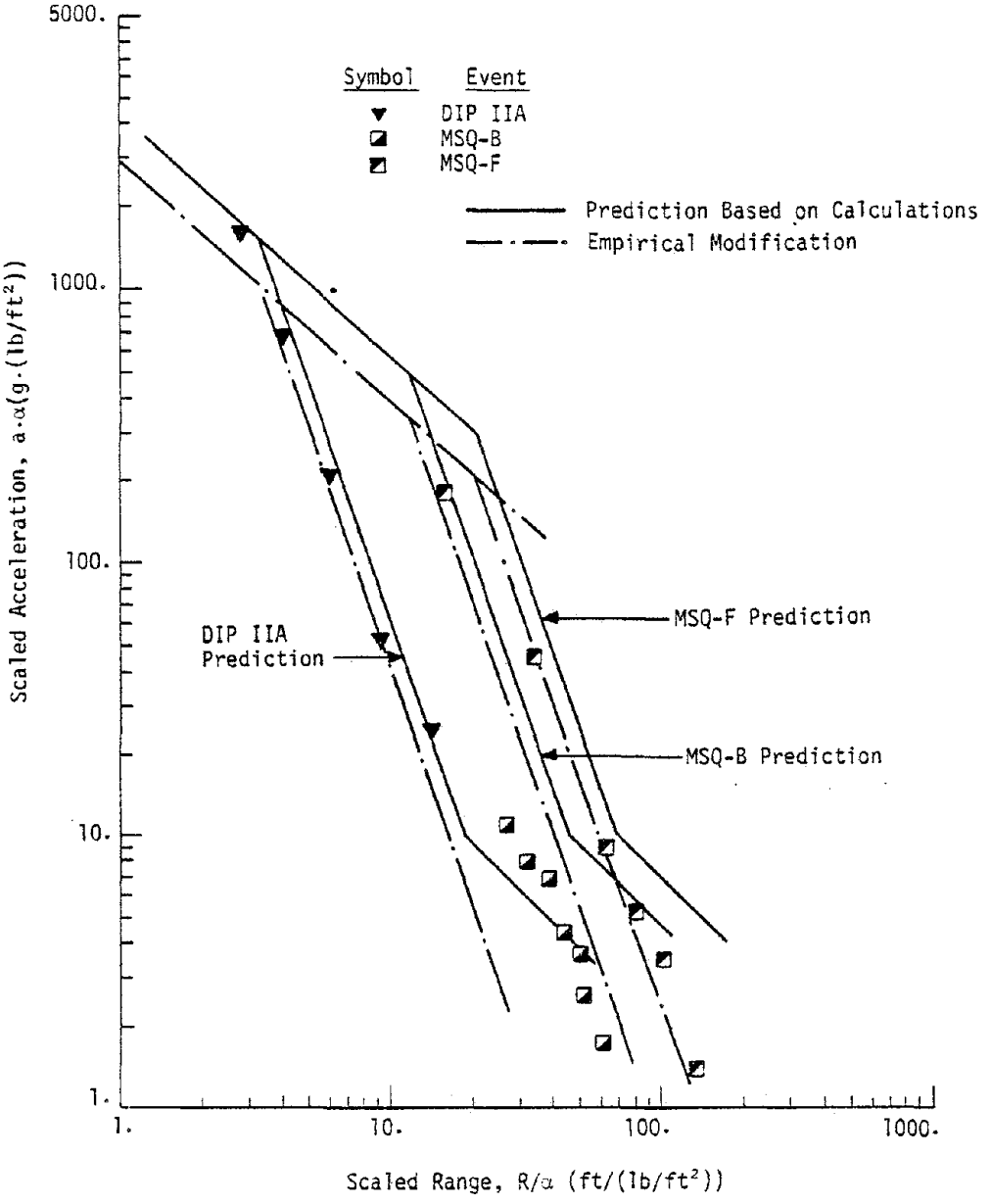

Figure VII-6. Planar Accelerations Predicted from Calculations Compared with Data

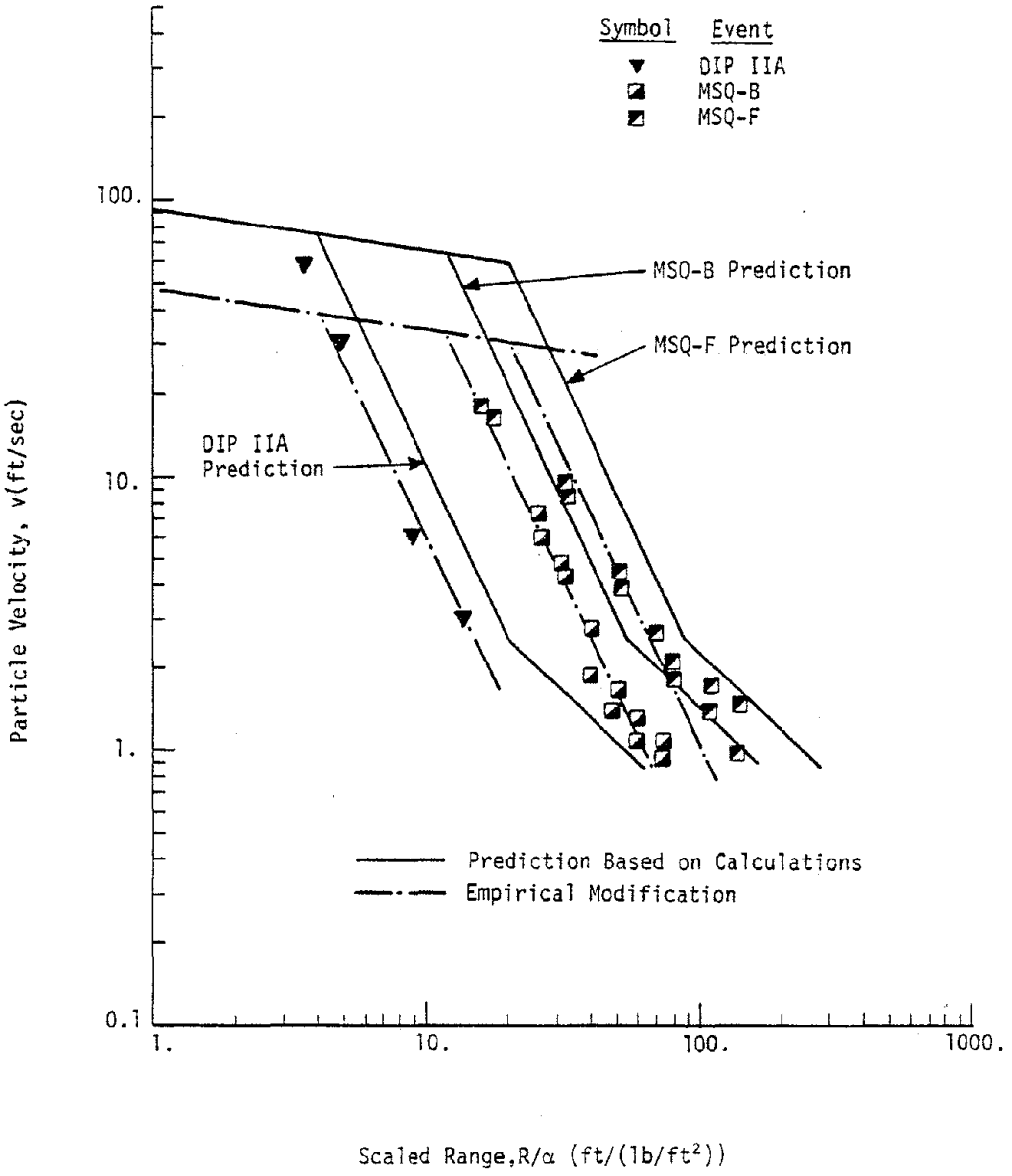

Figure VII-7. Planar Velocities Predicted from Calculations Compared with Data

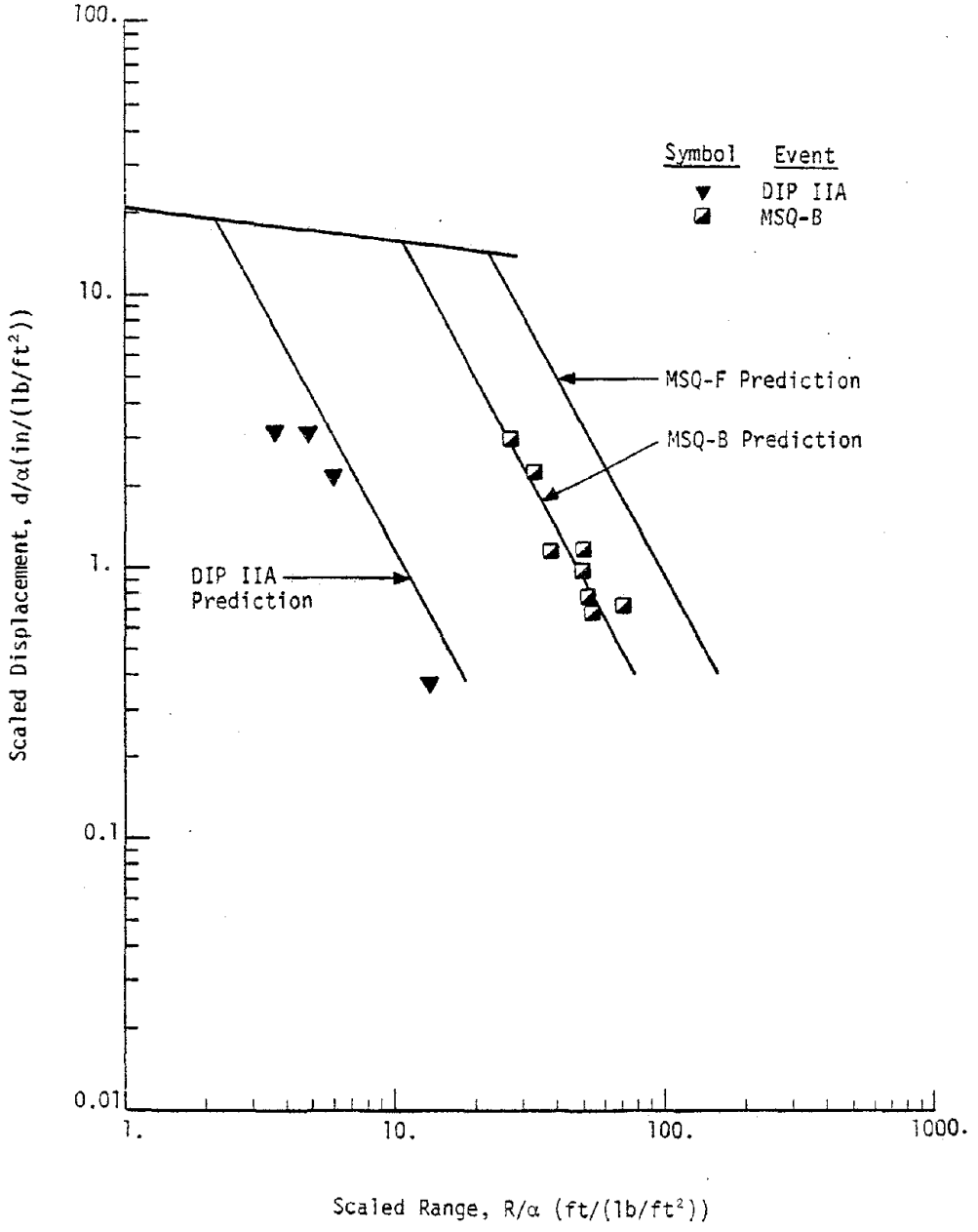

Figure VII-8. Planar Displacements Predicted from Calculations Compared with Data

for all the data. In addition, the acceleration and velocity data do not seem to exhibit a transition to elastic behavior. This later effect may be due to the finite lateral array dimensions in the field. Finite array width would be expected to cause a transition to spherical behavior beyond some range, and increased motion attenuation rates This effect may be counteracting the elastic reduction in attenuation in the field data. The effect, of course, is not modeled in two-dimensional calculations. The amplitude differences may be due to material model and/or input loading inadequacies.

The predicted displacements for DIP IIA are a factor of about 1.6 high while the predictions for MSQ-B are in excellent agreement with the data. Displacement data for MSQ-F are not given since they could not be interpreted in the data. This difficulty was due to the superposition of MSQ-B and MSQ-F effects in the sequenced experiment.

The calculated characteristic times exhibited little variation with range out to the elastic region and this agrees with the trends of the measured data. This behavior allows the average characteristic times to be evaluated as a function of scaled array height. The average characteristic times in the data are compared with the calculated relations as a function of scaled array height in figure VII-9. The trend of the calculations leads to a markedly different interpretation of the variation with array height than was made in Section IV. The data fit indicated a trend of initially high increases in characteristic times with array height. Beyond a scaled height of about 10 ft/(lb/ft^2), the times remained about constant. The calculations, on the other hand, indicate continually increasing characteristic times with increasing

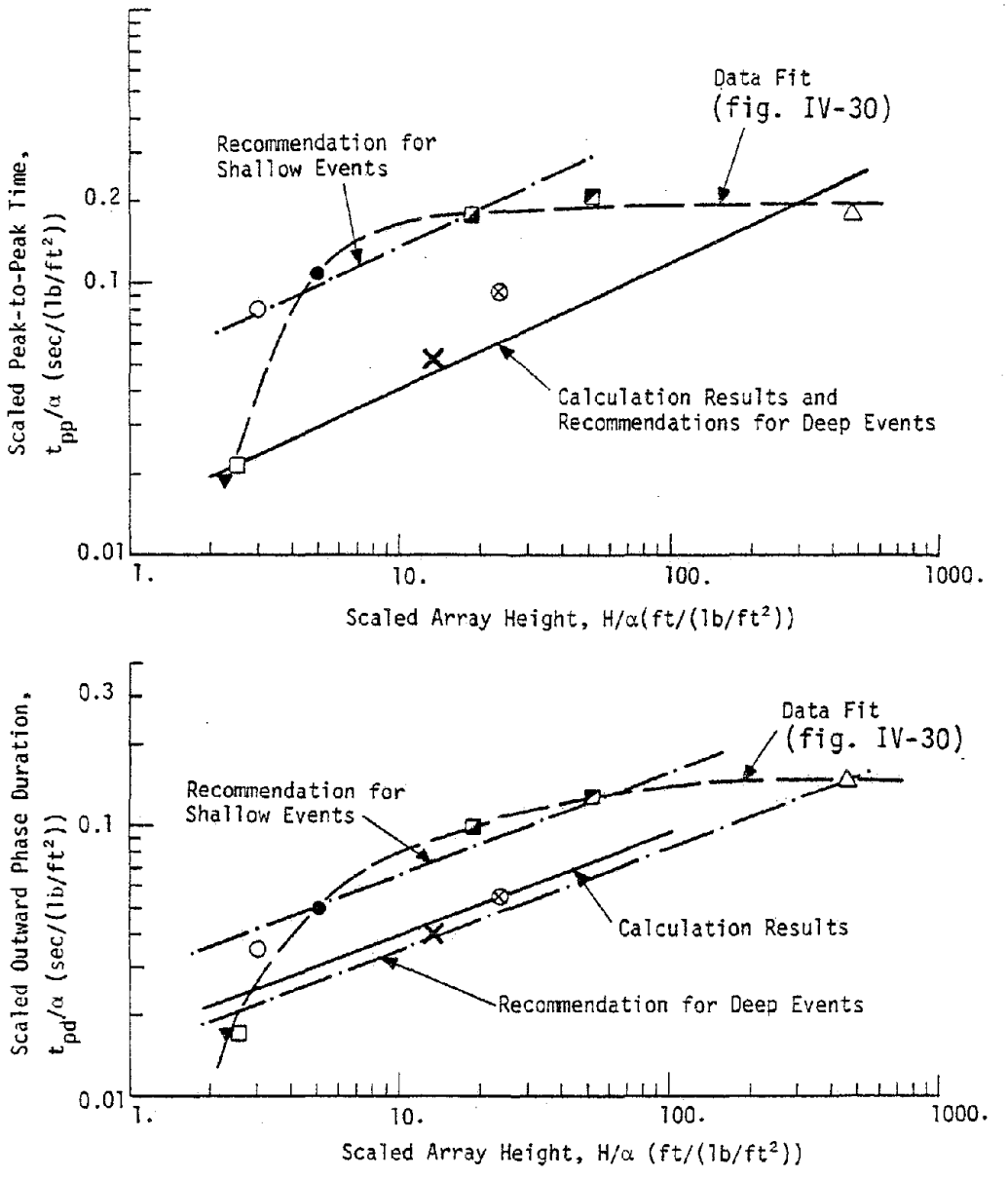

Note: See figure continuation for definitions of symbols.

Figure VII-9. Planar Characteristic Times Predicted from Calculations Compared with Data

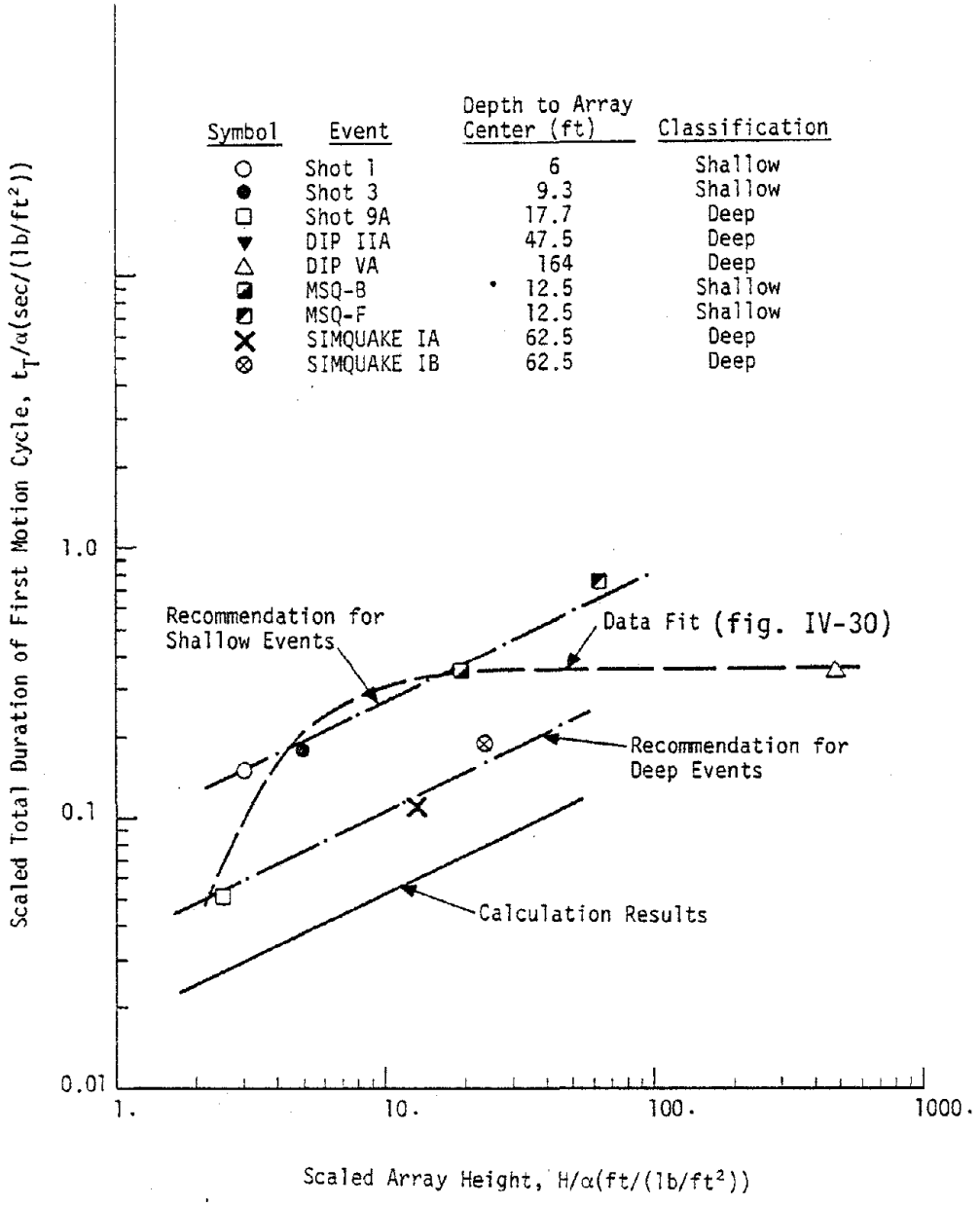

Figure VII-9 (cont.) Planar Characteristic Times Predicted from Calculations Compared with Data

array height. Some new data which recently became available from the SIMQUAKE IA and IB (SQIA and SQIB) events also indicate a different trend from the data available previously.

It appears that there is a depth of burst effect in the behavior of the characteristic times. The data for DIHEST enhancement Shots 1 and 3, and for MSQ-B and MSQ-F all are significantly higher than those of DIP IIA, Shot 9A, SQIA, SQIB and DIP VA. Shot 1, Shot 3, MSQ-B and MSQ-F all had array centerline depths at 12.5 feet and above while the centerline depths for the other events were significantly deeper. If the two groups of events are separated into shallow and deep categories, then the data in the individual groups show the same trend as the calculations, i.e., continually increasing characteristic times with increasing array height.

Gravity and/or material property differences may be exerting an influence. There is insufficient data to evaluate the potential effect of gravity. With regard to material properties, although McCormick Ranch is considered herein as a homogeneous site, there is an increase of seismic velocity with depth. In the near-surface region, the average seismic velocity is about 1650 ft/sec while between 15 feet and 85 feet it is about 2200 ft/sec. This difference, as well as strength differences, may partially account for the behavior.

The calculations were made with a material model which corresponds closest with the shallow events. The calculated characteristic times are lower than the data just as they were for the cylindrical results. Empirical fits to the shallow and deep data are shown in figure VII-9.

These fits which use the same slopes as derived from the calculations are recommended for future predictions.

The observations and comparisons discussed above can be used to select prediction relations for motion amplitudes on planar events. The recommended acceleration and velocity relations are

$$a\cdot\alpha = 2900(R/\alpha)^{-0.89} \qquad \text{for } R/\alpha \le 2(H/\alpha)^{0.6} \qquad \text{(a)}$$

$$a\cdot\alpha = 11{,}680(H/\alpha)^{1.21}(R/\alpha)^{-2.9} \qquad \text{for } R/\alpha > 2(H/\alpha)^{0.6} \qquad \text{(b)}$$

$$v = 49(R/\alpha)^{-0.16} \qquad \text{for } R/\alpha \le 2.6(H/\alpha)^{0.52} \qquad \text{(c)} \qquad \text{(VII-4)}$$

$$v = 313(H/\alpha)(R/\alpha)^{-2.1} \qquad \text{for } R/\alpha > 2.6(H/\alpha)^{0.52} \qquad \text{(d)}$$

where

a = acceleration in g's

v = velocity in ft/sec

R = range in feet

H = array height in feet

α = areal charge density in lb/ft^2 of TNT

These relations should not be altered in the elastic region since spherical effects seem to counteract the elastic attenuation reduction. These recommendations are compared with the data in figures VII-6 and VII-7.

The displacement correlation from the calculations should be taken as the basis for displacement estimates. The relation is

$$d/\alpha = 21(R/\alpha)^{-0.12} \quad \text{for } R/\alpha \le 1.15(H/\alpha)^{0.75} \qquad \text{(a)} \qquad \text{(VII-5)}$$

$$d/\alpha = 26.6(H/\alpha)^{1.28}\ (R/\alpha)^{-1.82} \quad \text{for } R/\alpha > 1.15(H/\alpha)^{0.75} \quad \text{(b)} \quad \text{(VII-5)}$$

where d = displacement in inches and the other variables are as defined for equation VII-4. This relation should be used without modification for shallow events. It appears that the calculations overestimate velocities and underestimate outward phase durations in such a way that they compensate each other and give good displacement estimates for shallow events. For deep events, the calculations slightly overestimate the outward phase durations so that equation VII-5 overestimates displacements. Deep event estimates should be taken as about 50 percent of the values given by equation VII-5.

Figure VII-10 compares the calculated ratios of peak inward to peak outward velocity with the available measured data. Overall, the data exhibit higher inward to outward ratios than the calculations. This trend is opposite to that in the cylindrical results where the calculated ratios were larger. It may be that the additional relief effects from the ends of the array are playing an important role in the field behavior. These three-dimensional effects are not modeled in the calculations.

The MSQ-F and DIP VA (H/α of 51.7 and 474 ft/(lb/ft^2)) inward to outward ratios are in good agreement with the calculated results for scaled array depths greater than about 11 ft/(lb/ft^2). It may be that the curve at which these calculated results and the data coincide forms an approximate lower bound to the ratios.

The results from the calculations indicate the proper scaling for the inward to outward ratios as a function of range. The data fits,

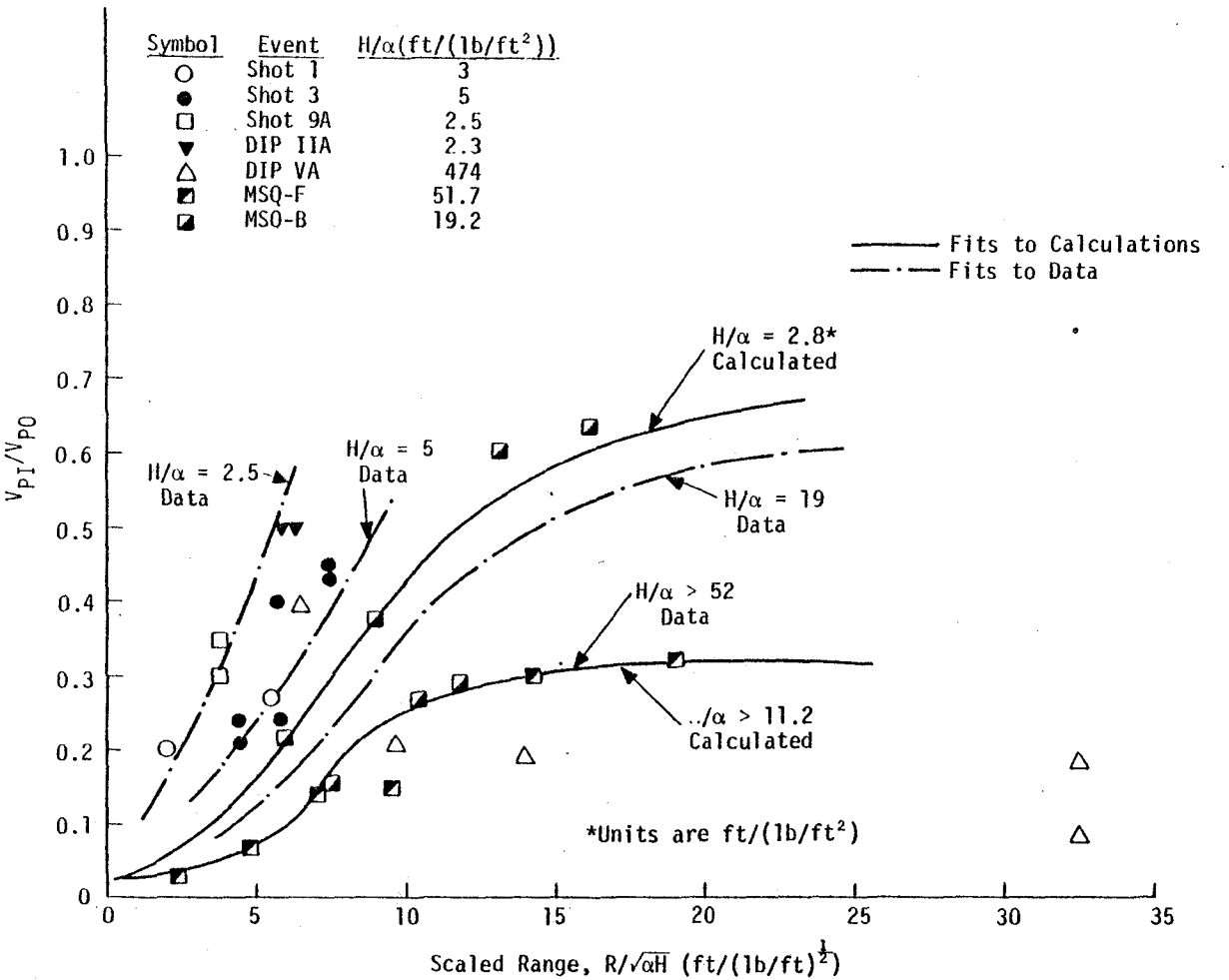

Figure VII-10. Ratios of Peak Inward to Peak Outward Velocities Predicted from Calculations in Planar Geometry Compared with Data

which have the same form as the calculated results, can provide a guide for empirical estimates. Additional data or calculations, perhaps three-dimensional, will be required to better define the parameters affecting the inward to outward ratios.

The planar data for cross-range motion amplitude variations and for free-surface effects are relatively sparse and contain significant scatter. The normalized results of the cylindrical calculations (figs. V-44 through V-47) are consistent with the cross-range data and may be used for cross-range estimates. Similarly, the normalized results of the planar free-surface calculations (figures V-72 through V-76) are consistent with the horizontal and vertical experimental data and may be used for estimates of free-surface effects.

5. ENHANCEMENT METHODS

This paragraph summarizes conclusions on the effects and potential usefulness of several simulation enhancement methods. The conclusions are based upon the data analysis of Section IV and the limited analytical and calculational studies of Section VI. In large part, the conclusions are qualitative since neither the data nor the calculations provide sufficient information for the derivation of quantitative prediction relations. There is sufficient information, however, to state firm conclusions on the usefulness of the various techniques and the direction of future work.

The enhancement methods considered initially were the following:

- Focused Arrays
- Explosives with Longer Burn Times
- Decoupling of Explosives

- Relief Trenches
- Shock Barriers
- Multiple, Time Sequenced Explosions

In the course of numerically evaluating relief trenches, trench considerations were extended to encompass the use of trench screens.

Existing data indicate that focused explosive arrays enhance stresses and accelerations more than velocities and displacements. This effect is contrary to that desired for earthquake ground motion simulation. Should some need be established for this type of enhancement in the future, the effect is probably susceptible to analysis with calculations.

The data on explosives with various burn times indicate that there is no significant influence on motion amplitudes or time histories for the explosives evaluated. Burn time effect, if any, for other explosives would probably be a second order effect, at most. It, therefore, appears that burn time variations will not provide an effective means of significantly enhancing explosive simulations.

The decoupling data (figs. IV-15 through IV-17) and calculations (figs. V-18 through V-20) indicate that increasing the size of the explosive cavity for a given amount of explosive results in increased displacements and correspondingly lower frequency content. At the same time, accelerations and velocities at intermediate to far ranges are not changed much. These effects suggest significant potential application to earthquake ground motion simulation. The data available to this study did not span a sufficient range of parameters (explosive density, array size, etc.) to enable derivation of general quantitative relations. SRI International is now conducting research concerned with controlling explosive gas vent-

ing from an explosive using a mechanical device. This work is closely related to decoupling and the SRI data should be evaluated for decoupling effects. In addition, other experiments and calculations should be pursued.

Relief trench data (figs. IV-48 through IV-52) and calculations (figs. VI-16 and VI-17) indicate that it is possible to enhance horizontal velocities and displacements in the region between the explosive source and the trench. Under certain design conditions, this effect may be desirable from a simulation viewpoint. However, relief trenches do not excite additional motion cycles in the cases for which data and calculations are available. Further experiments and numerical calculations will be necessary for the development of general relations for estimating the amount of velocity and displacement enhancement.

Numerical calculations suggest that the use of trench screens is a very viable method for diminishing the horizontal accelerations and, to a lesser extent, velocities in a region behind the trench. The ultimate horizontal displacement does not appear to be affected by the existence of a trench. Figure VII-11 plots the acceleration and velocity attenuation rates at the ground surface in the trench numerical calculations as a function of trench depth. In the specific case investigated, a factor of two reduction in acceleration can be obtained with a 15-foot trench. This size trench is quite practical. The relations of figure VII-11 as well as those shown previously in Section VI are for a single set of explosive conditions and a single trench range. The generalization of these relations will require additional calculations as well as field experiments.

Shock shield calculations and data indicate that it is possible to

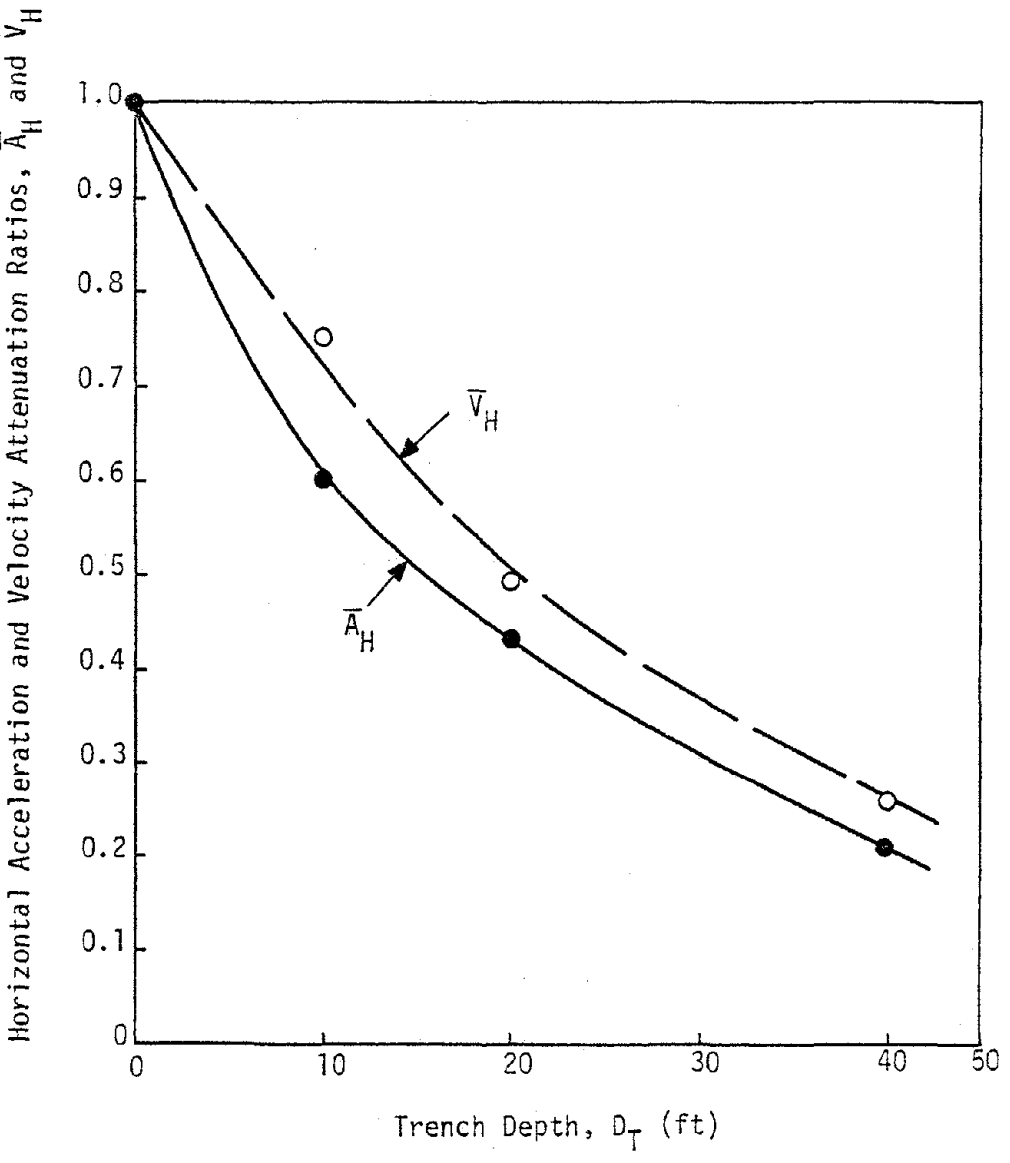

Figure VII-11. Attenuation of Horizontal Acceleration and Velocity as a Function of Trench Depth in the Numerical Calculations

diminish accelerations behind the shield, while causing a lesser effect on velocities and displacements. The size of the shield required for a given amount of attenuation is strongly dependent on the rise time contained in the input ground motion. In small scale simulation experiments, which will contain short rise times, shields of practical size can be selected. In large simulations, however, impractically large shields will be required because of the long rise times in the input ground motions.

Multiple, time sequenced explosions appear to be the most practical method available for inducing multiple cycles and long durations of ground shaking. Such explosions might be on the same side of the test area or on opposite sides. Since the time delays will generally be selected so that the motion from previous explosions is at a low level when later explosions occur, linear superposition of individual explosion effects will probably provide an adequate estimate of combined effects. This conclusion is supported by the Mini-SIMQUAKE results given previously in figure IV-47.

6. ESTIMATES OF FREQUENCY CONTENT AND SHOCK SPECTRA

The recommended relations of the previous paragraphs provide means for estimating ground motion amplitudes and time characteristics under a variety of explosive configuration conditions. These estimates implicitly contain frequency information. In designing a simulation, however, it is desirable to have explicit estimates of the main frequencies contained in the ground motions, as well as shock spectra estimates which can be used to estimate the level of response of the system of interest. The most accurate means of estimating these quantities

is the explicit generation of Fourier and shock spectra from either measured or calculated time histories. Calculated time histories should be modified empirically in amplitude and time characteristics by the relations previously presented. There are simpler means of estimating frequency content and shock spectra which will probably be satisfactory for initial design estimates. These methods are briefly described here.

The characteristic times of the velocity pulse can provide an estimate of the major frequencies of the ground motion. In general, the data seem to indicate that peak to peak times are about 1 to 2 times the outward phase duration, and the duration of the first motion cycle about 3 to 4 times the outward phase duration. The major frequency in the experiment will probably be associated with the outward phase duration and the frequency can be estimated roughly as

$$f_{pd} \simeq \frac{1}{2t_{pd}} \qquad \text{(VII-6)}$$

where

f_{pd} = approximate frequency associated with the outward phase duration in Hz

t_{pd} = outward phase duration in sec

Because of the differences between the outward phase duration and the peak to peak and first motion cycle times, significant frequencies will probably occur from f_{pd} to 1/4 f_{pd}.

Guides to shock spectra estimates are provided in reference VI-1 and VI-2. On a tripartite plot (see Section III), the undamped spectra bounds for a short impulsive motion (a parabolic velocity pulse with no inward component) can be estimated by using amplitude multipliers of

1 for displacements, 1.5 for velocity and 2 for acceleration (ref. VI-1). The corresponding multipliers for 10 percent damping are 0.9, 1.3, and 1.7. Average undamped spectra multipliers for earthquakes (ref VI-2) are about 1.15 for displacement, 1.75 for velocity, and 2 for acceleration. For 10 percent damping, the corresponding values are 1.15, 1.34, and 1.65. The earthquake multipliers are somewhat higher than those for short impulsive motions because of the more oscillatory nature of earthquake motions.

In simulation applications, the appropriate multipliers should be selected on the basis of range and experiment design. At large ranges from single arrays, and at all ranges from multiple arrays, the earthquake multipliers are recommended because the motions will be oscillatory. At near-ranges from single arrays, the motion will be more impulsive in nature. In this case, the multipliers for short impulsive motions would be appropriate.

7. REFERENCES

VI-1 Veletsos, A.S., et al, Design Procedures for Shock Isolation Systems of Underground Protective Structures, Vol. 13, Response Spectra of Single Degree of Freedom Elastic and Inelastic Systems, RTD TDR 63-3096, Vol. III, Air Force Weapons Laboratory, Kirtland AFB, New Mexico, June 1964.

VI-2 Newmark, N.M., Blume, J.A. and Kapur, K.K., "Seismic Design Spectra for Nuclear Power Plants," Journal of the Power Division, ASCE, Vol. 99, No. PO2, November 1973.

SECTION VIII
APPLICATION OF RESULTS

1. INTRODUCTION

Section VII summarizes improved empirical relations for predicting the ground motion environments from various unenhanced explosive configurations. Those relations can form the basis for designing simulations of earthquake-like ground motions on engineering systems. The other important aspect of the design problem is the system itself. The system characteristics and the prediction relations may be joined into the following procedure for designing a simulation:

a. Define the system and its important dynamic characteristics.

b. Define the prototype earthquake environment.

c. Define the scale of the experiment.

d. Define the desired level of system response.

e. Select an explosive configuration.

f. Estimate motions from candidate explosive configurations.

g. Estimate corresponding shock spectra or other measure of system response.

h. Select a simulation design and the range at which the system will be sited.

This procedure was recently applied by the University of New Mexico to the design of the SIMQUAKE I simulation experiments on nuclear power plant models for the Electric Power Research Institute. Although National

Science Foundation interest specifically excludes research uniquely related to nuclear power plants, the design method is general and the experiments represent the only case in which explosive tests have been designed and used to investigate specific earthquake-related behavior of large scale structures. Hence, it is of general interest and is outlined in the following paragraphs.

Before proceeding to that application, it is of interest to observe the range of motions that can be produced by an explosive simulation. Table VIII-1 lists predicted horizontal motions as a function of areal charge density at the 1 g acceleration level from planar arrays of 25, 50 and 75-ft heights. Corresponding surcharges of 10, 20 and 30 feet were assumed and free-surface effects were accounted for in the estimates. It appears possible to achieve particle velocities, displacements and frequency content which are well within the ranges expected in strong earthquakes. Durations and number of motion cycles are limited in single arrays but these may be increased if necessary by using multiple sequenced arrays.

2. ILLUSTRATIVE APPLICATION

a. The System

Containment structures of nuclear power plants are massive, rigid, reinforced concrete structures which are usually embedded to a significant depth. The rigid body translation/rocking response of containment structures is an important contributor to the loads transmitted to the reactor core and other internal components during earthquake excitation. Horizontal ground motions excite the translation/rocking response and are of prime concern.

Table VIII-1

Estimated Motions at the 1 g Acceleration Level at the Ground Surface from Various Arrays

Array Height(ft)	Areal Charge Density (lb/ft^2 TNT)	Range (ft)	Velocity (ips)	Displacement (in)	Frequency (Hz)	Duration* (sec)
25	2	135	13	2.0	3.0	0.24
	4	170	15	2.5	2.5	0.33
	8	180	18	2.5	2.5	0.40
50	2	165	18	3.5	2.0	0.33
	4	210	21	5.5	1.5	0.47
	8	225	25	5.5	1.5	0.58
75	2	195	28	8.0	1.5	0.48
	4	255	31	11.5	1.0	0.67
	8	285	35	14.0	0.9	0.80

*At array centerline

Individual containment structures vary in size, shape and embedment depending upon their specific design and site unique conditions. An average generic structure might be considered as an open cyclinder with the following characteristics

Height	: 180 feet
Diameter	: 120 feet
Base Thickness	: 14.5 feet
Wall Thickness	: 6.25 feet
Total Weight	: 40,500 tons
Embedment	: 1/4 to 1/3 the height

The base and wall thicknesses given above have been increased over typical dimensions to account for the added mass of internal equipment and the mass distribution with height in a typical structure since these parameters influence translation/rocking response.

Beredugo and Novak (ref. VIII-1) provide a method for estimating the translation/rocking frequencies of an embedded footing under small strain conditions. The system is a two degree of freedom system having two resonant frequencies, but the response is usually dominated by the fundamental vibration mode. The frequency solution is a function of the mass, mass moment of inertia and embedment of the structure, and the density and elastic properties of the adjacent soil. For 1/3 embedment of the generic structure presented above and assuming a soil unit of weight of 110 lb/ft^3, a shear wave velocity of 900 ft/sec and a Poisson's ratio of 0.25, the fundamental rocking frequency is about 2.0 Hz. An explosive simulation to excite high level translation/rocking response of this structure should be designed to produce frequencies at or, perferably, below 2.0 Hz. Less than 2.0 Hz is preferable because the rocking frequency may decrease at

high strain levels (i.e., softening soil conditions).

b. Prototype Earthquake Environment

A credible design environment might be that created at the 1 g acceleration level from a magnitude 7 or 8 earthquake. Motion estimates as a function of magnitude and distance are available from reference VIII-2 and were previously presented in figure III-1. Selecting a magnitude 8 earthquake, the 1 g level occurs at a range of 10 miles from the source and has corresponding velocity and displacement amplitudes of 36 in/sec and 18 in, respectively. The simulation should be designed to excite response on the order of that which would be excited by this selected prototype environment.

c. Experiment Scale

The generic full size structure described above would be quite expensive to build. The response of interest can probably be investigated on a smaller scale. The scale should not be too small, however, because of uncertainties in modeling in inelastic materials, gravity influences and the need for a practical structure size for instrumentation purposes. A 1/12 scale of the generic structure was selected as a reasonable compromise. This size is reasonable for instrumentation and modeling of details, if necessary, and is of reasonable cost. A 1/12 scale model of the 1/3 embedded generic structure using the same construction materials as in the prototype would have the following characteristics:

Height	: 15 feet
Diameter	: 10 feet
Base Thickness	: 1.21 feet

Wall Thickness : 0.52 feet

Total Weight : 23.4 tons

Embedment : 5 feet

Fundamental Rocking Frequency : 24 Hz

The simulation for this structure should be designed to contain frequencies at or below 24 Hz. In addition, the prototype design environment should be scaled appropriately. For a 1/12 scale experiment, the scaled environment should have an acceleration, velocity and displacement of 12 g, 36 in/sec and 1.5 in, respectively.

d. Desired Level of Response

A main concern in translation/rocking problems is the effect of large soil strains on the level of response. In earthquake applications, large shear strains are considered to be 0.1 percent and above, and this strain level might be selected as a minimum response criteria. The shear strain adjacent to the structure can be estimated approximately as the peak rocking angle of the structure during response. Assuming the center of rocking is near the structure base, a 0.1 percent soil shear strain implies a relative horizontal displacement between the top and base of the structure of 0.18 inch.

e. Explosive Configuration

A planar array was selected. The planar geometry assures that motions at the structure, which has large dimensions in spite of scaling, are relatively uniform. In addition, it provided a large experimental area which was used for additional experiments on embedment, structure size and backfill variations.

f. Estimated Motions

The selection of an appropriate array is a trial and error process. Equations VII-4 and VII-5 are used to estimate motions at the mid-depth of various candidate arrays. The mid-depth motions are then modified for off-center attenuation using figures V-67 through V-69. Finally, motions at the free-surface are estimated using figures V-72 through V-73. Figure VIII-1 shows predictions for a 75-foot high array loaded with 4 lbs/ft^2 of equivalent TNT. This configuration yields motions which are in the range of those required for the problem being considered. The surface amplitudes at the 100, 150 and 200-foot range are summarized in table VIII-2. The amplitudes do not precisely match the scaled environment requirements of 12 g, 36 in/sec and 18 inches at any range. However, if one of these motion parameters are considered more important than the others then a range corresponding to the appropriate parameter could be selected from the array illustrated or from another array. For example, if the 36 in/sec velocity is considered important then a range between 150 and 200 feet might be selected.

Table VIII-2

Predicted Motions at the Surface from a 75-foot High Planar Array Containing 4 lbs/ft^2 of Equivalent TNT Explosive

Range (ft)	Acceleration (g)	Velocity (in/sec)	Displacement (in)
100	6	85	9
150	2.5	53	7.2
200	1.4	32	6.4

A better method for selecting a range is to consider the desired response in the experiment rather than a particular motion amplitude

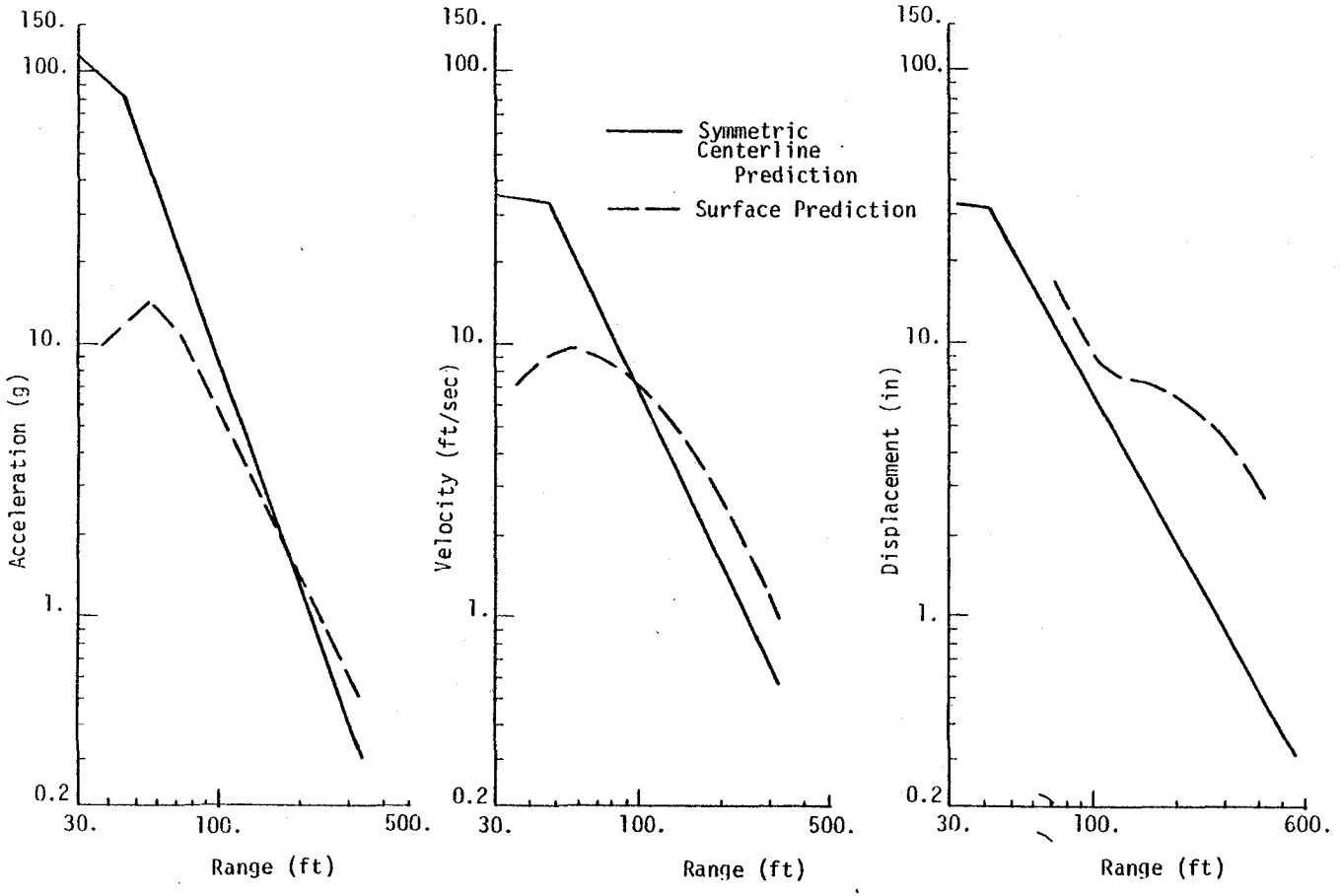

Figure VIII-1. Prediction of Ground Motions from a 75-foot High Planar Array of 4 lbs/ft^2 of Equivalent TNT at McCormick Ranch

value. This is discussed next. Before proceeding, however, it is interesting to note that the predicted motion amplitudes, with the exception of displacement, are very close to those of the design environment for the full scale structure (1 g, 36 in/sec, 18 in).

g. Shock Spectra and the Selection of a Design

Shock spectra provide a good means of estimating system response. Spectra may be estimated by the amplification factors given in Section VII. Since the explosive environment will be oscillatory in the anticipated siting region the same factors may be used for both the scaled earthquake environment and the explosive environment. Due to embedment, the structure will be highly damped, perhaps 10 percent of critical or greater. Hence, the amplification factors for 10 percent damping may be used. Those factors are 1.15 for displacement, 1.34 for velocity and 1.65 for acceleration.

Ten percent damped spectra for the 1/12 scale, 1 g earthquake environment, and for a 1/2 g environment in the same earthquake, as well as for the estimated ground motions at 100, 150 and 200-foot ranges are shown in figure VIII-2. The 1/12 scale structure with a 24 Hz fundamental frequency would have a very low response at any of the ranges shown compared with the 1 g earthquake. At 100 feet its response would be approximately that of the 1/2 g earthquake. However, the soil shear strain would only meet the minimum requirement of 0.18 in relative displacement. The low response is due to the relatively low frequency content of the explosive environment ($f_{pd} \simeq 2$ Hz) compared with the frequency of the system. Other large arrays also have a relatively low frequency content.

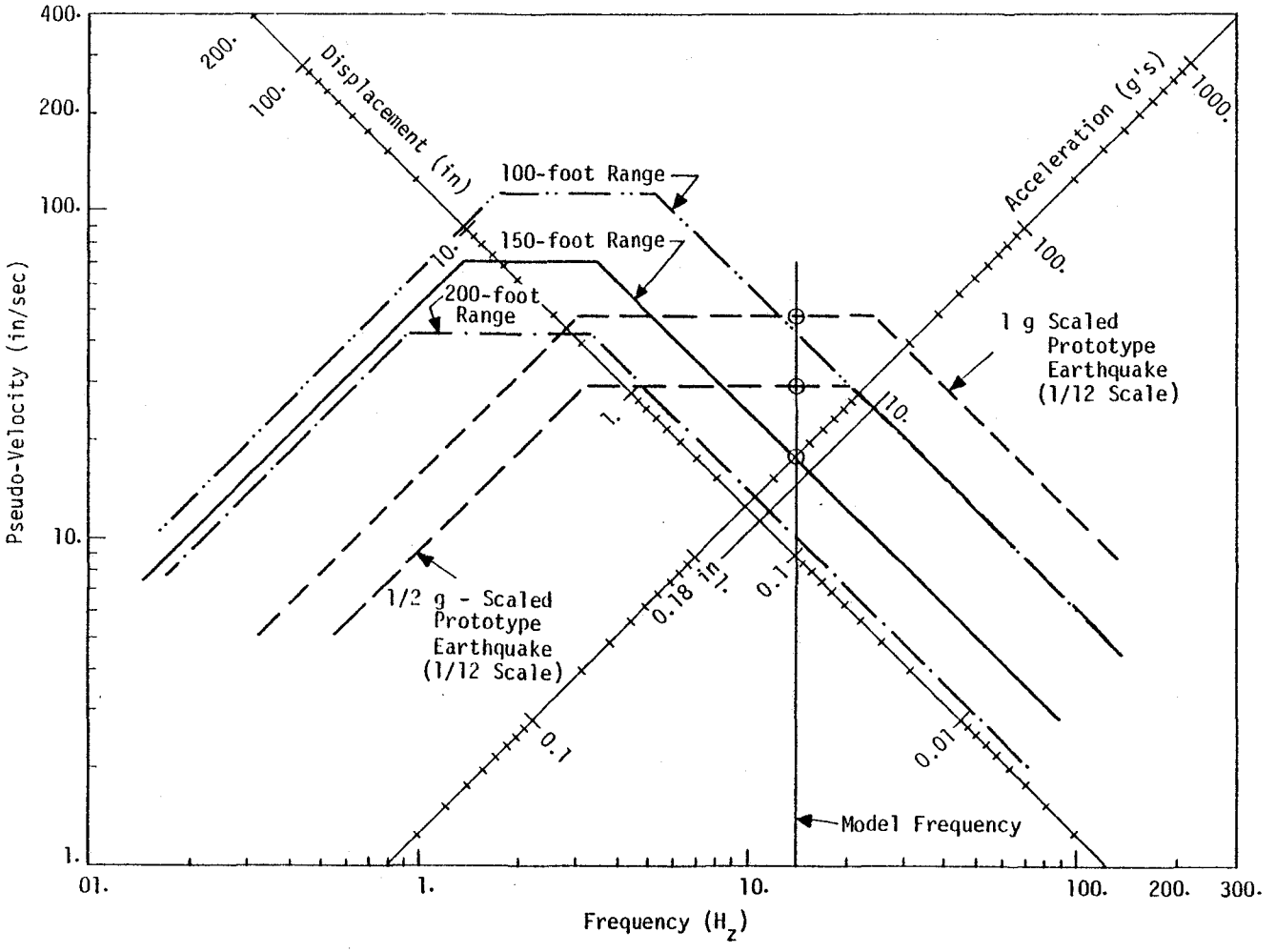

Figure VIII-2. Shock Spectra at Various Ranges from a 75-foot High Planar Array of 4 lbs/ft^2 of Equivalent TNT at McCormick Ranch Compared with Scaled Spectra from Credible Prototype Earthquakes

Increasing the structure base and wall thicknesses to 1.5 feet and 1.0 feet, respectively, and decreasing the embedment to 25 percent reduces the frequency of the model to about 14 Hz. Although no longer a perfectly scaled model of the generic prototype considered originally, this new model is still representative of a credible prototype and will contain similar translation/rocking response features. The 14 Hz model will have acceptable response at either the 100-foot or 150-foot range. At 100 feet, the response will be at least 90 percent that of the 1 g earthquake. At the 150-foot range the response will be at least 40 percent that of the 1 g earthquake and 65 percent that of the 1/2 g earthquake. The response is stated as being "at least" a given amount because large soil strains will be encountered in the experiment. At the 100 or 150-foot range, the relative displacement will exceed 0.18 in implying greater than 0.1 percent soil shear strain. These strain levels might be expected to reduce the structure frequency below 14 Hz and, therefore, increase response.

The results described are for a single explosive array. In other experiments, requirements may dictate the need for additional motion cycles. The experiment could be designed to include added arrays with little difficulty. A reasonable estimate of motions could be made using superposition.

h. Comments on the Illustration

The procedure described above illustrates both the steps involved in establishing a satisfactory simulation design as well as potential design problems that may be encountered. Although the data of the

SIMQUAKE I series are not yet fully analyzed and reported, quick look analyses indicate that the structure responded with a fundamental frequency in the range 3 to 6 Hz, well below the small strain estimate of 14 Hz. As a result, the level of response was near or above that of the 1 g prototype environment. The small strain frequency was measured in the field as about 18 Hz so that the pre-test estimate of 14 Hz was reasonable. The large reduction in frequency during the experiments appears to be a large strain phenomena. Hence, the SIMQUAKE I simulation series provided data on large strain response not previously available from real earthquakes or other simulation methods.

3. REFERENCES

VIII-1 Beredugo, Y.O. and Novak, M., "Coupled Horizontal and Rocking Vibration of Embedded Footings," Canadian Geotechnical Journal, Vol. 9, pp. 477-497, 1972.

VIII-2 Matthiesen, R.B., Howard, G. and Smith, C.B., "Seismic Considerations in Siting and Design of Power Plants," Nuclear Engineering and Design, Vol. 25, pp. 3-15, 1973.

SECTION IX
SIMULATION COST ANALYSIS

From inception to completion a well planned earthquake simulation experiment must encompass the following major tasks:

- Site Selection, Development, and Investigation
- Simulation Experiment Design
- Explosive Array Construction
- Free-Field Instrumentation
- Structure Design, Construction, and Instrumentation
- Data Reduction, Analysis, and Report Preparation
- Site Restoration

The University of New Mexico, Civil Engineering Research Facility, has conducted a series of such experiments at the McCormick Research Test Site during the past ten years. As a result, it has gained experience and assimilated a large amount of data for cost estimating purposes. It should be emphasized that the actual cost for such experiments depends greatly on the location and specific characteristics of the site, as well as on the size and complexity of the structures to be tested and the nature and completeness of the data that is sought. Consequently, the cost estimates presented herein are intended to provide only a rough measure of the order of magnitude of the costs involved.

Each of the tasks listed above will be discussed briefly.

1. SITE SELECTION, DEVELOPMENT, AND INVESTIGATION

(a) Site Selection: If a well documented site is available from previous experimental work, little or no additional cost for site selection will be necessary. However, if a new site possessing a specific geology is sought, there will be costs associated with a literature search, exploratory drilling, geophysical survey, and data analysis. Assuming that the exploratory drilling does not exceed a total of 1000 line ft and that the geophysical survey is limited to a preliminary assessment of the gross geologic features of the site, the total cost of the site selection phase should range between $30K and $40K.

(b) Site Development: The basic objective of this task is to make the site suitable for experimentation. It may include clearing and grading, drainage, road construction, and water and power development. Obviously, there will be little or no cost involved if a currently available site is used. If a new site is sought, the cost will be commensurate with the accessibility of the site. For a remote site the cost involved may range between $100K and $200K.

(c) Site Investigation: The site investigation includes detailed subsurface investigation and sampling, geophysical surveys, laboratory testing and, possibly, in-situ testing to establish dynamic geotechnical properties of the site. At a site in current use these investigations will be relatively small. At a new site they will depend on the complexities of the geology of the site and will consist of drilling and sampling; seismic surveys including refraction, uphole and crosshole; laboratory dynamic uniaxial, triaxial, and hydrostatic testing; in-situ dynamic testing (CIST); and material model fitting. It should be emphasized that in-situ dynamic testing is a major undertaking and the total cost

involved is greatly influenced by the in-situ dynamic testing. The total cost for the site investigation could range between $75K and $150K, depending on whether in-situ dynamic testing is undertaken or not.

2. SIMULATION EXPERIMENT DESIGN

The design of a simulation experiment entails empirical predictions as well as finite difference calculations of simulation behavior. On the basis of these findings, a simulation design is selected, which is followed by the selection of the free-field instrumentation including type, location, placement, and sensitivity. The cost for this phase of the experiment including computer time and manpower could range between $15K and $30K.

3. EXPLOSIVE ARRAY CONSTRUCTION

The explosive array construction phase of the experiment consists of shothole drilling, casing, explosive purchase and placement, firing system fabrication, and installation. The cost per ton of installed explosive varies according to the overall size of the experiment and the type of explosives used; however, assuming that ANFO is used for an explosive, the average cost may range between $1000 to $1200 per ton of in-place explosive.

4. FREE-FIELD INSTRUMENTATION

The free-field instrumentation consists of hole drilling, gage purchase and canister fabrication, cable hookup, gage placement, and grouting, calibration, checkout, and recording. Assuming that the instrumentation recording capability is already available, the average cost

of free-field instrumentation including all of the above items is approximately $1000 per new channel. Reused instrumentation for successive shots including materials and labor runs in the neighborhood of $600 per channel.

5. STRUCTURE DESIGN, CONSTRUCTION, AND INSTRUMENTATION

(a) Structure Design: The model design consists of establishing simulation criteria, structural response analysis, engineering design, and the preparation of construction drawings and specifications. The cost is structure dependent; however, previous experience indicates that it might entail between three to nine man-months of effort at a total cost ranging between $10K to $30K, depending on the type of structure.

(b) Structure Construction: The construction cost depends greatly on the type and size of the structure. The cost of construction for a large reinforced concrete structure may range between $800 to $1200 per cubic yard of concrete, while for a small size model structure the cost may range between $1400 to $1600 per cubic yard. Earthwork costs may range from $2 per cubic yard for large structures to $10 per cubic yard for small structures.

(c) Structure Instrumentation: The model instrumentation cost including gage purchase, cable hookup, gage assembly and placement, calibration, checkout, and recording is similar to that of free-field instrumentation. Assuming that a recording capability is available, the model instrumentation including labor will be about $100 per new channel and $600 per channel for reused channels in successive shots.

6. DATA REDUCTION, ANALYSIS, AND REPORT PREPARATION

(a) Data Reduction: The data reduction phase includes analog-to-digital conversion, noise removal, baseline correction, and integration and the generation of Fourier and Response spectra. The approximate cost for all the operations described above for data reduction is $600 per channel of data.

(b) Analysis and Report Preparation: The cost of data analysis and report preparation is a function of the overall size of the experiment, including the number of structures and the amount of instrumentation channels involved. It may entail anywhere between 1 to 2.0 man years of principal investigator's time including support functions at a total cost between $50K and $100K.

7. SITE RESTORATION

The site restoration phase of the simulation experiment includes the removal and/or demolition of structural models, the filling of craters, and the cleaning, grading, and environmental restoration of the site. The cost may range between $10K and $25K.

8. COST ESTIMATES FOR A TYPICAL EXAMPLE

It is assumed that initial simuaation experiments will be preferred at an existing, well documented site such as the McCormick Ranch Test Site. The example involves concrete structure models of approximately 35 cubic yards total and 120 channels of instrumentation including free-field and structure. It is further assumed that no in-situ dynamic testing will be performed. The estimated experimental cost including overhead is approximately as follows:

• Site Selection (No Cost)	$ ------
• Site Development (No Cost)	------
• Site Investigation - Nominal (w/o in-situ dynamic testing)	15,000
• Simulation Design	15,000
• Array Construction (80 tons ANFO)	80,000
• Free-Field Instrumentation (60 channels)	60,000
• Model Design (6 man months)	20,000
• Model Construction (35 yd^3 concrete)	35,000
• Structure Instrumentation (60 channels)	60,000
• Data Reduction (120 channels @ $600/channel)	72,000
• Data Analysis and Reporting (1.2 man year)	60,000
• Site Restoration	15,000
TOTAL -	$432,000

This typical example indicates that 120 channels of data for an earthquake simulation experiment can be obtained at a total cost of $432,000, or at a cost of $3600 per channel. This unit price per channel of instrumentation compares rather favorably with seismic instrumentation costs on prototype structures, which run well above the cost estimate for this simulation experiment (Ref. IX-1).

9. REFERENCES

IX-1 Hudson, D. E., "Earthquakes, Reliability of Records Panel," pp. 1.3-01 to 1.3-10, Sixth World Conference on Earthquake Engineering, New Delhi, India, January 10-14, 1977.

SECTION X
CONCLUSIONS AND RECOMMENDATIONS

1. CONCLUSIONS

a. General Conclusions

The overall objective of this investigation was the evaluation of the technical and economic feasibility of simulating earthquake-like ground motions with high explosives. The investigation results indicate that simulation is technically and economically feasible. The development of a simulation design requires that the engineering system of interest, the prototype earthquake environment and the ground motion environment from candidate explosive arrays be evaluated. The characteristics of the engineering system and the earthquake environment should be used to establish simulation criteria. An explosive design should then be chosen to meet that criteria.

Major general conclusions with regard to simulation criteria and explosive simulation capability are as follow:

(1) Simulation criteria should be based upon system response rather than specific environment details. This is necessary because the current state-of-the-art of detailed earthquake motion understanding is relatively weak on the one hand and it would be impractical to simulate every known earthquake detail on the other. The simulation should be designed to excite the types and amplitudes of response that might be expected in a

strong earthquake. The measured input and response data can then be used to evaluate and improve response models and analysis methods. Specific simulation criteria will probably be system dependent and will vary with the experiment scale. Shock spectra provide one means of evaluating response and establishing criteria.

(2) Explosives in various arrays can produce acceleration, velocity and displacement amplitudes which are in the range of those expected in earthquakes. Frequency content in the range of earthquake interest can also be produced. The equations and charts derived in this investigation can be used to predict the motion environments from candidate explosive arrays in dry alluvial materials.

(3) There is some degree of similarity between the wave structure of many earthquakes, as presently understood, and the wave structure of planar arrays. This similarity lies in shear wave content. Many earthquakes are thought to contain a large shear wave contribution in the horizontal motion. The loading waves in the near-surface region from a planar array also appear to contain large shear wave contributions. As a result, early arguments that explosive sources caused primarily compression phenomena and, therefore, were very dissimilar from earthquakes are not necessarily valid.

(4) Some simulation criteria may require modification of the ground motions from single explosions. If necessary, multiple motion cycles and longer time durations can be achieved with multiple, time sequenced explosions. Modification of the ground motion amplitudes is feasible through the use of shock shields, relief trenches and trench screens. However, these latter enhancement methods must be investigated experimentally and numerically in more detail before they can be used with confidence.

(5) High explosive simulations are economically feasible. This conclusion is based upon cost comparisons with simulation tests performed in the defense industry and costs per channel of recovered earthquake strong motion data. With regard to defense simulations, the federal government is willing to expend several million dollars a year to simulate nuclear weapon blast and shock effects on defense structures using high explosives. Earthquakes threaten billions of dollars worth of property and an unestimable number of lives. At the same time, the state of knowledge of earthquake behavior in some cases is behind the state of knowledge of weapon effects. Hence, it would appear that some Federal investment in explosive simulation of earthquake-like ground motions is quite justifiable.

With regard to costs of recoverable data, explosive simulations can be performed at a cost per recovered data channel of $3,000. to $5,000., including construction of the simulation and structures, geophysical investigation, and data reduction. This cost range is on the order of a factor of 2 to 5 lower than the cost per channel of recovered data from current earthquake strong motion networks.

b. Specific Conclusions

In the course of evaluating the general feasibility of simulating earthquake-like ground motions, several specific aspects of the analysis and behavior of ground motion environments created by high explosives were investigated. Detailed conclusions on these investigations were given at the end of each section. Major conclusions on some of the more important items are stated below.

(1) Numerical calculations can be used to evaluate ground motion

phenomena and to expand and aid in the interpretation of field data. The numerical calculations of this study yielded information which improved the level of certainty in the correlations of available data and, in addition, gave insight on some phenomena (e.g. free-surface effects) not available from data.

(2) Yield scaling in the same material is exact even if the material is inelastic. Deviations from yield scaling result from either material property differences or gravity effects.

(3) Techniques for scaling ground motion effects in different materials, which include only the explosive yield as a source parameter, are incomplete. Source parameters related to pressure must be included in order to obtain all of the necessary non-dimensional scaling terms.

(4) Source coupling, which is related to source peak pressure, can affect the amplitudes and frequency content of ground motions. This conclusion reinforces the scaling conclusions stated above and, in addition, suggests that source coupling may be a potential means of altering the ground motion environments from high explosives.

(5) The most common enhancement requirements may be acceleration reductions, multiple motion cycles and longer time durations. Trench screens appear to be the best potential method for reducing accelerations, while multiple, time sequenced explosions can induce multiple cycles and increased time durations.

2. RECOMMENDATIONS

Simulation design is technically feasible using the methods described in this report. However, there are other areas whose investigation would improve the options available in simulation design. These areas

and recommended approaches to their resolution are given below.

a. The only explosive simulation enhancement technique which can be employed with confidence is multiple, time sequenced explosions. There are several other candidate enhancement techniques with the potential for expanding simulation options. These include source coupling variations, shock shields, relief trenches and trench screens. There are insufficient data available on these techniques. Further investigation with both calculations and experiments is recommended.

b. The calculations performed in this investigation indicated that certain aspects of the ground motion environment were sensitive to the input loading assumptions and the material properties. Late time behavior and the ratio of inward to outward velocity were particularly affected. It would be desirable to quantify the sensitivity of the response to input and material property parameters, and to develop improved models for future calculations.

c. The analyses of this investigation were restricted to dry alluvial materials. At some point it will be desirable to extend these results to other geologies. The material property scaling analyses herein can form the basis for initial extrapolations. However, additional calculations and experiments will be needed to predict response in other materials with confidence.

d. Simulation criteria and simulation design are closely related to the engineering system of interest. An example application of the development of a design for a particular system is given in Section VIII. Simulation evaluations should be performed for other generic systems so that appropriate explosive simulations can be designed.

e. Explosive simulations should be used to investigate specific

engineering problems. Retaining structures, earth dams and underground lifelines are a few potential candidates. Experimentation can be done at small or large-scale.

In the case of large-scale simulations, major costs are involved in the explosive arrays and the free-field instrumentation. After this investment, however, there is a large amount of real estate available for experimentation. Multiple experiments on various applications can be included at a relatively small cost per individual experiment.

One approach to the planning of large-scale experiments would be the formation of a joint agency steering committee. The steering committee would have responsibility for assessing the requirements of various public and private agencies and, then, selecting, prioritizing, and coordinating individual projects to be fielded in a large-scale experiment. The costs of individual projects and a share of the explosive array and free-field instrumentation costs could be borne by the individual fielding agencies.

APPENDIX A
EXPLOSIVE EQUIVALENCIES

1. DISCUSSION

Existing ground motion data come from events which employed different types of explosives. The data evaluated herein were from events which utilized TNT, PETN and ammonium nitrate slurries. Future simulation designs may employ yet different explosives. ANFO (ammonium nitrate/fuel oil mixture) is a likely candidate because of its relatively low cost. Anaysis of existing data and predictions of future simulations require that some relative equivalence be established between the various explosives.

Explosive energy is the parameter currently in common use for correlating results from different explosives. The total available energy of an explosion is considered the most important quantity determining the available work potential of an explosive (ref. A-1). In cases where the explosion does not produce condensed solid or liquid products, the total available energy is about equal to the heat of detonation. The heat causes high pressures in the gaseous products which, in turn, do work on the surrounding soil. For explosions producing appreciable condensates, the total available energy will be less than the heat of detonation. This occurs because the energy residing in the condensates in the form of heat cannot transfer the heat to the gases fast enough to

allow work to be done on the surrounding soil during the short time of the explosion.

Table A-1 summarizes some information on energy and blast characteristics for the main explosives of interest in this study (Refs. A-1 through A-6). The data of table A-1 was used to select the representative explosive properties shown in table V-1 of the main text and the energy equivalencies used to correlate the data from different explosives.

2. REFERENCES

A-1 Cook, Melvin A., The Science of High Explosives, Robert E. Krieger Publishing Co., Inc., Huntington, N.Y., 1971.

A-2 Engineering Design Handbook, Explosive Series: Properties of Explosives of Military Interest, AMCP 706-177, U.S. Army Material Command, January 1971.

A-3 Effects of Impact and Explosion, Vol. 1, Summary Technical Report of Division 2, National Defense Research Committee, Office of Scientific Research and Development, Washington, D.C., 1946.

A-4 Johnson, S.M., Explosive Excavation Technology, Nuclear Cratering Group Technical Report No. 21, U.S. Army Nuclear Cratering Group, Livermore, California, June 1971.

A-5 Levmore, S., Principal Characteristics of the Gelled Slurry Explosive DBA-22M, Technical Report 4237, Ammunition Engineering Directorate, Picatinny Arsenal, Dover, New Jersey, July 1971.

A-6 Data from IRECO, West Jordan, Utah, reported in Simmons, K.B., DIHEST Improvement Program Tests (DIP IVA and VA), AFWL-TR-74-238, April 1975.

Table A-1

Energy and Blast Characteristics of Some Explosives

Explosive	Density (gm/cc)	Total Energy(Q) (cal/gm)	Available Energy(A) (cal/gm)	$\frac{A}{A(TNT)}$	Airblast Effectiveness(% TNT) Pressure	Airblast Effectiveness(% TNT) Impulse	Ground Shock Effectiveness(% TNT) Pressure	Ground Shock Effectiveness(% TNT) Impulse	Cratering Effectiveness(% TNT) Radius	Cratering Effectiveness(% TNT) Volume	Reference
TNT[a]	1.47	1130	1030[b]	1.00							A-1
TNT	1.59	1160	1045[b]	1.00							A-1
TNT	~1.56	1080	--	--	100	100	100	100	100	100	A-2
TNT	--	--	--	--							A-3
TNT	1.64	1030	--	--							A-4
PETN[a]	1.23	1380	1380		--	--	--	--	--	--	A-1
PETN	1.67	1410	1410	1.34 Avg	--	--	--	--	--	--	A-1
PETN	~1.7	1385	1385[b]		--	--	--	--	--	--	A-2
PETN	1.70	1360	--		--	--	--	--	--	--	A-4
AN[a]	~1.4	346	--	--	--	--	--	--	--	--	A-2
AN	1.07	327	--	--	--	--	--	--	--	--	A-4
ANFO[a]	--	850-900	850-900	0.85 Avg	--	--	--	--	--	--	A-1
ANFO	0.93	890	890[c]		--	--	--	--	--	100-110	A-4
AN Slurry(35%al)[a]	1.59	1950	--	--	--	--	--	--	--	160-180	A-4
AN Slurry(DBA-22M)	1.5-1.72	--	--	--	117 Avg	1.0	1.28[c]	--	111	160	A-5
AN Slurry(DBA-22M)	1.4	1915	1420		--	--	--	--	--	--	A-6
AN Slurry(DBA-65T2)	--	--	--	1.37 Avg	--	--	1.38	--	117	200	A-5
AN Slurry(DBA-65T2)	1.5	2050	1425		--	--	--	--	--	--	A-6
Black Powder[a]	1.75-1.9	684	684[b]	0.66	--	--	--	--	--	--	A-2

Footnotes:

a. Explosive Abbreviations

TNT = trinitroluene ($C_7H_5N_3O_6$)

PETN = pentaerythrital tetranitrate (C H N O)

AN = ammonium nitrate (NH_4NO_3)

ANFO = *ammonium nitrate/fuel oil mixture (94.5%/5.5%)*

AN Slurry = ammonium nitrate (40 to 75%), water (15 to 25%), stabilizing and gelling agent (1 to 5%), remainder aluminum and/or high explosive

DBA-22M = ammonium nitrate, water, bonding agents, 35% aluminum powder (manufactured by IRECO Chemical Company, West Jordan, Utah)

DBA-65T2 = ammonium nitrate, water, bonding agents, 20% TNT pellets, 35% aluminum powder (Manufactured by IRECO Chemical Co.)

Black Powder = 75 percent potassium nitrate, 15 percent charcoal, 10 percent sulvur

b. Interpreted from reference A-1.

c. Average or first and maximum seismic pulse measurements (assumed proportional to pressure or stress).

APPENDIX B
CRATER PREDICTION

1. DISCUSSION

Large high explosive simulations will generally produce craters and associated ejecta. Engineering systems will usually be sited sufficiently far from the explosive source so that the crater itself is not an immediate problem. Cratering and resulting large displacements are usually associated with horizontal particle velocities of about 10 ft/sec or greater. Particle velocities in strong earthquakes are about 3 to 4 ft/sec. Standard geometric scaling does not change the particle velocity. Hence, the particle velocity limitation will normally assure that the system is beyond the immediate crater region.

The material ejected from the crater will be thrown to relatively large distances. The ejecta will normally not be a problem because it arrives relatively late in time compared with the experimental time of interest. In addition, the ejecta mass will usually not be large enough to cause damage to the system.

Although cratering and ejecta will not normally be a serious problem, crater and ejecta estimates should be made in the design process to insure that they do not interfere with the simulation. In addition, these effects should be considered to insure personnel safety and the integrity of instrumentation systems.

Reference B-1 presents a correlation for crater dimensions from various high explosive simulation configurations. The correlation technique normalizes the crater dimensions by the depth of burst and

energy of the explosion by a geometric parameter of the explosive configuration. The geometric parameter is introduced to account for differences between the geometries of different explosive configurations. The normalized energy is called the mass-to-energy ratio in reference B-1. The assumed mass to energy ratios for different configurations are shown in figure B-1. The correlation between mass to energy ratio and normalized crater dimensions is shown in figure B-2.

Reference B-2 presents ejecta distribution measurements from buried line charges at various depths of burst. The results, shown in figure B-3, can be used as a guide to ejecta distributions from planar explosive arrays. The total ejecta mass from an experiment can be estimated by assuming a parabolic crater with a depth and width predicted by the method described above.

2. REFERENCES

B-1 Port, R.J., "Cratering and Ejecta Predictions for High Explosive Simulation Techniques," Proceedings of the Eric H. Wang Symposium on Protective Structures Technology, Air Force Weapons Laboratory, Kirtland AFB, New Mexico, 21-23 July 1970.

B-2 Carlson, R.H., "High-Explosive Ditching from Linear Charges," Journal of Geophysical Research, Vol. 68, No. 12, June 15, 1963.

(a) Single Charge Configuration

d = Depth of Burst

γ = Unit Weight of Soil

E = Energy in TNT Weight

$$\frac{M}{E} = \frac{\gamma \pi d^3}{3E}$$

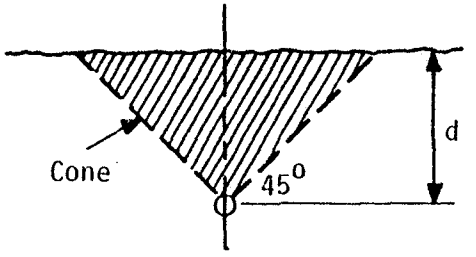

(b) Line Charge Configuration

d = Depth of Burst

γ = Unit Weight of Soil

E = Total Energy in TNT Weight

L = Length of Charge

$$\frac{M}{E} = \frac{\gamma d^2 L}{E}$$

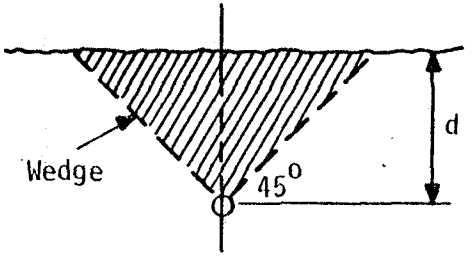

(c) Row Charge Configuration

d = Depth of Charges

γ = Unit Weight of Soil

E = Energy Per Charge in TNT Weight

S = Charge Spacing

$$\frac{M}{E} = \frac{\gamma d^2 S}{E}$$

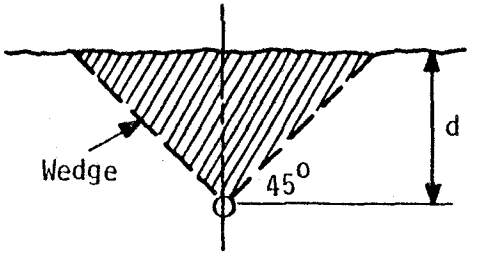

Figure B-1. Definition of Mass to Energy Ratios for Various Explosive Configurations (ref. B-1)

(d) Single Column Configuration

d = Depth to Column Center

L = Column Length

E = Energy Per Column in TNT Weight

γ = Unit Weight of Soil

$$\frac{M}{E} = \frac{\gamma\pi(d - \frac{L}{2})^2(d + \frac{L}{2})}{3E}$$

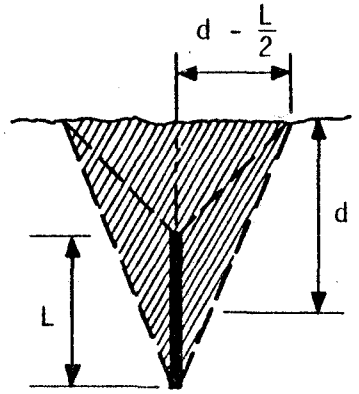

(e) Row of Column Charges

d, L, E, γ as above

S = Column Spacing

$$\frac{M}{E} = \frac{\gamma(d - \frac{L}{2})(d + \frac{L}{2})S}{E}$$

(f) Slab Charge Parallel to Surface

w = width of slab

L = Length of Slab > w

t = Thickness of Slab

d = Depth to Slab Centerline

E = Total Energy in TNT Weight

$$\frac{M}{E} = \frac{\gamma(d - \frac{t}{2})(d + \frac{t}{2})L}{E}$$

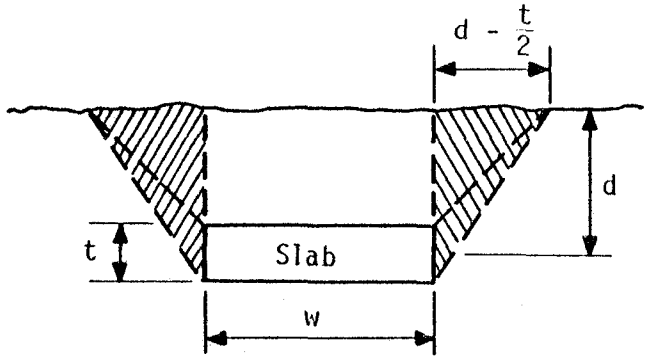

Figure B-1 (cont.) Definition of Mass-to-Energy Ratios for Various Explosive Configurations (cont.) (ref. B-1)

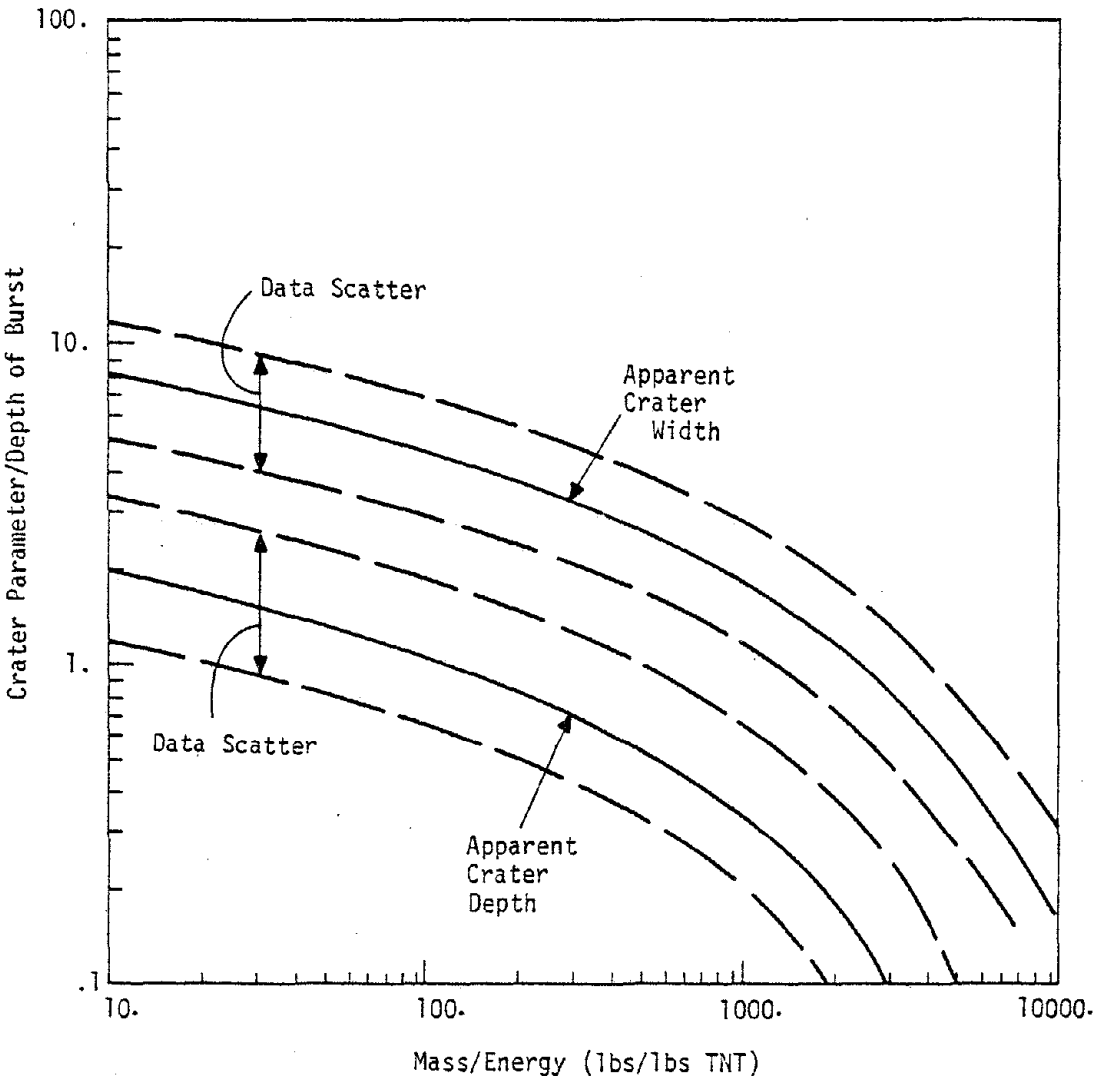

Figure B-2. Normalized Crater Parameters as a Function of Mass-to-Energy Ratio (Ref. B-1)

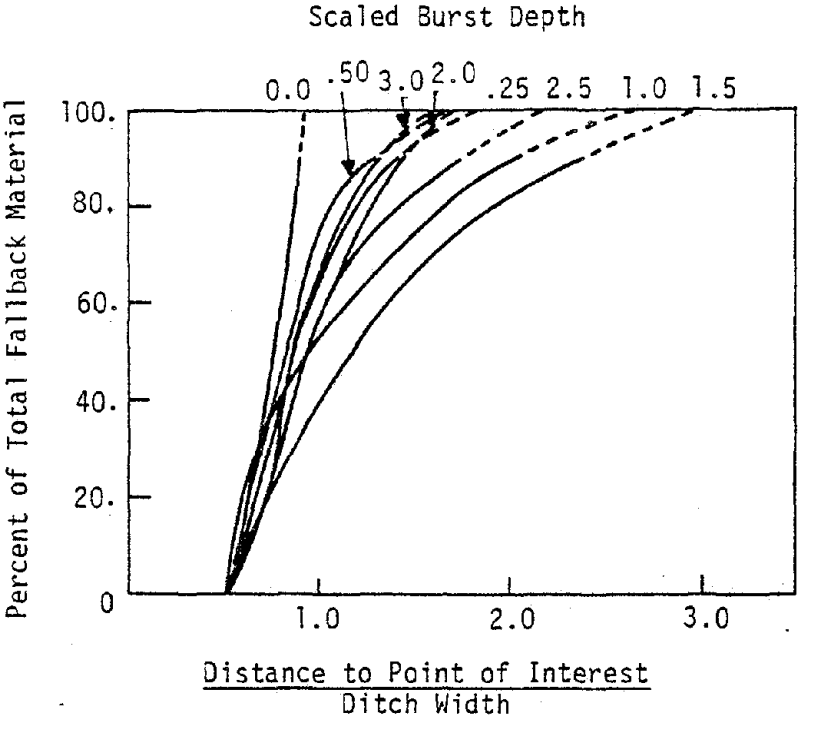

Figure B-3. Variation of Ejecta Outward From Longitudinal Ditch Axis (ref. B-2)

APPENDIX C
AIRBLAST PREDICTIONS

1. DISCUSSION

Earthquake simulations will usually require relatively deep explosion burial to achieve maximum energy coupling into the ground. As a result, the airblast from the explosion will be very small. However, airblast estimates should be made to insure that the simulation is not affected and that personnel and equipment are completely safe.

Reference C-1 observes that there are two sources of airblast in underground explosions: gas venting overpressure and ground shock induced overpressure. The amplitudes of both sources should be estimated. Empirical correlations for their amplitudes as well as total positive phase impulse from single charges (ref. C-1) are as follow:

Ground Shock Induced Peak Overpressure:

$$\Delta p = \frac{5(R/W^{\frac{1}{3}})^{-1.05}}{10\ \exp(0.6(DOB/W^{\frac{1}{3}}))} \qquad (C\text{-}1)$$

Gas Venting Overpressure:

$$\Delta p = \frac{70(R/W^{\frac{1}{3}})^{-0.93}}{10\ \exp(1.5(DOB/W^{\frac{1}{3}}))} \qquad (C\text{-}2)$$

Positive Phase Impulse:

$$I = \frac{15(R/W^{\frac{1}{3}})^{-0.5}}{10\exp(0.56(R/W^{\frac{1}{3}})^{0.17}(DOB/W^{\frac{1}{3}}))} \qquad \text{(C-3)}$$

where

Δp = peak overpressure in lb/in^2

I = total positive phase impulse in (lb/in^2)msec

R = range in feet

DOB = depth of burst in feet

W = yield in lbs of TNT

The effect of multiple charges on overpressure may be accounted for by the relation (ref. C-2):

$$\Delta p_{row} = n^{\alpha}\Delta p_{single} \qquad \text{(C-4)}$$

where

Δp_{single} = peak overpressure from a single charge

Δp_{row} = peak overpressure from a row of charges

n = number of charges

α = an exponent

The exponent α varies with depth of burst and charge spacing, and is different at locations perpendicular to the row than at locations off the ends of the row. Correlations for these variations have not been established. In the region perpendicular to the row of charges, α ranges from 0.41 to 0.8 for the ground shock induced overpressure and from 0.18 to 0.63 for the gas venting overpressure (ref. C-3).

2. REFERENCES

C-1 Vortman, L.J., "Close-In Airblast from Underground Detonations," Proceedings of Symposium on Engineering with Nuclear Explosives, Jan 14-16, 1970, The American Nuclear Society and U.S. Atomic Energy Commission, May 1970.

C-2 Vortman, L.J., Airblast and Craters From Rows of Two and Twenty Five Charges, SC-RR-68-655, Sandia Laboratories, Albuquerque, N.M., January, 1969.

C-3 Vortman, L.J., Airblast from Project Trinidad Detonations, SC-RR-71-0056, Sandia Laboratories, Albuquerque, N.M., June 1971.

APPENDIX D
SAMPLE CALCULATION OUTPUT

All calculation output was taken in plotted form. One-dimensional output at a typical target range in a spherical calculation (1S2) is shown in figure D-1. The output consists of time histories of normal stress (normal to the wave front), tangential stress, particle velocity and displacement. In addition, the stress path experienced by the material at the target location is plotted.

Two-dimensional output at a typical target point in a two-dimensional planar calculation with a free-surface (2P5) is shown in figures D-2, D-3 and D-4. Time history output (fig. D-2) consists of horizontal, vertical, transverse and shear stresses; horizontal and vertical velocities; and horizontal and vertical displacements. Deformed mesh plots (fig. D-3) and velocity vector plots (fig. D-4) can be obtained at selected time intervals. These latter plots are helpful in assessing calculational problems if they occur.

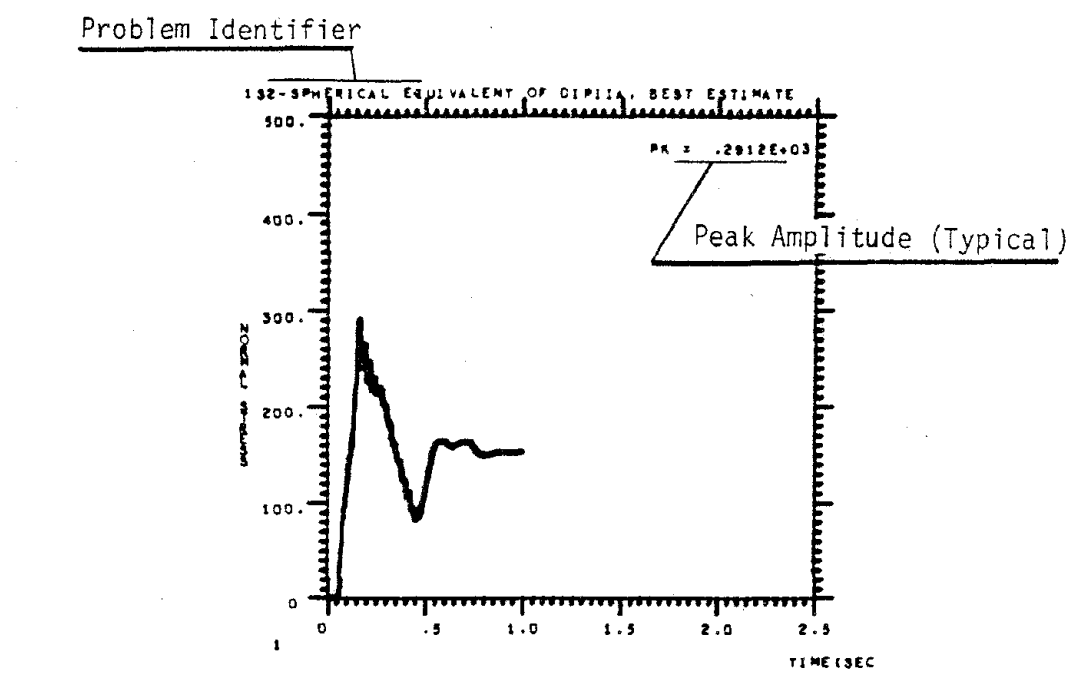

(a) Normal Stress in lb/in^2

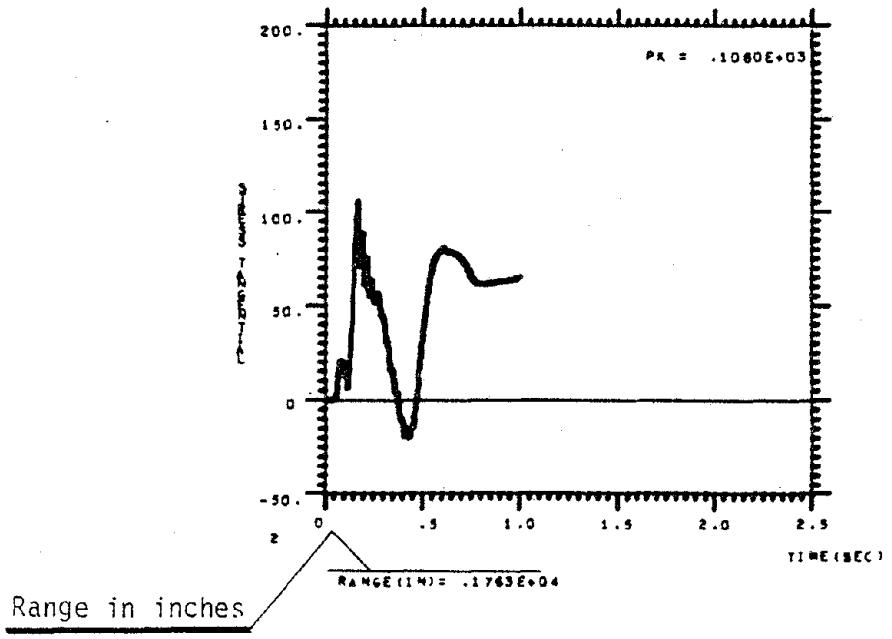

(b) Tangential Stress in lb/in^2

Figure D-1. Typical Plotted Output From a One-Dimensional Calculation

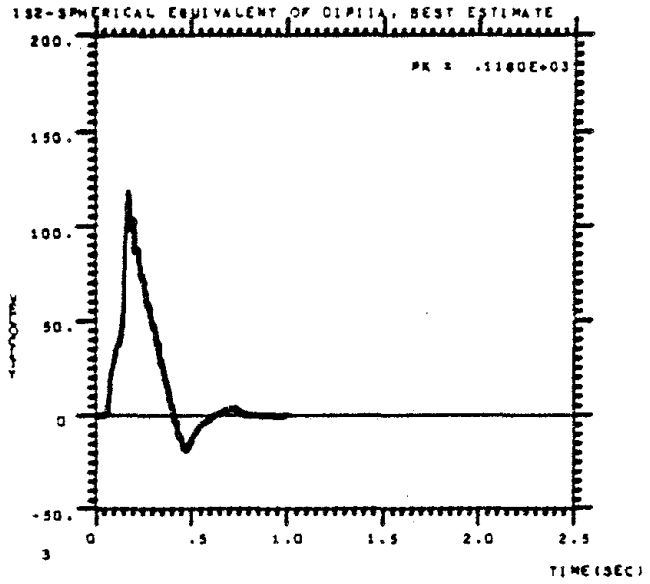

(c) Particle Velocity in in/sec

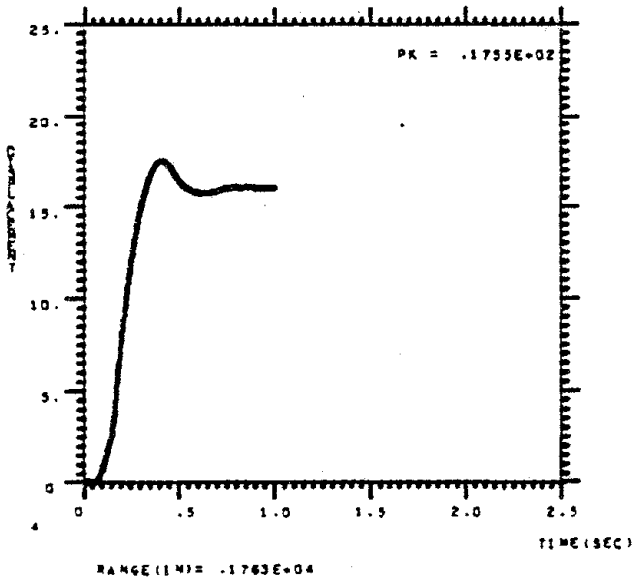

(d) Displacement in inches

Figure D-1 Typical Plotted Output From a One-Dimensional Calculation (cont.)

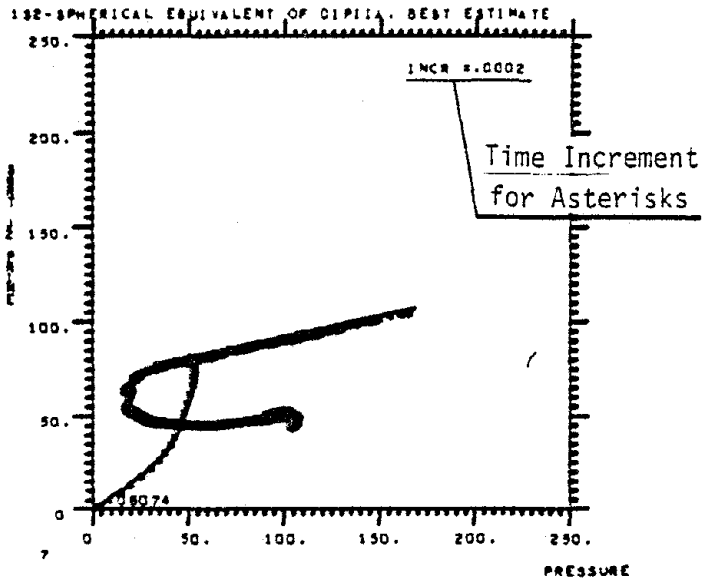

(e) Stress Path (Units are lb/in^2)

Figure D-1 Typical Plotted Output From a One-Dimensional Calculation (cont.)

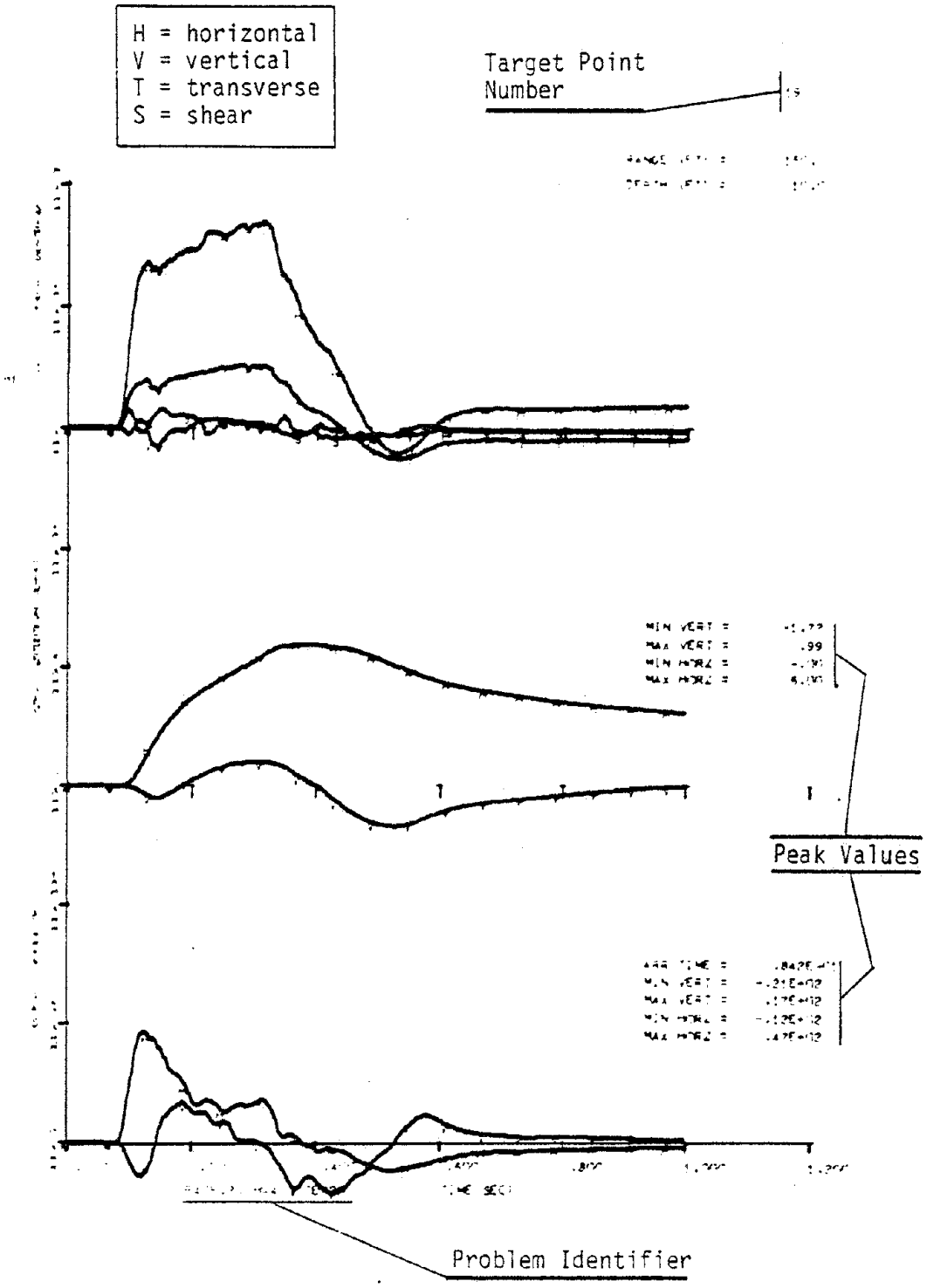

Figure D-2. Typical Plotted Time History Output From a Two-Dimensional Calculation

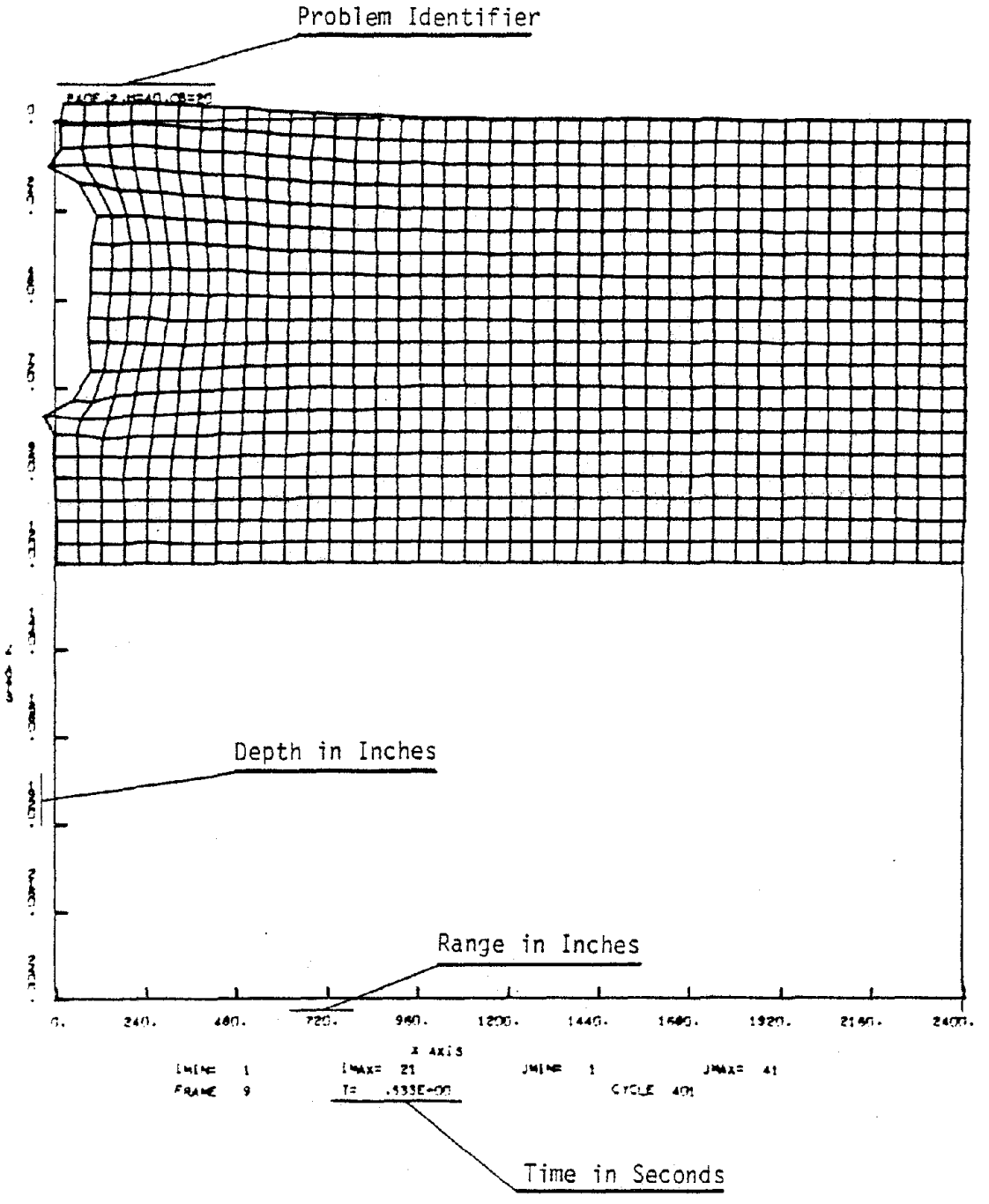

Figure D-3. Typical Deformed Mesh Plot From a Two-Dimensional Calculation

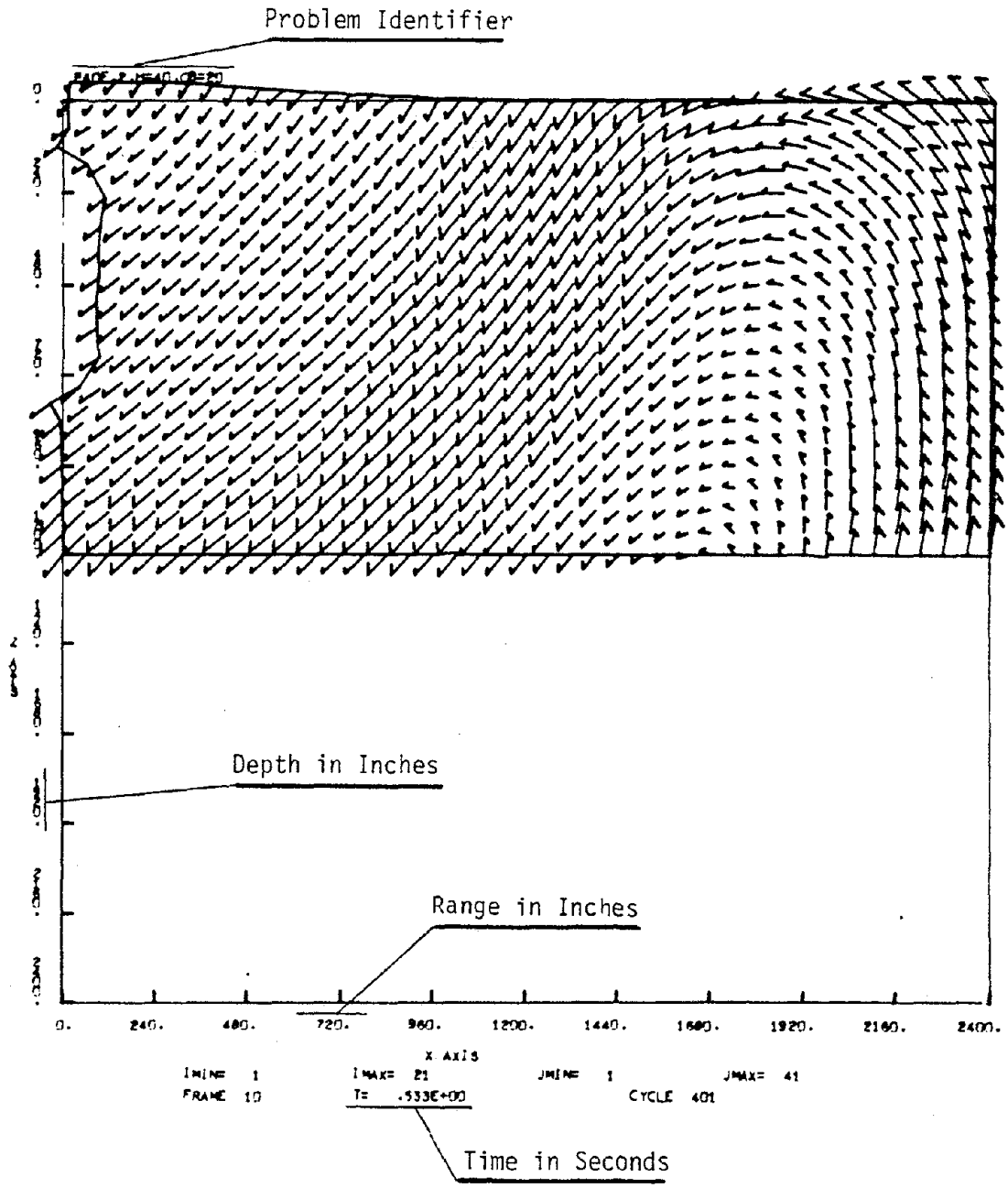

Figure D-4. Typical Velocity Vector Field From a Two-Dimensional Calculation